Advances in Atom and Single Molecule Machines
Series Editor: Christian Joachim

André Gourdon *Editor*

On-Surface Synthesis

Proceedings of the International Workshop On-Surface Synthesis, École des Houches, Les Houches 25–30 May 2014

Springer

Advances in Atom and Single Molecule Machines

More information about this series at http://www.springer.com/series/10425

André Gourdon
Editor

On-Surface Synthesis

Proceedings of the International Workshop On-Surface Synthesis, École des Houches, Les Houches 25–30 May 2014

Springer

Editor
André Gourdon
CEMES-CNRS
Toulouse
France

ISSN 2193-9691 ISSN 2193-9705 (electronic)
Advances in Atom and Single Molecule Machines
ISBN 978-3-319-26598-8 ISBN 978-3-319-26600-8 (eBook)
DOI 10.1007/978-3-319-26600-8

Library of Congress Control Number: 2015957046

Printed on acid-free paper

This Springer imprint is published by SpringerNature
The registered company is Springer International Publishing AG Switzerland

Preface

This book comprises contributions of the first PAMS workshop that was organized at the Ecole de Physique des Houches (France), in May 2014. This workshop has brought together a number of leading scientists working on various strategies to synthesize and study single molecules, 1D and 2D covalently bonded molecular architectures obtained by on-surface synthesis.

PAMS (for planar atomic and molecular scale devices) is a four-year large-scale integrating project funded by the European Commission's FET programme. It was launched in October 2013 with the objective to explore all scientific and technological aspects of the conception and the fabrication of planar atomic and molecular scale electronic devices on Si:H, Ge:H, AlN, $CaCO_3$ and CaF_2 surfaces, fabricated with atomic scale precision and reproducibility. The themes described in this volume have huge potential for the in situ preparation of large molecular logic gates and high-conductance molecular wires by on-surface synthesis, in ultra-clean environment as explored by the PAMS chemists, physicists and theoreticians.

In less than a decade, on-surface synthesis by covalent coupling of reactive precursors adsorbed on metallic, semiconducting or insulating surfaces has emerged as a powerful approach for the fabrication of novel molecular architectures with potential applications in nanoelectronics, optoelectronics and other fields where new low-dimensional materials with tailored properties are needed. Using this bottom-up route, atomically precise graphene nanoribbons, polyphthalocyanines films, metal coordination frameworks, porous metal networks, superhoneycomb frameworks, etc., have been synthesized. And it must be emphasized that most of these large molecular structures cannot be synthesized by standard in-solution syntheses.

The aim of this book is to regroup contributions at the forefront of advances in this very active field, focusing on the understanding of inter- or intramolecular chemical coupling mechanisms, on new reactions, on new substrates and on optimization of reactions.

I thank the ICT-FET programme, the Labex NEXT and EMPA, for financial support in organizing this workshop, and Marie Hervé, PAMS European Manager, for her help in preparing this workshop and this book.

André Gourdon

Contents

The Emergence of Covalent On-Surface Polymerization

Christophe Nacci, Stefan Hecht and Leonhard Grill

Abstract The covalent linking of molecular building blocks directly in the two-dimensional confinement of a surface, the so-called on-surface polymerization, has developed rapidly in the last years since it represents a reliable strategy to grow functional molecular nanostructures in a controlled fashion. Here, we review the growth of such structures via on-surface Ullmann coupling and highlight the major chemical and physical aspects. These systems are typically studied by scanning tunneling microscopy that allows exploration of the initial monomer species, intermediate products and final nanostructures with sub-molecular spatial resolution. In this way, the chemical structures of the ex situ synthesized molecular building blocks are directly correlated with the outcome of the chemical reaction. We also present examples with different monomer species in view of growing heterogeneous molecular structures as well as the importance of the molecular interaction with the template surface as a further key parameter to control the molecular diffusion and tune the final molecular architecture.

1 Introduction

Assembling functional molecular building blocks on a surface is a promising route toward central objectives of nanotechnology and in particular molecular electronics since it might allow the growth of electronic circuits based on the functionalities of individual molecular species [1, 2]. Other bottom-up strategies lead to the growth of

C. Nacci · L. Grill (✉)
Department of Physical Chemistry, Fritz-Haber-Institute of the Max-Planck-Society, 14195 Berlin, Germany
e-mail: leonhard.grill@uni-graz.at

C. Nacci · L. Grill
Department of Physical Chemistry, University of Graz, 8010 Graz, Austria

S. Hecht (✉)
Department of Chemistry, Humboldt-Universität zu Berlin, 12489 Berlin, Germany
e-mail: sh@chemie.hu-berlin.de

A. Gourdon (ed.), *On-Surface Synthesis*, Advances in Atom and Single Molecule Machines, DOI 10.1007/978-3-319-26600-8_1

extended surface supported two-dimensional networks with outstanding technological relevance [3, 4]. Thus, although the precursor molecules do not contain a function in these cases, the assembly of molecules in the two-dimensional confinement of a surface can be very efficient. In the field of weaker intermolecular interactions, many successful attempts of growing supramolecular patterns at surfaces [5–8] have been achieved. However, the use of covalent linking to stabilize molecular arrangements at surfaces attracted considerable attention in the last years [9–27], becoming nowadays a well-established technique. This approach results in the presence of molecular polymers on surfaces that could hardly be deposited onto the surface under clean conditions by using conventional techniques and preventing any defragmentation process [28]. The nature of the covalent bond provides high stability and robustness to the resulting nanostructures and allows for efficient "through bond" charge transport [29–31].

In this chapter, we review the development and conceptual foundation of the covalent on-surface polymerization technique. As our and many others' work is based on the Ullmann reaction [32], we focus on the aryl–aryl homocoupling of halogenated monomer building blocks typically performed on coinage metal surfaces. We first provide chemical considerations regarding the reaction mechanism and derive critical parameters for successfully carrying out on-surface polymerizations. Using this approach covalently bound molecular assemblies with a predefined shape and size are produced under ultrahigh vacuum (UHV) conditions. We show how the final topology of the desired molecular aggregates is intimately connected to the design of the single-molecule building constituents. Different growth strategies, e.g., one-step versus two-step (hierarchical) processes, can eventually lead to the same final molecular architecture: the major differences between the two cases are highlighted. The substrate surface corrugation can be furthermore exploited to drive on-surface synthesis processes along certain directions and promote the growth of nanostructures with predefined orientations. In this regard, the importance of the surface anisotropy is discussed.

2 Results and Discussions

2.1 On-Surface Polymerization Technique

In general, the on-surface assembly of molecular building blocks into large and extended structures according to a bottom-up scheme can be achieved by different strategies. If stabilized by rather weak non-covalent intermolecular interactions [5–8, 33], these nanostructures belong to the field of supramolecular chemistry [34]. For instance dipole–dipole interactions have been used to govern the molecular aggregation of porphyrin derivatives, carrying two *trans*-positioned cyanophenyl groups, into long linear chains on a Au(111) surface (Fig. 1a) [6]. Two opposing cyanophenyl groups can engage in a self-complementary dipolar interaction (hydrogen bond) thereby driving and directing the self-assembly into elongated porphyrin chains.

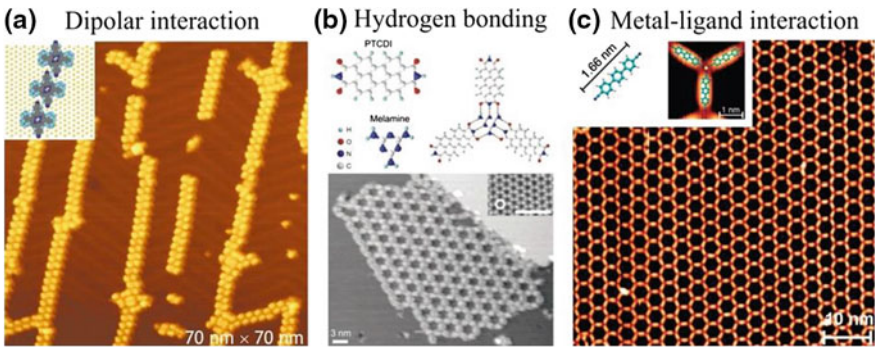

Fig. 1 Supramolecular self-assembled molecular structures. **a** STM image at 63 K of trans-BCTBPP wires hold together via dipole–dipole interactions on Au(111) (Reproduced from [6], with permission). **b** Two-dimensional networks of PTCDI and melamine molecules stabilized via H-bonding (model structures of the molecules and network in the upper panel). In the lower panel, an STM image of the network (−2 V, 0.1 nA). In the *inset*, a high-resolution view of the Ag/Si(111)-$\sqrt{3} \times \sqrt{3}$R30° is shown (Reprinted by permission from Macmillan Publishers Ltd: Nature [7], copyright 2003). **c** STM topographic image of an extended and highly regular networks formed by Codirected assembly of NC–Ph_3–CN linkers. In the *inset*, the structure of the molecule including its length and STM topography of the threefold *Co*–carbonitrile coordination motif with model structure is shown (Adapted with permission from Schlickum et al. [8]. Copyright 2007 American Chemical Society)

A more conventional and stronger multiple hydrogen bonding motif was used to stabilize a two-component mixture of 3,4,9,10-perylenetetracarboxylic diimide (PTCDI) and melamine molecules into a honeycomb pattern on a metal surface (Fig. 1b) [7]. The threefold symmetrical melamine molecules represent the branch points of the hexagonal network, while the PTCDI molecules serve as straight connectors (Fig. 1b). The assembly geometry allows for the local formation of three hydrogen bonds for each complementary melamine–PTCDI connection and this rather strong non-covalent interaction plays the key role in guiding the mentioned species into largely extended supramolecular networks. Moreover, many examples of two-dimensional molecular assemblies have been reported in the field of metallo-supramolecular chemistry where metal atoms are used to bridge suitably functionalized molecular units (ligands). The metal–ligand bond is typically stronger as compared to hydrogen bonding and this allows the formation of more robust networks [33]. Such metal–ligand interactions have, for example, been exploited to fabricate two-dimensional architectures based on the coordination of rod-like dinitrile molecules (NC–Ph_n–CN) to cobalt centers (Fig. 1c) [8].

In addition to these interactions, the formation of even stronger covalent carbon–carbon bonds between molecules on the surface gained large attention in the last years [9–18, 30, 31, 35]. The nature of the covalent bond allows to confer high stability and durability to the molecular structures, in contrast to non-covalent intermolecular bonds-based structures. This property is a key when thinking of potential use in future applications [2]. In analogy to the approach here, the

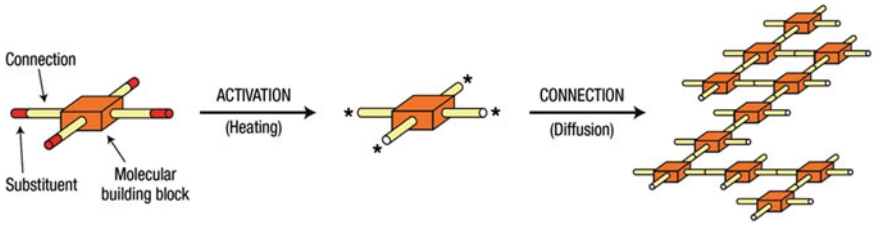

Fig. 2 Covalently linked molecular architectures by on-surface polymerization. Single building blocks are synthesized ex situ with halogen substituents. After being thermally activated, the species diffuse across a surface, interact to each other and the formation of new carbon–carbon covalent bonds take place at the activated sites positions [9]

bottom-up growth of large networks as graphene [3] and boron nitride [4] sheets also led to highly stable structures, because of the covalent nature of their links.

The concept of the on-surface polymerization technique is illustrated in Fig. 2. Each single building block is based on a chemically stable molecular unit carrying a certain number of potentially reactive sites at specific positions. These sites are represented by a carbon–halogen bond that has a bond dissociation energy lower than all other bonds in the molecular framework. After depositing the molecules on a surface, the halogen substituents are activated (i.e., halogen–carbon bond dissociation) thermally, leaving the chemical structure of the molecular building blocks intact. At the same time, the new species thermally diffuse over the surface and form new covalent C–C bonds at the activated site positions when they get close to each other.

The design and ex situ synthesis of molecules with different numbers and arrangements of interconnection points opens up the possibility to precisely tune the topology of the final molecular architecture. Before detailing the architectural control achievable using the on-surface polymerization approach, a few aspects regarding the chemistry of both the monomers as well as the surfaces need to be considered. Due to its dominant use in the field and its importance for our own work, we limit the following discussion to the Ullmann reaction.

3 Chemical Considerations

When considering an Ullmann coupling reaction [32] as the connection sequence for an on-surface polymerization, several key criteria have to be met. First, one needs to design monomers, which on the one hand have to be reactive at the desired connection sites to allow for regioselective activation, for example, by carrying labile halogen substituents, yet otherwise need to be stable at the deposition and reaction conditions. In addition, the activated monomers also have to be mobile on the surface to diffuse to other monomers and the growing polymer. The latter point inevitably also depends on the surface, which needs to stabilize the formed aryl

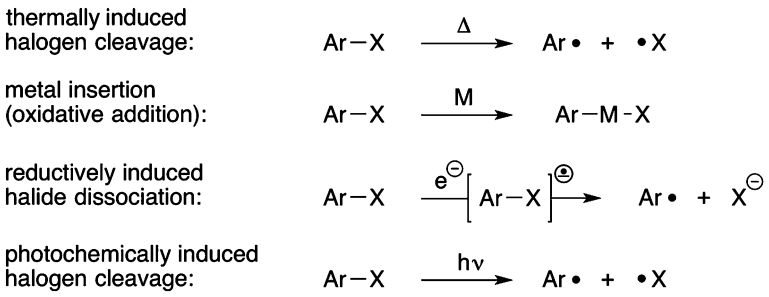

Fig. 3 Possible activation mechanisms for aryl halides to initiate covalent on-surface polymerization

radical intermediates, yet also has to provide mobility and ideally facilitate both the activation and connection steps, i.e., act as template and catalyst.

While these aspects generally apply to most on-surface polymerization reactions, there are some specific aspects when focussing on the Ullmann reaction. The reaction can be initiated by several different dissociation mechanisms caused simply by heat (in absence or presence of a metal catalyst), electrons (from the tip of an STM, and electrode or a reducing agent) or photons (Fig. 3).

While in all cases the aryl–halogen single bond is broken, the technique/stimulus used for activation potentially provides control over where the Ullmann reaction and hence polymerization is taking place. In contrast to the pioneering work of the Rieder group on the dimerization of iodobenzene induced with the STM tip at the step edge of a Cu(111) surface [36] the majority of the reported work has been exploring thermal activation mostly in conjunction with coinage metal substrates. Hereby, the temperature required for dissociation of the halogen substituent crucially depends on the type of halogen (and potentially also on the type of (het)aryl moiety) as well as the type of substrate. The first aspect has been exploited by us for the hierarchical growth of two-dimensional polyporphyrin networks (see below), where we utilize sequential activation of first iodine and then bromine substituents to separate the two orthogonal growth directions [35]. While the C–I bonds are cleaved at 120 °C, the C–Br bonds cleave at 250 °C on the employed Au(111) surface. Of course, the latter is important as well since similar C–I bonds cleave at much higher temperatures in the absence of a coinage metal as shown by the work of Gourdon, Kühnle, and coworkers on calcite ($CaCO_3$), where temperature above 300 °C are necessary for activation [37].

Clearly and not surprisingly in the context of the classic Ullmann work using copper species [32], coinage metals facilitate activation and aryl–aryl coupling [38]. However, there are two opposing effects when comparing the coinage metals with regard to their ability to aid on-surface Ullmann type polymerization: On the one hand the higher reactivity of less noble copper surfaces aids both the initial halide dissociation as well as the coupling of the activated aryl monomers but also significantly lowers the mobility and hence diffusion of the monomers and growing

polymers, thereby inhibiting growth. Fasel and coworkers have actually engaged in a detailed comparative study showing these opposing effects for the Cu(111), Ag (111), and Au(111) surfaces [39]. The authors found the onset of network formation from hexa(*meta*-phenylene) macrocyclic hexaiodide monomers to occur at 200 °C for Cu(111), while on Au(111) 250 °C and on Ag(111) 300 °C were required. However, the morphology of the obtained poly(1,3,5-phenylene)s differs significantly as the Cu(111) grown structures are highly branched fractal-like while in the case of Ag(111) extended high-quality 2D networks were formed. Based on their experimental findings as well as theoretical investigations, they conclude that the lower activity of Ag(111) in the aryl–aryl coupling combined with the higher monomer mobility (diffusion) on this surface, both compared to Cu(111), lead to better network formation. In our work we have been mostly focussing on gold surfaces that provide a good compromise between these features. Note that even with one and the same metal its surface reconstruction plays an important role as shown by our own work (see below) as well as others [40].

In addition, defects, step edges, and adatoms are of utmost importance as they can facilitate activation (see below) [41], stabilize intermediates, and even inhibit their coupling. This is nicely illustrated by the fact that activated aryl monomers cannot be considered as truly "free radicals" but are strongly stabilized be the metal surface [39]. This also prevents skeletal rearrangements to take place and thereby assures regioselective coupling at the initially halide-substituted positions (Fig. 4).

Depending on the presence of adatoms, an alternative coupling mechanism involves the formation of an aryl–metal–aryl intermediate, which can reductively eliminate to form the desired aryl–aryl connection (Fig. 4). While this sequence has in fact successfully been observed by Lin and coworkers to take place in the polymerization of 4,4″-dibromoterphenyl on a Cu(111) surface [42], in many cases the intermediately formed copper complexes are rather stable and cannot be forced to eliminate the desired products [43, 44]. For example, using hexabenzo-coronene (HBC) dibromide monomers on Cu(111) gave Cu-bridged HBC chains; however, on a Au(111) surface the corresponding gold complexes were not observed and hence covalent aryl–aryl connections could successfully be obtained (Fig. 5)

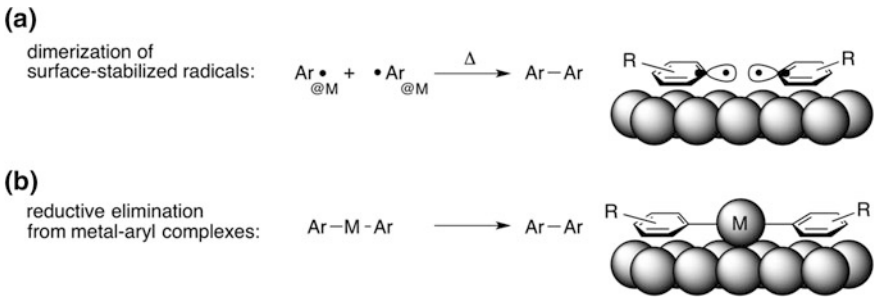

Fig. 4 Possible coupling mechanisms for aryl halides to initiate covalent on-surface polymerization: regioselective coupling (**a**) and aryl–aryl connection via an intermediate formation of an aryl–metal–aryl intermediate (**b**)

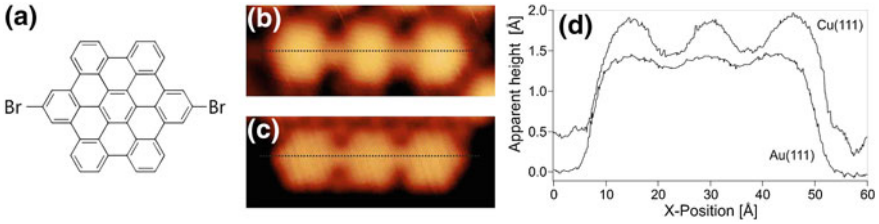

Fig. 5 **a** Chemical structure of Br_2–HBC. **b** Cu-bridged HBC chain on Cu(111) (5.5 × 2.0 nm^2, −300 mV, 0.3 nA). **c** HBC chain on Au(111) (5.5 × 2.0 nm^2, −300 mV, 0.1 nA). **d** Height profiles in STM images along a HBC trimer on Cu(111) and Au(111) [43]

[43]. Therefore, not only the type of surface but also the availability of adatoms seems to have a marked effect on the polymerization outcome.

In general, we note that using the Ullmann reaction poses two inherent limitations to the on-surface polymerization process. First and foremost, the reaction is irreversible under the employed conditions, i.e., formed defects cannot be healed. Therefore, the outcome of the reaction solely relies on kinetic control and equilibration to the global thermodynamic minimum structures cannot be used as often the case for non-covalent self-assembly or dynamic covalent chemistry [45]. Using other connections such as boronic esters or imines this drawback can be overcome, however, at the cost of stability (toward hydrolysis) and functionality (in an optoelectronic context). Second, the employed polymerization approach is that of a step growth, more precisely a polycondensation, and therefore intrinsic limitation with regard to polymerization efficiency and control over the polymerization outcome exist. After sketching the chemical basis for making aryl–aryl connections, we will now detail the method of covalent on-surface polymerization and highlight the means of controlling the formed polymer structures.

4 On-Surface Synthesis of Covalently Bound Nanostructures

Two alternative methods can be used for the activation of molecular building blocks (methods I and II) and the growth of covalently bound nanoarchitectures, leading to similar results [9]. In method I, intact molecules are first deposited onto a surface and subsequently thermally activated. Conversely, in method II, the activation of molecular species takes place already into the evaporator cell and they are deposited onto the surface.

In both cases, the covalent linking takes place on the supporting surface upon thermal diffusion. As a first candidate for on-surface synthesis, a porphyrin building block with four bromine substituents (Br_4TPP) has been used (inset of Fig. 6a). If the evaporator temperature was 550 K or lower during deposition, large and ordered islands of intact Br_4TPP were found as a result of molecular diffusion at the surface

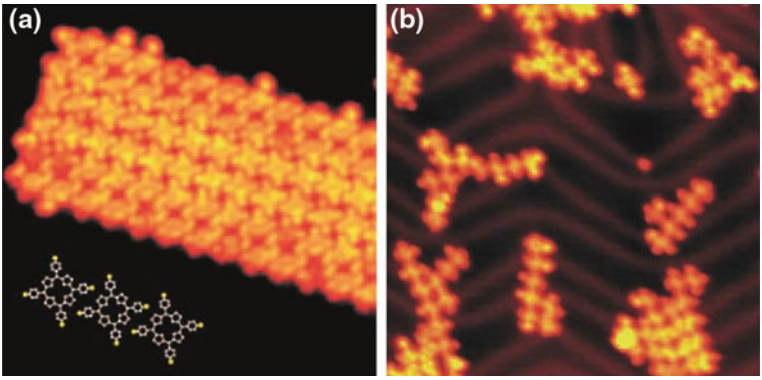

Fig. 6 Molecular nanostructures formed by different approaches (methods I and II). **a** STM image (20 × 20 nm^2) of a Br_4TPP molecular island on Au(111) after deposition at low evaporator temperature of 550 K onto the substrate surface kept at room temperature. Molecules are deposited intact onto the surface. The *inset* shows the chemical structure of Br_4TPP. **b** STM image (41 nm × 41 nm^2) for deposition at elevated evaporator temperature of 610 K. This causes the activation of the molecular species into the evaporator and subsequently the formation of covalently bound structures onto the surface. The Au(111) sample was cleaned by repeated Ne ion sputtering (E = 1.5 keV) and subsequent annealing up to 720 K. Measurements were performed under UHV conditions with a low-temperature STM operated at a temperature of 10 K. STM images were recorded in constant current mode with the bias voltage referring to the sample with respect to the STM tip [9]

(method I, Fig. 6a). A careful analysis of the outer border of the molecular island reveals that many molecules have only three Br atoms connected while there are four on the intact molecules. This suggests that the used evaporator temperature is enough to initiate the Br dissociation of a small amount of molecules (more than 90 % of the molecules remain intact).

At higher evaporator temperatures (Fig. 6b) most of the molecules are activated with the loss of several Br substituents in the evaporator (method II). The activated species can react with each other on the surface and form new intermolecular bonds upon thermal diffusion, leading to the formation of covalently bound structures with different sizes and shapes (Fig. 6b).

To investigate the ability to control the architecture of the final molecular nanostructures, different TPP-based monomer building blocks have been synthesized with one, two, and four Br substituents (Fig. 7a–c). Intact molecules have been identified by using low evaporator temperatures: the STM images after the preparation show clearly the expected different structures (Fig. 7d–f). All species have been deposited onto a Au(111) surface kept at low temperature (to suppress any carbon–halogen bond dissociation) and afterwards annealed to thermally activate the Br dissociation. Thus, the topology of the molecular architectures is intrinsically encoded in the design of the single monomer building block (cf. first and third rows of Fig. 7).

If the monomer building block provides just one reactive side (BrTPP, Fig. 7a), the only possible result is a dimer. Porphyrin building blocks carrying two reactive sides

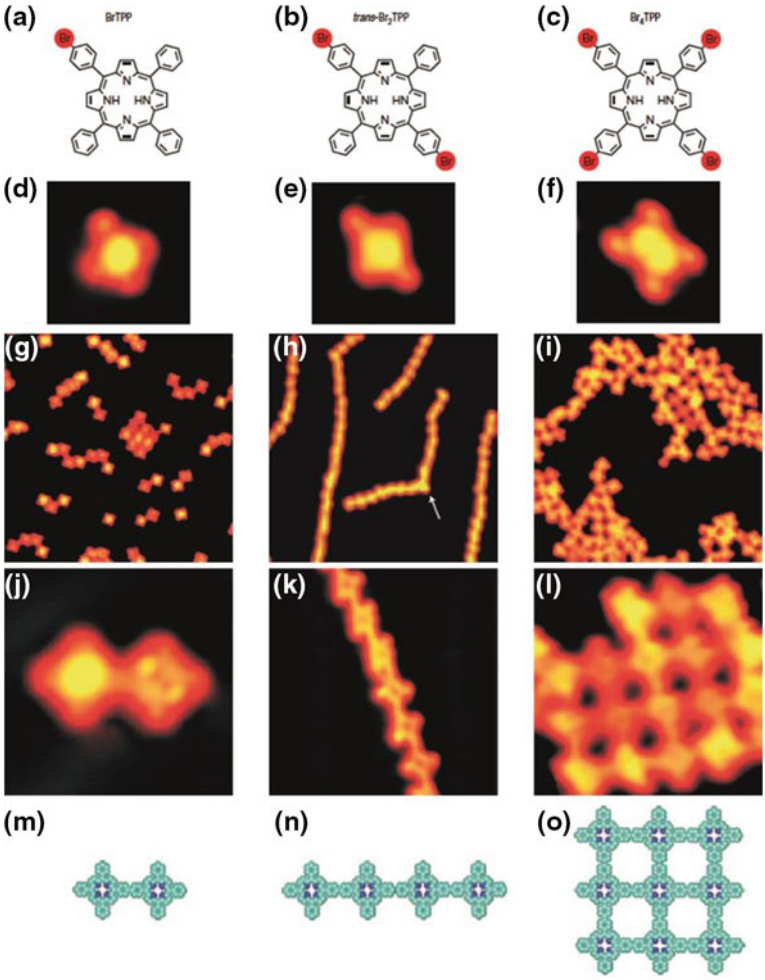

Fig. 7 Building nanoarchitectures using different monomer building blocks carrying one (*left column*, prepared by method I), two (*middle column*, prepared by method II) and four (*right column*, prepared by method I) Br substituents (**a–c**). STM images (3.5 × 3.5 nm^2) of the single intact molecules (**d–f**). Overview STM images (30 × 30 nm^2) of the nanostructures after activation and connection (**g–i**). Detailed STM images of the resulting nanoarchitectures (**j** 5 × 5 nm^2; **k** 10 × 10 nm^2; **l** 8.5 × 8.5 nm^2). Corresponding chemical structures of the nanostructures (**m–o**). Measurements were performed under ultrahigh vacuum (UHV) conditions with a low-temperature scanning tunneling microscope (STM) operated at a temperature of 10 K. Covalently linked molecular structures were produced in case of method I from molecular building blocks via on-surface polymerization [9], i.e., dehalogenation at a typical temperature of 523 K (bromine dissociation) for 10 min and subsequent covalent linking of the molecules [9]

as trans-Br_2TPP (Fig. 7b) allows accordingly the formation of long and linear chains as shown in Fig. 7h, k. When all four porphyrin unit legs carry Br substituents (Fig. 7c), the construction of two-dimensional molecular network is enabled (Fig. 7i, l). This proves that a careful choice of the molecular design, i.e., the arrangement of the active end groups within the molecular framework of the single building block, and a successful ex situ organic synthesis of the initial building blocks give high control over the final architecture of the molecular structures.

An important issue is the precise chemical nature of the newly formed intermolecular bonds (or intramolecular bonds in the final polymer, respectively). The first evidence comes from the distances between the building blocks, which is characteristic for such a bond. There is a good agreement between the experimentally measured neighboring porphyrin cores interdistance (17.2 ± 0.3 Å) and the DFT-calculated distance (17.1 Å) calculated for a covalently bound porphyrins dimer (Fig. 8d). Furthermore, the covalent nature of the intermolecular bonds can be investigated by STM single-molecule manipulation. Molecular islands made of intact Br_4TPP (Fig. 6a) are easily disassembled by STM-based lateral manipulation [9]. In contrast, dimers, chains, and molecular networks (Fig. 7) can follow the STM tip pathway during a pulling experiment [30, 31] without undergoing fragmentation processes. This is a clear signature for the robustness of the intermolecular bonds within the molecular structures after the end-group legs activation. Consequently, the interpretation as a covalent bond seems reasonable. Other

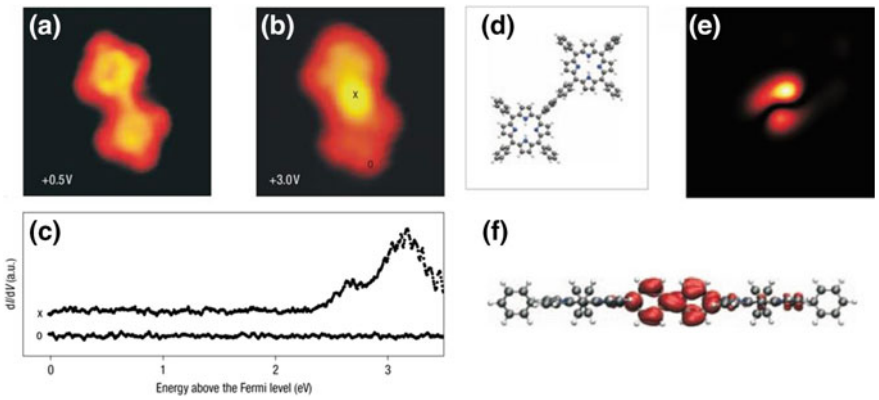

Fig. 8 The covalent nature of intermolecular bonds. STM images (5 × 5 nm^2) of a TPP dimer at 0.5 V (**a**) and 3.0 V (**b**). The bright protrusion in the middle of the dimer (**b**) is a signature related to an electronic feature clearly visible in the d*I*/d*V* curve marked by a *cross* in panel (**c**). The lower d*I*/d*V* curve (marked by a *circle*) taken on top of a porphyrin leg is featureless. DFT calculations reveal the formation of a covalent bond between the two neighboring phenyl legs, with corresponding C–C bonding (*s*) and antibonding (*s**) orbitals. **d** Calculated geometric structure of the isolated dimer. **e** Calculated contribution to the local density of states due to the state at about 2.8 eV above the HOMO (at 7 Å from the porphyrin plane). **f** Side view of a three-dimensional contourplot of the orbital density of this state at a much higher density. Scanning tunneling spectroscopy (STS) was performed at 10 K with a lock-in amplifier with 20 mV peak-to-peak modulation amplitude at 640 Hz (frequency) (see caption Fig. 7 for further experimental details) [9]

options, i.e., chemical bonds as H or metal-ligand bonding and π–π stacking, can be ruled out because of the molecular structure and adsorption geometry, and additionally they could hardly explain why the nanostructure remains stable when being pulled by an STM tip.

A clear signature for the covalent nature of the intramolecular bond within the dimer is provided by spectroscopy of single molecules (by scanning tunneling spectroscopy, STS). The interconnection site within the dimer appears homogenously at low bias voltages, while it appears as a bright protrusion when imaged at +3.0 V (Fig. 8a, b). This protrusion is indeed related to an electronic broad features localized at around +3.0 V (upper STS curve in Fig. 8c) suggesting the presence of a localized orbital [9]. DFT calculations prove the local formation of a covalent C–C intermolecular bond in full agreement with the experimentally measured porphyrin cores interdistance. Specifically, the calculations revealed the formation of C–C bonding (σ) and antibonding (σ*) orbitals that give rise to the signal in the d*I*/d*V* spectra. Hence, the peak at around 3 eV is a direct fingerprint of the chemical nature of the covalent bond. It is caused by the strong interaction with the two non-occupied antibonding π orbitals associated to the two legs, resulting in an in-phase and an out-of-phase combination, which are split by 1.3 eV. The in-phase combination is responsible for the increase of the calculated local density of states precisely located in between the porphyrin cores at about 2.8 eV (Fig. 8e, f) above the highest occupied molecular orbital (HOMO). This calculated electronic feature is associated to the experimentally probed electronic feature at about 3.0 eV shown in Fig. 8 [9].

Another clear example of Ullmann dehalogenation reaction that results in polymerization on the surface was reported by the group of Rosei [19]. They deposited diiodobenzene molecular species (**1** and **2** in Fig. 9a) on Cu(110) and found at first the formation of Cu bound phenylene intermediates, i.e., not yet linked by C–C

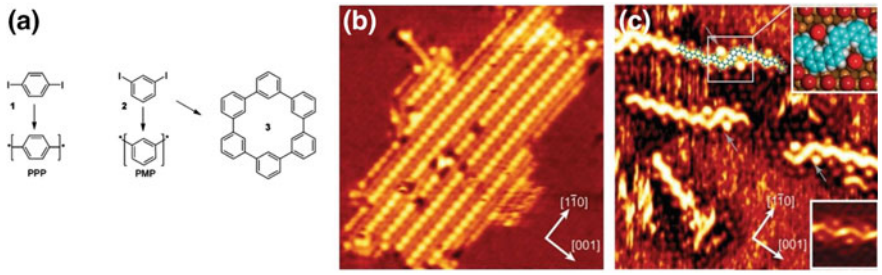

Fig. 9 Formation of polyphenylene-based polymers by on-surface polymerization. **a** Ullmann coupling of diiodobenzene molecules. **b** STM image (T = 115 K, 19 × 19 nm^2, V = −1.93 V, I = 1.06 nA) of PPP-based olygomers. 1,3-diodobenzene (*1* in panel **a**) were dosed on Cu(110) kept at room temperature and afterwards annealed to 500 K. **c** 0.2 L of 1,3-diiodobenzene dosed onto Cu(110) held at 500 K. STM topography (11.3 × 11.3 nm^2, V_s = −0.57 V, I_t = 0.82 nA) of oligomer branches. A model of PMP is overlaid on one of the oligomers. *Top-right inset* a force field relaxed model of PMP chain in the iodine matrix on a slab of Cu corresponding to the marked region in the STM image. *Bottom right inset* a scale portion of the RT deposited surface, showing a protopolymer of molecule *2* in panel **a**. Reproduced from [19]. © 2009 Wiley-VCH Verlag GmbH & Co. KGaA, Weinheim. doi:10.1002/smll.200801943

covalent bonds when depositing molecules on the surface kept at room temperature. Heating the sample to 500 K for 5–10 min is needed to induce the formation of straight conjugated PPP olygomers (Fig. 9b). The formation of zigzag PMP wires and macrocycles as well were promoted and observed when using 1,3-diiodobenzene (Fig. 9c, kinks are ascribed to the molecular symmetry) [19].

5 Controlling Nanostructures by Hierarchical Growth

The results presented so far are related to the growth of simple homogeneous molecular architectures, because they are based on a one-step process. Growing complex nanostructures, e.g., more complex molecular aggregates, requires a fine and accurate control of the reaction pathway that leads to the final molecular architecture. This can be achieved splitting the reaction pathway into individual connection steps and controlling their activation sequence, thus realizing a "programmed reactivity" of the molecules that allows *selective* activation of their reactivity at different sites. A sequential growth fashion can be implemented by designing single molecular building blocks that carry different types of halogen substituents. The sample temperature can be used as an "external knob" that allows to enable or suppress specified halogen dissociations, i.e., on-surface polymerization processes can be initiated and systematically controlled via the sample temperature. The temperature needed to break C–halogen bonds is mainly defined by the halogen species and the catalytic activity of the surface. The carbon–halogen bond dissociation is activated at temperatures that decrease with the halogen atomic number. In other words, the binding energy to the carbon atom can be tuned via the type of halogen atom. Iodine dissociation from molecules can be initiated already at room temperature and completed at around 120 °C, while this temperature range goes from 100 to 250 °C for Br substituents [35, 46]. A proper choice of the surface is crucial as it has been shown that the on-surface covalent linking occurs at different temperatures for different noble metal surfaces [39], or can even be suppressed for other surfaces. Gutzler et al. [16] reported on the growth of two-dimensional covalent bound networks by using polyaromatic molecules carrying halogen substituents. They deposited these molecular species on Cu(111) and Ag(110) and indeed verified the presence of activated species already at room temperature, i.e., without the need of additional activation energy. The same procedure repeated on graphite(001) resulted in the formation of well-ordered non-covalently bound networks stabilized by halogen–hydrogen bonding. This proves the importance of the surface in promoting the carbon–halogen dissociation at room temperature and the subsequent molecular assembly.

As mentioned above, the architecture of the final structures is encoded in the single monomer building block by incorporating distinct carbon–halogen bonds that dissociate and create active sites at the halogen sites. With this purpose, a porphyrin *trans*-Br_2I_2TPP unit has been designed and synthesized in order to carry two different types of halogen–phenyl side groups (Fig. 10a). *Trans*-Br_2I_2TPP

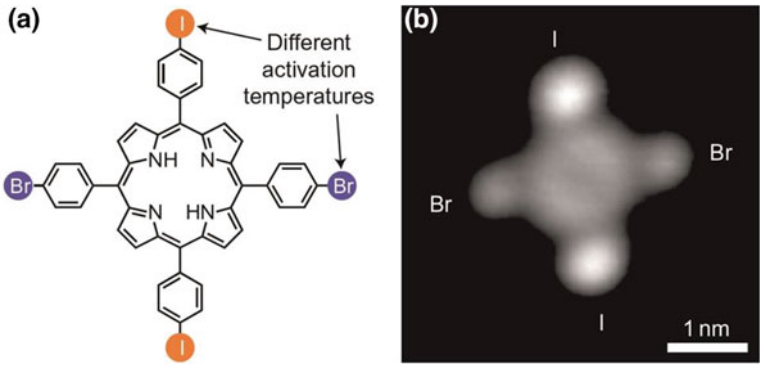

Fig. 10 Single monomer building blocks carrying Br and I substituents for sequential activation. **a** Chemical structure of the *trans*-Br_2I_2TPP. Br and I chemical groups have different chemical activation temperatures. **b** STM image (0.5 V, 0.1 nA) of a single intact *trans*-Br_2I_2TPP on Au (111). I substituents appear brighter than Br ones because of their different chemical structure. Measurements were performed under UHV conditions with a low-temperature STM operated at a temperature of 10 K. Molecules were sublimated at 593 K onto Au(111) kept at room temperature [35]

molecules have two pairs of halogen substituents (Br and I) each of them in a *trans* configuration on opposite sides of the porphyrin unit (see Fig. 10a). This chemical structure intrinsically encodes two different growth directions. As the two substituents have a pronounced difference in terms of bond dissociation energy (the binding energy of iodine–carbon is lower than that of bromine–carbon) [35], this allows to create active sites in the molecule step-by-step. In this way, new covalent intermolecular C–C bonds are formed with geometric control (via the temperature) and consequently sequential growth of nanostructures is achieved (see growth scheme in Fig. 10a). Low-temperature STM imaging allows to resolve with sub-molecular resolution the features of intact *trans*-Br_2I_2TPP molecules deposited on top of Au(111): the typical four-legs structure of the porphyrin unit is recognized and substituent halogens can be chemically distinguished because of their different appearance in STM (Fig. 10b): I and Br substituents have specific apparent heights and the former look brighter independent of the bias voltage over the investigated range (−1 V, +1 V) [35]. Thus, by comparison with other porphyrin derivatives that contain either only Br or only I substituents, it is possible to assign the characteristic apparent heights to iodine and bromine substituents. This precise knowledge of the chemical composition in an STM image (Fig. 10b) is important in the next step to identify which substituents remain after a heating step and which ones are dissociated.

Trans-Br_2I_2TPP molecules have been deposited onto Au(111) while keeping the substrate at a temperature of 80 K to suppress catalytically driven iodine dissociation from the molecules that occurs at higher temperatures, thus to keep the molecules intact with all four halogen substituents [35]. Under these conditions, molecular units are preferentially found in close-packed arrangements (Fig. 11b).

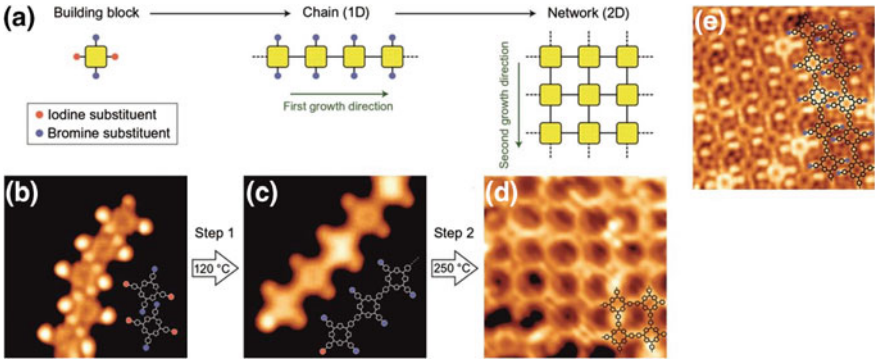

Fig. 11 Hierarchical growth of homogeneous molecular structures. **a** Scheme of the sequential activation mechanism (from *left* to *right*). In the first activation step, I substituents are dissociated and active sites in a *trans* geometry (*first growth direction*) are created enabling the formation of linear structures (from **b** to **c**). In the second step, Br are dissociated by annealing at higher temperatures. This further step allows to create lateral active sites that enable the growth along the second growth direction, i.e., the formation of 2D networks (from **c** to **d**). STM images (8×8 nm^2, **b**) of *trans*-Br_2I_2TPP molecules on Au(111), after heating up to 120 K (*step 1*, 8×8 nm^2, **c**), and after further annealing up to 250 K (*step 2*, 10×10 nm^2, **d**). **e** STM image (10×10 nm^2) of close-packed porphyrin chains after the first activation step. Further experimental details are in caption Fig. 9 and Ref. [35]

Annealing of the sample up to room temperature induces a partial I dissociation, while annealing up to 120 °C enables an efficient polymerization across the *trans*-iodine direction (first growth direction in panel Fig. 11a) during the first step. According to the *trans*-arrangement of halogen substituents within the single monomer, linear chains of porphyrin units are grown (Fig. 11c). This is in analogy to the *trans*-Br_2TPP molecules (Fig. 7h) but at lower temperatures because iodine is involved here. There are two important characteristics of these intermediate products (shown in Fig. 11c): (1) These chains always have a bright loves at their end, which reflects an iodine atom (as in Fig. 10b). Hence, all newly formed bonds are located at former iodine sites, which confirms the successful selective activation in this first step. (2) The Br substituents, which appear darker than the iodines, can be clearly seen sideways at the polymer chain and are therefore still present. However, they have not been activated yet and are therefore dormant, waiting to be activated at a suitable temperature.

Furthermore, covalently linked porphyrin chains arrange themselves parallel to each other into close-packed islands (Fig. 11e). In the next growth step, Br substituents are efficiently dissociated by thermal annealing up to 250 °C enabling the polymerization process along the second growth direction (as indicated in Fig. 8a) and triggering the formation of TPP-based two-dimensional networks (Fig. 11d). This represents an elegant way to grow two-dimensional networks in a sequential manner, and it is worth to compare it with the same structure obtained by the one-step growth process (TPP-based networks in Fig. 7i, l). An analysis of the

regularity of the TPP-based networks grown following both methods suggests that the hierarchical growth allows to prepare 2D architectures with less incorrectly connected building blocks, i.e. defects, and larger spatially extent regular networks (a detailed analysis is present in [35]).

Heterogeneous molecular architectures might be grown according to a hierarchical growth scheme. Covalently linked two-component structures on metal surfaces under UHV condition have already been achieved [10], although in a one-step growth process and thus limited control. The capability to activate different reaction pathways step-by-step allows a better tuning of the growth process. While the formation of two-dimensional TPP networks could also be achieved in a one-step process (Fig. 7l), the mixture of two molecular species in addition to the selective activation mechanism leads to molecular nanostructures that cannot be formed in one step. When combining *trans*-Br_2I_2TPP and DBTF molecules (Fig. 12a) on a Au (111) surface the two growth steps are sequentially activated when heating the sample at 250 °C. First, iodines of *trans*-Br_2I_2TPP molecules are dissociated and linear porphyrin chains are created while Br-phenyl groups remain intact (Fig. 11c). Second, Br sites are dissociated and DBTF molecules form linear chains that connect to the former Br site of porphyrin building blocks (Fig. 12b). In this way a ladder-type structure is formed that could not be achieved in one step.

A detailed analysis of the covalent links at the activated phenyl groups of porphyrin building blocks (shown in Fig. 12c) reveals the high selectivity of the process: 98 % of the former I sites of *trans*-Br_2I_2TPP molecules are connection points for further porphyrin units as desired from the molecular design. Only 2 % of

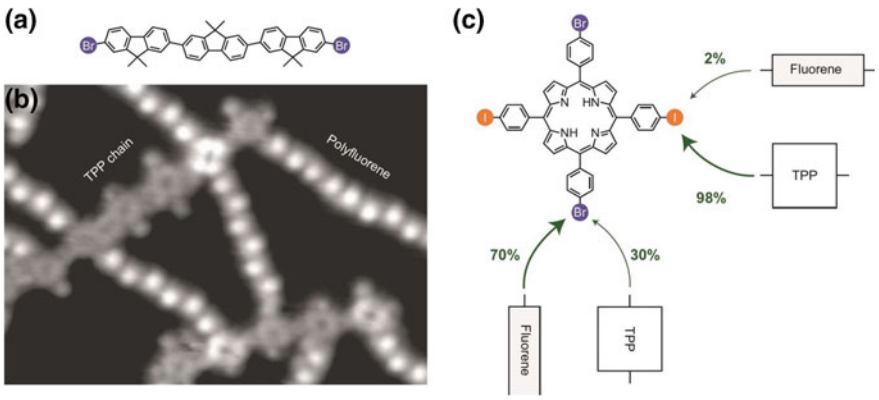

Fig. 12 Hierarchical growth of heterogenous architectures. **a** Chemical structure of DBTF molecules. **b** STM image (T = 10 K, 18 × 13 nm^2) of heterogenous networks based on DBTF and *trans*-Br_2I_2TPP on Au(111) by hierarchical growth after heating up to 250 °C. **c** Statistical analysis of porphyrin and fluorine attachment to the porphyrin *trans*-Br_2I_2TPP monomer at former bromine and iodine sites (number of evaluated sites: n_I = 489, n_{Br} = 269). Measurements were performed under UHV conditions with a low-temperature STM operated at a temperature of 10 K. A Knudsen cell was used to evaporate Br_4TPP molecules at 550 K and DBTF molecules at 503 K onto Au (111). The on-surface synthesis was achieved raising the sample temperature to 250 °C [35]

these sites are incorrectly used for fluorine connections. The second growth step determines a pronounced occupation of the remaining two Br sites by fluorene molecules (70 %, see Fig. 11c). The numbers are less impressive in this second case, because at the former Br sites also two porphyrin chains could be linked side to side, which represent a competition process for the planned ladder structure. This proves that the hierarchical growth leads to the formation of copolymers assisted by a remarkable degree of selectivity of the chemical species involved in the process.

6 Substrate-Directed Growth by On-Surface Synthesis

The on-surface synthesis consists of two processes at work: activation and diffusion of the single monomer building blocks across the surface. Elevated temperatures are required to enable these processes, but this also favors disorder into the molecular assembly and can therefore reduce the efficiency of the polymerization process. It should be noted, however, that the substrate surface is not a passive support for chemical species [16] but can play an active role in terms of activation of the molecular species in virtue of its catalytic properties [16, 41].

Any crystalline surface exhibits a certain corrugation, depending on the crystal structure and the surface orientation, which plays a crucial role for molecular diffusion. This feature can be used in order to introduce a further degree of freedom, thus improving the covalent linking and varying the final orientation of a nanostructure compared to the underlying substrate surface. By choosing properly the surface it is possible to restrict the molecular diffusion along the lowest corrugation directions and favor the formation of specific molecular architectures with a predefined orientation. For instance, the Au(110)-1 × 3 surface has been used to constrain the diffusion and subsequent polymerization of alkyl chains along its missing rows [40]. The confinement of molecular diffusion to one dimension (Fig. 13) leads to intermolecular interactions between neighboring molecules that result in the formation of linear molecular chains [40].

The effect of surface anisotropy on the growth of two-dimensional networks has been studied with an Au(100) single-crystal surface. The reconstructed surface shows a quasi-hexagonal (5 × 20) superstructure with straight rows of vertically displaced atoms [47], as shown in Fig. 14a [35]. *Trans*-Br_2I_2TPP molecules have been deposited on Au(100) at low temperature in order to keep all halogen–phenyl groups intact. Afterwards the sample was annealed to 120 °C. After this procedure, covalently bound porphyrin chains with a preferential orientation are found as illustrated in Fig. 14a. Hence, the surface reconstruction determines the orientation of the final nanostructure.

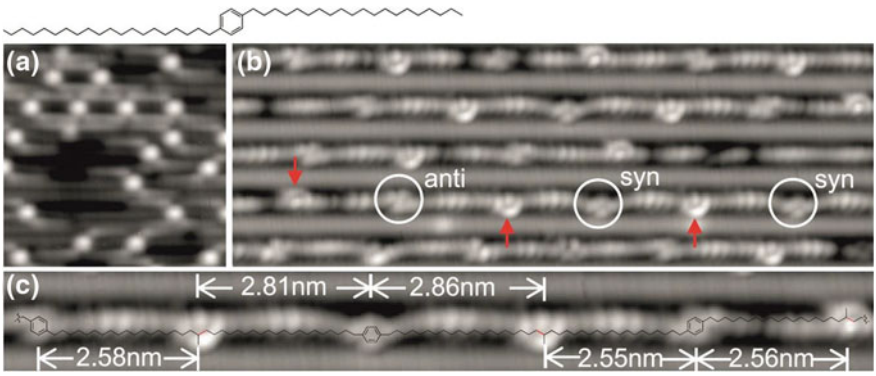

Fig. 13 Polymerization of hydrocarbons on an anisotropic gold surfaces. **a** STM topographic image of DEB molecules (12 × 12 nm^2, −0.5 V, 0.5 nA) on Au(110)-1 × 2 at 300 K. **b** STM topographic image (17.5 × 6 nm^2, −1 V, 2 nA) polymerized DEB chains located in the missing rows of Au(110)-1 × 3 after heating at 420 K for 10 h. *Circles* denote the phenylene groups; *arrows* denote the methyl side groups. **c** A section of DEB polymer chain and superimposed the molecular structure (14.4 × 1.6 nm^2, −1 V, 2 nA). The newly formed C–C bonds are shown in *red*. From [40]. Reprinted with permission from American Association for the Advancement of Science

An analysis of the chains angular distribution reveals a preferred angle at 51° between chains and atomic rows (Fig. 14b). This finding can be easily rationalized by geometric arguments since all porphyrin units are adsorbed on equivalent sites (Fig. 14c), thus reducing the total energy by this particular angle [35]. This is in contrast to the rather flat Au(111) surface where the angular distribution of chains is less defined (Fig. 7 and Ref. [1]) and underlines the importance of the surface corrugation. After heating to 250 °C (the second activation step), formation of rectangular networks is again found (Fig. 14d) with a clear orientation off the Au (100) atomic rows orientation [35]. Small networks reveal deviations from the rectangular shape (angle $\beta = 101 \pm 3°$ instead of 90°) as shown in Fig. 14d. This effect is most likely ascribed to the reduced relative contribution of intermolecular bond energy compared to the interaction of the molecular assembly with the surface [35] for small networks. Furthermore, a larger average size of networks is achieved as compared to the Au(111) surface [35], which can directly be assigned to the surface anisotropy. The corrugation rows lead to a parallel arrangement of the intermediate products (as illustrated in Fig. 14a) that results in a sort of zipping mechanism for the two-dimensional linking in the second step: If the first link between two chains is established, all other porphyrin units are in a perfect arrangement with respect to each other and a rather efficient linking of long chain segments can occur. As a consequence, the final nanostructures are larger for hierarchical growth on a corrugated surface than in a single-step process.

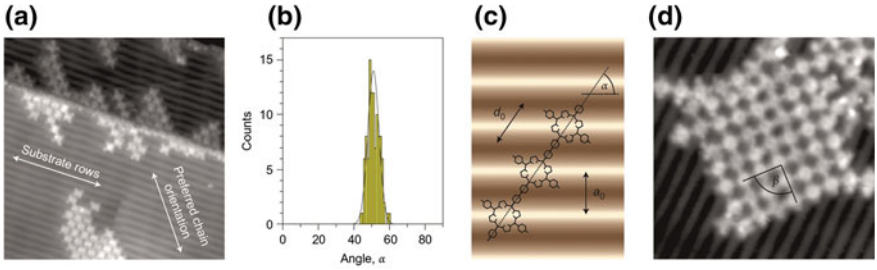

Fig. 14 Substrate-directed growth of networks. **a** STM image (42 × 42 nm^2) of *trans*-Br_2I_2TPP chains grown on Au(100) after the first activation process. **b** Angular distribution for chains shown in panel **a**. **c** Adsorption geometry scheme of polymeric chain on Au(100) surface with an angle of 55° for equivalent adsorption sites for all porphyrins (a_0 = 1.44 nm and d_0 = 1.76 nm). **d** STM image (20 × 20 nm^2) of an approximately squared covalently linked molecular network after the second activation process. Measurements were performed under UHV conditions with a low-temperature scanning tunneling microscope (STM) operated at a temperature of 10 K. A Knudsen cell was used to evaporate Br_4TPP molecules at 550 K onto Au(100). The first and second activation steps were induced by heating to 120 and 250 °C, respectively [35]

7 Summary

The growth of molecular nanostructures on surfaces via Ullmann coupling can be controlled by both the chemical structure of the initial building blocks, which is precisely reflected in the final products, as well as the surface underneath, in particular the presence of defects, step edges, and adatoms. Diffusion of the activated monomers and intermediate oligomers is another key issue since it defines the rate of polymerization and the possibility of substrate-directed growth that allows improved linking reactions. Various molecules have been used in the last years and it turns out that on-surface polymerization represents a very feasible method to create stable covalent 1D and 2D polymers on a surface and to image them by scanning probe microscopy in real space as successfully demonstrated in many cases. The covalent nature of the newly created bond is not only evident from the real space distances and orientations, but could additionally be proven by spectroscopic detection of characteristic electronic states. When using different halogen substituents, a hierarchical growth scheme could be realized since selective and sequential activation of the different substituents results in a programmed reactivity of the molecules. Based on the gathered mechanistic insight and with the ability to direct reactivity by designing proper monomer building blocks as well as using the surface as a template, 1D and 2D polymers of increasing structural and compositional complexity will emerge. Besides this continued exploration of on-surface polymerization as a new method for generating defined nanostructures, their resulting properties and functions will become increasingly important in the future.

References

1. Joachim, C., Gimzewski, J.K., Aviram, A.: Electronics using hybrid-molecular and mono-molecular devices. Nature **408**, 541–548 (2000)
2. Heath, J.R., Ratner, M.A.: Molecular Electronics. Phys. Today **56**, 43–49 (2003)
3. Wintterlin, J., Bocquet, M.-L.: Graphene on metal surfaces. Surf. Sci. **603**, 1841–1852 (2009)
4. Nagashima, A., Tejima, N., Gamou, Y., Kawai, T., Oshima, C.: Electronic dispersion relations of monolayer hexagonal boron nitride formed on the Ni(111) surface. Phys. Rev. B **51**, 4606–4613 (1995)
5. Rabe, J.P., Buchholz, S.: Commensurability and mobility in two-dimensional molecular patterns on graphite. Science **253**, 424–427 (1991)
6. Yokoyama, T., Yokoyama, S., Kamikado, T., Okuno, Y., Mashiko, S.: Selective assembly on a surface of supramolecular aggregates with controlled size and shape. Nature **413**, 619–621 (2001)
7. Theobald, J.A., Oxtoby, N.S., Phillips, M.A., Champness, N.R., Beton, P.H.: Controlling molecular deposition and layer structure with supramolecular surface assemblies. Nature **424**, 1029–1031 (2003)
8. Schlickum, U., Decker, R., Klappenberger, F., Zoppellaro, G., Klyatskaya, S., Ruben, M., Silanes, I., Arnau, A., Brune, H., Barth, J.V.: Metal-organic honeycomb nanomeshes with tunable cavity size. Nano Lett. **7**, 3813–3817 (2007)
9. Grill, L., Dyer, M., Lafferentz, L., Persson, M., Peters, M.V., Hecht, S.: Nano-architectures by covalent assembly of molecular building blocks. Nature Nanotech. **2**, 687–691 (2007)
10. Weigelt, S., Busse, C., Bombis, C., Knudsen, M.M., Gothelf, K.V., Strunskus, T., Wöll, C., Dahlbom, M., Hammer, B., Lægsgaard, E., Besenbacher, F., Linderoth, T.R.: Covalent interlinking of an aldehyde and an amine on an Au(111) surface in ultrahigh vacuum. Angew. Chem. Int. Ed. **46**, 9227–9230 (2007)
11. Champness, N.R.: Surface chemistry: building with molecules. Nature Nanotech. **2**, 671–672 (2007)
12. Matena, M., Riehm, T., Stöhr, M., Jung, T.A., Gade, L.H.: Transforming surface coordination polymers into covalent surface polymers: linked polycondensed aromatics through oligomerization of N-heterocyclic carbene intermediates. Angew. Chem. Int. Ed. **47**, 2414–2417 (2008)
13. Veld M.I., Iavicoli P., Haq S., Amabilino D.B., Raval R.: Unique intermolecular reaction of simple porphyrins at a metal surface gives covalent nanostructures. Chem. Commun. 1536–1538 (2008)
14. Zwaneveld, N.A.A., Pawlak, R., Abel, M., Catalin, D., Gigmes, D., Bertin, D., Porte, L.: Organized formation of 2D extended covalent organic frameworks at surfaces. J. Am. Chem. Soc. **130**, 6678–6679 (2008)
15. Gourdon, A.: On-surface covalent coupling in ultrahigh vacuum. Angew. Chem. Int. Ed. **47**, 6950–6953 (2008)
16. Gutzler, R., Walch, H., Eder, G., Kloft, S., Heckl, W.M., Lackinger, M.: Surface mediated synthesis of 2D covalent organic frameworks: 1,3,5-tris(4-bromophenyl)benzene on graphite (001), Cu(111), and Ag(110). Chem. Commun. 4456–4458 (2009)
17. Perepichka, D.F., Rosei, F.: Extending polymer conjugation into the second dimension. Science **323**, 216–217 (2009)
18. Sakamoto, J., Van Heijst, J., Lukin, O., Schlüter, A.D.: Two-dimensional polymers: Just a dream of synthetic chemists? Angew. Chem. Int. Ed. **48**, 1030–1069 (2009)
19. Lipton-Duffin, J.A., Ivasenko, O., Perepichka, D.F., Rosei, F.: Synthesis of polyphenylene molecular wires by surface-confined polymerization. Small **5**, 592–597 (2009)
20. Bartels, L.: Tailoring molecular layers at metal surfaces. Nature Chem. **2**, 87–95 (2010)
21. Lipton-Duffin, J.A., Miwa, J.A., Kondratenko, M., Cicoira, F., Sumpter, B.G., Meunier, V., Perepichka, D.F., Rosei, F.: Step-by-step growth of epitaxially aligned polythiophene by surface-confined reaction. Proc. Natl. Acad. Sci. **107**, 11200–11204 (2010)

22. Lackinger, M., Heckl, W.M.: A STM perspective on covalent intermolecular coupling reactions on surfaces. J. Phys. D Appl. Phys. **44**, 464011 (2011)
23. Mendez, J., Lopez, M.F., Martin-Gago, J.A.: On-surface synthesis of cyclic organic molecules. Chem. Sov. Rev. **40**, 4578–4590 (2011)
24. Ouchi, M., Badi, N., Lutz, J.-F., Sawamoto, M.: Single-chain technology using discrete synthetic macromolecules. Nature Chem. **3**, 917–924 (2011)
25. Palma, C.-A., Samorì, P.: Blueprinting macromolecular electronics. Nature Chem. **3**, 431–436 (2011)
26. Colson, J.W., Dichtel, W.R.: Rationally synthesized two-dimensional polymers. Nat. Chem. **5** (6), 453–465 (2013)
27. El Garah, M., MacLeod, J.M., Rosei, F.: Covalently bonded networks through surface-confined polymerization. Surf. Sci. **613**, 6–14 (2013)
28. Grill, L.: Functionalized molecules studied by STM: motion, switching and reactivity. J. Phys.: Condens. Matter **20**, 053001 (2008)
29. Nitzan, A., Ratner, M.A.: Electron transport in molecular wire junctions. Science **300**, 1384–1389 (2003)
30. Lafferentz, L., Ample, F., Yu, H., Hecht, S., Joachim, C., Grill, L.: Conductance of a single conjugated polymer as a continuous function of its length. Science **323**, 1193–1197 (2009)
31. Koch, M., Ample, F., Joachim, C., Grill, L.: Voltage-dependent conductance of a single graphene nanoribbon. Nature Nanotech. **7**, 713–717 (2012)
32. Ullmann, F., Bielecki, J.: Ueber synthesen in der Biphenylreihe. Chem. Ber. **34**, 2174 (1901)
33. Barth, J.V., Costantini, G., Kern, K.: Engineering atomic and molecular nanostructures at surfaces. Nature **437**, 671–679 (2005)
34. De Greef, T.F.A., Smulders, M.M.J., Wollfs, M., Schenning, A.P.H.J., Sijbesma, R.P., Meijer, E.W.: Supramolecular polymerization. Chem. Rev. **109**, 5687–5754 (2009)
35. Lafferentz, L., Eberhardt, V., Dri, C., Africh, C., Comelli, G., Esch, F., Hecht, S., Grill, L.: Controlling on-surface polymerization by hierarchical and substrate-directed growth. Nature Chem. **4**, 215–220 (2012)
36. Hla, S.-W., Bartels, L., Meyer, G., Rieder, K.H.: Inducing all steps of a chemical reaction with the scanning tunneling microscope tip: towards single molecule engineering. Phys. Rev. Lett. **85**(13), 2777–2780 (2000)
37. Kittelmann, M., Rahe, P., Nimmrich, M., Hauke, C.M., Gourdon, A., Kühnle, A.: On-surface covalent linking of organic building blocks on a bulk insulator. ACS Nano **5**, 8420–8425 (2011)
38. Hassan, J., Sévignon, M., Gozzi, C., Schulz, E., Lemaire, M.: Aryl-aryl bond formation one century after the discovery of the Ullmann reaction. Chem. Rev. **102**, 1359–1470 (2002)
39. Bieri, M., Nguyen, M.-T., Gröning, O., Cai, J., Treier, M., Aït-Mansour, K., Ruffieux, P., Pignedoli, C.A., Passerone, D., Kastler, M., Müllen, K., Fasel, R.: Two-dimensional polymer formation on surfaces: insight into the roles of precursor mobility and reactivity. J. Am. Chem. Soc. **132**, 16669–16676 (2010)
40. Zhong, D., Franke, J.H., Podiyanachari, S.K., Blömker, T., Zhang, H., Kehr, G., Erker, G., Fuchs, H., Chi, L.: Linear alkane polymerization on a gold surface. Science **334**, 213–216 (2011)
41. Saywell, A., Schwarz, J., Hecht, S., Grill, L.: Polymerization on stepped surfaces: alignment of polymers and identification of catalytic sites. Angew. Chem. Int. Ed. **51**, 5096–5100 (2012)
42. Wang, W., Shi, X., Wang, S., Van Hove, M.A., Lin, N.: Single-molecule resolution of an organometallic intermediate in a surface-supported Ullmann coupling reaction. J. Am. Chem. Soc. **133**, 13264–13267 (2011)
43. Koch, M., Gille, M., Viertel, A., Hecht, S., Grill, L.: Substrate-controlled linking of molecular building blocks: Au(111) vs. Cu(111). Surf. Sci. **627**, 70–74 (2014)
44. Villagomez, C.J., Sasaki, T., Tour, J.M., Grill, L.: Bottom-up assembly of molecular wagons on a surface. J. Am. Chem. Soc. **132**, 16848 (2010)
45. Rowan, S.J., Cantrill, S.J., Cousins, G.R., Stoddart, J.K., Sanders, J.F.: Dynamic covalent chemistry. Angew. Chem. Int. Ed. **41**, 898–952 (2002)

46. Krasnikov, S.A., Doyle, C.M., Sergeeva, N.N., Preobrajenski, A.B., Vinogradov, N.A., Sergeeva, Y.N., Zakharov, A.A., Senge, M.O., Cafolla, A.A.: Formation of extended covalently bonded Ni porphyrin networks on the Au(111) surface. Nano Res. **4**, 376–384 (2011)
47. Havu, P., Blum, V., Havu, V., Rinke, P., Scheffler, M.: Large-scale surface reconstruction energetics of Pt(100) and Au(100) by all-electron density functional theory. Phys. Rev. B **82**, 161418 (2010)

Transition Metals Trigger On-Surface Ullmann Coupling Reaction: Intermediate, Catalyst and Template

L. Dong, S. Wang, W. Wang, C. Chen, T. Lin, J. Adisoejoso and N. Lin

Abstract In this chapter, we report on our recent studies of on-surface Ullmann coupling reaction and focus on the roles of the transition metals in the reaction. First, we discuss an organometallic intermediate state, which separates the reaction into two steps. Next, we examine the catalytic efficiency of Cu, Au, Ag, Pt, and Pd in the reaction. We analyze the bond formation yields when the reaction takes place in the presence of these metals. In particular, we determine the rate constants and activation energy of Cu- and Pd-catalyzed reaction. In the last part, we demonstrate a strategy of using metal coordination template to steer the reaction toward specific products.

1 Introduction

Molecular self-assembly on surfaces is a fundamental strategy for the bottom-up fabrication of nanostructures [1]. Various intermolecular interactions such as van der Waals interaction [2], hydrogen bonds [3, 4], halogen bonds [5], and metal–organic coordination bonds [6] have been utilized to build nanostructures. Taking the advantage of the reversibility of such bonding, long-range-ordered organizations have been formed. However, such structures are inherently fragile due to the weak intermolecular interactions, which lead to poor mechanical stability and low charge-transport efficiency. Robust and irreversible covalent bonding offers a way to overcome these limitations. Ullmann reaction [7], the C–C coupling between halogen aromatics via catalysts, has been employed onto surface for the synthesis of covalent-linked oligomers and polymers. A wide range of one-dimensional (1D) [8–10] and two-dimensional (2D) [11–13] materials has been successfully obtained via this route. Moreover, on-surface chemistry under ultrahigh vacuum (UHV) allows a much

L. Dong · S. Wang · W. Wang · C. Chen · T. Lin · J. Adisoejoso · N. Lin (✉)
Department of Physics, The Hong Kong University of Science and Technology, Clear Water Bay, Kowloon, Hong Kong, China
e-mail: phnlin@ust.hk

A. Gourdon (ed.), *On-Surface Synthesis*, Advances in Atom and Single Molecule Machines, DOI 10.1007/978-3-319-26600-8_2

broader range of reaction temperatures, and the 2D confined geometry could favor reactions not accessible in the three dimensional space. Many of these studies utilized scanning tunneling microscopy (STM), which is a powerful tool not only imaging at the sub-molecular level, but also revealing molecular orbitals. The active research in this field provides unprecedented insights into the reaction mechanism [14].

In this chapter, we report on the STM studies of Ullmann reaction taking place in the presence of different transition metals. These metal species are in the form either as substrate (*intrinsic*) or as deposit (*extrinsic*). Our focus is to understand the roles the transition metals play in the Ullmann reaction. In Sect. 2, we present a combined experimental and theoretical study which reveals topographic and electronic signatures of an organometallic intermediate state containing C–Cu–C moieties. In Sect. 3, we first analyze the activity of *intrinsic* Cu, Ag, and Au and *extrinsic* Pt catalysts and conclude that the catalytic efficiency in the two reaction steps is very different for different metals. Furthermore, we compare the pathways of the reaction catalyzed by *extrinsic* Cu and Pd catalysts and determine the activation energy quantitatively. In Sect. 4, we demonstrate a strategy of using metal coordination bonds as template to steer the Ullmann reaction, which allows us to control the on-surface polymerization processes toward size-limited macromolecular structures.

2 Organometallic Intermediate State

A typical Ullmann reaction generally involves multiple steps from the halogen-contained molecules to the final coupled product. In the surface-confined reaction path, an essential intermediate state has been proposed by several groups [13, 15–18]. The study of the formation and structure of this intermediate state can give us a better understanding of the reaction mechanisms and dynamics [14]. It has been proposed that the radicals in the intermediate were connected by molecule–molecule and surface–mediated interactions [16, 19]. A Cu-atom-linked intermediate was also suggested based on the distance between two neighboring radicals [15, 17].

2.1 Topographic Identification

Here, we used STM measurements and DFT calculations to identify an organometallic intermediate incorporating C–Cu–C bridges in the on-surface Ullmann reaction [20]. As illustrated in Fig. 1a, after the deposition to a Cu(111) surface kept at room temperature, molecules of 4,4″-dibromo-*p*-terphenyl (compound **1**) are completely debrominated resulting in a Cu-bridged polymeric organometallic intermediate; an annealing at 473 K triggers the C–C coupling with the Cu atoms released and poly(*para*-phenylene) oligomers formed.

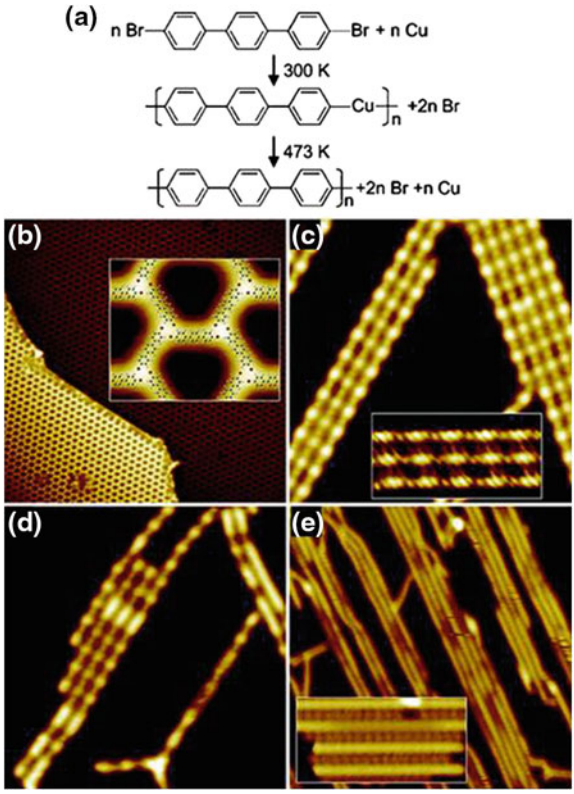

Fig. 1 **a** Surface-supported Ullmann coupling reaction path of compound **1** to poly(*para*-phenylene). **b** STM image of self-assembly of the molecules on Cu(111) at 77 K (120 nm × 120 nm). *Inset* Magnified STM image of the network with molecular models superimposed (6 nm × 5 nm). **c** STM image of the sample annealed to 300 K (20 nm × 20 nm). *Inset* Br atoms trapped between the linear structures (8 nm × 4 nm). **d** STM image of the sample annealed to 393 K (20 nm × 20 nm). **e** STM image of sample annealed to 473 K (40 nm × 40 nm). *Inset* Br atoms lying between the poly(*para*-phenylene) oligomers (8 nm × 4 nm) [20]

As shown in Fig. 1b, the STM image reveals a honeycomb network on the Cu (111) surface at 77 K after the adsorption of **1**. A vortex structure is resolved at the joint of three molecules in the inset of Fig. 1b. With the molecular model superimposed, we can see that a terminal Br atom (in red) points toward an H atom of the neighboring molecule. The distance between the Br and the H atoms is 3.2 ± 0.5 Å. Therefore, we propose that the molecules are yet intact at 77 K and this molecular network is stabilized by Br…H–C hydrogen bonds. A 473 K annealing treatment destroyed the well-ordered honeycomb network and left newly formed linear chains (see Fig. 1e). No apparent periodicity was resolved in the chains. Electronic band structures of poly(*para*-phenylene) oligomers were observed [21]. Both topographic and electronic features indicate that these chains are poly(*para*-phenylene) oligomers, which means Ullmann coupling has successfully completed. Another

interesting feature is the small dots between the chains (inset of Fig. 1e). Similar features have been observed for iodine-aromatic systems adsorbed on Cu(110) surface and assigned as dissociated iodine atoms adsorbed on the surface [15]. It was reported that on Cu(111) surface Br atoms are dissociated from the phenyl group at 300 K [17]. We attribute these dots to be adsorbed Br atoms cleaved from the molecules.

After annealing at 300 K, the 2D honeycomb networks converted to linear structures (Fig. 1c). In comparison with the final product aforementioned, a periodical feature emerged in these linear structures. These linear structures are commensurate with the Cu lattice: each three periods matches 11 Cu atoms in the $[11\bar{2}]$ direction, that is, with a periodicity of 16.2 ± 0.2 Å. This distance is much larger than the length of a single debrominated $(ph)_3$ unit, which is 11.4 Å as calculated by DFT. In contrast to the sample prepared at 77 K, Cu surface at room temperature provides sufficient 2D Cu adatom gas, which could be easily incorporated in the organometallic intermediate. We hence propose that the brighter oval features are $(ph)_3$ biradicals that are connected by Cu adatoms. A DFT optimized linear periodical structure is shown in Fig. 2a. The side view of the structure reveals that the Cu atoms are almost in the same plane of the phenyl rings and do not bind strongly to the substrate.

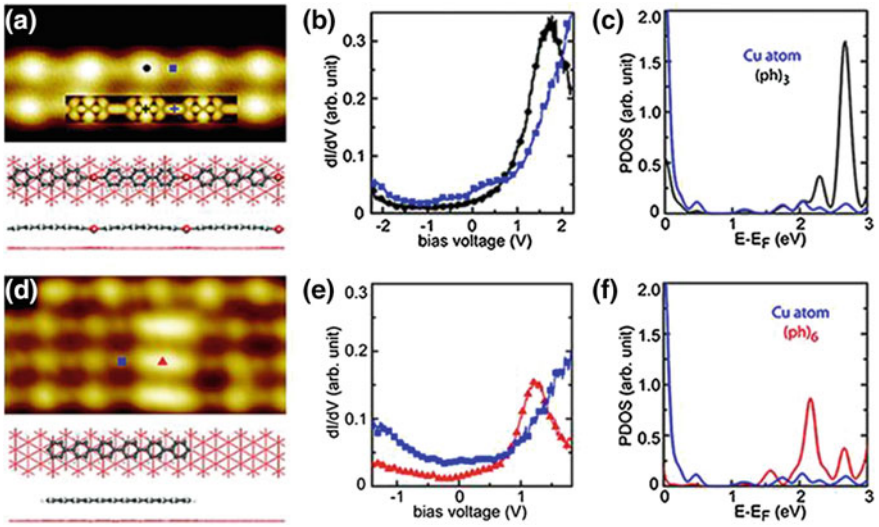

Fig. 2 **a** High-resolution STM image of the intermediate (8 nm × 4 nm) and the DFT calculated structure. *Inset* simulated STM image at +2.7 V. **b** d*I*/d*V* spectra measured at $(ph)_3$ (*black*) and Cu (*blue*) sites marked in **a**. **c** Calculated PDOS of $(ph)_3$ (*black*) and Cu (*blue*) in the inset of **a**. **d** STM image of the intermediate annealed to 393 K (8 nm × 4 nm) and calculated structure. **e** and **f** Experimental d*I*/d*V* and PDOS of $(ph)_6$ (*red*) and Cu (*blue*) in **d** [20]

2.2 Electronic Characterization and DFT Calculation

We conducted tunneling spectroscopic (d*I*/d*V*) measurements on the intermediate states. The $(ph)_3$ part shows a prominent peak at +1.7 V, while the Cu atom shows only a gradual climbing state starting from +1.0 V (Fig. 2b), which is in good agreement with the calculated projected density of states (PDOS) in Fig. 2c, where the $(ph)_3$ has an electronic state at +2.7 V while the Cu atom shows no apparent features (Fermi level is commonly offset in the DFT calculations). A simulated STM image of the intermediate at +2.7 V is shown in Fig. 2a which reproduces well the main features of the experimental results.

Between the intermediate and the final oligomer, furthermore, a mixed state was identified after an annealing of 393 K. As shown in Fig. 2d, besides the periodical features observed in Fig. 1c, bright segments of different length emerge in the linear structures, and the shortest one is identified with a length of 2.5 nm, equal to the dimension of a $(ph)_6$ oligomer. In the dI/dV spectra shown in Fig. 2e, such a $(ph)_6$ oligomer has a peak at +1.2 V, which is 0.5 V lower than main state of $(ph)_3$, which is consistent with the isolated $(ph)_6$ oligomer result [21]. The Cu atom shows similar feature as the intermediate case. In the calculated PDOS, the prominent peak of $(ph)_6$ oligomer (+2.2 V) is 0.5 V lower than $(ph)_3$ (Fig. 2f), which agrees well with the experimental values. On basis of both the topographic and electronic properties of the bright segments, we believe that they are short poly(*para*-phenylene) oligomers formed by covalent-linked $(ph)_3$ units. The length of the poly (*para*-phenylene) oligomers ($(ph)_{3n}$) is shorter than the chain containing the same number (n) of $(ph)_3$ units, implying the fact that Cu atoms are released during this transition.

Besides Cu, other transition metal atoms are also found to form organometallic intermediates including Ag [22] and Pt, which will be discussed later.

3 Transition Metal Catalysts

3.1 Intrinsic Ag, Au, Cu, and Extrinsic Pt Catalysts

In this part, we discuss a series of comparative experiments of Ullmann coupling of 1,3,5-tris(4-bromophenyl)benzene (compound **2**) molecules on fcc(111) transition metal surfaces of Ag, Au, and Cu. We also examined the catalytic behavior *of extrinsic* Pt deposits on Ag surface. As illustrated in Fig. 3, three distinct states can be identified by STM: an initial state of intact molecules (IS), an intermediate state of organometallic state (IntS), and a final state of covalently linked molecules (FS). We quantitatively analyzed the yields of the FS when the reaction was catalyzed by different catalysts.

It has been reported that deposition of **2** onto Cu(111) held at room temperature resulted in an IntS with C–Cu–C bond, but the deposition onto the substrate held at

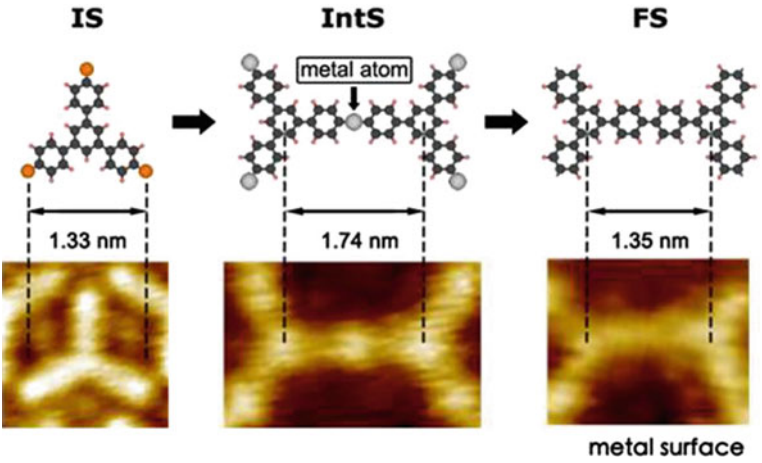

Fig. 3 Scheme of the on-surface Ullmann reaction path of **2** on Ag(111) surface with corresponding topographic structures in STM: IS to IntS to FS. *Black* C; *Red* H; *Orange* Br; *Gray* Ag

80 K kept the molecules intact [17]. Thus, the transition from IS to IntS occurs below the temperature of 300 K. Here, we focused on the transition from IntS to FS. We annealed the sample step-wisely to monitor when the conversion from the IntS to FS happens. As shown in Fig. 4a, after a 370 K annealing, the IntS developed into larger and regular organometallic networks stabilized by C–Cu–C bonds, indicating that the C–Cu–C bonds are quite stable at this temperature. Further annealing to 390 K disrupted the regular networks of the IntS and a small fraction of the IntS was converted into FS. The IntS-to-FS conversion became significant above 400 K and reached over 90 % at 410 K as shown in Fig. 4b.

Ullmann Coupling of **2** on Au(111) was reported by Blunt et al. [23], revealing that molecules are intact as deposited on a room-temperature sample, then form covalently coupled dimers at ~380 K and fully connected covalent networks at ~450 K. These results were reproduced in our study. Figure 4d shows that the IS (up-right corner) and the dimer phase coexisted after being heated to 370 K [23, 24]. Further annealing at 430 K led to irregular polymer network structures associated with the molecules fully converted to the FS (Fig. 4e). Differing from the Cu(111) case, we did not observe any IntS on the Au(111) surface in the temperature range between 300 and 450 K.

Walch et al. [17] reported that molecules **2** keep intact on Ag(111) surface at room temperature. Here, we examined its high-temperature behavior. As shown in Fig. 4g, after an annealing at 390 K, an open network structure consisting of polygons replaced the close-packed molecular monolayer formed at room temperature. The sides of the polygons consist of a pair of **2** linked in a head-to-head manner. The center-to-center distance between two neighboring molecules is about 1.74 nm with a protrusion in the middle. The distance indicates that this configuration is a C–Ag–C IntS [25]. We found that this C–Ag–C IntS was very robust

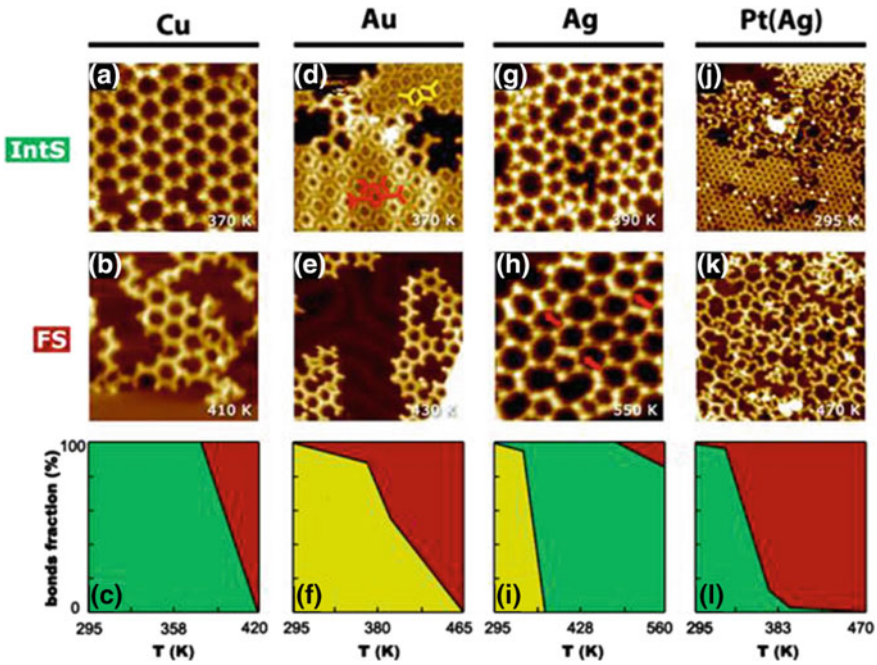

Fig. 4 STM images of the representative products and the bonds fraction in the reaction process on various metal surfaces: **a–c** Cu; **d–f** Au; **g–i** Ag; **j–l** Ag dosed with Pt. *Yellow* IS; *Green* IntS; *Red* FS. **a** and **b** 16.5 nm × 16.5 nm. **d** 14.4 nm × 14.4 nm. **e** 19.8 nm × 19.8 nm. **g** 18.9 nm × 18.9 nm. **h** 13.8 nm × 13.8 nm. **j** 23.0 nm × 23.0 nm. **k** 21.0 nm × 21.0 nm

against annealing. After 550 K heating, only 10 % of IntS was converted into FS (cf. Fig. 4h).

Based on the experimental observation, we analyzed the number of different types of bonds formed on the three substrates at various temperatures (from 295 K to 420, 465 and 560 K for Cu, Au, and Ag, respectively). The fraction of the three states, IS (yellow), IntS (green) and FS (red), is plotted in the bottom panels of Fig. 4. Apparently, the Ullmann reaction proceeds comparatively different on the three metals: (1) At 295 K, IS is present on Au and Ag but not on Cu, indicating that the IS is stable on Au(111) and Ag(111) but more reactive on Cu(111); (2) Cu and Ag form organometallic IntS but no Au organometallic species being observed, presumably C–Au–C is either unstable or having a short lifetime; (3) On Cu or Au, all molecules are converted into FS at 420 or 465 K, but the conversion is only $\sim$10 % on Ag even at a much high temperature of 560 K.

Pt is a widely used catalyst in organic synthesis [26]. To explore the catalytic activity of Pt, we deposited Pt at Ag(111). As discussed before, on Ag(111) the yield of C–C bond formation is very low even upon 550 K annealing, hence Ag is an ideal surface for exploring the catalytic ability of Pt deposits. Figure 4j shows that after adding Pt at room temperature onto predeposited monolayer of **2**, the

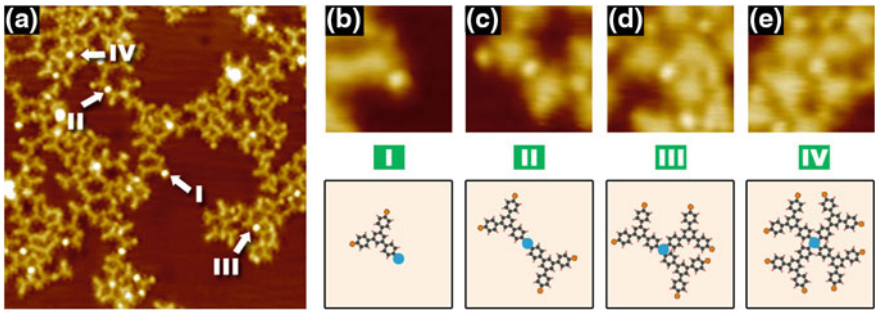

Fig. 5 **a** STM image of the IntS formed by Pt and **2**, which shows different coordination numbers for single Pt atom (25.4 nm × 25.4 nm). **b–e** STM images with corresponding schematic models of Pt coordinated with 1, 2, 3 and 4 molecules, respectively (3.2 nm × 3.2 nm)

close-packed monolayer is disrupted. One can see that lots of bright dots are scattered in the molecular layer. From the larger apparent height than Ag atom in the IntS, we attribute them to be Pt atoms. Figure 5a shows a STM topography of the sample after an annealing at 320 K. One can see that the bright dots are attached to the corners of the triangular shape molecules. Figure 5c shows that two monomers are linked by a dot in which the molecular center-to-center distance is 1.74 nm. This value agrees with an organometallic intermediate state containing C–Pt–C bonding. In contrast to the Ag or Cu linked organometallic states in which the metal atoms are always in a twofold coordination, the Pt atoms may coordinate to one, two, three, or four molecules. Figure 5b–e shows several such examples with the corresponding models illustrated in Fig. 5f–i. Further annealing at 380 K converted 90 % of the IntS into FS. Finally, annealing at 470 K achieved almost a 100 % conversion (cf. Fig. 4k). The temperature-dependent fraction of different states of Pt-catalyzed reaction is plotted in Fig. 4l. Compared to what happened on the pristine Ag surface, we conclude that Pt deposits significantly enhance the Ullmann reaction.

The yield of the Ullmann reaction, defined as the conversion ratio of the FS, catalyzed by the four metals is summarized in Fig. 6a. The ratios account for an overall catalytic activity sequence of Pt > Au > Cu > Ag. As we have aforementioned, the Ullmann reaction proceeds in two steps that are separated by the IntS. Based on the fractions of the three states shown in Fig. 4, we propose a qualitative energy diagram shown in Fig. 6b. The energy barrier I defines the conversion of IS to IntS. Upon deposition on the substrates held at room temperature, **2** is in IS on Ag and Au but completely forms IntS on Cu- and Ag-dosed with Pt. Thus, barrier I in the Cu- or the Pt-catalyzed reaction is lower than that in the Ag- or Au-catalyzed process. The barrier II defines converting the IntS to FS in the second step. Since Ag-stabilized organometallic state is stable up to 550 K, barrier II on Ag is the highest. On Au, because no IntS was detected, we assume that the barrier II is very low or absent.

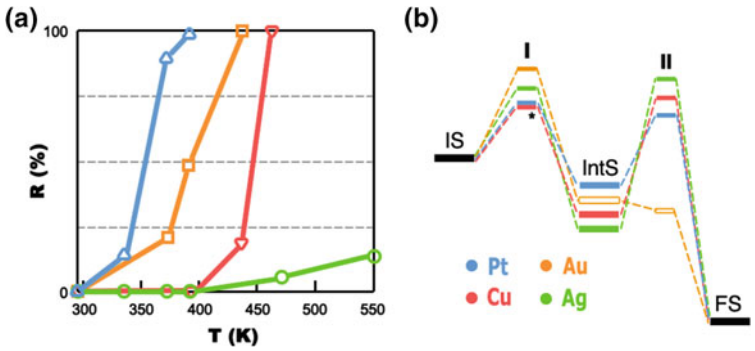

Fig. 6 **a** Conversion ratios defined in the text as a function of annealing temperatures for different transition metals. **b** Schematic energy diagram of the reaction process for all the metals

3.2 Extrinsic Pd and Cu Catalysts

We chose the polymerization reaction of 5,15-bis-(4-bromo-phenyl)-10,20-diphenyl porphyrin (compound **3**, see the inset of Fig. 7a) as our model system to investigate *extrinsic* Cu and Pd catalysts [27]. As a prototypical catalyst of Ullmann reaction, Cu catalysis is vital in the reaction process. Pd is the most

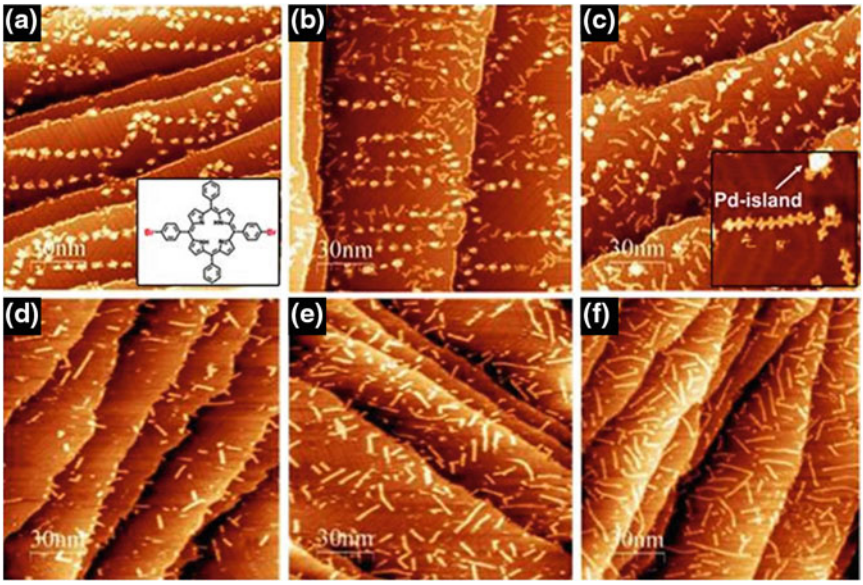

Fig. 7 **a**–**c** STM images of polymeric chains formed by **3** and Pd with annealing of 447 K for 5, 45, 105 min, respectively. *Inset* of **c** high-resolution STM image of the **3**-Pd chain (25 nm × 25 nm). **d**–**f** STM images of polymeric chains formed by **3** and Cu with annealing of 453 K for 5, 75, 160 min, respectively [27]

versatile catalyst used in homo-coupling and cross-coupling reactions [28, 29]. Here, we used STM to monitor the isothermal reaction and then determined the reaction yields, rate constants, and activation energy. In addition, kinetic Monte Carlo (KMC) simulation was utilized to explore the reaction mechanism.

After depositing **3** onto a Au(111) surface with predosed Pd, periodical chains were formed with a center-to-center distance of 1.74 ± 0.04 nm for the adjacent units, indicating covalently connected polymers (Fig. 7a–c). Similar chains were obtained when we conducted the Cu-catalyzed experiment on Au(111) surface (Fig. 7d–f). As contrast, annealing the same molecules on clean Au(111) up to 453 K for 30 min only gave us only 1.5 % covalently linked species, which confirms the catalytic influence of Pd or Cu on this Ullmann coupling reaction.

To study the reaction kinetics of C–C bond formation of **3** catalyzed by Pd, we annealed the sample at a defined temperature in 10–12 steps with 8–10 min for each. STM measurements were carried out after each step when the sample was cooled down to room temperature. The same procedure was conducted at different annealing temperatures. The discerning of dimers and even longer chains in STM images allows for the determination of the number of bonds formed as a function of reaction time and temperature. The increase of polymeric chains with longer reaction time is apparent in Fig. 7a–c, and this similar phenomenon was observed for each annealing temperature (Fig. 8). At higher temperatures, bond concentration rises rapidly until reaching a saturation value; At lower temperature, 393 K for example, a two-phase behavior emerges: A slow increase (0–60 min, defined as phase I) is followed by a rapid one (60–140 min, phase II). Such a two-phase behavior implies that the coupling reaction involves multiple steps. We suppose that phase I accounts for an initial activation process, and phase II is related to the C–C bond formation.

At higher temperature, e.g., 429 K, phase II is always the rate-limiting process while phase I is almost undetectable (Fig. 8a). As a result, by counting the number of formed C–C bond, activation energy could be calculated. We define [bond] and [phenyl–Br] as the concentration of the C–C bonds and intact phenyl–Br bonds, respectively, so the rate equation can be expressed as follows:

$$d[\text{bond}]/d\text{t} = k[\text{phenyl}-\text{Br}]^2 \tag{1}$$

Then the concentration of C–C bonds is given as:

$$[\text{bond}] = \frac{k\text{t}[\text{phenyl--Br}]_0^2}{1 + 2k\text{t}[\text{phenyl -- Br}]} + [\text{bond}]_0 \tag{2}$$

where $[\text{phenyl–Br}]_0$ and $[\text{bond}]_0$ refer to the initial concentration before the annealing.

In Fig. 8b, $\ln(k)$ versus T^{-1} is plotted according to the Arrhenius equation, where the k stands for the rate constant. By fitting the three reaction rate constants at higher temperature linearly, activation energy of (0.41 ± 0.03) eV and a prefactor of $(3 \times 10^{6\pm1})$ s^{-1} nm^{-2} for the entire reaction are obtained. Since the much faster

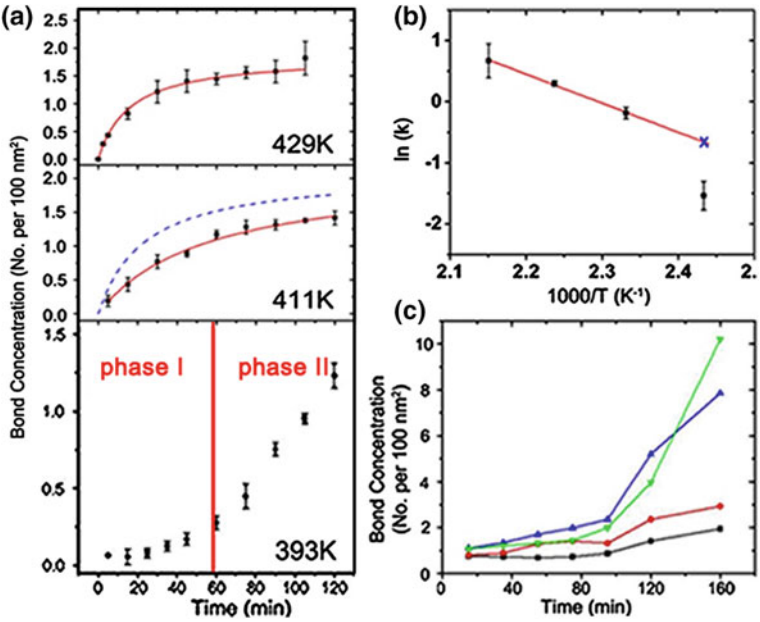

Fig. 8 **a** Bond concentration in Pd-catalyzed coupling of **3** on Au(111) as a function of reaction time at 393 K, 411 K, and 429 K. **b** Arrhenius plot of rate constant *k* obtained from experimental data. **c** Bond concentration in Cu-catalyzed coupling of **3** on Au(111) as a function of reaction time at 399 K (*black*), 417 K (*red*), 435 K (*blue*), and 453 K (*green*). The 453 K data are scaled down by a factor of five [27]

kinetics of phase I indicates an extremely low activation energy, the acquired value is more close to that of phase II alone. Considering the reported activation energy of the Ullmann coupling of iodobenzene on Cu(111) is 1.12 eV [30, 31], and the fact that iodine is more reactive than bromine, our result manifests the higher catalytic activity of Pd than Cu. At 411 K, phase I process cannot be neglected so the equations above are not completely suitable. A higher rate constant could be expected if we neglect phase I at that temperature, as the mark "×" in Fig. 8b, which corresponds to a bond concentration behavior described by the dashed curve in Fig. 8a. The lower value for the experimental bond concentration compared to this hypothesized one indicates the limiting effect of phase I at this temperature.

We found Pd and Cu result in distinct C–C bond formation yield and length distribution of the polymeric chains. When the initial molecule dosage was kept constant, at higher temperatures, Cu-catalyzed reactions show rapid increase (Fig. 8c) in the yield rather than the slight decline for Pd-catalyzed ones (Fig. 8a). Moreover, at specific temperature, Cu-catalyzed reaction always has a much higher yield and longer polymeric chains (Fig. 7), which is as well supported by the length distribution shown in Fig. 9a, b. Dimers are most favored in the Pd-catalyzed reactions with other chains no longer than hexamer, but no apparent length preference is observed in the Cu-catalyzed coupling.

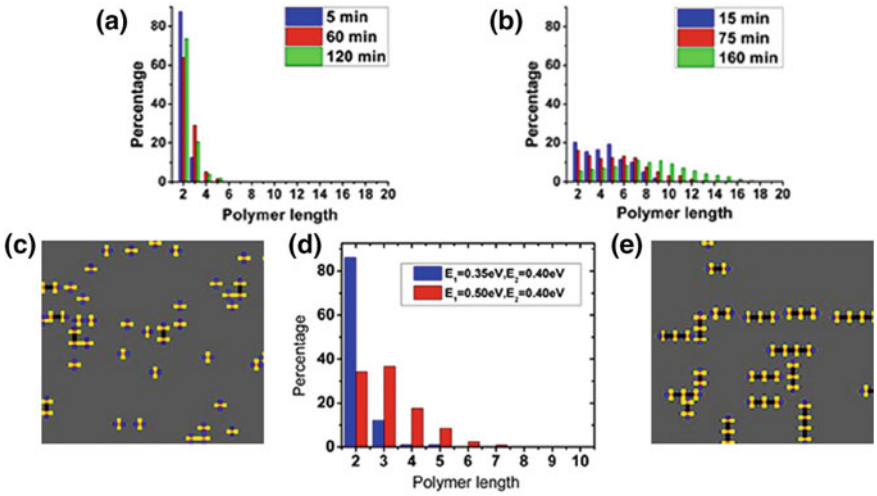

Fig. 9 Length distribution of the polymers catalyzed by **a** Pd at 465 K and **b** Cu at 453 K. **c** and **e** KMC simulated polymeric chains with E_1 = 0.35 eV and E_1 = 0.50 eV, whose length distributions are plotted in **d** [27]

For a better understanding of the difference between Pd and Cu, we carried out KMC simulations [32]. The reaction consists of two irreversible steps: the activation of a monomer's phenyl–Br bond with energy barrier E_1, and the C–C bond formation with energy E_2 between an activated monomer and an inactivated one. According to our experimental results, E_1 was set to be larger for Cu (0.50 eV) than for Pd (0.35 eV), and E_2 was set at 0.40 eV for both. As shown in Fig. 9c, e, a lower E_1 leads to shorter chains. The distribution of polymeric length in the simulation illustrated in Fig. 9d is well reproduces the experimental observation. In the other aspect, the lower E_1 gives a lower yield (10.5 %) of C–C bonds than the higher one (67.7 %).

4 Metal-Coordination Template

Since the first surface-assisted realization of covalent-linked molecular nanostructure by polymerization via Ullmann coupling, as mentioned in the former sections, there has been a big challenge to control the final product. Due to the non-reversibility of covalent bonds, if kinetic trapping would be inevitably introduced in the polymerization processes, then it is difficult to control the size and distribution of the final macromolecular product on surface. Many effect has been made to eliminate this hindrance [33–38]. It was found that polycondensation of boronic acid could generate well-ordered covalent networks with the assistance of water [34, 35]. Gold surface with troughs was also exploited for the confinement

of alkene's polymerization [33]. Besides, molecules functionalized with different halogens were proved to be coupled step by step [38].

When "molecular and supramolecular science meet" [39], it brings out the template synthesis, that is, utilizing non-covalent structure to steer highly ordered covalent organization [40]. For the predesigned templates, various connections, including π–π interactions, hydrogen bond, and metal-ligand bond, have been adopted [41]. As we know, in comparison with covalent bond, coordination bond is less robust but reversible and specifically more flexible. In such consideration, we developed an effective approach of using metal–ligand coordination as template to steer the on-surface polymerization process. The resulting macromolecular structures exhibit a very narrow size distribution and are organized hierarchically through supramolecular assembly.

4.1 Verification of On-Surface Polymerization

Porphyrin derivatives with various end groups were utilized in our experiments [42]. The precursor of 5,15-bis-(4-bromophenyl)-10,20-diphenyl porphyrin (compound **4**) possesses both py(pyridine) groups as coordination sites for metal atoms and bromine groups for Ullmann coupling. It could form 1D metallorganic single-row (SR) chains with Cu atoms on a Au(111) surface at room temperature. In these SR chains, the adjacent molecules have a center-to-center separation of 1.9 nm, featuring py–Cu–py coordination bonds as the linkages (Fig. 10a) [43]. Cu atoms cannot be resolved probably due to electronic effects or tip conditions.

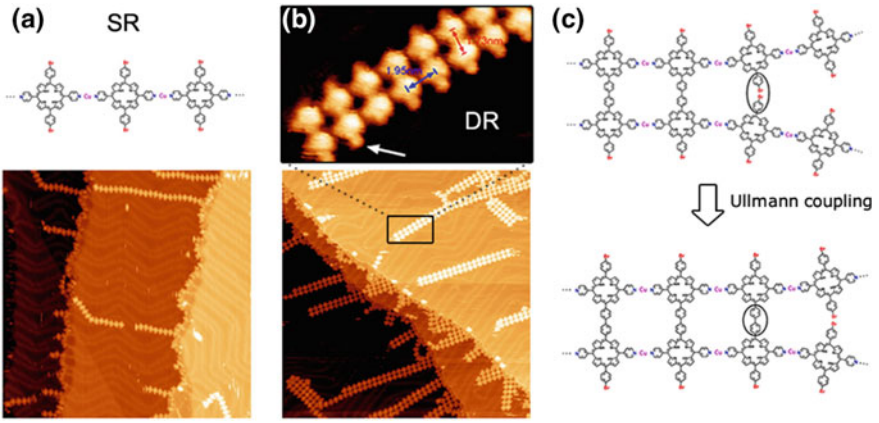

Fig. 10 **a** STM image of SR coordination chain formed from **4** and Cu on Au(111) surface at 298 K (100 nm × 100 nm) with the proposed model. **b** STM image of DR and TR chains after annealing of 453 K (100 nm × 100 nm), with a DR magnified. **c** Scheme of Ullmann coupling assisted by the py–Cu–py coordination template [42]

An annealing of 453 K for 30 min converted these SR chains to ladder-shaped double rows (DR) or triple rows (TR), as shown in Fig. 10b. A close inspection of the DR chain reveals two distinct center-to-center distances: 1.73 nm perpendicular to the chain (red arrow) and 1.95 nm along the chain (blue arrow). While the larger distance is the same as the SR case, the smaller distance is in good agreement with covalent-linked porphyrins. These structural characteristics clearly indicate that the DR chains consist of covalently bonded dimeric macromolecules linked by py–Cu–py coordination bonds along the chain direction, whose model is illustrated in Fig. 10c. It is also notable that there are small protrusions at the side of the chains pointed out with white arrow. These features have been observed on the SR chains and identified as bromine atoms. This phenomenon provides another piece of evidence that the molecules are arranged with their Br groups at the side in the DR chains. It is clear that 453 K annealing has already triggered the coupling of **4** forming covalent-linked dimers [5, 8, 9, 11, 12, 15, 38]. Such a lower activation temperature compared to the case on the pristine Au(111) surface is due to the catalytic effect of Cu.

4.2 Metal-Directed Template

To unravel the role of py functions, we carried out control experiments to explore the difference between **4** and **3** (see Sect. 3.2). Figure 11a shows the Au(111) surface deposited with **4** and Cu with an annealing of 453 K for 60 min. It shows

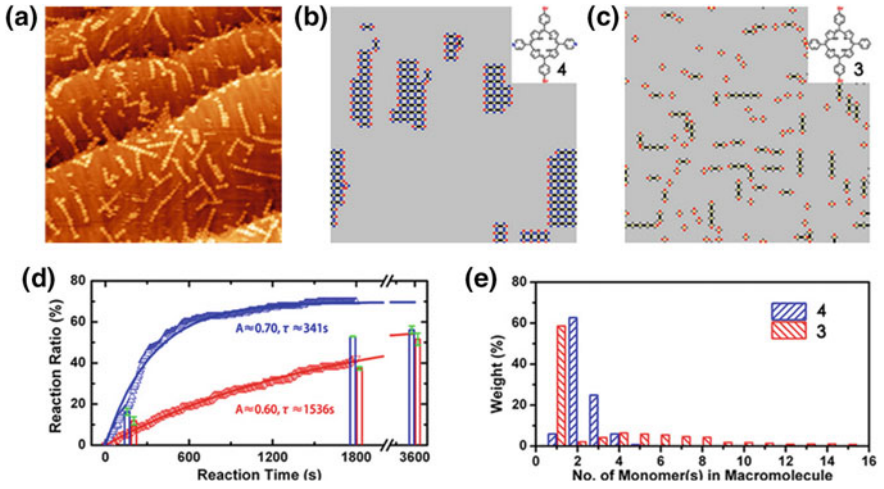

Fig. 11 Comparison of the polymerization of **4** and **3**. **a** STM image of SR chains formed from **3** (100 nm × 100 nm). **b** and **c** KMC simulated structures formed out of **4** and **3**. **d** Reaction ratios of **4** and **3** as a function of reaction time. *Triangle* Simulation results. *Solid line* Exponential fittings. *Vertical bars* Experimental values. *Blue* **4**. *Red* **3**. **e** Experimental weight distribution of the macromolecular structures formed out of **4** and **3** as a function of the size of macromolecule [42]

covalently bonded polymeric chains [12]. Under the same Cu dosage and annealing treatment, we found that the reaction ratios of **3** were always lower than those of **4**, which can be seen from the vertical bars in Fig. 11d. We also conducted KMC simulation of **4** and **3** with Cu at 453 K for 30 min (Fig. 11b, c). For **4**, ladder-like structure is formed with py–Cu–py bonds in one direction (blue) and C–C covalent bond in the orthogonal direction (black). For **3**, only short single chains are generated. Moreover, most of **4** are involved in the coupled architecture, while about 60 % of **3** are adsorbing as isolated monomers. The simulated reaction ratios versus annealing time are plotted in Fig. 11d. With the fitting using function $A(1 - e^{-t/\tau})$, time constant could be obtained, and the value of **4** (341 s) is merely one-fifth of that of **3** (1536 s). However, the prefactor A is comparable for **3** and **4**. Therefore, the simulation verifies that the formation of coordination bonds can significantly enhance the coupling reaction rates.

Distribution of the macromolecular structures of certain sizes was also analyzed for the samples of **3** or **4** after 60-min annealing at 453 K, as shown in Fig. 11e. One can see that monomers account for 5 % in **4** but almost 60 % in **3**, reflecting the lower reaction rates of **3**. Apart from that, the macromolecular structures formed from **3** exhibit a much wider size distribution than from **4**. Majority of **4** (63 %) are coupled in dimeric configuration, and they are organized in order by coordination bonds in contrast to the random distribution of **3**.

Two possible mechanisms might take place during the reaction: (1) the SR chains are decomposed by the annealing and then the free monomers are coupled by covalent bonds. Coordination bonds reform as the sample is cooled down. However, such a process would generate macromolecules of a broad size distribution, and the final coordinated chains would be composed by them and have an inhomogeneous width. As this is not observed in the experiment, this presumption is ruled out. (2) A template-assisted coupling reaction as illustrated in Fig. 10c: a DR chain is grown from a dimeric molecule seed step by step. When two more monomers are anchored separately to the dimer via py–Cu–py bonds, to avoid the spatial conflict, those flexible bonds have to be bent as the model highlighted by circle in Fig. 10c, which could be found in the real structure as circled in Fig. 12b. In this configuration, the Br atoms are brought into proximity to facilitate the Ullmann coupling reaction as in topochemical polymerization processes [44]. According to our simulation, most C–C bonds were formed between the neighboring monomers anchored to the existing chains though coordination bonds; hence, we propose that Cu plays a dual role in promoting the C–C bond formation: One is reducing the reaction barrier as catalyst; one is ligating with py as template to speed up the reaction.

4.3 Size-Limited Polymerization

As discussed in the previous section, dimeric and trimeric chains predominate after the 453 K annealing, as shown in Figs. 10b and 11e. Different annealing temperatures were tested for the reaction of **4** and Cu. In Fig. 12a, it can be found that most of the

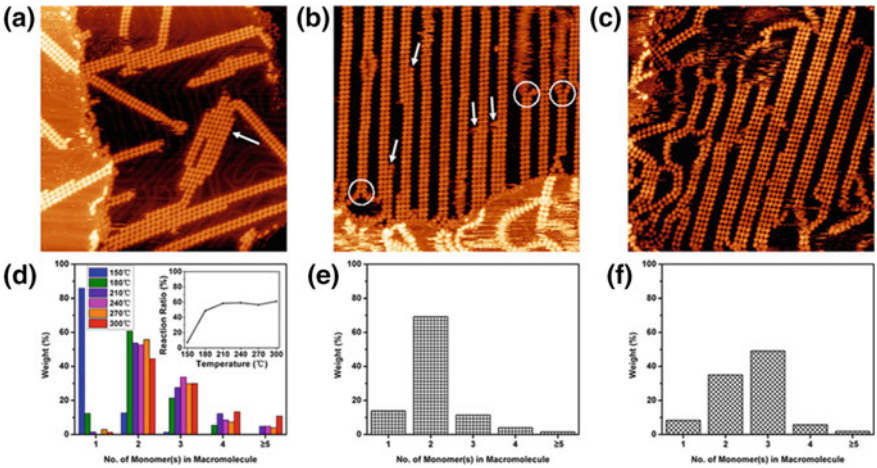

Fig. 12 STM images (100 nm × 100 nm) and weight distribution of chains formed from **4** with different preparation parameters. **a** Molecules were deposited on Au(111) held at 298 K and annealed to 573 K. **b** Weight distribution with different annealing treatments. *Inset* the corresponding reaction ratio. **c** and **d** Deposition was done on the substrate held at 298 K and then annealed to 453 K. **e** and **f** Deposition was done on the substrate with precovered Cu at 513 K [42]

products are DR chains after a 573 K annealing. The size distribution of the macromolecular structures produced at different annealing temperatures is plotted in Fig. 12d. The high-temperature annealing did not significantly enhance the formation of larger oligomers. Tetramers or larger ones are rarely observed, and the largest structure found is heptamer, as marked by the arrow in Fig. 12a. It is worth noting that DR chains are always the predominant structure when the annealing temperature is higher than 453 K.

Besides the size limitation, the chains always show very smooth edges. It implies that the attachment of individual monomers to the side of a chain is unfavorable, and even if it happens, a new row will grow along the side of the chain due to the template effect. In other word, the coordination template steered the polymerization process to favor the replication of the existing smaller (dimeric or trimeric) seed structures over the growth of larger structures, which led to the predominant formation of the dimeric macromolecules.

We prepared a sample with DR chains of low surface coverage, then put more Cu and **4** onto the surface with an additional annealing of 453 K for 30 min. As marked by arrows in Fig. 12b, some sections of several DR chains had been widened to TR chains. However, DR chains are still the main structures, as shown in the size distribution in Fig. 12e. Therefore, most of the lately added molecules either formed new DR chains or prolonged the existing ones, which is consistent with the proposed mechanism. It indicates that for a higher yield of wider chains, larger macromolecular structures must be generated at the early stage as seeds, which will grow longer via a self-replicating process. To verify this proposal, we deposited **4** onto a hot surface (513 K) predosed with Cu. More covalent-linked

trimers or larger macromolecules formed, which triggered the formation of wider chains, as shown in the STM image of Fig. 12c and the size distribution in Fig. 12f. The ratio of the TR chains reached 50 %, exceeding that of the DR chains.

5 Summary and Conclusions

In this chapter, we have discussed the roles of several transition metals in the on-surface Ullmann coupling reaction focusing on three aspects: (1) metal atoms form an organometallic intermediate in the reaction; (2) *intrinsic* metal substrates and *extrinsic* metal deposits catalyze the two reaction steps, and (3) metal-coordination template controls the polymerization via Ullmann coupling.

1. We have identified an organometallic state as an intermediate phase in the reaction. STM and DFT calculations revealed at a single-molecular level that the intermediate consists of biradical terphenyl $(ph)_3$ units that are connected by single Cu atoms through C–Cu–C bridges.
2. We have investigated the catalytic behavior of five transition metals of Ag, Pt, Au, Cu, and Pd. We found that Cu, Ag, and Pt form the organometallic intermediates. Based on statistical analysis of the yields of different species, we propose that the overall catalytic activity ranks as Pt > Au > Cu > Ag while the rate-limiting step varies with the different metals. By means of analyzing the isothermic series of Pd- and Cu-catalyzed reactions, we discovered that the two catalysts result in distinctive bond formation yields as well as reaction rates. We attribute these differences to the distinctive roles the two catalysts play in different reaction steps. We also determined the activation energy of Pd catalysis to be (0.41 ± 0.03) eV, which is lower than the Cu catalysis.
3. Using specially designed bifunctional porphyrin compounds, we have demonstrated that metal coordination can effectively alter the products of the on-surface polymerization. First, the dimeric structure is formed with a very high yield. Second, the macromolecules are organized by metal coordination into supramolecular chains on the surface. These results may shed lights on the design and synthesis of size- and shape-controlled macromolecular systems in the fast emerging field of on-surface synthesis.

The results presented in this chapter highlight the active roles that the transition metals play in the on-surface Ullmann reaction. We emphasize that in spite of the fact that this reaction is one of the most-studied on-surface reactions, more work must be done to get a better understanding as many open questions remain. For example, how does debromination occur? How to describe the molecules after debromination (radical might not be an accurate term)? How do the intermediate states form and convert to the final state? We believe that these questions are to be addressed for other on-surface reactions too.

References

1. Barth, J.V.: Molecular architectonic on metal surfaces. Annu. Rev. Phys. Chem. **58**, 375 (2007)
2. De Feyter, S., Miura, A., Yao, S., Chen, Z., Würthner, F., Jonkheijm, P., Schenning, A.P.H.J., Meijer, E.W., De Schryver, F.C.: Two-dimensional self-assembly into multicomponent hydrogen-bonded nanostructures. Nano Lett. **5**, 77 (2005)
3. Barth, J.V., Weckesser, J., Trimarchi, G., Vladimirova, M., De Vita, A., Cai, C., Brune, H., Günter, P., Kern, K.: Stereochemical effects in supramolecular self-assembly at surfaces: 1-D versus 2-D enantiomorphic ordering for PVBA and PEBA. J. Am. Chem. Soc. **124**, 7991 (2002)
4. Cañas Ventura, M.E., Xiao, W., Wasserfallen, D., Müllen, K., Brune, H., Barth, J.V., Fasel, R.: Self-assembly of periodic bicomponent wires and ribbons. Angew. Chem. Int. Ed. **46**, 1814 (2007)
5. Berger, G., Soubhye, J., Meyer, F.: Halogen bonding in polymer science: from crystal engineering to functional supramolecular polymers and materials. Polym. Chem. **6**, 3559 (2015)
6. Stepanow, S., Lin, N., Barth, J.V.: Modular assembly of low-dimensional coordination architectures on metal surfaces. J. Phys. Cond. Mat. **20**, 184002 (2008)
7. Ullmann, F., Bielecki, J.: Ueber Synthesen in der Biphenylreihe. Ber. Dtsch. Chem. Ges. **34**, 2174 (1901)
8. Grill, L., Dyer, M., Lafferentz, L., Persson, M., Peters, M.V., Hecht, S.: Nano-architectures by covalent assembly of molecular building blocks. Nature Nanotech. **2**, 687 (2007)
9. Lipton Duffin, J.A., Miwa, J.A., Kondratenko, M., Cicoira, F., Sumpter, B.G., Meunier, V., Perepichka, D.F., Rosei, F.: Step-by-step growth of epitaxially aligned polythiophene by surface-confined reaction. PNAS **107**, 11200 (2010)
10. Cai, J., Ruffieux, P., Jaafar, R., Bieri, M., Braun, T., Blankenburg, S., Muoth, M., Seitsonen, A.P., Saleh, M., Feng, X., Müllen, K., Fasel, R.: Atomically precise bottom-up fabrication of graphene nanoribbons. Nature **466**, 470 (2010)
11. Gutzler, R., Walch, H., Eder, G., Kloft, S., Heckl, W.M., Lackinger, M.: Surface mediated synthesis of 2D covalent organic frameworks: 1,3,5-tris(4-bromophenyl)benzene on graphite (001), Cu (111), and Ag (110). Chem. Commun. 4456 (2009)
12. Lafferentz, L., Eberhardt, V., Dri, C., Africh, C., Comelli, G., Esch, F., Hecht, S., Grill, L.: Controlling on-surface polymerization by hierarchical and substrate-directed growth. Nature Chem. **4**, 215 (2012)
13. Bieri, M., Nguyen, M.-T., Gröning, O., Cai, J., Treier, M., Aït-Mansour, K., Ruffieux, P., Pignedoli, C.A., Passerone, D., Kastler, M., Müllen, K., Fasel, R.: Two-dimensional polymer formation on surfaces: insight into the roles of precursor mobility and reactivity. J. Am. Chem. Soc. **132**, 16669 (2010)
14. El Garah, M., MacLeod, J.M., Rosei, F.: Covalently bonded networks through surface-confined polymerization. Surf. Sci. **613**, 6 (2013)
15. Lipton Duffin, J.A., Ivasenko, O., Perepichka, D.F., Rosei, F.: Synthesis of polyphenylene molecular wires by surface-confined polymerization. Small **5**, 592 (2009)
16. McCarty, G.S., Weiss, P.S.: Formation and manipulation of protopolymer chains. J. Am. Chem. Soc. **126**, 16772 (2004)
17. Walch, H., Gutzler, R., Sirtl, T., Eder, G., Lackinger, M.: Material-and orientation-dependent reactivity for heterogeneously catalyzed carbon-bromine bond homolysis. J. Phys. Chem. C **114**, 12604 (2010)
18. Blake, M.M., Nanayakkara, S.U., Claridge, S.A., Fernandez-Torres, L.C., Sykes, E.C.H., Weiss, P.S.: Identifying reactive intermediates in the Ullmann coupling reaction by scanning tunneling microscopy and spectroscopy. J. Phys. Chem. A **113**, 13167 (2009)

19. Sykes, E.C.H., Han, P., Kandel, S.A., Kelly, K.F., McCarty, G.S., Weiss, P.S.: Substrate-mediated interactions and intermolecular forces between molecules adsorbed on surfaces. Acc. Chem. Res. **36**, 945 (2003)
20. Wang, W., Shi, X., Wang, S., Van Hove, M.A., Lin, N.: Single-molecule resolution of an organometallic intermediate in a surface-supported ullmann coupling reaction. J. Am. Chem. Soc. **133**, 13264 (2011)
21. Wang, S., Wang, W., Lin, N.: Resolving band-structure evolution and defect-induced states of single conjugated oligomers by scanning tunneling microscopy and tight-binding calculations. Phys. Rev. Lett. **106**, 206803 (2011)
22. Chung, K.-H., Koo, B.-G., Kim, H., Yoon, J.K., Kim, J.-H., Kwon, Y.-K., Kahng, S.-J.: Electronic structures of one-dimensional metal-molecule hybrid chains studied using scanning tunneling microscopy and density functional theory. Phys. Chem. Chem. Phys. **14**, 7304 (2012)
23. Blunt, M.O., Russell, J.C., Champness, N.R., Beton, P.H.: Templating molecular adsorption using a covalent organic framework. Chem. Comm. **46**, 7157 (2010)
24. Russell, J.C., Blunt, M.O., Garfitt, J.M., Scurr, D.J., Alexander, M., Champness, N.R., Beton, P.H.: Dimerization of tri(4-bromophenyl)benzene by aryl-aryl coupling from solution on a gold surface. J. Am. Chem. Soc. **133**, 4220 (2011)
25. Park, J., Kim, K.Y., Chung, K.-H., Yoon, J.K., Kim, H., Han, S., Kahng, S.-J.: Interchain interactions mediated by Br adsorbates in arrays of metal-organic hybrid chains on Ag (111). J. Phys. Chem. C **115**, 14834 (2011)
26. Wintterlin, J., Volkening, S., Janssens, T., Zambelli, T., Ertl, G.: Atomic and macroscopic reaction rates of a surface-catalyzed reaction. Science **278**, 1931 (1997)
27. Adisoejoso, J., Lin, T., Shang, X.S., Shi, K.J., Gupta, A., Liu, P.N., Lin, N.: A single-molecule-level mechanistic study of Pd-catalyzed and Cu-catalyzed homocoupling of aryl bromide on an Au(111) surface. Chem. Eur. J. **20**, 4111 (2014)
28. Molnar, A.: Efficient, selective, and recyclable palladium catalysts in carbon-carbon coupling reactions. Chem. Rev. **111**, 2251 (2011)
29. Yin, L., Liebscher, J.: Carbon-carbon coupling reactions catalyzed by heterogeneous palladium catalysts. Chem. Rev. **107**, 133 (2007)
30. Nguyen, M.-T., Pignedoli, C.A., Passerone, D.: An ab initio insight into the Cu(111)-mediated Ullmann reaction. Phys. Chem. Chem. Phys. **13**, 154 (2011)
31. Meyers, J.M., Gellman, A.J.: Effect of substituents on the phenyl coupling reaction on Cu (111). Surf. Sci. **337**, 40 (1995)
32. Li, Y., Lin, N.: Combined scanning tunneling microscopy and kinetic Monte Carlo study on kinetics of Cu-coordinated pyridyl-porphyrin supramolecular self-assembly on a Au(111) surface. Phys. Rev. B **84**, 125418 (2011)
33. Zhong, D., Franke, J.-H., Podiyanachari, S.K., Blömker, T., Zhang, H., Kehr, G., Erker, G., Fuchs, H., Chi, L.: Linear alkane polymerization on a gold surface. Science **334**, 213 (2011)
34. Dienstmaier, J.F., Medina, D.D., Dogru, M., Knochel, P., Bein, T., Heckl, W.M., Lackinger, M.: Isoreticular two-dimensional covalent organic frameworks synthesized by on-surface condensation of diboronic acids. ACS Nano **6**, 7234 (2012)
35. Dienstmaier, J.F., Gigler, A.M., Goetz, A.J., Knochel, P., Bein, T., Lyapin, A., Reichlmaier, S., Heckl, W.M., Lackinger, M.: Synthesis of well-ordered COF monolayers: surface growth of nanocrystalline precursors *versus* direct on-surface polycondensation. ACS Nano **5**, 9737 (2011)
36. Guan, C.-Z., Wang, D., Wan, L.-J.: Construction and repair of highly ordered 2D covalent networks by chemical equilibrium regulation. Chem. Comm. **48**, 2943 (2012)
37. Weigelt, S., Bombis, C., Busse, C., Knudsen, M.M., Gothelf, K.V., Lægsgaard, E., Besenbacher, F., Linderoth, T.R.: Molecular self-assembly from building blocks synthesized on a surface in ultrahigh vacuum: kinetic control and topo-chemical reactions. ACS Nano **2**, 651 (2008)

38. Lafferentz, L., Eberhardt, V., Dri, C., Africh, C., Comelli, G., Esch, F., Hecht, S., Grill, L.: Controlling on-surface polymerization by hierarchical and substrate-directed growth. Nature Chem. **4**, 215 (2012)
39. Anderson, S., Anderson, H.L., Sanders, J.K.M.: Expanding roles for templates in synthesis. Acc. Chem. Res. **26**, 469 (1993)
40. Thompson, M.C., Busch, D.H.: Reactions of coordinated ligands. IX. Utilization of the template hypothesis to synthesize macrocyclic ligands *in situ.* J. Am. Chem. Soc. **86**, 3651 (1964)
41. Sprafke, J.K., Kondratuk, D.V., Wykes, M., Thompson, A.L., Hoffmann, M., Drevinskas, R., Chen, W.-H., Yong, C.K., Kärnbratt, J., Bullock, J.E., Malfois, M., Wasielewski, M.R., Albinsson, B., Herz, L.M., Zigmantas, D., Beljonne, D., Anderson, H.L.: Belt-shaped π-systems: relating geometry to electronic structure in a six-porphyrin nanoring. J. Am. Chem. Soc. **133**, 17262 (2011)
42. Lin, T., Shang, X.S., Adisoejoso, J., Liu, P.N., Lin, N.: Steering on-surface polymerization with metal-directed template. J. Am. Chem. Soc. **135**, 3576 (2013)
43. Adisoejoso, J., Li, Y., Liu, J., Liu, P.N., Lin, N.: Two-dimensional metallo-supramolecular polymerization: toward size-controlled multi-strand polymers. J. Am. Chem. Soc. **134**, 18526 (2012)
44. Nagahama, S., Matsumoto, A.: Two-dimensional polymer synthesis through the topochemical polymerization of alkylenediammonium muconate as a multifunctional monomer. J. Polym. Sci. Part A: Polym. Chem. **42**, 3922 (2004)

On-Surface (Cyclo-)Dehydrogenation Reactions: Role of Surface Diffusion

José A. Martín-Gago, Anna L. Pinardi and José I. Martínez

Abstract Creating or connecting together large organic molecules, as polycyclic aromatic hydrocarbons (PAH), readily on surfaces arises as a step of paramount importance towards a true advance in the field of nanotechnology, and particularly of molecular electronics. On-surface synthesis can be regarded as an efficient means to build new molecular species by using bottom-up strategies. In particular, temperature-driven surface-catalysed cyclodehydrogenation (CDH) processes have burgeoned in last years as a novel and powerful route to efficiently transform (hetero-) aromatic molecular precursors into a large variety of *a la carte* hierarchical nanostructures: from fullerenes and triazafullerenes, aromatic domes, or nanotubes, to polymeric nanonetworks and, depending on the specific precursor utilized, even to pristine and functionalized graphene. In the first section of this chapter, the foundations and main aspects of the on-surface synthesis methodology and CDH reactions are revised, as well as the current status in the field up to the date. In Sect. 2, the most advanced first-principles theoretical tools currently available for the characterization of CDH processes will be summarized and described, including the novel theoretical strategies to monitorize CDH reaction paths and to calculate STM images. The following two sections will report on a very recently paradigmatic example related to the tailored formation of *N*-doped nanoarchitectures by diffusion-controlled on-surface (cyclo-)dehydrogenation of heteroaromatics, where the strength of the PAH–substrate interaction dramatically rules the competitive reaction pathways (CDH versus dehydrogenative polymerization). On the basis of those findings, the stepwise formation of *N*-doped nanohelicenes, nanographenes, nanodomes, molecular networks and graphene from the same heteroaromatic precursor through subsequent dehydrogenations on Pt(111) upon thermal-annealing will be fully described. The combined experimental (in situ UHV-STM, XPS and NEXAFS) and detailed computational DFT-based studies provide a full atomistic and chemical description of the intermediate reaction stages along the dehydrogenation path.

J.A. Martín-Gago (✉) · A.L. Pinardi · J.I. Martínez
Department Surfaces, Coatings and Molecular Astrophysics,
Institute of Materials Science of Madrid (ICMM-CSIC), 28049 Madrid, Spain
e-mail: gago@icmm.csic.es

A. Gourdon (ed.), *On-Surface Synthesis*, Advances in Atom and Single Molecule Machines, DOI 10.1007/978-3-319-26600-8_3

1 Introduction

1.1 Towards an On-Surface Synthesis

The outstanding electronic properties of molecular assemblies have generated significant expectations about the capability of fabricating new devices directly on surfaces. Nowadays, molecular electronics is regarded, not only as a mean of extending Moore's law beyond presently foreseen limits, but also as the emergence of exciting new potentialities for faster, smaller and cheaper electronic devices.

One of the most promising bottom-up strategies consists of the development of new on-surface synthesis methodologies for fabricating cyclic molecular compounds. Molecules or organic networks are now readily assembled on a surface, either created or fused from their constituent building blocks throughout the establishment of covalent bonds, as a molecular puzzle or origami [1–3]. This idea of assembling molecules to form superior architectures was originally proposed by Coté and co-workers almost a decade ago [4]. These authors designed and synthesized periodic extended organic structures in which the building blocks were linked by strong covalent bonds, organized as porous and stable networks. Chemical reactions of cyclic molecules were first obtained on surfaces nearly simultaneously by different groups. Hence, two years later, Grill et al. reported the formation of nanoarchitectures of controlled dimensionality by covalent assembly of molecular building blocks [5], Weigelt et al. achieved the synthesis of imine [6], and Rim et al. [7] showed the formation of molecular aromatic hemispheres. In the following months, an assortment of different reactions leading to large tailor-made organic molecules was reported. Although this synthetic route is still in its embryonic state, the first breakthroughs have already been reported. Thus, in less than a decade, the formation of new fullerene species [8, 9], nanographene [10], graphene nanoribbons [11], domes and aromatic hemispheres [6, 12, 13], surface networks and molecular chains [12], or nanotubes [14, 15], among others, has been achieved. Therefore, highly attractive π-electron systems on metal [5, 7–20], semiconductor or insulator [21, 22] surfaces are becoming available.

On-surface chemistry presents several figures of merit. First, the structures formed attain high stability leading to steady conformations and consequently, to time invariability with a low thermal degradation of the structural properties. Thus, they could be transferred from the substrate where have been grown, usually a metal, to another one, more suitable for applications. A second outstanding feature of covalent assemblies is an efficient electron transport throughout the formed bonds, which makes the networks appropriate for molecular applications [1, 2]. Third, these mechanisms could give rise to the formation of molecular species that cannot be synthetized by standard wet-chemistry protocols. Finally, this strategy requires the use of surface science characterization techniques and highly controlled environments, and this decreases the possibility of contamination leading to chemically pure structures.

On the other hand, during the last decade, surface science has developed a powerful set of experimental techniques enabling us to unveil the atomic structure of surfaces and ad-layers with a precision of hundredths of an Å and accurately reproduce most electronic features by using first-principles frameworks, as well as predicting and monitoring the reaction paths. These surface-sensitive techniques make it possible to investigate reaction mechanisms at the nanoscale and sometimes even real-time processes. Among them, scanning tunnelling microscopy (STM) has become an established technique for exploring molecular assemblies. Its ability to work in different environments and temperature makes it a valuable tool in the exploration of reaction mechanisms. Unfortunately, STM does not always provide chemical information. Although molecular-resolved STM images of the new molecules or created networks are well resolved, they do not unequivocally prove that a particular reaction has taken place, i.e., which are the bonds behind the structures displayed in the images. STM images need to be combined with other complementary spectroscopic techniques or theoretical methods, such as X-ray photoemission spectroscopy (XPS), infrared spectroscopy, ultra-violet photoemission spectroscopy (UPS) and near-edge X-ray absorption spectroscopy (NEXAFS). All these techniques can be used to determine which are the chemical reactions coupling molecules between them or transforming the molecular precursors. Current ab initio calculations based on density functional theory (DFT) approximation can be regarded as truly in silico experiments, helping us to understand the basis of reaction mechanisms.

A general mechanism for producing covalently bonded molecular networks or new molecular species is schematically described in Fig. 1. As it can be seen, the

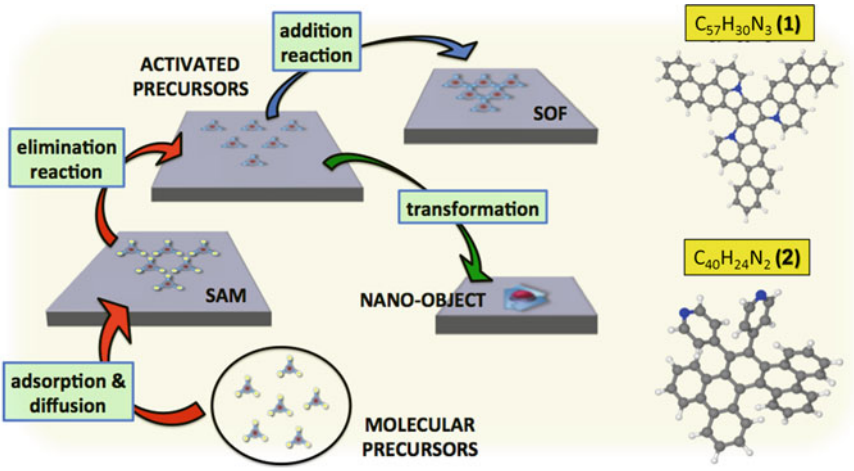

Fig. 1 *Right* Schematic representation of the on-surface synthesis process (adapted from Ref. [3]). The first step indicates the deposition of the molecular precursor on the surface; the second one, the formation of a self-assembled monolayer (*SAM*) on the surface; the third, a temperature-driven elimination reaction of the protecting groups, and the fourth the formation of either individual nanostructures or extended frameworks. *Left* Ball-and-stick models of the heteroaromatic molecules used as molecular building blocks in this chapter: (**1**) $C_{57}H_{33}N_3$; (**2**) $C_{40}H_{24}N_2$

aim of on-surface synthesis is the formation of macromolecular assemblies or new molecular nanoarchitectures through the molecular transformation of the constituent building blocks [5]. Two are the main routes for achieving this goal. The first one leads to polymeric networks of variable dimensionality, whereas the second transforms a molecular precursor into another molecular structure (see Fig. 1). The idea is to use molecular precursors to build-up complex nanostructures that can range from purely 2D organic layers, networks or templates, to 1D nanowires or zero-dimensional (0D) nanoobjects. In this outlined picture, the first step is to obtain the desired molecular bricks or reagents. Thus, the desired precursor, represented in Fig. 1 by reddish spheres, is usually synthesized with a molecular connector at the borders (small yellow ball in Fig. 1). These linkers, connectors or end-groups stabilize the molecule termination and they could be halide elements, methyl, amine groups or simply hydrogen atoms.

The on-surface covalent coupling methodology [5, 16–18, 21–27] makes use so far of a limited portfolio of useful carbon-carbon bond forming reactions: cyclodehydrogenation (CDH) (analogous to Scholl reaction), dehydrogenative oligomerization or polymerization, radical dimerization (analogous to Ullmann coupling), carbene dimerization and aryl halide-alkyne coupling (analogous to Sonogashira reaction). Among these reactions, CDH (intramolecular oxidative C–C coupling) and dehydrogenative oligo- or polymerization (intermolecular oxidative C–C coupling) are especially attractive. The processes formally correspond to C–H activation of both precursors followed by their (cross)coupling [3].

After this introduction, it should be clear that the bottom-up approach to achieve new functional nanostructures and two-dimensional (2D) materials should retain the key features of a traditional synthesis, but also exploit specific phenomena such as on-surface self-assembly and reactivity of individual molecular components to covalently interconnect the outcome. This is particularly important when doping is required to modify the electronic properties of the new 2D materials, such as graphene. Substitutional doping is a powerful way of tailoring the material properties [28], and the use of heteroaromatic precursors for the bottom-up reaction permits an easy and rational control of the doping in the final reaction outcome.

1.2 The Supporting Surface

The surface structure plays an important role in the reactions. Not only because it lowers the energy barrier, but also because it brings together different adsorbed precursors through a diffusion mechanism. The first process is related to the energetics of the system, whereas the second to kinetical aspects. Whether the reaction is driven by kinetics or thermodynamics depends on the diffusion/deposition-rate ratio. A kinetic regime during growth makes possible the formation of metastable assemblies, whereas a thermodynamically controlled process leads to equilibrium structures [29].

The knowledge acquired with heterogeneous catalysis tells us that the reactivity of a metal is intimately related to the structure of its surface, and in particular on the electronic configuration of its d-band. The 12 atomic elements of groups VIII–XI of the periodic table are the ones that exhibit catalytic properties, and can be divided into two different groups. Both, the physical properties and their ability to react with particular species change dramatically when moving from a group to another. These are the Platinum group metals (Ru, Rh, Pd, Os, Ir and Pt), the base metals (Fe, Co, Ni) and the coinage metals (Cu, Ag, Au). The role of a metal surface on the CDH mechanism was studied experimentally and theoretically in detail for the specific case of Cu(111) [10], where nanographene was formed following a rational methodology from a PAH precursor.

In the next sections, we will see that the strength of the surface–adsorbate interaction can control the formation of new tailored nanostructures with different dimensionality. This interaction depends on the type of surface and thus, controlling the diffusion of the precursors with the choice of the metal surface, one can drive the reaction towards the formation of zero-dimensional nanoobjects, or towards the formation of covalent polyaromatic networks.

1.3 (Cyclo-)Dehydrogenation Reactions

Dehydrogenation and CDH reactions are among the most common in heterogeneous catalysis, because of the outstanding properties of the platinum group metals to cleave the C–H bond. For example, the Pt(111) surface is known to be a good catalyst towards dehydrogenation of hydrocarbons and of PAHs [3, 8, 30, 31], because of the particular electronic structure of its d-band. In some cases, such as for methane and ethylene, the molecules readily dehydrogenate at room temperature (RT) [30]; however, depending on the precursor, sometimes this reaction needs to be promoted by an external injection of energy, which can be provided by the annealing of the sample. Dehydrogenation of many aromatic molecules, such as benzene, takes place spontaneously at room temperature just after the molecule reaches many metallic surfaces. Thus, a large number of small PAH, as well as linear hydrocarbons, easily dehydrogenate upon adsorption on a Pt(111) surface due to the spontaneous scission of the C–H bond [32]. Note the strong catalytic effect of the substrate to overcome the 4.5 eV needed to break the C–H bond [33].

There are many examples of organic molecules readily dehydrogenated on surfaces [3]. However, the undersized H atom is difficult to detect. These types of reactions are unappreciated by STM and hardly followed by the XPS technique. As we will see in Sect. 4, the core-level shifts induced by dehydrogenation are usually smaller of 0.5 eV, and therefore, synchrotron radiation-based XPS is required. Hence, thermal programmed desorption (TPD) appears to be the most suitable technique to follow dehydrogenation. However, in order to detect these processes, and particularly due to the experimental difficulty to differentiate hydrogen atoms

specifically emitted from the PAH under study, the use of deuterium atoms substituting some of the hydrogen atoms of the precursor is appealing, as in the example of Ref. [8].

On the other hand, latest advances in atomistic and molecular modelling have permitted the possibility of fully characterizing metal–organic interfaces within a high degree of accuracy. These theoretical techniques lately have been applied to fully characterize a large variety of CDH reactions, manifesting an excellent agreement with the experimental evidence and, even in some cases, showing a highly predictive added value.

1.4 Background and Current Status of On-Surface CDH Reactions

Let us chronologically revisit the most important advances in the field of the CDH reactions up to the date. Almost a decade ago, Rim and co-workers activated the field and burgeoned as the pioneer group investigating by the first time the temperature-driven and surface-catalysed CDH of PAH [7]. In their original work, the authors described the chemical transformations of hexabenzocoronene (HBC) deposited on a clean Ru(0001) surface after thermal-annealing up to 750 K, where the original precursor resulted in aromatic hemispheres after observing a sequential CDH process. The fundamental inspiration for this work was the interest of the mentioned precursor and its interaction with transition metal surfaces, which was driven by its relationship to the end cap of a carbon nanotube, to polynuclear aromatic hydrocarbons, and to reactor carbonization. Even though HBC is a large and multifunctional molecule, the unique advantages offered by its high symmetry (there are only five types of C atoms) simplify the interpretation of the fundamental surface-molecule chemistry. On the other hand, Ruthenium played a very important role in this investigation as a metallic scaffold able to p-bond to HBC, and due to its excellent catalytic activity in many processes such as Fischer–Tropsch and olefin metathesis.

A step forward in the CDH reactions field was given by Otero and co-workers thanks to the synthesis of the heteroaromatic PAH $C_{57}H_{33}N_3$ [34, 35]. In this work, the formation, for the first time, of triazafullerene $C_{57}N_3$ molecules by using a highly efficient surface-catalysed CDH process was achieved. Its shape was specifically designed to yield to the formation of a triazafullerene via CDH. The precursor was deposited under UHV conditions on a clean Pt(111) surface: upon annealing at 720 K, it underwent a complete surface-catalysed CDH and transformed, like a nanoorigami, into the corresponding triazafullerene molecules with about 100 % yield. The same procedure was repeated, and the same result was obtained, using the similar precursor $C_{60}H_{30}$. Details about this transformation reaction will be given in subsequent sections.

Amsharov and collaborators [9] also investigated formation of fullerenes from similar precursors. In particular, they achieved the on-surface synthesis of the higher fullerene C_{84} from CDH of $C_{84}H_{42}$. In their work, Amsharov et al. focused on the importance of the design of the precursor for achieving the desired result. They provided evidence that only the correctly programmed precursor can transform into the desired outcome. To this goal, they synthesized two different isomers of $C_{60}H_{30}$ molecules and showed that only one of them can turn into a fullerene via on-surface CDH. Therefore, they proved that the surface-catalysed CDH processes do not involve C–C bond rearrangement and that the "cage formation proceeds through dehydrogenation and the zipping of newly formed bonds at preselected positions only" [9]. These authors also showed that the CDH of the modified isomer of $C_{60}H_{30}$ precursor led to open-cage fullerene, discerning among four types of open-cage fullerenes, depending on which C–H bonds broke to form new C–C bonds. Therefore, they were able to superimpose the models of open-cage fullerenes to the STM images. Importantly, they found that the molecules bend downwards upon annealing.

Following this line, Treier and co-workers proposed in 2011 a surface chemical route that allowed for the atomically precise fabrication of tailored nanographenes from polyphenylene precursors [10]. In their original work, the CDH of a prototypical polyphenylene on Cu(111) was studied combining STM and DFT. They found that the thermally induced CDH proceeded via several intermediate steps, two of which can be stabilized on the surface, yielding unprecedented insight into a dehydrogenative intramolecular aryl–aryl coupling reaction. The authors also proved that, although the reaction was catalysed on this particular substrate, a hybrid simulation suggested that the reaction could also proceed—although in a different way—on an inert substrate that interacts with the adsorbate through dispersive interactions only, hence favouring planarized conformations. Through chemical synthesis of appropriate polyphenylene precursors (bearing structural resemblance to, or comprising cyclohexa-o-p-o-p-o-p-phenylene (CHP) units) and on-surface CDH, this might offer a route to substrate-supported, tailor-made graphene nanoribbons and nanographenes on technologically relevant substrates.

Very recently, on-surface CDH has been extended to the synthesis of ultrasoft singly capped single-wall carbon nanotubes (SWCNTs), that is, SWCNT end cap with a short tube segment attached. Such molecules represent ideal seeds for subsequent epitaxial elongation into isomerically pure SWCNTs. This idea was previously suggested by Mueller et al. [14], but the key point in this process is to avoid uncontrolled, spontaneous nucleation of end caps by providing ultrasoft nanotube seeds (specially designed molecular precursors), which unambiguously dictates the chiral index of these SWCNTs forming on epitaxial elongation. To tackle this challenge, Sánchez-Valencia and co-workers [15] have recently designed and synthesized by multistep organic synthesis the precursor $C_{96}H_{54}$. Upon intramolecular CDH, it affords seed S1, an ultra-short singly capped (6,6) SWCNT bearing a carbon nanotube segment.

1.5 Designing the Molecular Precursors

Nowadays, many different kinds of molecular precursors can be synthesized *a la carte* by organic chemists. New synthetic routes based on catalytic elements become more efficient in the determination of the reaction products. As the organic chemists synthetize more complex and focused molecular precursor, new blue-printed nanostructures will be fabricated. The adequate choice of the geometry of the precursor is of paramount importance to programme the outcome of the CDH reaction [7–9]. Thus, the work together with organic chemists has become essential.

Another advantage of the CDH methodology is that heteroatoms can be easily included into the fabricated nanoarchitecture and thus permits an easy and rational control of the doping in the final reaction outcome. In order to illustrate these ideas, the examples of Chaps. 3 and 4 are performed with two different heteroaromatic precursors, **1** and **4** (see Fig. 1), which have been intentionally fabricated to obtain a final targeted outcome.

The threefold symmetric clover-shaped and nearly flat crushed-fullerene precursor **1** ($C_{57}H_{33}N_3$) was already shown in Sect. 1.4 to undergo CDH [8] on single-crystal platinum surfaces yielding triazafullerene **2** ($C_{57}N_3$) by removing 33 H atoms and the consequent formation of new C–C bonds. This molecule was synthesized by Gómez-Lor et al. [34]; its shape was specifically designed to yield to the formation of a triazafullerene via CDH.

The easily accessible pyridyl-substituted dibenzo[5]helicene **4** ($C_{40}H_{24}N_2$) is a non-planar helical molecule. Precursor **4** can flatten through on-surface CDH by the removal of 8 H atoms: the resultant formation of four new C–C bonds leads to the achievement of 2,5-diazahexabenzocoronene **5** ($C_{40}H_{16}N_2$), 2 N-HBC, namely *N*-doped nanographene.

2 Theoretical Characterization Tools for CDH Processes

2.1 Ground-State Characterization

2.1.1 Structure and Energetics of the Interfaces

The latest advances in atomistic and molecular modelling have allowed the possibility of fully characterizing metal–organic interfaces within a high degree of accuracy, showing an excellent agreement with the experimental evidence. In particular, one of the most accurate and feasible theoretical frameworks for the structural characterization of the different systems involved in (cyclo-)dehydrogenation reactions is DFT. DFT is powerful to obtain optimal structures and total energies through an effective combination of several atomistic simulation packages, such as the fast and efficient localized-basis-set codes [36–38], and the accurate plane-wave simulation packages [39–41]. At this point, it is important to remark

that the geometrical optimization processes can be faced by structural relaxations at 0 K, or by finite-temperature dynamical quenching molecular dynamics when the effect of an external temperature has to be included. On the other hand, depending on the nature of the system, size or electronic character, the geometric structure can be described by a large variety of different exchange-correlation parametrizations, such as local-density approximation (LDA), density gradient-dependent approximation (GGA), or hybrid functionals (combining both the previous schemes). LDA arises as a more adequate scheme for systems with metallic character, while GGA yields to more accurate results for semiconductors and insulators. Both the localized-basis set and the plane-wave DFT-based implementations previously mentioned [36–41] allow using accurate parametrizations for the van der Waals forces and energies, as described in next subsection.

2.1.2 van der Waals (vdW) Interaction

There is strong evidence that van der Waals (vdW)—or dispersion forces—play a paramount role in the adsorption mechanism of aromatic molecules on metal surfaces [12, 22, 42], usually leading, in comparison with non-vdW DFT calculations, to a significant increase of the adsorption energies and distances, and, what is even more relevant, to non-negligible geometric distortions of both the organic and the substrate. On this basis, in order to properly account van der Waals interactions for the different systems participating in (cyclo-)dehydrogenation reactions, both DFT schemes introduced in previous paragraph [36–41] can be improved by the inclusion of essentially equivalent parametrizations of the vdW interaction. Many different ways can be adopted to implement the vdW interaction in this kind of DFT-based implementations. Nevertheless, herein we will summarize the main points of the most (in our opinion) adequate ones, according to the systems currently participating in the (cyclo-)dehydrogenation reactions from the theoretical point of view. On one side, we can treat the vdW forces and energies within the localized-basis-set codes by the dipolar approximation, where all the atomic dipoles can be obtained from all the counterparts involved in the whole system by a summation rule. The total sum of those contributions will provide the vdW correction to the conventional DFT results [43, 44]. On the other side, plane-wave simulation packages can use an empirical efficient van der Waals (vdW) R^{-6} correction to add dispersive forces to conventional density functionals (DFT-D) [45]. In this method, the vdW correction is added to the DFT total energy by the expression $E_{\mathrm{vdW}} = \sum_{i,j} \frac{C_{ij}}{R_{ij}^6} f(R_{ij})$, where C_{ij} and R_{ij} are the vdW coefficients and the distance between atom i and j, respectively. The vdW coefficients can be calculated as described by Elstner et al. [46] and $f(R_{ij})$ is a damping function which prevents a divergence in the energy as R_{ij} tends to zero as. $f(R_{ij}) = \left(1 - \exp\left[-3.0\left(\frac{R_{ij}}{R_{0ij}}\right)^7\right]\right)^4$, where R_{0ij} is the sum of atomic van der Waals radii. They can be calculated from the vdW radii provided by Gavezzotti and co-workers [47–49].

2.1.3 Improving the Electronic Structure Description: Many-Body Perturbation Theory Corrections

For the description of the electronic structure, when a conventional DFT-based framework is sufficient, both previously mentioned implementations can be employed [36–41]. Nevertheless, DFT calculations of energy band structures have well-known limitations due to the approximate description of exchange and correlation (XC) effects between the electrons, such as the incorrect asymptotic behaviour of the XC potential and the underestimation of the magnitude of the electronic energy gap in semiconductors [50]. A similar error can be expected for the gap between occupied and unoccupied electronic states (HOMO–LUMO gap) in finite clusters, nanoparticles [51] and metal–organic interfaces (which is the case in most temperature-driven and surface-catalysed CDH processes) [52, 53]. Those errors could affect the energies of the excited electronic states, and thus the band structure, the photoabsorption spectrum, the electron–phonon coupling and, what is even more important in this case, theoretical spectroscopical quantities. For this reason, it is possible to correct, when necessary, the DFT band structures using many-body perturbation theory. For this purpose, once the LDA (GGA or hybrid) electronic band structure is established, one can calculate the many-body corrections to the electronic band structure by combining two different techniques. First, the quasi-particle corrections within the 0th-order Green function screened-interaction approach (G_0W_0) [54–56] to account for the exchange-correlation self-energy, which is poorly described by conventional DFT. A basic input ingredient in the G_0W_0 calculations will be the LDA electronic structure as extracted from the conventional DFT codes. On the other hand, it is well known that the G_0W_0 calculations lead to more accurate band gaps and to an improved description of the k-dispersion of the band structure [55]. Second, taking the corrected G_0W_0 electronic structure as input, it is possible to apply the Bethe–Salpeter equation (BSE) formalism [51, 57, 58], where the aforementioned quasi-particle G_0W_0 approach is further corrected to account for excitonic effects in the unoccupied and excited states. These excitonic effects (related to the electron–hole interaction) are of particular importance in systems involving transition metal atoms, which will be the case in most of temperature-driven and surface-catalysed CDH processes. To successfully apply the mentioned many-body corrections, a large amount of unoccupied electronic bands will be necessary to obtain converged self-consistent results.

2.2 *(Cyclo-)Dehydrogenation Kinetic Barriers: Reaction-Path Energy Characterization*

One of the most important issues to take into account when dealing with (cyclo-) dehydrogenation processes of heteroaromatics on surfaces is that, during the thermal-annealing process, not all the hydrogens of the molecules are lost and

detached at the same temperature. This fact is related to the necessary energy to remove hydrogen atoms in different positions and forming different C–H bonds, with different binding energies. This fact causes the formation of stable intermediate structures upon annealing, and governs the (cyclo-)dehydrogenation reaction path. Is at this point where an accurate theoretical framework can be used to predict the binding energies of the different hydrogen atoms forming the molecules, and the strength of the different C–H bonds in the molecule? If one knows a priori which are the hydrogen atoms with a lower binding energy, the possibilities to predict a realistic and feasible (cyclo-)dehydrogenation path are substantially increased. The connection between different molecules or the formation of reaction intermediates from the initial precursor (via the formation of new C–C bonds from dehydrogenated C atoms) with the increasing temperature will be more intuitive and evident towards the prediction of the subsequent steps along the dehydrogenation reaction. For that purpose, DFT-based calculations can be used to efficiently evaluate binding energies of the different hydrogen atoms forming an organic molecule just by taking total energy differences between the molecule with and without a particular hydrogen atom (see Fig. 2). On the basis of that information, the reaction path can be constructed by sequentially removing the less bonded hydrogen atoms [12].

Of course, this procedure could be seen as a naïf starting point that has to be validated. The effect of the interaction with the surface atoms can strongly modify the energy balance. Also, steric arguments become important, as it will be later discussed. Nevertheless, this initial strategy could be an adequate guide, mainly for those cases where the interaction with the surface is weak.

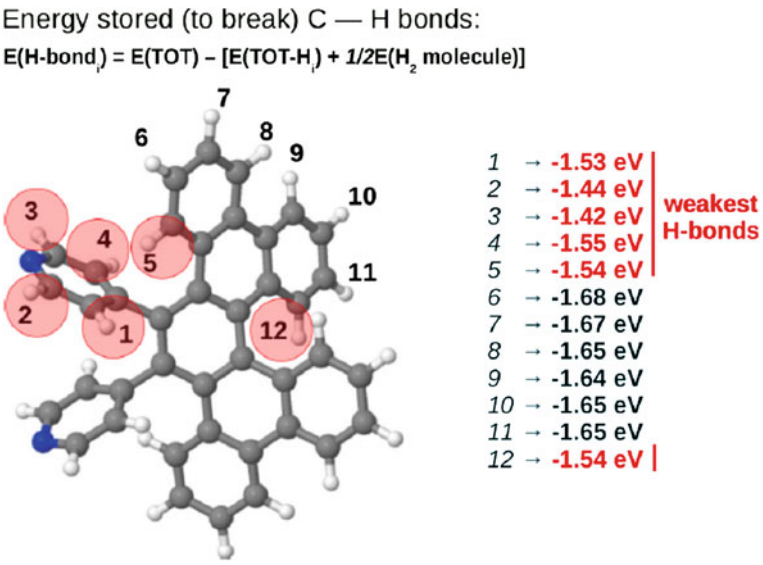

Fig. 2 Schematic representation of the "weakest" C–H bonds (highlighted in *red*) in a pyridine-type organic precursor evaluated by ab initio calculations

On the other hand, as one goes sequentially removing the hydrogen atoms from the molecule, kinetic formation barriers can be obtained from the structure with an instantaneously removed hydrogen atom towards its optimal configuration, obtaining in this way the different intermediates along the reaction path as the hydrogen atoms are removed, as well as the values of the kinetic formation barriers to reach the consecutive intermediates. Besides enthalpies of formation, H, for a particular process the important feature to ascertain its feasibility is the height of the barrier at the transition state (TS), ΔE. These TSs can be efficiently investigated within the climbing-image nudge elastic band (CI-NEB) approach [59–61] implemented in some of the most used commercial and free-source simulation packages (Ref. [39] as an example); where the initial, the final, and all the intermediate image states were free to fully relax. The transition-state energies obtained from the CI-NEB calculations can been used to determine the Boltzmann probability for a thermal fluctuation to overcome the kinetic barriers along the thermal-annealing process, yielding even the time scale for an event to occur. This strategy can be used to rationalize the possible routes to predict realistic on-surface (cyclo-)dehydrogenation reaction paths.

2.3 Improved Theoretical STM Imaging Approach

Theoretical STM imaging arises as a powerful tool to characterize and monitorize the structural configurations along the (cyclo-)dehydrogenation reaction paths in metal-organic interfaces: from the starting precursors to the final products, including the reaction intermediate configurations. Theoretical STM calculations can be carried out to be compared with the experimental UHV-STM images. In order to obtain accurate STM images and tunnelling currents, it is possible to use an efficient STM theoretical simulation technique that includes—by construction—a detailed description of the electronic properties of both the tip and the sample (this formalism has been fully implemented in the Fireball atomistic simulation code [36]). Using this technique, based on an effective combination of a Keldysh–Green's function formalism and local-orbital DFT [62, 63], the system is split into sample and tip (see Fig. 3). Given the versatility of this approach, we will be able to use a great variety of scanning tips [64], with different shapes and sizes (including the standard W- and Au-based pyramidal tips), even applying different tip-functionalizations, or accounting for tip-contamination effects [65]. Within this approach, in the tunnelling regime at low temperature, the STM current is given by Refs. [62, 63] as:

$$I = \frac{4\pi e^2}{\hbar} \int_{E_F}^{E_F + eV_s} \mathrm{d}\omega \mathrm{Tr}[\boldsymbol{T}_{ts}\boldsymbol{\rho}_{ss}(\omega)\boldsymbol{T}_{st}\boldsymbol{\rho}_{tt}(\omega - eV)], \tag{1}$$

where V_s is the surface voltage, ρ_{tt} and ρ_{ss} are the density of states (DOS) matrices—in the local-orbital basis—associated with the tip and sample, while T_{ts} and T_{st} are

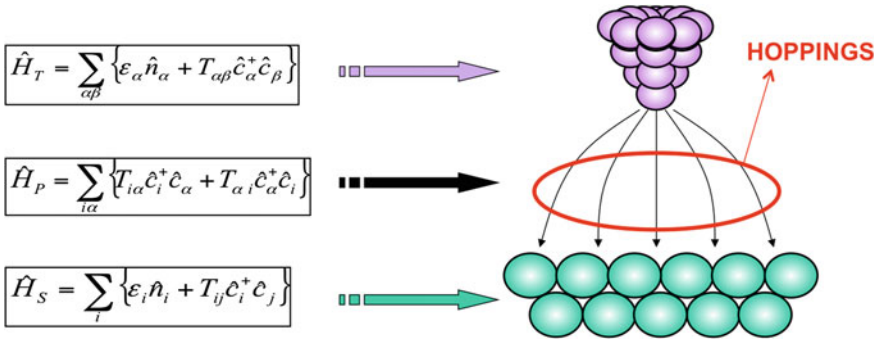

Fig. 3 Pictorial representation of the tip ($\widehat{H}_T$) sample ($\widehat{H}_S$) and overlapping ($\widehat{H}_P$) Hamiltonians used to calculate the tunnel current within the Keldish–Green's function formalism [62, 63]

the local-orbital Hamiltonian matrices coupling tip and sample (see Refs. [62, 63] for further details). The Hamiltonian hopping matrix elements between tip and sample are then obtained by using a dimer approximation: the interaction of a dimer formed by each contributing atom of the scanning tip and each contributing atom in the sample is calculated for different atom–atom distances and for all the nonzero interactions, using the Keldysh–Green formalism to propagate the tunnel current between both subsystems [62, 63]. Some recent examples of the application of this approach for organic molecules on surfaces can be found in Refs. [64, 66]. It is important to remark that this formalism dramatically improves the theoretical STM imaging description within the standard application of the Tersoff–Hamman approach, [67, 68] in which the STM tunnelling current is simply proportional to the DOS at the Fermi level (E_F) of the sample at the position of the tip; thus, contour maps of this DOS have been frequently used to generate theoretical STM images. This method has proven being very useful, obtaining qualitatively correct STM images for moderately simple interfaces. Nevertheless, this theoretical approach fails for slightly more complex systems, for instance, when p (or d) orbitals in the tip play a significant role in the STM current, [69] or in the case of tip contamination.

On the other hand, simply using the LDA Kohn–Sham energy levels provides molecular transport gaps that are too small, and this is an important issue for obtaining accurate and realistic STM images with respect to the conventional DFT-based STM imaging formalisms, when we have organics adsorbed on metal surfaces (which are the cases visited in this chapter) [53, 64, 66]. However, the effective charging energy of the molecule, U, can be used to effectively correct the Kohn–Sham energy gap, E^{KS}, and calculate the transport gap as $E^t = E^{KS} + U$. This correction can be easily introduced in a conventional localized-basis-set DFT implementation (see Ref. [35] as an example) via a scissor operator in the molecular orbitals before the self-consistency DFT process. The use of this operator will also permit accounting for image potential effects, electronic screening, as well as the correct energy-level alignment between the substrate and the adsorbates (a variety of organic molecules in this case), which will permit to tunnel at the same bias

voltage used in the experiments, [64, 66] as well as obtaining an improved description of charge transfers and the created induced dipoles, and other related quantities. The mentioned scissor operator can be also used to incorporate valuable electronic structure information previously obtained from improved many-body calculations to the STM imaging calculation process.

3 Tailored Formation of *N*-Doped Nanoarchitectures by Diffusion-Controlled on Surface (Cyclo-) Dehydrogenation of Heteroaromatics

3.1 Introduction

As discussed in Sect. 1, surface-assisted CDH and dehydrogenative polymerization of polycyclic (hetero-)aromatic hydrocarbons (PAH) are among the most important and novel strategies for bottom-up assembly of new nanostructures from their constituent molecular building blocks. Although diverse compounds have been formed in recent years using this methodology (see Introduction Section), a limited knowledge on the molecular machinery operating at the nanoscale has so far disallowed to control the reaction outcome. In this section, it will be shown that the strength of the PAH–substrate interaction rules the competitive reaction pathways (CDH versus dehydrogenative polymerization). So, starting from the same molecular precursor and controlling its diffusion by selecting the metal to be used as the supporting surface, temperature-triggered dehydrogenation takes place to provide molecular or polymeric structures of variable dimensionality. In situ ultra-high vacuum scanning tunnelling microscopy (UHV-STM) is employed to achieve the understanding of the self-assembling of molecular precursors on surfaces. By choosing the appropriate N-heteroaromatic precursors and by controlling their diffusion, the on-surface (cyclo-)dehydrogenation can either lead to monomolecular triazafullerenes, diazahexabenzocoronenes (*N*-doped nanographene), or to *N*-doped polymeric networks.

A sketch of the reaction pathways and of the selected precursors is represented in Fig. 4.

3.2 Cyclodehydrogenation on a Highly Reactive Surface: The Case of Pt(111)

Pt is known to be a highly reactive surface and a good catalyst for dehydrogenation reactions of organic molecules [8]. In this subsection, the deposition of precursors **1** and **4** under UHV conditions on Pt(111) at room temperature (RT) is shown, and this is represented in Fig. 5 (left-panels). At low coverage (about 0.3 monolayers),

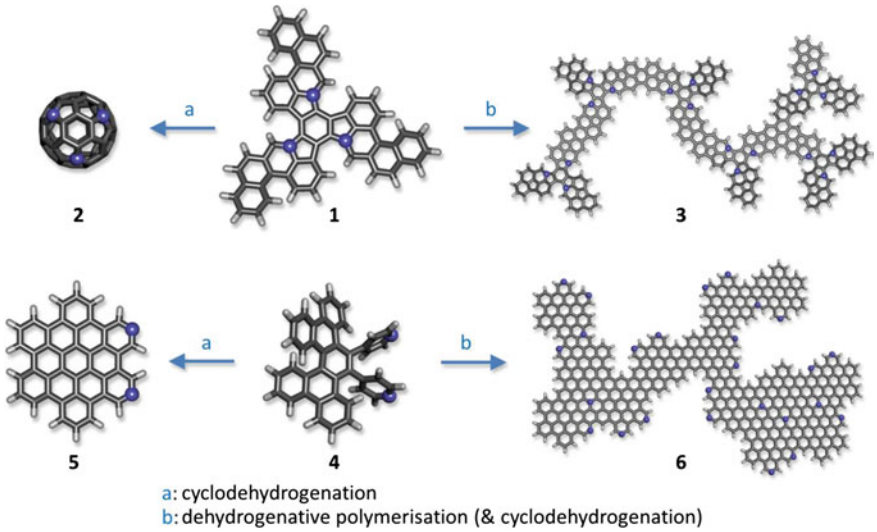

Fig. 4 Heteroaromatic precursors **1** and **4** are subjected to controlled on-surface dehydrogenation. **1** and **4** may form, respectively, (i) nitrogen-doped triazafullerene **2** or 2,5-diazahexabenzocoronene **5** (both through intramolecular cyclodehydrogenation) or (ii) branched and cross-linked 2D polyaromatic architectures **3** or **6** (both through intermolecular dehydrogenative polymerization accompanied by intramolecular cyclodehydrogenation). Nitrogen atoms are highlighted as *blue balls*. **3** and **6** represent only conjectural structures. Reprinted (adapted) with permission from (*ACS Nano*, 2013, 7(4), pp. 3676–3684). Copyright (2013) American Chemical Society

the STM images show individual molecules of **1** (Fig. 5a) and **4** (Fig. 5c) scattered over the surface with no preferential adsorption at the step edges. This indicates that both precursors are well anchored to their adsorption sites and, accordingly, their diffusion is substantially restricted. However, the molecule–substrate interaction is not strong enough to disrupt the molecular structure [35].

DFT-based calculations for the case of **4** on Pt(111) shows that precursor **4** adsorbs 0.31 nm above the surface and reacts with the Pt by electrostatic interactions derived from van der Waals forces with a binding energy of 1.5 eV per molecule, which is high enough to prevent its diffusion. However, the electrostatic nature of this interaction and, thus, the absence of covalent bonding does not modify the structure of the molecule as it is experimentally observed: in the STM images the shape of individual molecules is distinguishable, and it is possible to resolve the submolecular structure of **1** and **4** (insets of Fig. 5a, c, respectively).

Upon annealing **1** and **4** on Pt(111) at about 720 K, they both change their shape, size and intramolecular structure (Fig. 5b, d). The shape of **1** turns from triangular to spherical (**2**) (Fig. 5b). The transformation of **1** to triazafullerene **2** is caused by the cleavage of all the C–H bonds and the spontaneous formation of new C–C bonds without rearranging the present bonds. This transformation is accompanied by significant morphological changes: the width decreases from 2.2 to 1.2 nm and

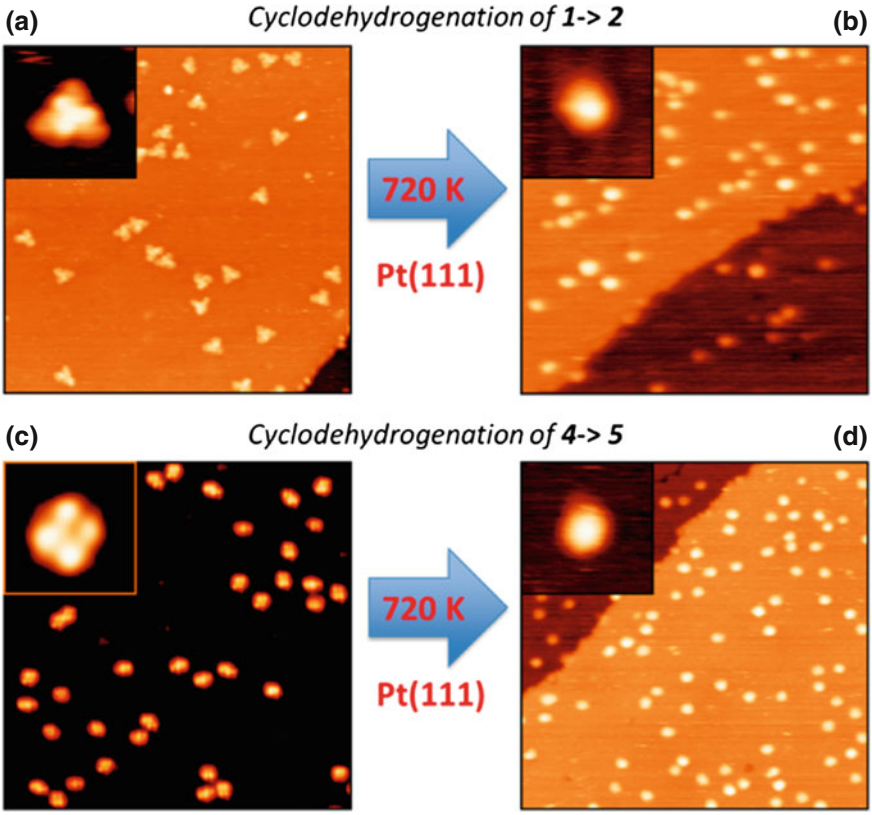

Fig. 5 Dehydrogenation of 1 and 4 on the Pt(111) single-crystal surface. UHV-STM images of about 0.3 monolayers of precursor **1** in (**a**) (30 × 30 nm^2, the *inset* 4 × 4 nm^2, V_s = +0.5 V) and precursor **4** in (**c**) (30 × 30 nm^2, *inset* 4 × 4 nm^2, V_s = +2.0 V) deposited on Pt(111) at room temperature show individual molecules with intramolecular structure corresponding to molecular orbitals. After annealing at 720 K, the cyclodehydrogenation process occurs and **1** is transformed into the spherical triazafullerene **2** in (**b**) (30 × 30 nm^2, *inset* 4 × 4 nm^2, V_s = +0.5 V) and **4** into the flat 2,5-diazahexabenzocoronene **5** in (**d**) (30 × 30 nm^2, *inset* 4 × 4 nm^2, V_s = +2.0 V). Reprinted (adapted) with permission from (*ACS Nano*, 2013, 7(4), pp. 3676–3684). Copyright (2013) American Chemical Society

the apparent height increases from 0.20 to 0.37 nm. These observations are in agreement with related studies on fullerene nanostructures deposited on the same surface [9, 70].

Concerning precursor **4**, its internal structure with four bright lobes disappears upon annealing and rounded features are imaged with the STM (Fig. 5d). The lateral size (diameter) changes from 1.7 to 1.4 nm and the apparent height from 0.28 to 0.23 nm. This newly formed nanostructure features a loss of the intermolecular resolution (see inset) indicating the breakage of C–H bonds compatible with the formation of 2 N-HBC, *N*-doped nanographene **5**. This agrees with previous studies

on forming and imaging HBC structures on surfaces [7, 71, 72]. Finer details of this transformation will be discussed in next section.

The transformation of **1** into **2** is a process of complete CDH, as the thermal activation involves the cleavage of all the C–H bonds, and the C dangling bonds link between neighbouring ones to form new cycles. However, only partial CDH occurs in the process of transformation of precursor **4** into **5**, since only the inner H atoms detach, while the peripheral ones are maintained. The differences can be related to steric reasons. The first CDH reactions on **1** create some pentagons that induce a height to the planar molecule. This curvature approaches H atoms from different molecular wings to each other, assisting the formation of a new cycle. This is not the case of **4**. Only the rings having a neighbour close enough to form a new cycle dehydrogenate. In another words, and following the notation of Fig. 2, atoms 2, 3, 6, 7, 8, 9, 10 and 11 do not have a neighbouring ring one to form a new cycle.

3.3 Cyclodehydrogenation on a Weakly Interacting Surface: The Case of Au(111)

Intriguingly, an entirely different reaction outcome is obtained when changing the substrate from platinum to gold (Fig. 6). In contrast to Pt(111), the Au(111) single-crystal surface is known to interact weakly with adsorbed aromatics and, accordingly, it is considered to be inert towards some catalytic reactions [73] Indeed, after the deposition of about 0.4 monolayers (ML) of **1** or **4** on the Au(111) surface at room temperature, no molecules are seen by STM because they diffuse faster than the scanning speed (Fig. 6a, c, respectively). The presence of **1** and **4** in its molecular form on the surface was corroborated by XPS and NEXAFS. These spectroscopic techniques also confirm the presence of N in the molecules on the surface (see next section).

However, upon annealing **1** and **4** to 700 K, it is possible to observe the formation of 2D polymeric cross-linked networks **3** and **6** (Fig. 6b, d, respectively). The highly diffusing precursors **1** and **4** partially cyclodehydrogenate and dehydrogenate, respectively, meet other diffusing (and also dehydrogenated) adsorbed precursor to covalently bind together.

After a few molecules merge via dehydrogenative oligomerization, the diffusion of such nanoclusters diminishes. Once these molecular seeds fix on the gold surface, a random network of branched molecules forms, since polymerization does not follow any preferential crystallographic direction. In some sections of the network, it is possible to distinguish a triangular or round topology in their constituent units resembling that of the original precursor **1** and **4**, respectively.

These results have also been observed for other coinage surfaces as Cu(111) and Cu(100).

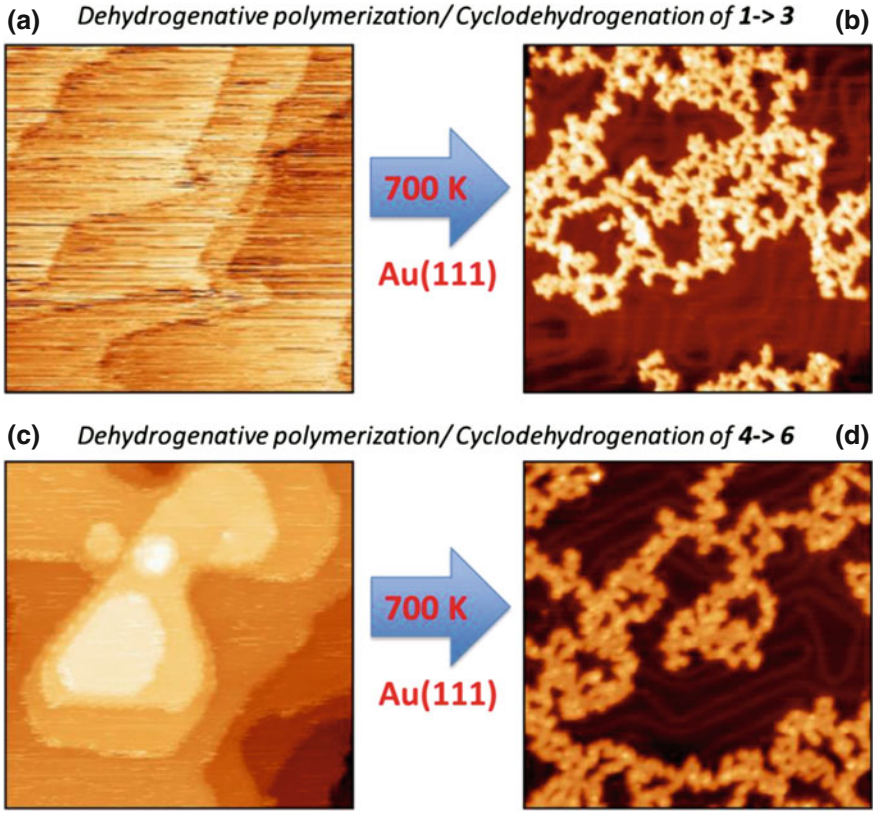

Fig. 6 Dehydrogenation of 1 and 4 on the single-crystal Au(111) surface. STM images of 0.4 ML of precursor **1** in (**a**) (30 × 30 nm^2, V_s = +0.5 V) and precursor **4** in **c** (30 × 30 nm^2, V_s = +2.0 V) deposited on Au(111) at room temperature do not show individual molecules. After annealing **1** and **4** at 700 K, the dehydrogenative polymerization/cyclodehydrogenation processes occur and **1** is transformed into the 2D heteroaromatic network **3** in (**b**) (40 × 40 nm^2, V_s = +0.75 V) and similarly **4**–**6** in (**d**) (40 × 40 nm^2, V_s = +2.0 V). Reprinted (adapted) with permission from (*ACS Nano*, **2013**, 7(4), pp. 3676–3684). Copyright (2013) American Chemical Society

Figures 5 and 6 indicate that surface diffusion is the key mechanism driving CDH and dehydrogenative polymerization of the same molecular precursor (**1** and **4**) either to the formation of individual nanoobjects (**2** and **5**) or extended networks (**3** and **6**) as schematically represented in Fig. 4. The interplay between molecule–surface and molecule–molecule interactions causes the reaction to move towards either the left or the right in Fig. 4.

The degree of polymerization of the precursors **1** and **4** and, accordingly, the structure and dimensionality of the formed nanoobjects can be controlled by two experimental parameters, namely by the annealing temperature and by the surface coverage of the precursor (Fig. 7). Temperature effects will be deeply discussed in the next section.

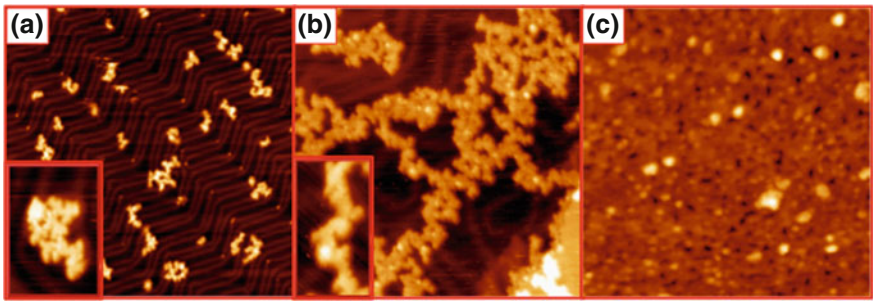

Fig. 7 (Cyclo-)dehydrogenation of **1** to form new nanoarchitectures with different dimensionality. STM images of **1** deposited on Au(111) at different coverage. **a** Small oligomeric clusters nucleate at the corner of the surface reconstruction (formation of 0-D nanostructures) for 0.1 ML deposited at 540 K (30 × 30 nm^2). *Inset* shows a detail of one oligomeric structure. **b** The formation of a linear polymeric network made up of individual molecules indicates a 2-D cross-linking of the deposited precursor when depositing 0.3 ML at 600 K, (30 × 30 nm^2). *Inset* shows a detail of the unimolecular branches of the **c** *N*-doped carbon 2D layer is formed with a series of interlinked partially folded structures when 1 ML is deposited at 900 K (40 × 40 nm^2). Presence of N in all these nanoarchitectures was confirmed by XPS. Typical bias and tunnel current were 750 mV and 0.1 nA, respectively

Indeed, depositing a lower coverage of **1** (0.1 ML) on Au(111) and annealing at a lower temperature (540 K), small zero-dimensional oligomeric clusters **3** become visible by STM, as they anchor to the surface at the elbows of the herringbone reconstruction (Fig. 7a, b) or at the step edges. High-resolution STM images show that the oligomeric clusters **3** consist of a few covalently bound subunits where some retain the triangular shape of the precursor **1**, meaning that only partial (cyclo-) dehydrogenation of **1** took place, which leads to oligomerization rather than folding. Their height corresponds to that of individual intact molecules **1**. These nanostructures can be easily moved with the STM tip, which manifests their weak interaction with the surface. Thus, they could be possibly transferred to a more technologically useful surface. In some images, we have found semi-intact molecules that link to each other for a small wedge. The CDH of these precursors is only partial, since they maintain their pristine shape; however, the dehydrogenative oligomerization is effective here.

Curiously, the final morphology of the two different polymeric chains formed using **1** and using **4** as building blocks is similar. At low annealing temperature, the apparent height and width of the chains are in general those of a single intact molecule, meaning that most chains are unimolecular and that the CDH of the building blocks is partial. Upon increasing the activation temperature to 600 K polymeric chains **3** topologically similar to those shown in Fig. 6b are formed. However, in a few cases one can still distinguish the intermolecular structure of the original precursor **1**. This shows that CDH is also not complete at this temperature.

In order to form a complete two-dimensional *N*-doped carbonaceous monolayer, the coverage shall be increased up to 1 ML and, to favour the CDH process, the

temperature of the substrate to 900 K (see Fig. 7c). Then, all triangular-shaped substructures disappear and a dense carbonaceous sheet structure forms. Evidently, extensive dehydrogenative polymerization took place but, at the same time, CDH proceeded to a higher degree than at 600 K since open-cage and completely closed triazafullerene **2**, could be identified within the layer.

Figure 7c shows that the morphology of the layer is rough. The origin of the roughness is twofold. On the one hand, one has to keep in mind that *N* atoms are included in the layer, and the local DOS at the *N* sites can be much higher, and therefore, STM images show bumped structures due to electronic effects [74] Secondly, **1** includes both pentagons and hexagons, and therefore, the precursor should (partially) fold upon (partial) CDH. As mentioned above, the triangular features are not visible at this temperature, indicating an almost complete removal of H atoms and an intermolecular recombination process.

3.4 Conclusions

In this section, we have shown that the adsorbate–surface interaction plays a key role in tailoring the outcome of the on-surface dehydrogenation of suitable (hetero-) aromatic precursors. Under temperature and substrate control, CDH and dehydrogenative polymerization compete to govern the on-surface reaction in favour of either individual molecular nanostructures (when their initial diffusion is minimized) or polymeric networks (when diffusion is enhanced).

It is found that either (i) a strong coupling of heteroaromatic precursors with the Pt(111) surface blocks the diffusion of molecules and, accordingly, thermally induced intramolecular CDH dominates; or, in contrast, (ii) a weak coupling of heteroaromatic precursors with the Au(111), Cu(110) or Cu(111) surface allows the diffusion of activated molecules and, therefore, intermolecular dehydrogenative polymerization takes place (along with CDH).

Thus, by using the same heteroaromatic precursor, it is possible to steer the reaction towards the formation of individual molecular nanostructures or complex heteroaromatic networks. Importantly, it can be evidenced a straightforward bottom-up approach to nanoscale carbon-rich heteroarchitectures such as triazafullerenes, *N*-doped nanographene, *N*-doped polymeric networks and *N*-doped carbonaceous overlayers, which are not accessible by standard tools of chemical synthesis. In particular, the use of heteroaromatic precursors allows a controllable way of achieving a doped outcome. Weakly reactive substrates such as Au(111) are also promoting surface chemistry, even though to a lower extent than the highly reactive one such as Pt(111).

4 Controlling the Cyclodehydrogenation Sequence

4.1 Introduction

As discussed in previous section, the pyridyl-substituted dibenzo[5]helicene (DiPy[5]DBH) can form either *N*-doped nanographene units, or polymerize to form covalent heteroaromatic chains. We have seen that the choice of the surface is a crucial parameter for driving the reaction towards one or the other product, by promoting either CDH or dehydrogenative polymerization (see Fig. 4).

For this purpose, the temperature was increased to obtain substantial dehydrogenation. In the present section, we will study the formation of other intermediate reaction products that can be obtained for partial dehydrogetated structures along the reaction path. For this goal, we will characterize the deposition of the same molecular precursors, **1** and **4**, on two typical surfaces with different properties. Pt(111) as a prototypical example of the platinoid group metals on the periodic table, and Cu(111) as example of coinage metals. We illustrate these examples with STM, NEXAFS, and XPS at different temperatures, which are effectively combined with the advanced DFT-based techniques, introduced and detailed in Sect. 2. NEXAFS and XPS provide precise element-resolved chemical information on the processes and are therefore very useful to understand the mechanisms of (cyclo-)dehydrogenation from an atomistic point of view. These results are complemented with STM images, which provide a visual understanding of the situation.

4.2 Sequentially Formed Species on Highly Reactive Surfaces

4.2.1 Experimental Characterization of DiPy[5]DBH on Pt(111)

In this section, we will focus on how to control the (cyclo-)dehydrogenation to form stable intermediate structures, by monitoring the annealing temperature. We will show that the different C–H binding energy of different C–H bonds determines the existence of stable intermediates.

Following the scheme presented in Fig. 1, the first step is the deposition of the precursor on the surface. Figure 8a represents an STM image of 0.4 monolayers of pyridyl-substituted dibenzo[5]helicene (DiPy[5]DBH, $C_{40}H_{24}N_2$) on Pt(111). Randomly scattered four-lobe structures are observed. The apparent height (AH) of the objects is 0.28 ± 0.02 nm, while the width is about 1.70 ± 0.15 nm: since their size is comparable to the one of the molecules, we conclude that each four-lobe object represents a single molecule. The zoom in Fig. 8b represents a single molecule, and the internal features correspond to a mixture of the topography (the tilted rings) with electronic effects [the spatial distribution of the lowest unoccupied molecular orbital (LUMO)].

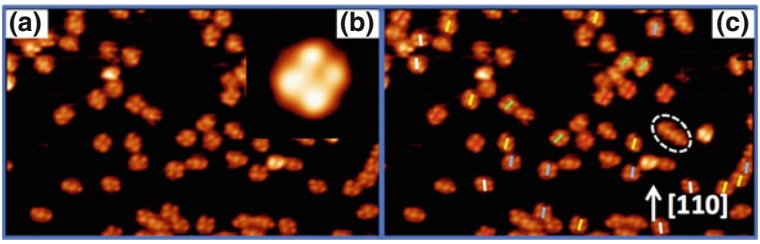

Fig. 8 STM images of DiPy[5]DHB as deposited on Pt(111) at room temperature. **a** 30 × 15 nm^2; Voltage applied to the sample (V_s) = + 0.5 V. **b** 4 × 4 nm^2 zoom of a single molecule **c** Same image than in **a** indicating by different coloured lines the different on-surface orientation of the molecules

Upon deposition, the molecules stick where they land: this indicates that the interaction with the surface is stronger than the intermolecular forces, meaning that the heteroaromatics cannot diffuse and form ordered islands. However, the fact that it is possible to actually observe the intramolecular resolution indicates that the interaction between the molecules and the Pt is not strong enough to fully disrupt the molecular structure, even though it is high enough to prevent diffusion.

When deposited, **4** sits in five different directions, represented in Fig. 8c by different coloured lines. Due to the threefold symmetry of the system, the molecular orientations turn out to be only three: at 30 ± 5°, 15 ± 5° and 7 ± 5° with respect to the $[1\bar{1}0]$ crystallographic direction of Pt. Although the real angle is hard to determine, because of the error in determining the Pt crystallographic directions from the STM, the rotational difference between the molecules on a particular image is accurate. These angles would correspond to the main directional axis of the molecules oriented, respectively, along the (1,1), (1,3) and (1,6) directions with respect to the Pt(111) surface (see Fig. 9). These directions originate angles of 30°, 15.9° and 8.7°, respectively, in good agreement with the angles reported by the STM. Unfortunately, the registry of the surface cannot be determined by STM. The fact that the molecule can only orient in three ways indicates that even though the molecules are not energetically allowed to diffuse, they rotate and slightly

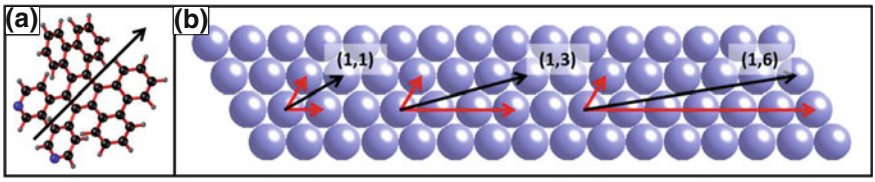

Fig. 9 Orientation of the main directional axis of the molecules with respect to the Pt(111) surface directions. **a** A possible main directional axis of the molecule is indicated by a *black arrow* superimposed to the ball-and-stick model of DiPy[5]DBH. **b** The lilac spheres indicate atoms of the Pt(111) surface; the main directional axis of the molecule can orient in three different directions, namely (1,1), (1,3) and (1,6); the resultant vector is indicated by a *black arrow*

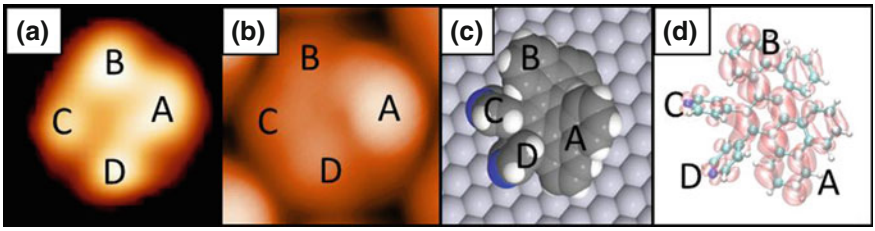

Fig. 10 STM image, STM simulation and structure of a deposited molecule at RT on Pt(111). The letters *A*–*D* represent a different lobe. **a** An experimental STM image of **1** exhibiting four bright lobes (2×2 nm^2; $V_s = +2.0$ V). **b** The theoretical simulation of the intact molecule at RT. **c** The calculated structure of the relaxed precursor at RT, oriented in the same way as (**b**). **d** The free molecule molecular orbital (LUMO) obtained with an isosurface of 4×10^{-5} electrons/Å^2

displace to adjust with respect to the surface in order to find the minimum energy configuration, as in the case of other large PAHs on the same surface [35].

Figure 10a represents the STM image of **4** compared with its theoretical simulation (Fig. 10b), and the LUMO representation of the free molecule (Fig. 10d), obtained with an isosurface of 4×10^{-5} electrons/Å^2; both experimental and theoretical images are oriented as the structure shown in Fig. 10c. Since Fig. 10d does not exhibit four clear lobes, we can conclude that the features observed with the STM are mainly due to a topographical effect rather than to an electronic one.

The experimental STM image of the molecule presents four bright lobes, reproduced by the theoretical simulation, which includes the surface. The similarity between the two indicates that the molecule remains intact upon deposition. The model structure is oriented so that they can be superimposed to the theoretical simulation and the experimental image (each letter on top of each lobe indicates an analogous feature); hence, the brightest lobe A is caused by the phenyl ring of the helicene, which is tilted with respect to the substrate. Lobes C and D are related to the two pyridine rings (ring D is standing higher than ring C) and lobe B to one of the two benzene rings. The interaction between the pristine molecule and the Pt surface is electrostatic at room temperature, and this allows the molecule to maintain its three-dimensional shape caused by its helical structure.

To study the catalytic effects of Pt(111) on this molecule, the samples are annealed to different temperatures, up to 830 K, in steps, to have a full picture of the different chemical stages undergone by the precursor. Above 830 K, the molecules disrupt to form graphene (not shown). Figure 11 shows STM images of different stable steps. As displayed in Fig. 11a, d, STM images indicate that the structure with the four lobes of the molecular orbitals is present up to about 400 K. At this point, the precursor changes aspect, and only two lobes (one brighter than the other) are visible. The change of the aspect of the molecule reflects a structural change caused by the annealing. This structure is explained in detail below, and it will be referred to as **7**, as indicated in Fig. 12.

Figure 11b, c, e, f shows the complete loss of molecular orbital resolution triggered when further heating the sample to 650 K and to 770 K: the molecules

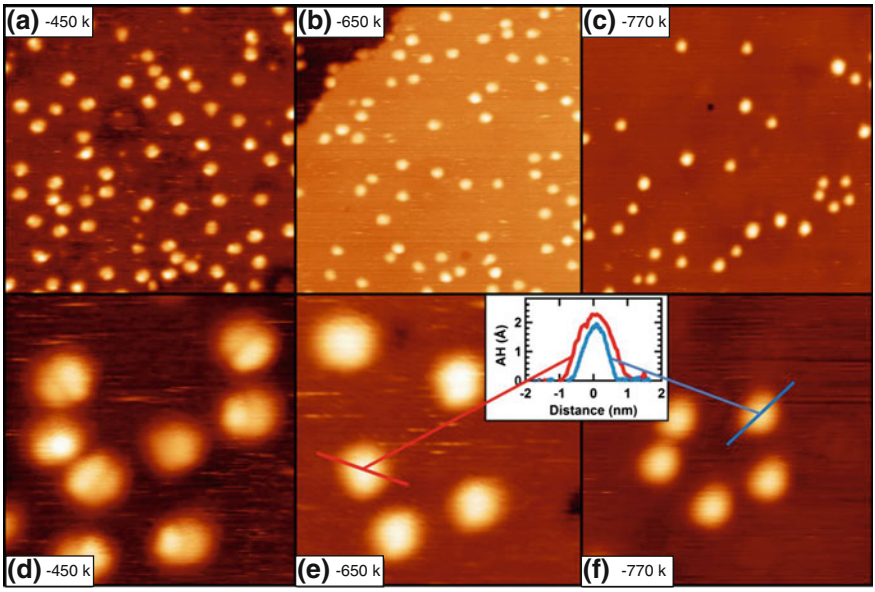

Fig. 11 Three different types of molecules arise when annealing DiPy[5]DHB/Pt(111) at 450, 650 and 770 K. The images at the *top* have the same size (25 × 25 nm^2) as the images at the *bottom* (7 × 7 nm^2). **a** When the sample is annealed at 450 K, the molecule transforms and only two lobes are visible, a brighter and a dimmer one (25 × 25 nm^2; V_s = +2.0 V). **b** As the sample is annealed at 650 K, the intramolecular resolution is lost (25 × 25 nm^2; V_s = +2.0 V). **c** If the sample is further heated to 770 K, most molecules become smaller than the ones observed in (**b**) (25 × 25 nm^2; V_s = +2.0 V). **d** A 7 × 7 nm^2 zoom of (**a**) highlights the features of the molecules at 450 K: these molecules will be referred to as **7**. **e** A more detailed image of the sample annealed to 650 K: these molecules will be referred to as **5** (7 × 7 nm^2; V_s = +2.0 V). **f** A smaller image of the sample annealed at 770 K showing five molecules: these molecules will be referred to as **8** (7 × 7 nm^2; V_s = +2.0 V). The *inset* in between (**e**) and (**f**) shows the apparent height profiles of one molecule annealed to 650 K (*red*) compared with the one of a molecule annealed to 770 K (*blue*): the latter is smaller both in width and in height

transform into uniform round features. The zooms (Fig. 11e, f) clearly show that in both cases no intramolecular resolution is present. An attentive reader may relate the absence of such feature to a poor resolution of the tip. However, after scanning hundreds of images of annealed samples, no intramolecular resolution was ever seen, while for the un-annealed samples the MOs were routinely observed. Interestingly, the panorama after annealing to 650 K is different from the one after heating to 770 K. Figure 11b, c compare two 25 × 25 nm^2 images after annealing at 650 and 770 K, respectively. The molecules at 650 K (referred to as **5**) seem broader than the majority of the molecules at 770 K (**8**), and this is highlighted by the 7 × 7 nm^2 zooms (Fig. 11e, f). The apparent height profiles of **5** and **8** in the inset clearly indicate that annealing the precursor at 650 K (**5**, red) triggers the formation of a new molecular structure, which differs from the outcome obtained when increasing the temperature further (**8**, blue).

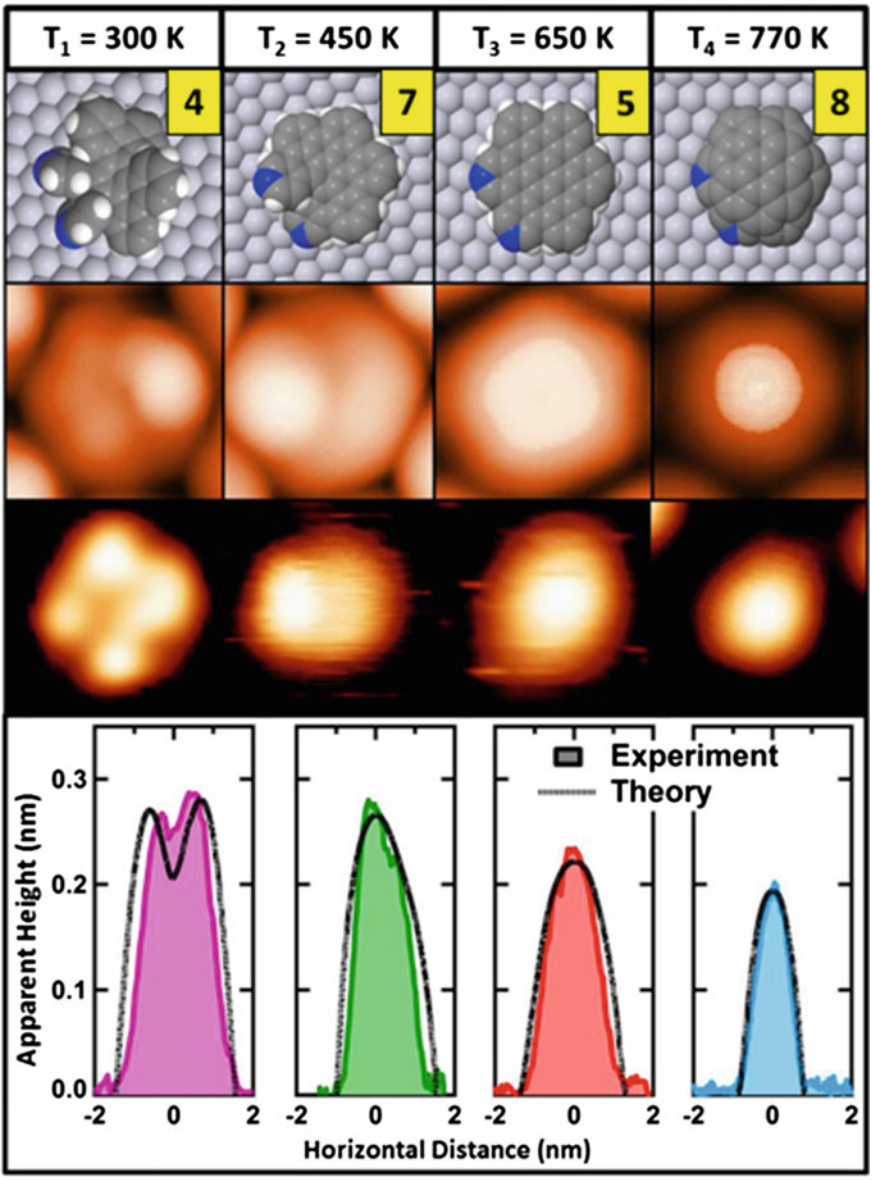

Fig. 12 Each column of this image represents one of the four main stages of the transformation of the pristine molecule **4** into the intermediate step **7**, to *N*-doped nanographene **5** and to a *N*-doped nanodome **8**, upon thermal activation. The *first row* represents the annealing temperature. The *second panel* reveals the structure of a given stage: this structure is oriented so that it can be superimposed onto the STM simulation, shown in the *third panel*. The *fourth row* represents the experimental STM image of each stage (2×2 nm^2; $V_s = +2.0$ V). Finally, the last panel shows the experimental apparent height (*solid coloured line*) as compared to the theoretical apparent height (*dashed black line*). Reprinted (adapted) with permission from (Chem. Commun. 2013, 50 (13), pp. 1555). Copyright (2013) Royal Society of Chemistry

Table 1 The apparent height and the width of DiPy[5]DBH annealed at four different temperatures

Annealing T (K) + molecule type	Maximum apparent height (±0.02 nm)	Width (±0.15 nm)	MOs at V_s = 2.0 V
RT (DiPy[5]DBH: **4**)	0.28	1.70	4 lobes
450 (nanohelicene: **7**)	0.28/0.23	1.50	2 lobes
650 (2 N-HBC or nanographene: **5**)	0.23	1.44	NO
770 (nanodome: **8**)	0.19	1.25	NO

The height and width of the non-annealed sample **4** (observed with four lobes in the STM) are compared with the ones of the molecule annealed at 450 K (**7**), 650 K (**5**) and to 770 K (**8**): the four molecules are different. The apparent height profiles were measured on about 30 molecules at each stage, to obtain statistical validity. The last column indicates whether molecular orbitals are observed with the STM. The apparent heights of the brighter and dimmer lobes of **7** are both shown

Table 1 summarizes these experimental findings. It shows the typical apparent height and width of an intact precursor at room temperature **7**, compared with the outcomes arising after the structural changes upon annealing at 450 K (**7**), 650 K (**5**) and 770 K (**8**). Notice how both the height and the width of the representative molecules decrease with temperature. Therefore, the precursor must undergo at least three structural transformations upon annealing (before forming graphene). The apparent height profiles were recorded for about thirty molecules at each temperature, to achieve statistical validity.

Interestingly, Fig. 11c indicates that not all the molecules annealed to 770 K undergo the full transformation from **5** to **8**: some exceptions exhibit the same size as the precursors annealed to 650 K of Fig. 11a, b, showing that at this temperature the structural transition is only partial and the transformation process is slow.

4.2.2 Theoretical STM Imaging of DiPy[5]DBH on Pt(111) Along the Cyclodehydrogenation Reaction Path

As mentioned above, the change of the observed intramolecular structure in **4**, **7**, **5** and **8** and the decrease in the apparent height and width imply a structural change of the molecule itself. In order to understand these variations, we performed theoretical STM simulations (with the formalism explained in Sect. 2), which are shown in Fig. 12. In this image, each column represents a different temperature. The top row shows the annealing temperature, the second row the structure of the molecule (oriented as the next two rows), the third row the theoretical STM simulation of the precursor at a given temperature, the fourth row the experimental STM image (2×2 nm^2) and the last row the experimental apparent height compared with the theoretical one. As explained in Sect. 2, within STM approach, tunnelling currents for the STM images have been calculated using a Keldysh–Green function formalism, together with the first-principles tight-binding Hamiltonian obtained from the local-orbital DFT–Fireball method [36]. The theoretical STM images have been

obtained at constant-current scanning conditions, moving the W-tip perpendicularly to the sample in each scanning stage to search a preselected fix value of the tunnel current. The theoretical scanning parameters used here were I_{tunnel} = 0.2 nA, and $V_{\text{substrate}}$ = +2.0 V, in order to mimic the experimental procedure.

The first column of Fig. 12 represents **4** at room temperature. As discussed above, the essential features of the four bright lobes of the experimental STM image are replicated by the simulation. Compound **7** is an intermediate stage between **4** and **5,** and it is represented in the second column of Fig. 12. Upon thermal activation at 450 K, **4** undergoes a partial CDH, in which six C–H bonds break and three new C–C bonds form to create three new aromatic rings. The two tails of the helicene bind together as a consequence of CDH, and the two pyridine rings bind with the benzene rings. At this point, the only C–H left are the ones at the edges of the molecules and the C–H bonds in between the pyridinic rings. This change is reflected in the experimental and theoretical STM images, where a drastic change occurs: three of the bright lobes of **4** merge to form a unique lobe. This result reflects the formation of three new aromatic rings in the molecule. According to the apparent height profile, the experimental STM image reveals a brighter lobe (0.28 nm) and a dimmer lobe (0.23 nm). The bright part corresponds to one of the pyridine rings being farther from the surface due to steric and geometrical effects.

Further, thermal activation allows the cleavage of the two C–H bonds in between the two pyridinic rings, and the subsequent formation of a new C–C link which creates a new aromatic ring, forming **5**, diazahexabenzocoronene (2 N-HBC), also known as *N*-doped nanographene. The transformation from **7** to **5** results in a structural change which is reflected in the experimental and theoretical STM as a complete loss of molecular orbital resolution, as represented in the third column of Fig. 12, which shows a molecule from the sample annealed at 650 K. The profile shows a decrease in apparent height to 0.23 nm and in width to 1.44 nm. Curiously, the central part of the molecule is not flat, as it would be expected by a flat molecule such as this one: the reason for this may be assigned to the tip geometry: this is reproduced by the pyramidal scanning W-tip employed in the calculations. The use of a tip with large curvature can account for the experimental shape.

The fourth column of Fig. 12 shows the next annealing step at 770 K, which has the effect of cleaving all the remaining H atoms, namely the ones at the edges, from the molecule. As for the case of Rim et al. [7], the effect of the complete dehydrogenation of the molecule is to curve the precursor into an *N*-doped nanodome (**8**). Since the breakage of the C–H bonds at the edge does not generate any organic cycle, we must refer to this process as to dehydrogenation, as opposed to CDH, which is the formation of an aromatic ring caused by the cleavage of one or more C–H bonds.

The energy to break the internal C–H bonds is lower than the one needed to cleave the bonds at the edge due to steric effects [75]; therefore, the first H atoms to leave the molecule are the more central ones. However, if we supply high enough energy to the system the edge atoms detach as well. This sequence allows obtaining a hierarchical order for the dehydrogenation of the molecule. Firstly, the internal H atoms cleave and the carbons cyclodehydrogenate; secondly, the carbons at the perimeter

dehydrogenate. This gives us the power to select the desired outcome, simply by controlling the annealing temperature and hence the energy supplied by the system.

As for the case of **5**, **8** does not exhibit any intramolecular resolution. However, its width decreased to 1.27 nm and its height to 0.19 nm. This is somewhat unexpected, since upon this last dehydrogenation step the molecule bends, and the central core is elevated with respect to the edges, as shown in the second row of the last column of Fig. 12. The reason for the decrease of the apparent height of **8** with respect to **5** is that the dangling C bonds at the edges bind covalently with the Pt underneath. So, even if **8** is three-dimensional and **5** is planar, the *N*-doped nanodome is much closer to the Pt surface than the *N*-doped nanographene, whose edges are passivated by the H atoms. Therefore, the nanodome **8** appears smaller than the nanographene **5**.

4.2.3 Theoretical Structural and Energy Characterization of the CDH Reaction Path

The (cyclo-)dehydrogenation process previously outlined is catalysed by the Pt surface, which lowers the energy barrier required to break the C–H bond. To better understand the CDH steps of the transformation of **4** into **5**, we performed DFT calculations, by means of large-scale ab initio simulations including all molecule–surface interactions, as van der Waals, in a DFT framework within a local-density approximation (see Sect. 2). This investigation was not restricted to the ground state of the isolated species, but gave detailed insights of intramolecular C–C coupling by explicitly computing CI-NEB reaction barriers to explain the formation of *N*-doped nanographene out of our heteroaromatic precursor (see Fig. 13).

Figure 13 summarizes the main results extracted from the calculations. Upon deposition (step I), DiPy[5]DBH remains intact (**4**), with its three-dimensional shape, and no hydrogen atoms are lost. As described above, the pyridinic rings are not lying flat on the surface, but they are almost perpendicular, and we obtained a minimum energy structure with the precursor located at a perpendicular distance of 3.2 Å above the substrate. This indicates that the molecules are not covalently bonded with the surface, but a strong electrostatic interaction prevents diffusion and allows the molecule to remain intact upon deposition.

At this point, it is adequate to propose a reaction energy path consisting in the consecutive CDH of DiPy[5]DBH. The characterization of the energy of each C–H bond forming the molecule reveals that some hydrogen atoms are participating in weaker bonds with C. The reaction energy path is composed by intermediate steps (II–VIII), as shown in Fig. 13. Step VII corresponds to **7** in Fig. 12.

The complete reaction is a sequence of mechanisms, involving: (a) thermal and kinetic-promoted removal of a "weak" hydrogen (energy barrier, 1.5 eV); and (b) slight rotation of the corresponding dehydrogenated aromatic ring towards the neighbouring "weak" C–H bond and the fracture of this C–H bond to form a new C–C bond by radical aromatic addition (energy barrier, 1.4–1.6 eV). These mechanisms are repeated four times to complete the formation of four C–C bonds.

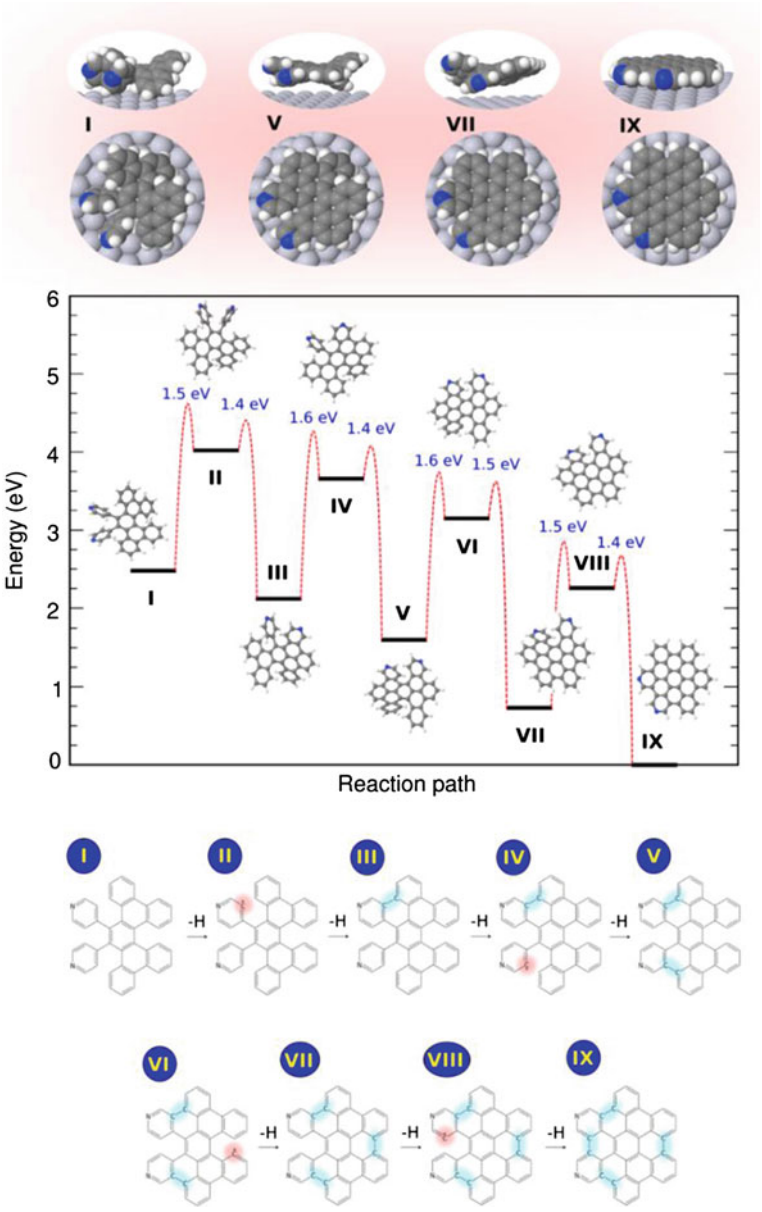

The full reaction pathway (Fig. 13) is completed with a net energy gain of 2.48 eV in favour of the *N*-doped nanographene 5 reaction product.

UHV-STM on-surface synthesis of nanographene was also performed by Treier et al. [10] by cyclodehydrogenating cyclohexa-o-p-o-p-o-p-phenylene (CHP) on Cu (111). The authors observed with the STM different stages undergone by the

◀ **Fig. 13** The computed reaction path of the cyclodehydrogenation of DiPy[5]DBH on Pt(111) upon annealing (steps IV–V). The reaction proceeds via seven metastable intermediates (II–VII). All energies (in eV) are referred to the final *N*-doped nanographene reaction product (step IX). Energy barriers (in eV) are shown for each elementary step. Images of the most representative metastable states (I, V, VII, IX) along the surface-assisted cyclodehydrogenation process are also depicted (*top panels*). A chemical structure diagram is included (*bottom panel*) to visually illustrate the different dehydrogenation steps (highlighted in *red*) and the subsequent C–C bond formations (highlighted in *blue*). Reprinted (adapted) with permission from (*ACS Nano*, 2013, 7 (4), pp. 3676–3684). Copyright (2013) American Chemical Society

molecules and interpreted them as different steps of partial CDH up to the formation of nanographene. Moreover, they also performed large-scale DFT. Surface-assisted CDH started with a copper-promoted cleavage of the C(sp^2)–H bond to generate an aryl radical that attaches to a neighbouring aromatic units via radical aromatic addition forming thus the aryl–aryl bond. The reaction is completed by the copper-promoted removal of hydrogen and final release of recombined H_2. Importantly, as for the present case revised in this section, when the system overcame a given energetic barrier, it fell back to the next minimum and it needed another energy injection to overcome the next barrier.

As discussed above, according to DFT, when more energy is injected in the system, a further structural phase transition occurs after the formation of 2 N-HBC **3**, which involves the full dehydrogenation of the molecule, by cleaving also the H atoms at the edge (see Fig. 14).

The calculations hence suggest that the C atoms at the edge bond with the surface and the *N*-doped nanographene **5** bends into an *N*-doped nanodome **8**. Figure 14a represents a ball-and-stick model of the dome. Figure 14b shows the STM simulation of **8**: it confirms that no intramolecular resolution should be observed, as for the case of the experimental STM images.

The STM simulation of the two structural phase transitions of **4** into **5** and subsequently into **8** allowed us to record the theoretical apparent height profile and to compare it with the experimental one (Fig. 15). The left panel of Fig. 15 represents the experimental apparent height profiles of a typical 2 N-HBC (red) and a typical N-dome (blue): as discussed above (see Table 1), 2 N-HBC is wider and taller than the N-dome. This is confirmed by the theoretical apparent height profiles (right panel). The width of the theoretical simulations is about 5 % broader than the one of the experiment, but it lies within the error.

The final value of the apparent height of the N-domes (0.19 nm) resembles the apparent height of the domes grown with HBC on Ru(0001) by Rim et al. [7] (0.20 nm); in their case, the molecule was flat at room temperature; therefore, the transformation into a hemisphere results in an overall increase in the apparent height. The apparent height of 0.28 nm measured at room temperature is due to various factors, such as the three-dimensional nature of the precursor and to the electrostatic interaction with the surface (as opposed to a stronger bond which would bring the molecule closer to the surface). Moreover, the height measured with the STM is a convolution of the topographical and electronic effects, which

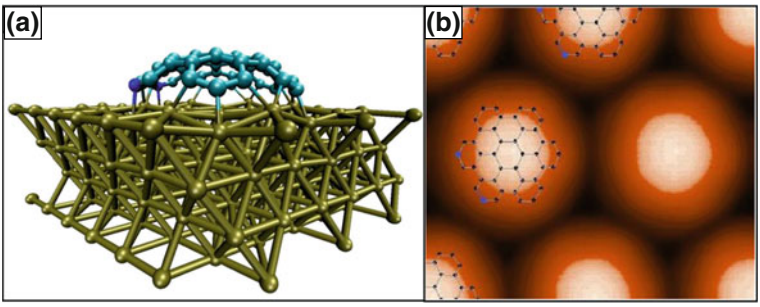

Fig. 14 DFT representation of the complete dehydrogenation of DiPy[5]DBH/Pt(111) and subsequent formation of *N*-doped domes **8**. **a** A three-dimensional representation of the formation of **8** on Pt(111); the *light blue atoms* indicate the C and the *dark blue ones* the *N*, while the *green ones* the Pt. Notice how the C atoms at the edge bond with the Pt causing the bending of the molecule. **b** A ball-and-stick model of the dome is superimposed to the simulation of the STM images, measured with a current of 0.1 nA and a sample voltage of +2.0 V

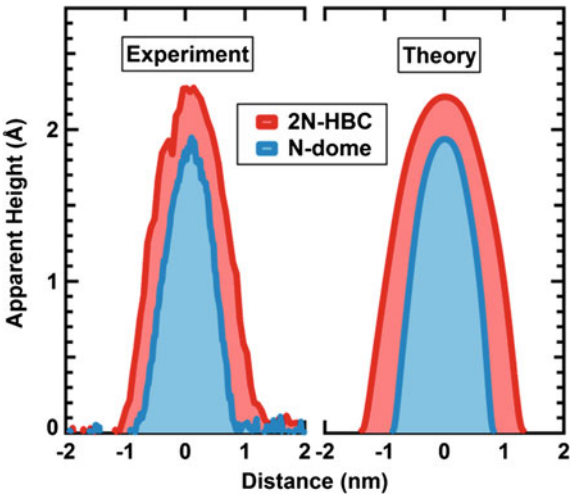

Fig. 15 Experimental and theoretical apparent height profiles of 2 N-HBC 5 and N-dome 8. The left (*right*) panel shows the apparent height profile of the experimental (theoretical) evolutions of DiPy[5]DBH, namely 2 N-HBC (*red*) and N-domes (*blue*). The N-dome is shorter and narrower than the 2 N-HBC. The sample voltage of both theoretical and experimental images was +2.0 V

may play a great role at room temperature, due to the presence of the N dopants. The decrease in apparent height from **4** (0.28 nm) to **3** (0.23 nm) reflects the flattening of the molecule due to the 2 N-HBC formation caused by the CDH. As discussed before, further annealing to 830 K leads to the observation of large graphene flakes. Previously, we have showed that graphene islands coexist with the *N*-doped nanographene domes. Upon further annealing the STM shows no more nanographene fragments, just large graphene islands.

The mechanism of formation of graphene has been the topic of different experiments [76]. In the present case, the bonds that formed the molecules break to form larger graphene islands at the Pt steps. The steps are in general more reactive sites, ideal for triggering the formation of graphene.

4.2.4 Controlling the CDH Sequence for Fullerene Precursors on Pt (111): Formation of Open-Cage Fullerenes

Figure 16 shows three STM images along the CDH path at different annealing temperatures (RT, 300 and 450 °C).

At RT and after annealing at 100 °C, the topology of the precursors is characterized at the STM by a triangular structure, which can be easily related to the structure of a flat precursor with all its hydrogen atoms intact. On the contrary, at 300 °C a drastic change in the topographical images of the molecules takes place. At this temperature, the precursor loses a substantial amount of hydrogen atoms. The images exhibit an intermediate aspect between the triangular shape and a more rounded profile, which can be related to partially closed fullerenes. At this temperature, it is estimated that the molecule has lost around an average of 6 H atoms per structural branch. Nevertheless, other different intermediate dehydrogenation steps can be detected at this temperature, which indicates that not all the PAHs have lost the same amount of hydrogen atoms. Moreover, in some cases, STM images are not symmetric, and some of the corners of the molecules exhibit a lower apparent height tan the rest. This effect may be interpreted in terms that not all the branches of the PAHs lost the same amount of H atoms for a same annealing temperature. Those branches of the molecules adsorbed on the Pt surface in an

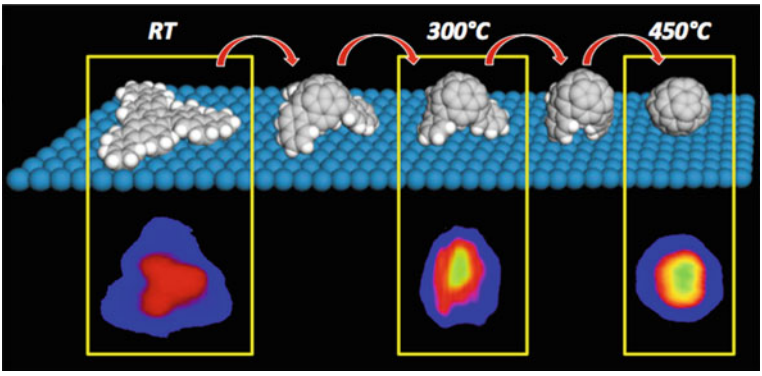

Fig. 16 Path of cyclodehydrogenation towards the fullerene formation and topographical images corresponding to annealing at RT, 300 and 450 °C. The planar precursor bends downwards as folding to form a triazafullerene. The path shows conjectural intermediate steps with partially dehydrogenated molecules, from a fully hydrogenated planar precursor to the dehydrogenated fullerene. *Bottom* topographical images show that at intermediate temperatures molecules are partially cyclodehydrogenated (I = 0.2 nA/V_s(RT) = +0.75 V/V_s(300/450 °C) = +0.5 V)

energetically more favourable configuration could start losing H atoms at higher temperatures tan the rest ones.

Nowadays, the most extended methodologies to obtain partially open fullerenes are based on the opening of a fullerene by means a series of chemical reactions. In the present case, the methodology is the opposite one, by which starting from flat molecular precursors it is possible to obtain partially open fullerenes at intermediate annealing temperatures (for instance at 300 °C). Finally, for annealing temperatures around 450 °C, the STM images reveal rounded structures that can be directly identified as fullerenes (or triazafullerenes depending on the precursor used). The detection of deuterium atoms in the TPD experiments occurs at the same temperature for which the precursor topography changes in the STM images, indicating that both processes (the dehydrogenation and the topological transformation of the PAHs) happen simultaneously. Besides, hydrogen desorbs from the Pt(111) surface at 50 °C, while when a precursor is present this occurs at 200–250 °C to start the dehydrogenation, which means that at RT the hydrogen atoms still remains attached to the PAHs.

4.3 Sequentially Formed Species on Weakly Interacting Surfaces: DiPy[5]DBH on Cu(111)

In this final subsection, we give some insights on the spectroscopic characterization of the formed structures, by means a combined NEXAFS/XPS analysis at the ALOISA beamline in the Elettra synchrotron radiation facility, for one monolayer of DiPy[5]DBH (**4**) deposited on Cu(111). DiPy[5]DBH on Cu(111) behaves similarly as on Au(111), that is, the as-deposited molecular heteroaromatic diffuses at room temperature and then upon annealing partially (cyclo-)dehydrogenates and forms polymeric networks. Hence, the interaction between the precursor and the substrate is weak, contrasting with the strong interaction observed for the previously analysed case of the DiPy[5]DBH on Pt(111). By weak interaction, we mean that the strength of the substrate-adsorbate coupling is not enough to stop surface diffusion at room temperature and that molecular structure resembles that of the free molecule, as it will be shown next.

4.3.1 High-Resolution C-K Edge NEXAFS of DiPy[5]DBH/Cu(111)

Figure 17 shows the C1s-NEXAFS of DiPy[5]DBH/Cu(111) prior to annealing, recorded for both s- and p-polarized light (dashed black and solid red lines, respectively). The room temperature partial electron yield (PEY) p-polarized NEXAFS exhibits: one asymmetric main peak *A* at 284.9 eV; four smaller peaks at *B* = 286.4 eV, *C* = 287.3 eV, *D* = 288.0 eV and *E* = 289.4 eV; a continuum after

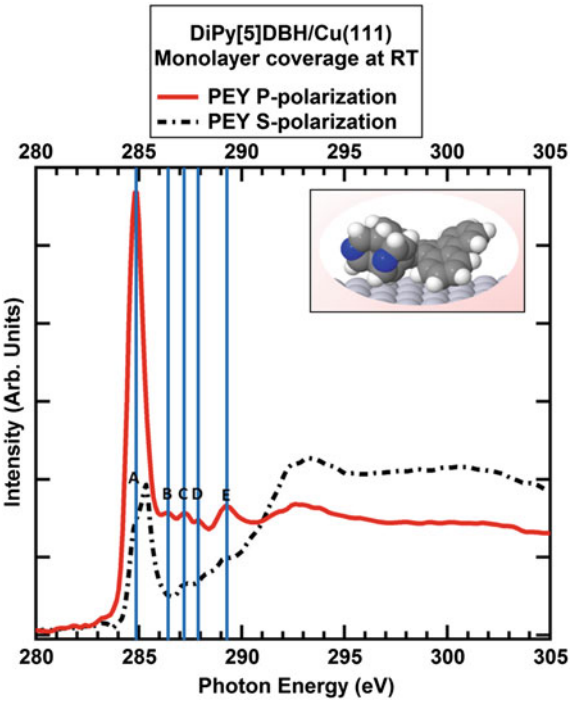

Fig. 17 RT C-K edge NEXAFS of DiPy[5]DBH/Cu (111). The solid *red line* represents the partial electron yield (PEY) p-polarized scan, while the *black dotted* one the PEY s-polarized scan. In the *inset*, the three-dimensional intact molecule is shown. The *blue lines* indicate the position of the five peaks A–E

291 eV. The s-polarized scan shows similar features; however, the asymmetry of peak A turned into two defined peaks, the second one being at 285.3 eV.

The most intense peaks at 284.9 and 285.3 eV can be assigned to the C1s transitions to the LUMO π* states of non-equivalent C sites in the molecules [77, 78]. There is a large dichroism between the s- and p-polarized signals, even though the s-polarized signal does not vanish. The π* region is less intense for s-polarized light and the σ* region is less intense for the p-polarized light. This means that the molecules are not completely flat because they conserve the 3D structure of an intact gas-phase molecule (see inset in Fig. 17). However, the s-polarized intensity is smaller than the p-one, so the benzene rings of the molecules are laying on the surface at an average angle lower than 45°, as they try to couple their aromatic rings parallel to the surface.

Moreover, for p-polarized light, the peak at 284.9 eV is the most intense, while for s-polarized light the one at 285.3 eV is prominent. This asymmetry suggests again that the as-deposited diffusing molecule is three-dimensional since the contribution to the LUMO of the C1s electrons of carbon atoms in two different positions is geometrically different. The small peaks B, D and E at 286.4, 288.0 and 289.4 eV can be associated to transitions of the C1s electrons related to the C–H groups [77, 79–81]. Peak C at 287.3 eV is likely to represent the carbon atoms in the pyridinic rings [82]. The broad features above 291 eV represent C1s transitions to the σ* symmetry [83–85].

NEXAFS spectroscopy can also be used to follow dehydrogenation process. As reported in reference [12] after annealing above 500 K the spectral line-shape changes importantly. First, most of the peaks in the region 286–289 eV, related to C–H groups, disappear. Thus, the p-spectrum becomes featureless, indicating that important chemical changes take place. Second, the dichroic behaviour of the π* region is strongly enhanced. The molecules react to each other and get planarized upon reaction, leading to the evanescence of the π* features observed in s-polarization conditions.

4.3.2 High-Resolution N1s and C1s XPS Spectra of DiPy[5]DBH/Cu (111)

Let us now move to the N1s and C1s XPS spectra recorded at various temperatures, as shown in Fig. 18. The C1s scans were fitted with five peaks and the N1s with

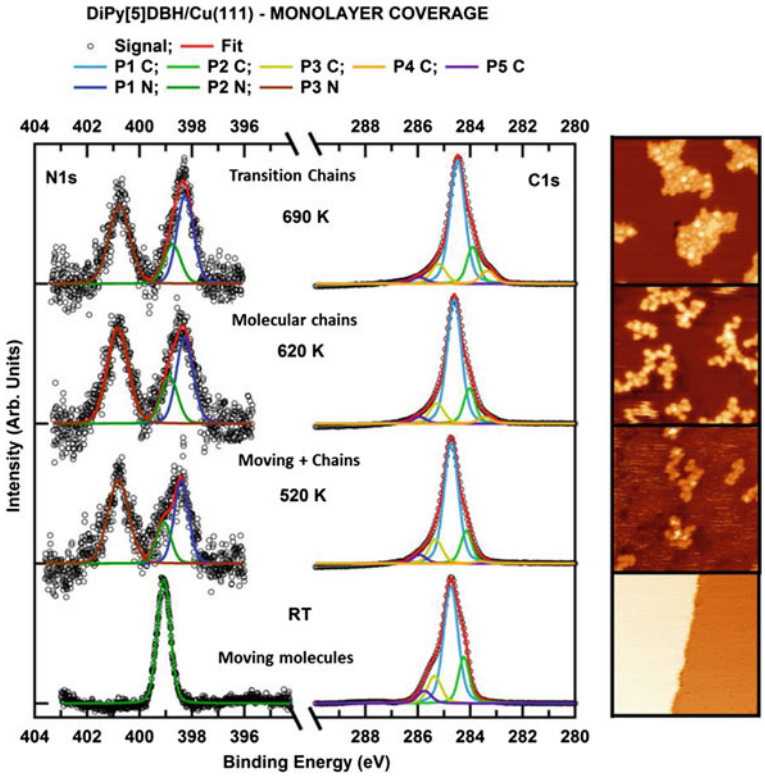

Fig. 18 N1 s and C1s XPS of one monolayer of DiPy[5]DBH/Cu(111) at various temperatures. The STM images on the *right* (20 × 20 nm^2; V_s = +2.0 V) represent the stage of the molecules upon the annealing. The intensity y-axis is not in scale for C1s and N1s. The photon energy for measuring the N1s and C1s spectra is 450 eV

three. The trend of the area of each peak with temperature helps to understand and explain the transformations of the molecules. P1-C (indicating C in aromatic rings) represents about 60 % of the intensity, and upon annealing, it peaks and then its intensity decreases: the increase is due to a decrease in P2-C (the C–H peak) caused by the dehydrogenating molecule, while the rise of the interaction with the surface (represented by P4-C) causes the final reduction.

The molecules diffuse at room temperature, so they interact weakly with the metal. However, as they (cyclo-)dehydrogenate, their motion ceases and their interaction with the surface increases. This is observed as a rise in the relative importance of P4-C (the C–Cu peak). P3-C represents the contribution of carbon atoms bonded to the N dopants and it is constant throughout the annealing meaning that N atoms are not lost up to 700 K.

At the right-hand side of the Fig. 18, STM images corresponding to the indicated annealing temperature are shown.

The N1s evolution elucidates what is occurring with the pyridinic rings of the molecule. At room temperature, when the three-dimensional molecules are moving, 100 % of N is in pyridinic form as indicated by the fact that one single component P2-N is present in the XPS. However, upon annealing, P1-N and P3-N rise at the same time: the molecules dehydrogenate so the C dangling bonds meet other molecules forming graphitic N (P3-N) or bonding with the metal surface (P1-N) as a consequence of a rotation of the pyridinic ring towards the surface.

4.4 Conclusions

The aim of this section is to uncover all the details of the partial (cyclo-)dehydrogenation of some paradigmatic organic precursors DiPy[5]DBH and $C_{57}H_{33}N_3$ to achieve different nanoarchitectures (*N*-doped nanographene/nanodomes, hetero-aromatic polymeric networks, *N*-doped nanographene and triazafullerenes) just controlling the final annealing temperature on different transition metal surfaces.

In the previous sections, it was discussed that the control over on-surface diffusion can be achieved by changing the nature of the substrate and we demonstrated how the state of the as-deposited precursor is crucial to determine the final outcome. In this section, we demonstrate that a combination of the most advanced first-principles theoretical calculations (explained in Sect. 2), STM, XPS and NEXAFS allow us to follow the structural and chemical transformations experienced by the molecular precursor step by step.

On Pt(111), a hierarchical transformation of DiPy[5]DBH is observed. Upon deposition, the non-annealed precursor is intact and exhibits a four-lobes molecular orbital structure. When heated, the precursor undergoes four phase transitions. At 450 K, an intermediate cyclodehydrogenated phase occurs. At 650 K, 2 N-HBC (*N*-doped nanographene) is formed via CDH of the precursor. Further, annealing allows the complete cleavage of the C–H bonds and the bending of the molecules

into *N*-doped nanodomes covalently bonded with the surface. The final phase transition results in the decomposition of the molecule to form *N*-doped graphene at 850 K.

Some insights are also given about the control of the CDH sequence in the formation of fullerene on Pt(111). Controlling the annealing temperature, open-cage structures can be formed on the surface. We finally conclude summarizing the main chemical aspects of the temperature-assisted CDH of DiPy[5]DBH on Cu(111) from a point of view framed on a NEXAFS and XPS analysis, which spectroscopically shows spectroscopic fingerprints of all the intermediates formed.

References

1. Champness, N.R.: Surface chemistry: Building with molecules. Nat. Nanotechnol. **2**, 671 (2007)
2. Martín-Gago, J.A.: Polycyclic aromatics: On-surface molecular engineering. Nat. Chem. **3**, 11 (2011)
3. Méndez, J., López, M.F., Martín-Gago, J.A.: On-surface synthesis of cyclic organic molecules. Chem. Soc. Rev. **40**, 4578 (2011)
4. Côté, A.P., Benin, A.I., Ockwig, N.W., O'Keeffe, M., Matzger, A.J., Yaghi, O.M.: Porous, crystalline, covalent organic frameworks. Science **310**, 1166 (2005)
5. Grill, L., Dyer, M., Lafferentz, L., Persson, M., Peters, M.V., Hecht, S.: Nano-architectures by covalent assembly of molecular building blocks. Nat. Nanotechnol. **2**, 687 (2007)
6. Weigelt, S., Busse, C., Bombis, C., Knudsen, M.M., Gothelf, K.V., Strunskus, T., Dahlbom, M., Besenbacher, F., Linderoth, T.R.: Covalent interlinking of an aldehyde and an amine on a Au(111) surface in ultrahigh vacuum. Angew. Chem. Int. Ed. **46**, 9227 (2007)
7. Rim, K.T., Siaj, M., Xiao, S., Myers, M., Carpentier, V.D., Liu, L., Su, C., Steigerwald, M.L., Hybertsen, M.S., McBreen, P.H., Flynn, G.W., Nuckolls, C.: Forming aromatic hemispheres on transition-metal surfaces. Angew. Chem. Int. Ed. **46**, 7891 (2007)
8. Otero, G., Biddau, G., Sánchez-Sánchez, C., Caillard, R., López, M.F., Rogero, C., Palomares, F.J., Cabello, N., Basanta, M.A., Ortega, J., Méndez, J., Echavarren, A.M., Pérez, R., Gómez-Lor, B., Martín-Gago, J.A.: Fullerenes from aromatic precursors by surface-catalysed cyclodehydrogenation. Nature **454**, 865 (2008)
9. Amsharov, K., Abdurakhmanova, N., Stepanow, S., Rauschenbach, S., Jansen, M., Kern, K.: Towards the isomer-specific synthesis of higher fullerenes and buckybowls by the surface-catalyzed cyclodehydrogenation of aromatic precursors. Angew. Chem. Int. Ed. **49**, 9392 (2010)
10. Treier, M., Pignedoli, C.A., Laino, T., Rieger, R., Müllen, K., Passerone, D., Fasel, R.: Surface-assisted cyclodehydrogenation provides a synthetic route towards easily processable and chemically tailored nanographenes. Nat. Chem. **3**, 61 (2011)
11. Cai, J., Ruffieux, P., Jaafar, R., Bieri, M., Braun, T., Blankenburg, S., Muoth, M., Seitsonen, A.P., Saleh, M., Feng, X., Müllen, K., Fasel, R.: Atomically precise bottom-up fabrication of graphene nanoribbons. Nature **466**, 470 (2010)
12. Pinardi, A.L., Otero-Irurueta, G., Palacio, I., Martínez, J.I., Sánchez-Sánchez, C., Tello, M., Rogero, C., Cossaro, A., Preobrajenski, A., Gómez-Lor, B., Jancarik, A., Stará, I.G., Stary, I., López, M.F., Méndez, J., Martín-Gago, J.A.: Tailored formation of N-doped nanoarchitectures by diffusion-controlled on-surface (cyclo)dehydrogenation of heteroaromatics. ACS Nano **7**, 3676 (2013)
13. Pinardi, A.L., Martínez, J.I., Jancarik, A., Stará, I.G., Stary, I., López, M.F., Méndez, J., Martín-Gago, J.A.: Sequential formation of N-doped nanohelicenes, nanographenes and

nanodomes by surface-assisted chemical (cyclo)dehydrogenation of heteroaromatics. Chem. Commun. **50**, 1555 (2014)
14. Mueller, A., Amsharov, K.: Synthesis of precursors for large-diameter hemispherical buckybowls and precursors for short carbon nanotubes. Eur. J. Org. Chem. **36**, 7153 (2012)
15. Sánchez-Valencia, J.R., Dienel, T., Gröning, O., Shorubalko, I., Mueller, A., Jansen, M., Amsharov, K., Ruffieux, P., Fasel, R.: Controlled synthesis of single-chirality carbon nanotubes. Nature **512**, 61 (2014)
16. Bieri, M., Nguyen, M., Gro, O., Cai, J., Treier, M., Aït-Mansour, K., Ruffieux, P., Pignedoli, C.A., Passerone, D., Kastler, M., Mu, K.: Two-dimensional polymer formation on surfaces: insight into the roles of precursor mobility and reactivity. J. Amer. Chem. Soc. **132**, 16669 (2010)
17. Lipton-Duffin, J.A., Ivasenko, O., Perepichka, D.F., Rosei, F.: Synthesis of polyphenylene molecular wires by surface-confined polymerization. Small **5**, 592 (2009)
18. Lafferentz, L., Ample, F., Yu, H., Hecht, S., Joachim, C., Grill, L.: Conductance of a single conjugated polymer as a continuous function of its length. Science **323**, 1193 (2009)
19. Dinca, L.E., Fu, C., MacLeod, J.M., Lipton-Duffin, J., Brusso, J.L., Szakacs, C.E., Ma, D., Perepichka, D.F., Rosei, F.: Unprecedented transformation of tetrathienoanthracene into pentacene on Ni(111). ACS Nano **7**, 1652 (2013)
20. Lafferentz, L., Eberhardt, V., Dri, C., Africh, C., Comelli, G., Esch, F., Hecht, S., Grill, L.: Controlling on-surface polymerization by hierarchical and substrate-directed growth. Nat. Chem. **4**, 215 (2012)
21. Kittelmann, M., Rahe, P., Nimmrich, M., Hauke, C.M., Ku, A.: On-Surface Covalent Linking of Organic Building Blocks on a Bulk Insulator. ACS Nano **5**, 8420 (2011)
22. Sánchez-Sánchez, C., Martínez, J.I., Lanzilotto, V., Biddau, G., Gómez-Lor, B., Pérez, R., Floreano, L., López, M.F., Martín-Gago, J.A.: Chemistry and temperature-assisted dehydrogenation of $C_{60}H_{30}$ molecules on TiO_2(110) surfaces. Nanoscale **5**, 11058 (2013)
23. Bartels, L.: Tailoring molecular layers at metal surfaces. Nat. Chem. **2**, 87 (2010)
24. Gourdon, A.: On-surface covalent coupling in ultrahigh vacuum. Angew. Chem. Int. Ed. **47**, 6950 (2008)
25. Lackinger, M., Heckl, W.M.: Perspective on covalent intermolecular coupling reactions on surfaces. J. Phys. D Appl. Phys. **44**, 1 (2011)
26. Palma, C.A., Samori, P.: Homo-coupling of terminal alkynes on a noble metal surface. Nat. Chem. **3**, 431 (2011)
27. Zhong, D., Franke, J.H., Podiyanachari, S.K., Blömker, T., Zhang, H., Kehr, G., Erker, G., Fuchs, H., Chi, L.: Linear alkane polymerization on a gold surface. Science **334**, 213 (2011)
28. Usachov, D., Vilkov, O., Grüneis, A., Haberer, D., Fedorov, A., Adamchuk, V.K., Preobrajenski, A.B., Dudin, P., Barinov, A., Oehzelt, M., Laubschat, C., Vyalikh, D.V.: Nitrogen-doped graphene: efficient growth, structure, and electronic properties. Nanoletters **11**, 5401 (2011)
29. Barth, J.V., Costantini, G., Kern, K.: Engineering atomic and molecular nanostructures at surfaces. Nature **437**, 671 (2005)
30. Fuhrmann, T., Kinne, M., Tränkenschuh, B., Papp, C., Zhu, J.F., Denecke, R., Steinrück, H.P.: Activated adsorption of methane on Pt(1 1 1) — an in situ XPS study. New J. Phys. **7**, 107 (2005)
31. Ugeda, M., Fernández-Torre, D., Brihuega, I., Pou, P., Martínez-Galera, A., Pérez, R., Gómez-Rodríguez, J.: Point defects on graphene on metals. Phys. Rev. Lett. **107**, 116803 (2011)
32. Manner, W.L., Girolami, G.S., Nuzzo, R.G.: Sequential dehydrogenation of unsaturated cyclic C_5 and C_6 hydrocarbons on Pt(111). J. Phys. Chem. B **102**, 10295 (1998)
33. Streitwieser, A., Heathcock, C.H.: Introduction to Organic Chemistry. Macmillan, New York (1985)
34. Gómez-Lor, B., Echavarren, A.M.: Synthesis of a triaza analogue of crushed-fullerene by intramolecular palladium-catalyzed arylation. Org. Lett. **6**, 2993 (2004)

35. Otero, G., Biddau, G., Ozaki, T., Gómez-Lor, B., Méndez, J., Pérez, R., Martín-Gago, J.A.: Spontaneous discrimination of polycyclic aromatic hydrocarbon (PAH) enantiomers on a metal surface. Chemistry. A Eur. J. **16**, 13920 (2010)
36. Lewis, J.P., Jelínek, P., Ortega, J., Demkov, A.A., Trabada, D.G., Haycock, B., Wang, H., Adams, G., Tomfohr, J.K., Abad, E., Wang, H., Drabold, D.A.: Advances and applications in the FIREBALL ab initio tight-binding molecular-dynamics formalism. Phys. Stat. Sol. B **248**, 1989 (2011)
37. GAUSSIAN, Gaussian, Inc., Wallingford. URL: www.gaussian.com (2009)
38. Soler, J.M., Artacho, E., Gale, J.D., García, A., Junquera, J., Ordejón, P., Sánchez-Portal, D.: The SIESTA method for ab initio order-N materials simulation. J. Phys. Cond. Matt. **14**, 2745 (2002)
39. Giannozzi, P., et al.: QUANTUM ESPRESSO: a modular and open-source software project for quantum simulations of materials. J. Phys.: Condens. Matter **21**, 395502 (2009)
40. Hafner, J.: Ab-initio simulations of materials using VASP: density-functional theory and beyond. J. Comput. Chem. **29**, 2044 (2008)
41. Gonze, X., et al.: ABINIT: First-principles approach to material and nanosystem properties. Comput. Phys. Commun. **180**, 2582 (2009)
42. Abad, E., Dappe, Y.J., Martínez, J.I., Flores, F., Ortega, J.: C_6H_6/Au(111): Interface dipoles, band alignment, charging energy, and van der Waals interaction. J. Chem. Phys. **134**, 044701 (2011)
43. Dappe, Y.J., Basanta, M.A., Ortega, J., Flores, F.: Weak chemical interaction and van der Waals forces between graphene layers: a combined density functional and intermolecular perturbation theory approach. Phys. Rev. B **74**, 205434 (2006)
44. Basanta, M.A., Dappe, Y.J., Ortega, J., Flores, F.: Van der Waals forces in the local-orbital density functional theory. Europhys. Lett. **70**, 355 (2005)
45. Barone, V., Casarin, M., Forrer, D., Pavone, M., Sambi, M., Vittadini, A.: Role and effective treatment of dispersive forces in materials: polyethylene and graphite crystals as test cases. J. Comput. Chem. **30**, 934 (2009)
46. Elstner, M., Hobza, P., Frauenheim, T., Suhai, S., Kaxiras, E.: Hydrogen bonding and stacking interactions of nucleic acid base pairs: a density-functional-theory based treatment. J. Chem. Phys. **114**, 5149 (2001)
47. Gavezzotti, A.: The calculation of molecular volumes and the use of volume analysis in the investigation of structured media and of solid-state organic reactivity. J. Am. Chem. Soc. **105**, 5220 (1983)
48. Dunitz, J.D., Gavezzotti, A.: Attractions and repulsions in organic crystals: what can be learned from the crystal structures of condensed-ring aromatic hydrocarbons? Acc. Chem. Res. **32**, 677 (1999)
49. Filippini, G., Gavezzotti, A.: Empirical intermolecular potentials for organic crystals: the 6-exp' approximation revisited. Acta Crystallogr. Sect. B: Struct. Sci. **49**, 868 (1993)
50. Mowbray, D.J., Martínez, J.I., García-Lastra, J.M., Thygesen, K.S., Jacobsen, K.W.J.: Stability and electronic properties of TiO_2 nanostructures with and without B and N doping. J. Phys. Chem. C **113**, 12301 (2009)
51. Martínez, J.I., García-Lastra, J.M., López, M.J., Alonso, J.A.: Optical to ultraviolet spectra of sandwiches of benzene and transition metal atoms: time dependent density functional theory and many-body calculations. J. Chem. Phys. **132**, 044314 (2010)
52. Martínez, J.I., Abad, E., Flores, F., Ortega, J.: Simulating the organic-molecule/metal interface TCNQ/Au(111). Phys. Stat. Sol. B **248**, 2044 (2011)
53. Martínez, J.I., Abad, E., Flores, F., Ortega, J., Brocks, G.: Barrier height formation in organic blends/metal interfaces: case of tetrathiafulvalene-tetracyanoquinodimethane/Au. Chem. Phys. **390**, 14 (2011)
54. Hybertsen, M.S., Louie, S.G.: First-principles theory of quasiparticles: calculation of band gaps in semiconductors and insulators. Phys. Rev. Lett. **55**, 1418 (1985)
55. Hybertsen, M.S., Louie, S.G.: Electron correlation in semiconductors and insulators: band gaps and quasiparticle energies. Phys. Rev. B **34**, 5390 (1986)

56. Marini, A., Hogan, C., Grüning, M., Varsano, D.: YAMBO: An ab initio tool for excited state calculations. Comput. Phys. Commun. **180**, 1392 (2009)
57. Rohlfing, M., Louie, S.G.: Excitons and optical spectrum of the Si(111)−(2×1) surface. Phys. Rev. Lett. **83**, 856 (1999)
58. Onida, G., Reining, L., Rubio, A.: Electronic excitations: density-functional versus many-body Green's-function approaches. Rev. Mod. Phys. **74**, 601 (2002)
59. Berne, B.J., Cicotti, G., Coker, D.F.: Classical and Quantum Dynamics in Condensed Phase Simulations. World Scientific Publishing Company, Singapore (1998)
60. Henkelman, G., Jonsson, H.J.: Improved tangent estimate in the nudged elastic band method for finding minimum energy paths and saddle points. Chem. Phys. **113**, 9978 (2000)
61. Henkelman, G., Uberuaga, B.P., Jonsson, H.J.: A climbing image nudged elastic band method for finding saddle points and minimum energy paths. Chem. Phys. **113**, 9901 (2000)
62. Blanco, J.M., González, C., Jelínek, P., Ortega, J., Flores, F., Pérez, R.: First-principles simulations of STM images: from tunneling to the contact regime. Phys. Rev. B **70**, 085405 (2004)
63. Blanco, J.M., Flores, F., Pérez, R.: STM-theory: image potential, chemistry and surface relaxation. Prog. Surf. Sci. **81**, 403 (2006)
64. Martínez, J.I., Abad, E., González, C., Flores, F., Ortega, J.: Improvement of scanning tunneling microscopy resolution with H-sensitized tips. Phys. Rev. Lett. **108**, 246102 (2012)
65. Sánchez-Sánchez, C., González, C., Jelínek, P., Méndez, J., de Andres, P.L., Martín-Gago, J.A., López, M.F.: Understanding atomic-resolved STM images on TiO_2(110)-(1×1) surface by DFT calculations. Nanotechnology **21**, 405702 (2010)
66. Martínez, J.I., Abad, E., González, C., Ortega, J., Flores, F.: Theoretical characterization of the TTF/Au(111) interface: STM imaging, band alignment and charging energy. Org. Electron. **13**, 399 (2012)
67. Tersoff, J., Hamann, D.R.: Theory and application for the scanning tunneling microscope. Phys. Rev. Lett. **50**, 1998 (1983)
68. Tersoff, J., Hamann, D.R.: Theory of the scanning tunneling microscope. Phys. Rev. B **31**, 805 (1985)
69. Gross, L., Moll, N., Mohn, F., Curioni, A., Meyer, G., Hanke, F., Persson, M.: High-resolution molecular orbital imaging using a p-wave STM tip. Phys. Rev. Lett. **107**, 086101 (2011)
70. Pinardi, A.L., Biddau, G., van de Ruit, K., Otero-Irurueta, G., Gardonio, S., Lizzit, S., Schennach, R., Flipse, C.F.J., López, M.F., Méndez, J., Pérez, R., Martín-Gago, J.A.: Vacancy formation on C_{60}/Pt (111): unraveling the complex atomistic mechanism. Nanotech. **25**, 385602 (2014)
71. Weiss, K., Beernink, G., Dötz, F., Birkner, A., Müllen, K., Wöll, C.: Template-mediated synthesis of polycyclic aromatic hydrocarbons: cyclodehydrogenation and planarization of a hexaphenylbenzene derivative at a copper surface. Angew. Chem. Int. Ed. **38**, 3748 (1999)
72. Beernink, G., Gunia, M., Dötz, F., Öström, H., Weiss, K., Müllen, K., Wöll, C.: Synthesis of polycyclic aromatic hydrocarbons and graphite islands via surface-induced reaction of small molecules. ChemPhysChem **2**, 317 (2001)
73. Martínez-Galera, A.J., Brihuega, I., Gómez-Rodríguez, J.M.: Ethylene irradiation: a new route to grow graphene on low reactivity metals. Nanolett. **11**, 3576 (2011)
74. Zhao, L., He, R., Rim, K.T., Schiros, T., Kim, K.S., Zhou, H., Gutierrez, C., Chockalingam, S. P., Arguello, C.J., Palova, L., Nordlund, D., Hybertsen, M.S., Reichman, D.R., Heinz, T.F., Kim, P., Pinczuk, A., Flynn, G.W., Pasupathy, A.N.: Visualizing individual nitrogen dopants in monolayer graphene. Science **333**, 999 (2011)
75. Violi, A.: Cyclodehydrogenation reactions to cyclopentafused polycyclic aromatic hydrocarbons. J. Phys. Chem. A **109**, 7781 (2005)
76. Lizzit, S., Baraldi, A.: High-resolution fast X-ray photoelectron spectroscopy study of ethylene interaction with Ir(111): from chemisorption to dissociation and graphene formation. Catal. Today **154**, 68 (2010)

77. Oji, H., Mitsumoto, R., Ito, E., Ishii, H., Ouchi, Y., Seki, K., Yokoyama, T., Ohta, T., Kosugi, N.: Core hole effect in NEXAFS spectroscopy of polycyclic aromatic hydrocarbons: benzene, chrysene, perylene, and coronene. J. Chem. Phys. **109**, 10409 (1998)
78. Zhang, W., Nefedov, A., Naboka, M., Cao, L., Wöll, C.: Molecular orientation of terephthalic acid assembly on epitaxial graphene: NEXAFS and XPS study. PhysChemChemPhys **14**, 10125 (2012)
79. Weiss, K., Gebert, S., Wühn, M., Wadepohl, H., Wöll, C.: Near edge x-ray absorption fine structure study of benzene adsorbed on metal surfaces: comparison to benzene cluster complexes. J. Vac. Sci. Tech. A **16**, 1017 (1998)
80. Lee, V., Park, C., Jaye, C., Fischer, D.A., Yu, Q., Wu, W., Liu, Z., Bao, J., Pei, S.S., Smith, C., Lysaght, P., Banerjee, S.: Substrate hybridization and rippling of graphene evidenced by near-edge X-ray absorption fine structure spectroscopy. J. Phys. Chem. Lett. **1**, 1247 (2010)
81. Schultz, B.J., Patridge, C.J., Lee, V., Jaye, C., Lysaght, P.S., Smith, C., Barnett, J., Fischer, D. A., Prendergast, D., Banerjee, S.: Imaging local electronic corrugations and doped regions in graphene. Nat. Commun. **2**, 372 (2011)
82. Schmidt, N., Fink, R., Hieringer, W.: Assignment of near-edge x-ray absorption fine structure spectra of metalloporphyrins by means of time-dependent density-functional calculations. J. Chem. Phys. **133**, 054703 (2010)
83. Kikuma, J., Yoneyama, K., Nomura, M., Konishi, T., Hashimoto, T., Mitsumoto, R., Ohuchi, Y., Seki, K.: Surface analysis of CVD carbon using NEXAFS, XPS and TEM. J. Elec. Spec. Rel. Phen. **88**, 919 (1998)
84. Preobrajenski, A.B., Ng, M.L., Vinogradov, A.S., Mårtensson, N.: Controlling graphene corrugation on lattice-mismatched substrates. Phys. Rev. B **78**, 073401 (2008)
85. Dedkov, Y.S., Sicot, M., Fonin, M.: X-ray absorption and magnetic circular dichroism of graphene/Ni(111). J. Appl. Phys. **107**, 09E121 (2010)

Enediyne Cyclization Chemistry on Surfaces Under Ultra-High Vacuum

Dimas G. de Oteyza

Abstract The synthesis of complex molecular materials directly on surfaces under ultra-high vacuum is a new chemical approach attracting increasing interest. Inspired in the well-established conventional organic chemistry, an increasing number of reactions are being tested and demonstrated to work also under vacuum. Among those reactions, we find enediyne cyclizations, which open up promising new routes to create π-conjugated molecular materials that can be tailored through the choice of appropriate precursors and substrates. This chapter reviews the pioneering experiments of enediyne-based chemistry on atomically clean surfaces under ultra-high vacuum, put in relation to available knowledge from the conventional wet-chemistry analogues.

1 Introduction

The tunable properties of molecular materials place them among the favorites for a variety of future generation devices. Beyond the readily commercialized organic electronic devices, the range of potential applications foreseen for supramolecular materials is dramatically increasing and includes functionalities and device structures with great degrees of sophistication. For example, self-assembly of well-defined molecular structures is considered among the most promising strategies to maintain the current trend of device miniaturization, for which a significant modification of the present top-down production methods will soon be required. A reliable synthesis of functional supramolecular structures from the bottom-up

D.G. de Oteyza (✉)
Donostia International Physics Center, Paseo Manuel Lardizabal, 4,
20018 San Sebastián, Spain
e-mail: d_g_oteyza@ehu.es; d_g_oteyza@ehu.eus

D.G. de Oteyza
Centro de Física de Materiales CSIC-UPV/EHU, Paseo Manuel Lardizabal, 5,
20018 San Sebastián, Spain

A. Gourdon (ed.), *On-Surface Synthesis*, Advances in Atom and Single Molecule Machines, DOI 10.1007/978-3-319-26600-8_4

could pave the way toward industrial production of single-/few-molecule devices with dramatically reduced length scales. And the potential of precisely controlled molecular structures reaches even further. It would, for example, allow control over new and fascinating properties emerging in nanoscale-structured systems, which could in turn be used for optimized macroscopic devices such as sensors, filters, solar cells, or catalysts.

Along these lines, the main challenge remains to synthesize appropriate materials optimized for each particular functionality, which depending on the latter might require structures of substantial complexity. This in turn necessitates on the one hand a sufficient understanding of the structure–property relations to allow the rational design of molecular structures with the desired properties, and on the other hand the capability to build those previously designed structures. Acquisition of such understanding and control of matter at the molecular scale has been the goal of countless investigations over the last decades, which have indeed led to significant advances. Molecular self-assembly has, for example, been successfully used to create many kinds of supramolecular structures [1, 2]. Even restricting ourselves to materials on solid surfaces under ultra-high vacuum (UHV), an enormous variety of two-dimensional, one-dimensional, or zero-dimensional molecular structures with diverse compositions, symmetries, electronic, optic, or magnetic properties have been synthesized [1, 2]. However, self-assembly typically relies on weak, non-covalent intermolecular interactions such as hydrogen bonds or metal coordination. This carries some disadvantages, as is the reduced assembly's resistance and consequently the compromised durability of a potential device, or also a strong localization of the electronic states, which limits the charge carrier mobility and thereby the structure's efficiencies in many electronic or optical processes.

Only recently, formation of covalently bonded supramolecular structures directly on surfaces was demonstrated [3, 4]. And although the first pioneering examples still relied on the manual guidance of the reactions by means of a scanning tunneling microscope (STM), inspiring works demonstrating the self-assembled growth of covalently bonded molecular networks, tailored by appropriate design of the precursors, began appearing in 2007 [5, 6]. The consequences of this approach are far reaching. Not only is the stability of the molecular structures greatly increased and the charge transfer integral along the network enhanced, but it also allows the synthesis of complex molecular structures directly on surfaces of technological interest. Most applications require solid supports, and the transfer of complex molecular building blocks synthesized ex situ by conventional chemistry is often hampered by solubility problems or by thermal fragmentation if deposited by sublimation. Therefore, in addition to the intrinsic advantages of covalently linked structures, further compelling aspects of this so-called on-surface chemistry are that tedious transfer procedures [7] might be avoided, as well as that it can allow the occurrence of reactions and the synthesis of materials not achievable by other means [8, 9].

Among the multiple differences between conventional organic chemistry and on-surface chemistry under UHV is the absence of a traditionally crucial and tunable parameter: the solvent. However, here it is the surface which, in a somewhat

related role, becomes a key player. In addition to the 2D confinement that it imposes on the reactants (or even 1D if appropriately structured surfaces are used [9–11]), it might act itself as a catalyzer [11, 12]. Understanding the role of the surfaces to rationally use it according to our needs thus becomes one of the important challenges lying ahead toward the full exploitation of on-surface chemistry's potential.

2 Enediyne Cyclization Chemistry

In spite of the associated research having boomed in the last years, it is believed that only an insignificant part of the potential of UHV on-surface chemistry has been unveiled to date. Most efforts have been aimed at the demonstration of particular chemical reactions inspired in conventional wet chemistry [13, 14]. The positive verification of some of those reactions on surfaces even under UHV has been extremely stimulating, since it places a vast wealth of knowledge accumulated over decades in conventional organic chemistry as an enormous test bed for UHV on-surface chemistry. Among the successfully run reactions, we find the cyclization of enediynes [15].

After Bergman's seminal report on the cyclization of enediynes upon thermal activation [16], the interest in this reaction sparked when enediynes were found to be the bioactive site of naturally occurring antibiotics [17]. The diradicals formed upon enediyne cyclization (Fig. 1) can abstract hydrogen from the DNA backbone, causing DNA cleavage and cell death. But in addition to its relevance in biochemistry, it was John and Tour who noticed the potential of the Bergman cyclization reaction for the material science community and demonstrated its use for the synthesis of conjugated aromatic polymers (such as polyphenylenes or polynaphthalene derivatives) by radical step-growth polymerization (Fig. 1) [18, 19]. However, it was soon found that in addition to the radical step growth, initially

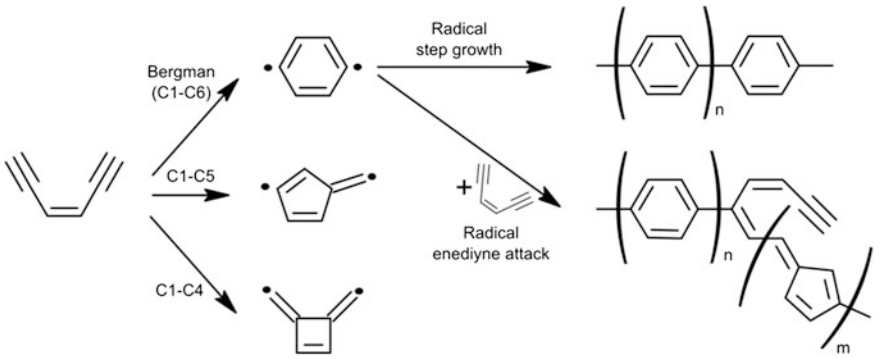

Fig. 1 Schematic representation of various possible cyclization and polymerization routes of an enediyne

generated radicals can also attack the alkynes of still unreacted enediynes, greatly increasing the possible reaction paths. This translates into associated products including highly irregular structures with 6- and also 5-membered rings, branched chains, and unreacted alkynes (Fig. 1) [20].

Besides, in addition to the Bergman or C1–C6 cyclization, different C1–C5 and even C1–C4 cyclizations can equally occur (Fig. 1). While the two latter are generally thermodynamically unfavored [21], several factors have been shown to sway the energetic balance toward C1–C5 cyclizations [22]. This is, for example, the case if bulky alkyne terminal groups are present, causing steric congestion upon cyclization [21–23]. Electronic effects have a similarly significant influence on the cyclization, in which two mutually perpendicular arrays of π-orbitals play along with different roles. In-plane π-orbitals are sacrificed to form a σ-bond and two radicals, while out-of-plane π-orbitals evolve smoothly toward the cyclic aromatic π-system product [22, 24, 25]. The relative energies of in-plane and out-of-plane molecular orbitals cross along the cyclization. Thus, while the highest occupied and lowest unoccupied molecular orbitals (HOMO and LUMO, respectively) of the reactant typically involves out-of-plane π-orbitals, in the cyclization product the frontier orbitals are normally localized in in-plane (radical) orbitals. This crossing has little importance in the thermal reactivity of neutral unexcited enediynes, but becomes relevant if the LUMO (HOMO) gets populated (depopulated) by reduction (oxidation) or photochemical excitation, often favoring C1–C5 cyclizations [22, 25, 26]. In particular, as a result of this crossing and additional aromaticity changes upon enediyne reduction, calculations show that the radical–anionic cyclization mechanism differs substantially from the thermal counterpart. Energetically, radical–anionic cyclization of reduced enediynes lowers the transition state and increases the exothermicity of both C1–C6 and C1–C5 cyclizations, but shows a significantly stronger influence on the latter [22, 25]. Also, the presence of certain catalysts has been reported to favor the C1–C5 pathway for thermal cyclizations [27]. Besides, different reactions such as alkyne homocoupling might also occur and contribute to possible dimerization or polymerization processes of yet uncyclized enediynes [12, 28, 29].

Altogether, the use of enediyne cyclization chemistry for synthetic applications is challenging due to the great number of possible reaction pathways: multiple cyclization options, each allowing both for subsequent radical step growth or radical attack of still unreacted enediynes (Fig. 1), alkyne coupling, and combinations thereof. Nevertheless, in spite of all the complexity, enediyne cyclization has become an important platform for conventional wet-chemistry-based synthesis of functional polymers [30]. Furthermore, a similarly interesting application of enediyne cyclizations is for the transformation of readily synthesized polymers. The cyclization chain reaction of poly-alkynes arranged in what can be seen as overlapping enediyne units has, for example, been proposed as a potential synthesis route to obtain graphene nanoribbons with atomically controlled structures (Fig. 2a) [31, 32].

All the above is referred to enediyne chemistry in solution, but is expected to apply at least to some extent also on surfaces under ultra-high vacuum. Under these

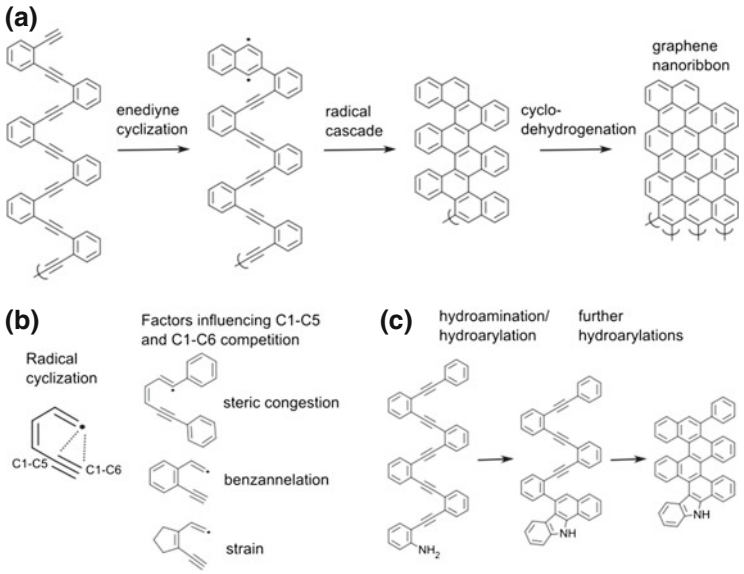

Fig. 2 **a** Example of poly-alkyne on which an initial enediyne cyclization triggers a subsequent radical cascade that may afford graphene nanoribbons upon additional cyclodehydrogenation. **b** C1–C5 and C1–C6 radical cyclizations, and some of the factors influencing their competing balance. **c** Gold(I)-catalyzed cyclization cascade by hydroamination and hydroarylations reported in Ref. [34]

new conditions, the substrate may additionally influence the chemical processes by acting as a catalyst, as a template, causing molecule-substrate charge transfer, etc. In this frame, it is interesting to remark that enediyne cyclization in principle does not require catalyzing agents. Thus, while the experiments under UHV reported to date have been performed on metal surfaces, this reaction holds promise to work also on insulators, as would be ultimately required for many technological applications. In the following, experiments performed on surfaces under UHV will be described and put in relation to our available knowledge from wet chemistry for each of these two approaches: chain reaction in poly-alkynes and radical step-growth polymerization of cyclized enediynes.

3 Chain Reactions

In molecular structures as shown in Fig. 2a, featuring coupled alkynes that form "overlapping enediynes," an initial cyclization generates diradicals that subsequently attack the neighboring alkynes and thereby trigger a chain reaction [32]. These radical cyclization cascades differ from the analogous thermal single enediyne cyclization reactions, but the product structures still result from the balance of

competing C1–C5 and C1–C6 pathways [33]. Among the factors affecting that balance we find the benzannelation of the conjugated radical reactants, steric congestion from bulky alkyne terminal groups, or strain (Fig. 2b) [33]. While the two former tend to favor C1–C5 cyclizations, the latter reverses the selectivity and favors C1–C6 cyclizations. Noteworthy, strain is particularly relevant in cascade radical cyclizations where rigid polycyclic frameworks are created.

A phenomenologically different example of chain reaction is displayed in Fig. 2c, by means of which polycyclic conjugated frameworks have been created in solution [34]. In that case, in the presence of a gold(I) catalyst, an initial hydroamination forming a 5-membered ring triggers subsequent hydroarylations with the available alkynes that form exclusively 6-membered rings, as would be desirable, for example, for graphene nanoribbon formation from longer polymeric chains. However, experiments on surfaces under UHV following this approach have not yet been reported, in contrast to radical cyclization cascades.

In particular, the cyclization cascade of 1,2-bis((2-ethynylphenyl)ethynyl)benzene on Ag(100) surfaces under UHV has been studied at the single molecule level with a powerful combination of scanning tunneling microscopy (STM) and tuning fork-based non-contact atomic force microscopy (nc-AFM), by means of which the local density of states (LDOS) and internal bond structure of the molecules can be imaged, respectively [35, 36]. The product structures resulting after annealing the precursor-decorated Ag(100) surface to temperatures above 90 °C are multiple, although close to 80 % is made up by the two majority structures displayed in Fig. 3a.

The reactivity of the precursor can be rationalized considering it as three independent but overlapping benzannelated enediyne systems with terminal alkyne substitutions of two phenyl rings for the central enediyne, or one phenyl ring and one hydrogen atom in the terminal segments (Fig. 3). This treatment suggests three potential cyclizations along the reaction pathway. However, additional isomerization processes such as [1,2]-radical shifts and bond rotations are required to explain the reactant transformation into the majority products. Combinations of those processes leading to the products in a minimal number of steps were explored and analyzed using density functional theory (DFT) calculations displayed in Fig. 3b, c [36]. The calculations indicate that due to the exothermic character of the initial cyclizations, all barriers associated with subsequent isomerization steps remain at lower energies and are thus not rate limiting. That is, the effective transition state is found along the initial cyclization. This is in line with the experimental observations: The reactant molecules on Ag(100) are stable up to temperatures of $\sim$90 °C, and above that threshold temperature, no intermediates on the reaction pathway to the final products is observed. Consequently, the order of the various processes following the rate limiting initial cyclizations cannot be strictly determined experimentally. However, the sequence does not change the overall reaction kinetics and thermodynamics discussed above.

Interestingly, both reaction pathways involve C1–C5 cyclizations. This can be explained by the multiple factors applying to this system that, as described above, tend to favor C1–C5 versus C1–C6 cyclizations: (i) bulky phenyl substituents at the

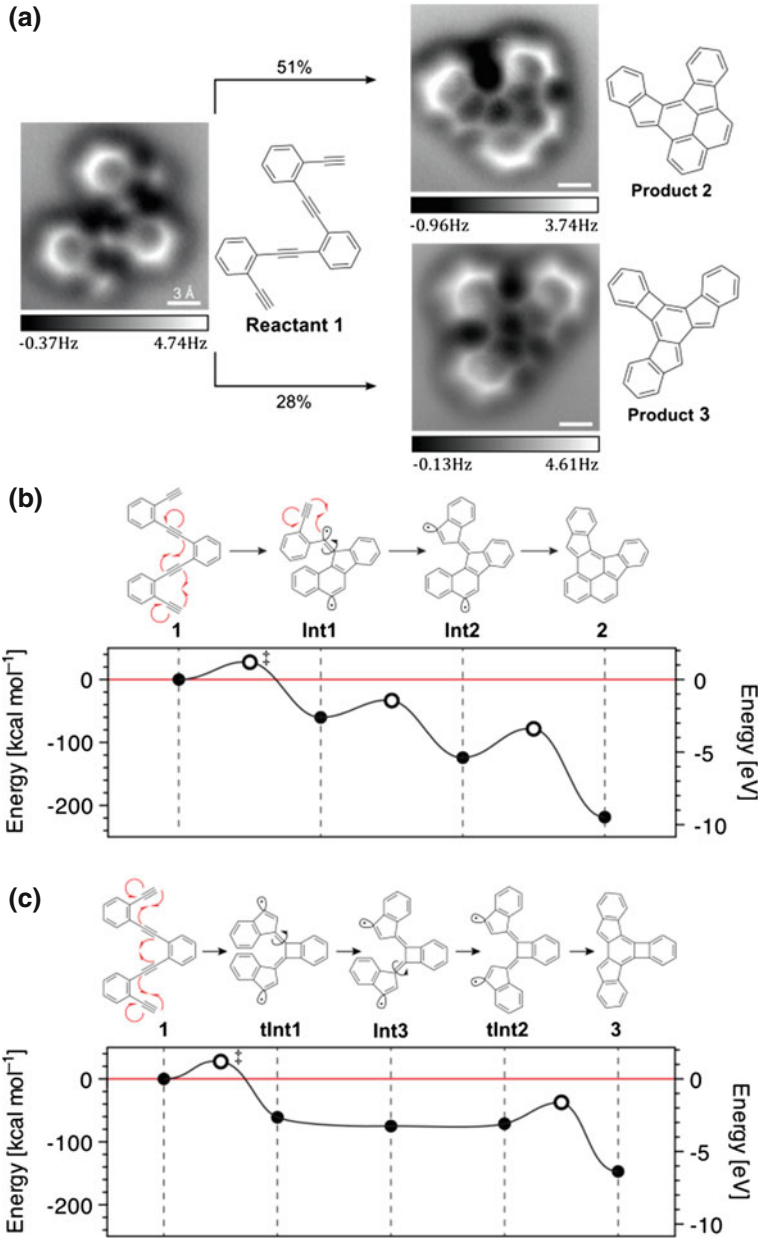

Fig. 3 **a** Frequency shift nc-AFM microscopy images at constant height (together with the corresponding wireframe chemical structures) of reactant **1** before annealing and of the majority products **2** and **3** generated in yields of 51 and 28 %, respectively, after annealing the sample at $T > 90$ °C. **b** Reaction pathway and the associated energies as calculated by DFT for the transformation of **1** into **2**. **c** Same for the transformation of **1** into **3**. Adapted from Ref. [36]. Reprinted with permission from AAAS

alkyne ends, (ii) a catalytic metallic substrate, (iii) a molecular reduction (DFT calculations predict a charge transfer of 0.5 electrons from substrate to reactant), and (iv) the radical cyclization (as opposed to the initial thermal cyclization) of some of the enediyne units. And also of interest is to see that in both reaction pathways, the isomerization processes include an intramolecular recombination of the diradicals initially generated by the enediyne cyclizations. The result is an additional cyclization involving in both cases a great energetic gain (Fig. 3b, c), making it thermodynamically very favorable. Its occurrence further explains the quenching of a subsequent polymerization by radical step growth, and the consequently scarce amount of dimers or oligomers among the products.

4 Radical Step-Growth Polymerization

The use of enediyne cyclization to form conjugated polymers by radical step growth, as initially proposed by John and Tour [18, 19], has been recently applied with 1,6-di-2-naphthylhex-3-ene-1,5-diyne molecules on Cu(110) surfaces under UHV [15]. As opposed to the scenario described above with more complex molecules used in chain reactions, these simpler precursors lack easily accessible isomerization steps that could end up in a thermodynamically favorable cyclization by intramolecular radical recombination. Instead, the radicals remain available for step-growth polymerization, as schematically displayed in Fig. 4a. Indeed, STM measurements reveal the pristine reactants as single molecules after deposition on a cold substrate (Fig. 4b), which are then transformed into regular and uniaxially aligned molecular chains upon annealing the sample to 400 K (Fig. 4c). This temperature is thus sufficient to overcome the initial Bergman cyclization barrier, generating diradical species, and provide them enough mobility to diffuse on the surface and meet each other, setting in a radical step-growth polymerization. The discrete azimuthal chain alignment along the Cu[1-10] direction (just as the discrete azimuthal orientation of the precursors before cyclization and their preferential diffusion directions along the Cu[1-10] direction) remarks the relevant role of the substrate in the growth process. DFT-based STM simulations of the expected polymer structure show a good agreement with high-resolution experimental images (Fig. 4d) and thus support the proposed growth scenario (Fig. 4a) and product structure (Fig. 4e) [15].

Another example of enediyne cyclization-based radical step-growth polymerization under UHV is that of 1,2-bis(2-ethynylphenyl)ethyne (Fig. 5a). Low-temperature (T = 4 K) STM and nc-AFM characterizations provide detailed insight into the involved chemistry and electronic properties of reactant and products [37]. nc-AFM images of the reactants deposited on Au(111) surfaces held at room temperature (Fig. 5b) display two different isomer conformations: a C_{2h} symmetric trans-conformation and a C_{2v} symmetric cis-conformation. Annealing of the submonolayer reactant-decorated Au(111) surface at 160 °C brings about two intramolecular cyclizations per monomer. Most common is the occurrence of two

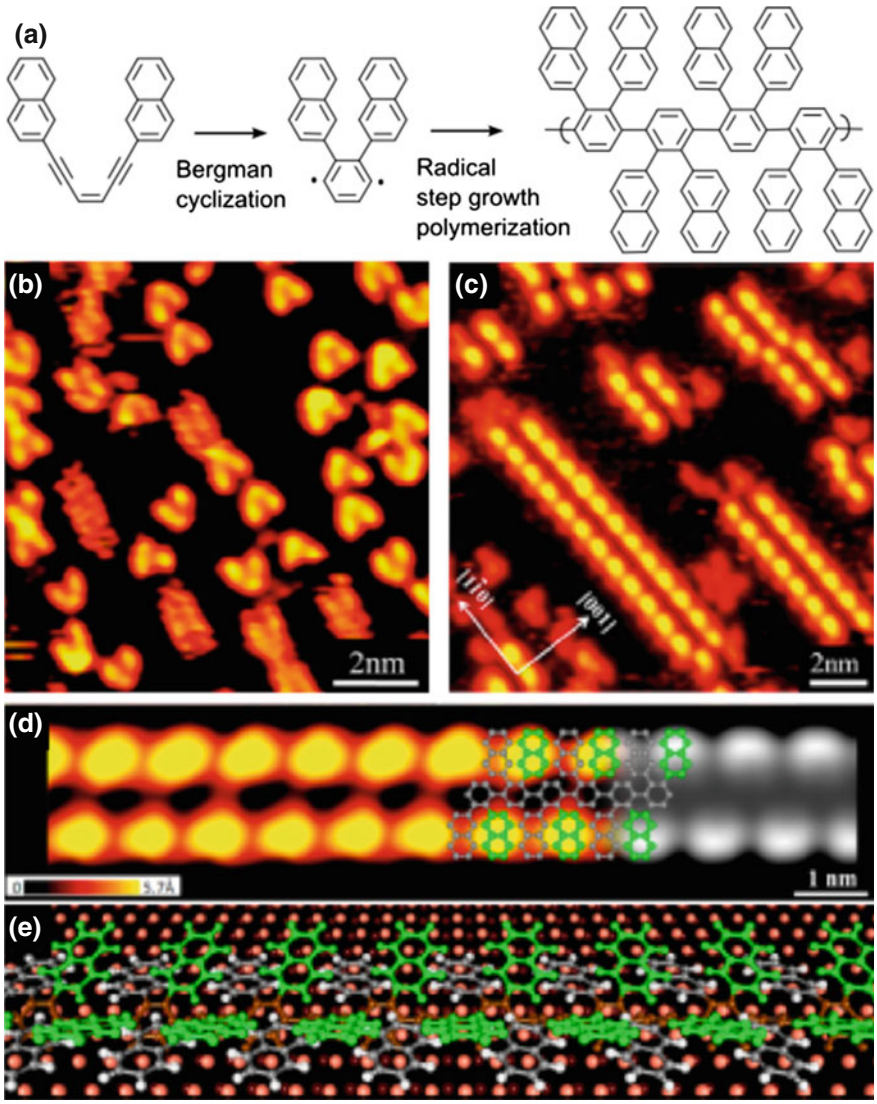

Fig. 4 **a** Wireframe molecular structure of the reactant and the associated reaction mechanism. **b** STM image of the reactant deposited on Cu(110) held at 170 K. **c** STM image showing the formation of one-dimensional molecular chain structures along the [1-10] direction after annealing the substrate to 400 K. **d** High-resolution close-up image of the molecular chain and DFT-based STM simulation (*right part*) of the proposed product structure. **e** Perspective view of the structural model showing the alternatingly tilted naphthyl groups. Adapted with permission from Ref. [15]. Copyright (2013) American Chemical Society

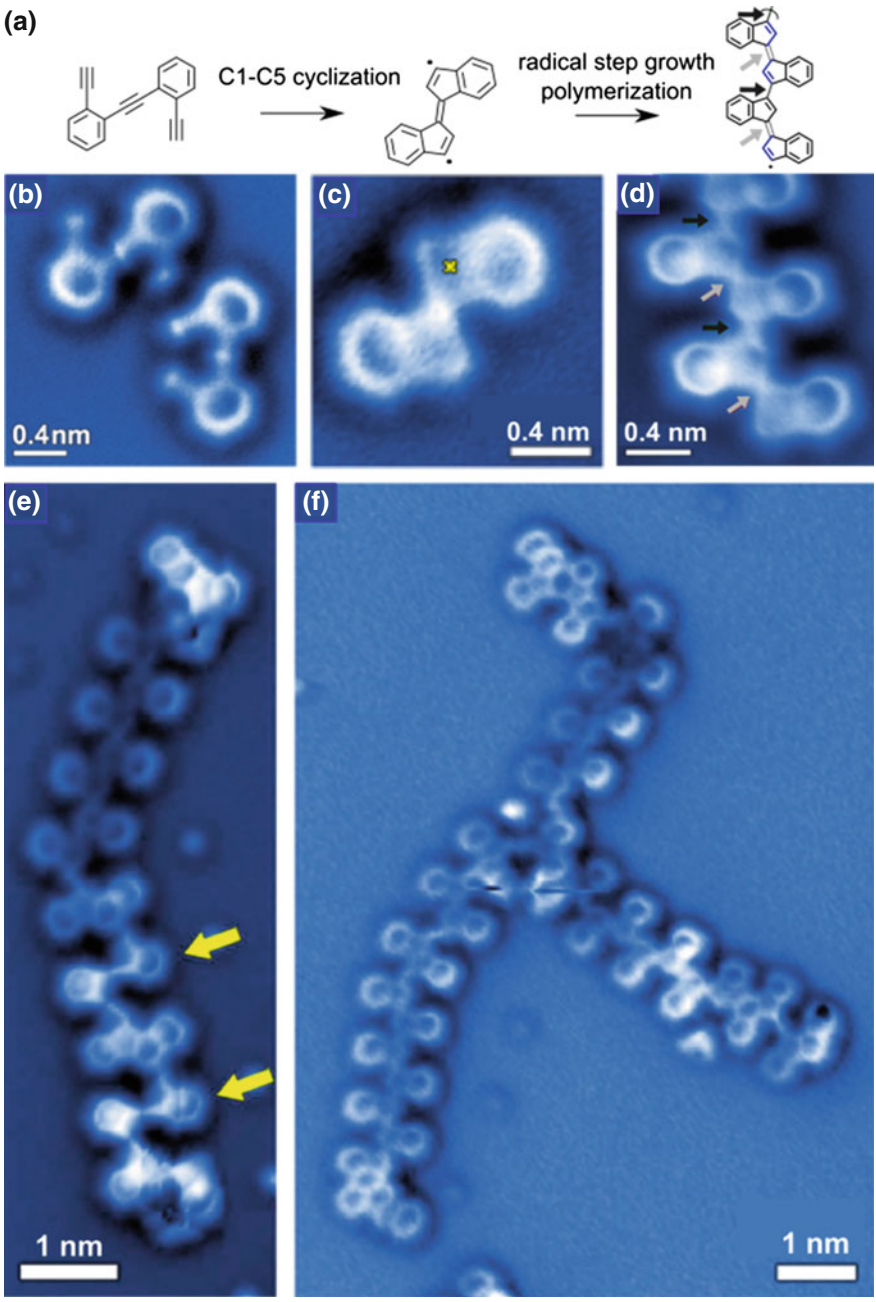
(a)
C1-C5 cyclization
radical step growth
polymerization
(b)
0.4nm
(c)
0.4 nm
(d)
0.4 nm
(e)
1 nm
(f)
1 nm

◀ **Fig. 5** **a** Wireframe chemical structure of the pristine reactant, intermediate product after cyclization, and final product after radical step-growth polymerization. The correspondent nc-AFM images on a Au(111) surface are shown in **b** (reactant), **c** (cyclized monomer), and **d** (polymer). *Dark* (*light*) *arrows mark* the long (short) bonds between indenyl units in the polymer (color coded accordingly in the wireframe structure above). **e** Polymer including non-cyclized reactants (highlighted with *yellow arrows*) and differently cyclized units (next to non-cyclized reactants). **f** Image of branched polymer chains. Adapted from Ref. [37] with permission under CC BY

C1–C5 cyclizations to yield the highly reactive 3,3′-diradical structure displayed in Fig. 5c. In turn, recombination of these resultant diradicals in a step-growth polymerization process leads to covalently linked oligo-(E)-1,1′-bi-(indenylidene) chains (Fig. 5c). More than 70 % of the material on the surface ends up forming covalently linked molecular assemblies with lengths $n \geq 3$ (where n denotes the number of monomer subunits), most chains containing 5–10 monomer units and the longest chains sometimes exceeding 20 units.

However, a defect-free oligo-(E)-1,1′-bi-(indenylidene) structure as shown in Fig. 5a, d is typically retained only over segments of three to five monomers, since different monomer cyclizations also occur (e.g., C1–C6) whose product structures are equally included into the polymer chains. Examples thereof are shown in Fig. 5e. In fact, even non-cyclized monomer units are found within the molecular chains (marked with arrows in Fig. 5e). This is attributed to an attack of the radicals in cyclized species to the terminal alkyne carbon in non-cyclized precursors. While an analogue situation with the precursors described in Fig. 4 is presumably prevented by steric hindrance, this process is already known from solution-based enediyne polymerization reactions [20]. And as displayed in Fig. 1, it may cause irregular structures with different cyclization patterns, unreacted alkynes, and branched chains. An example of the latter is provided in Fig. 5f. Furthermore, cyclization of a monomer unit readily linked to a molecular chain implies a more complex "reactant" structure. In analogy to the chain reactions of 1,2-bis ((2-ethynylphenyl)ethynyl)benzene on Ag(100) described in the previous section, following the exothermic cyclizations it could undergo additional isomerization reactions ending up in an intramolecular radical recombination that quenches the polymer step growth. This may indeed be an explanation to the common occurrence of irregular monomer subunits at the chain ends (Fig. 5e, f) reported in Ref. [37].

The main polymerization product oligo-(E)-1,1′-bi-(indenylidene) is an oligoacetylene derivative with a π-conjugated carbon backbone (Fig. 5a). Bond length alternation, defined as the difference in length between long (C–C) and short (C=C) carbon–carbon bonds in a conjugated molecule, is considered as one of the phenomenological measures of aromaticity [38]. Smaller bond length alternation implies enhanced aromaticity and π-electron delocalization, as well as a smaller bandgap in extended conjugated systems. In spite of the small dimensions of such bond length variations, tuning fork-based nc-AFM measurements with carbon monoxide functionalized probes artificially enhance that difference in the images and thereby allow its visualization [39]. This is observed best in the bonds between the five-membered rings of adjacent indenyl groups (Fig. 5d), for which the bond

length variation measured experimentally reaches ~50 %, while density functional theory predictions amount only to about 3 % [37]. Shorter bonds are highlighted with light gray arrows and longer ones with dark arrows (Fig. 5d), corresponding to double and single bonds, respectively (as displayed in the accordingly marked molecular structure drawing of Fig. 5a). Also, the bonds within the five-membered rings exhibit bond length modulation. In particular, the double bonds in indenyl end groups show a distinctive deviation compared to indenyl groups along the extended oligomer chain. This different geometry resembles that in cyclized monomers (Fig. 5c) and might thus be related to the interaction of a radical with the surface [40].

The bandgap of organic semiconductors is known to scale inversely proportional to the number of π-conjugated electrons both in linear [38, 41] and 2D structures [42]. Combining on-surface synthesis, which provides varied product structures, with scanning tunneling spectroscopy to probe the electronic properties of each structure independently, the same effect could be concluded from the reduced energy of the LUMO of polyphenylene oligomers with increasing length [43]. An equivalent phenomenology is observed on oligo-(E)-1,1′-bi-(indenylidene) chains, whose LUMO energy with respect to the Fermi level drops from ~1.2 to ~0.13 eV by going from a cyclized monomer (Fig. 5c) to an oligomer containing four monomer subunits [37]. Mapping of the local density of states at the LUMO energy further reveals its delocalization along the π-conjugated oligomer backbone and agrees with the distribution calculated by density functional theory. Altogether, it provides a fully coherent picture of the experimental findings on enediyne cyclization-based oligomers synthesized on Au(111) surfaces under UHV by radical step-growth polymerization. Moreover, it highlights the potential of this approach for the synthesis of fully conjugated low-bandgap derivatives of all-trans polyacetylene [37].

5 Summary and Conclusions

The use of enediyne cyclizations for on-surface chemistry under UHV has been demonstrated following two different approaches. On the one hand, cyclization-induced diradical species have been linked in a step-growth polymerization process to afford conjugated molecular chains. On the other hand, previously available alkyne chains in what can be seen as overlapping enediyne systems have been transformed via cyclization cascades into polycyclic aromatic hydrocarbons. Experiments following both approaches evidence, in line with the conventional wet-chemistry analogues, a significant complexity in the involved chemistry: multiple reaction pathways competing in a subtle balance that is in turn affected by many different parameters. Nevertheless, with a sufficient understanding of their respective effects, a rational choice of molecular precursors and substrate surfaces might convert enediyne-based chemistry into a versatile UHV synthetic route.

References

1. Barth, J.V., Costantini, G., Kern, K.: Engineering atomic and molecular nanostructures at surfaces. Nature **437**, 671–679 (2005)
2. Elemans, J.A.A.W., Lei, S., de Feyter, S.: Molecular and supramolecular networks on surfaces: from two-dimensional crystal engineering to reactivity. Angew. Chem. Int. Ed. **48**, 7298–7332 (2009)
3. Hla, S.W., Bartels, L., Meyer, G., Rieder, K.-H.: Inducing all steps of a chemical reaction with the scanning tunneling microscope tip: towards single molecule engineering. Phys. Rev. Lett. **85**, 2777–2780 (2000)
4. Okawa, Y., Aono, M.: Nanoscale control of chain polymerization. Nature **409**, 683–684 (2001)
5. Grill, L., Dyer, M., Lafferenz, L., Persson, M., Peters, M.V., Hecht, S.: Nano-architectures by covalent assembly of molecular building blocks. Nat. Nanotech. **2**, 687–691 (2007)
6. Weigelt, S., Busse, C., Bombis, C., Krudsen, M.M., Gothelf, K.V., Strunkus, T., Woll, C., Dahlbom, M., Kammer, B., Laegsgaard, E., Besenbacher, F., Linderoth, T.R.: Covalent interlinking of an aldehyde and an amine on a Au(111) surface in ultrahigh vacuum. Angew. Chem. Int. Ed. **46**, 9227 (2007)
7. Bennett, P., Pedramrazi, Z., Madani, A., Chen, Y.-C., de Oteyza, D. G., Chen, C., Fischer, F., Crommie, M., Bokor, J.: Bottom-Up Graphene Nanoribbon Field-Effect Transistors. Appl. Phys. Lett. **103**, 253114–1-4 (2013)
8. Cai, J., Ruffieux, P., Jaafar, R., Bieri, M., Braun, T., Blankenburg, S., Muoth, M., Seitsonen, A.P., Saleh, M., Feng, X., Mullen, K., Fasel, R.: Atomically precise bottom-up fabrication of graphene nanoribbons. Nature **466**, 470–473 (2010)
9. Zhong, D., Franke, J.-H., Podiyanachari, S.K., Blomker, T., Zhang, H., Kehr, G., Erker, G., Fuchs, H., Chi, L.: Linear alkane polymerization on a gold surface. Science **334**, 213–216 (2011)
10. Ruffieux, P., Cai, J., Plumb, N.C., Patthey, L., Prezzi, D., Ferreti, A., Molinari, E., Feng, X., Mullen, K., Pignedoli, C.A., Fasel, R.: Electronic structure of atomically precise graphene nanoribbons. ACS Nano **6**, 6930–6935 (2012)
11. Saywell, A., Schwarz, J., Hecht, S., Grill, L.: Polymerization on stepped surfaces: alignment of polymers and identification of catalytic sites. Angew. Chem. Int. Ed. **51**, 5096–5100 (2012)
12. Gao, H.-Y., Wagner, H., Zhong, D., Franke, J.-H., Studer, A., Fuchs, H.: Glaser coupling at metal surfaces. Angew. Chem. Int. Ed. **52**, 4024–4028 (2013)
13. Mendez, J., Lopez, M.F., Martin-Gago, J.A.: On-surface synthesis of cyclic organic molecules. Chem. Soc. Rev. **40**, 4578–4590 (2011)
14. Bjork, J., Hanke, F.: Towards design rules for covalent nanostructures on metal surfaces. Chem. Eur. J. **20**, 928–934 (2014)
15. Sun, Q., Zhang, C., Li, Z., Kong, H., Tan, Q., Hu, A., Xu, W.: On-surface formation of one-dimensional polyphenylene through bergman cyclization. J. Am. Chem. Soc. **135**, 8448–8451 (2013)
16. Jones, R.R., Bergman, R.G.: p-Benzyne. generation as an intermediate in a thermal isomerization reaction and trapping evidence for the 1,4-Benzenediyl Structure. J. Am. Chem. Soc. **94**, 660–661 (1972)
17. Nicolaou, K.C., Dai, W.-M.: Chemistry and biology of the enediyne anticancer antibiotics. Angew. Chem. Int. Ed. **30**, 1387–1416 (1991)
18. John, J.A., Tour, J.M.: Synthesis of polyphenylenes and polynaphthalenes by thermolysis of enediynes and dialkynylbenzenes. J. Am. Chem. Soc. **116**, 5011–5012 (1994)
19. John, J.A., Tour, J.M.: Synthesis of polyphenylene derivatives by thermolysis of enediynes and dialkynylaromatic monomers. Tetrahedron **53**, 15515–15534 (1997)
20. Johnson, J.P., Bringley, D.A., Wilson, E.E., Lewis, K.D., Beck, L.W., Matzger, A.J.: Comparison of "polynaphthalenes" prepared by two mechanistically distinct routes. J. Am. Chem. Soc. **125**, 14708 (2003)

21. Prall, M., Wittkopp, A., Schreiner, P.R.: Can fulvenes form from enediynes? A systematic high-level computational study on parent and benzannelated enediyne and enyne-allene cyclizations. J. Phys. Chem. A **105**, 9265–9274 (2001)
22. Mohamed, R.K., Peterson, P.W., Alabugin, I.V.: Concerted reactions that produce diradicals and zwitterions: electronic, steric, conformational, and kinetic control of cycloaromatization processes. Chem. Rev. **113**, 7089–7129 (2013)
23. Vavilala, C., Byrne, N., Kraml, C.M., Ho, D.M., Pascal Jr, R.A.: Thermal C1–C5 diradical cyclization of enediynes. J. Am. Chem. Soc. **130**, 13549–13551 (2008)
24. Galbraith, J.M., Schreiner, P.R., Harris, N., Wei, W., Wittkopp, A., Shaik, S.: A valence bond study of the bergman cyclization: geometric features, resonance energy, and Nucleus-Independent Chemical Shift (NICS) values. Chem. Eur. J. **6**, 1446–1454 (2000)
25. Alabugin, I.V., Manoharan, M.: Radical-anionic cyclizations of enediynes: remarkable effects of benzannelation and remote substituents on cyclorearomatization reactions. J. Am. Chem. Soc. **125**, 4495–4509 (2003)
26. Alabugin, I.V., Kovalenko, S.V.: C1–C5 photochemical cyclization of enediynes. J. Am. Chem. Soc. **124**, 9052–9053 (2002)
27. Lee, C.-Y., Wu, M.-J.: Synthesis of benzofulvenes by palladium-catalyzed cyclization of 1,2-dialkynylbenzenes. Eur. J. Org. Chem. **2007**, 3463–3467 (2007)
28. Batsanov, A.S., Collings, J.C., Fairlamb, I.J.S., Holland, J.P., Howard, J.A.K., Lin, Z., Marder, T.B., Parsons, A.C., Ward, R.M., Zhu, J.: Requirement for an oxidant in Pd/Cu co-catalyzed terminal alkyne homocoupling to give symmetrical 1,4-disubstituted 1,3-diynes. J. Org. Chem. **70**, 703–706 (2005)
29. Zhang, Y.-Q., Kepcija, N., Kleinschrodt, M., Diller, K., Fischer, S., Papageorgiou, A.C., Allegretti, F., Bjork, J., Klyatskaya, S., Klappenberger, F., Ruben, M., Barth, J.V.: Homo-coupling of terminal alkynes on a noble metal surface. Nat. Commun. **3**, 1286 (2012)
30. Xiao, Y., Hu, A.: Bergman cyclization in polymer chemistry and material science. Macromol. Rap. Comm. **32**, 1688–1698 (2011)
31. Byers, P.M., Alabugin, I.V.: Polyaromatic ribbons from oligo-alkynes via selective radical cascade: stitching aromatic rings with polyacetylene bridges. J. Am. Chem. Soc. **134**, 9609–9614 (2012)
32. Alabugin, I.V., Gilmore, K., Patil, S., Manoharan, M., Kovalenko, S.V., Clark, R.J., Ghiviriga, I.: Radical cascade transformations of tris(o-aryleneethynylenes) into substituted benzo[a] indeno[2,1-c]fluorenes. J. Am. Chem. Soc. **130**, 11535–11545 (2008)
33. Alabugin, I.V., Manoharan, M.: Thermodynamic and strain effects in the competition between 5-exo-dig and 6-endo-dig cyclizations of vinyl and aryl radicals. J. Am. Chem. Soc. **127**, 12583 (2005)
34. Hirano, K., Inaba, Y., Takasu, K., Oishi, S., Takemoto, Y., Fujii, N., Ohno, H.: Gold(I)-catalyzed polycyclizations of polyenyne-type anilines based on hydroamination and consecutive hydroarylation cascade. J. Org. Chem. **76**, 9068–9080 (2011)
35. Gross, L., Mohn, F., Moll, N., Liljeroth, P., Meyer, G.: The chemical structure of a molecule resolved by atomic force microscopy. Science **325**, 1110–1114 (2009)
36. de Oteyza, D.G., Gorman, P., Chen, Y.-C., Wickenburg, S., Riss, A., Mowbray, D.J., Etkin, G., Pedramrazi, Z., Tsai, H.-Z., Rubio, A., Crommie, M.F., Fischer, F.R.: Direct imaging of covalent bond structure in single-molecule chemical reactions. Science **340**, 1434–1437 (2013)
37. Riss, A., Wickenburg, S., Gorman, P., Tan, L.Z., Tsai, H.-Z., de Oteyza, D.G., Chen, Y.-C., Bradley, A.J., Ugeda, M.M., Etkin, G., Louie, S.G., Fischer, F.R., Crommie, M.F.: Local electronic and chemical structure of oligo-acetylene derivatives formed through radical cyclizations at a surface. Nano Lett. **14**, 2251–2255 (2014)
38. Kertesz, M., Choi, C.H., Yang, S.: Conjugated polymers and aromaticity. Chem. Rev. **105**, 3448–3481 (2005)
39. Gross, L., Mohn, F., Moll, N., Schuler, B., Criado, A., Guitian, E., Pena, D., Gourdon, A., Meyer, G.: Bond-Order discrimination by atomic force microscopy. Science **337**, 1326–1329 (2012)

40. Van der Lit, J., Boneschanscher, M. P., Vanmaekelbergh, D., Ijas, M., Uppstu, A., Ervasti, M., Harju, A., Liljeroth, P., Swart, I.: Suppression of electron–vibron coupling in graphene nanoribbons contacted via a single atom. Nat. Commun. **4**, 2023 (2013)
41. Torras, J., Casanovas, J., Aleman, C.: Reviewing extrapolation procedures of the electronic properties on the π-conjugated polymer limit. J. Phys. Chem. A **115**, 7571–7583 (2012)
42. Gutzler, R., Perepichka, D.F.: π-electron conjugation in two dimensions. J. Am. Chem. Soc. **135**, 16585–16594 (2013)
43. Wang, S., Wang, W., Lin, N.: Resolving band-structure evolution and defect-induced states of single conjugated oligomers by scanning tunneling microscopy and tight-binding calculations. Phys. Rev. Lett. **106**, 206803 (2011)

On-Surface Synthesis by Azide–Alkyne Cycloaddition Reactions on Metal Surfaces

Oscar Díaz Arado, Harry Mönig and Harald Fuchs

Abstract On-surface synthesis of covalently bond nanostructures under ultrahigh vacuum conditions has received increased attention in the recent years. This approach allows to study solvent-free chemical reactions and moreover to use well-defined substrates, which act as a catalyst and/or exerting steric effects leading to kinetic and regioselective control of the chemical process at hand. Recently, successful 1,3-dipolar azide–alkyne cycloaddition reactions were performed on metal substrates with complete regioselectivity of a specific product. This chapter presents a summary of these experimental efforts on different metal substrates, while also focusing on a comprehensive understanding of the catalyst prerequisite for on-surface coupling reactions and a quantitative description of steric effects dominating the coupling mechanism and the regioselectivity of the reaction products. Future perspectives for the bottom-up development of functional nanostructures involving on-surface azide–alkyne cycloadditions are discussed.

1 Introduction

Decades of organic synthesis research have accomplished an extensive pool of suitable chemical processes in solution, which are nowadays increasingly investigated in the two-dimensional confinement of surfaces [1–3]. On-surface synthesis

O. Díaz Arado (✉) · H. Mönig · H. Fuchs
Physikalisches Institut, Westfälische Wilhelms-Universität Münster, Wilhelm-Klemm Strasse 10, 48149 Münster, Germany
e-mail: arado@uni-muenster.de

H. Mönig
e-mail: hmoenig@uni-muenster.de

H. Fuchs
e-mail: fuchsh@uni-muenster.de

O. Díaz Arado · H. Mönig · H. Fuchs
Center for Nanotechnology (CeNTech), Heisenbergstrasse 11, 48149 Münster, Germany

A. Gourdon (ed.), *On-Surface Synthesis*, Advances in Atom and Single Molecule Machines, DOI 10.1007/978-3-319-26600-8_5

under ultrahigh-vacuum (UHV) conditions for the bottom-up growth of covalently bound organic nanostructures with well-defined functionalities has become an attractive field of study in modern nanoscience and nanotechnology. Among the many possible cases of study, cycloaddition reactions [4], commonly referred to as "click" reactions, are highly attractive candidates for on-surface synthesis efforts. Such by-product-free reactions, performed as solution-phase processes, are widely used for the modification of surfaces and nanoparticles [5, 6] and also for the preparation of biologically active compounds in pharmaceutical research [7, 8]. In this field, one of the most widely used reactions is the azide–alkyne 1,3-dipolar cycloaddition [9] leading to 1,4 and 1,5 triazoles (Fig. 1). The so-called uncatalyzed pathway (Huisgen azide–alkyne [3 + 2] cycloaddition) is a thermal process which delivers a mixture of both regioisomers. However, the use of a Cu(I) catalyst provides 1,4-triazoles with high efficiency and regioselectivity under ambient conditions (CuAAC) [9].

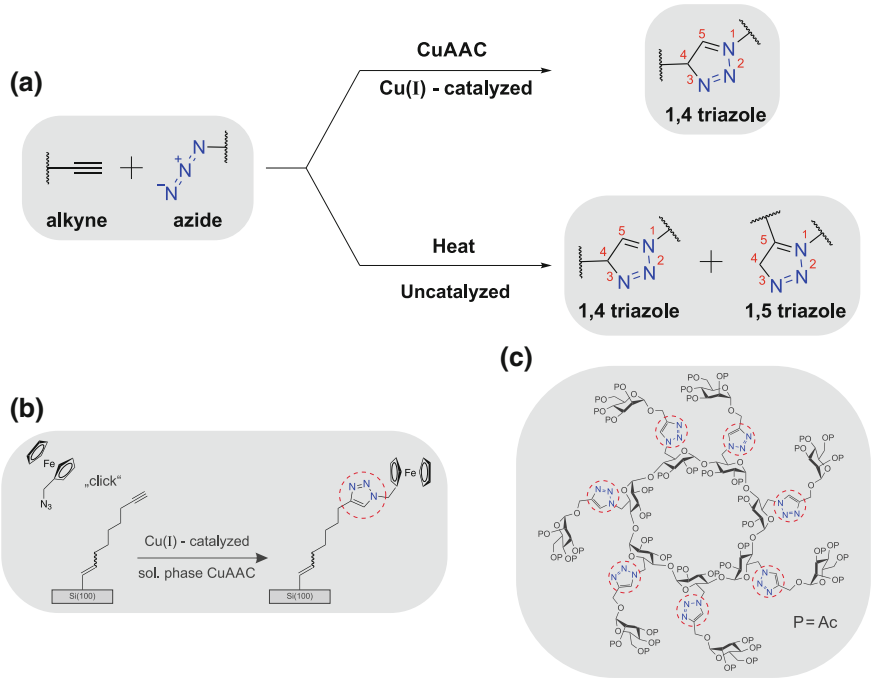

Fig. 1 Solution-phase 1,3-dipolar cycloaddition reaction between azides and alkynes. **a** General reaction scheme, including the Cu-catalyzed (*top*) and the Huisgen uncatalyzed (*bottom*) reaction pathways. Adapted with permission from [10]. Copyright (2013) American Chemical Society. **b** Schematic depiction of a "click" reaction investigated for the immobilization of azidomethylferrocene on the alkyne-terminated silicon electrode. Adapted with permission from [6]. Copyright (2008) WILEY-VCH Verlag. **c** Application of the Cu(I)-catalyzed triazole formation in drug discovery, in particular for multivalent neoglycoconjugates. Adapted with permission from [8]. Copyright (2013) American Chemical Society

Resembling the CuAAC mechanism in solution, a successful cycloaddition between 9-ethynylphenanthrene (alkyne) and 4-azidobiphenyl (azide) was recently accomplished on a Cu(111) surface at room temperature under UHV conditions, with complete regioselectivity toward the formation of the corresponding 1,4-triazoles [10]. In that study, two different precursor molecules were charged with a single alkyne or azide moiety (Fig. 2a), allowing dimerization after successful coupling. As for the solution-phase process, the observed complete regioselectivity and the low activation temperature for the reaction were discussed considering the involvement of a copper acetylide (C–H activation) and bonding of the alkyne group to the Cu(111) surface. However, the Cu surface was shown to be very reactive toward the organic reactants, in particular causing the azide moieties to degrade. Such degradation was found to be the limiting factor and furthermore explained the low yield ($\sim$1.1 %) of the coupling reaction on this surface.

In a different study, the reactivity of *N*-(4-azidophenyl)-4-ethynylbenzamide (AEB) monomers on a Au(111) surface (AuAAC) under UHV conditions (Fig. 2b) was investigated with a combination of cryogenic scanning tunneling microscopy (STM) and density functional theory (DFT) [11]. In this case, the inert Au(111) surface was chosen since it can be expected to have a weaker interaction with the azide moiety, and thus improve the coupling rate of the on-surface azide–alkyne cycloaddition reaction. Furthermore, the AEB monomers were designed with two

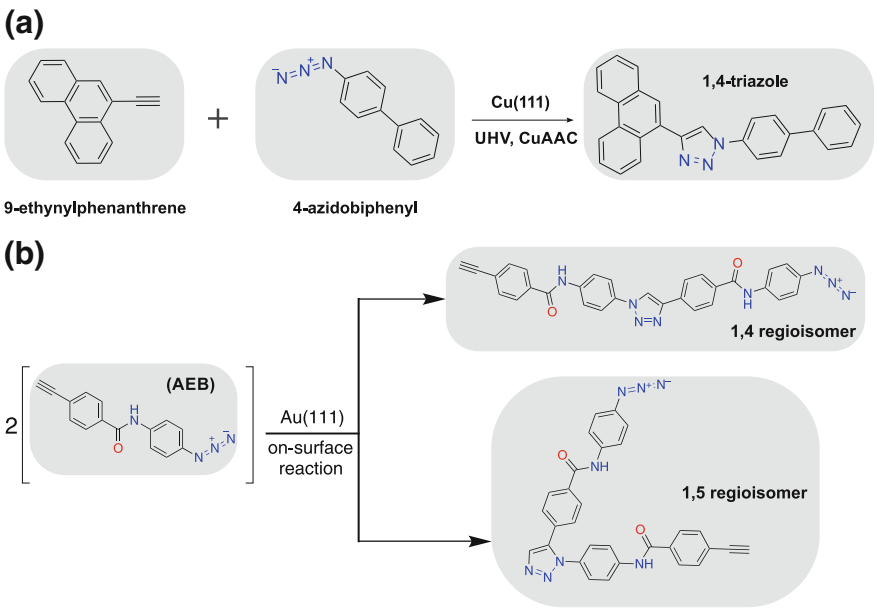

Fig. 2 On-surface Azide–Alkyne cycloaddition reactions. **a** Dimerization on Cu(111). **b** Dimerization on Au(111). The obtained dimers are also charged with alkyne and azide moieties, leading to oligomerization. Adapted with permission from [10, 11]. Copyright (2013) American Chemical Society

phenyl rings connected through an amide linker as backbone. These features allow the reactants to be thermally deposited on the surface, where they can lay flat and diffuse, thus increasing the probability of the alkyne and azide groups to meet and react. In addition, the amide linker could form intermolecular hydrogen bonds perpendicular to the targeted reaction direction. This makes possible to aim for supramolecular ordering after the deposition and therefore enhance the reaction probability accordingly. Moreover, a single AEB reactant is charged with an azide and an alkyne moiety which allows this compound to undergo oligomerization.

In this chapter, a comprehensive comparison between the completely regioselective on-surface CuAAC [10] and AuAAC [11] processes will be presented. Section 2 presents a summary of the experimental efforts for each process. Given that Au complexes have not been shown to catalyze chemical reactions of this kind, detailed DFT calculations for the AuAAC process are presented in Sect. 3. These not only explain the low temperatures required to trigger this chemical process on a metal substrate, but also the role of the substrate in the reaction, and how its careful selection can improve the regioselectivity of the reaction output. Finally, a brief discussion about the future perspectives for this on-surface synthesis approach to develop functional nanostructures on surfaces is presented in Sect. 4.

2 On-Surface Azide–Alkyne Cycloaddition Reactions

In the following section, up-to-date experimental efforts for the on-surface azide–alkyne cycloaddition reactions will be presented. Emphasis is given to critical points involving the relatively low-temperature requirement for C–H activation of the alkyne moiety on both substrates, the reaction yield and the reactivity limitations.

2.1 Deposition and On-Surface Reaction at Room Temperature

As mentioned before, the on-surface azide–alkyne cycloaddition reaction on the Cu (111) surface at room temperature mimics the CuAAC solution-phase process and leads to the exclusive formation of 1,4-triazoles. On the other hand, the Au(111) surface might not act as a catalyst for this specific reaction, and therefore, the evolution of this system at the same experimental conditions was investigated [11]. Molecular deposition of the monomers always resulted in a partially covered surfaces, showing a first layer mixture of reactants along with reacted compounds (Fig. 3a). Around these features, it was always found a disordered molecular phase, which was ascribed to the azide end group degradation occurring on both Cu(111) and Au(111) surfaces.

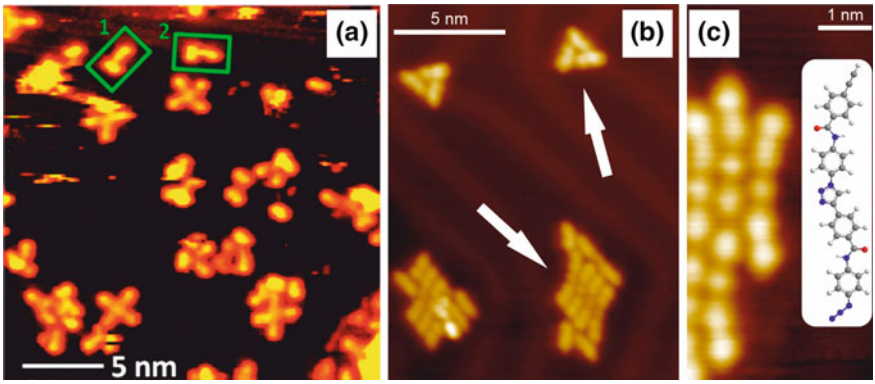

Fig. 3 STM images after the reactants deposition onto the metal surfaces at room temperature. **a** Deposition onto Cu(111) results in the formation of the corresponding 1,4-triazole (enclosed in *green*) surrounded by a disordered phase ascribed to the azide degradation. Such a degradation was also observed on Au(111). **b** Arrangement of AEB monomers and dimers on Au(111) after the reaction. **c** AEB dimers and trimers formed as a result of the successful azide–alkyne "click" reaction. The *inset* in (**c**) shows the molecular structure of the 1,4 regioisomer. Adapted with permission from [10, 11]. Copyright (2013) American Chemical Society

The potential degradation of the azide moiety does not represent a major limiting factor for the coupling reaction on Au(111). High-resolution STM images (Fig. 3b) show a mixture of reacted and unreacted molecules on the substrate. A number of monomers were oriented in a way that the alkyne group of one monomer and the azide group of the other were in close proximity and hence properly positioned to undergo the targeted cycloaddition reaction. Besides the dimerization, the formation of longer linear structures confirmed that the corresponding trimers were also formed, i.e., the targeted oligomerization of AEB monomers can be achieved. Furthermore, the successful formation of trimers (Fig. 3c) strongly supports the occurrence of the proposed azide–alkyne "click" process since the formation of such trimeric structures should only be feasible if the reaction of an AEB monomer and a dimer occurs between the azide and alkyne end groups of these two reaction partners (Fig. 2). It is important to note that Au complexes have not been shown to catalyze azide–alkyne cycloadditions; therefore, the success of the reaction without further thermal annealing is surprising on this surface.

The inset in Fig. 3c represents the molecular structure of a 1,4-triazole regioisomer on Au(111). This structure matches very well the STM observations, since the alternative 1,5-regioisomer would present an *L*-shaped configuration instead of the observed linear structure (Fig. 2). It is emphasized that for all the experiments on Au(111), only the formation of the 1,4-regioisomer was also observed. However, the thermal azide–alkyne cycloaddition in the absence of a Cu catalyst generally requires high temperatures resulting in a mixture of 1,4 and 1,5 triazoles [9]. If the cycloaddition products were formed in the crucible during the heating process prior to the deposition and subsequently deposited on the surface, a mixture

of both regioisomers is to be expected in the STM images. Therefore, also the observed complete regioselectivity strongly pointed toward an on-surface reaction. It is likely that the Au substrate lowers the activation energy and also steers the regioselectivity of the [3 + 2] cycloaddition reaction (mechanistic studies will be discussed in Sect. 3).

DFT calculations further confirmed the correct assignment of the on-surface dimerization products to the 1,4-regioisomer structure. On Au(111) (Fig. 4), the reactants and the proposed products were verified by comparing experimentally determined distances with the theoretical values calculated for the gas phase of the AEB monomer, dimer, and trimer. The center-to-center distance between the two aryl rings of the AEB monomer was found to be 0.65 ± 0.03 nm (calculated, 0.65 nm); for the dimer, the measured distance between the adjacent minima of the 1,4-triazole group is 0.57 ± 0.02 nm (calculated, 0.50 nm); the same distance, measured for the triazoles of the AEB trimer, is 0.55 ± 0.01 and 0.56 ± 0.01 nm (calculated, 0.50 nm), respectively. Evidently, the triazole groups corresponding to the dimers and trimers have the same size. Therefore, not only a good qualitative agreement with the STM images was found, but also a good quantitative agreement between the theoretically and experimentally determined distances. The small differences can be ascribed to the absence of the Au(111) surface in the gas-phase calculations, which restrains out-of-plane movements of the molecular components. As a result, bonding angles can differ leading to deviations of the calculated center-to-center distances.

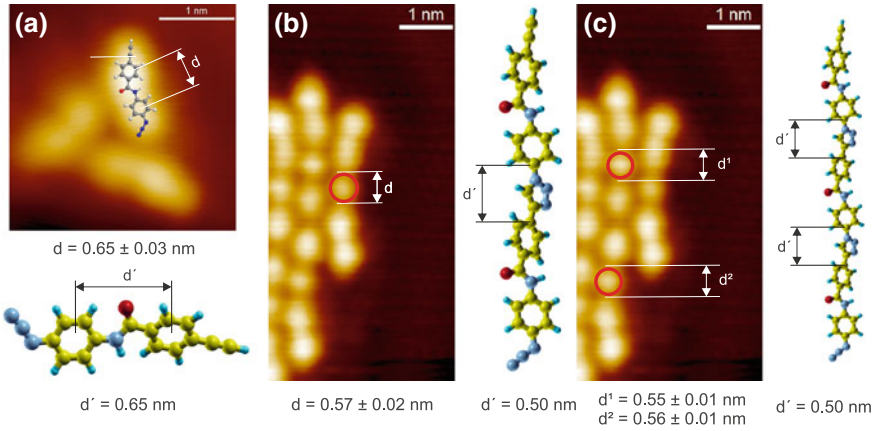

Fig. 4 A good quantitative agreement was found between the experimental and the center-to-center theoretical distances for the three AEB species observed on the Au(111) surface. Adapted with permission from [11]. Copyright (2013) American Chemical Society

2.2 *Yield of the On-Surface Azide–Alkyne Cycloaddition Reactions*

Another important aspect that should be addressed is to estimate the real amount of products obtained after the reactions (Fig. 5). Therefore, a detailed comparison between the reaction outputs on the Cu(111) and Au(111) substrates is hereinafter presented, with special attention on the monomers' reactivity and the formation of higher order structures. On one hand, a total of 35 observations of the 1,4-triazoles products were made in 8 independent experiments on the Cu(111) surface (sampling ~3200 deposited molecules). On the other hand, in the study performed on Au(111), a representative sampling from four different deposition experiments of AEB on Au(111) was chosen. From a total of 1083 intact molecules observed in this case, 689 (63.6 %) were AEB monomers. For the AEB 1,4-dimer and the trimers, a total of 310 (28.6 %) and 84 (7.8 %) molecules was identified, respectively.

A substantial amount of monomers remained unreacted on the Cu(111) surface, as compared with the amount on Au(111). This could be ascribed to limited diffusion on the surface. It is known that copper substrates are more reactive toward organic compounds, hence limiting their free diffusion on the surface at room temperature. On the other hand, the dimerization yield for the azide–alkyne cycloaddition on Au(111) is considerably larger than the one observed on Cu(111). Although the large amount of unreacted monomers on the latter is certainly influencing the low yield obtained, the viability of using gold surfaces instead of copper for more efficient on-surface reactions involving azides cannot be neglected. Furthermore, it confirms that the degradation the azide moieties undergo on the

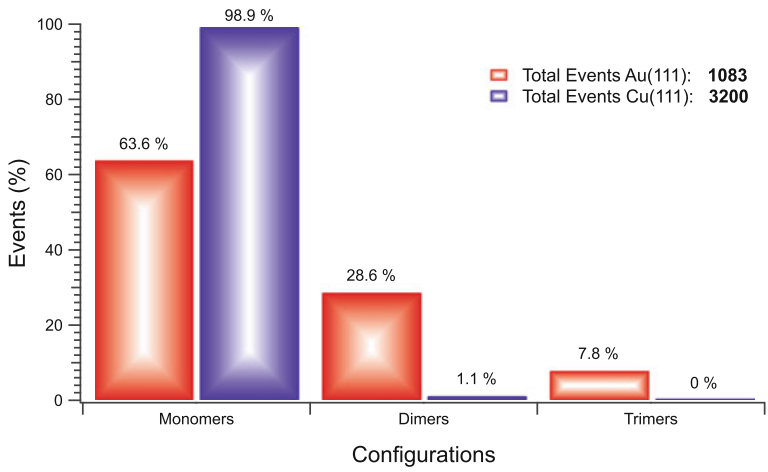

Fig. 5 Estimated yield for the on-surface azide–alkyne cycloaddition reaction on Cu(111) [10] and on Au(111) [11]. The successful dimerization rate was increased by ~27 % on the Au(111) substrate with respect to Cu(111)

Au(111) is not as severe when compared to their degradation on Cu(111), hence not being a major limiting factor for the reaction. Unfortunately, a direct comparison of the trimerization yields is not possible at the moment, given that the design of the reactants in the experiments performed on Cu(111) did not target oligomerization, but more importantly, it was focused on probing the viability of the on-surface coupling reaction (Fig. 2a).

2.3 *Controlled STM Tip Manipulations*

In Sect. 2.1, the correct assignment of the on-surface reaction products was assessed by direct comparison between experimentally determined and DFT calculated center-to-center distances. To ensure that the observed species are indeed covalently connected monomers, controlled STM tip manipulations were performed. Due to the high mechanical stability of the triazole groups, mechanical perturbations induced by the STM tip must not lead to the dissociation of the products.

Therefore, extensive controlled manipulations with the STM tip were carried out on the dimers and the trimers formed on Au(111). Figure 6 shows a sequence of STM images with consecutive manipulations, where the starting point of the experiment was an arrangement of a dimer and two trimers. After a successful

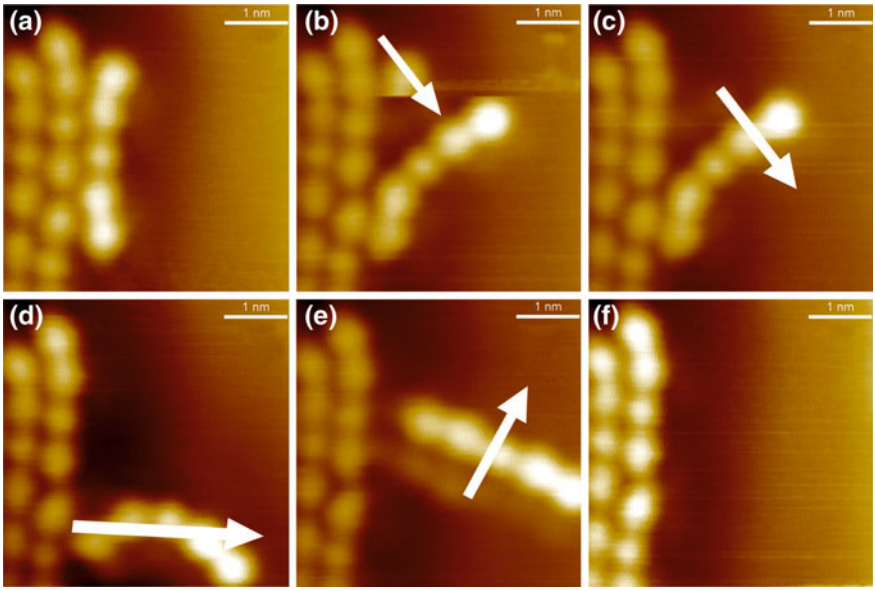

Fig. 6 Mechanical manipulation of a 1,4-dimer structure with the STM tip. Manipulations were conducted at $T \leq 5$ K with 100 pA $\leq I \leq 3$ nA and $V = 5$ mV. The *white arrows* represent the manipulation vectors. Reprinted with permission from [11]. Copyright (2013) American Chemical Society

manipulation, the dimer was partially detached from the two linear trimers (Fig. 6b). Subsequent manipulations led to a complete separation of the dimer from the two trimers (Fig. 6c–f). Importantly, the structure of the dimer remained intact after the STM tip manipulations, which confirms the covalent nature of the linkage of the two monomers for the build-up of the 1,4-dimeric structure. The amide functionality between the phenyl rings combined with the triazole group in the dimer provides the product large torsional freedom. The trimers could also be successfully manipulated although a complete detachment from the adjacent molecules was a challenging task. This can be attributed to the stronger van der Waals forces, and probably also to the larger number of hydrogen bonds (between amide bonds), between the linear structures upon switching from the dimer to trimer. These STM manipulations demonstrated that AEB dimers and the corresponding trimers display high mechanical stability, as it is expected for covalently bonded chemical structures, particularly triazoles.

2.4 *Analysis of the Reactivity*

Another interesting point when comparing the experiments on Cu(111) and Au (111) is the amount of reactants that did not form the corresponding dimer and trimer products. It is important to note that for a successful on-surface reaction, two reactants must diffuse toward each other so that the reactive alkyne and azide functionalities are close enough for the successful coupling. Therefore, the isolated monomers and/or the self-assembled structures obtained after initial deposition must somehow relate to their reactivity (as discussed in Sect. 2.2). For example, in STM images acquired after the deposition onto Au(111) showed that the AEB monomers that did not react are present in three different configurations (Fig. 7):

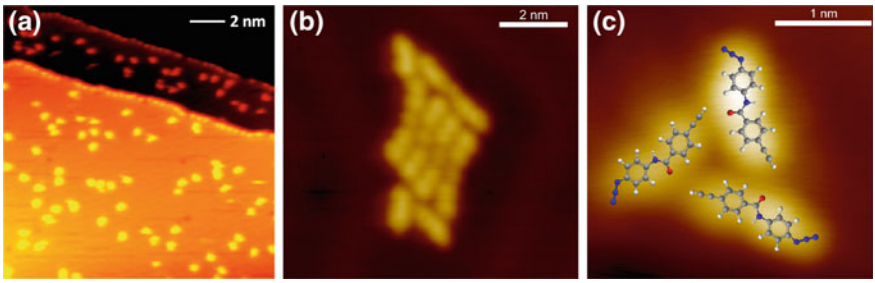

Fig. 7 Analysis of the AEB monomers reactivity. Unreacted monomers appear in three distinct configurations which probably hinder the reaction. **a** Nucleated along step edges, in this case the alkyne reactant on Cu(111). **b** AEB monomers agglomerated adjacent to molecular islands on Au (111). **c** AEB monomers self-assembled in a triangular arrangement on Au(111). Here, the *inset* represents one of the possibilities of how similar end groups facing each other would prevent a successful reaction. Adapted with permission from [10, 11]. Copyright (2013) American Chemical Society

(i) nucleated along the step edges. This behavior has been also observed on Cu(111) for the alkyne reactant [10], which is in general known to have high affinity for reactive sites on surfaces, such as step edges; (ii) agglomerated adjacent to molecular islands, possibly as a result of diffusion of the molecules on the Au(111) surface and self-assembly steered by van der Waals forces; and (iii) self-assembled in a three-monomers arrangement, forming a stable triangular shaped island. This configuration was observed quite frequently ($\sim$27.4 % of the AEB monomers which remain intact after the deposition), being the only configuration where exclusively monomers self-assembled independently (see also Fig. 3b).

It is quite interesting that for molecules which are able to undergo dimerization at room temperature, such stable triangular configuration can be found under similar experimental conditions. However, as for most of the on-surface synthesis reactions, the pre-arrangement of the reactants is crucial [3, 12, 13]. Therefore, one possibility why the reaction does not occur in the triangular configuration is that this particular configuration is too stable and therefore fixed. Moreover, the functional end groups are sterically blocked within this configuration (model structure in Fig. 7c), which leads to reduced reactivity.

3 Reaction Mechanism

The last open question remaining is related to the reaction mechanism dominating the observed azide–alkyne cycloaddition reactions. On the Cu(111) surface, di–σ bonding of the alkyne to the substrate was observed, in analogy to the mechanism involving formation of a Cu(I) π complex with the alkyne triple bond. Only the 1,4-regioisomer was obtained in these experiments under UHV conditions, but when liquid-phase synthesis with the protocol of the uncatalyzed path was performed, only the 1,4-product was obtained as well. Therefore, steric hindrance effects driving the observed regioselectivity were qualitatively assigned as responsible for the reaction to proceed with complete regioselectivity in a surface-confined situation. On the Au(111) experiments, however, di–σ bonding of the alkyne to the bare substrate was not observed; thus, a purely AuAAC-like mechanism should not be feasible at the experimental conditions. Therefore, DFT calculations were carried out for this case, to elucidate the on-surface coupling mechanism and more importantly to clarify the role of the Au substrate on the regioselectivity.

3.1 Involvement of the Surface in the Reaction

To simplify the calculations, a *para*-alkynylazidobenzene (*p*-AAB) monomer was chosen as a suitable model compound for the representation of the observed on-surface azide–alkyne cycloaddition reaction on Au(111) [11]. First, the transition-state energies

of the dimerizations of AEB and the model compound *p*-AAB in vacuum were determined. In a second step, the transition state energy of the dimerization of *p*-AAB on a flat unreconstructed Au(111) surface (see Fig. 8a–c) was calculated and subsequently compared with the calculated vacuum barrier. Interestingly, all three calculated barrier heights for the cycloadditions were comparable: The same value (0.72 eV) was determined for the reaction of the model compound in vacuum and on the Au substrate, whereas a value of 0.69 eV was obtained for the AEB dimerization in vacuum. These calculated reaction barriers are low when compared to other on-surface reactions that require higher temperatures to be triggered [12, 13]. Moreover, the reaction was found to be strongly exothermic by 2.78 eV for the *p*-AAB in vacuum and on the flat Au(111) substrate. These results explain why the reaction readily proceeded on Au(111) at room temperature without di–σ bonding of the alkyne to the substrate.

On the other hand, the flat unreconstructed surface initially used in the DFT calculations does not resemble the actual herringbone-reconstructed Au(111) substrate. To assess the potential catalytic role played by the gold atoms of the surface, the "click" reaction was simulated on Au(111) with one uncoordinated additional Au atom (Fig. 8d–f). To take into account the complete surface reconstruction would require a very large unit cell and therefore resulting in different locations where the molecules could adsorb. The extreme case where a single uncoordinated

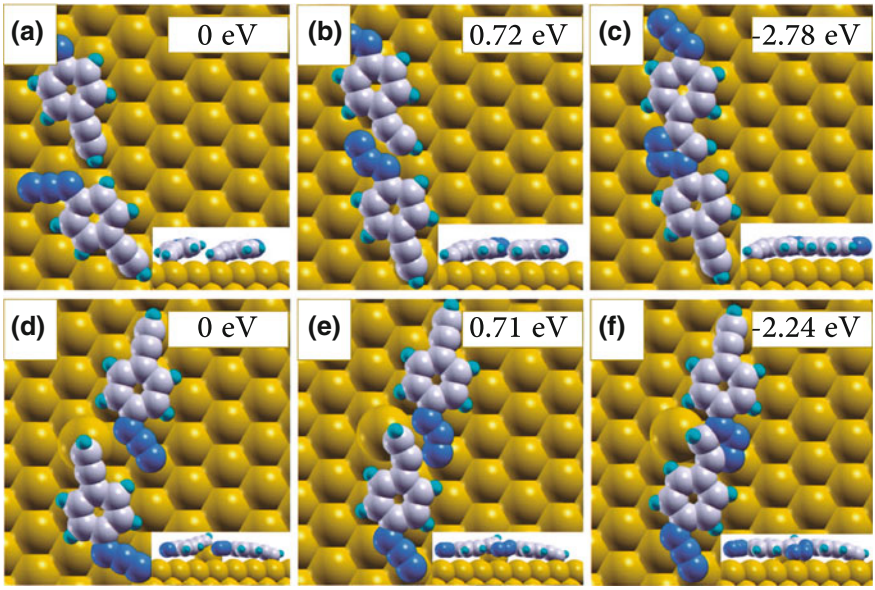

Fig. 8 On-surface dimerization of the model compound *p*-AAB on the Au(111) surface. **a**–**c** Reaction on a flat Au(111) surface. **d**–**f** Reaction with the reacting terminal carbon atom bound to an additional Au atom on the surface. Initial state energies are defined as 0 eV for both reactions. Adapted with permission from [11]. Copyright (2013) American Chemical Society

atom stands out as the most reactive site is more feasible for the calculations and provides valuable information regarding surface catalysis when compared with the counter extreme case, i.e., the flat unreconstructed surface. It was found that the strong binding of the alkyne group to the additional gold atom increases the binding energy of the initial state of this configuration (Fig. 8d) by 0.51 eV when compared to the flat surface (Fig. 8a). In this case, the exothermicity decreases down to 2.24 eV, and more importantly, the transition state energy is 0.71 eV, barely different from the 0.72 eV calculated for the flat surface. The small difference between these transition state energies indicates a negligible catalytic effect of uncoordinated Au atoms for the on-surface cycloaddition of *p*-AAB at room temperature. It is reasonable to expect that other surface sites of a herringbone reconstruction will show, at best, a catalytic activity as good as the one observed for the extreme case of an additional uncoordinated Au atom on the surface.

3.2 Role of Steric Effects on the Complete Regioselectivity

As described in Sect. 3, the metal surface seems to play only a negligible role in the on-surface azide–alkyne cycloaddition coupling reactions. Therefore, the observed complete regioselectivity for each case could not be explained in terms of surface catalysis. Instead, steric hindrance effects could be responsible for the experimentally observed complete regioselectivity. To quantify this effect on Au(111), the energy difference between the two possible regioisomers after coupling was calculated. The 1,5-regioisomer was found to be less stable than the 1,4 version by 0.72 eV on the Au(111) surface. This significant energy difference induced by steric hindrance between the aryl rings (Fig. 9) affects the reaction considerably and therefore increases the transition state energy of the 1,5-regioisomer formation process accordingly. This clearly shows that the selectivity of this reaction can be

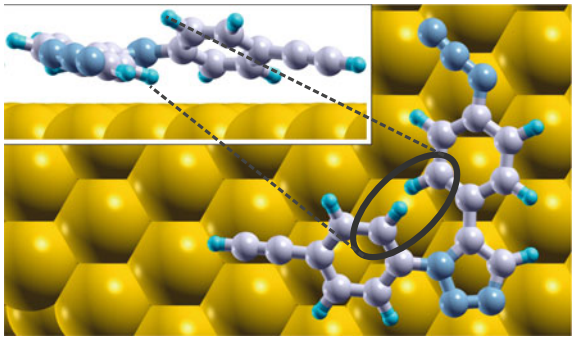

Fig. 9 Representation of the steric hindrance effect affecting the 1,5-regioisomer. Reprinted with permission from [11]. Copyright (2013) American Chemical Society

strongly enhanced by moving from a solution phase which proceeds in a three-dimensional space, to the analogous on-surface process that occurs restricted to two dimensions. This was the first report where the beneficial effect of two-dimensional confinement on the complete regioselectivity of an on-surface reaction was quantitatively explained.

4 Outlook and Perspectives

The success of azide–alkyne cycloadditions on metal substrates under mild reaction conditions has been demonstrated to be a promising alternative to develop functional nanostructures on surfaces. Furthermore, the complete regioselectivity being tuned by steric hindrance should be considered a more general effect, especially in cases where the surface does not play a catalytic role in the reaction, rendering it as a key factor to control on-surface regioselectivity. Taking all this into consideration, future work could follow two different lines: (i) to systematically probe the viability of the same reactions (including the same reactants) on different substrates, e.g., insulators, semiconductors or oxides; and (ii) to exploit the low activation temperature of this reaction and combine it with reactions with a higher activation barrier.

For the first case, the choice of a more inert surface renders itself promising. By lowering the reactivity of the substrate toward the azide moiety and the monomers in general, i.e., choosing a Au(111) substrate instead of a Cu(111), the efficiency of the on-surface cycloaddition was enhanced by almost 30 %. Such behavior could also be expected if the reaction is performed on an insulating or oxide substrate or thin layer. There has been promising advances in on-surface synthesis via Ulmann coupling on insulators, for example [14]. On the other hand, the second case could be a promising route to obtain advanced supramolecular nanostructures on surfaces. The products of on-surface cycloadditions between terminal azides and alkynes have been proven to be extremely robust, while maintaining considerable flexibility (see Sect. 2.3). Given the low activation temperature required to induce the covalent coupling, orthogonal cross-coupling reactions can be envisioned. To combine the azide–alkyne cycloaddition reaction with a different on-surface reaction may be an alternative to control functionalities in two-dimensional networks at surfaces. This would allow to mix the optimal mechanical properties from the triazoles with, for example, optoelectronic properties. In summary, there is still plenty of room for new research regarding the on-surface azide–alkyne cycloadditions, making it an interesting candidate for future on-surface synthesis studies.

Acknowledgements The authors gratefully acknowledge the support of the Deutsche Forschungsgemeinschaft (DFG) through the collaborative research center SFB 858 (project B2) and the transregional collaborative research center TRR 061 (projects B3 and B7).

References

1. Gourdon, A.: On-surface covalent coupling in ultrahigh vacuum. Angew. Chem. Int. Ed. **47** (37), 6950 (2008)
2. Perepichka, D., Rosei, F.: Chemistry: extending polymer conjugation into the second dimension. Science **323**(5911), 216 (2009)
3. Champness, N.: Surface chemistry: making the right connections. Nat. Chem. **4**(3), 149 (2012)
4. Kolb, H., Finn, M., Sharpless, K.: Click chemistry: diverse chemical function from a few good reactions. Angew. Chem. Int. Ed. **40**(11), 2004 (2001)
5. Li, Y., Cai, C.: Chem. Click chemistry-based functionalization on non-oxidized silicon substrates. Asian J. **6**(10), 2592 (2011)
6. Ciampi, S., Le Saux, G., Harper, J.B., Gooding, J.J.: Optimization of click chemistry of ferrocene derivatives on acetylene-functionalized silicon(100) surfaces. Electroanalysis **20** (14), 1513 (2008)
7. Kolb, H., Sharpless, K.: The growing impact of click chemistry on drug discovery. Drug Discovery Today **8**(24), 1128 (2003)
8. Pérez-Balderas, F., Ortega-Muñoz, M., Morales-Sanfrutos, J., Hernández-Mateo, F., Calvo-Flores, F.G., Calvo-Asín, J.A., Isac-García, J., Santoyo-González, F.: Multivalent neoglycoconjugates by regiospecific cycloaddition of alkynes and azides using organic-soluble copper catalysts. Org. Lett. **5**(11), 1951 (2003)
9. Rostovtsev, V., Green, L., Fokin, V., Sharpless, K.: Angew. A stepwise huisgen cycloaddition process: copper(i)-catalyzed regioselective "ligation" of azides and terminal alkynes. Chem. Int. Ed. **41**(14), 2596 (2002)
10. Bebensee, F., Bombis, C., Vadapoo, S., Cramer, J., Besenbacher, F., Gothelf, K., Linderoth, T.: On-surface azide-alkyne cycloaddition on cu(111): does it "click" in ultrahigh vacuum? J. Am. Chem. Soc. **135**(6), 2136 (2013)
11. Díaz Arado, O., Mönig, H., Wagner, H., Franke, J.H., Langewisch, G., Held, P.A., Studer, A., Fuchs H.: On-surface azide-alkyne cycloaddition on au(111). ACS Nano **7**(10), 8509 (2013)
12. Zhong, D., Franke, J.H., Podiyanachari, S., Blömker, T., Zhang, H., Kehr, G., Erker, G., Fuchs, H., Chi, L.: Linear alkane polymerization on a gold surface. Science **334**(6053), 213 (2011)
13. Gao, H.Y., Wagner, H., Zhong, D., Franke, J.H., Studer, A., Fuchs, H.: Glaser coupling at metal surfaces. Angew. Chem. Int. Ed. **52**(14), 4024 (2013)
14. Kittelmann, M., Rahe, P., Nimmrich, M., Hauke, C., Gourdon, A., Kühnle, A.: On-surface covalent linking of organic building blocks on a bulk insulator. ACS Nano **5**(10), 8420 (2011)

On-Surface Synthesis of Phthalocyanine Compounds

E. Nardi, M. Koudia, S. Kezilebieke, J.-P. Bucher and M. Abel

Abstract In this chapter, we review the recent progress in the synthesis of phthalocyanine compounds at metallic surfaces under ultra-high vacuum conditions. Starting with tetra-carbonitrile-benzene molecules and magnetic atoms such as iron and manganese, we show that metal–organic coordination networks are formed at room temperature; then annealing at 500–600 K leads to the on-surface formation of phthalocyanine compounds. This reaction has been studied step-by-step by scanning tunneling microscopy and spectroscopy. The last part of this chapter is dedicated to the study of larger precursors functionalized with tetra-carbonitrile groups that react with copper atoms to form original polymers linked by phthalocyanine cores.

1 Introduction

Among technologically relevant molecules for organic electronic devices, the metallophthalocyanines (MPc) are very extensively studied for their chemical and optoelectronic properties [1]. They can be employed as building blocks for a wide range of applications such as gas sensors, field effect transistors, organic light emitting diodes, or data storage devices. The polymeric forms of phthalocyanines have been known for a long time [2–7] but the isolation of single sheet of 2D

E. Nardi · M. Koudia · M. Abel (✉)
Institut Matériaux, Microélectronique et Nanosciences de Provence, CNRS UMR7334, Aix Marseille Université, Marseille 13397, France
e-mail: mathieu.abel@im2np.fr

E. Nardi
e-mail: elena.nardi@im2np.fr

S. Kezilebieke · J.-P. Bucher
Université de Strasbourg, Institut Universitaire de France, 23 rue du Loess, Strasbourg 67034, France
e-mail: jean-pierre.bucher@ipcms.unistra.fr

A. Gourdon (ed.), *On-Surface Synthesis*, Advances in Atom and Single Molecule Machines, DOI 10.1007/978-3-319-26600-8_6

polymer has never been obtained. One of the main interests is the combination of magnetic properties given by the central metals with pi-conjugated electrons of phthalocyanines. The molecular magnetism arises from the unpaired spins residing in the *d*-orbitals of the atom. Such molecules adsorbed on metallic substrates have recently gained special interest in view of emerging field of spintronics and spin-based devices. Preparation of supramolecular assemblies at surfaces under ultra-high vacuum (UHV) conditions usually requires deposition of the molecular building blocks by thermal sublimation from a crucible. Therefore, there is a limit to the weight of molecular building blocks that can be utilized in these studies: the high temperature required for their evaporation leads to thermal decomposition or to polymerization in the crucible before evaporation. A possible approach to the problem is to use smaller molecular precursors which react with atoms on the surface and form phthalocyanine compounds (Scheme 1).

Density functional theory (DFT) calculations predict very interesting properties for polymeric phthalocyanine (Table 1) [8]. Series of magnetic atoms have been theoretically studied and it appears that only Mn has a ferromagnetic coupling, whereas the coupling of the other metals is antiferromagnetic. However, the most important behavior is a high exchange energy in case of Mn (E_{ex} = 125 meV) accompanied by a half-metallic character. This gives hope for remarkable properties for the development of materials for spintronic applications.

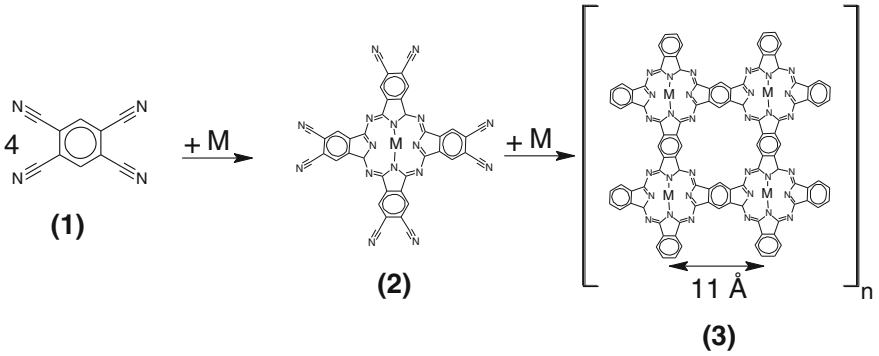

Scheme 1 Schematic diagram of the reaction between tetra-carbonitrile benzene (TCNB) molecules (**1**) and metallic atoms to form octacyano metallophthalocyanine (**2**) when the reaction goes on, it can form the polymeric–phthalocyanine compound (**3**) [1]

Table 1 Density functional theory calculations in the framework LDA + U of the magnetic configuration of the 2D polymers

	Cr	Mn	Fe	Co	Ni	Cu	Zn
E_{ex}	−29	124	−14	−6	–	−7	–
M	4	3	2	1	0	1	0
E_g	0.36	Half-metal	0.24	0.10	0.34	0.31	0.30

E_{ex} Exchange energy per supercell (E_{ex} in meV); total magnetic moment per supercell (M in μB), and energy band gap (E_g in eV) Ref. [8]

In the first part of this chapter, the possibility to induce surface reactions between small ligands—tetra-carbonitrile benzene (TCNB)—and magnetic atoms (Scheme 1) is demonstrated. This is done by depositing metallic atoms (Fe or Mn) and TCNB molecules under UHV conditions. At room temperature, TCNB molecules form large metal–organic networks with both Fe and Mn atoms in 1:4 and 1:2 stoichiometries [9–11]. For the reaction to occur, it is necessary to heat the surface to 500–550 K [12, 13]. At these temperatures, a significant proportion of molecules desorbs from the surface, necessitating a fine tuning between reaction and desorption. Since the Mn is slightly more reactive than Fe, the reaction evolves more efficiently in the former case, leading to comparatively larger MnPc domains. Further activation at higher annealing temperatures then leads to the formation of small domains of polymeric Mn-phthalocyanine.

In the second part of this chapter, it is shown on the example of Fe-TCNB that low-temperature, high-resolution scanning tunneling spectroscopy (STS) provides a powerful identification of the step-by-step evolution of the chemical reaction. In particular, a deeper insight into the genesis of the magnetic properties of such compounds is achieved. A good illustration of the convergence toward the covalent properties is the emergence of the Kondo resonance in FePc.

The last part of this chapter describes the potentiality and versatility of this method to access to a diversity of hybrid organic–inorganic compounds. New molecular precursors functionalized by tetra-carbonitrile groups are used in combination with copper atoms to form original 1D and 2D polymers linked by phthalocyanine cores. In that case, the homogeneity of the reaction allows full conclusive X-ray photoelectron spectroscopy (XPS) measurements of the chemical reaction [14].

2 Reaction Between Tetra-Carbonitrile Benzene and Magnetic Atoms (Fe or Mn)

In this example, the stepwise identification of the reaction between molecular TCNB and atomic Fe toward the final FePc product is achieved. The self-assembly of the vapor deposited TCNB molecules and Fe atoms on Au(111) first leads to tetra-coordinated $Fe(TCNB)_4$ and $Fe(TCNB)_2$ precursors [9]. However, among the two tetra-coordinate phases, only the $Fe(TCNB)_2$ network has the appropriate stoichiometry for the synthesis of FePc on Au(111). This phase is composed of Fe atoms interconnected with TCNB molecules (Fig. 1a, b) [12]. Large homochiral and mirror symmetric $Fe(TCNB)_2$ domains with a lateral extension up to 50 nm are present on the surface (Fig. 1a). It is worth mentioning that a similar result is obtained on Ag(100), indicating that the coordination network is relatively insensitive to the surface template, i.e., to the crystallography and, to some extent, to the chemical nature of the underlying substrate. A careful analysis of the STM data shows that the $Fe(TCNB)_2$ network has a square structure with a measured periodicity of 1.15 ± 0.1 nm in both orthogonal directions (Fig. 1b). The unit cell of the

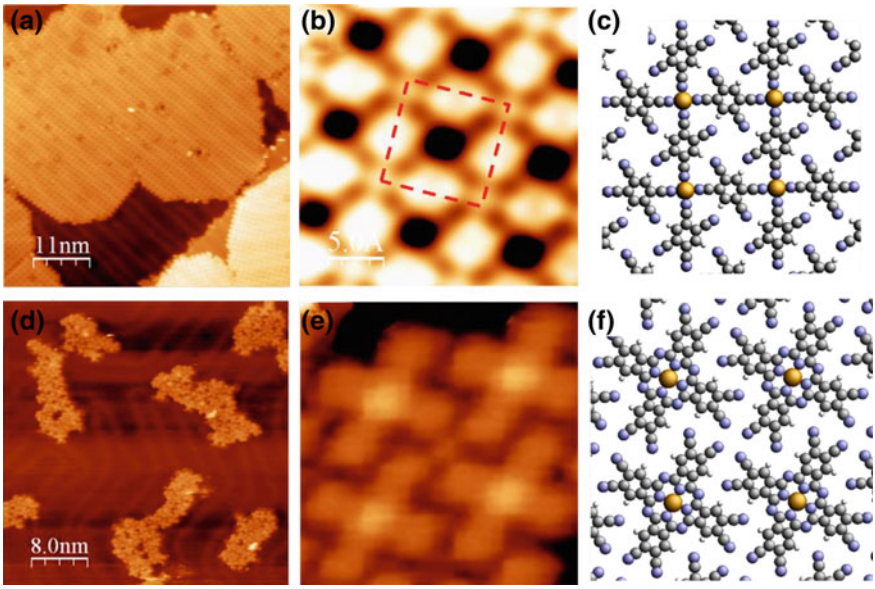

Fig. 1 STM topography images. **a**, **b** $Fe(TCNB)_2$ network on Au(111) acquired at $I = 0.2$ nA and $V = -0.9$ V. **c**, **d** Units of $FePc(CN)_8$ on Au(111), obtained upon annealing the previous Fe $(TCNB)_2$ structure at 550 K, acquired at $I = 1.8$ nA and $V = -0.9$ V. **e**, **f** Corresponding schematics. Adapted with permission from Ref. [12]. Copyright 2014 American Chemical Society

$Fe(TCNB)_2$ network (Fig. 1b, c) contains eight nitrogen atoms, four of which having a coordination bond with one single Fe atom. Annealing the $Fe(TCNB)_2$ phase to 550 K leads to the formation of cross-like molecules of octacyano-FePc ($FePc(CN)_8$) (Fig. 1e, f). The Fe atoms appear as bright protrusions (Fig. 2f), confirming the presence of d_{z2} orbitals of Fe while the organic ligands appear as four symmetric lobes. Full transformation into covalent bonds is further ascertained from the absence of chirality of the ligands around the central metal.

The annealing used for the reaction between Fe and TCNB at 550 K produces large desorption of the molecules and dilution of the metallic atoms into the substrate. In that case, the reaction has a limited yield and it results in small domains of iron phthalocyanine. Using manganese instead of iron atoms for the reaction with TCNB molecules allows a modification of the reaction efficiency because Mn, which has a less filled *d*-band than Fe, is more reactive. The room temperature phase obtained with Mn and TCNB (Fig. 2a) is very similar to the room temperature phase previously obtained with Fe and TCNB. Its annealing at 370 K allows the activation of the reaction and the formation of a Mn-phthalocyanine (Mn-Pc) network linked by hydrogen bonding (Fig. 2b). Additional Mn atoms can be found between the Mn-Pc (dotted circle in Fig. 2c) coordinating half of the available carbonitrile groups. Using the same STM tip is now possible to distinguish two electronic behaviors of Mn atoms: Mn in the cross-like compounds (solid line circles) that appears 0.4 Å above the molecular plane while Mn in between the

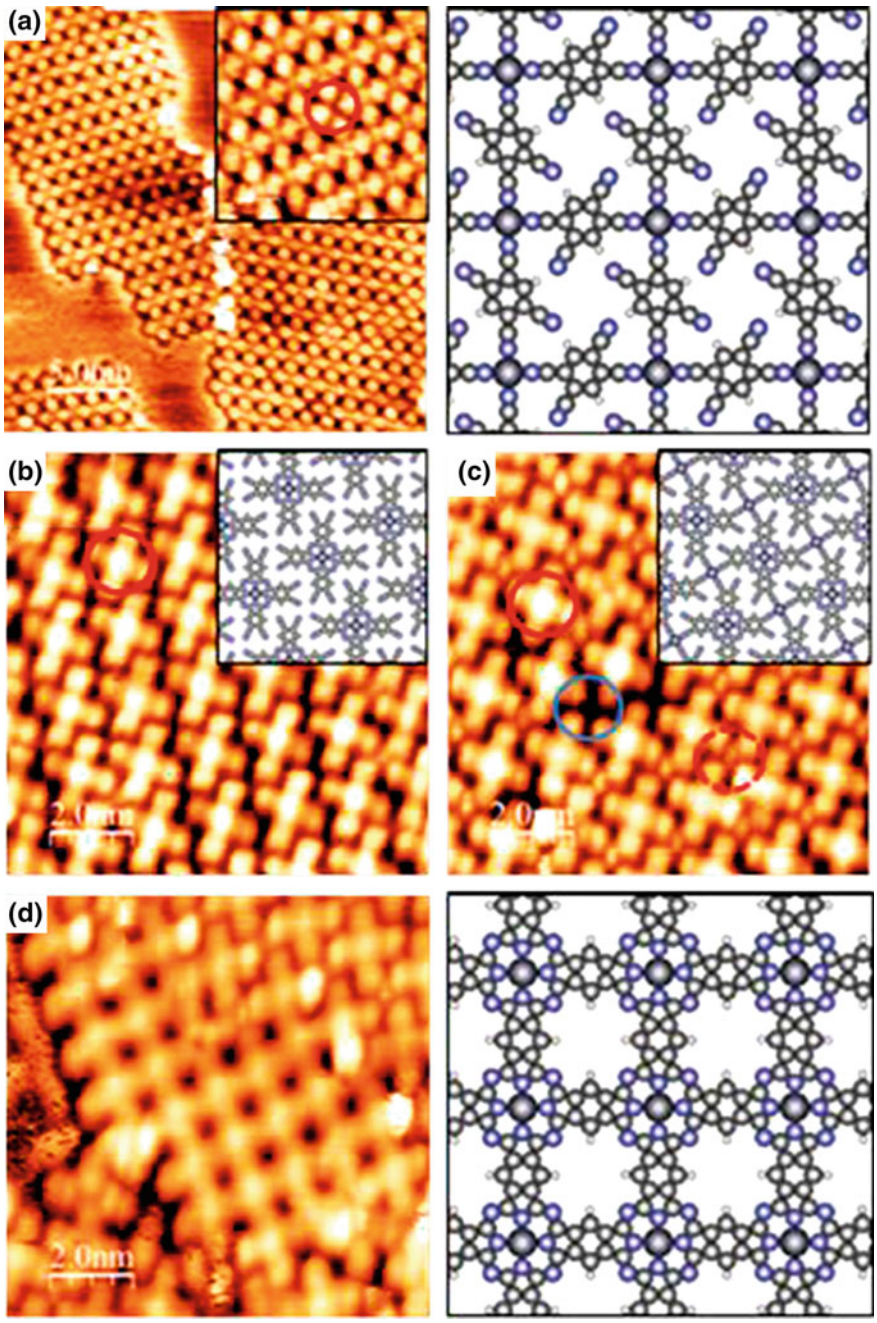

Fig. 2 STM topography images. **a** $Mn(TCNB)_2$ networks on Ag(111); **b** $MnPc(CN)_8$ on Ag(111) obtained after annealing at 370 K linked by hydrogen bonding **c** $MnPc(CN)_8$ obtained after annealing at 370 K linked by metal–ligand interactions; **d** Polymeric form of the MnPc obtained after annealing at 500 K. Adapted from Ref. [13] with permission from The Royal Society of Chemistry

Mn–Pcs (dotted line circle) that appears 0.1 Å lower. The temperature needs to be increased up to 500 K for the reaction to proceed further and to form small domains of polymeric Mn-phthalocyanines (Fig. 2d).

2.1 STS Identification of Chemical Bonds During the Synthesis of Fe-Phthalocyanine on Au(111)

Scanning tunneling spectroscopy has become a key tool to access properties of metal–organic molecules adsorbed on surfaces. In this context, the MPc's have been extensively studied due to their advantageous face-on adsorption providing easy access to metal atoms and ligands with the STM probe tip [15–22]. STS has been applied on FePc on Au(111) to track the covalent self-assembly of organic ligands and metal atoms [12]. The STS characterization of $FePc(CN)_8$ complexes reveals a strong similarity with the results obtained for FePc in the literature. This comes from a small influence of the peripheral functionalization (CN instead of H) on the orbital configuration of Fe atom. Thus, magnetic moment and spin state are expected to be the same in both systems which are further ascertained by comparing the projected density of states (PDOS) calculations for both systems [12].

To get a deeper insight into the hierarchy of chemical bonding of the iron atom, STS measurements on the freshly deposited FePc on Au(111) have been compared with those of the $Fe(TCNB)_2$ phase on Au(111) [12]. The measurements were performed in a low-temperature STM operating at a temperature of 4.6 K and UHV conditions. Two dI/dV spectra taken above the Fe atom (red) and on the benzene rings (black) of a FePc molecule are presented in Fig. 3 (upper panels). There are seven main features at sample bias of −0.9, −0.79, −0.72, −0.37, −0.17, +0.5, and 0 V. Relevant features in the dI/dV spectra are only expected when a significant overlap between tip states and molecular orbitals is achieved. This is possible for example in the case of d_{z2}, d_{xz}, and d_{yz} orbitals above the Fe atom. The sharp peak labeled No. 1 (Fig. 3) and located at −0.9 V corresponds to the lower occupied molecular orbital (HOMO-1) while the shoulder at −0.79 V (No. 2) has been attributed to the $d_{xz/yz}$ orbitals of iron [16]. The peak at −0.72 V (No. 3) on the ligand is attributed to the HOMO which is in good agreement with valence-band photoemission studies on FePc/Au(111) [23]. The relatively intense resonance at −0.38 V (labeled No. 4) is similar to the one observed by Gao et al. [16] most probably arising from the hybridization of the Fe atom in the FePc molecule with the Au(111) electronic surface state. Such surface-induced states (Fig. 3b labeled SI) have been observed for FePc on other substrates and are quite common for atoms on noble metal surfaces [20, 22]. The peak located at −0.17 V (No. 5) was not reported in the previous studies of FePc on Au(111) although a similar feature has been observed for FePc on Ag(100) [22] and Ag(111) [17] surfaces. The peak close to the Fermi level (No. 6) is a well-known Kondo signature previously observed in FePc on Au(111) [16, 21]. Additional information on the spatial

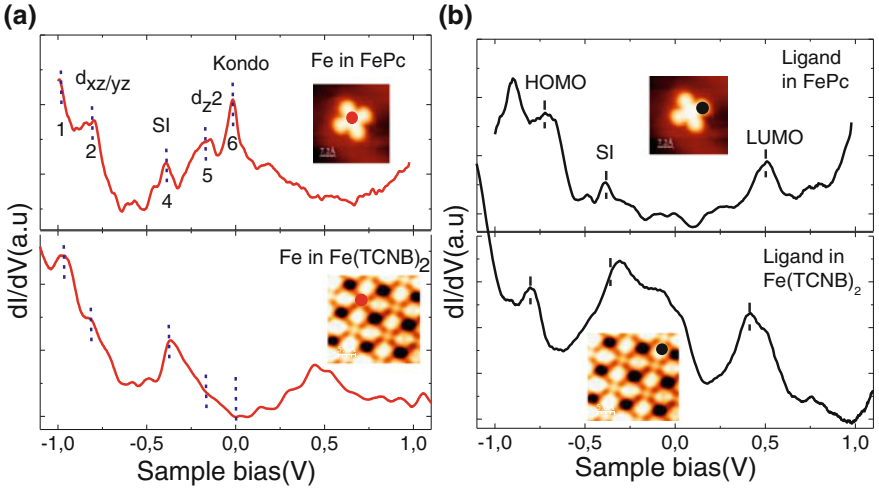

Fig. 3 Comparison of d*I*/d*V* spectra taken on the $Fe(TCNB)_2$ network and on the FePc molecule on Au(111) under the same conditions (feedback loop opened at $V = -0.7$ V, $I = 0.2$ nA). **a** d*I*/d*V* spectra taken above the Fe in FePc and in $Fe(TCNB)_2$, respectively, **b** d*I*/d*V* taken above the ligands of $Fe(TCNB)_2$ and above the lobes of FePc, respectively. Adapted with permission from Ref. [12]. Copyright 2014 American Chemical Society

distribution of the molecular orbitals can be obtained by recording the constant-height differential conductance (d*I*/d*V*) maps at different bias voltages [12, 18], thus providing information on dominant conduction channels above the molecules. Thereby, it was confirmed that the localized contrast associated with peak No. 5 and No. 6 in the d*I*/d*V* maps both originates from out-of-plane d_{z2} state of the Fe atom [12].

Although each Fe atom in the $Fe(TCNB)_2$ phase has four neighbor nitrogens as in the FePc molecule, the spectra in both systems show significant differences but also remarkable similarities. The differences mainly come from different chemical bonding between Fe and ligands: from metal–ligand interactions in $Fe(TCNB)_2$ to covalent bonds in FePc. Figure 3 shows d*I*/d*V* spectra for both $Fe(TCNB)_2$ and FePc with the STM tip above the Fe atom (Fig. 3a) and above the ligand (Fig. 3b). The two systems show three similar features: two similarities are observed on the Fe atom and one on the ligand. In particular, the feature at −0.79 V on the Fe, attributed to the d_π (d_{xz} and d_{yz}) orbitals, is similar in both systems indicating that the Fe has a similar environment in the two cases. The second remarkable feature is the surface-induced state (No. 4 in Fig. 3a) found above the Fe atom at −0.38 V indicating that Fe atom has the same influence on the Au(111) sp surface state. The spectra acquired on the ligand (Fig. 3b) show that both LUMO and HOMO of $Fe(TCNB)_2$ and FePc appear at the same energy (+0.50 V and −0.72 eV, respectively). These similarities are summarized in Table 2.

The presence of a Kondo resonance for FePc on Au(111) (No. 6 in Fig. 3a) with a corresponding Kondo temperature of about 200 K deserves a special attention as it

Table 2 Summary of the similar peak positions for FePc and $Fe(TCNB)_2$ on Au (111) given in eV

	No.	FePc	$Fe(TCNB)_2$
$d_{xz/yz}$	2	−0.79	−0.79
HOMO	3	−0.72	−0.76
SI	4	−0.38	−0.38
d_{z2}	5	−0.17	–
Kondo	6	Yes	No
LUMO	7	+0.5	+0.5

Ref. [12]

disappears in $Fe(TCNB)_2$. In FePc, the oxidation state of the iron is Fe(II) with the electronic configuration $(d_{xy})^2$, $(d_{z2})^1$, $(d_\pi)^3$ inducing a spin $S = 1$. The fact that the Kondo resonance of FePc/Au(111) is located at the metal ion can be related to a screened Kondo spin originating from the d_{z2} orbital (local moment Kondo system). This result is far from being trivial since on similar MPc systems (adsorbed on noble metals) the maximum of the Kondo resonance intensity was found on the ligands, arising from unpaired spins in the d_π orbital [22]. It is also in contrast to the fully delocalized Kondo resonance observed over the Co-porphyrin molecules on Cu(111) [24]. Finally, the above result related to the Kondo resonance of FePc by Kezilebieke et al. is in good agreement with the work of Minamitani et al. [21] who found that for FePc on Au(111) the strong coupling of the d_{z2} orbital overcomes the zero-field splitting providing a temperature window where the Kondo screening becomes dominant (effective Hamiltonian with $S = 1/2$). The partial screening of the $S = 1$ spin of FePc was also reported by Stepanow et al. [25]. To evaluate the hybridization of the Fe d_{z2} state with the substrate, STS measurements were carried out on FePc adsorbed on Au(111), Cu(111), and a cobalt nano-island [12]. The corresponding d*I*/d*V* spectra exhibit an increasing shift of the Fe *d*-state toward the Fermi level. The positions of the Fe *d*-states are summarized in Table 3 for different surfaces.

The *d*-states shift over the Fe is rationalized by means of the *d*-band model [26, 27] whose key parameter is the position of the *d*-band center with respect to the Fermi energy. As shown in Table 3, the *d*-state shift follows the same order as the *d*-band filling and the *d*-band center position: Ag < Au < Cu < Co. As a result, in case of Ag where the *d*-band center is lower in energy, the interaction with adsorbates gives rise to a large fraction of antibonding states which results in the lower adsorption energy. On the contrary, the Co surface has a *d*-band center close to the Fermi level. A large fraction of the antibonding states between the adsorbate and the surface is pushed above the Fermi level resulting in the higher adsorption energy. This might explain the strong Fe *d*-states shift observed for FePc adsorbed on the cobalt nano-islands. Experimental results for FePc molecules and Fe $(TCNB)_2$ complexes are in good agreement with DFT calculations [12]. The

Table 3 Positions of the d_{z2} resonance of Fe for FePc molecules adsorbed on metallic surfaces

	Ag(111)	Ag(100)	Au(111)	Cu(111)	Co island
Peak position (mV)	−250	−250	−170	−50	−10

Refs. [12, 17, 22]

calculation for the $Fe(TCNB)_2$ complex shows that the broad peak in the STS spectrum at +0.5 eV corresponds to an empty d_{z2} state, whereas FePc shows an occupied d_{z2} resonance just below the Fermi level. Therefore, the lack of Kondo signature for $Fe(TCNB)_2$ cannot be ascribed to a different Fe-substrate distance and is most probably due to the intrinsic differences mentioned above. As expected, the calculation clearly shows a localized spin density on the Fe of FePc with $S = 1$, whereas $Fe(TCNB)_2$ shows a weekly delocalized spin density on the ligand with Fe bearing only a fraction ($S = 0.68$) of the total spin [12].

In conclusion, the information gathered from high-resolution d*I*/d*V* spectroscopic labeling and spin-polarized DFT calculations shows that the d_π features appear already on the intermediate $Fe(TCNB)_2$ complex. The contribution of the covalent character of the surface-synthesized FePc is evidenced by the appearance of the d_{z2} state close to the Fermi energy and the related Kondo resonance, as demonstrated by studying the hybridization of the d_{z2} orbital of Fe to various substrates (Cu, Au, and Co) by STS. The lack of Kondo resonance in $Fe(TCNB)_2$ is related to the absence of the d_{z2} feature just below E_F and appears to be intrinsic to the complex.

2.2 *Reaction Between Pyrazino Phenanthroquinoxaline-Tetracarbonitrile and Copper Atoms*

Here, we show that a copper-phthalocyanine derivative is synthesized at the surface from a larger organic component, the pyrazino phenanthroquinoxaline-tetracarbonitrile (PPCN) (Scheme 2). The tunability of the electronic and structural properties of phthalocyanines makes this class of molecules ideal for both

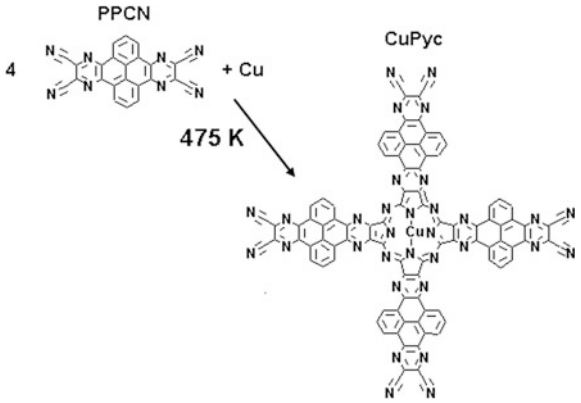

Scheme 2 Reaction between pyrazino phenanthroquinoxaline-tetracarbonitrile (PPCN) and copper atoms leading to octacyano-copper pyrenopyrazinocyanines (CuPycs)

fundamental science and technological applications, such as optoelectronic devices, sensors, and thin-film transistors.

PPCN was sublimated from a crucible onto a clean Au(111) surface. Submonolayer deposition of PPCN at room temperature in UHV results in the formation of well-ordered two-dimensional molecular domains extended over entire terraces and stabilized by weak interactions. Electron beam evaporator was used to deposit Cu atoms on top of the PPCN layer. After annealing at T = 355 K, well-ordered regular structures, in which metal centers connect to organic molecules, emerge in domains up to 120 nm in size [14].

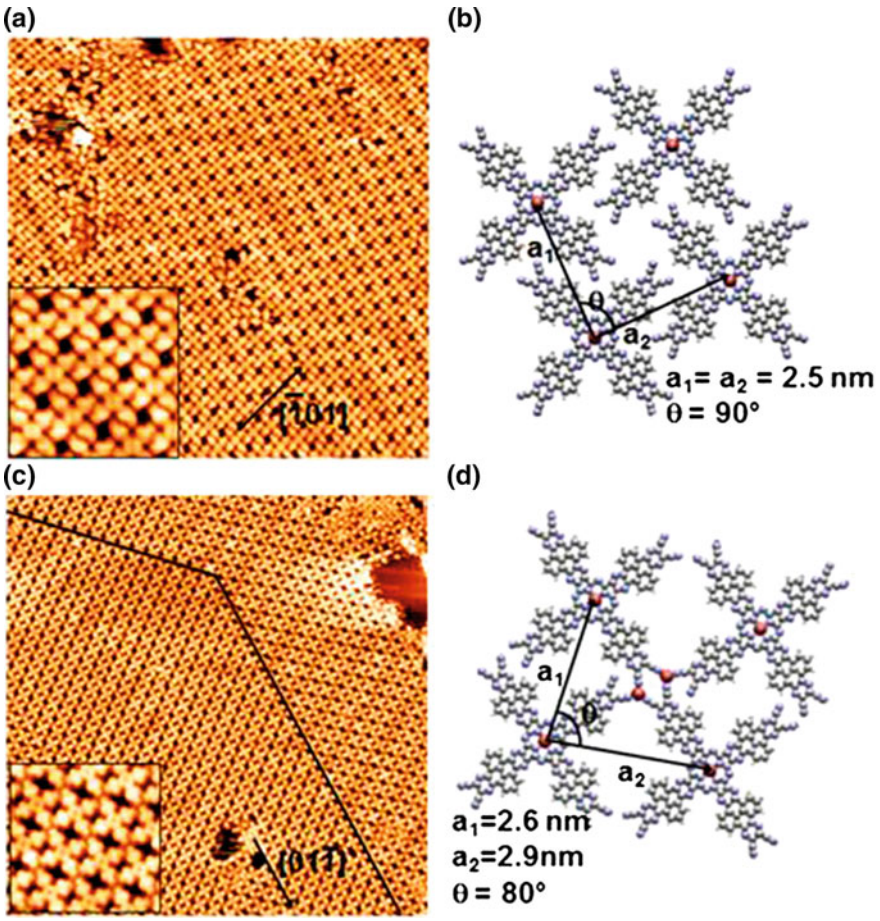

Fig. 4 Copper pyrenopyrazinocyanine (CuPyc) networks. **a** STM image (50 × 50 nm^2) of CuPycs linked by C–N···H–C bonds. *Inset* zoom (1.8 × 1.8 nm^2). **b** DFT model of the CuPyc network. **c** STM image (80 × 80 nm^2) showing the CuPycs linked by metal–organic interactions. Two mirror domains are present, separated by the *black line*. *Inset* zoom (2 × 2 nm^2). **d** DFT model of the CuPyc network linked by metal–ligand interaction. Adapted with permission from Ref. [14]. Copyright 2014 American Chemical Society

The phthalocyanine network (Fig. 4a–d) is obtained upon annealing at 475 K: the PPCN molecules react with Cu atoms to form new macromolecules derived from phthalocyanines (CuPyc, Copper pyrenopyrazinocyanine). Deposition of Cu atoms on this layer results in an extended coordination network, with domains up to 100 nm in size, in which each Cu atom is coordinated to three CuPycs (Fig. 4c). Finally, the increase in annealing temperature to 540 and 675 K leads to the formation of 1D and 2D phthalocyanine polymers, respectively (Fig. 5a–d).

An ultimate proof of the reaction between copper and PPCN is given by XPS core-level measurements of the different elements (C, N, and Cu) in the molecular film [14]. The modification of the shape of the C1s photoemission spectrum as a

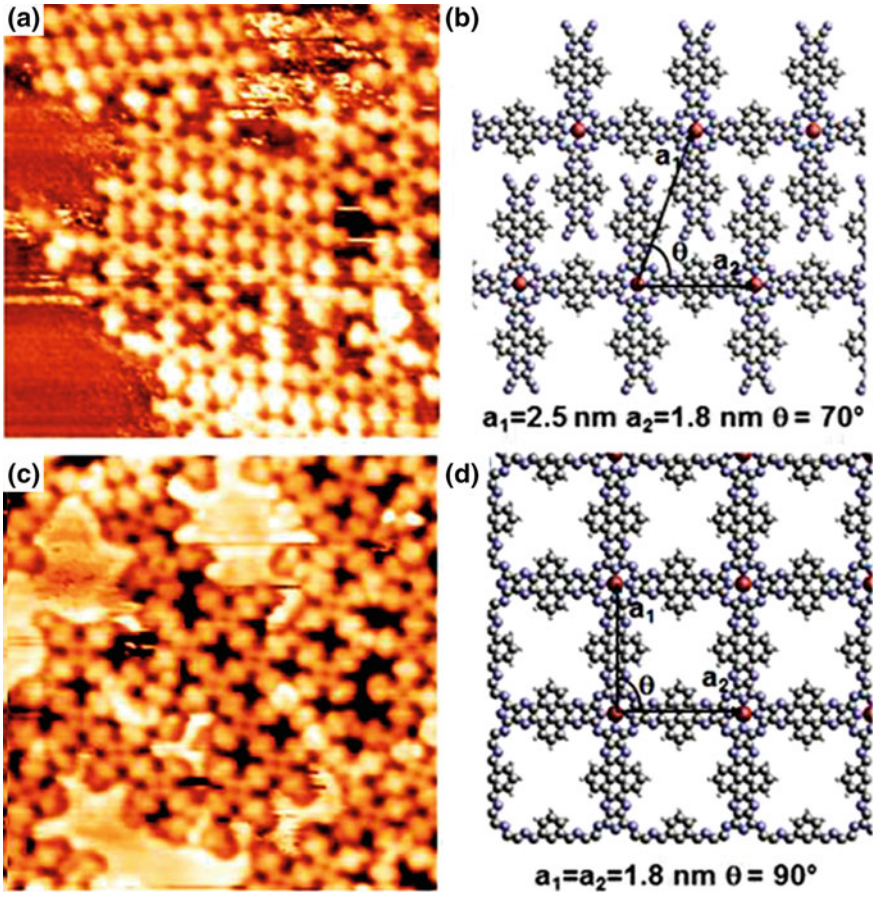

Fig. 5 Copper pyrenopyrazinocyanine (CuPyc) polymeric networks. **a** STM image (15 × 15 nm^2) of polymeric CuPyc chains, obtained by annealing the substrate at 540 K. **b** DFT model of polymeric chains. **c** STM image (15 × 15 nm^2) of the polymeric grid obtained by annealing the substrate at 675 K. **d** DFT model of polymeric grid. Adapted with permission from Ref. [14]. Copyright 2014 American Chemical Society

function of sample temperature and a new feature in the Cu2p3/2 photoemission spectrum allows a fully conclusive XPS analysis (Fig. 6). The C1s spectrum of the PPCN self-assembled network is composed of two main peaks, related to carbons of the aromatic rings (C1), carbons bonded with nitrogen atoms (C2), and a satellite of this latter (S2) [28, 29]; the C1s spectrum of the non-reacted metal–organic network (MOCN) presents the same shape slightly shifted toward higher binding energy. An evolution of the C2 peak is observed with increasing annealing temperature: Its intensity decreases and it shifts toward lower binding energy. The reaction involves the transformation of half of the carbonitrile carbons into pyrrole carbons whose binding energy is about 0.4 eV lower [30, 31]; as the reaction proceeds further to form the CuPycs, the polymeric chains, and the polymeric grid, the pyrrole component becomes more significant, thus explaining the change in the C2 peak. The Cu2p3/2 spectrum of MOCN exhibits one peak, at the same binding energy of Cu deposited on Au(111); after 475 K annealing, a new peak at about 935.4 eV appears. This value of binding energy is in good agreement with the binding energy of the Cu(II) copper peak measured for bulk CuPc and CuPc on Au

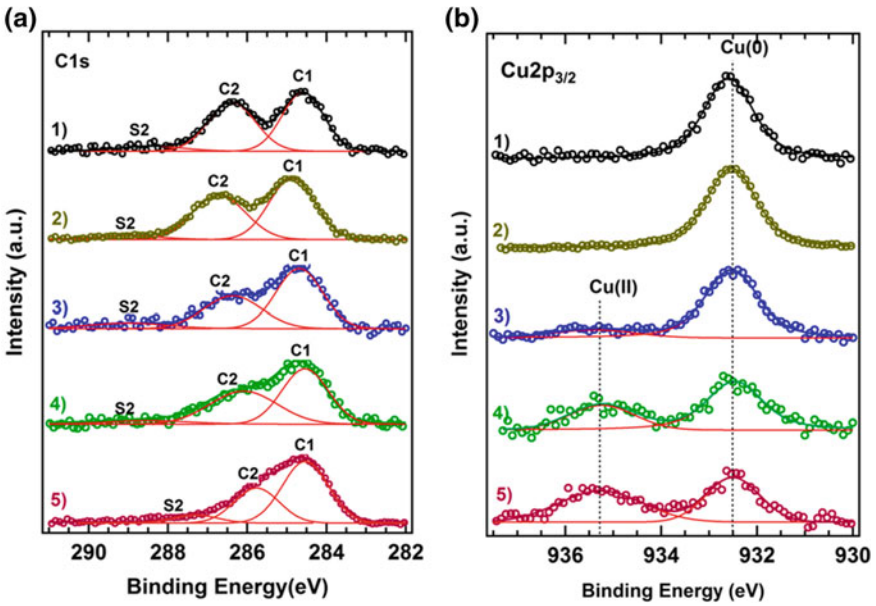

Fig. 6 X-ray photoemission spectroscopy as a function of the annealing temperature. **a** C1s spectra of, *1* PPCN self-assembled network, *2* MOCN1, *3* CuPyc coordination network (475 K annealing), *4* CuPyc polymeric chains (540 K annealing) *5* CuPyc polymeric network (675 K annealing). All the spectra were normalized to the same total area. **b** Cu2p3/2 spectra of, *1* Cu on Au(111), *2* MOCN1, *3* CuPyc coordination network (475 K annealing), *4* CuPyc polymeric chains (540 K annealing), *5* CuPyc polymeric grid (675 K annealing). All the spectra were normalized to the same total area. *Circular markers* represent the experimental data, *solid lines* the fit. The individual components of the fit are represented with *red line*. Adapted with permission from Ref. [14]. Copyright 2014 American Chemical Society

(100) [31, 32]; we interpret this peak as the signature of the CuPycs formation. Furthermore, the Cu(II):N:C ratio of the CuPyc coordination network is about 1:31:98, which is consistent with the 1:32:96 ratio of the CuPyc molecule formed on the whole surface. The intensity of the Cu(II) peak increases after 540 and 675 K annealing: this increase confirms the interpretation of the STM images and the temperature-dependent nature of the reaction, as with the formation of polymeric chains and polymeric grid more and more Cu–N bonds are indeed created.

3 Conclusion

In this chapter, we review on-surface synthesis of pi-conjugated 2D metal–organic materials, opening an access to a diversity of hybrid organic–inorganic compounds with possibly interesting transport properties. We take advantage of on-surface reaction between metallic atoms and organic precursors to confine the reaction in two dimensions. This method appeared in the last few years as a new way to form 2D materials. The choice and comparison between different molecular precursors (TCNB, PPCN) and different metallic atoms (Fe, Mn and Cu) allows us to discriminate between non-reacted and reacted species by a drastic difference in the symmetry of the self-assembled networks. Furthermore, the reaction yield obtained in the case of PPCN, close to 90 % of the surface coverage, allows a fully conclusive XPS analysis. Finally, completely new 1D and 2D pi-conjugated polymers are formed. The hierarchical synthesis of new pi-conjugated molecules embedding metals, obtained using 2D confinement of molecular precursors on surfaces, is a key step forward toward new nano-materials combining organic and inorganic species and the bottom-up production of sophisticated structures for electronic devices.

Acknowledgments We thank Dr. L. Chen, Dr. S. Clair, Dr. L. Giovanelli, Prof. X. Feng, Prof. L. Porte, and Prof. K. Muellen for fruitful discussions. This research was supported by the International Center for Frontier Research in Chemistry (Grant FRC-2010-JBu-0001). JPB thanks the Institut Universitaire de France (IUF) for support.

References

1. Leznoff, C.C., Lever A.B.P. (eds.): Phthalocyanines and related compounds, vol. 1–4.VCH, Cambridge (1996)
2. Bannehr, R., Meyer, G., Wohrle, D.: Polymer phthalocyanines and their precursors .2. the structure of polyphthalocyanines.2. Polym. Bull. **2**, 841 (1980)
3. Yudasaka, M., Nakanishi, K., Hara, T., Tanaka, M., Kurita, S., Kawai, M.: Metal phthalocyanine polymer film formation by the double source evaporation of tetracyanobenzene and metal. Synth. Met. **19**, 775 (1987)
4. Yanagi, H., Ueda, Y., Ashida, M.: Characterization of monomeric and polymeric (octacyanophthalocyaninato)metals in thin-films. Bull. Chem. Soc. Jpn. **61**, 2313 (1988)
5. Sanjai, B., Raghunathan, A., Natarajan, T.S., Rangarajan, G.: Electrical conduction in heat-treated poly metallo phthalocyanines. Mater. Sci. Eng., C **3**, 227 (1995)

6. Wöhrle, D.: Phthalocyanines in macromolecular phases – methods of synthesis and properties of the materials. Macromol. Rapid Commun. **22**, 68 (2001)
7. McKeown, N.B.: Phthalocyanine-containing polymers. J. Mater. Chem. **10**, 1979 (2000)
8. Zhou, J., Sun, Q.: Magnetism of phthalocyanine-based organometallic single porous sheet. J. Am. Chem. Soc. **133**, 15113 (2011)
9. Kezilebieke, S., Amokrane, A., Boero, M., Clair, S., Abel, M., Bucher, J.-P.: Steric and electronic selectivity in the synthesis of Fe-1,2,4,5-tetracyanobenzene (TCNB) complexes on Au(111): From topological confinement to bond formation. Nano Res. **7**, 888 (2014)
10. Abel, M., Clair, S., Ourdjini, O., Mossoyan, M., Porte, L.: Single layer of polymeric Fe-phthalocyanine: an organometallic sheet on metal and thin insulating film. J. Am. Chem. Soc. **133**, 1203 (2010)
11. Giovanelli, L., Savoyant, A., Abel, M., Maccherozzi, F., Ksari, Y., Koudia, M., Hayn, R., Choueikani, F., Otero, E., Ohresser, P., Themlin, J.-M., Dhesi, S.S., Clair, S.: Magnetic coupling and single-ion anisotropy in surface-supported Mn-based metal–organic networks. J. Phys. Chem. C **118**, 11738 (2014)
12. Kezilebieke, S., Amokrane, A., Abel, M., Bucher, J.-P.: Hierarchy of chemical bonding in the synthesis of Fe-phthalocyanine on metal surfaces: a local spectroscopy approach. J. Phys. Chem. Lett. **5**, 3175 (2014)
13. Koudia, M., Abel, M.: Step-by-step on-surface synthesis: from manganese phthalocyanines to their polymeric form. Chem. Comm. **50**, 8565 (2014)
14. Nardi, E., Chen, L., Clair, S., Koudia, M., Giovanelli, L., Feng, X., Müllen, K., Abel, M.: On-surface reaction between tetracarbonitrile-functionalized molecules and copper atoms. J. Phys. Chem. C **118**, 27549 (2014)
15. Brede, J., Atodiresei, N., Kuck, S., Lazic, P., Caciuc, V., Morikawa, Y., Hoffmann, G., Bluegel, S., Wiesendanger, R.: Spin- and energy-dependent tunneling through a single molecule with intramolecular spatial resolution. Phys. Rev. Lett. **105**, 047204 (2010)
16. Gao, L., Ji, W., Hu, Y.B., Cheng, Z.H., Deng, Z.T., Liu, Q., Jiang, N., Lin, X., Guo, W., Du, S.X., Hofer, W.A., Xie, X.C., Gao, H.J.: Site-specific Kondo effect at ambient temperatures in iron-based molecules. Phys. Rev. Lett. **99**, 106402 (2007)
17. Gopakumar, T.G., Brumme, T., Kroeger, J., Toher, C., Cuniberti, G., Berndt, R.: Coverage-driven electronic decoupling of Fe-phthalocyanine from a Ag(111) substrate. J. Phys. Chem. C **115**, 12173 (2011)
18. Heinrich, B.W., Iacovita, C., Brumme, T., Choi, D.-J., Limot, L., Rastei, M.V., Hofer, W.A., Kortus, J., Bucher, J.-P.: Direct observation of the tunneling channels of a chemisorbed molecule. J. Phys. Chem. Lett. **1**, 1517 (2010)
19. Iacovita, C., Rastei, M.V., Heinrich, B.W., Brumme, T., Kortus, J., Limot, L., Bucher, J.P.: Visualizing the spin of individual cobalt-phthalocyanine molecules. Phys. Rev. Lett. **101**, 116602 (2008)
20. Li, Z., Li, B., Yang, J., Hou, J.G.: Single-molecule chemistry of metal phthalocyanine on noble metal surfaces. Acc. Chem. Res. **43**, 954 (2010)
21. Minamitani, E., Tsukahara, N., Matsunaka, D., Kim, Y., Takagi, N., Kawai, M.: Symmetry-driven novel Kondo effect in a molecule. Phys. Rev. Lett. **109**, 086602 (2012)
22. Mugarza, A., Robles, R., Krull, C., Korytar, R., Lorente, N., Gambardella, P.: Electronic and magnetic properties of molecule-metal interfaces: transition-metal phthalocyanines adsorbed on Ag(100). Phys. Rev. B **85**, 155437 (2012)
23. Ahmadi, S., Shariati, M.N., Yu, S., Gothelid, M.: Molecular layers of ZnPc and FePc on Au (111) surface: charge transfer and chemical interaction. J. Chem. Phys. **137**, 084705 (2012)
24. Perera, U.G.E., Kulik, H.J., Iancu, V., Dias da Silva, L.G.G.V., Ulloa, S.E., Marzari, N., Hla, S.W.: Spatially extended kondo state in magnetic molecules induced by interfacial charge transfer. Phys. Rev. Lett. **105**, 106601 (2010)
25. Stepanow, S., Miedema, P.S., Mugarza, A., Ceballos, G., Moras, P., Cezar, J.C., Carbone, C., de Groot, F.M.F., Gambardella, P.: Mixed-valence behavior and strong correlation effects of metal phthalocyanines adsorbed on metals. Phys. Rev. B **83**, 220401 (2011)

26. Hammer, B., Morikawa, Y., Norskov, J.K.: CO chemisorption at metal surfaces and overlayers. Phys. Rev. Lett. **76**, 2141 (1996)
27. Norskov, J.K.: Covalent effects in the effectiveness-medium theory of chemical binding hydrogen heats of solution in the 3D metals. Phys. Rev. B **26**, 2875 (1982)
28. Lindquist, J.M., Hemminger, J.C.: High-resolution core level photoelectron spectra of solid TCNQ: determination of molecular orbital spatial distribution from localized shake-up features. J. Phys. Chem. **92**, 1394 (1988)
29. Lindquist, J.M., Hemminger, J.C.: High energy resolution X-ray photoelectron spectroscopy studies of tetracyanoquinodimethane charge transfer complexes with copper, nickel, and lithium. Chem. Mat. **1**, 72 (1989)
30. Ottaviano, L., Lozzi, L., Ramondo, F., Picozzi, P., Santucci, S.J.: Copper hexadecafluoro phthalocyanine and naphthalocyanine: the role of shake up excitations in the interpretation and electronic distinction of high-resolution X-ray photoelectron spectroscopy measurements. Electr. Spectr. Rel. Phen. **105**, 145 (1999)
31. Schwieger, T., Peisert, H., Golden, M.S., Knupfer, M., Fink, J.: Electronic structure of the organic semiconductor copper phthalocyanine and K-CuPc studied using photoemission spectroscopy. Phys. Rev. B **66**, 155207 (2002)
32. de Oteyza, D.G., El-Sayed, A., Garcia-Lastra, J.M., Goiri, E., Krauss, T.N., Turak, A., Barrena, E., Dosch, H., Zegenhagen, J., Rubio, A., Wakayama, Y., Ortega, J.E.: Copper-phthalocyanine based metal-organic interfaces: the effect of fluorination, the substrate, and its symmetry. J. Chem. Phys. **133**, 214703 (2010)

Molecular On-Surface Synthesis: Metal Complexes, Organic Molecules, and Organometallic Compounds

J. Michael Gottfried

Abstract This article covers aspects of the on-surface synthesis of large molecular systems, in particular metal complexes, organometallic compounds, and organic molecules. It is shown that this approach is especially useful if the desired molecular species are too large or thermally unstable for vapor deposition, or when their synthesis in solution is not possible. Another advantage is the possible formation of well-ordered two-dimensional network structures with a hybrid covalent/van der Waals bonding scheme. The first part of the article focuses on the on-surface synthesis of metalloporphyrins, metallocorroles, and metallophthalocyanines by direct metalation of the respective ligand molecules with coadsorbed metal atoms. The underlying metalation reaction proceeds with high yields and without by-products except hydrogen, which readily desorbs. The second part is devoted to the on-surface synthesis of hydrocarbon macrocycles by means of the surface Ullmann reaction and also discusses the organometallic reaction intermediates with C–Cu–C bonds.

List of abbreviations

(a) General

CV	Cyclic voltammetry
DFT	Density functional theory
EC-STM	Electrochemical scanning tunneling microscopy
LDOS	Local density of states
LT-STM	Low-temperature scanning tunneling microscopy
MOCN	Metal-organic coordination network
NEXAFS	Near-edge X-ray absorption fine structure
RT	Room temperature
SERRS	Surface-enhanced resonance Raman scattering
STM	Scanning tunneling microscopy

J. Michael Gottfried (✉)
Philipps-Universität Marburg, Fachbereich Chemie, Hans-Meerwein-Str. 4, 35032 Marburg, Germany
e-mail: michael.gottfried@chemie.uni-marburg.de

A. Gourdon (ed.), *On-Surface Synthesis*, Advances in Atom and Single Molecule Machines, DOI 10.1007/978-3-319-26600-8_7

STS	Scanning tunneling spectroscopy
TPD	Temperature programmed desorption
TPR	Temperature programmed reaction
UHV	Ultra-high vacuum
UPS	Ultraviolet photoelectron spectroscopy
XPS	X-ray photoelectron spectroscopy

(b) Chemical compounds

DABCO	1,4-diazabicyclo[2.2.2]octane
DMTP	4,4″-dibromo-*m*-terphenyl
DPP	5,15-diphenylporphyrin
MTP	*meta*-terphenyl biradical
OEP	2,3,7,8,12,13,17,18-octaethylporphyrin
P	Porphin
Pc	Phthalocyanine
PPIX	Protoporphyrin IX (3,7,12,17-tetramethyl-8,13-divinyl-2,18-porphindipropionic acid)
TBPP	5,10,15,20-tetrakis-(3,5-di-tert-butyl)-phenylporphyrin
TBrPP	5,10,15,20-tetrakis(4-bromophenyl)porphyrin
TCNB	1,2,4,5-tetracyanobenzene
TMP	*Meso*-tetramesitylporphyrin (5,10,15,20-tetrakis(2,4,6-trimethyl)phenylporphyrin)
TMPA	5,10,15,20-tetrakis[4-(trimethylammonio)phenyl]-porphyrin
$TMPyP^{4+}$	5,10,15,20-tetra(*N*-methyl-4-pyridinium)porphyrin
TPCN	5,10,15,20-tetra[(4-cyanophenyl)phen-4-yl]porphyrin
TPP	5,10,15,20-tetraphenylporphyrin
TPyP	5,10,15,20-tetra(4-pyridyl)porphyrin

Prefixes for porphyrin and phthalocyanine ligands: 2H or 2D = freebase, M = metal complex

1 Introduction

The synthesis of metal complexes, organic molecules, and organometallic compounds at the solid/vacuum interface is a promising approach for surface modification and functionalization. It is an important alternative to the direct vapor deposition of the required molecules or metal complexes and has substantial advantages especially in the following cases:

1. The substance cannot be synthesized as a bulk material and then (vapor) deposited onto a surface, either because no bulk synthesis is available or because the substance is too labile for vapor deposition. The former issue typically arises

in the case of large conjugated hydrocarbons, where a solution-based synthesis often requires that long alkyl chains are attached to the parent structure in order to achieve sufficient solubility [1–3]. The corresponding naked parent structures have only been accessible by on-surface synthesis [4]. In addition, catalytic and template effects exerted by the surface can help driving the reaction in the desired direction, especially in the case of planar molecular structures.

2. The on-surface synthesis of covalently bonded two-dimensional networks is often hampered by large defect concentrations. This issue results from the irreversible character of the bond formation, which prevents the healing of initially formed structural defects. An alternative strategy uses the on-surface synthesis of large molecular moieties, which are still sufficiently mobile to self-assemble and to segregated defect structures. The resulting van der Waals network can then be fused by covalent bonds in a subsequent step.

In this contribution, both cases will be addressed and illustrated by examples from the recent literature. The first part focuses on the surface-confined synthesis of large metal complexes based on porphyrins, corroles, and phthalocyanines. Monolayers and multilayers of these complexes can be synthesized by the reaction of the metal-free macrocycle ligands with coadsorbed metal atoms (or metal atoms from the substrate), sometimes followed by the attachment of another ligand on the metal center. Mechanistic details of this in situ redox reaction and properties of the resulting complexes will be discussed. The second part deals with reactions of bromoarenes on Cu surfaces. Temperature-dependent studies show that the C–Br bonds dissociate already at low temperatures and are replaced by C–Cu–C bonds, which lead to the formation of linear, cyclic, or two-dimensional organometallic oligomers and polymers. A prominent example for a molecule for which no solution-based synthesis is available, but which can be made by on-surface synthesis, is hyperbenzene, a hexagonal octadecaphenylen, which is formed by an Ullmann-type reaction from six dibromo-*m*-terphenyl molecules. As a room temperature stable intermediate, the corresponding organometallic macrocycle with 6 C–Cu–C bridges was found, accompanied by other cyclic and chain-like organometallic oligomers.

2 On-Surface Synthesis of Porphyrin, Phthalocyanine, and Corrole Complexes

Formation of coordinative bonds between adsorbed ligand molecules and coadsorbed (or substrate) metal atoms has frequently been used to synthesize two-dimensional metal-organic coordination networks [5–8]. With a similar approach, molecular complexes can be synthesized on surfaces, as has been shown for various porphyrins and phthalocyanines. Their parent structures are displayed in Fig. 1.

Porphyrins and their metal complexes are widespread in nature as the active centers of many enzymes and other functional biomolecules, such as hemoproteins

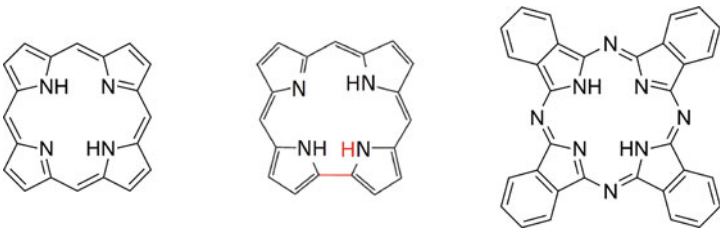

Porphin (2HP) Corrole (3HC) Phthalocyanine (2HPc)

Fig. 1 Porphin, corrole, and phthalocyanine, the parent structures of the respective classes of molecules. Corrole differs from porphin only by the absence of one *meso*-carbon atom in the macrocycle (position marked in *red*); the hydrogen atom from this *meso*-position (formally) goes to one of the *N* atoms, resulting in three pyrrolic nitrogens (–NH–) in the corrole

[9, 10] or chlorophylls [11]. Porphyrin derivatives also find widespread application in science and technology, such as heterogeneous catalysis [12, 13], electrocatalysis [14], photocatalysis [15], sensor systems [16–18], organic electronics [19, 20], and various types of light-harvesting systems [21, 22]. Porphyrins have also been employed in the medical context as sensitizers in photodynamic therapy for cancer treatment [23–26].

Phthalocyanines are not found in nature, but can efficiently be synthesized from phthalonitriles in the presence of metals [27]. They are produced on an industrial scale and find their main applications as pigments in printing inks, paints, plastics, and other mass products, including color filters for LCD and TFT displays [27]. They are also used as oxidation catalysts [28], in organic semiconductors in thin-film transistors [29], organic light-emitting diodes [30], and molecular organic photovoltaics [31–33], in liquid crystalline materials [34, 35], as photoactive element in photocopies and laser printers [32, 36], and as photosensitizers in dye solar cells [37] and for photodynamic cancer therapy [38, 39].

Porphyrins and phthalocyanines possess a rich and diverse coordination chemistry, which arises from the large variety of complexes which they form with most stable elements in the periodic table, except nitrogen, the halogens, and the rare gases (Figs. 2 and 3) [40]. A similar rich coordination chemistry was observed at solid/vacuum interfaces [41], although there are characteristic mechanistic differences, which partly result from the presence or absence of a solvent: In solution, stabilization by solvatation favors ionic reactants, products, and intermediates, especially in polar solvents, while in the absence of solvatation, reactions preferentially proceed via neutral species. This is well known for gas-phase reactions, where atoms and radicals dominate the reaction mechanism, but also holds true for many surface reactions. It also applies to the formation of metalloporphyrins and metallophthalocyanines by direct metalation of the ligand. In solution, the metalation reaction proceeds as a replacement of two protons by a metal ion, i.e., as an ion exchange [42]. In contrast, the corresponding surface reaction follows a redox mechanism, resulting in the oxidation of a metal atom to its dication and the related

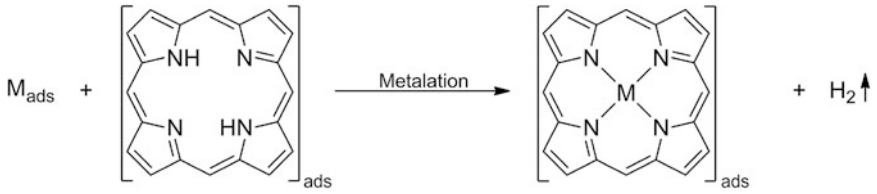

Fig. 2 Metalation of a porphyrin (here: porphin, 2HP) in the adsorbed state

reduction of the protons to H_2 (Fig. 2) [43–45]. Besides the coordination reactions at the center of the macrocycle and the coordination of axial ligands to the metal center, porphyrins with suitable substituents can also form coordinative bonds at the molecule's periphery [7].

2.1 Synthesis of Complexes Using Pre-deposited Ligand Molecules

Adsorbed metalloporphyrins and phthalocyanines at the solid/vacuum interface can be synthesized by reaction between the pre-adsorbed ligand molecules and post-deposited metal atoms. This type of reaction was first reported for Co and *meso*-tetraphenylporphyrin (2HTPP) [43, 46], Zn and 2HTPP [43, 47], Fe and *meso*-tetrapyridylporphyrin (2HTPyP) [48], as well as Fe and 2HTPP [49]. In all these experiments, the metals were vapor deposited onto monolayers of the ligands on an inert metal surface. The metal atoms reacted with the porphyrin molecules as is shown in Fig. 2.

The reaction proceeds at room temperature for V [50], Cr [51], Mn [52], Fe, Co [43], and Ni [53], but requires elevated temperatures for Ti [54], Zn [43], and Rh [52], as will be discussed in Sect. 2.3. A periodic table with all elements that form metal complexes with porphyrins and those for which on-surface metalation was achieved (gray-shaded boxes) is shown in Fig. 3. As can be seen, there are plenty of opportunities for the further exploration of on-surface metalation.

The reaction progress was monitored mainly with XPS, STM, and NEXAFS. Representative N 1*s* XPS spectra for the metalation of a 2HTPP monolayer on Ag (111) with post-deposited Fe atoms are displayed in Fig. 4 [55]. The XP spectrum of a 2HTPP monolayer shows two components: one for the iminic nitrogen (–N=) at lower binding energy (398.2 eV) and another for pyrrolic nitrogen (–NH–) at higher binding energy (400.1 eV) [56]. Upon deposition of Fe atoms, the two 2HTPP related peaks are increasingly replaced by a single peak at 398.7 eV, which indicates the formation of iron(II) *meso*-tetraphenylporphyrin (FeTPP), because the four nitrogen atoms are chemically equivalent in the complex.

The reaction progress can also be monitored by STM, if there is sufficient contrast between the unmetalated and the metalated species. Figure 4b shows STM

Li												B	C	
Na	Mg											Al	Si	P
K	Ca	Sc	Ti	V	Cr	Mn	Fe	Co	Ni	Cu	Zn	Ga	Ge	As
Rb	Sr	Y	Zr	Nb	Mo	Tc	Ru	Rh	Pd	Ag	Cd	In	Sn	Sb
Cs	Ba	Ln	Hf	Ta	W	Re	Os	Ir	Pt	Au	Hg	Tl	Pb	Bi
		An												

Fig. 3 All elements shown in this periodic system form porphyrin and phthalocyanine complexes. To date, on-surface metalation in UHV was achieved only with the elements in the *gray-shaded* boxes

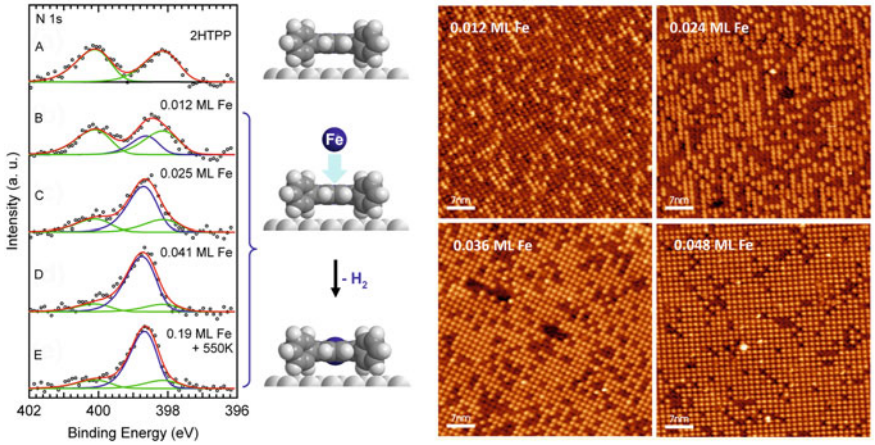

Fig. 4 On-surface synthesis of iron(II) *meso*-tetraphenylporphyrin (FeTPP) by metalation of *meso*-tetraphenylporphyrin (2HTPP) with vapor-deposited Fe. *Left*, N 1*s* XP spectra for increasing dosages of Fe (from *top* to *bottom*). The STM images (*right*) show the 2HTPP monolayer after deposition of 0.012, 0.024, 0.036, and 0.048 ML Fe, resulting in metalation degrees of 29, 60, 73, and 89 %, respectively. The indicated Fe coverages are relative to the number of surface Ag atoms. The stoichiometric Fe coverage would be 0.037 ML (one Fe atom per one 2HTPP molecule). Adapted with permission from Ref. [55], © (2008) American Chemical Society (*left*). Adapted with permission from Ref. [49] (*right*), © (2007) John Wiley and Sons (*right*)

images of a 2HTPP monolayer on Ag(111) during metalation with Fe [49]. The first image was taken after the deposition of 0.012 ML Fe, which led to the metalation of 29 % of the molecules in the monolayer. The FeTPP complexes appeared bright because of the large contribution of iron *d*-orbitals near E_F [57]. The subsequent images show the monolayer after additional Fe deposition steps, resulting in the metalation of 60, 73, and 89 % of the molecules. Typical yields were 70–90 % relative to the deposited amount of metal atoms. Excessive metal deposition onto

the porphyrin monolayer led to the formation of metal clusters, which preferentially formed at substrate step edges. For deposition of Fe onto 2HTPP/Ag(111), the Fe clusters were reported to sit between the Ag surface and the FeTPP layer formed by metalation [58]. Similar observations were made for the metalation of 2HTPP with Ni on Au(111) [53].

Up to now, there is no evidence for a significant influence of the peripheral substituents at the porphyrin core on the metalation reaction with post-deposited metal atoms (but see Sect. 2.2 for substitutent effects on the metalation with pre-deposited or substrate metal atoms). Metalation of 2HTPP [49, 55], 2HTPyP [48], and 2HOEP [59] with Fe on Ag(111) led to very similar results; all these reactions were found to take place at room temperature, if the metal was deposited onto the porphyrin layer.

Metalation with post-deposited metal atoms was also used as part of a two-step on-surface synthesis of porphyrin complexes with an additional axial ligand: (NH_3) ZnTPP was made on Ag(111) by metalation of 2HTPP with Zn followed by coordination of NH_3 at the Zn ion [47]. With a similar approach, the complex (NO) FeTPP was synthesized by successive reaction of Fe and nitric oxide (NO) with a 2HTPP monolayer on Ag(111) [60, 61].

Metalation of porphyrin monolayers is not limited to metallic substrates, but can also be performed on oxides. On a $TiO_2(110)$-(1×1) surface, 2HTPP (sub)monolayers were metalated with post-deposited Ni atoms to from NiTPP. The yield was found to be lower than in the case of metalation on metal surfaces, reaching only 60 % even with a threefold Ni excess [62].

Phthalocyanines undergo similar metalation reactions as porphyrins. 2HPc monolayers have been metalated with Fe [58, 63] and V [50] on Ag(111). The yields were similar to those found for porphyrin metalation. Another example is the metalation of 2HPc with Fe on thin Pb films on Si(111), which was dependent on the thickness of the Pb film (cf. Sect. 2.3) [64].

Corroles, which differ from porphyrins by the lack of one of the four *meso*-carbon atoms, have also been shown to undergo metalation. Since the corrole macrocycle contains three pyrrolic nitrogen atoms (–NH–), the metal atom can be oxidized to its +III state, as was shown for the metalation of 2,3,8,12,17, 18-hexaethyl-7,13-dimethyl-corrole with Co on Ag(111) [65].

Instead of vapor-deposited metal atoms, metal carbonyls can be used for metalation. $Ru_3(CO)_{12}$ was reported to metalate a 2HTPP derivative on Ag(111). (The 2HTPP derivative was formed by surface-assisted partial dehydrogenation.) After adsorption of the carbonyl at room temperature, the reaction was induced by heating to 550 K [66].

Double-decker complexes containing a metal ion in a formal +IV oxidation state sandwiched between two porphyrins or phthalocyanine ligands are formed by metals with large atomic radii and preference for higher oxidation states, such as rare earth metals. Complexes of this structure were produced by exposing 2HTPP multilayers on Ag(111) to a beam of Ce atoms. After heating to 500 K, which induces the metalation reaction and ensures desorption of excessive 2HTPP, $Ce(TPP)_2$ double-decker complexes were observed by LT-STM. Additional bright features in

the STM images were interpreted as $Ce_2(TPP)_3$ triple-decker complexes [67]. If only (sub)monolayers of 2HTPP are available, Ce deposition leads to the formation of CeTPP complexes. Due to its size, the Ce ion sits outside the porphyrin plane, but it is not clear whether it points toward or away from the surface [68].

If the metalation reaction does not proceed spontaneously, it can be induced by manipulation with an STM tip, as was demonstrated by Sperl et al. with the metalation of a single phthalocyanine (2HPc) molecule on a Ag(111) surface at 7 K, resulting in the formation of AgPc [69]. The first step of the forced metalation consisted in the dehydrogenation of the pyrrolic nitrogen atoms (–NH–) by applying voltage pulses with the STM tip (Fig. 5). In the second step, the Ag-coated W tip was approached to the molecular center at low bias voltage. At a certain distance, a sudden change of the tunneling current indicated the transfer of an Ag atom from the tip to the ligand. The identity of the synthesized AgPc was established by comparison with the tunneling spectra with those of directly deposited AgPc. Note that spontaneous formation of silver(II) phthalocyanine (AgPc) (or any Ag porphyrin) on Ag(111) by reaction with substrate atoms has not been observed as yet. Due to its large ion radius, the Ag center is located outside the molecular plane of the Pc ligand. After the STM-induced synthesis, the Ag ion points to the vacuum side (Ag-up position). By applying a voltage pulse, the ion can be pushed downward to a position between the substrate surface and molecular plane of the Pc ligand (Ag-down position). A similar conversion was reported for SnPc on Ag (111). SnPc molecules in direct contact to the Ag surface can only be switched from a Sn-up to a Sn-down position. If the molecules sit on a decoupling layer of other SnPc molecules, reversible switching in both directions was possible [70].

2.2 *Synthesis of Complexes Using Post-deposited Ligand Molecules*

Synthesis of porphyrin and phthalocyanine complexes is also possible by applying the reverse order of deposition, as was first demonstrated for a Zn/Ag(111) substrate, onto which 2HTPP was deposited. Subsequent heating to 550 K induced reaction to ZnTPP, as was shown by XPS [71]. A similar reaction was observed between 2HTPP and Fe/Ag(111): Initial vapor deposition of small amounts of Fe onto Ag(111) led to the formation cluster at monatomic step edges (Fig. 6a). In the next step, 2HTPP was deposited, which formed an ordered monolayer on the terraces (Fig. 6b). At room temperature, the Fe and 2HTPP coexisted without reaction. Upon heating to 550 K, however, the clusters dissolved and the Fe atoms reacted with the 2HTPP molecules on the terraces to form FeTPP. The fact the bright protrusions of FeTPP are randomly distributed over the terraces (and not clustered around the original positions of the Fe clusters at the step edges) indicates that the reactants are sufficiently mobile at this temperature to allow multiple diffusion events before the actual metalation reaction occurs [55]. Similar results were obtained for the metalation of 2HTPP on Ni/Au(111) [53].

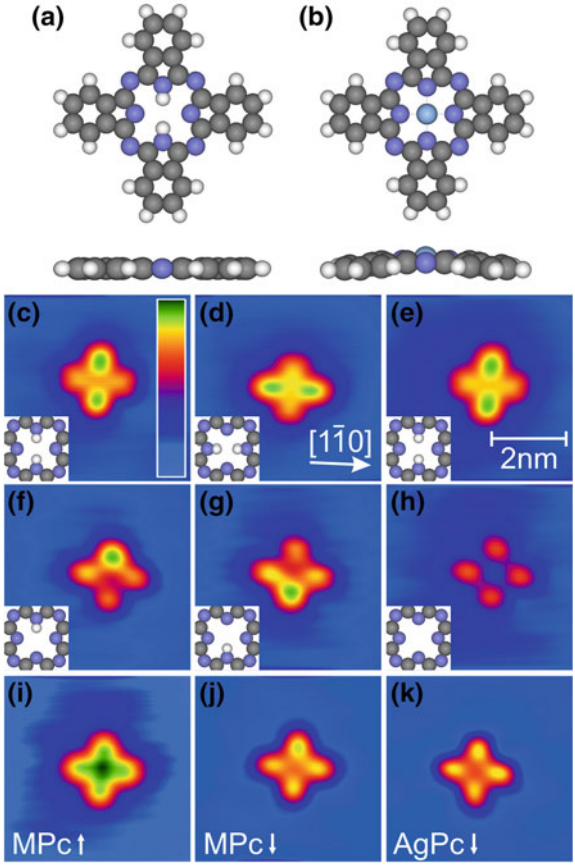

Fig. 5 Synthesis of silver(II) phthalocyanine (AgPc) by forced metalation of phthalocyanine (2HPc) on Ag(111) with a Ag atom from the STM tip. **a**, **b** Gas-phase structures of 2HPc and AgPc. **c**–**j** Constant-current STM images of 2HPc and derived molecules, along with molecular models (*Insets*). **c**–**e** Tautomerization of 2HPc induced by voltage pulses of 1.6 V. **f**, **g** STM images of HPc obtained after removal of one pyrrolic H atom from 2HPc by a pulse of 3.0 V. Hopping of the remaining pyrrolic H atom was induced by pulses of 2.5 V. **h** Pc molecule fabricated by pulsing the voltage to 3.5 V. **i** After approach of the Ag tip to the center of the Pc, MPc-up (MPc$^{\uparrow}$) is formed. **j** A voltage pulse of 3.0 V leads to an interconversion of MPc into MPc-down (MPc$\downarrow$). By comparison with the image of AgPc on Ag(111) prepared by sublimation from a heated crucible (**k**), the molecule in (**j**) was identified as AgPc, with the Ag atom between the surface and the molecular plane (AgPc$\downarrow$). Adapted with permission from Ref. [69], © (2011) John Wiley and Sons

At higher coverages of pre-deposited Fe, metalation at room temperature is possible. This has been shown for thin films of γ-Fe(110) (15 ML) on Cu(110). Vapor deposition of 1 ML 2HTPP onto this Fe layer led to immediate formation of FeTPP. A similar reactivity was found for 2HTPP on Ni(111): Deposition of 1 ML 2HTPP onto this substrate held at room temperature resulted in complete metalation

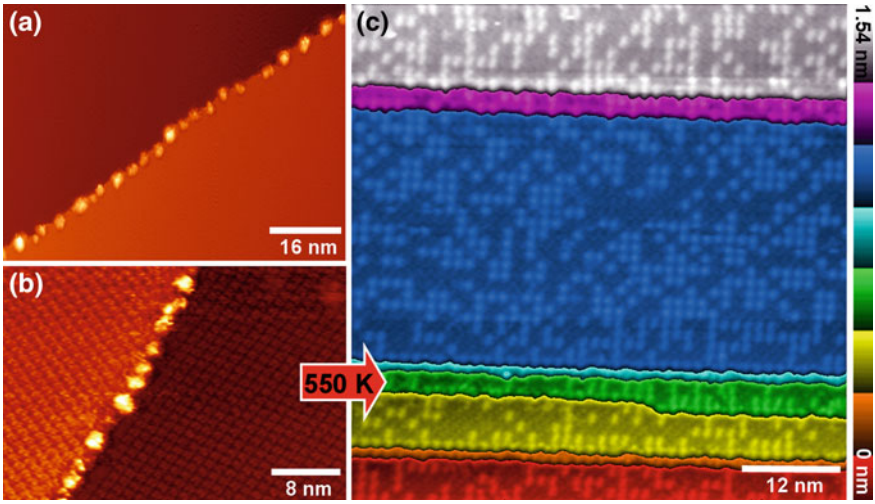

Fig. 6 Synthesis of FeTPP from 2HTPP on Fe/Ag(111). **a** STM image taken after deposition of 0.025 ML Fe onto Ag(111) at room temperature, showing Fe clusters at the step edges of a Ag(111) surface. **b** Coexistence of Fe clusters and a 2HTPP monolayer at the terraces after subsequent deposition of a 2HTPP monolayer. **c** After heating to 550 K, terraces individually color-coded. The bright spots in (**c**) indicate FeTPP formed by metalation of 2HTPP. Adapted with permission from Ref. [55], © (2008) American Chemical Society

to NiTPP [52]. 2HOEP deposited onto Ni islands on Cu(111) gave also rise to metalation, whereas no metalation was observed for 2HTPP on the same substrate [72].

The finding of room temperature metalation on Fe or Ni films and single-crystal surfaces also explains why elevated temperatures are necessary for the metalation with submonolayers of Fe or Ni on inert surfaces such as Ag(111) or Au(111): Apparently, not the metalation reaction itself is rate-limiting, but rather the supply of metal atoms by 2D evaporation of the metal clusters. At room temperature, the 2D vapor pressure of the clusters is too low for efficient metalation.

Metalation by substrate metal atoms, sometimes termed "self-metalation," has also been studied on Cu surfaces [73–80]. The reaction of 2HP and 2HTPP with a Cu(111) surface was studied in great detail by Diller et al. [73, 74] using LT-STM, XPS, and NEXAFS. A 2HP submonolayer was found to undergo complete metalation upon heating to 423 K, as was deduced by STM. Detailed XPS studies of a 2HP bilayer revealed that complete reaction of both layers to CuP occured already between 373 and 393 K [73]. A 2HTPP monolayer on Cu(111) was shown to react to CuTPP starting at 420 K [74]. Ditze et al. used the slow reaction of 2HTPP with Cu on Cu(111) at 400 K to determine the reaction activation energy (cf. Sect. 2.3 below) [78]. For 2HTBPP on Cu(111), it was found that 57 % of a monolayer was metalated after heating to 350 K for 3.5 h. In contrast, substantial metalation of a 2HPc monolayer on Cu(111) occurred already below room temperature [81].

Reaction of 2HTPP with substrate Cu atoms was reported to be facilitated by the presence of chemisorbed oxygen atoms. On an oxygen-($\sqrt{2} \times \sqrt{2}$)*R*45° reconstructed Cu(001) surface, metalation of 2HTPP was found to be complete already at 285 K, whereas 450 K was required on the bare Cu(001) surface [75]. Interestingly, the oxygen-containing porphyrin 2HPPIX was reported to undergo metalation on Cu(100) and Cu(110) surfaces at room temperature. It is not clear whether the oxygen of the molecule plays a role in this reaction as well or whether the high adatom density on the Cu(100) and Cu(110) surfaces was decisive, as was suspected by the authors [76].

The metalation of 2HTPP on Cu(111) was found to be strongly dependent on the 2HTPP coverage [82]. While disordered 2HTPP submonolayers on Cu(111) reacted only slowly to CuTPP, an increased reaction rate was observed for an ordered supramolecules "checkerboard" structure, which was formed at higher coverages [83].

2.3 *Mechanism, Energetics, and Kinetics of Direct Metalation*

In contrast to metalation in solution, where a metal ion replaces two protons at the pyrrolic N atoms of the porphyrin core, direct metalation with metal atoms is a redox reaction. In the course of this reaction, the metal atom is oxidized to its dication and hydrogen is released as H_2. Thus, this reaction formally resembles the dissolution of a metal in a Brønsted acid [43].

Gas-phase DFT calculations of the reaction between a porphin molecule (2HP) and various metal atoms (Fe, Co, Ni, Zn, Cu) were reported by Shubina et al. [43, 44]. Figure 7 shows the computed lowest energy profile of the reaction between 2HP and Zn, together with selected minimum and transition state structures.

As can be seen in the diagram, the metalation reaction starts with the coordination of the neutral metal atom by the intact porphin molecule. This initial step is exothermic and leads to a deformation of the ligand, such that the pyrrolic hydrogen atoms are bent out of the molecular plane. The resulting complex closely resembles the sitting-atop (SAT) complex postulated for metalation in solution [84, 85]. In the following two elementary steps, which have substantial activation barriers in the case of Zn, the pyrrolic hydrogen atoms are transferred to the coordinated Zn atom, from which they desorb as H_2. As a result, the Zn atom is formally oxidized to its dication, while the porphin ligand acquires two negative charges. In this example (Zn + 2HP), the rate-limiting step is the first H transfer, which has a computed barrier of $\Delta E^{\neq}$ = 136 kJ/mol or $\Delta G^{\neq}$ = 137 kJ/mol [43]. The fact that $\Delta E^{\neq}$ and $\Delta G^{\neq}$ are almost identical indicates that the activation entropy $\Delta S^{\neq}$ is very small. This is consistent with an intramolecular H transfer step in a porphyrin molecule [86].

The release of H_2 provides a convenient method for the experimental determination of the overall reaction barrier. For this purpose, *N*-deuterated 2DTPP was

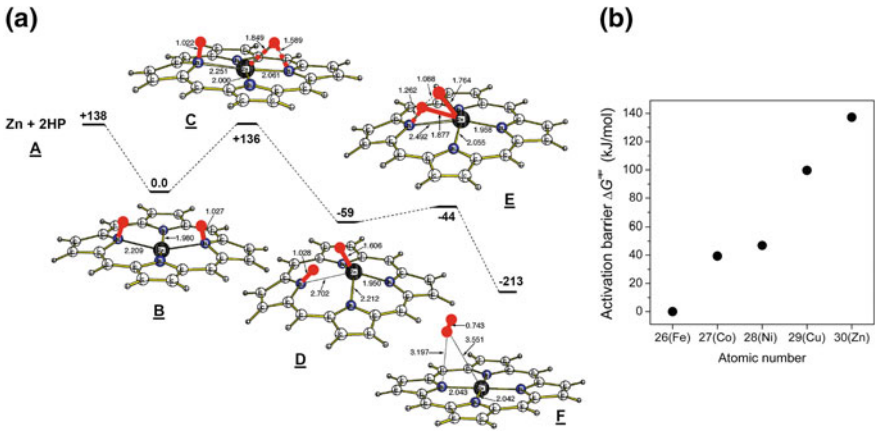

Fig. 7 **a** Schematic energy diagram of the metalation of porphin (2HP) with Zn, according to gas-phase DFT calculations. Energies are given in kJ/mol, bond lengths in Å. The pyrrolic hydrogen atoms are marked in *red*. **b** Calculated activation energies for the gas-phase metalation of 2HP with as a function of the atomic number. Values were taken from Ref. [43]. Adapted with permission from Ref. [43], © (2007) American Chemical Society

reacted with Zn, while the evolution of D_2 was monitored with mass spectrometry. The resulting experimental $\Delta G^{\neq}$ value of 134 kJ/mol was found to agree well with theory [43, 44].

The height of the rate-limiting barrier depends strongly on the type of the metal center. While no barrier was computed for Fe, the activation energy was predicted to increase in the order Fe < Co < Ni < Cu < Zn, as shown in Fig. 7b. According to these barriers, one should expect metalation with Fe, Co, and Ni to occur below room temperature, whereas elevated temperatures should be required for Cu and Zn. This was confirmed by various experimental studies, including Refs. [43, 46, 52, 53, 55].

Experimental observations of the initial (SAT-like) complex provide further evidence for the proposed reaction mechanism as shown in Fig. 7. SAT complexes were first observed at room temperature by XPS for Zn-2HTPP on Ag(111) [43] and Cu-2HTBrPP on Cu(111) [87]. A Cu-2HTPyP SAT complex and its transition to CuTPyP were observed by STM after the deposition of Cu onto a 2HTPyP submonolayer on Au(111) [88].

A separate determination of the activation energy and the pre-exponential factor of porphyrin metalation with substrate atoms was achieved with isothermal rate measurements using STM [78]. 2HTPP and CuTPP were discriminated and quantified by their different mobilities, due to which only 2HTPP molecules appeared as individual moieties in the STM images, whereas the more mobile CuTPP gave rise to blurry areas. This approach yielded an activation energy of 143 ± 12 kJ/mol and a pre-exponential factor of $10^{(15\pm1.6)}$ s^{-1}. At higher coverages, a reduced barrier for the metalation was observed [82]. For comparison, DFT values for the activation energy, computed for the corresponding gas-phase reaction of

2HP with Cu, range from 100 to 155 kJ/mol, depending on the level of theory and the applied basis sets [43, 88]. The measured frequency factor is remarkably high, indicating a large positive activation entropy. This result points toward a dissociation reaction such as the final release of H_2, rather than an intramolecular H transfer, as the rate-limiting step. This could indicate an active participation of the substrate surface in the metalation mechanism, as was also suggested on the basis of metalation experiments with *N*-deuterated tetraphenylporphyrin (2DTPP) on Cu(111) [89]. In addition, the metalation of adsorbed corroles may also be surface-mediated, because the third pyrrolic H atom cannot easily desorb as molecular hydrogen by the mechanism in Fig. 7a, and desorption of atomic H is energetically unfavorable. Therefore, it is likely that at least the third H atom migrates to the substrate surface and recombines there with another H atom before desorption as H_2 [65]. Furthermore, for the metalation of monolayers, substantial influences of the substrate's electronic structure have been observed. Song et al. studied the metalation of a 2HPc monolayer on Pb islands deposited on Si(111) [64]. The Pb islands had different thicknesses ranging from 9 to 19 monolayers. Due to the electron confinement between the semiconductor bandgap and the vacuum barrier, the electronic structure of the Pb film was found to be thickness dependent with an odd–even transition at 17 ML (Fig. 8) [90–96]. After deposition of substoichiometric amounts of Fe onto the 2HPc monolayer, the amounts of FePc on the islands of different heights were determined by STM. The yield of FePc was found to have a one-to-one correspondence to the local density of states at the Fermi level (LDOS(E_F)), as shown in Fig. 8 [64]. Considering these findings of substantial surface influences, one may question the relevance of the (gas-phase) mechanism shown in Fig. 7a [43, 44]. However, it was shown that the metalation reaction also proceeds when metal atoms are deposited onto thick porphyrin multilayers, i.e., in the absence of a surface that could participate in the reaction [55] (cf. Sect. 2.5). This reaction most likely follows the mechanism shown in Fig. 7a.

Coadsorption of other species can also influence the rate of the metalation reaction. This has been shown for metalation of 2HTPP on oxygen-covered Cu(001) [75]. As already briefly mentioned in Sect. 2.2, the reaction rate is dramatically enhanced by the presence of chemisorbed atomic oxygen, such that the reaction proceeds already at 285 K, compared to a minimum of 450 K on the bare Cu(001) surface. This was attributed to the fact that not H_2, but H_2O is formed as the second reaction product besides CuTPP. This reduces the energy of the final state by $\sim$73 kJ/mol and likely also reduces the corresponding activation barrier. This hypothesis is supported by the loss of surface oxygen observed with XPS. As a possible mechanism, the initial incorporation of a Cu–O species into the porphyrin ring was proposed, which then reacts to H_2O and the Cu porphyrin [75].

DFT calculations of the reaction between 2HTPP and Ni(111) were reported by Goldoni et al. [52]. In particular, an initial state configuration where a Ni adatom remains on a Ni(111) surface far from the adsorbed molecule was compared with a final state, in which the Ni atom has reacted with 2HTPP to form NiTPP and H_2. This process was found to be exothermic by 86 kJ/mol. In contrast, when the reacting Ni atom was not an adatom, but was removed from a terrace site creating a

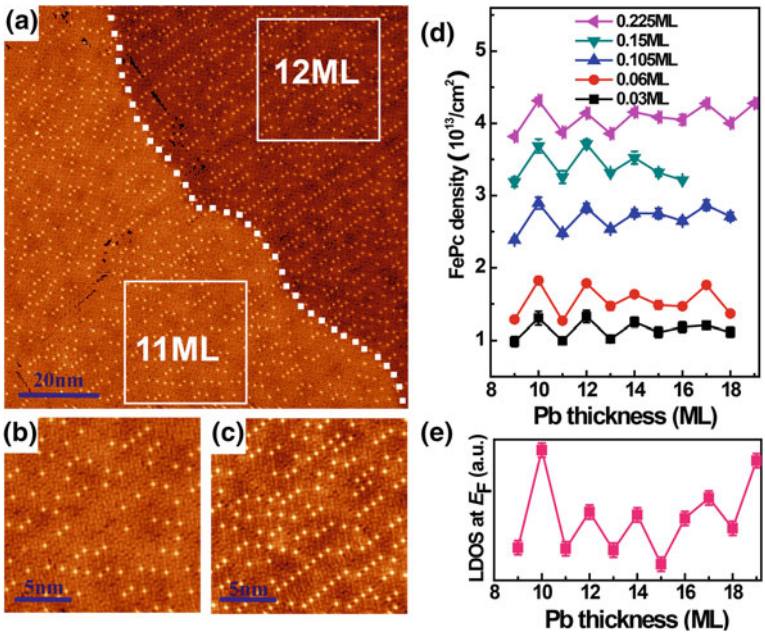

Fig. 8 Metalation of a 2HPc monolayer with Fe on Pb islands of different thickness on Si(111). **a** STM image showing different areal densities of the FePc product on 11 ML and 12 ML Pb films. The *white dotted line* indicates the boundary between the 11 and 12 ML Pb islands. **b** and **c** Magnified STM images from the marked regions in (**a**) depicting the thickness-dependent metalation. **d** Thickness-dependent FePc density at different Fe coverage. Each data point was obtained by averaging over ~1300 molecules. **e** Experimental LDOS(E_F) as a function of Pb film thickness. There is an obvious one-to-one correspondence between the FePc areal density and LDOS (E_F). Adapted with permission from Ref. [64], © (2010) American Chemical Society

vacancy, the process was endothermic by 67 kJ/mol. The importance of adatom availability was also thoroughly discussed by Diller et al. for metalation with substrate atoms on Cu surfaces [74].

2.4 Metalation and Synthesis of Two-Dimensional Networks

The metalation reaction can be accompanied by the formation of two-dimensional networks with covalent, organometallic, or coordination bonds, if the periphery of the ligand molecules possesses suitable functionalities for reaction with metal atoms and neighboring molecules. A prototypical example is the reaction of 2HTPyP with Cu atoms. In the absence of Cu, submonolayers of 2HTPyP on Au(111) were found to form densely packed, ordered islands. Deposition of Cu led to the formation of a two-dimensional metal-organic coordination network (2D-MOCN) with a square unit cell. In this structure, Cu atoms occupied the bridging positions between two

pyridyl groups of neighboring molecules, forming linear N–Cu–N links. Additional Cu atoms coordinated to the centers of the porphyrin molecules. At room temperature, the reaction between Cu and the porphyrin core reached only the stage of the initial SAT complex, which means that only Cu(0) is present in the structure. Heating to 450 K induced completion of the metalation reaction, by which the Cu in the porphyrin centers was oxidized to Cu(II), according to XPS. The bridging Cu atom between the pyridyl groups maintained their position and zero oxidation state. As a result, a mixed-valence network with a regular arrangement of Cu(0) and Cu(II) centers was obtained [88]. Deposition of Fe instead of Cu onto a 2HTPyP submonolayer on Au(111) and annealing resulted in the formation a coordination network, in which each four pyridyl groups of neighboring molecules were connected by a vertically oriented pair of Fe atoms, besides metalation of some of the porphyrin centers [97]. It is also possible to have different metal species in the center and in the bridging position, either by linking adsorbed metalloporphyrins with another metal species or by sequential deposition of metal atoms onto the adsorbed freebase porphyrin. The latter has been demonstrated for 5,10,15,20-tetra [(4-cyanophenyl)phen-4-yl]porphyrin (2HTPCN), which forms a close-packed assembly on Ag(111). Vapor deposition of Gd onto this assembly results in the formation of a metal–organic coordination network with a square unit cell. In this network, each Gd atom links four cyano groups, whereas no Gd is found in the centers of the porphyrin molecules. Subsequent deposition of Co results in the metalation of the porphyrin centers [98].

On more reactive surfaces, the dehydrogenation of the porphyrin is not limited to the pyrrolic N–H bonds, as in the case of the metalation reaction; instead, also C–H bonds at the periphery can be dissociated. This can eventually lead to the formation of metal-organic frameworks with C–M–C bonds and covalent frameworks with C–C bonds. This type of reaction has been observed for 2HTMP of Cu(110) upon annealing to 423–473 K. Besides the metalation of the porphyrin core, the molecules formed oligomers by C–C bond formation between the peripheral mesityl groups [99]. Not only the peripheral substituent, but also the porphyrin core itself can undergo dehydrogenation, as was reported for 2HP and 2HDPP on Cu(110). Annealing submonolayers to temperatures up to 670 K led to metalation of the porphyrin core and to the formation of 2D organometallic networks, in which the dehydrogenation porphyrin cores were linked by C–Cu–C bonds [100, 101].

A related approach is the on-surface synthesis on phthalocyanine derivatives by tetramerization of phthalonitriles, as was first proposed by Abel et al. [102]. Coadsorption of 1,2,4,5-tetracyanobenzene (TCNB) with Fe atoms on Au(111) at room temperature resulted in structures that were attributed to individual Fe(II)-octacyanophthalocyanine ($FePc(CN)_8$) molecules and covalently linked FePc-polymers, depending on the ratio between Fe and TCNB. However, later work suggested that these structures did not represent phthalocyanines, but rather 2D metal-organic coordination networks (2D-MOCNs), in which the intact TCNB molecules coordinated to Fe with their CN groups [103–105]. Koudia and Abel [106] later modified this approach and succeeded in the on-surface synthesis of Mn (II)-octacyanophthalocyanine ($MnPc(CN)_8$) by codeposition of TCNB and Mn

atoms on Ag(111). At room temperature, similar 2D-MOCNs as in the case of the Fe-TCNB system were obtained. Post-annealing at 415 K induced the cyclotetramerization reaction resulting in the formation of $MnPc(CN)_8$. Polymerization of the $MnPc(CN)_8$ molecules by reaction of the peripheral cyano group and formation of a 2D covalent MnPc network was achieved by annealing to 615 K [106]. Similar codeposition experiments with Mn and TCNB on Ag(111) were reported by Piantek et al. [104], who obtained $MnPc(CN)_8$ molecules after annealing to 423 K. The on-surface synthesis of $FePc(CN)_8$ was eventually achieved by annealing coadsorbed Fe and TCNB on Au(111) to 550 K [105].

2.5 *Synthesis of Complexes with Ligand Multilayers and at Bulk Interfaces*

Metal complexes of porphyrins and phthalocyanines can also be obtained by vapor deposition of metal atoms onto multilayers of the organic ligands or by reaction of the multilayers with the underlying metal substrate. A related approach is the codeposition of metal and porphyrin, which also leads to the respective metal complexes.

Multilayer metalation was first reported by Buchner et al., who vapor deposited Fe onto a 2HTPP multilayer on Ag(111) (Fig. 9). The reaction was not complete, i.e., not all deposited Fe atoms reacted, despite an excess of unreacted 2HTPP [55]. Similar experiments were reported by Di Santo et al. for the metalation of thin multilayers ($\sim$4 layers) of 2HTPP on Ag(111). This thin multilayer was almost completely metalated, as was shown by XPS. In addition, the thereby produced FeTPP multilayer was removed by thermal desorption, leaving a FeTPP monolayer on the surface [107]. 2HOEP multilayers ($\sim$4 layers) on Ag(111) were successfully metalated by the same approach [59]. Metalation of 2HTPP multilayers with vapor-deposited Ce atoms and subsequent desorption of excessive 2HTPP was used by Ecija et al. for the on-surface synthesis of $Ce(TPP)_2$ double-decker and $Ce_2(TPP)_3$ triple-decker complexes [67]. The codeposition of Er and 2HTPP was used for the synthesis of clean ErTPP multilayers of up to 60 nm thickness. Composition and electronic structure of the ErTPP film were studied by XPS and UPS [108].

Metalation of multilayers by reaction with a single-crystalline metal substrate has been observed for 2HTPP, 2HP, and 2HPc on Cu(111). Diller et al. reported XPS data which show that a thin 2HTPP multilayer reacts completely with Cu atoms from the substrate, forming CuTPP, upon annealing at 420 K [74]. Similar results were reported for a 2HP bilayer [73].

Reaction of a multilayer with substrate atoms raises the question how the reactants come into contact. There are two principal possibilities: diffusion of the metal into the organic phase or exchange within the organic phase, such that all molecules in the multilayer get into contact with the metal surface. This question

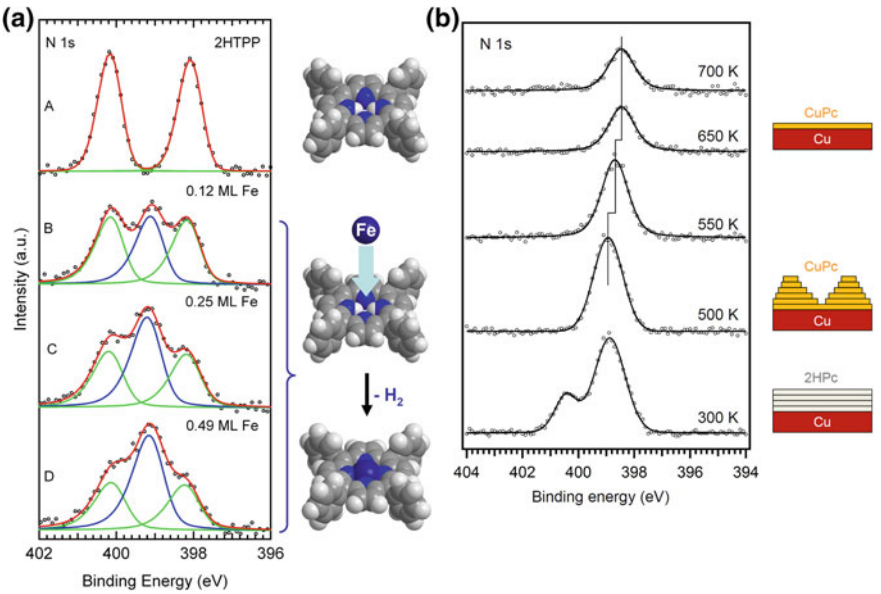

Fig. 9 Multilayer metalation. **a** Vapor deposition of the metal onto the organic layer: N 1*s* XP spectra of the metalation of 2HTPP multilayers (ca. 20 layers) with vapor-deposited Fe atoms at room temperature. (*A*) 2HTPP multilayer. (*B*)–(*D*) After vapor deposition of Fe as indicated. The central peak in the spectra (*B*)–(*D*) represents the newly formed FeTPP, while the two outer peaks stem from residual 2HTPP. **b** Vapor deposition of the organic multilayer onto the metal: N 1*s* XP spectra taken after deposition of 2HPc onto Cu(111) at 300 K with an initial coverage of 4 monolayers and after heating to the indicated temperatures. Adapted with permission from Refs. [55, 81], © (2008) and (2014) American Chemical Society

was addressed by Chen et al., who investigated the metalation of 2HPc multilayers on Cu(111) with XPS (Fig. 9b) and TPD/TPR [81]. TPD/TPR performed after deposition of a 2HPc bilayer on Cu(111) led to desorption of CuPc around 550 K, while XPS showed that a CuPc monolayer remained on the surface. Likewise, it was found that a NiPc monolayer did not desorb at temperatures up to 650 K (instead, decomposition occurs above that temperature, according to XPS). In contrast, when a bilayer of 2HPc was deposited onto 0.8 monolayers of NiPc on Cu (111), NiPc was found to desorb along with CuPc and residual 2HPc. A similar experiment with a NiPc bilayer yielded a similar result. This experiment was explained with an exchange of molecules between the first layer and the higher layers, bringing 2HPc into contact with the Cu surface and NiPc into higher layers, from which it can desorb. Therefore, a possible mechanism for multilayer metalation was shown to be the exchange of molecules between the first layer and the higher layers [81]. However, the findings by Chen et al. could also be explained by an exchange of metal centers between the NiPc and Cu(111) surface, as was shown for another system by Doyle et al. [109].

2.6 Synthesis of Porphyrin Complexes by Metalation at Solid–Liquid Interfaces

Porphyrins adsorbed at solid–liquid interfaces can also undergo metalation. Hai et al. studied this process at an electrochemical interface using the cationic porphyrin 2HTMPyP^{4+} on Cu(100) in a solution containing HCl and 2HTMPyP^{4+} tosylate. Cu^{2+} ions formed during anodic oxidation of the Cu electrode were incorporated into the adsorbed porphyrin molecules, resulting in the formation of Cu(II)TMPyP^{4+}. This was concluded from cyclic voltammetry (CV) in combination with electrochemical STM (EC-STM) and UV–vis measurements. The mechanism of the metalations is apparently based on an ion exchange process: Similar to the homogeneous reaction in solution, but unlike the metalation reaction at the solid–vacuum interface, the two pyrrolic protons are replaced by one Cu(II) ion [110].

Metalation of porphyrins adsorbed at the metal/liquid interface has also been observed by surface-enhanced resonance Raman scattering (SERRS). For 2HTMPyP^{4+} adsorbed on Ag colloids, it was found that 2HTMPyP^{4+} exists only under acidic conditions, while metalation to Ag(II)TMPyP^{4+} occurred in neutral and alkaline environments. On mixed Ag–Cu colloids with up to 5 at.% Cu, all adsorbates were converted to Cu(II)TMPyP^{4+} [111]. The metalation kinetics of 2HTMPyP^{4+} on Ag colloids was investigated by time-dependent SERRS and was found to be highly dependent on the presence of anions in the system [112, 113]. In another study, Zn(II) ions adsorbed on silica gel reacted rapidly with solutions of 2HTPP to ZnTPP [114].

2.7 Synthesis of Complexes with Axial Ligands

The on-surface metalation of porphyrins and phthalocyanines described in the previous sections results in adsorbed complexes with a vacant axial coordination site, to which a ligand can be attached in a subsequent step. Such two-step syntheses have rarely been performed; notable examples are the synthesis of (NH_3)ZnTPP from 2HTPP, Zn, and NH_3 successively adsorbed on a Ag(111) surface [47]. The same approach was used for the synthesis of (NO)FeTPP on the same substrate [61]. In both cases, it would not have been possible to vapor deposit the intact complexes because of their insufficient thermal stability. In other work, small molecules were coordinated to directly deposited metalloporphyrins and metallophthalocyanines, again to produce complexes which would have been thermally too labile for direct vapor deposition. Examples include (CO)MTPP and *cis*-($CO)_2$MTPP with M=Co, Fe [115, 116], (CO)FePc [117, 118], (CO)MnPc [119], (DABCO)ZnTBPP [120], (H)MPc with M=Fe, Mn [121, 122], (NH_3)FePc [117, 123, 124], (NH_3)MnPc [125], (NH_3)NiTPP [126], (NO)CoOEP [127], (NO)CoTPP [60, 61, 115, 125, 128–134], (NO)FeOEP [135], (NO)FePc [117, 118, 124, 136], (NO)FeTPP [61, 115, 125], (NO)MnTPP [125], (pyridine)FePc [117], and (O)TiTPP [54]. In the case of (N)MnPc, thermal activation of N_2 was necessary [137].

The attachment of the axial ligand can influence the bond between the coordinated metal center and the substrate (surface trans effect [61]), and the magnetic properties of the complex (surface spin trans effect [138]). As an illustrative example, the coordination of NO and CO to CoTPP and FeTPP on an Ag(111) surface will be compared in the following. NO formed exclusively the mononitrosyl species (NO)MTPP (M=Fe, Co) and had a large impact on the geometric and electronic structure of the porphyrins. In particular, the M–Ag(111) interaction (M=Fe, Co) was suppressed by the NO ligand, resulting in changes of the electronic structure in the valence region [60, 61]. In contrast, CO was found to form both monocarbonyl and *cis*-dicarbonyl species, while leaving the properties of the metalloporphyrin almost unaffected [115]. The carbonyl species were generated by dosing CO at very low temperatures of 6–20 K. Transfer of the CO molecules between neighboring CoTPP molecules by LT-STM manipulation was demonstrated [115, 116]. In contrast to NO, CO did not suppress the valence states

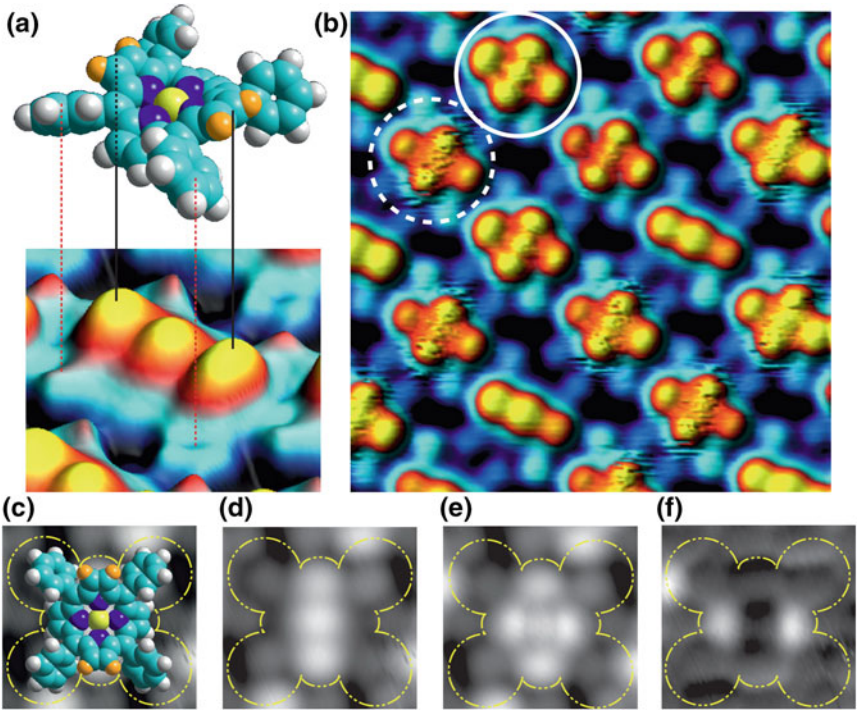

Fig. 10 Synthesis of $(CO)_xCoTPP$ on Ag(111), STM images. **a** Conformational adaptation with saddle-shape distortion of CoTPP adsorbed on Ag(111). **b** CoTPP monolayer array on Ag(111) after exposure to CO, comprising CoTPP, (CO)CoTPP (*dashed circle*), and $(CO)_2CoTPP$ (*solid circle*). **c** Top-view model of CoTPP overlaid on an STM image. **d**, **e** Top-view topography of undecorated CoTPP (**d**) and dicarbonyl (**e**) species. The corresponding difference image (**f**) emphasizes the relatively large distance of ~5.3 Å between the CO-related maxima. Adapted with permission from Ref. [116], © (2011) Nature Publishing Group

induced by the interaction of the Fe and Co centers with the Ag surface, as was shown by STS [115]. STM images of the *cis*-dicarbonyl species $(CO)_2$FeTPP and $(CO)_2$CoTPP revealed a relatively large distance between the two CO molecules, compared to dicarbonyls formed with metal adatoms. This was explained with a bonding geometry in which the CO ligands occupy bridge positions between the metal center and a porphyrin N atom (Fig. 10) [116]. Overall, CO appears to have a weaker influence on the metal centers than NO.

3 On-Surface Synthesis of Organometallic and Covalent Nanostructures

3.1 The Surface Ullmann Reaction

In contrast to the wide range of C–C bond formation reactions available in solution-based organic chemistry, only few reactions suitable for C–C bond formation at solid surfaces have been identified so far. The most prominent example is the Ullmann reaction between bromo- and iodoarenes on metal surfaces. Originally performed in solution with solid Cu metal as a reactant [139] and widely used in organic synthesis [140, 141], this heterogeneous reaction can also be used for C–C bond formation on well-defined metal surfaces in ultra-high vacuum (UHV) [142]. To date, detailed insight into the mechanism of this surface Ullmann reaction has been obtained by a combination with spectroscopic and microscopic techniques [143–147], complemented by theoretical investigations [148, 149].

3.2 Hierarchical Molecular Approach Toward a Hydrocarbon-Based Two-Dimensional Network

The surface Ullmann reaction has been used for the on-surface synthesis of large π-conjugated hydrocarbon macrocycles consisting of phenyl rings, i.e., cyclo-oliphenylenes. This type of model systems will be discussed here in more detail for two reasons: First, the naked parent structures of these macrocycles are only available by on-surface synthesis. Previous solution-based syntheses required the presence of large solubility enhancing alkyl substituents. As an example, Hensel and Schlüter reported a hexagonal cyclotetraicosa-phenylene macrocycle containing 24 phenyl rings and, for enhanced solubility, 12 hexyl side chains [3]. Similar compromises were necessary for the synthesis of other large, shape-persistent macrocycles [1]. In addition, even if it was possible to make the parent structures of these macrocycles in solution, they would be too large for undecomposed vapor deposition in UHV.

Second, the macrocycles made by on-surface synthesis are suitable for the fabrication of porous networks with a combined covalent and van der Waals

linkage. Compared to the conventional all-covalent linkage, this approach has distinct advantages: As illustrated in Fig. 11, the on-surface synthesis of porous graphene-like structures requires careful kinetic control of the reaction conditions, which include the usage of appropriate precursors. In most cases, the reaction still results in structures with very high defect concentrations. This is rather unfortunate, because the reactions need to be performed under conditions at which the C–C bond formation is not reversible (e.g., at moderate temperatures). Otherwise, the thermodynamic equilibrium structure will be formed, which is regular graphene. Considering this fundamental issue, it appears questionable whether the direct synthesis of two-dimensional hydrocarbon nanostructures is possible at all with this approach. Therefore, alternative approaches should be developed.

The problem of defect formation and a possible solution are illustrated in Fig. 12: Molecular precursors that undergo C–C bond formation in two dimensions form covalent networks, which are usually defect-rich (left). The irreversible nature of the C–C bond (under the required experimental conditions) makes these defects permanent. Another hierarchical strategy is shown in the right column of Fig. 12. The precursors used in this approach can only link in one dimension and form large

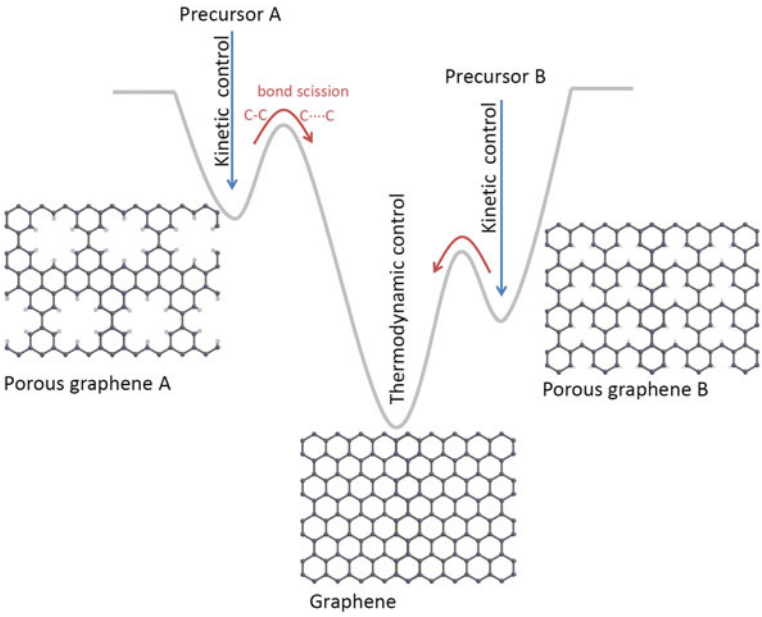

Fig. 11 Kinetic versus thermodynamic control on the example of the on-surface synthesis of (porous) graphene structures. The global minimum of the potential energy surface is usually graphene, which is formed under conditions where the C–C bond formation is reversible. In contrast, the porous graphene derivatives represent only local minima of the potential energy surface. Their synthesis therefore requires kinetic reaction control and suitable precursors. Initially formed defects cannot be healed by annealing, because this would lead to the formation of (unwanted) regular graphene

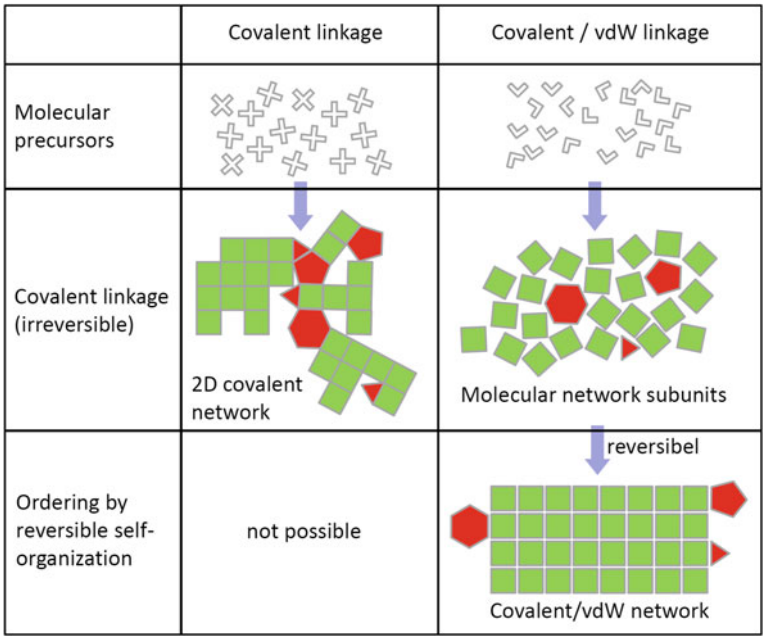

Fig. 12 Network formation exclusively based on covalent linkage results in defect-rich structures which cannot be improved by annealing (*left*). In contrast, the hybrid approach shown in the *right* column starts with the on-surface synthesis of mobile molecular subunits, which are mobile and can form ordered supramolecular structures by reversible self-assembly. "Wrong" structural elements (*red*) are expelled from the lattice

molecular network subunits (with the formation of oligomer or polymer chains as a possible side reaction). If these subunits are still sufficiently mobile on the surface, they can self-assemble to form ordered arrays. Since this process is reversible, defects can heal and unwanted structural elements (shown in red) are able to segregate. If necessary, additional covalent linkage of the now well-ordered subunits can be achieved in an additional reaction step.

3.3 *Formation of Hyperbenzene and Organometallic Intermediates*

An example for the strategy outlined in Sect. 3.2 is the on-surface synthesis of hyperbenzene $C_{108}H_{72}$, a hexagonal hydrocarbon macrocycle consisting of 18 phenyl rings, using the surface Ullmann reaction [4]. The reaction proceeds most likely via an intermediate state with C–Cu–C bonds [145, 150], which are stable at and well above room temperature.

3.3.1 Organometallic Intermediates with C–Cu–C Bonds

Deposition of the bromoarene precursor molecule, 4,4″-dibromo-*m*-terphenyl (DMTP), onto Cu(111) at room temperature resulted in the dissociation of the C–Br bonds (which occurs already below 240 K on this surface [146]) and the subsequent formation of C–Cu–C bonds between neighboring molecular *m*-terphenyl (MTP) fragments [150]. This process led to the formation of organometallic $(MTP\text{-}Cu)_n$ zigzag chains (as shown schematically in Fig. 13a) and cyclic $(MTP\text{-}Cu)_n$ (n = 6, 8, 14, 16, 18, 22) structures [150]. STM images of these chains are shown in Fig. 14. Deposition at elevated temperatures (440 K) yielded large islands consisting of the $(MTP\text{-}Cu)_n$ zigzag chains (Fig. 14d) [150]. The chains have preferential orientations relative to the high-symmetry directions of the Cu(111) substrate (see Fig. 14a). The lattice constant *along* the chains is 26.5 Å, which is larger than the value expected for direct C–C linkage (21.8 Å) and confirms that the MTP fragment is linked by Cu atoms (in line with related work, in which dibromo-*p*-terphenyl was used [145]). The apparent height in STM varies along the chains, and the terphenyl units (located at the bends, large maxima in Fig. 14g) can be distinguished from the C–Cu–C bridges (at the straight parts of the chain, small maxima in Fig. 14g). Residual Br atoms sit between the chains or form

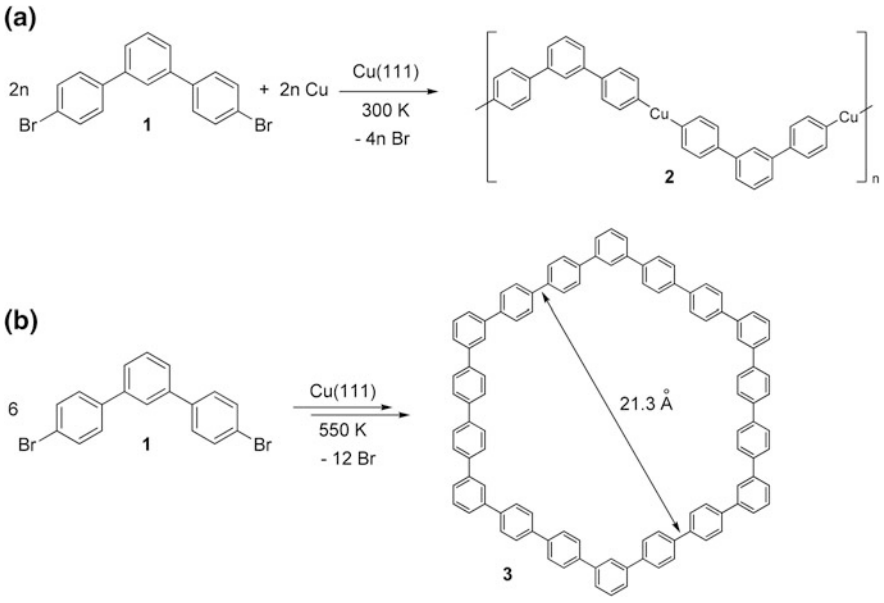

Fig. 13 Surface-assisted Ullmann coupling reaction of 4,4″-dibromo-*m*-terphenyl (DMTP) on Cu (111), resulting in the formation of **a** organometallic polymers at 300 K and **b** hyperbenzene molecules at 550 K. Adapted with permission from Ref. [4], © (2013) John Wiley & Sons

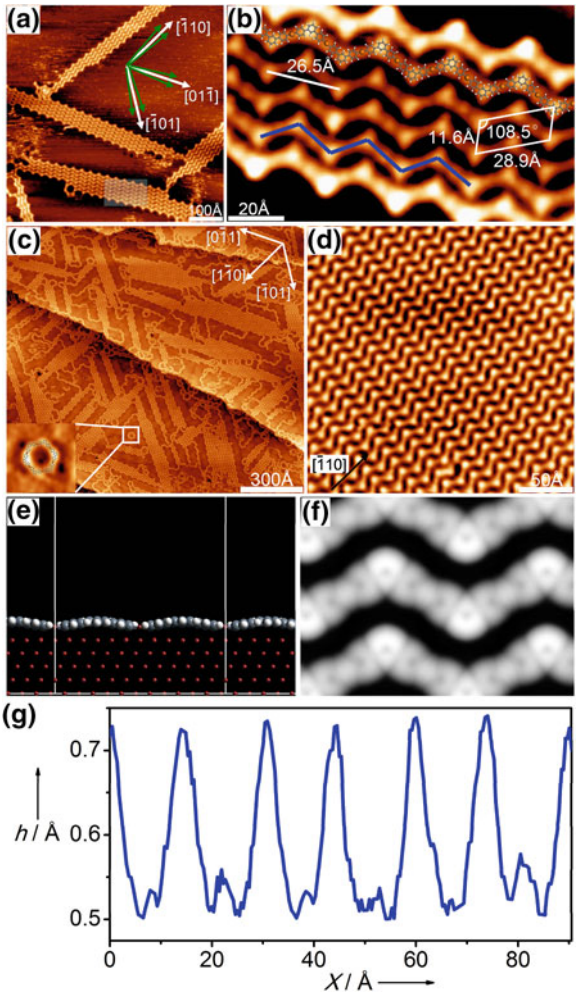

Fig. 14 STM study of the reaction of dibromo-*m*-terphenyl (DMTP) on Cu(111) at 300 K and formation of organometallic oligomers and polymers with C–Cu–C bonds: **a** Constant-current STM image after deposition of DMTP onto Cu(111) at 300 K at low coverage. The islands consist of chains of the organometallic polymer $(MTP\text{-}Cu)_n$, which are oriented at angles of ±5° relative to the [−110] (and equivalent) directions, as marked with *green arrows*. **b** Higher resolution image of the shaded area in (**a**) with overlaid molecular model and unit cell. **c** $(MTP\text{-}Cu)_n$ polymers at higher precursor coverage. *Inset* Magnified view of a cyclic hexamer $(MTP\text{-}Cu)_6$ superimposed with molecular model. **d** After deposition of DMTP onto Cu(111) held at 440 K, which leads to larger $(MTP\text{-}Cu)_n$ islands. **e** *Side view* of a structure from periodic DFT calculations, illustrating the non-planar geometry of the $(MTP\text{-}Cu)_n$ chains. **f** DFT-calculated STM image for the tunneling parameters in (**b**). **g** Apparent height profile along the *blue zigzag line* in (**b**) from *left* to *right*. Adapted with permission from Ref. [4], © (2013) John Wiley & Sons

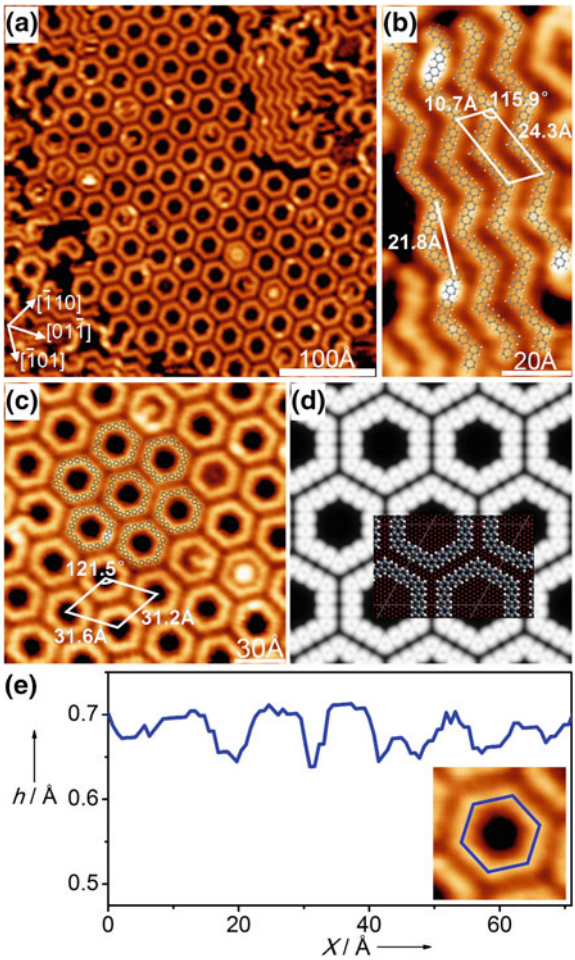

Fig. 15 Hyperbenzene: **a** Overview constant-current STM image obtained at 300 K after deposition of 4,4″-dibromo-*m*-terphenyl (DMTP) onto Cu(111) held at 550 K. The resulting hexagonal rings (hyperbenzene) show a preferential orientation relative to the high-symmetry directions of the substrate. **b** Magnified view of a small section with oligophenylene chains. **c** Magnified view of a hyperbenzene island with several defects and inclusions in the central cavities. Molecular models and a unit cell are overlaid. **d** DFT-calculated STM images with overlaid model of the relaxed computed structure. **e** Apparent height profile along the perimeter of a hyperbenzene molecule, as marked by the blue hexagon in the inset. Note that the height axis is identical to that in Fig. 14g for direct comparison. Adapted with permission from Ref. [4], © (2013) John Wiley & Sons

separate islands with a $(\sqrt{3} \times \sqrt{3})R30°$ structure and a hexagonal unit cell [151]. The C–Cu bond was found to be remarkably stable, requiring temperatures above 440 K for the release of the Cu atom and formation of the C–C bond [4, 147, 150, 151].

3.3.2 On-Surface Synthesis of Hyperbenzene Molecules

Hyperbenzene was synthesized according to the scheme in Fig. 13b by deposition of DMTP onto a hot Cu(111) surface at 550 K [4]. Besides hyperbenzene, which was found to account for ∼70 % of the reaction products, oligophenylene chains (13 %) and other oligophenylene structures (17 %) were observed as side products (Fig. 15) [4]. Synthesis by heating the organometallic precursor phase from 300 K to temperatures above 500 K also induced the formation of C–C bonds, but the yield of well-defined products (and especially hyperbenzene) was considerably lower, most likely because the islands of the organometallic $(MTP\text{-}Cu)_n$ chains (as can be seen in Fig. 14d) are too dense for the formation of hyperbenzene.

In line with the scheme in Fig. 12 (right column), the hyperbenzene molecules self-assemble to form a hexagonal lattice with the unit cell dimensions displayed in Fig. 15c. Products with other structures (such as chain fragments) are not embedded in the hyperbenzene islands, but segregate to the periphery (Fig. 15a).

The distance between the edges of two adjacent hyperbenzene molecules of 9.3 Å is almost identical to the distance between the coordination polymer chains in Fig. 14, indicating that the assembly is mainly driven by van der Waals interactions and that there are no C–C bonds between the rings. The variation of the apparent height along the ring is small compared to the case of the coordination oligomers (compare the height profile in Fig. 15e with Fig. 14g).

4 Summary

In this chapter, it has been shown that structurally complex molecular coordination compounds, organometallic compounds, and conjugated hydrocarbons can be synthesized on metal surfaces from suitable molecular precursors. Some of the reactions proceed with high yields and lead to by-products that desorb under the reaction conditions, while in other cases the synthesis is hamped by formation of multiple products, which remain adsorbed. Two examples have been discussed in more detail.

Adsorbed porphyrins, corroles, and phthalocyanines react with coadsorbed metal atoms such as Ti, V, Cr, Mn, Fe, Co, Ni, Cu, Zn, Ru, and Ce, resulting in the formation of the respective metal complexes. In the course of this reaction, porphyrins and phthalocyanines oxidize metal atoms to their +II ions, while corroles cause oxidation to the +III ions. The metal atoms can be provided by the substrate, vapor deposited before or after the deposition of the molecules, or delivered as carbonyls. The reaction follows a two-step mechanism, which starts with the initial coordination of the neutral metal atom by the intact freebase macrocyle, and includes two hydrogen transfer steps and is completed by with the release of H_2 from the oxidized metal center. The activation barriers vary strongly with the type of the metal center. Participation of the surface in the reaction has been observed in some cases. In the resulting metal complexes, one of the two axial coordination

sites at the metal center points away from the surface and can bind one or more additional ligands, which can affect the electronic and magnetic properties of the metal center. Multilayers can be metalated in the same way by the deposition of metals onto the organic phase.

The surface Ullmann reaction can be employed for the on-surface synthesis of large organic molecules, as has been shown on the example of hyperbenzene, a hexagonal macrocycle consisting of 18 phenyl rings, formed at a Cu(111) surface by covalent linking of six *meta*-terphenyl fragments. The macrocycles undergo self-assembly to form a honeycomb network. Extension to other and larger macrocycles as well as functionalized species appears feasible. Subsequent covalent linking of the honeycomb network could provide a possible way to well-ordered covalent networks with large pores.

References

1. Grave, C., Schlüter, A.D.: Shape-persistent, nano-sized macrocycles. Eur. J. Org. Chem. **18**, 3075–3098 (2002)
2. Hensel, V., Lutzow, K., Jacob, J., Gessler, K., Saenger, W., Schlüter, A.D.: Repetitive construction of macrocyclic oligophenylenes. Angew. Chem.-Int. Edit. **36**, 2654–2656 (1997)
3. Hensel, V., Schlüter, A.D.: A cyclotetraicosaphenylene. Chem.-Eur. J. **5**, 421–429 (1999)
4. Fan, Q.T., Wang, C.C., Han, Y., Zhu, J.F., Hieringer, W., Kuttner, J., Hilt, G., Gottfried, J.M.: Surface-assisted organic synthesis of hyperbenzene nanotroughs. Angew. Chem.-Int. Edit. **52**, 4668–4672 (2013)
5. Barth, J.V.: Molecular architectonic on metal surfaces. Annu. Rev. Phys. Chem. **58**, 375–407 (2007)
6. Barth, J.V.: Fresh perspectives for surface coordination chemistry. Surf. Sci. **603**, 1533–1541 (2009)
7. Lin, N., Stepanow, S., Ruben, M., Barth, J.V.: Surface-confined supramolecular coordination chemistry. In: Broekmann, P., Dotz, K.H., Schalley, C.A. (eds.) Templates in Chemistry III, Topics in Current Chemistry, pp. 1–44 (2009)
8. Stepanow, S., Lin, N., Barth, J.V.: Modular assembly of low-dimensional coordination architectures on metal surfaces. J. Phys.-Condens. Matter **20**, 184002 (2008)
9. Aldridge, W.N., De Matteis, P.: Heme and Hemoproteins. Springer, Berlin (1977)
10. Oohora, K., Hayashi, T.: Hemoprotein-based supramolecular assembling systems. Curr. Op. Chem. Biol. **19**, 154–161 (2014)
11. Milgrom, L.R.: The Colors of Life. Oxford University Press, Oxford (1997)
12. Mochida, I., Suetsugu, K., Fujitsu, H., Takeshita, K.: Enhanced catalytic activity of cobalt tetraphenylporphyrin on titanium dioxide by evacuation at elevated temperatures for intensifying the complex support interaction. J. Phys. Chem. **87**, 1524–1529 (1983)
13. Rezaeifard, A., Jafarpour, M.: The catalytic efficiency of Fe-porphyrins supported on multi-walled carbon nanotubes in the heterogeneous oxidation of hydrocarbons and sulfides in water. Catal. Sci. Technol. **4**, 1960–1969 (2014)
14. Qiao, J.L., Liu, Y.Y., Hong, F., Zhang, J.J.: A review of catalysts for the electroreduction of carbon dioxide to produce low-carbon fuels. Chem. Soc. Rev. **43**, 631–675 (2014)
15. Wang, C., Li, J., Mele, G., Duan, M.Y., Lu, X.F., Palmisano, L., Vasapollo, G., Zhang, F.X.: The photocatalytic activity of novel, substituted porphyrin/TiO_2-based composites. Dyes Pigm. **84**, 183–189 (2010)

16. Takulapalli, B.R., Laws, G.M., Liddell, P.A., Andreasson, J., Erno, Z., Gust, D., Thornton, T.J.: Electrical detection of amine ligation to a metalloporphyrin via a hybrid SOI-MOSFET. J. Am. Chem. Soc. **130**, 2226–2233 (2008)
17. Jiang, S., Cheng, R., Wang, X., Xue, T., Liu, Y., Nel, A., Huang, Y., Duan, X.F.: Real-time electrical detection of nitric oxide in biological systems with sub-nanomolar sensitivity. Nat. Commun. **4**, 2225 (2013)
18. Dedigama, A., Angelo, M., Torrione, P., Kim, T.-H., Wolter, S., Lampert, W., Atewologun, A., Edirisoorya, M., Collins, L., Kuech, T.F., Losurdo, M., Bruno, G., Brown, A.: Hemin-functionalized InAs-based high sensitivity room temperature NO gas sensors. J. Phys. Chem. C **116**, 826–833 (2012)
19. Klauk, H.: Organic Electronics—Materials, Manufacturing and Applications. Wiley-VCH (2006)
20. Tuffy, B.: Porphyrin Materials for Organic Light Emitting Diodes: A Route to Phosphorescent Emission. Lambert Academic Publishing (2011)
21. Imahori, H.: Giant multiporphyrin arrays as artificial light-harvesting antennas. J. Phys. Chem. B **108**, 6130–6143 (2004)
22. Li, L.-L., Diau, E.W.-G.: Porphyrin-sensitized solar cells. Chem. Soc. Rev. **42**, 291–304 (2013)
23. Ackroyd, R., Kelty, C., Brown, N., Reed, M.: The history of photodetection and photodynamic therapy. Photochem. Photobiol. **74**, 656–669 (2001)
24. Nyman, E.S., Hynninen, P.H.: Research advances in the use of tetrapyrrolic photosensitizers for photodynamic therapy. J. Photochem. Photobiol. B Biology **73**, 1–28 (2004)
25. O'Connor, A.E., Gallagher, W.M., Byrne, A.T.: Porphyrin and Nonporphyrin photosensitizers in oncology: preclinical and clinical advances in photodynamic therapy. Photochem. Photobiol. **85**, 1053–1074 (2009)
26. Middelburg, T.A., de Vijlder, H.C., de Bruijn, H.S., van der Ploeg-van den Heuvel, A., Neumann, H.A.M., de Haas, E.R.M., Robinson, D.J.: Topical photodynamic therapy using different porphyrin precursors leads to differences in vascular photosensitization and vascular damage in normal mouse skin. Photochem. Photobiol. **90**, 896–902 (2014)
27. Erk, P., Hengelsberg, H.: Phthalocyanine dyes and pigments. In: Kadish, K.M., Guilard, R., Smith, K.M. (eds.) The Porphyrin Handbook, vol. 19, pp. 105–150. Academic Press (2003)
28. Sorokin, A.B.: Phthalocyanine metal complexes in catalysis. Chem. Rev. **113**, 8152–8191 (2013)
29. Dimitrakopoulos, C.D., Malenfant, P.R.L.: Organic thin film transistors for large area electronics. Adv. Mater. **14**, 99–117 (2002)
30. Blochwitz, J., Pfeiffer, M., Fritz, T., Leo, K.: Low voltage organic light emitting diodes featuring doped phthalocyanine as hole transport material. Appl. Phys. Lett. **73**, 729–731 (1998)
31. Bottari, G., de la Torre, G., Guldi, D.M., Torres, T.: Covalent and noncovalent phthalocyanine-carbon nanostructure systems: synthesis, photoinduced electron transfer, and application to molecular photovoltaics. Chem. Rev. **110**, 6768–6816 (2010)
32. Hains, A.W., Liang, Z.Q., Woodhouse, M.A., Gregg, B.A.: Molecular semiconductors in organic photovoltaic cells. Chem. Rev. **110**, 6689–6735 (2010)
33. Cao, W.R., Xue, J.G.: Recent progress in organic photovoltaics: device architecture and optical design. Energy Environ. Sci. **7**, 2123–2144 (2014)
34. Ayhan, M.M., Durmus, M., Gurek, A.G.: Synthesis, photophysical and photochemical studies of novel liquid crystalline phthalocyanines. J. Porph. Phthalocyanines **13**, 722–738 (2009)
35. Basova, T.V., Parkhomenko, R.G., Igumenov, I.K., Hassan, A., Durmus, M., Gurek, A.G., Ahsen, V.: Composites of liquid crystalline nickel phthalocyanine with gold nanoparticles: liquid crystalline behaviour and optical properties. Dyes Pigm. **111**, 58–63 (2014)
36. Gregory, P.: Industrial applications of phthalocyanines. J. Porph. Phthalocyanines **4**, 432–437 (2000)

37. Ince, M., Yum, J.H., Kim, Y., Mathew, S., Gratzel, M., Torres, T., Nazeeruddin, M.K.: Molecular engineering of phthalocyanine sensitizers for dye-sensitized solar cells. J. Phys. Chem. C **118**, 17166–17170 (2014)
38. Bonnett, R.: Photosensitizers of the porphyrin and phthalocyanine series for photodynamic therapy. Chem. Soc. Rev. **24**, 19–33 (1995)
39. Taquet, J.P., Frochot, C., Manneville, V., Barberi-Heyob, M.: Phthalocyanines covalently bound to biomolecules for a targeted photodynamic therapy. Curr. Med. Chem. **14**, 1673–1687 (2007)
40. Buchler, J.W.: Static coordination chemistry of metalloporphyrins. In: Smith, K.M (ed.) Porphyrins and Metalloporphyrins, pp. 157–232. Elsevier (1975)
41. Gottfried, J.M., Marbach, H.: Surface-confined coordination chemistry with porphyrins and phthalocyanines: aspects of formation, electronic structure, and reactivity. Z. Phys. Chem. **223**, 53–74 (2009)
42. Hambright, P.: Dynamic coordination chemistry of metalloporphyrins. In: Smith, K.M. (ed.) Porphyrins and Metalloporphyrins, pp. 234–278. Elsevier (1975)
43. Shubina, T.E., Marbach, H., Flechtner, K., Kretschmann, A., Jux, N., Buchner, F., Steinrück, H.P., Clark, T., Gottfried, J.M.: Principle and mechanism of direct porphyrin metalation: joint experimental and theoretical investigation. J. Am. Chem. Soc. **129**, 9476–9483 (2007)
44. Shubina, T.E.: Computational studies on properties, formation, and complexation of M(II) porphyrins. In: VanEldik, R., Harvey, J. (ed.) Advances in Inorganic Chemistry: Theoretical and Computational Inorganic Chemistry, vol. 62, pp. 261–299 (2010)
45. Panighel, M., Santo, G.D., Caputo, M., Lal, C., Taleatu, B., Goldoni, A.: Review of 2H-tetraphenylporphyrins metalation in ultra-high vacuum on metal surfaces. J. Phys. Conf. Series **470**, 012012 (2013)
46. Gottfried, J.M., Flechtner, K., Kretschmann, A., Lukasczyk, T., Steinrück, H.P.: Direct synthesis of a metalloporphyrin complex on a surface. J. Am. Chem. Soc. **128**, 5644–5645 (2006)
47. Flechtner, K., Kretschmann, A., Bradshaw, L.R., Walz, M.M., Steinrück, H.P., Gottfried, J.M.: Surface-confined two-step synthesis of the complex (ammine)(*meso*-tetraphenylporphyrinato)-zinc(II) on Ag(111). J. Phys. Chem. C **111**, 5821–5824 (2007)
48. Auwärter, W., Weber-Bargioni, A., Brink, S., Riemann, A., Schiffrin, A., Ruben, M., Barth, J.V.: Controlled metalation of self-assembled porphyrin nanoarrays in two dimensions. ChemPhysChem **8**, 250–254 (2007)
49. Buchner, F., Schwald, V., Comanici, K., Steinrück, H.-P., Marbach, H.: Microscopic evidence of the metalation of a free-base porphyrin monolayer with iron. ChemPhysChem **8**, 241–243 (2007)
50. Eguchi, K., Nakagawa, T., Takagi, Y., Yokoyama, T.: Direct synthesis of vanadium phthalocyanine and its electronic and magnetic states in monolayers and multilayers on Ag (111). J. Phys. Chem. C **119**, 9805–9815 (2015)
51. Schouteden, K., Ivanova, T., Li, Z., Iancu, V., Janssens, E., Van Haesendonck, C.: Probing magnetism in 2D molecular networks after in situ metalation by transition metal atoms. J. Phys. Chem. Lett. **6**, 1048–1052 (2015)
52. Goldoni, A., Pignedoli, C.A., Di Santo, G., Castellarin-Cudia, C., Magnano, E., Bondino, F., Verdini, A., Passerone, D.: Room temperature metalation of 2H-TPP monolayer on iron and nickel surfaces by picking up substrate metal atoms. ACS Nano **6**, 10800–10807 (2012)
53. Chen, M., Feng, X.F., Zhang, L., Ju, H.X., Xu, Q., Zhu, J.F., Gottfried, J.M., Ibrahim, K., Qian, H.J., Wang, J.O.: Direct synthesis of nickel(II) tetraphenylporphyrin and its interaction with a Au(111) surface: a comprehensive study. J. Phys. Chem. C **114**, 9908–9916 (2010)
54. Duncan, D.A., Deimel, P.S., Wiengarten, A., Han, R., Acres, R.G., Auwarter, W., Feulner, P., Papageorgiou, A.C., Allegretti, F., Barth, J.V.: Immobilised molecular catalysts and the role of the supporting metal substrate. Chem. Commun. **51**, 9483–9486 (2015)
55. Buchner, F., Flechtner, K., Bai, Y., Zillner, E., Kellner, I., Steinrück, H.P., Marbach, H., Gottfried, J.M.: Coordination of iron atoms by tetraphenylporphyrin monolayers and

multilayers on Ag(111) and formation of iron-tetraphenylporphyrin. J. Phys. Chem. C **112**, 15458–15465 (2008)
56. Khandelwal, S.C., Roebber, J.L.: Photoelectron spectra of tetraphenylporphine and some metallotetraphenylporphyrins. Chem. Phys. Lett. **34**, 355–359 (1975)
57. Lu, X., Hipps, K.W.: Scanning tunneling microscopy of metal phthalocyanines: d(6) and d(8) cases. J. Phys. Chem. B **101**, 5391–5396 (1997)
58. Buchner, F., Kellner, I., Steinrück, H.-P., Marbach, H.: Modification of the growth of iron on Ag(111) by predeposited organic monolayers. Z. Phys. Chem. **223**, 131–144 (2009)
59. Borghetti, P., Di Santo, G., Castellarin-Cudia, C., Fanetti, M., Sangaletti, L., Magnano, E., Bondino, F., Goldoni, A.: Adsorption geometry, conformation, and electronic structure of 2H-octaethylporphyrin on Ag(111) and Fe metalation in ultra high vacuum. J. Chem. Phys. **138**, 144702 (2013)
60. Flechtner, K., Kretschmann, A., Steinrück, H.P., Gottfried, J.M.: NO-induced reversible switching of the electronic interaction between a porphyrin-coordinated cobalt ion and a silver surface. J. Am. Chem. Soc. **129**, 12110–12111 (2007)
61. Hieringer, W., Flechtner, K., Kretschmann, A., Seufert, K., Auwärter, W., Barth, J.V., Görling, A., Steinrück, H.P., Gottfried, J.M.: The surface trans effect: influence of axial ligands on the surface chemical bonds of adsorbed metalloporphyrins. J. Am. Chem. Soc. **133**, 6206–6222 (2011)
62. Wang, C., Fan, Q., Hu, S., Ju, H., Feng, X., Han, Y., Pan, H., Zhu, J., Gottfried, J.M.: Coordination reaction between tetraphenylporphyrin and nickel on a TiO2(110) surface. Chem. Commun. **50**, 8291–8294 (2014)
63. Bai, Y., Buchner, F., Wendahl, M.T., Kellner, I., Bayer, A., Steinrück, H.-P., Marbach, H., Gottfried, J.M.: Direct metalation of a phthalocyanine monolayer on Ag(111) with coadsorbed iron atoms. J. Phys. Chem. C **112**, 6087–6092 (2008)
64. Song, C.L., Wang, Y.L., Ning, Y.X., Jia, J.F., Chen, X., Sun, B., Zhang, P., Xue, Q.K., Ma, X.C.: Tailoring phthalocyanine metalation reaction by quantum size effect. J. Am. Chem. Soc. **132**, 1456–1457 (2010)
65. Chen, M., Schmid, M., Schweyen, P., Bröring, M., Gottfried, J.M.: Oxidation state tuning in ligand-metal surface reaction: formation of Co(III)-Corrole on Ag(111). submitted
66. Papageorgiou, A.C., Fischer, S., Oh, S.C., Saglam, O., Reichert, J., Wiengarten, A., Seufert, K., Vijayaraghavan, S., Ecija, D., Auwärter, W., Allegretti, F., Acres, R.G., Prince, K.C., Diller, K., Klappenberger, F., Barth, J.V.: Self-terminating protocol for an interfacial complexation reaction in vacuo by metal-organic chemical vapor deposition. ACS Nano **7**, 4520–4526 (2013)
67. Ecija, D., Auwärter, W., Vijayaraghavan, S., Seufert, K., Bischoff, F., Tashiro, K., Barth, J. V.: Assembly and manipulation of rotatable cerium porphyrinato sandwich complexes on a surface. Angew. Chem.-Int. Edit. **50**, 3872–3877 (2011)
68. Weber-Bargioni, A., Reichert, J., Seitsonen, A.P., Auwärter, W., Schiffrin, A., Barth, J.V.: Interaction of cerium atoms with surface-anchored porphyrin molecules. J. Phys. Chem. C **112**, 3453–3455 (2008)
69. Sperl, A., Kröger, J., Berndt, R.: Controlled metalation of a single adsorbed phthalocyanine. Angew. Chem.-Int. Edit. **50**, 5294–5297 (2011)
70. Wang, Y.F., Kröger, J., Berndt, R., Hofer, W.A.: Pushing and pulling a sn ion through an adsorbed phthalocyanine molecule. J. Am. Chem. Soc. **131**, 3639–3643 (2009)
71. Kretschmann, A., Walz, M.-M., Flechtner, K., Steinrück, H.-P., Gottfried, J.M.: Tetraphenylporphyrin picks up zinc atoms from a silver surface. Chem. Commun., 568–570 (2007)
72. Ditze, S., Röckert, M., Buchner, F., Zillner, E., Stark, M., Steinrück, H.P., Marbach, H.: Towards the engineering of molecular nanostructures: local anchoring and functionalization of porphyrins on model-templates. Nanotechnology **24**, 115305 (2013)
73. Diller, K., Klappenberger, F., Allegretti, F., Papageorgiou, A.C., Fischer, S., Wiengarten, A., Joshi, S., Seufert, K., Ecija, D., Auwärter, W., Barth, J.V.: Investigating the

molecule-substrate interaction of prototypic tetrapyrrole compounds: adsorption and self-metalation of porphine on Cu(111). J. Chem. Phys. **138**, 154710 (2013)
74. Diller, K., Klappenberger, F., Marschall, M., Hermann, K., Nefedov, A., Wöll, C., Barth, J. V.: Self-metalation of 2H-tetraphenylporphyrin on Cu(111): an x-ray spectroscopy study. J. Chem. Phys. **136**, 014705 (2012)
75. Nowakowski, J., Wäckerlin, C., Girovsky, J., Siewert, D., Jung, T.A., Ballav, N.: Porphyrin metalation providing an example of a redox reaction facilitated by a surface reconstruction. Chem. Commun. **49**, 2347–2349 (2013)
76. Gonzalez-Moreno, R., Sanchez-Sanchez, C., Trelka, M., Otero, R., Cossaro, A., Verdini, A., Floreano, L., Ruiz-Bermejo, M., Garcia-Lekue, A., Martin-Gago, J.A., Rogero, C.: Following the metalation process of protoporphyrin IX with metal substrate atoms at room temperature. J. Phys. Chem. C **115**, 6849–6854 (2011)
77. Xiao, J., Ditze, S., Chen, M., Buchner, F., Stark, M., Drost, M., Steinrück, H.-P., Gottfried, J. M., Marbach, H.: Temperature-dependent chemical and structural transformations from 2H-tetraphenylporphyrin to Copper(II)-tetraphenylporphyrin on Cu(111). J. Phys. Chem. C **116**, 12275–12282 (2012)
78. Ditze, S., Stark, M., Drost, M., Buchner, F., Steinrück, H.-P., Marbach, H.: Activation energy for the self-metalation reaction of 2H-tetraphenylporphyrin on Cu(111). Angew. Chem.-Int. Edit. **51**, 10898–10901 (2012)
79. Bürker, C., Franco-Cañellas, A., Broch, K., Lee, T.L., Gerlach, A., Schreiber, F.: Self-metalation of 2H-tetraphenylporphyrin on Cu(111) studied with XSW: influence of the central metal atom on the adsorption distance. J. Phys. Chem. C **118**, 13659–13666 (2014)
80. Stark, M., Ditze, S., Lepper, M., Zhang, L., Schlott, H., Buchner, F., Röckert, M., Chen, M., Lytken, O., Steinrück, H.P., Marbach, H.: Massive conformational changes during thermally induced self-metalation of 2H-tetrakis-(3,5-di-tert-butyl)-phenylporphyrin on Cu(111). Chem. Commun. **50**, 10225–10228 (2014)
81. Chen, M., Röckert, M., Xiao, J., Drescher, H.-J., Steinrück, H.-P., Lytken, O., Gottfried, J. M.: Coordination reactions and layer exchange processes at a buried metal-organic interface. J. Phys. Chem. C **118**, 8501–8507 (2014)
82. Röckert, M., Ditze, S., Stark, M., Xiao, J., Steinrück, H.P., Marbach, H., Lytken, O.: Abrupt coverage-induced enhancement of the self-metalation of tetraphenylporphyrin with Cu(111). J. Phys. Chem. C **118**, 1661–1667 (2014)
83. Röckert, M., Franke, M., Tariq, Q., Ditze, S., Stark, M., Uffinger, P., Wechsler, D., Singh, U., Xiao, J., Marbach, H., Steinrück, H.P., Lytken, O.: Coverage- and temperature-dependent metalation and dehydrogenation of tetraphenylporphyrin on Cu(111). Chem.-Eur. J. **20**, 8948–8953 (2014)
84. Fleischer, E.B., Wang, J.H.: The detection of a type of reaction intermediate in the combination of metal ions with porphyrins. J. Am. Chem. Soc. **82**, 3498–3502 (1960)
85. De Luca, G., Romeo, A., Scolaro, L.M., Ricciardi, G., Rosa, A.: Sitting-atop metallo-porphyrin complexes: experimental and theoretical investigations on such elusive species. Inorg. Chem. **48**, 8493–8507 (2009)
86. Braun, J., Schlabach, M., Wehrle, B., Kocher, M., Vogel, E., Limbach, H.H.: NMR-study of the tautomerism of porphyrin including the kinetic HH/HD/DD isotope effect in the liquid and the solid state. J. Am. Chem. Soc. **116**, 6593–6604 (1994)
87. Doyle, C.M., Krasnikov, S.A., Sergeeva, N.N., Preobrajenski, A.B., Vinogradov, N.A., Sergeeva, Y.N., Senge, M.O., Cafolla, A.A.: Evidence for the formation of an intermediate complex in the direct metalation of tetra(4-bromophenyl)-porphyrin on the Cu(111) surface. Chem. Commun. **47**, 12134–12136 (2011)
88. Li, Y., Xiao, J., Shubina, T.E., Chen, M., Shi, Z., Schmid, M., Steinrück, H.-P., Gottfried, J. M., Lin, N.: Coordination and metalation bifunctionality of Cu with 5,10,15,20-tetra (4-pyridyl)porphyrin: toward a mixed-valence two-dimensional coordination network. J. Am. Chem. Soc. **134**, 6401–6408 (2012)

89. Röckert, M., Franke, M., Tariq, Q., Lungerich, D., Jux, N., Stark, M., Kaftan, A., Ditze, S., Marbach, H., Laurin, M., Libuda, J., Steinrück, H.-P., Lytken, O.: Insights in reaction mechanistics: isotopic exchange during the metalation of deuterated tetraphenyl-21, 23D-porphyrin on Cu(111). J. Phys. Chem. C **118**, 26729–26736 (2014)
90. Aballe, L., Barinov, A., Locatelli, A., Heun, S., Kiskinova, M.: Tuning surface reactivity via electron quantum confinement. Phys. Rev. Lett. **93**, 196103 (2004)
91. Chiang, T.C.: Photoemission studies of quantum well states in thin films. Surf. Sci. Rep. **39**, 181–235 (2000)
92. Czoschke, P., Hong, H., Basile, L., Chiang, T.C.: Quantum size effects in the surface energy of Pb/Si(111) film nanostructures studied by surface x-ray diffraction and model calculations. Phys. Rev. B **72**, 075402 (2005)
93. Czoschke, P., Hong, H.W., Basile, L., Chiang, T.C.: Quantum beating patterns observed in the energetics of Pb film nanostructures. Phys. Rev. Lett. **93**, 036103 (2004)
94. Danese, A.G., Curti, F.G., Bartynski, R.A.: Quantum size effect induced modification of the chemisorption properties of thin metal films. Phys. Rev. B **70**, 165420 (2004)
95. Ma, X., Jiang, P., Qi, Y., Jia, J., Yang, Y., Duan, W., Li, W.-X., Bao, X., Zhang, S.B., Xue, Q.-K.: Experimental observation of quantum oscillation of surface chemical reactivities. Proc. Natl. Acad. Sci. U.S.A. **104**, 9204–9208 (2007)
96. Zhang, Y.F., Jia, J.F., Han, T.Z., Tang, Z., Shen, Q.T., Guo, Y., Qiu, Z.Q., Xue, Q.K.: Band structure and oscillatory electron–phonon coupling of Pb thin films determined by atomic-layer-resolved quantum-well states. Phys. Rev. Lett. **95**, 096802 (2005)
97. Lin, T., Kuang, G., Wang, W., Lin, N.: Two-Dimensional lattice of out-of-plane dinuclear iron centers exhibiting kondo resonance. ACS Nano **8**, 8310–8316 (2014)
98. Urgel, J.I., Ecija, D., Auwärter, W., Stassen, D., Bonifazi, D., Barth, J.V.: Orthogonal insertion of lanthanide and transition-metal atoms in metal-organic networks on surfaces. Angew. Chem.-Int. Edit. **54**, 6163–6167 (2015)
99. In't Veld, M., Iavicoli, P., Haq, S., Amabilino, D. B., Raval, R.: Unique intermolecular reaction of simple porphyrins at a metal surface gives covalent nanostructures. Chem. Commun., 1536–1538 (2008)
100. Haq, S., Hanke, F., Dyer, M.S., Persson, M., Iavicoli, P., Amabilino, D.B., Raval, R.: Clean coupling of unfunctionalized porphyrins at surfaces to give highly oriented organometallic oligomers. J. Am. Chem. Soc. **133**, 12031–12039 (2011)
101. Hanke, F., Haq, S., Raval, R., Persson, M.: Heat-to-connect: surface commensurability directs organometallic one-dimensional self-assembly. ACS Nano **5**, 9093–9103 (2011)
102. Abel, M., Clair, S., Ourdjini, O., Mossoyan, M., Porte, L.: Single layer of polymeric Fe-phthalocyanine: an organometallic sheet on metal and thin insulating film. J. Am. Chem. Soc. **133**, 1203–1205 (2011)
103. Kezilebieke, S., Amokrane, A., Boero, M., Clair, S., Abel, M., Bucher, J.-P.: Steric and electronic selectivity in the synthesis of Fe-1,2,4,5-tetracyanobenzene (TCNB) complexes on Au(111): from topological confinement to bond formation. Nano Res. **7**, 888–897 (2014)
104. Piantek, M., Serrate, D., Moro-Lagares, M., Algarabel, P., Pascual, J.I., Ibarra, M.R.: Manganese phthalocyanine derivatives synthesized by on-surface cyclotetramerization. J. Phys. Chem. C **118**, 17895–17899 (2014)
105. Kezilebieke, S., Amokrane, A., Abel, M., Bucher, J.-P.: Hierarchy of chemical bonding in the synthesis of Fe-phthalocyanine on metal surfaces: a local spectroscopy approach. J. Phys. Chem. Lett. **5**, 3175–3182 (2014)
106. Koudia, M., Abel, M.: Step-by-step on-surface synthesis: from manganese phthalocyanines to their polymeric form. Chem. Commun. **50**, 8565–8567 (2014)
107. Di Santo, G., Castellarin-Cudia, C., Fanetti, M., Taleatu, B., Borghetti, P., Sangaletti, L., Floreano, L., Magnano, E., Bondino, F., Goldoni, A.: Conformational adaptation and electronic structure of 2H-tetraphenylporphyrin on Ag(111) during Fe metalation. J. Phys. Chem. C **115**, 4155–4162 (2011)

108. Nardi, M., Verucchi, R., Tubino, R., Iannotta, S.: Activation and control of organolanthanide synthesis by supersonic molecular beams: erbium-porphyrin test case. Phys. Rev. B **79**, 125404 (2009)
109. Doyle, C.M., Cunniffe, J.P., Krasnikov, S.A., Preobrajenski, A.B., Li, Z.S., Sergeeva, N.N., Senge, M.O., Cafolla, A.A.: Ni–Cu ion exchange observed for Ni(II)-porphyrins on Cu(111). Chem. Commun. **50**, 3447–3449 (2014)
110. Hai, N.T.M., Furukawa, S., Vosch, T., De Feyter, S., Broekmann, P., Wandelt, K.: Electrochemical reactions at a porphyrin-copper interface. Phys. Chem. Chem. Phys. **11**, 5422–5430 (2009)
111. Itoh, K., Sugii, T., Kim, M.: Surface-enhanced resonance Raman-scattering study on tetrakis (4-N-methylpyridinium)porphine adsorbed on mixed silver and copper colloids. J. Phys. Chem. **92**, 1568–1571 (1988)
112. Prochazka, M., Hanzlikova, J., Stepanek, J., Baumruk, V.: Metalation of positively charged water soluble mesoporphyrins studied via time-resolved SERRS spectroscopy. J. Mol. Struct. **410**, 77–79 (1997)
113. Hanzlikova, J., Prochazka, M., Stepanek, J., Bok, J., Baumruk, V., Anzenbacher, P.: Metalation of 5,10,15,20-tetrakis(1-methyl-4-pyridyl)porphyrin in silver colloids studied via time dependence of surface-enhanced resonance Raman spectra. J. Raman Spectr. **29**, 575–584 (1998)
114. Tsukahara, S., Suzuki, N.: Characteristics of complexation reaction of tetraphenylporphine with zinc(II) at solid–liquid interface. Inorg. Chim. Acta **245**, 105–108 (1996)
115. Seufert, K., Auwärter, W., Barth, J.V.: Discriminative response of surface-confined metalloporphyrin molecules to carbon and nitrogen monoxide. J. Am. Chem. Soc. **132**, 18141–18146 (2010)
116. Seufert, K., Bocquet, M.L., Auwärter, W., Weber-Bargioni, A., Reichert, J., Lorente, N., Barth, J.V.: Cis-dicarbonyl binding at cobalt and iron porphyrins with saddle-shape conformation. Nat. Chem. **3**, 114–119 (2011)
117. Isvoranu, C., Wang, B., Schulte, K., Ataman, E., Knudsen, J., Andersen, J.N., Bocquet, M. L., Schnadt, J.: Tuning the spin state of iron phthalocyanine by ligand adsorption. J. Phys.-Condens. Matter **22**, 472001 (2010)
118. Isvoranu, C., Wang, B., Ataman, E., Knudsen, J., Schulte, K., Andersen, J.N., Bocquet, M. L., Schnadt, J.: Comparison of the carbonyl and nitrosyl complexes formed by adsorption of CO and NO on mono layers of iron phthalocyanine on Au(111). J. Phys. Chem. C **115**, 24718–24727 (2011)
119. Strozecka, A., Soriano, M., Pascual, J.I., Palacios, J.J.: Reversible change of the spin state in a manganese phthalocyanine by coordination of CO molecule. Phys. Rev. Lett. **109**, 147202 (2012)
120. Williams, F.J., Vaughan, O.P.H., Knox, K.J., Bampos, N., Lambert, R.M.: First observation of capping/uncapping by a ligand of a Zn porphyrin adsorbed on Ag(100). Chem. Commun., 1688–1689 (2004)
121. Liu, L.W., Yang, K., Xiao, W.D., Jiang, Y.H., Song, B.Q., Du, S.X., Gao, H.J.: Selective adsorption of metal-phthalocyanine on Au(111) surface with hydrogen atoms. Appl. Phys. Lett. **103**, 023110 (2013)
122. Liu, L.W., Yang, K., Jiang, Y.H., Song, B.Q., Xiao, W.D., Li, L.F., Zhou, H.T., Wang, Y.L., Du, S.X., Ouyang, M., Hofer, W.A., Neto, A.H.C., Gao, H.J.: Reversible single spin control of individual magnetic molecule by hydrogen atom adsorption. Sci. Rep. **3**, 1210 (2013)
123. Isvoranu, C., Wang, B., Ataman, E., Schulte, K., Knudsen, J., Andersen, J.N., Bocquet, M. L., Schnadt, J.: Ammonia adsorption on iron phthalocyanine on Au(111): influence on adsorbate-substrate coupling and molecular spin. J. Chem. Phys. **134**, 114710 (2011)
124. Tran, N.L., Kummel, A.C.: A density functional theory study on the binding of NO onto FePc films. J. Chem. Phys. **127**, 214701 (2007)
125. Wäckerlin, C., Tarafder, K., Siewert, D., Girovsky, J., Hahlen, T., Iacovita, C., Kleibert, A., Nolting, F., Jung, T.A., Oppeneer, P.M., Ballav, N.: On-surface coordination chemistry of

planar molecular spin systems: novel magnetochemical effects induced by axial ligands. Chem. Sci. **3**, 3154–3160 (2012)
126. Wäckerlin, C., Tarafder, K., Girovsky, J., Nowakowski, J., Hahlen, T., Shchyrba, A., Siewert, D., Kleibert, A., Nolting, F., Oppeneer, P.M., Jung, T.A., Ballav, N.: Ammonia coordination introducing a magnetic moment in an on-surface low-spin porphyrin. Angew. Chem.-Int. Edit. **52**, 4568–4571 (2013)
127. Hermanns, C.F., Bernien, M., Kruger, A., Miguel, J., Kuch, W.: Switching the electronic properties of Co-octaethylporphyrin molecules on oxygen-covered Ni films by NO adsorption. J. Phys.-Condens. Matter **24**, 394008 (2012)
128. Buchner, F., Seufert, K., Auwärter, W., Heim, D., Barth, J.V., Flechtner, K., Gottfried, J.M., Steinrück, H.P., Marbach, H.: NO-induced reorganization of porphyrin arrays. ACS Nano **3**, 1789–1794 (2009)
129. Burema, S.R., Seufert, K., Auwärter, W., Barth, J.V., Bocquet, M.L.: Probing nitrosyl ligation of surface-confined metalloporphyrins by inelastic electron tunneling spectroscopy. ACS Nano **7**, 5273–5281 (2013)
130. Kim, H., Chang, Y.H., Lee, S.H., Lim, S., Noh, S.K., Kim, Y.H., Kahng, S.J.: Visualizing tilted binding and precession of diatomic NO adsorbed to Co-porphyrin on Au(111) using scanning tunneling microscopy. Chem. Sci. **5**, 2224–2229 (2014)
131. Wäckerlin, C., Chylarecka, D., Kleibert, A., Müller, K., Iacovita, C., Nolting, F., Jung, T.A., Ballav, N.: Controlling spins in adsorbed molecules by a chemical switch. Nat. Commun. **1**, 61 (2010)
132. Wäckerlin, C., Siewert, D., Jung, T.A., Ballav, N.: On-surface coordination chemistry: direct imaging of the conformational freedom of an axial ligand at room temperature. Phys. Chem. Chem. Phys. **15**, 16510–16514 (2013)
133. Kim, H., Chang, Y.H., Lee, S.H., Kim, Y.H., Kahng, S.J.: Switching and sensing spin states of Co-porphyrin in bimolecular reactions on Au(111) using scanning tunneling microscopy. ACS Nano **7**, 9312–9317 (2013)
134. Domke, K.F., Pettinger, B.: In situ discrimination between axially complexed and ligand-free Co porphyrin on Au(111) with tip-enhanced Raman spectroscopy. ChemPhysChem **10**, 1794–1798 (2009)
135. Miguel, J., Hermanns, C.F., Bernien, M., Kruger, A., Kuch, W.: Reversible manipulation of the magnetic coupling of single molecular spins in Fe-porphyrins to a ferromagnetic substrate. J. Phys. Chem. Lett. **2**, 1455–1459 (2011)
136. Bishop, S.R., Tran, N.L., Poon, G.C., Kummel, A.C.: Dynamics of analyte binding onto a metallophthalocyanine: NO/FePc. J. Chem. Phys. **127**, 214702 (2007)
137. Zhang, J.L., Wang, Z., Zhong, J.Q., Yuan, K.D., Shen, Q., Xu, L.L., Niu, T.C., Gu, C.D., Wright, C.A., Tadich, A., Qi, D., Li, H.X., Wu, K., Xu, G.Q., Li, Z., Chen, W.: Single-molecule imaging of activated nitrogen adsorption on individual manganese phthalocyanine. Nano Lett. **15**, 3181–3188 (2015)
138. Ballav, N., Wäckerlin, C., Siewert, D., Oppeneer, P.M., Jung, T.A.: Emergence of on-surface magnetochemistry. J. Phys. Chem. Lett. **4**, 2303–2311 (2013)
139. Ullmann, F., Meyer, G.M., Loewenthal, O., Gilli, E.: Ueber symmetrische biphenylderivate. Justus Liebigs Ann. Chem. **332**, 38–81 (1904)
140. Fanta, P.E.: Ullmann synthesis of biaryls 1945–1963. Chem. Rev. **64**, 613–632 (1964)
141. Fanta, P.E.: Ullmann synthesis of biaryls. Synthesis, 9–21 (1974)
142. Xi, M., Bent, B.E.: Mechanisms of the Ullmann coupling reaction in adsorbed monolayers. J. Am. Chem. Soc. **115**, 7426–7433 (1993)
143. Blake, M.M., Nanayakkara, S.U., Claridge, S.A., Fernandez-Torres, L.C., Sykes, E.C.H., Weiss, P.S.: Identifying reactive intermediates in the Ullmann coupling reaction by scanning tunneling microscopy and spectroscopy. J. Phys. Chem. A **113**, 13167–13172 (2009)
144. Lewis, E.A., Murphy, C.J., Liriano, M.L., Sykes, E.C.H.: Atomic-scale insight into the formation, mobility and reaction of Ullmann coupling intermediates. Chem. Commun. **50**, 1006–1008 (2014)

145. Wang, W.H., Shi, X.Q., Wang, S.Y., Van Hove, M.A., Lin, N.: Single-molecule resolution of an organometallic intermediate in a surface-supported Ullmann coupling reaction. J. Am. Chem. Soc. **133**, 13264–13267 (2011)
146. Chen, M., Xiao, J., Steinrück, H.-P., Wang, S., Wang, W., Lin, N., Hieringer, W., Gottfried, J.M.: Combined photoemission and scanning tunneling microscopy study of the surface-assisted Ullmann coupling reaction. J. Phys. Chem. C **118**, 6820–6830 (2014)
147. Di Giovannantonio, M., El Garah, M., Lipton-Duffin, J., Meunier, V., Cardenas, L., Fagot Revurat, Y., Cossaro, A., Verdini, A., Perepichka, D.F., Rosei, F., Contini, G.: Insight into organometallic intermediate and its evolution to covalent bonding in surface-confined Ullmann polymerization. ACS Nano **7**, 8190–8198 (2013)
148. Nguyen, M.T., Pignedoli, C.A., Passerone, D.: An ab initio insight into the Cu(111)-mediated Ullmann reaction. Phys. Chem. Chem. Phys. **13**, 154–160 (2011)
149. Björk, J., Hanke, F., Stafström, S.: Mechanisms of Halogen-based covalent self-assembly on metal surfaces. J. Am. Chem. Soc. **135**, 5768–5775 (2013)
150. Fan, Q., Wang, C., Han, Y., Zhu, J., Kuttner, J., Hilt, G., Gottfried, J.M.: Surface-assisted formation, assembly, and dynamics of planar organometallic macrocycles and zigzag shaped polymer chains with C–Cu–C bonds. ACS Nano **8**, 709–718 (2014)
151. Fan, Q., Wang, C., Liu, L., Han, Y., Zhao, J., Zhu, J., Kuttner, J., Hilt, G., Gottfried, J.M.: Covalent, organometallic, and halogen-bonded nanomeshes from tetrabromo-terphenyl by surface-assisted synthesis on Cu(111). J. Phys. Chem. C **118**, 13018–13025 (2014)

On-Surface Synthesis of Single Conjugated Polymer Chains for Single-Molecule Devices

Yuji Okawa, Swapan K. Mandal, Marina Makarova, Elisseos Verveniotis and Masakazu Aono

Abstract Although single-molecule electronic devices have been of great interest for several decades, the fabrication of practical circuits remains challenging due to the lack of reliable ways to wire individual molecules. On-surface synthesis of single conductive polymer chains will be a key technology to solve this problem. We already found that stimulating a molecular layer of diacetylene compound by the tip of scanning tunneling microscope (STM) could initiate chain polymerization. As a result, we could systematically fabricate a single conjugated polydiacetylene chain at designated positions. Subsequently, we developed a novel method ('chemical soldering') for connecting the conjugated polymer chains to single organic molecules. The connection of two polydiacetylene chains to a single phthalocyanine molecule was demonstrated. Nanoscale characteristics of the connection were also experimentally and theoretically investigated. Here, we briefly review tip-induced chain polymerization and the chemical soldering methods. This work will help to advance single-molecule electronics.

1 Introduction

To go beyond silicon-based complementary metal-oxide semiconductor (CMOS) technology, recent research focused on single-molecule nanoelectronic devices. In these single-molecule devices, the individual molecules function as electronic components such as rectifiers, transistors, switches, or memories. Since the first

Y. Okawa (✉) · S.K. Mandal · M. Makarova · E. Verveniotis · M. Aono
International Center for Materials Nanoarchitectonics (WPI-MANA),
National Institute for Materials Science (NIMS), Tsukuba, Ibaraki 305-0044, Japan
e-mail: OKAWA.Yuji@nims.go.jp

S.K. Mandal
Department of Physics, Visva-Bharati University, Santiniketan 731 235, India

M. Makarova
Institute of Physics, Prague 18200, Czech Republic

A. Gourdon (ed.), *On-Surface Synthesis*, Advances in Atom and Single Molecule Machines, DOI 10.1007/978-3-319-26600-8_8

proposal of a single-molecular rectifier 40 years ago [1], many experimental and theoretical studies have been performed to realize single-molecule devices [2–15]. Despite such efforts, the fabrication of a usable single-molecule integrated circuit has yet to be demonstrated. This is partly due to the absence of reliable ways to wire or connect each functional molecule. Such wiring is also a very good way to understand the electronic properties of the component molecules. Most previous efforts focused on directly connecting metal electrodes to single molecules. However, it is difficult to reduce the width of metal wires to the size of single molecules. The best way to do so is to use single conductive polymer chains, which are probably the thinnest wires among all materials.

Single conductive polymer chains will thus be a key component in single-molecule electronics. On-surface chain polymerization of diacetylene moieties was already demonstrated with the tip of a scanning tunneling microscope (STM) on a molecular layer of diacetylene compound [16, 17]. As a result, we could fabricate a single conjugated polydiacetylene chain at designated positions. We then developed a novel method, 'chemical soldering,' for connecting the single polydiacetylene chains to individual organic molecules [18, 19]. In this chapter, we briefly review these methods of fabricating and connecting single conductive polymer chains on a surface.

2 Nanoscale Control of Chain Polymerization

Chain polymerization was performed with diacetylene compounds as monomer molecules, which have the general formula R–C≡C–C≡C–R′, where C≡C–C≡C is the diacetylene moiety and R and R′ are various substituent groups. It is well known that diacetylene compounds in the form of solid crystals [20] and Langmuir-Blodgett films [21] polymerize into polydiacetylene chains when exposed to heat or ultraviolet light (Fig. 1). Since the polydiacetylene chain has a π-conjugated backbone, it can be an electrical conductor when charge carriers are injected. We mostly experimented with 10,12-nonacosadiynoic acid ($CH_3(CH_2)_{15}$–C≡C–C≡C–$(CH_2)_8$COOH) or 10,12-pentacosadiynoic acid ($CH_3(CH_2)_{11}$–C≡C–C≡C–$(CH_2)_8$COOH).

Molecular layers of diacetylene compounds were prepared by transferring a thin film of the molecules from the surface of purified water to a substrate by nearly horizontal dipping. It is also possible to prepare such layers by direct droplet casting and by thermal evaporation. Once the molecular layers have been prepared on a flat

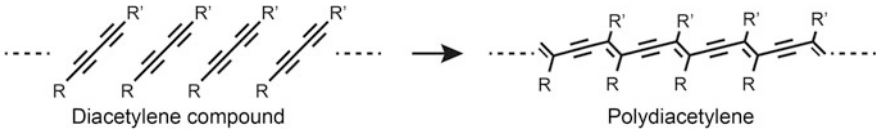

Fig. 1 Polymerization of diacetylene compound, which results in a conjugated polydiacetylene chain

substrate, STM and atomic force microscopy (AFM) experiments can be performed at room temperature both in air and in ultra-high vacuum.

Typical STM images of molecular layers of 10,12-nonacosadiynoic acid and 10,12-pentacosadiynoic acid on highly oriented pyrolytic graphite (HOPG) are shown in Figs. 2a and 3a, respectively. In both cases, parallel bright lines are clearly observed, which indicates that the molecules are self-ordered on the substrate. Figure 2b, c shows magnified STM images of 10,12-nonacosadiynoic acid layers on HOPG and molybdenum disulfide (MoS_2) substrates, respectively. In this case, we can resolve individual molecules. From these high-resolution images, we proposed the model of molecular ordering, as shown in the superimposed models in the figure. In this model, the molecules form flat-lying and closely packed straight rows. The rows are arranged so that COOH end groups in one row are opposite to those of a neighboring row [17, 22].

Though all domains have the same structure on HOPG, we found that the arrangement of molecules varies for different domains on MoS_2. On the former, the

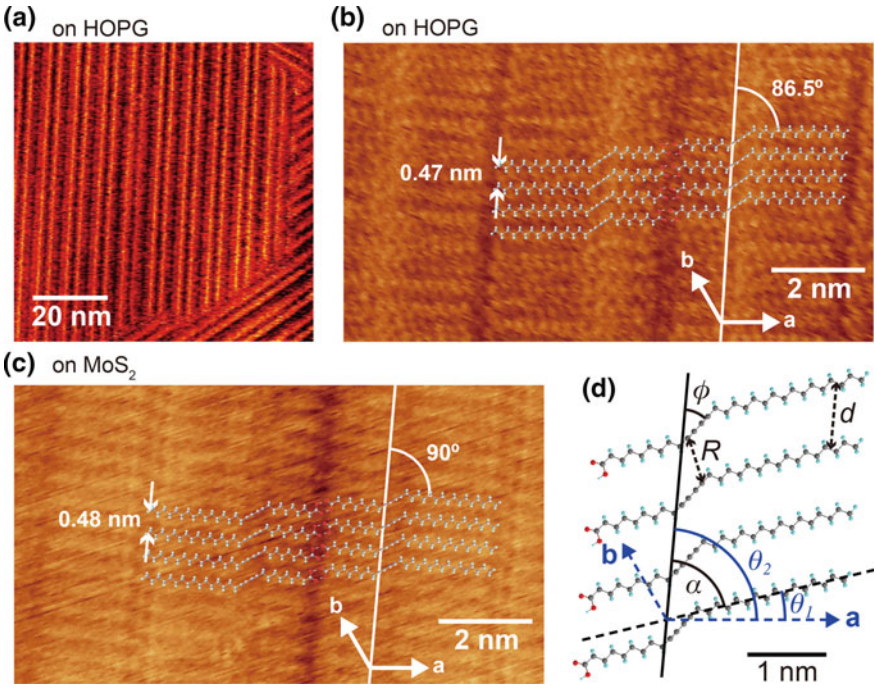

Fig. 2 **a** STM image of a molecular layer of 10,12-nonacosadiynoic acid on a HOPG substrate. **b**, **c** Magnified STM images of the molecular layer on HOPG and MoS_2 substrates, respectively. Molecular models are superimposed in the images. **d** Schematic sketch of the molecular arrangement indicating the structural parameters. Vectors *a* and *b* indicate the directions of the underlying substrate lattice. Image **a** adapted from Ref. [19] with permission from The Royal Society of Chemistry. Images **b**–**d** adapted with permission from Ref. [22]. Copyright 2011, American Chemical Society

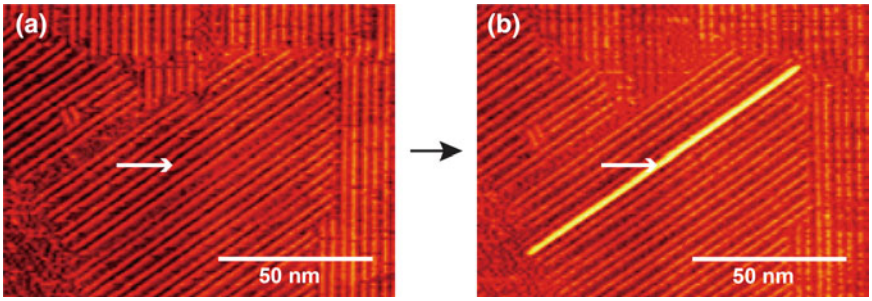

Fig. 3 **a** STM image of a molecular layer of 10,12-pentacosadiynoic acid on a HOPG substrate. **b** STM image of the same area after applying a pulsed sample bias voltage (–4 V in amplitude, 5 μs in width) at the point indicated by the *arrow*. The fabricated single polydiacetylene chain is imaged as a *brighter line*. Adapted with permission from Ref. [17]. Copyright 2001, AIP Publishing LLC

orientation of the alkyl side chains is parallel to the main graphite crystal axis. Additionally, the spacing d between neighboring molecules along the direction of the molecular row is always 0.47 nm, and the angle α between the alkyl side chains and the molecular row is 86.5° (see Fig. 2d). On MoS_2, the angle θ_1 between the alkyl side chains and the main MoS_2 crystal axis varies from −7 to 7°. In this case, the α and d values vary between 85–95° and 0.41–0.48 nm, respectively [22]. The fluctuation of the molecular arrangement on MoS_2 is probably related to the weaker interactions between the alkyl chains and the MoS_2, compared to graphite [22].

Tip-induced chain polymerization on a molecular layer of 10,12-pentacosadiynoic acid is shown in Fig. 3. After depositing the layer, we positioned the STM tip over the diacetylene molecule indicated by the arrow, and applied a pulsed sample bias (–4 V in amplitude, 5 μs in width), as illustrated in Fig. 3a. Figure 3b shows the pulse application product. It reveals a bright line, originating from the point of stimulation. This is a single polydiacetylene chain formed by the tip-induced chain polymerization. Thus, a single straight polydiacetylene chain can be fabricated at any designated position with nm spatial precision. Note that the polymerization is terminated when it encounters a domain boundary (Fig. 3b) [17], a substrate step [23], or an artificial defect [16]. Therefore, when chain polymerization is initiated on larger, defect-free domains, the polydiacetylene chains can be micron-long [24].

3 Lifted-Up Structure of Single Polydiacetylene Chains

Figure 4a shows a typical high-resolution STM image of 10,12-pentacosadiynoic acid monomers and a polymer on a HOPG substrate. A model of the molecular arrangement in the monomer row is depicted in Fig. 4b. We see that the alkyl side chains are oriented parallel to the main graphite crystal axis. Among the

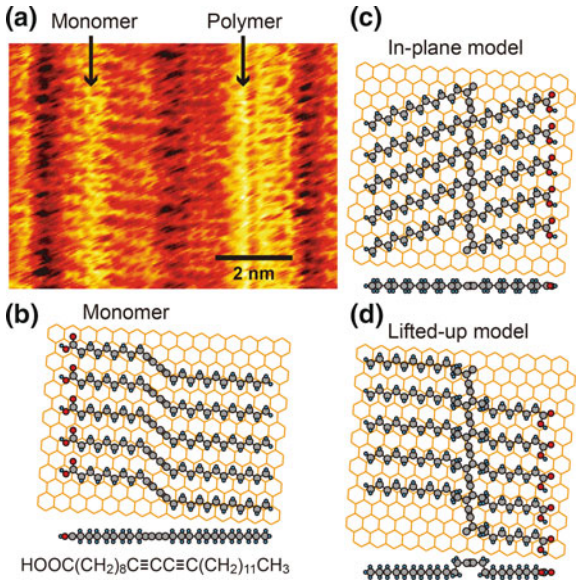

Fig. 4 **a** STM image of a molecular layer of 10,12-pentacosadiynoic acid on a HOPG substrate obtained after ultraviolet irradiation. A photo-polymerized polydiacetylene chain and an unpolymerized monomer row are resolved in the same image. **b** *Top and side views* of the monomer molecular arrangement. **c**, **d** 'In-plane' and 'lifted-up' conformation models of the polydiacetylene, respectively. Adapted from Ref. [25] with permission from The Royal Society of Chemistry

considerable structure models of the polymer, the simplest one is the 'in-plane' structure model (Fig. 4c). In this model, all carbon atoms in the polymer lie in the same plane, parallel to the substrate surface. If this was the case, then, under the experimentally observed condition that the polymer backbone has the same orientation as the linear array of diacetylene monomers, the alkyl side chains should have orientation changes as depicted in Fig. 4c. This is because C–C bonds connecting the alkyl side chains to the polydiacetylene backbone are restricted in directions that satisfy sp^2 and sp^3 bond angles. However, this is inconsistent with STM images such as in Fig. 4a, where orientations of polymer side chains are observed to be parallel to those of monomer side chains. Thus, we proposed a 'lifted-up' conformation model (Fig. 4d) [17, 25]. In this model, the alkyl side chains of the polymer are tilted by rotating C–C single bonds which makes the model consistent with the experimental observations. The polydiacetylene backbone is geometrically raised from the level of alkyl side chains.

In first-principles density-functional calculations of the optimized lifted-up structure [25], the height of the polydiacetylene backbone from the alkyl side chains is 0.15 nm. From the total energy calculation, it was suggested that the conformation of the polymer is determined by the stability of an oligomer as an intermediate rather than the stability of a long polymer as a final product. The intermediate oligomer is

restricted between the neighboring monomers which will form chemical bonds with it in the process of chain polymerization. In the case of in-plane structure, the alkyl side chains of the oligomer are not parallel to those of neighboring monomers, thus the alkyl side chains of the oligomer collide with those of the monomers. Hence, the lifted-up oligomer structure is more stable than that of in-plane structure due to the steric hindrance between the alkyl side chains.

The lifted-up structure enables us to observe the single polydiacetylene chains with AFM. In AFM images, the polydiacetylene chains were 0.05–0.16 nm higher than the unpolymerized monomer rows [25], which is consistent with the lifted-up structure model.

Initially, we assumed that only one CH_2 group is lifted at each side of the backbone, symmetrically, as shown in Fig. 4d. However, a recent calculation suggested that the total energy of oligomer could be more stable if one CH_2 group was lifted on one side and two CH_2 groups were lifted on the other side. Further investigations are required to resolve the structure.

4 Reaction Mechanism and Rate-Determining Factors

Figure 5 illustrates the reaction probability P of tip-induced polymerization as a function of applied pulsed sample bias voltage V_s for typical domains of 10,12-nonacosadiynoic acid on HOPG and MoS_2 substrates [22]. The P/V_s dependence is very similar on both substrates. However, the absolute values differ, making the reaction probability on MoS_2 about 4 times higher than that on HOPG. Nevertheless, the similar V_s dependence indicates that the reaction mechanism is the same on both substrates. Furthermore, the plots are nearly symmetric with respect to the polarity of voltage, and the threshold is $\pm 2.7 \pm 0.2$ V on both substrates. This value roughly corresponds to the 3.1 eV energy difference between the diacetylene π–π ground state and the lowest excited π–π^* triplet state [26]. Thus, we can assume that at the first step in chain polymerization, electrons tunneling between the tip and

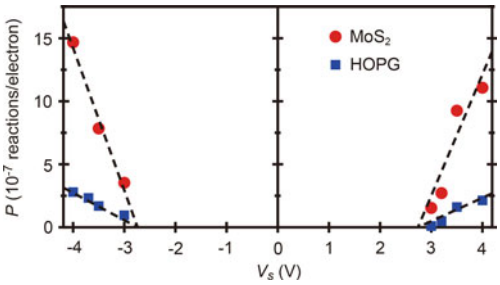

Fig. 5 Plot of tip-induced polymerization rate P per tunneling electron against pulsed sample bias voltage V_s, measured on typical domains of 10,12-nonacosadiynoic acid on HOPG and MoS_2 substrates. Adapted with permission from Ref. [22]. Copyright 2011, American Chemical Society

the substrate pass inelastically through the molecular layer and excite the diacetylene moiety.

This observation is consistent with the process of tip-induced chain polymerization schematically shown in Fig. 6 [17]. This is based on the proposed process for three-dimensional crystals of diacetylene compounds [27]. Initially, a single diacetylene moiety is inelastically excited by tunneling electrons, as described above, creating a reactive diradical state (Fig. 6b). This state has a finite lifetime before relaxing into the underlying substrate. If, within the lifetime of the diradical state, a neighboring diacetylene moiety approaches the diradical via thermal vibrations (Fig. 6c), an addition reaction can take place between them, creating a diacetylene dimer (Fig. 6d). Because the created dimer also has reactive terminals, similar addition reactions can take place on either side. The one-dimensional polymer is thus extended by spontaneously repeating this process along the molecular row (Fig. 6e). During the chain propagation, chain ends have reactive carbenes as illustrated in Fig. 6e.

The greater polymerization reactivity on the MoS_2 substrates can be attributed to the weaker interactions of the alkyl side chains with the MoS_2 compared to graphite. Due to the weaker interaction, molecules on MoS_2 experience more thermal vibrations, which increase the frequency of close-approaching diacetylene moieties favouring dimer formation (Fig. 6c), effectively promoting chain polymerization.

As mentioned above, the arrangement of molecules is always the same on HOPG, but varies in different domains on MoS_2. This structural variation allows us to investigate how the reaction probability is affected by molecular geometry. We determined the structural parameter d and α (Fig. 2d) for each domain from high-resolution STM images such as Fig. 2c. Using these parameters, we then estimated the distance between two reactive carbon atoms that are to be bound by

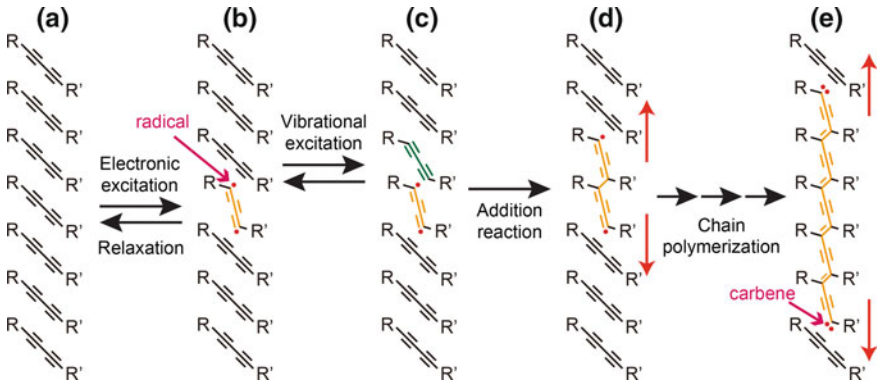

Fig. 6 Illustration of chain polymerization process. **a** Original array of diacetylene compound monomers. **b** A single diacetylene moiety is inelastically excited by tunneling electrons to a reactive diradical state. **c** A neighboring diacetylene moiety approaches one side of the diradical via thermal vibrations. **d** Dimer formation by an addition reaction. **e** Extended polymer formation by chain propagation reaction. The propagating polymer has reactive carbenes at both ends

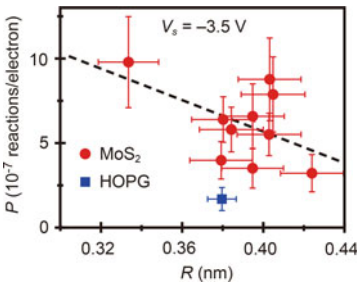

Fig. 7 Plot of tip-induced polymerization rate P per tunneling electron against the reactive carbon–carbon distance, R, for MoS_2 and HOPG substrates. Pulse amplitude V_s and duration were always −3.5 V and 5 μs, respectively. Adapted with permission from Ref. [22]. Copyright 2011, American Chemical Society

the polymerization reaction, R. This parameter R is a factor of the reaction probability, as seen in the plot in Fig. 7 [22]. This plot indicates that when R decreases by 0.1 nm, the reaction probability P doubles. This is consistent with the reaction mechanism described above. This means that R has a pronounced effect on the occurrence (or not) of the first addition reaction (Fig. 6c, d) within the lifetime of the diradical state.

Recently, we also found that similar molecular layers of diacetylene compound can be formed on a cleaved surface of hexagonal boron nitride (h-BN) nanosheets [28]. H-BN is a layered compound having a similar structure to graphite, except that the two carbon basis set is replaced by boron and nitrogen. It is an insulator with a band gap of 5.97 eV [29]. We found that the photo-polymerization rate on h-BN was approximately 100 times faster than that on graphite. As the band gap of h-BN is larger than the excited energy of diacetylene moiety (5.97 vs. 3.1 eV), the excited state is prevented to relax into the substrate. In contrast, the excited energy can easily relax into graphite or MoS_2. Thus, the excited diradical state (Fig. 6b) has a much longer lifetime on h-BN, resulting in a higher probability of the first addition reaction.

5 Chemical Soldering: New Method for Single-Molecule Wiring

'Chemical soldering' is a novel method for connecting conjugated polymer chains to individual organic molecules [18, 19]. The concept is illustrated in Fig. 8. Initially, a target functional molecule is adsorbed on a molecular layer of diacetylene compound. Then, an STM tip is positioned on the same molecular row of the diacetylene compound that the functional molecule is adsorbed, and chain polymerization is initiated as described in Sect. 2. As previously described, the propagating terminals of the chain have the reactive carbenes, as shown in Fig. 6e.

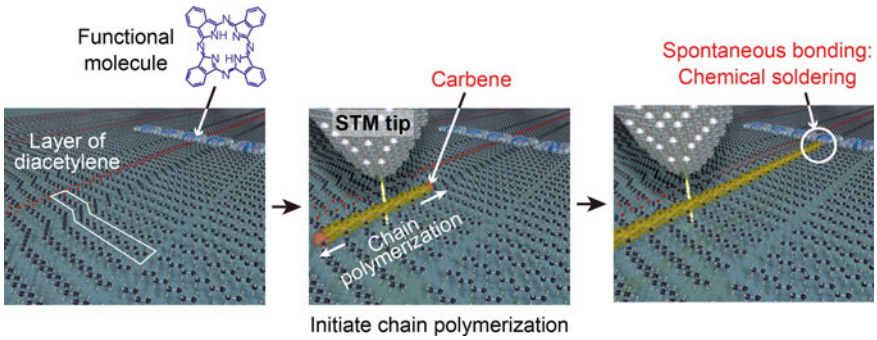

Fig. 8 Illustration of chemical soldering method. After a functional molecule is placed on a molecular layer of diacetylene compound, chain polymerization is initiated using an STM tip. The reactive carbene at the front edge of the chain polymerization spontaneously reacts and bonds with the functional molecule

When the chain polymerization encounters the adsorbed functional molecule, the carbene at the terminal of the polymer reacts not only with a neighboring diacetylene molecule but also with the adsorbed molecule. As a result, a chemical bond is spontaneously formed between the polydiacetylene chain and the target functional molecule. Since the target functional molecule is located above the molecular layer of diacetylene, the lifted-up structure of polydiacetylene is very important for this process, as it enables the reactive carbene to approach the functional molecule.

We initially used phthalocyanine (Pc) as the target functional molecules. They are planar functional dyes with unique electronic and optical properties [30]. Pc molecules are very mobile on HOPG, so it is impossible to observe STM images of isolated Pc molecules at room temperature. However, we found that Pc molecules are stabilized on a molecular layer of 10,12-nonacosadiynoic acid (Fig. 9) [18, 19].

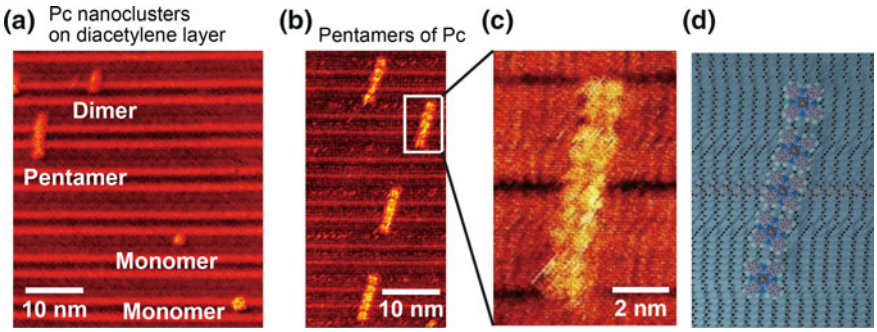

Fig. 9 **a** STM image after depositing a small quantity of copper phthalocyanine molecules on a molecular layer of 10,12-nonacosadiynoic acid lying on HOPG. Monomers, a dimer, and a pentamer of Pc are shown. **b** STM image of Pc pentamers. **c** Magnified STM image of a Pc pentamer. **d** Model of a Pc pentamer. Adapted with permission from Ref. [18]. Copyright 2011, American Chemical Society

In Fig. 9a, the smallest protrusions (labeled 'monomer') are isolated single Pc molecules adsorbed above the alkyl side chains of the 10,12-nonacosadiynoic acid molecules. The larger protrusion labeled 'dimer' consists of two Pc molecules, and the largest protrusion labeled 'pentamer' consists of five Pc molecules, which are shown in Fig. 9b, c. As illustrated in Fig. 9d, a Pc pentamer adsorbs across two rows of 10,12-nonacosadiynoic acid. As the pentamers are frequently observed (Fig. 9b), they most likely represent a stable structure on the molecular layer of 10,12-nonacosadiynoic acid. The first demonstrations of chemical soldering were performed on such pentamers of Pc [18].

Figure 10a shows an STM image of a Pc pentamer adsorbed onto a molecular layer of 10,12-nonacosadiynoic acid on HOPG. Chain polymerization was initiated by applying a pulsed bias voltage to the diacetylene row the Pc was adsorbed onto.

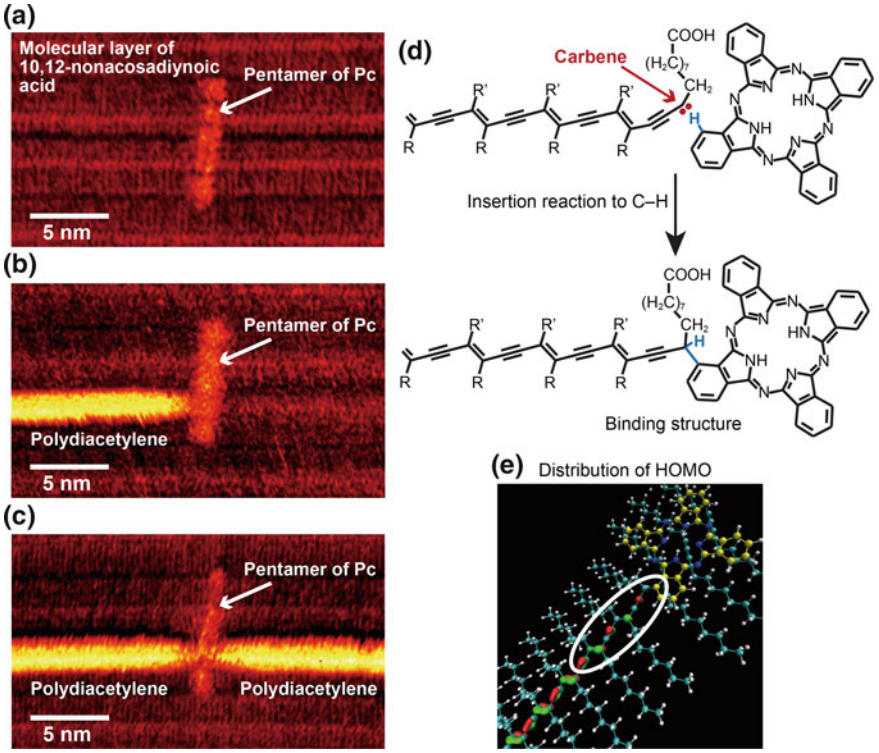

Fig. 10 **a** STM image of a Pc pentamer on a molecular layer of 10,12-nonacosadiynoic acid lying on HOPG. **b** Same area after chain polymerization initiation. A fabricated single polydiacetylene chain (*bright line*) is connected to a Pc molecule. **c** Same area after two polydiacetylene chains are connected to the same Pc molecule. **d** Proposed chemical reaction. The reactive end of polydiacetylene is inserted into a C–H bond of Pc. **e** Optimized structure model for the binding structure. Calculated distribution of HOMO density is also shown. The *white oval* indicates the region of smaller HOMO density. Adapted with permission from Ref. [18]. Copyright 2011, American Chemical Society

As a result, the polydiacetylene chain was connected to the Pc molecule (Fig. 10b). Then, the STM tip was positioned on the other side of the Pc and initiated the second chain polymerization (Fig. 10c), effectively connecting two polydiacetylene chains to the same Pc molecule.

Careful observation of Fig. 10b, c reveals that the image contrast of the polydiacetylene backbone near the Pc connecting point decreased. By repeating similar experiments more than 60 times, we found that approximately 70 % of the images exhibited similar decreased contrast. In the other 30 %, the contrast of the polydiacetylene backbone was relatively unchanged [18]. We considered several possible chemical reactions of the terminal carbene and performed structural optimizations of them [18] via the density-functional first-principles calculations with a wavelet basis set (BigDFT) designed for large-scale calculations [31]. We found that the binding structure, shown in Fig. 10d, e, gives the lowest energy among calculated structures. In this structure, the carbene at the terminal of the polydiacetylene chain is inserted into a C–H bond of Pc, resulting in the formation of chemical bond between them, as shown in Fig. 10d. Figure 10e shows the optimized structure of this binding structure. The calculated density distribution of highest occupied molecular orbital (HOMO) is also depicted in the figure. The calculated HOMO density in the two or three units of the polymer closest to the connecting point (white oval in Fig. 10e) is less than that in the center of the polymer. This is consistent with the decreased contrast in the STM images that reflect the HOMO density. With 70 % of the images showing decreased contrast, we conclude that polymer connection to Pc (chemical soldering) is the main reaction. The remaining 30 % of the images, not exhibiting decreasing contrast, are assigned to a structure where the carbene is inactivated through 1,2-rearrangement of a hydrogen atom, without binding to the Pc.

Concerning the future applications of chemical soldering to Pc, it is suggested that the system where the Pc molecule is connected to two polydiacetylene chains could act as a molecular resonant tunneling diode [18]. As illustrated in Fig. 10d, the terminal carbon atom of the polydiacetylene is converted to sp^3 hybridization by the insertion reaction. Those sp^3 carbon atoms become tunneling barriers between the polydiacetylene and Pc. If the bias voltage is adjusted such that the energy level of the polydiacetylene is equivalent to that of the Pc, then an electron can directly tunnel from the polydiacetylene into the Pc. Thus, electrons can flow from one side to the other through the Pc molecule. If the bias is lower or higher than this voltage, the flow of electrons could be restrained. Such could be a useful component of future single-molecule electronics.

We also succeeded in chemical soldering with fullerene (C_{60}) molecules [32]. When a chain polymerization is initiated to C_{60} nanoislands adsorbed on the molecular layer of 10,12-pentacosadiynoic acid, a cycloaddition reaction occurs between the carbene at the end of polydiacetylene and a single C_{60} molecule. STM observation has proved that the C_{60} molecule is covalently connected to the end of polydiacetylene [32].

6 Summary

In this chapter, we discussed a method for on-surface synthesis of single conjugated polymer chains, using STM tip-induced chain polymerization. This method enables us to fabricate in ambient conditions, single straight polydiacetylene chains at designated positions with nm spatial precision. Using this method, we have proposed and demonstrated 'chemical soldering,' for connecting conjugated polymer chains to a single functional molecule. Phthalocyanine and C_{60} molecules have been used in our demonstrations, but we believe that many other functional molecules can be connected using this method. Thus, this method will be a key technology for the fabrication of single-molecule devices.

Acknowledgments We are grateful to our collaborators, Prof. J.K. Gimzewski (UCLA), Prof. C. Joachim (CNRS), Prof. S. Goedecker (Univ. of Basel), Prof. T. Hasegawa (Waseda Univ.), Dr. C. Hu (Tokyo Univ. of Science), Dr. S. Tsukamoto (Forschungszentrum Jülich and JARA), Dr. D. Takajo (Osaka Univ.), Prof. M. Nakaya (Nagoya Univ.), Dr. Y. Tateyama, Dr. J.P. Hill, Dr. K. Ariga, Dr. T. Taniguchi, and Dr. T. Nakayama (NIMS). This work was supported by World Premier International Research Center Initiative (WPI), the Ministry of Education, Culture, Sports, Science and Technology of Japan (MEXT), and partially supported by JSPS KAKENHI Grant Numbers 21310078 and 24241047.

References

1. Aviram, A., Ratner, M.A.: Molecular rectifiers. Chem. Phys. Lett. **29**, 277 (1974)
2. Joachim, C., Gimzewski, J.K., Aviram, A.: Electronics using hybrid-molecular and mono-molecular devices. Nature **408**, 541 (2000)
3. Wada, Y., Tsukada, M., Fujihira, M., Matsushige, K., Ogawa, T., Haga, M., Tanaka, S.: Prospects and problems of single molecule information devices. Jpn. J. Appl. Phys. **39**, 3835 (2000)
4. Kwok, K.S., Ellenbogen, J.C.: Moletronics: future electronics. Mater. Today **5**, 28 (2002)
5. Joachim, C., Ratner, M.A.: Molecular electronics: some views on transport junctions and beyond. Proc. Natl. Acad. Sci. U.S.A. **102**, 8801 (2005)
6. Natelson, D., Yu, L.H., Ciszek, J.W., Keane, Z.K., Tour, J.M.: Single-molecule transistors: electron transfer in the solid state. Chem. Phys. **324**, 267 (2006)
7. Tao, N.J.: Electron transport in molecular junctions. Nat. Nanotechnol. **1**, 173 (2006)
8. Choi, H., Mody, C.C.M.: The long history of molecular electronics. Microelectronics origins of nanotechnology. Social Stud. Sci. **39**, 11 (2009)
9. Scott, G.D., Natelson, D.: Kondo resonances in molecular devices. ACS Nano **4**, 3560 (2010)
10. Song, H., Reed, M.A., Lee, T.: Single molecule electronic devices. Adv. Mater. **23**, 1583 (2011)
11. de Ruiter, G., van der Boom, M.E.: Sequential logic and random access memory (RAM): a molecular approach. J. Mater. Chem. **21**, 17575 (2011)
12. Fuentes, N., Martín-Lasanta, A., De Cienfuegos, L.Á., Ribagorda, M., Parra, A., Cuerva, J.M.: Organic-based molecular switches for molecular electronics. Nanoscale **3**, 4003 (2011)
13. Prauzner-Bechcicki, J.S., Godlewski, S., Szymonski, M.: Atomic- and molecular-scale devices and systems for single-molecule electronics. Phys. Status Solidi A **209**, 603 (2012)
14. Pathem, B.K., Claridge, S.A., Zheng, Y.B., Weiss, P.S.: Molecular switches and motors on surfaces. Annu. Rev. Phys. Chem. **64**, 605 (2013)

15. Ratner, M.: A brief history of molecular electronics. Nat. Nanotechnol. **8**, 378 (2013)
16. Okawa, Y., Aono, M.: Nanoscale control of chain polymerization. Nature **409**, 683 (2001)
17. Okawa, Y., Aono, M.: Linear chain polymerization initiated by a scanning tunneling microscope tip at designated positions. J. Chem. Phys. **115**, 2317 (2001)
18. Okawa, Y., Mandal, S.K., Hu, C., Tateyama, Y., Goedecker, S., Tsukamoto, S., Hasegawa, T., Gimzewski, J.K., Aono, M.: Chemical wiring and soldering toward all-molecule electronic circuitry. J. Am. Chem. Soc. **133**, 8227 (2011)
19. Okawa, Y., Akai-Kasaya, M., Kuwahara, Y., Mandal, S.K., Aono, M.: Controlled chain polymerisation and chemical soldering for single-molecule electronics. Nanoscale **4**, 3013 (2012)
20. Wegner, G.: Topochemical polymerization of monomers with conjugated triple bonds. Macromol. Chem. Phys. **154**, 35 (1972)
21. Tieke, B., Lieser, G., Wegner, G.: Polymerization of diacetylenes in multilayers. J. Polym. Sci. Pol. Chem. **17**, 1631 (1979)
22. Mandal, S.K., Okawa, Y., Hasegawa, T., Aono, M.: Rate-determining factors in the chain polymerization of molecules initiated by local single-molecule excitation. ACS Nano **5**, 2779 (2011)
23. Sullivan, S.P., Schnieders, A., Mbugua, S.K., Beebe Jr, T.P.: Controlled polymerization of substituted diacetylene self-organized monolayers confined in molecule corrals. Langmuir **21**, 1322 (2005)
24. Takajo, D., Okawa, Y., Hasegawa, T., Aono, M.: Chain polymerization of diacetylene compound multilayer films on the topmost surface initiated by a scanning tunneling microscope tip. Langmuir **23**, 5247 (2007)
25. Okawa, Y., Takajo, D., Tsukamoto, S., Hasegawa, T., Aono, M.: Atomic force microscopy and theoretical investigation of the lifted-up conformation of polydiacetylene on a graphite substrate. Soft Matter **4**, 1041 (2008)
26. Bertault, M., Fave, J.L., Schott, M.: The lowest triplet state of a diacetylene. Chem. Phys. Lett. **62**, 161 (1979)
27. Neumann, W., Sixl, H.: The mechanism of the low temperature polymerization reaction in diacetylene crystals. Chem. Phys. **58**, 303 (1981)
28. Makarova, M., Okawa, Y., Verveniotis, E., Taniguchi, T., Joachim, C., Aono, M.: Self-assembled diacetylene molecular wires polymerization on an insulating hexagonal boron nitride (0001) surface. (in preparation)
29. Watanabe, K., Taniguchi, T., Kanda, H.: Direct-bandgap properties and evidence for ultraviolet lasing of hexagonal boron nitride single crystal. Nat. Mater. **3**, 404 (2004)
30. de la Torre, G., Claessens, C.G., Torres, T.: Phthalocyanines: old dyes, new materials. Putting color in nanotechnology. Chem. Commun. 2000 (2007)
31. Genovese, L., Neelov, A., Goedecker, S., Deutsch, T., Ghasemi, S.A., Willand, A., Caliste, D., Zilberberg, O., Rayson, M., Bergman, A., Schneider, R.: Daubechies wavelets as a basis set for density functional pseudopotential calculations. J. Chem. Phys. **129**, 014109 (2008)
32. Nakaya, M., Okawa, Y., Joachim, C., Aono, M., Nakayama, T.: Nanojunction between fullerene and one-dimensional conductive polymer on solid surfaces. ACS Nano **8**, 12259 (2014)

On-Surfaces Synthesis on Insulating Substrates

Markus Kittelmann, Robert Lindner and Angelika Kühnle

Abstract On-surface synthesis has attracted great attention in recent years due to its promising potential for creating functional structures on surfaces. An important aspect of on-surface synthesis is the capability to arrive at covalently linked thermally stable structures that offer the possibility for application even in harsh environments outside ultra-high vacuum conditions. Additionally, covalent linking allows for fabricating conjugated structures with superior electron transport properties. Especially, the latter is of tremendous interest when considering future applications in the field of molecular electronics. Having molecular electronics applications in mind explains the need for decoupling of the electronic structure of the molecular network from the underlying support surface. Thus, it is highly interesting to transfer on-surface synthesis strategies from metallic to insulating surfaces. Albeit, insulating surfaces pose several challenges for on-surface synthesis. First, many prototypical insulating support materials interact only weakly with organic molecules. This weak binding frequently results in molecule desorption rather than reaction activation when thermally initiating the reaction. Second, it is known that metals act as catalyst for several reactions that have been performed successfully on metallic surfaces. A simple transfer of these reactions to insulating surfaces in the absence of metal atoms is, therefore, questionable and requires different reaction pathways to be considered. In this chapter, we review the current state-of-the-art in on-surface synthesis on electrically insulating substrates carried out in ultra-high vacuum. Proof-of-principle reactions are discussed with an emphasis on strategies to overcome challenges related to the weak molecule-surface binding often present on insulating surfaces, e.g., by means of photochemical activation. Site-specific and sequential reactions are presented as a promising way for enhancing control and structural complexity of on-surface synthesis on insulating support materials. Finally, the influence of the substrate is shown to induce directionality in on-surface synthesis by favoring specific surface directions.

M. Kittelmann · R. Lindner · A. Kühnle (✉)
Institut für Physikalische Chemie, Johannes Gutenberg-Universität Mainz,
Duesbergweg 10–14, 55099 Mainz, Germany
e-mail: kuehnle@uni-mainz.de

A. Gourdon (ed.), *On-Surface Synthesis*, Advances in Atom and Single Molecule Machines, DOI 10.1007/978-3-319-26600-8_9

1 Introduction

Despite being a relatively young field of research, on-surface synthesis has attracted tremendous interest in the past decade. Impressive progress has been made from one of the first proof-of-principle experiments carried out in 2007 [1] to hierarchical synthesis in a sequential and site-specific manner [2]. Compared to self-assembled structures, molecular networks created by on-surface synthesis provide higher stability, which is of importance when considering applications in a harsh environment outside ultra-high vacuum (UHV). From a synthesis point of view, novel reaction pathways might be possible on the surface due to the confinement of the educts to the two-dimensional surface plane. Moreover, the absence of solvent might enable reactions that are difficult in solution due to low solubility of the reaction product [3]. A further aspect is providing structures that can be incorporated into future molecular electronic devices, such as molecular wires and switches. Here, it is of special interest to create covalently coupled structures that are conjugated and, thus, exhibit high electron transport capabilities.

When discussing molecular electronic applications, however, it is mandatory to decouple the electronic structure of the molecular network from the underlying substrate. Thus, metal surfaces are largely incompatible with molecular electronic applications. Attempts to electronically decouple the molecular structure from the support while still working with metallic substrates have been made to maintain the experimental accessibility of the system by scanning tunneling microscopy (STM). One approach is using so-called "Lander" molecules [4], featuring spacer groups that can act as legs to separate the conjugated core form the surface. Another approach is evaporating a thin insulating film on a metal support [5]. However, both strategies bear sever limitations in terms of materials flexibility. Thus, from an application point of view and for enlarging the materials basis for on-surface synthesis, it is highly desirable to transfer the concept from metallic to bulk insulating substrates.

Bulk insulators, however, have rarely been studied in the context of on-surface synthesis. This is mainly due to experimental restrictions, as insulating surfaces are more difficult to investigate. In particular, STM as a powerful tool for real-space imaging [6] cannot be used as it requires electrically conducting substrates. But also when considering the physico-chemical mechanisms of on-surface synthesis, insulating surfaces pose significant challenges as compared to metal substrates. A major obstacle is the comparatively weak molecule–surface interaction on insulating substrates, which frequently leads to desorption rather than reaction initiation upon annealing. This is why alternative routes for reaction initiation, e.g., by photochemical means are of particular importance for insulating substrates. Moreover, the classical Ullmann reaction that has often been exploited for on-surface covalent linking, which is known to be catalyzed by the presence of copper (or other metal) atoms [1]. These facts readily illustrate that a transfer of on-surface synthesis strategies to nonmetallic systems might not be straightforward. Indeed, only few examples of on-surface synthesis reactions have been presented

on an insulating surface so far. An important tool toward investigating such systems is the scanning force microscope operated in the noncontact mode, as this technique allows for direct imaging in UHV with atomic or molecular resolution [7].

Here, we review the current state-of-the-art of on-surface synthesis on insulating surfaces carried out in UHV. First, the specific situation arising from the use of insulating surfaces is briefly discussed. We commence the presentation of experimental results by briefly introducing early studies that have been performed on thin insulating films to maintain the experimental accessibility by STM and other electron-based surface characterization methods. After that, the first proof-of-principle reaction carried out on the surface of a bulk insulator is presented, which has been performed with a benzoic acid derivative on calcite(104). The flexibility of this system has been demonstrated by varying the number and position of the reactive sites. We show the possibility to extend this approach for performing sequential and site-specific reaction to enhance structural control. Photochemical initiation of an on-surface synthesis reaction has been demonstrated using C_{60} molecules on calcite(104). With this system, we also address the option of guiding the on-surface reaction by the underlying substrate, thereby gaining further control over the resulting structures. Finally, the current status is concluded and an outlook discussing future trends is given.

2 Specific Situation on Insulating Substrates

Many studies have addressed on-surface synthesis reaction on metallic substrates. However, only little is known about on-surface synthesis on insulating substrates. A main hurdle when investigating insulating surfaces arises from the comparably poor experimental accessibility of insulating substrates. Standard surface science methods such as STM, photoelectron emission spectroscopy (PES) or low-energy electron diffraction (LEED) rely on electrically conducting materials, thus, they usually cannot be applied to nonconducting surfaces. Only since the advent of scanning force microscopy, this experimental limitation has been partially overcome [7]. Substantial improvements of noncontact atomic force microscopy (NC-AFM) have now developed this technique from an emerging method into a standard routine for direct-space imaging of surfaces with atomic resolution.

However, besides this technical aspect, on-surface synthesis on insulating substrates also pose specific challenges arising from the comparably weak and typically unknown interaction of the educt molecules with the supporting substrate. In fact, compared to metal surfaces, the interaction of organic molecules with electrically insulating surfaces is rather poorly understood. In part, this is a consequence of the limited experimental accessibility discussed above. Besides this technical issue, however, the limited understanding also arises from the fact that the class of insulating materials is much more heterogeneous than the class of metals. The class of insulators spans a wide range from covalently linked crystals such as diamond or titanium dioxide, ionic crystals like sodium chloride or calcium fluoride to van der

Waals bonded molecular crystals. Thus, general statements regarding the interaction of organic molecules with "an insulating surface" are difficult to make.

For prototypical insulating surfaces studied so far, namely KBr(001), CaF_2(111), and NaCl(001), the interaction with organic molecules has been found to be comparatively weak. This statement includes both, the binding energy of the molecules towards the surfaces as well as the diffusion barrier on the surface [8–13]. However, precise values of binding energies and diffusion barriers are generally lacking, except for a few examples [12, 14]. The weak interaction hinders molecular self-assembly on these surfaces, and in most cases it prevents on-surface synthesis reaction to be performed as annealing would lead to desorption instead of reaction initiation. Thus, a prerequisite effort is to explore means to enhance the molecule–surface interaction [15]. Several strategies have been followed in this context, including modification of the surface by electron irradiation [16] and equipping the molecules with specific anchor groups [12, 17]. Besides these modifications, it is also important to consider the reactivity of the surface by comparing the surface energies [18]. In this context, the natural cleavage plane of calcite, calcite(104), has taken a special role. It exhibits a surface energy of approximately 600 mJ/m^2, which is not as high as those of typical metals (e.g., Au (111) with more than 1000 mJ/m^2), but still considerably higher than those of the prototypical insulator surfaces discussed above (e.g., KBr(001) having a surface energy of around 140 mJ/m^2). The high surface energy is synonymous to a reactive surface, which can be understood from the fact that calcite(104) provides several binding sites for electrostatic anchoring as well as hydrogen bonding.

An alternative approach to induce on-surface reactions without risking desorption of the educts from the surface is using other stimuli rather than thermal annealing. This is why photochemical initiation is of special interest when discussion on-surface synthesis on insulating substrates. In principle, photochemical initiation can be used to induce a reaction without heating the educts on the surface. Thus, it can be speculated that problems associated with desorption can be substantially reduced by photochemical initiation.

In addition to the weak interaction, non-metallic surfaces pose another challenge. For many reactions initiated so far on surfaces, the metallic substrate is known to act as a catalyst. The most prominent reaction studied so far is the Ullmann reaction, which is catalyzed by the presence of copper (or, generally speaking any other metal with *d* electrons available) atoms. For this reason, it remains questionable, how on-surface reactions relying on the presence of metal atoms can be transferred to insulating surfaces.

3 Reactions on Thin Insulating Films

For maintaining the accessibility by standard surface science characterization methods such as STM, experiments have been carried out on a thin insulator film supported by a metallic substrate. One example has been the synthesis of a

two-dimensional polymeric network of Fe phthalocyanine obtained from the stoichiometric co-deposition of iron and the tetracyanobenzene precursor [19]. These educts have been deposited onto an Ag(100) surface that has been partially covered with monatomic NaCl islands. Due to the weak interaction of the molecules with the thin insulating film, the educts have been observed to preferentially adsorb on the free metal areas. Thus, it has appeared necessary to first cover the metallic parts of the surface with molecules before growth could be obtained on the insulating film. A highly ordered, monodomain network has been achieved on the NaCl islands, again illustrating the high molecular mobility on the insulating surface (see Fig. 1a).

The formation of a molecular wire connecting both metallic and insulating parts on a surface has been demonstrated by the synthesis of poly (9,9-dimethylfluorene) on an Au(111) surface exhibiting NaCl islands [20]. In this work, the wire synthesis has been taken part on the metallic areas of the surface with the NaCl islands repelling the molecular wires. Above a critical NaCl coverage, however, the wires have been observed to rise to the top of the NaCl islands due to space limitations (see Fig. 1b). Scanning tunneling spectroscopy data have been collected at various positions of the wire. The latter data have demonstrated that three NaCl layers appeared insufficient for decoupling of the electronic structure of the wire from the underlying metal support; illustrating that thicker layers are needed for a more efficient decoupling.

From these investigations, the above-mentioned weak molecule–surface interaction in case of an insulating surface becomes apparent, indicating that strategies for molecule–surface anchoring are mandatory for on-surface synthesis on insulating surfaces. Moreover, thin films have been shown to fail when asking for efficient electronic decoupling from the metallic support.

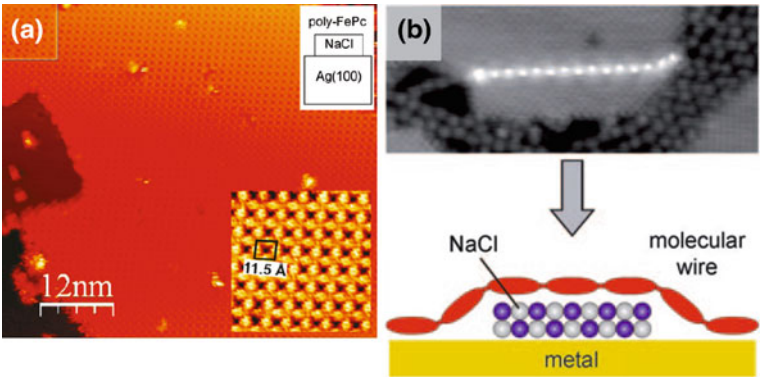

Fig. 1 **a** Two-dimensional network of Fe phthalocyanine on an NaCl island on Ag(100). Reproduced with permission from Abel et al. [19]. **b** Molecular wire of poly(9,9-dimethylfluorene) on an NaCl island on Au(111). Reproduced with permission from Bombis et al. [20]

4 Current State-of-the-Art on Bulk Insulators

In the following section, we review the current state-of-the-art in on-surface synthesis on the surface of a bulk insulator. The first proof-of-principle of an on-surface reaction carried out on an insulating substrate is presented in Sect. 4.1. Varying both number and position of the reactive sites at the molecular building blocks provides a reliable way for controlling the success of the reaction [21]. Based on these results, enhanced reaction control has been achieved by site-specific and sequential reaction initiation [22], which constitutes a promising means for fabricating more complex structures (see Sect. 4.2). Finally, results demonstrating photochemical initiation are reviewed in Sect. 4.3. These results provide a route to overcome problems with desorption of weakly bonded molecules. Moreover, the direction of the oligomerization has been shown to be governed by the underlying substrate, providing an interesting possibility for further structural control by substrate-guided reactions.

Calcite, the most stable modification of calcium carbonate, has been used in the investigations presented here. Calcite has a band gap of 6.0 eV [23], i.e., it constitutes an electrically insulating material. Calcite can be easily cleaved in UHV [24], resulting in the formation of the energetically most favorable (104) cleavage plane (see Fig. 2a). Moreover, as discussed above, calcite(104) has a high surface energy compared to many other insulating surfaces, indicating an increased molecule–surface interaction. This increased interaction is, indeed, observed for many molecules [25].

The molecules that have been used in the studies presented here are shown in Fig. 2b. These include 4-iodobenzoid acid (4-IBA), biphenyl-4,4′-dicarboxylic acid (BPDCA), 2,5-diiodobenzoic acid (DIBA), 3,5-diiodosalicylic acid (DISA), 2-(4-bromophenyl)-6-(4-chlorophenyl)pyridine-4-carboxylic acid (BPCPPCA) as well as C_{60}.

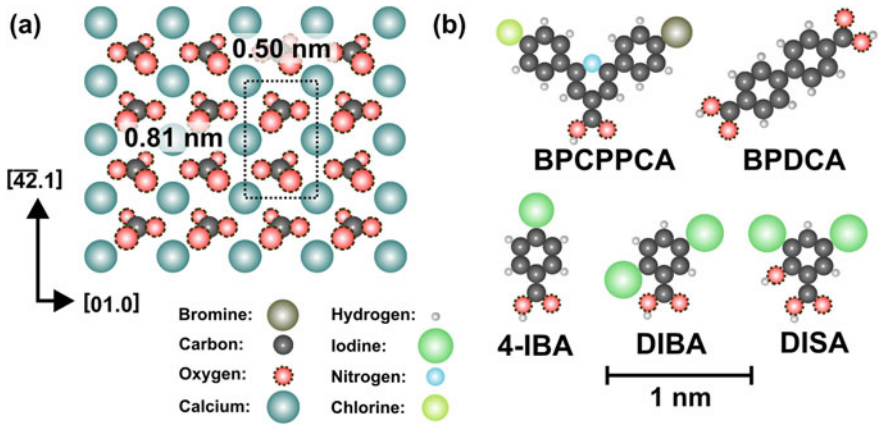

Fig. 2 **a** Calcite crystal structure and **b** molecules studied in this chapter (drawn to scale)

4.1 Proof-of-Principle on a Bulk Insulating Surface

As a first proof-of-principle study, the reaction of several organic molecules has been tested on calcite(104). Among many molecules that have been tested, only few turned out to provide sufficient anchoring towards the surface to initiate the linking reaction by thermal means. Surprisingly, the comparably simple benzoic acid derivatives have been found to be among the successful molecules. The carboxylic acid functionality provides an anchor towards the surface, while the benzene core can be equipped with reactive species. In the simplest case, iodobenzoic acid can be studied. Upon annealing, the iodine atom is cleaved from the molecule, creating reactive radicals on the surface. These radicals diffuse on the surface until they meet another radical to react with.

An important aspect to consider is the deprotonation of the acid group. Depending on the pK_A value of the investigated benzoic acid derivative, the molecules might deprotonate upon annealing before the reaction is initiated. Based on the large number of carboxylic acid molecules deposited onto calcite(104) in UHV [21, 26, 27], a rough estimate can be given regarding the deprotonation state at room temperature. Although the deprotonation surely depends on many other aspects than the pK_A value alone (e.g., the substrate surface and the specific binding geometry), the benzoic acids presented here have been found to obey the following trend. At a pK_A value around 3, the molecule has been observed to deprotonate at room temperature, giving the possibility to follow this transition directly by NC-AFM [27]. Molecules with a pK_A value smaller than 3 are already deprotonated at room temperature, while molecules with a pK_A value larger than 3 require an additional annealing step to induce deprotonation. The latter is of importance when performing on-surface synthesis, as two annealing steps can be required for molecules with a pK_A value larger than 3: In the first step, the molecules become deprotonated, which changes the molecular arrangement on the surface but which is not associated with a covalent linking. Only upon further annealing in the second step, the molecules become dehalogenated and form radicals that can link on the surface. This two-step process has, indeed, been observed for 4-IBA on calcite(104), in agreement with a pK_A value of 4.02 [26].

As shown in Fig. 3, 4-IBA can be covalently linked on calcite(104) using thermal activation. When deposited onto calcite(104) held at room temperature, the molecules are found to be highly mobile, indicating the small diffusion barrier discussed above. As a consequence of the high mobility, molecules are only observed on the surface when confined, e.g., in surface troughs (see Fig. 3a). The situation is changed drastically when annealing the surface to 520 K. This change is ascribed to a deprotonation step. Now, negatively charged molecules exist on the surface, which interact much stronger with the ionic calcite surface than the neutral molecules before annealing. Consequently, a molecular wetting layer is formed with the molecules standing upright and anchoring towards the surface calcium cations (Fig. 3b) [26]. A second annealing step is required for inducing a further structural change. Upon annealing the substrate to 580 K, a molecular structure is found that can be explained by covalently linked dimer molecules arranged in a

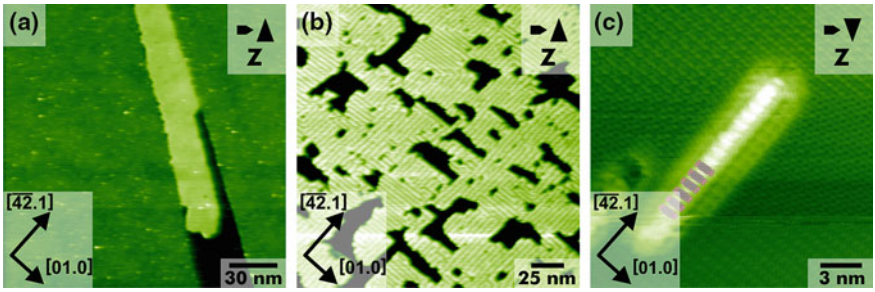

Fig. 3 Proof-of-principle of an on-surface reaction on a bulk insulating substrate [21]. **a** Upon deposition of 4-IBA onto calcite(104) held at room temperature, molecules are only visible when confined into troughs. **b** Moderate annealing to 520 K results in deprotonation and the formation of an extended wetting layer [26]. **c** Upon annealing to 580 K, 4-IBA forms covalently linked molecular dimers on the surface. These dimers resemble their protonated counterparts, which can be obtained from direct deposition of the dimer species, BPDCA [25]

side-by-side fashion (Fig. 3c). This assignment is corroborated by the size of the observed features and by comparing the structure with the appearance of the molecules obtained when directly depositing the reacted species, namely BPDCA [25]. While direct deposition of BPDCA results in two different structures, only the side-by-side structure is obtained for reacted 4-IBA. This can be readily understood from the fact that the reacted 4-IBA is deprotonated, while directly deposited BPDCA is not. Therefore, BPDCA can form a hydrogen-bonded structure with the molecules arranging in a head-to-tail fashion.

To further prove the reaction shown for 4-IBA, the number and the position of the iodine atoms can be changed. When changing the number of the iodine atoms to two in positions 2 and 5 as in DIBA, extended molecular rows are expected on the surface upon covalent linkage. As shown in Fig. 4a, DIBA forms a wetting island upon deposition onto calcite(104) held at room temperature. This indicates a comparatively strong interaction that has been observed with 4-IBA only after the first annealing step. It can, thus, be speculated that DIBA exists on the surface in the deprotonated state already at room temperature. This assumption is supported by the lower pK_A value of 2.51. Upon annealing to 530 K, the structure is changed completely. Now, rows oriented along the [-4-21] substrate direction are found on the surface (Fig. b). This structure can be understood by a twofold dehalogenation of the molecules and covalent linkage of the resulting radicals. Interestingly, the registry of the calcite(104) surface along the [-4-21] direction appears to support the reaction, as the negatively charged carboxylate groups within the row can be positioned atop a calcium ion (see model in Fig. 4c).

As an additional test for the on-surface reaction, the position of the iodine groups at the benzene core can be changed. For this check, DISA has been used, having iodine atoms at position 3 and 5 [21]. Upon linkage, a zigzag pattern is expected if the molecules arrange in an alternating fashion (in fact, also other structures are

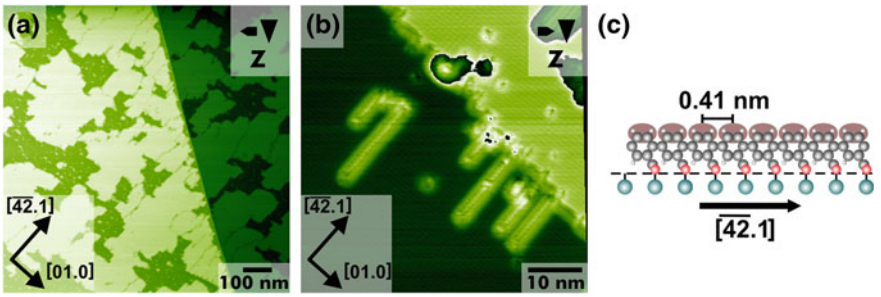

Fig. 4 Changing the number of reactive sites from one to two: DIBA on calcite(104) [21]. **a** Upon deposition of DIBA onto calcite(104) held at room temperature, an extended layer is found on the surface. **b** The structure changes significantly after annealing the surface to 530 K. Now, rows aligned along the [-4-21] substrate direction are formed. **c** Model of the conjugated row on the surface with the negatively charged carboxylate groups anchoring toward the calcite calcium ions

expected for a non-alternating linkage). Again, when depositing this molecule onto calcite(104) held at room temperature, an extended wetting layer is formed as shown in Fig. 5a. In the case of DISA, a perfect (1 × 1) overlayer is obtained, which can be understood by anchoring of the negatively charged carboxylate groups towards the surface calcium ions. This assignment is in agreement with a pK_A of 2.07. A structural change is induced by annealing the surface to 580 K. Now, a structure with reduced height is observed, indicating that the molecules are now lying flat on the surface (Fig. 5b). Among the various patterns observed, also a distinct zigzag structure can be identified. The superposition of the expected zigzag structure illustrates the excellent size match of the obtained structure (see Fig. 5c).

The observed direct response of the resulting structures to the monomer building blocks provides a clear indication for the successful covalent linkage of the molecules. As further evidence, the required temperature can be studied depending

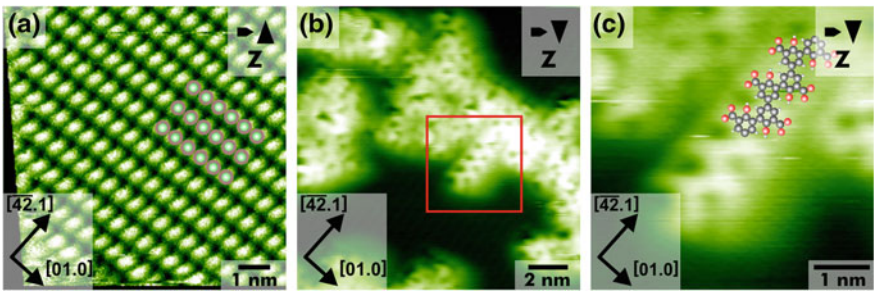

Fig. 5 Changing the position of the reactive sites [21]: DISA on calcite(104). **a** Upon deposition of DISA onto calcite(104) held at room temperature, a (1 × 1) overlayer is formed. **b** After annealing the surface to 580 K, another structure with reduced height is observed. **c** Among the structures seen, also a zigzag pattern is found, which precisely matches the structure expected when having an alternating arrangement of the DISA units within a covalently linked row

on the involved halogen atom. Depending on the halogen-phenyl bond strength, the temperature to induce radical formation is likely to increase when changing the halogen in the order iodine, bromine, chlorine, with the respective bond energies 268, 336 and 399 kJ/mol. This has been tested for the pair DIBA and 2,5-dichlorobenzoic acid. While DIBA has been shown to react at a temperature of 530 K, a temperature of 565 K was needed for radical formation of DCBA on calcite(104). Thus, although the details of the cleavage mechanism remain unclear, the energy required to induce the reaction follows a rather straightforward trend, again corroborating the interpretation of a dehalogenation and covalent linkage reaction.

This discussion directly points to another open question, namely the role of the calcite surface for the dehalogenation step. As mentioned above, the presence of copper is required as a catalyst for the well-known Ullmann reaction. As no metal has been available in the presented studies, another mechanism has to be at play. A possible explanation is a bond weakening of the phenyl-iodine bond upon adsorption of the carboxylate onto the calcite surface. Elucidating the details of the reaction mechanism will, however, require a close interplay of the experimental results with theoretical calculations.

4.2 Site-Specific and Sequential Reaction

A key goal of on-surface synthesis is providing tailor-made molecular networks on surfaces with precise control over structure and functionality. This goal requires enhancing the reaction control, e.g., from a simple one-step process as described above to a two-step reaction with site-specific linkage. This approach has been followed on a metallic surface [2] by using a molecule that has been equipped with both, bromine and iodine substituents. It has been shown that iodine can be cleaved off first, providing site-specific reaction sites that are available for the first-step linking. Only after a second annealing step to slightly higher temperatures, the bromine atoms are removed, making these reaction sites available in the second linking step. Inspired by these results, a similar approach has been taken on calcite(104). A molecule, namely BPCPPCA, has been chosen that provides both, two different halide substituents as well as a carboxylic acid anchor group (see Fig. 2b).

Upon deposition of BPCPPCA onto calcite(104) held at room temperature, molecular islands are observed on the surface as shown in Fig. 6a. These islands exhibit a mirror symmetry axis along the [-4-21] substrate direction. This mirror symmetry can be readily understood by the fact that the molecules form a (2 × 4) superstructure on the surface, which can be arranged in two mirror-symmetric ways on the surface. The islands changes drastically upon a first annealing step at 570 K. Now, row-like features are found on the surface (Fig. b). These rows are aligned along two distinct surface directions, forming an opening angle of about 48°. Considering the molecular structure allows for speculating about the structural details of the rows. A moderate annealing step is expected to exclusively cleave off

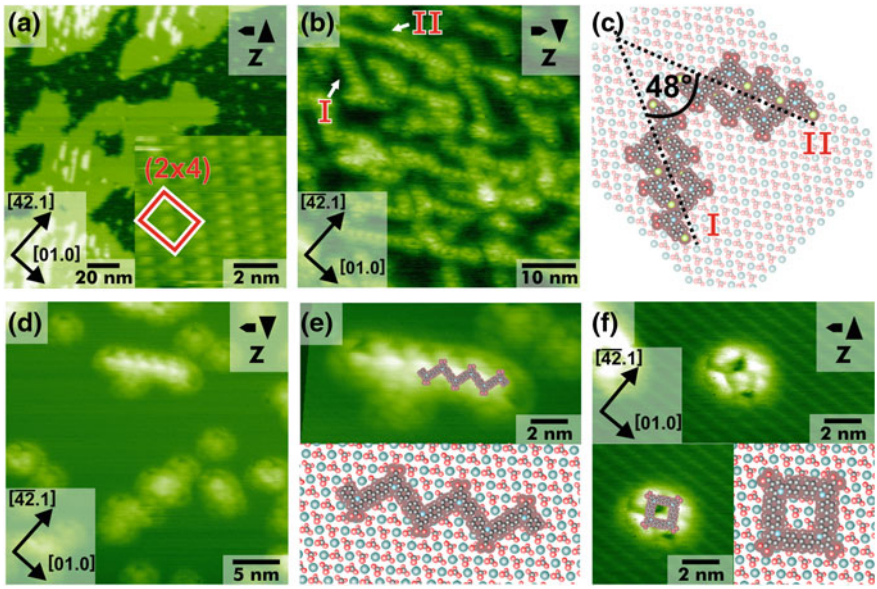

Fig. 6 Site-specific and sequential on-surface reaction on calcite(104) [22]. **a** Upon deposition of BPCPPCA onto calcite(104) held at room temperature, molecular islands with a mirror symmetry axis along [-4-21] exist on the surface. **b** Moderate annealing to 570 K results in the formation of row-like features, oriented along specific surface directions, i.e., resulting in a well-defined opening angle of 48°. **c** Model for the structural arrangement of the row-like features, illustrating the origin of the characteristic opening angle. **d** Further annealing to 610 K induces a second structural change. Now, zigzag chains and ring-like structures are present on the surface. **e** Zoom and structural model of the zigzag chain. **f** Zoom and structural model of a ring structure

the bromine atoms. This results in the formation of molecular dimers either with an "S" or "U" shape. The intermolecular interaction is larger when S-shaped molecules arrange side-by-side. If we now further assume that the carboxylate groups should be positioned atop a surface calcium ion, only two distinct directions are reasonable, as shown in the model in Fig. 6c. These two directions include an opening angle of 48°, precisely as observed in the experiment.

A further structural change is induced when annealing the substrate to 610 K. Upon this second annealing step, the chlorine atoms are expected to dissociate from the dimers, allowing for coupling of the dimers into larger molecular structures. Depending on the conformation of the dimers (S or U-shaped), either zigzag chains (coupling of S-shaped dimers) or ring structures (coupling of two U-shaped dimers) should be formed on the surface. Indeed, two types of structures exist on the surface after the second annealing step as shown in Fig. 6d. Among them, it is possible to identify zigzag chains, as shown in the zoom in Fig. 6e. Superimposing a model of the expected chains demonstrates a perfect size match of the observed periodicity along the chain with the repeat distance of the zigzag structure. Moreover, a specific direction of the chains with respect to the underlying substrate is expected from the

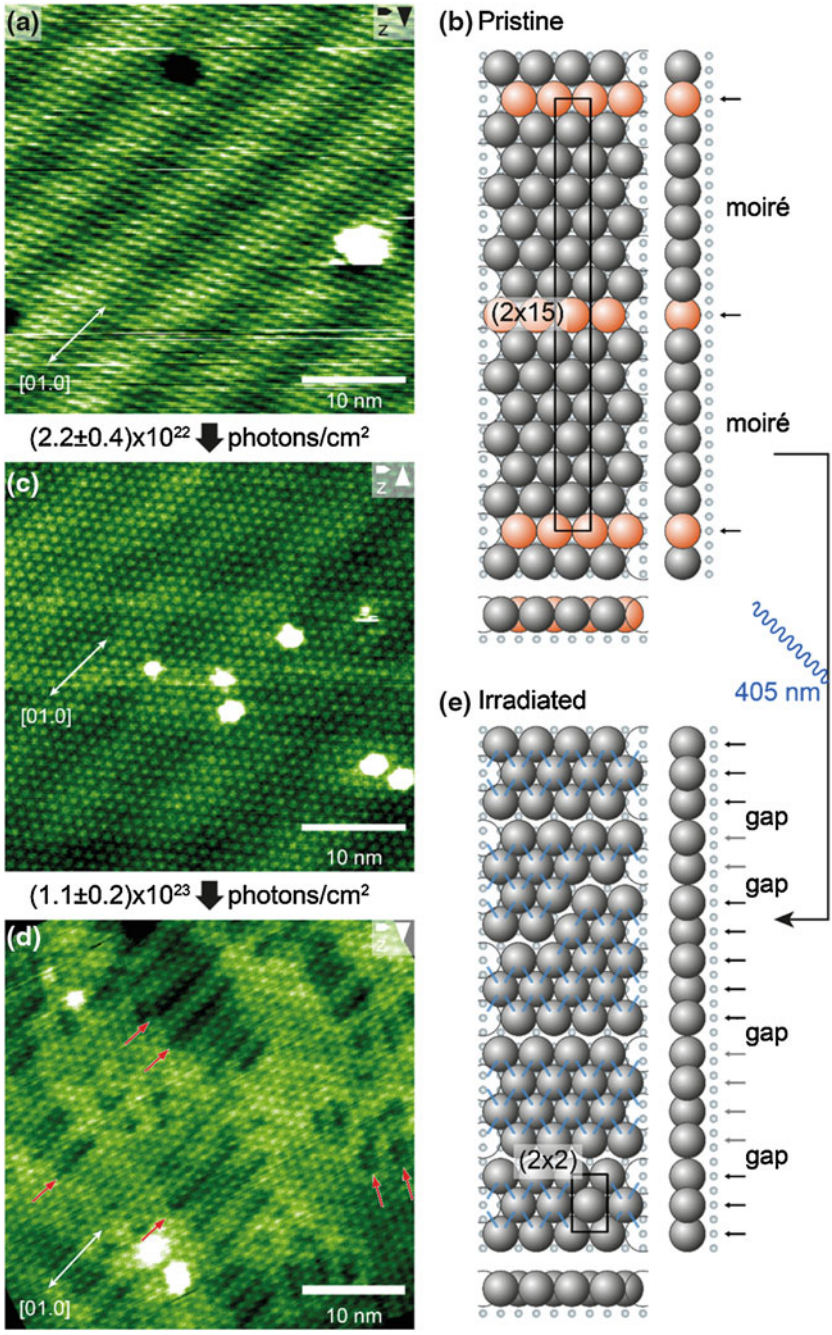
(a)
[01.0]
10 nm
(2.2±0.4)x10²² photons/cm²
(c)
[01.0]
10 nm
(1.1±0.2)x10²³ photons/cm²
(d)
[01.0]
10 nm
(b) Pristine
(2x15)
moiré
moiré
405 nm
(e) Irradiated
(2x2)
gap
gap
gap
gap

◀ **Fig. 7** Photochemical initiation of an on-surface reaction on a bulk insulator surface [28]. **a** Upon deposition of C_{60} onto calcite(104), elongated islands are formed that show a distinct moiré pattern [18]. **b** The moiré pattern can be readily explained by the different lattice mismatch in the two surface directions as shown in the model. **c** Irradiation with a total of about 10^{22} photons results in an alteration of the structure. The moiré pattern becomes aperiodic. **d** Upon further irradiation with a total of 10^{23} photons, the moiré pattern is vanished. Gaps are formed in the molecular film, which can be understood by considering the molecular model (**e**)

fact that the carboxylate groups of the chain should be placed atop surface calcium ions. One specific direction allows for optimizing this carboxylate–calcium interaction, which is the one drawn in the model in Fig. 6e. This direction is precisely what is observed experimentally, giving further evidence for the proposed model. Besides the chains, also roundish features are revealed on the surface as shown in Fig. 6f. These features can be understood by covalent coupling of two U-shaped dimers. Again, the superimposed model fits in size with the observed ring-like structures. For this structure, it is not possible to optimize the position of all four carboxylate groups within the ring atop a surface calcium ion. The different adsorption positions might be the reason for the somewhat asymmetric appearance of the ring structures. This example demonstrates the feasibility to transfer the strategy of sequential and site-specific reactions to a bulk insulator surface, namely calcite(104).

4.3 Photochemical Initiation

In the above examples, the reaction was initiated by annealing the substrate to a specific temperature, thereby inducing homolytic bond cleavage at the phenyl-halide bond. Although this approach is straightforward experimentally, it bears a severe drawback, which arises from the comparatively weak molecule–surface interaction.

For many molecule–surface systems studied, annealing of the substrate with the aim to initiate the linking reaction only resulted in desorption of the educt molecules from the surface. Thus, it appears mandatory to explore other means of reaction initiation. In this context, photochemical linking is an obvious strategy to decouple reaction initiation from desorption [28–30].

As a straightforward example, C_{60} molecules were chosen, which are known to polymerize in a [2 + 2] cycloaddition when irradiated with light [28]. Upon deposition of C_{60} onto calcite(104) held at room temperature, elongated islands are found on the surface [18]. These islands are formed by C_{60} molecules that arrange in a hexagonal pattern as shown in Fig. 7a. Considering the C_{60}–C_{60} distance in bulk C_{60} of 1.02 nm readily shows that the molecular repeat distance fits nicely to the twofold substrate periodicity of 0.50 nm along the [010] direction. This is why one close-packed direction of the hexagonal molecular layer is aligned along the [010] substrate direction. For the other substrate direction, however, the substrate

periodicity of 0.81 nm does not fit to the periodicity of the molecular film of 1.02 nm · sin (60°) = 0.88 nm. Consequently, a moiré pattern is formed, which is readily observed as a height modulation in the image shown in Fig. 7a. A model for the pristine molecular layer is given in Fig. 7b, showing the molecular (2 × 15) superstructure. Molecules that adopt the same adsorption positions (except for a rotation of the underlying carbonate groups) are marked by arrows, directly reflecting the observed moiré pattern. When irradiating the surface covered with molecules with light (405 nm laser diode), the structure changes considerably. Upon a first irradiation step, the moiré pattern starts to degrade and becomes aperiodic as shown in Fig. 7c [28]. Further irradiation results in vanishing of the moiré pattern and the appearance of gaps between the molecules, as marked by the arrows in Fig. 7d. Interestingly, the majority of these gaps are aligned along the [010] direction. Both observations, the vanishing of the moiré pattern as well as the formation of gaps aligned along the [010] direction, can be explained by a simple model in a straightforward manner. As no lattice mismatch exists along the [010] direction, there is no driving force for a linking reaction along this direction. However, linking along the other close-packed row directions of the molecular film, as indicated by the short lines in the model in Fig. e results in a reduction of the molecule–molecule distance along the [-4-21] substrate direction. Interestingly, when C_{60} trimers are formed, the molecule–molecule distance of 0.92 nm [31] projected to the [-4-21] direction becomes 0.80 nm. Thus, upon covalent coupling of the C_{60} molecules along this direction, the lattice mismatch can be lifted, explaining the vanishing of the moiré pattern. As a consequence of the linking along these specific directions, the molecules move closer only in [-4-21] direction, thereby creating a gap that opens along the [010] direction (see Fig. 7e).

These results show that photochemical initiation is possible on a bulk insulator surface. Moreover, the studied system of C_{60} on calcite(104) illustrates how the underlying substrate can be exploited deliberately for guiding the reaction in a specific direction. This constitutes a promising strategy for increasing the structural control in addition to the sequential approach presented above.

5 Summary and Outlook

In recent years, on-surface synthesis has attracted considerable attention due to the impressive potential of this strategy for fabricating novel functional structures at surfaces. This is especially true for the field of future molecular electronics, where tailor-made molecular structures such as wires and switches are needed for constructing functional devices. Having these applications in mind requires strategies to decouple the electronic structure of the molecular network from the underlying substrate. Consequently, electrically insulating rather than metallic substrates are highly interesting for these applications. Compared to metallic substrates, however, little is known about on-surfaces synthesis principles on bulk insulating surfaces. A simple transfer of on-surface synthesis strategies developed on metallic surfaces

towards insulating substrates has been demonstrated to be difficult. This is due to the comparably weak molecule–surface interaction present on many insulating surfaces studied so far. Thus, on-surface synthesis on insulating substrates requires to carefully consider the molecule–surface interaction of the system of interest. For the systems studied so far, it has been shown that choosing educt molecules with dedicated anchor functionality appears to be essential for avoiding desorption upon thermal activation of the on-surface reaction. While this need can be partially met by choosing standard educt molecules, the impressive variability of organic synthesis will surely boost the success of on-surface synthesis by providing tailored molecules with dedicated anchor functionalities and reaction sites. Moreover, reaction mechanisms usually requiring the presence of metal atoms, e.g., the Ullmann reaction, need to be reconsidered for transferring these principles to insulating substrates. So far, little is known about the details of on-surface reactions on insulating substrates, clearly asking for theoretical efforts to elucidate the individual reaction steps.

A major effort of future research will be dedicated to increasing the library of available reaction types by exploring suitable educt molecules. Various means of reaction initiation need to be tested as well as co-deposition of two or more educt molecules. Moreover, it will be mandatory to further increase structural control by extending and combining control strategies such as sequential or substrate-guided reactions.

References

1. Grill, L., Dyer, M., Lafferentz, L., Persson, M., Peters, M.V., Hecht, S.: Nano-architectures by covalent assembly of molecular building blocks. Nature Nanotech. **2**(11), 687–691 (2007)
2. Lafferentz, L., Eberhardt, V., Dri, C., Africh, C., Comelli, G., Esch, F., Hecht, S., Grill, L.: Controlling on-surface polymerization by hierarchical and substrate-directed growth. Nat. Chem. **4**(3), 215–220 (2012)
3. Gourdon, A.: On-surface covalent coupling in ultrahigh vacuum. Angew. Chem. Int. Ed. **47** (37), 6950–6953 (2008)
4. Gourdon, A.: Synthesis of "molecular landers". Eur. J. Org. Chem. **1998**(12), 2797–2801 (1998)
5. Repp, J., Meyer, G., Stojkovic, S.M., Gourdon, A., Joachim, C.: Molecules on insulating films: Scanning-tunneling microscopy imaging of individual molecular orbitals. Phys. Rev. Lett. **94**(2), 026803 (2005)
6. Rosei, F., Schunack, M., Naitoh, Y., Jiang, P., Gourdon, A., Lægsgaard, E., Stensgaard, I., Joachim, C., Besenbacher, F.: Properties of large organic molecules on metal surfaces. Prog. Surf. Sci. **71**(5–8), 95–146 (2003)
7. Giessibl, F.J.: Advances in atomic force microscopy. Rev. Mod. Phys. **75**(3), 949–983 (2003)
8. Kunstmann, T., Schlarb, A., Fendrich, M., Wagner, T., Möller, R., Hoffmann, R.: Dynamic force microscopy study of 3,4,9,10-perylenetetracarboxylic dianhydride on KBr(001). Phys. Rev. B **71**(12), 121403 (2005)
9. Nony, L., Bennewitz, R., Pfeiffer, O., Gnecco, E., Baratoff, A., Meyer, E., Eguchi, T., Gourdon, A., Joachim, C.: Cu-TBPP and PTCDA molecules on insulating surfaces studied by ultra-high-vacuum non-contact AFM. Nanotechnology **15**(2), S91 (2004)

10. Burke, S.A., Ji, W., Mativetsky, J.M., Topple, J.M., Fostner, S., Gao, H.J., Guo, H., Grütter, P.: Strain induced dewetting of a molecular system: Bimodal growth of PTCDA on NaCl. Phys. Rev. Lett. **100**(18), 186104 (2008)
11. Schütte, J., Bechstein, R., Rohlfing, M., Reichling, M., Kühnle, A.: Cooperative mechanism for anchoring highly polar molecules at an ionic surface. Phys. Rev. B **80**(20), 205421 (2009)
12. Such, B., Trevethan, T., Glatzel, T., Kawai, S., Zimmerli, L., Meyer, E., Shluger, A.L., Amijs, C.H.M., de Mendoza, P., Echavarren, A.M.: Functionalized Truxenes: Adsorption and diffusion of single molecules on the KBr(001) surface. ACS Nano **4**(6), 3429–3439 (2010)
13. Pawlak, R., Nony, L., Bocquet, F., Olson, V., Sassi, M., Debierre, J.M., Loppacher, C., Porte, L.: Supramolecular assemblies of 1,4-Benzene Diboronic Acid on KCl(001). J. Phys. Chem. C **114**(20), 9290–9295 (2010)
14. Loske, F., Lübbe, J., Schütte, J., Reichling, M., Kühnle, A.: Quantitative description of C_{60} diffusion on an insulating surface. Phys. Rev. B **82**(15), 155428 (2010)
15. Rahe, P., Kittelmann, M., Neff, J.L., Nimmrich, M., Reichling, M., Maass, P., Kühnle, A.: Tuning molecular self-assembly on bulk insulator surfaces by anchoring of the organic building blocks. Adv. Mater. **25**(29), 3948–3956 (2013)
16. Mativetsky, J.M., Burke, S.A., Fostner, S., Grutter, P.: Nanoscale pits as templates for building a molecular device. Small **3**(5), 818–821 (2007)
17. Hinaut, A., Lekhal, K., Aivazian, G., Bataillé, S., Gourdon, A., Martrou, D., Gauthier, S.: NC-AFM study of the adsorption of hexamethoxytriphenylene on KBr(001). J. Phys. Chem. C **115**(27), 13338–13342 (2011)
18. Rahe, P., Lindner, R., Kittelmann, M., Nimmrich, M., Kühnle, A.: From dewetting to wetting molecular layers: C_{60} on $CaCO_3(10\underline{1}4)$ as a case study. Phys. Chem. Chem. Phys. **14**(18), 6544–6548 (2012)
19. Abel, M., Clair, S., Ourdjini, O., Mossoyan, M., Porte, L.: Single layer of polymeric Fe-phthalocyanine: An organometallic sheet on metal and thin insulating film. J. Am. Chem. Soc. **133**(5), 1203–1205 (2011)
20. Bombis, C., Ample, F., Lafferentz, L., Yu, H., Hecht, S., Joachim, C., Grill, L.: Single molecular wires connecting metallic and insulating surface areas. Angew. Chem. Int. Ed. **48** (52), 9966–9970 (2009)
21. Kittelmann, M., Rahe, P., Nimmrich, M., Hauke, C.M., Gourdon, A., Kühnle, A.: On-surface covalent linking of organic building blocks on a bulk insulator. ACS Nano **5**(10), 8420–8425 (2011)
22. Kittelmann, M., Nimmrich, M., Lindner, R., Gourdon, A., Kühnle, A.: Sequential and site-specific on-surface synthesis on a bulk insulator. ACS Nano **7**(6), 5614–5620 (2013)
23. Baer, D.R., Blanchard, D.L.: Studies of the calcite cleavage surface for comparison with calculation. Appl. Surf. Sci. **72**(4), 295–300 (1993)
24. Tröger, L., Schütte, J., Ostendorf, F., Kühnle, A., Reichling, M.: Concept for support and cleavage of brittle crystals. Rev. Sci. Instrum. **80**(6), 063703 (2009)
25. Kittelmann, M., Rahe, P., Kühnle, A.: Molecular self-assembly on an insulating surface: interplay between substrate templating and intermolecular interactions. J. Phys.: Condens. Matter **24**(35), 354007–354013 (2012)
26. Kittelmann, M., Nimmrich, M., Neff, J.L., Rahe, P., Gren, W., Bouju, X., Gourdon, A., Kühnle, A.: Controlled activation of substrate templating in molecular self-assembly by deprotonation. J. Phys. Chem. C **117**(45), 23868–23874 (2013)
27. Kittelmann, M., Rahe, P., Nimmrich, M., Hauke, C.M., Gourdon, A., Kühnle, A.: Direct visualization of molecule deprotonation on an insulating surface. ACS Nano **6**(8), 7406–7411 (2012)
28. Lindner, R., Rahe, P., Kittelmann, M., Gourdon, A., Bechstein, R., Kühnle, A.: Substrate templating guides the photoinduced reaction of C_{60} on calcite. Angew. Chem. Int. Ed. **53**(30), 7952–7955 (2014)
29. Sloan, D., Sun, Y.M., Ihm, H., White, J.M.: Photochemistry of iodobenzene adsorbed on sapphire(0001). J. Phys. Chem. B **102**(35), 6825–6830 (1998)

30. Palma, C.A., Diller, K., Berger, R., Welle, A., Bjork, J., Cabellos, J.L., Mowbray, D.J., Papageorgiou, A.C., Ivleva, N.P., Matich, S., Margapoti, E., Niessner, R., Menges, B., Reichert, J., Feng, L., Rader, H.J., Klappenberger, F., Rubio, A., Müllen, K., Barth, J.V.: Photoinduced C–C reactions on insulators toward photolithography of graphene nanoarchitectures. J. Am. Chem. Soc. **136**(12), 4651–4658 (2014)
31. Onoe, J., Nakayama, T., Nakao, A., Hashi, Y., Esfarjani, K., Kawazoe, Y., Aono, M., Takeuchi, K.: In Situ FTIR, XPS, and STM studies of the nano-structure of a photopolymerized C_{60} Film. Mol. Cryst. Liq. Cryst. **340**(1), 689–694 (2000)

Bottom-Up Fabrication of Two-Dimensional Polymers on Solid Surfaces

Markus Lackinger

Abstract Two-dimensional polymers are a novel class of future materials that are not purely hypothetical anymore, but have not been realized in full yet. A promising and versatile synthetic approach is the bottom-up fabrication by polymerization of monomers into covalently cross-linked nanostructures on solid surfaces. This chapter introduces the synthetic approach consisting of monomer deposition and activation, and describes a typical characterization scheme by established surface science techniques—high-resolution Scanning Tunneling Microscopy for structures and X-ray Photoelectron Spectroscopy for chemical state. The coupling chemistry is largely predetermined by monomer functionalization and various coupling reactions can be utilized to achieve cross-linking on surfaces. A major aim of this chapter is to compare and discuss the most popular interlinking chemistry and to highlight important implications when classical reactions are transferred from a beaker to a solid surface. The most important distinction is whether coupling proceeds irreversibly and remains kinetically controlled or whether thermodynamical control is possible. Ullmann coupling is a prominent example for an irreversible reaction. Recent achievements with focus on defect formation as well as the occurrence and utility of organometallic intermediates are discussed. Long-range ordered covalent organic frameworks were demonstrated based on boronic acid condensation. In this context, emphasis will be put on the importance of bond reversibility. Moreover, coupling reactions of terminal alkynes are introduced, and both possibilities and limitations are illustrated by referring to recent examples.

M. Lackinger (✉)
Deutsches Museum, Museumsinsel 1, 80538 Munich, Germany
e-mail: markus@lackinger.org; markus.lackinger@tum.de

M. Lackinger
Physik-Department, Technische Universität München, James-Franck-Straße 1, 85748 Garching, Germany

A. Gourdon (ed.), *On-Surface Synthesis*, Advances in Atom and Single Molecule Machines, DOI 10.1007/978-3-319-26600-8_10

1 Motivation and Aim

Molecular self-assembly has been studied on surfaces for almost three decades now. Although this research could already be considered as a first liaison between surface science and organic chemistry, this relationship grew more intense in 2007–2008 when the two seminal papers by Grill et al. and Porte et al. on Ullmann coupling and boronic acid condensation indicated that solid surfaces may also be an advantageous venue for coupling reactions between comparatively large organic molecules [1, 2]. This had at least two implications: On the one hand, the whole tool-box of microscopic and spectroscopic surface science techniques became available to study the progression, intermediates, and products of chemical reactions. On the other hand, the apparent templating effect of surfaces by confinement of the reacting species in two dimensions has ignited ideas to use "flatlands" for the synthesis of extended 2D networks or ultimately for the fabrication of novel 2D materials. It is intriguing to compare self-assembled monolayers (SAMs) on surfaces with graphene, the most prominent 2D material. As illustrated in Fig. 1, graphene is extremely stable and the strong coupling between its carbon atoms by covalent bonds promotes the ability to conduct electrons, not to mention the unique electronic band structure and the unprecedented charge carrier mobilities. The properties of graphene, however, are mostly predetermined by its unalterable structure, and an atomically precise modification remains extremely challenging. On the other hand, SAMs are structurally and chemically extremely versatile, owing to the diversity and variability of its constituents, the organic molecules. Yet, the typical intermolecular bonds that stabilize these monolayers, i.e. van-der-Waals, hydrogen, or metal coordination bonds, are relatively weak. This not only accounts for the comparatively low chemical, mechanical, and thermal stability of SAMs, but also precludes electronic transport across these structures. This direct comparison naturally sets the goal of getting the best of both worlds—versatility and stability—

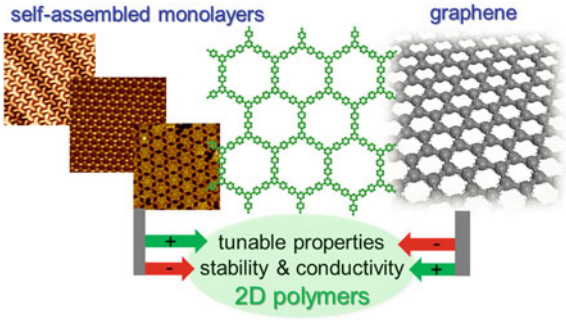

Fig. 1 SAMs versus graphene. Major advantages of SAMs are tunability and versatility which in turn are disadvantages of graphene. On the contrary, high stability and conductivity are application-relevant properties of graphene, but substantial drawbacks of SAMs. Both advantages are united in 2D polymers that bridge these two materials

by upgrading SAMs to two-dimensional (2D) polymers through covalent cross-linking. The terminology of the field has not settled yet, so 2D polymers are not rigorously defined. Distinctions could be made concerning the degree of structural order or the thickness—one atom versus one monomeric unit. Nevertheless, the materials which are the ultimate goal of the subsequently described endeavors would be defined as organic, fully covalently cross-linked networks which are only one atom thick and crystalline, i.e., exhibit long-range order and translational symmetry. The pursued synthetic approach toward 2D polymers is on-surface polymerization, where the coupling reactions are inspired by synthetic organic chemistry and the preparation and characterization tools are provided by surface science.

2 Typical Approach

A scheme of the typical approach for on-surface polymerization experiments is shown in Fig. 2 and comprises three steps: deposition, activation, and characterization. All individual steps can be carried out either under ambient or ultra-high vacuum (UHV) conditions. The benefit of working under ambient conditions is the low experimental effort, but this approach can suffer from limitations, e.g. concerning the usage of more reactive surfaces. Deposition under ambient conditions is typically performed from solution by drop-casting or spin-coating. Albeit relatively straightforward, sample homogeneity can still be a challenge.

Deposition in UHV is typically performed through the vapor phase of the compound. Smaller molecules with sufficiently high vapor pressure at room temperature can just be dosed through a leak valve, for compounds with larger sublimation enthalpies standard deposition sources with heated crucibles (Knudsen

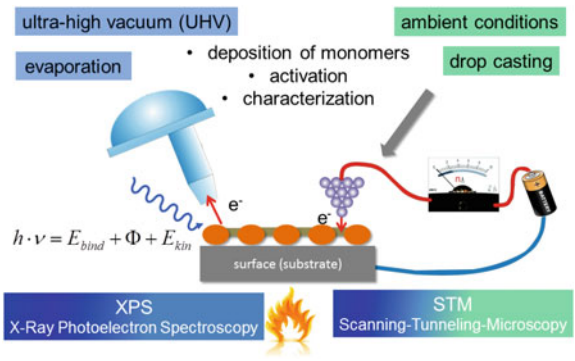

Fig. 2 Illustration of the typical experimental approach consisting of the three steps: deposition, activation, and characterization. Deposition and activation can both be conducted under UHV (*blue*) and ambient (*green*) conditions. Similarly, STM can be carried out in both environments, whereas XPS measurements are restricted to UHV, but are applicable to ex situ prepared samples

cells) are used. Limitations can arise for both deposition methods: solution deposition can be limited by low solubility, especially for larger molecules, whereas the reactivity of a compound can preclude thermal sublimation. Heating the crucible initiates a kinetic competition between sublimation and reaction. Depending on the respective enthalpies or activation barriers, reactions in the crucible can become favored, leading to the formation of larger aggregates that cannot be sublimed anymore.

Thermal annealing is the most common method for activating reactions on surfaces. However, alternative means of activation include irradiation with electrons—globally by an electron gun or locally by an STM tip—or energetic light. Depending on the reactivity of the system, thermal energy at room temperature can already be sufficient; hence, further annealing is not needed. Again external energy input activates two competing processes, i.e., the intended reaction on the surface, but also desorption from the surface. A typical solution to this "desorption problem" is increasing the adsorption energy of the monomers by enlarging the size of the organic backbone or using already preformed dimers, trimers etc. instead of monomers. However, by the same token the temperature required for deposition via sublimation increases. Accordingly, a compromise concerning the monomer size has to be found, where deposition via sublimation is still possible, and thermal activation of the polymerization on the surface is not impaired by desorption. In principle, it is also possible to work with protecting groups for sublimation and subsequent deprotection on the surface or to use more sophisticated deposition techniques for thermally instable compounds as electrospray ionization. It is noteworthy, that the reactivity arises from the specific combination of monomer and surface. This was nicely demonstrated by the example of alkanes on Au(110), where even the combination of relatively inert molecules with a relatively noble surface gave rise to unexpected coupling reactions [3].

For characterization mostly typical surface science techniques are used. Since on-surface polymerization has largely been developed from the self-assembly community, scanning tunneling microscopy (STM) is one of the favorite characterization tools. Molecular resolution can relatively easily be accomplished with widely available instruments, and imaging in real space facilitates a direct structure assessment. Moreover, in many cases, STM derived inter- or intramolecular distances already facilitate unambiguous verification of covalent coupling. In this context, it is particularly important that STM is not restricted to long-range ordered structures, because the covalent networks are in most cases less well-ordered than their supramolecular counterparts and exhibit high defect densities. The basic STM sample requirement of electrical conductivity is so far not a serious limitation, as for many coupling reactions the catalytic activity of metals is indispensable. Nevertheless, insulator surfaces are particularly interesting, especially for electronic transport measurements through the covalent nanostructures. On insulators, not only the reaction mechanisms can be expected to be very different, but also more sophisticated tools as non-contact atomic force microscopy (NC-AFM) become necessary.

Even though formation of new covalent bonds is often concluded from distance measurements in STM images, a complementary, chemically more sensitive characterization can be quite useful. Therefore, X-ray photoelectron spectroscopy (XPS) is ideally suited: Chemical core level shifts can unambiguously prove the proposed reaction or facilitate identification of the chemical state, especially when STM images are inconclusive. Moreover, the global character of XPS efficiently leads to solid statistical conclusions that are cumbersome to derive from local STM data. This is particularly useful for studying the progression of a reaction, e.g. the ratio between reacted and unreacted monomers in dependence of a specific activation protocol. At the moment, alternative spectroscopic techniques are less commonly used, despite their potential to provide additional complementary information. In particular, vibrational spectroscopy can also reveal the formation of new bonds or molecular groups. For instance, ex situ Raman spectroscopy was successfully employed to verify the formation of atomically precise graphene nano-ribbons [4]. Also first steps to access the electronic structure were taken by scanning tunneling spectroscopy and photoelectron spectroscopy experiments [5].

At present, the lack of long-range order in most covalent networks precludes the use of surface-sensitive diffraction techniques as low electron energy diffraction (LEED). Such experiments facilitate a very efficient and reliable structural characterization on a more global scale and would increase the precision of structural data. Furthermore, the epitaxial relation between covalent networks and supporting surface could easily be derived. More sophisticated techniques as Spot-Profile Analysis LEED may even give access to a global characterization of domain sizes. The recent advancements of structural quality will also bring LEED experiments on covalent nanostructures within reach.

3 Coupling Reactions

The volume of organic chemistry textbooks impressively demonstrates the richness and versatility of suitable functional groups and reactions for chemical coupling. A distinction can be made between homo- and crosscoupling, i.e., whether the same or different molecular species react with each other. Crosscouplings are much more versatile, but their implementation in surface chemistry remains challenging. Co-deposition of two different monomers in a stoichiometric ratio may be cumbersome, but is not a principal problem. However, both functional groups involved in crosscoupling are reactive and very often have a pronounced affinity for homocoupling which is difficult to fully suppress. In synthetic organic chemistry, a kinetic competition between different coupling reactions results in a lower yield, but on surfaces it hampers the formation of ordered networks. Nevertheless, first examples such as, for instance, Sonogashira coupling of iodobenzene and phenylacetylene was demonstrated on Au(111) [6]. The art is finding reaction conditions, i.e., surfaces, coverages, temperatures, deposition sequences, etc. that exclusively promote crosscoupling.

A further distinction can be made between reactions that can become reversible under suitable conditions or remain irreversible in any event. Condensation where a smaller molecule is formed and eliminated during the coupling is a prototypical type of possibly reversible reaction. An example is the release of H_2O during the self-condensation (dehydration) of boronic acids or the Schiff base reaction. According to Le Chatelier's principle, increasing the amount of H_2O in the system shifts the chemical equilibrium toward the unreacted starting material. In other words, a water atmosphere induces bond reversibility, and hence promotes error correction which is so far considered a necessity for the growth of long-range ordered structures of any kind. A more detailed description of boronic acid condensation on surfaces is provided in the next section. Ullmann coupling is a prominent example for an irreversibly proceeding coupling reaction on surfaces. The newly formed bonds are kinetically inert and cannot be opened up again under normal reaction conditions. This implies that Ullmann polymerization is kinetically controlled and any type of error correction mechanism is absent. Consequently, the structural quality is significantly lower than for SAMs, or the networks can even be entirely irregular, respectively. The dimensionality of the targeted covalent nanostructure plays an important role here: 1D structures as graphene nano-ribbons or polyphenylene chains do not suffer from high defect densities, because the monomers are just stringed together and this binding motif does not allow for topological defects. 2D networks, however, have many more possibilities to form defects, rendering the growth of long-range ordered structures based on irreversible coupling reactions truly challenging or even impossible.

4 Boronic Acid Condensation

The introduction of covalent organic frameworks (COF)—purely organic crystalline porous materials based on covalently cross-linked organic entities—by Yaghi and co-workers initiated a new and ever growing research direction [7, 8]. COFs are exclusively composed of light elements and exhibit high permanent porosities. This leads to ultralow densities which render these materials particularly promising for mobile gas storage applications. Most COFs exhibit a layered structure comparable to graphite, i.e. covalent bonds within the layers, whereas relatively weak interlayer bonds mediate a defined stacking. The first COFs were obtained by either the self-condensation of 1,4-benzene diboronic acid (BDBA) into COF-1 or the co-condensation with hexahydroxytriphenylene (HHTP) into COF-5 [7]. X-ray powder diffractometry revealed a high degree of crystallinity that was attributed to slightly reversible reaction conditions in the solvothermal synthesis. Apparently, the layered COF structure was inspiring for surface scientists, and Porte et al. were the first to demonstrate boronic acid coupling on Ag(111) [1]. Even though the BDBA monomer is only ditopic, the resulting networks are fully cross-linked in two dimensions. The reason can be understood by means of the reaction scheme for para-diboronic acids in Fig. 3a illustrating the cyclocondensation of three

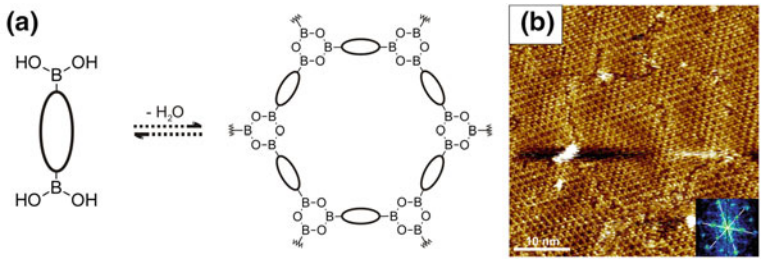

Fig. 3 **a** Reaction scheme of the self-condensation of para-diboronic acids into 2D COFs. **b** STM image of a 2D COF-1 monolayer synthesized from BDBA on graphite(0001) under reversible reaction conditions. The *inset* shows the corresponding FFT. Reprinted with permission from Refs. [12, 13]. Copyright 2012 and 2011 American Chemical Society

monomers: three boronic acid groups form a B_3O_3 boroxine ring, whereby three water molecules are released. Detailed atomistic simulations of the polymerization on Ag(111) suggest coupling via an intermediate dimer and propose an overall endothermic reaction [9]. The driving force of the boronic acid polycondensation is the entropy gain through the water release. Boronic acid condensation on surfaces was first demonstrated under UHV conditions, where the released water is immediately removed from the system by the vacuum pumps [1]. In the absence of gaseous water, boronic acid condensation proceeds irreversibly, i.e. without the possibility for error correction, resulting in less regular networks with many defects. To improve the networks, Porte et al. systematically studied the dependence between structural quality and reaction parameters, e.g., different metal surfaces, temperatures, and deposition rates [10]. For a meaningful comparison and solid conclusions, a quantitative assessment of the structural quality becomes necessary. For rather irregular networks, a statistical analysis of STM data is most appropriate. An elaborate statistical analysis based on the minimal spanning tree revealed that in UHV the best boronic acid networks could be grown on silver surfaces by working with higher deposition rates [10].

Yet, the key to structural perfection is taking advantage of bond reversibility. For boronic acid condensation this means that the polymerization has to be carried out in a water atmosphere. So far it is not quantitatively known how much water is actually required. From own experiments, we conclude that a water partial pressure in the order of 10^{-6} mbar—the highest bearable in a UHV system—is not sufficient. Consequently, ambient conditions are the best environment to realize reversible reaction conditions. In this synthetic approach, the monomers are typically deposited from solution and the polymerization is activated in a small autoclave or reactor by heating to temperatures of 100–150 °C. The reversibility inducing water can be supplied either by adding pure liquid water or by the thermally activated release of crystal water from hydrates [11]. For instance, blue vitriol ($CuSO_4 \cdot 5H_2O$) reversibly releases part of its crystal water already around 100 °C. A representative STM image of a 2D COF obtained by reversible condensation of BDBA on graphite is depicted in Fig. 3b. One interesting aspect of this approach is

that bond reversibility can be switched on and off at will, just by the presence or absence of water. Even though no in situ microscopic studies of the polymerization are available, it appears reasonable that a slow transition from the fully reversible (non-bonding) to the irreversible regime is an important ingredient for high-quality networks, in order to always remain close to equilibrium. This transition is achieved by reducing the water partial pressure and/or the temperature. Water can be removed by working in an open system or when using $CuSO_4 \cdot 5H_2O$ as a water source, by rehydration at lower temperature.

In bulk COF synthesis, almost infinite structural versatility is achieved by co-condensation of boronic acids with diols. Proof of principle for this co-condensation on surfaces has already been provided with HHTP and BDBA in the seminal UHV work [1]. However, generally applicable protocols of how this crosscoupling on surfaces can yield high-quality networks have so far not been developed. A promising approach to bimolecular covalent networks is deposition of one monomer onto the surface and supplying the other monomer through the vapor phase, as nicely demonstrated for the co-condensation of amines and aldehydes [14]. In case the reactor has to be heated to either activate the reaction or to increase the vapor pressure of the compound in the gas phase, desorption of the compound on the surface has to be prevented by a high adsorption energy. Moreover, it is important to suppress homocoupling on the surface, i.e., by adsorbing a relatively inert compound.

Yet, structural versatility can already be achieved with the self-condensation of para-diboronic acids. For instance, tailoring of pore sizes by varying the length of the organic backbone has been demonstrated with a homologous series of diboronic acids with backbones ranging from phenyl to quaterphenyl [12]. Similarly, pyrene-based 2D COFs indicated possibilities to tune the chemical nature of the organic scaffold. A serious limitation for solution-based approaches, however, arises from the limited solubility of larger molecules. Deposition of larger boronic acids by vacuum sublimation is also not possible, because the relatively high sublimation temperatures required for larger monomers already activate the preferential polymerization in the crucible of the deposition source. Alternative concepts would be using protecting groups for sublimation and subsequent deprotection on the surface [15]. On the other hand, the high reactivity of boronic acids can also be used for the "in-crucible" synthesis of more complex molecules from abundantly available smaller boronic acids as p-bromobenzene boronic acid and 3,5-dibromophenyl boronic acid [16, 17]. Already these smaller boronic acids are too large for thermal sublimation. Accordingly, when heating the crucible, three monomers condensate into the corresponding trimer with a newly formed boroxine ring as threefold symmetry center. These compounds are then sufficiently inert for thermal sublimation.

The reversibility of boronic acid condensation in a water atmosphere is a blessing and a curse. On one hand, it provides the grounds for the synthesis of long-range ordered covalently cross-linked networks that feature the anticipated thermal and mechanical stability. On the other hand, not only the surface-supported 2D COFs but also their bulk counterparts degrade under ambient conditions, due to humidity-induced bond breaking.

Moreover, it is instructive to study the electronic properties of boronic acid-derived COFs. Experimental band structure data are unfortunately not available; however, density functional theory (DFT) simulations for a COF-1 monolayer suggest a semiconducting behavior with a band gap in the order of ~3 eV [17]. Apart from the band gap, the dispersion relation is equally important. The 2D COF-1 bands come out essentially flat, indicating localized electrons with high effective mass. The reason for this is the insulating effect of the boroxine rings which effectively decouple the phenyl rings from each other. In other words, any 2D COF synthesized by boronic acid condensation will not be suitable as an electronically active material. It is worth mentioning that nominally π-conjugated networks can be synthesized by condensation reactions, whereby the condensation of amines with aldehydes is a proven example for on-surface polymerization [18].

Based on the combined properties of boronic acid-derived 2D COFs—structural versatility, high mechanical stability, and water solubility—applications where a porous network is required as a template for one processing step, while it should be removed in a subsequent processing step appear most promising.

5 Ullmann Coupling

The enormous interest in highly stable and electronically conjugated networks calls for a coupling chemistry that establishes new C–C bonds. To this end, the surface variant of classical Ullmann coupling as introduced by Grill et al. is highly appropriate [2]. The principal reaction scheme is relatively straightforward: brominated or iodinated precursor molecules are deposited onto a metal surface, typically Cu, Ag, or Au. Upon adsorption, the weakly bonded halogen substituents are split off with the aid of the catalytic properties of the metal surface. DFT simulations propose an activation barrier in the order of 0.5–1.0 eV for the overall exothermic dehalogenation [19]. The energy gain is partly related to the relatively strong adsorption of the spit off halogens. The activation barrier decreases in the order Au > Ag > Cu, i.e., with increasing reactivity of the metal surface, and is for all surfaces studied ~0.3 eV lower for iodine than for bromine substituents. This trend appears plausible, considering the differences in carbon–halogen bond strength. However, the bond dissociation energy of C–I is ~0.65 eV lower than for C–Br in iodobenzene versus bromobenzene [20], indicating a distinct surface influence. In any case, iodinated precursors are more reactive, and deiodination readily takes place at room temperature (RT) even on less-reactive gold surfaces [21]. On the contrary, the reactivity of the metal surface plays a decisive role for brominated compounds: on copper, debromination already occurs at room temperature, whereas on gold additional heating to ~150–200 °C is required [22]. The vast differences in activation temperatures for deiodination versus debromination on gold can be used for a defined sequential coupling by selective activation of iodine and bromine sites [23, 24]. Silver surfaces occupy an interesting intermediate position, where partial debromination is observed at room temperature, whereas full

debromination also requires additional heating [25]. The incomplete debromination on silver cannot simply be explained with a fixed value for the reaction barrier, and detailed studies may shine more light on the actual mechanism of surface-catalyzed dehalogenation.

Dehalogenation results in so called surface-stabilized radicals (SSR), where the dangling bonds of the dehalogenated carbons bind to the underlying metal surface. The further progression of the coupling reaction strongly depends on the metal surface. On Au(111), the generally accepted picture is that the SSR are mobile, diffuse around and form covalent bonds upon encounter. However, the detailed atomistic knowledge of these processes is not very advanced: The nucleation behavior is not well studied, e.g., the role of step-edges for immobilization of monomers. It is also not clear, how fast the coupling step takes place, i.e., whether there are effective entropic or even energetic barriers. Nevertheless, the coupling reaction is kinetically controlled and the irreversibility of newly formed interlinks typically results in irregular networks with high defect densities. In most studies, Ullmann polymerization is carried out under UHV conditions, however, drop-casting of respective solutions onto preheated Au(111) surfaces under ambient conditions has also yielded covalent structures [26, 27].

On the more, reactive Cu and Ag surfaces intrinsic adatoms interfere with the coupling step. Instead of directly establishing covalent bonds, the SSR form intermediate organometallic complexes and networks based on carbon-metal-carbon interlinks [28–30]. Upon further annealing, the metal atoms can be released; whereby the metastable organometallic bonds are irreversibly converted into covalent bonds (see Fig. 4a). For example, room temperature deposition of 1,3,5-tris-(bromophenyl) benzene (TBB) onto Cu(111) results in disordered organometallic networks [30], a typical STM image is depicted in Fig. 4b. The disorder is attributed to the irreversibility of the relatively strong C–Cu bonds. The resulting covalent networks are similarly disordered, suggesting that the initial organometallic arrangement is maintained during the conversion. On Ag(111) partly ordered organometallic networks were observed [31]. This may be viewed as an

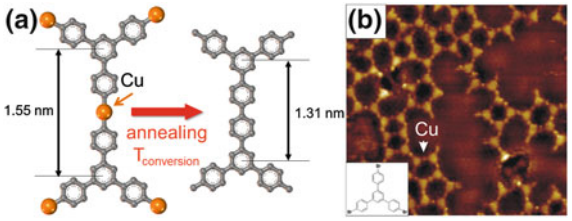

Fig. 4 **a** Structure of an organometallic dimer with triphenylbenzene backbones. Annealing at $T_{conversion}$ triggers the conversion from organometallic to covalent. According to gas-phase DFT calculations the center-to-center distance shrinks from 1.55 to 1.31 nm. **b** STM image acquired after room temperature deposition of TBB (cf. *inset* for structure) onto Cu(111). Fully debrominated molecules are interlinked via organometallic C–Cu–C bridges into networks. The linking copper atoms are imaged as dots between molecules (example marked by *arrow*)

indication for reversibility of the weaker C–Ag bonds, indicating possibilities for error correction. At present, the role of the adatoms for the initial reaction step—the dehalogenation—has not been clarified; however, it appears likely that the under-coordinated, thus more reactive, adatoms also promote halogen cleavage. On Au(111) organometallic networks have only rarely been observed [32]. The differences of the metal surfaces with respect to dehalogenation and organometallic intermediates are summarized in Table 1.

An intriguing question is, whether the structural quality of covalent networks obtained by kinetically controlled coupling reactions can be improved by optimization of reaction parameters (e.g. temperatures, heating or deposition rates) or the preparation sequence (e.g. room temperate deposition and subsequent heating versus deposition at elevated substrate temperature). A detailed comparison requires a quantitative measure of the network quality. Ideal networks based on threefold symmetric, straight connecting precursors as TBB are hexagonal. However, irregular tetragonal, pentagonal, heptagonal, and octagonal pores are commonly observed defects [22]. Consequently, a statistical analysis just by counting the different pore types in a significant number of STM images provides first insights. Yet, even networks that exclusively consist of ideal hexagonal pores can be far from perfect, due to frequently observed branching or vacancies [33]. Therefore, additional statistical indicators as the average number of adjacent pores have to be evaluated. For Ullmann polymerization of 1,3-bis(-bromophenyl)-5-(p-iodophenyl) benzene (BIB, c.f. inset to Fig. 5a) on Au(111), the influence of different reaction parameters on the network quality was studied in detail [24]. This brominated and iodinated precursor was also designed to compare hierarchical versus direct polymerization: room temperature deposition onto Au(111) selectively activates the iodine sites, resulting in covalent and kinetically inert dimers; only further annealing above the debromination threshold (∼175 °C) activates full polymerization; whereas upon high temperature deposition, both iodine and bromine sites become activated, resulting in the direct polymerization into networks. However, no substantial differences could be found for the two different polymerization protocols.

In the following, we focus on the influence of deposition rate and surface temperature for direct polymerization. Figure 5 depicts representative STM images

Table 1 Dehalogenation of brominated versus iodinated precursors and occurrence of organometallic intermediates for different metal surfaces

$d^{10}s^1$ metal	Bromine cleavage	Iodine cleavage
Cu(111) organometallic → disordered	Full @ RT	Full @ RT
Ag(111) organometallic → ordered	Partial @ RT Full @ ∼150 °C	Full @ RT
Au(111) *rarely* organometallic intermediates	None @ RT Full @ ∼180 °C	Full @ RT

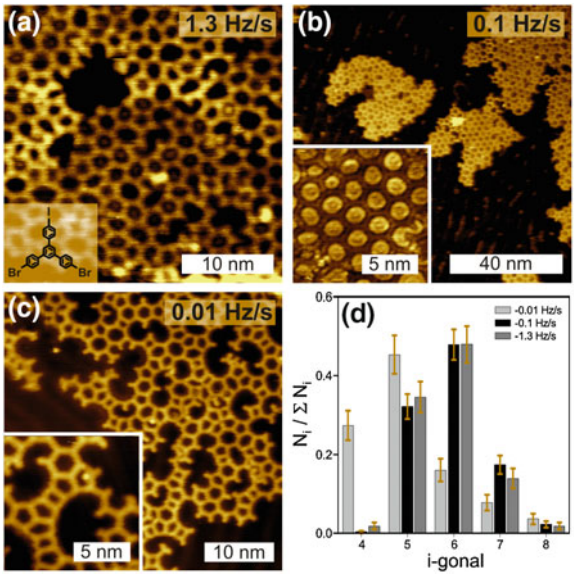

Fig. 5 STM images of covalent networks obtained by deposition of BIB (structure in *inset* to **a**) onto Au(111) held at 250 °C with different deposition rates (indicated in the *upper right* corners as frequency decline rates of a quartz crystal microbalance); **a** "normal" and **b** "slow" deposition with 1.3 and 0.1 Hz/s lead to comparable network quality; **c** whereas networks obtained by "ultraslow" deposition with 0.01 Hz/s exhibit a substantial amount of tetragonal and pentagonal pores, as also apparent from the corresponding pore geometry distribution in (**d**). Reprinted with permission from Ref. [24]. Copyright 2014 American Chemical Society

of covalent networks obtained by deposition of BIB onto Au(111) held at 250 °C with rates spanning over two orders of magnitude. The corresponding pore geometry distributions are summarized in Fig. 5d. Deposition with "normal" and "slow" rates (cf. Fig. 5a and b) leads to comparable distributions, while "ultra-slow" deposition results in a markedly increased number of pentagonal and even tetragonal pores, as also evident from the STM image in Fig. 5c. A comparable series of experiments where the surface temperature was varied while the deposition rate was kept constant revealed an increasing amount of pentagonal pores for increasing surface temperatures.

To develop strategies for improving the network quality, an atomistic understanding of defect formation is useful. Increased numbers of pentagonal pores were experimentally observed for higher surface temperatures or extremely low deposition rates. Both dependencies can consistently be explained by a relatively simple model. During polymerization, a stage occurs where a five-membered open ring which is missing one monomer is not yet closed. As sketched in Fig. 6, two different reaction pathways are conceivable: either the five-membered open ring is closed in a bimolecular reaction into an ideal hexagonal pore by addition of one

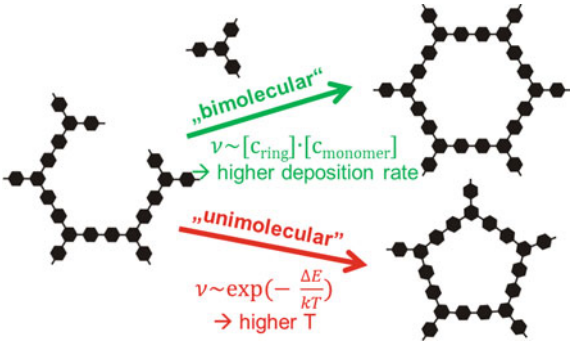

Fig. 6 Illustration of the kinetic competition between the bimolecular reaction (*green*) that yields ideal hexagonal pores versus the unimolecular reaction (*red*) that results in irregular pentagonal pores

more monomer or the five-membered ring becomes an irregular pentagonal pore in an unimolecular ring-closing reaction. The latter process requires bond distortion and is hence associated with an energy barrier. According to chemical kinetics, the bimolecular reaction rate depends on the concentration product of five-membered open rings and available monomers which increases with deposition rate. The unimolecular ring-closing reaction has to overcome an energy barrier, thus the rate becomes enhanced at higher surface temperatures according to an Arrhenius law.

The studies above have indicated possibilities to improve the quality of covalent networks by optimizing reaction parameters. Yet, structural perfection or at least long-range order appears to be beyond this approach. Alternatively, reversibility of organometallic bonds on Ag(111) might bear the potential to yield significantly better networks. The basic idea is taking advantage of a two stage protocol: The first step employs bond reversibility in organometallic networks for equilibration into highly ordered structures. This can be viewed as a self-assembly process. Yet, slightly higher temperatures $T_{\text{equilibration}}$ are required, due to the relative strength of C–Ag bonds as compared to supramolecular interactions. In the second step, these ordered organometallic networks are converted into similarly ordered covalent networks by additional heating at $T_{\text{conversion}}$ that is ideally significantly higher than $T_{\text{equilibration}}$. This scheme is far from being a topochemical reaction, because the conversion is accompanied by a considerable shrinkage of intermolecular distances (cf. Fig. 4a), hence obtaining very large domains might still be difficult. Nevertheless, the proof of concept is illustrated by the STM images in Fig. 7, where (a) was acquired directly after room temperature deposition of BIB onto Ag(111). In the STM contrast of this particular image, the interconnecting Ag atoms appear as clearly recognizable bright features between the fainter molecules. Molecule–molecule distances are in accord with organometallic bonds. The corresponding room temperature C 1s XP spectrum in Fig. 7d exhibits both a shoulder at higher binding energy corresponding to still brominated carbon (C_{Br}) and a shoulder at lower binding energy corresponding to Ag-bound carbon (C_{Ag}). The STM image in

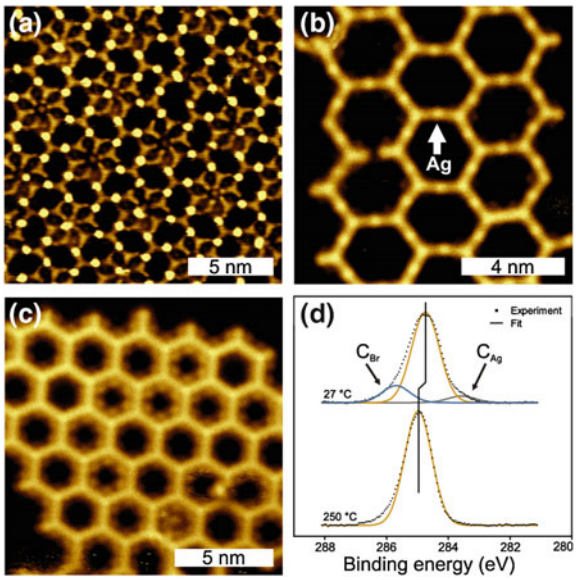

Fig. 7 STM images of BIB on Ag(111) obtained after **a** room temperature deposition **b** annealing at 125 °C, and **c** annealing at 250 °C [25]. **d** C 1s XP spectra acquired directly after room temperature deposition and after annealing to 250 °C. Reproduced with permission from The Royal Society of Chemistry

Fig. 7b was obtained after moderate heating at 125 °C for extended periods of time and shows a quite regular porous hexagonal network. The faint dots between interconnected molecules (example marked by the arrow) correspond to still present Ag atoms. A comparison of Fig. 7a and b makes obvious: annealing induced a massive structural reorganization that inevitably required breaking and reforming of C–Ag bonds, thereby proving their reversible nature at slightly elevated temperature. First indications of a conversion to covalent were only observed at higher temperatures of ~150 °C, whereas a sizable conversion required ~170 °C. Accordingly, further annealing at 250 °C ultimately results in fully covalent networks. The STM image in Fig. 7c shows a structurally perfect domain obtained via an ordered organometallic intermediate. The annealing was carried out extremely carefully with a low heating rate, in order to stay close to equilibrium structures during the progressive conversion. Both shoulders in the C 1s XPS data have disappeared after annealing, indicating a full conversion of all active sites into C–C bonds (cf. Fig. 7d).

6 Coupling of Terminal Alkynes

A drawback of Ullmann coupling is surface contamination by strongly adsorbing byproducts. The split off halogens chemisorb and in particular iodine can block part of the surface and hamper further polymerization [21]. In this respect, exploring alternative reactions can be rewarding and ethynyl groups appear to be sufficiently reactive for on-surface chemistry, but also sufficiently inert for deposition via

thermal sublimation. The only possible reaction byproduct is H_2 which readily desorbs from the surface. Terminal alkynes were already used for the synthesis of bulk COFs that are porous but not crystalline [34]. A priori different coupling reactions are conceivable: Glaser-Hay coupling, where a new C–C σ-bond is formed and only H_2 is released as a byproduct; cyclo-trimerization—an atom-economic reaction, where three ethynyl groups form a new phenyl ring; but also more complex coupling reaction schemes can occur; In the following, the surface chemistry of 1,4-diethynylbenzene (DEB) on Cu(111) is discussed as an example [35]. After room temperature deposition, STM reveals ordered structures of presumably intact molecules. Thermal annealing induces massive structural changes, leading to disordered structures and filamentous networks, representative STM images are shown in Fig. 8. The structures are imaged with uniform apparent height, suggesting a more or less well-defined coupling. Obtaining these structures is rather insensitive to the precise preparation protocol. Differences were neither observed for different annealing temperatures in the range of 175–350 °C nor for deposition onto a preheated surface. Despite the disorder, reoccurring motifs can be identified, most frequently: threefold-stars as well as larger and shorter dumbbells. The limited possibilities of coupling reactions facilitate identification of the reaction products by overlaying geometry-optimized candidate structures on the STM images (see Fig. 8). Accordingly, all these structures can be derived from DEB using only Glaser-Hay coupling and trimerization, the respective reaction schemes are depicted in Fig. 9: The threefold stars simply result from trimerization of three DEB into 1,3,5-tris(4′-ethynylphenyl)benzene (TEB) molecules. The larger dumbbells originate from a secondary Glaser-Hay coupling of two TEB molecules, whereas the shorter dumbbells form by secondary trimerization of one TEB lobe with two more DEB. However, also more complex reaction products were observed, in accord with bulk COF synthesis.

The lack of a clear preference for a specific coupling reaction among the different possibilities—i.e. the limited regioselectivity—inhibits polymerization into ordered

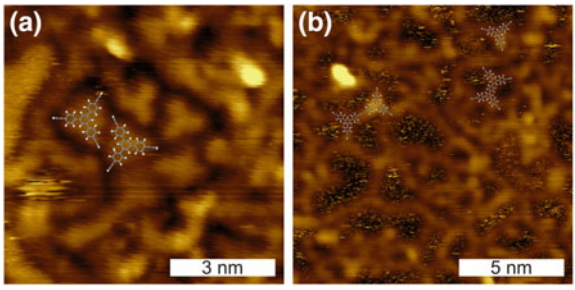

Fig. 8 STM images obtained after the thermally activated polymerization of DEB on Cu(111). Frequently encountered motifs as **a** threefold stars as well as **b** longer and shorter dumbbell are overlaid with optimized geometries of candidate structures. Size and shape consistency aids in the identification of reaction products [35]. Reproduced with permission from The Royal Society of Chemistry

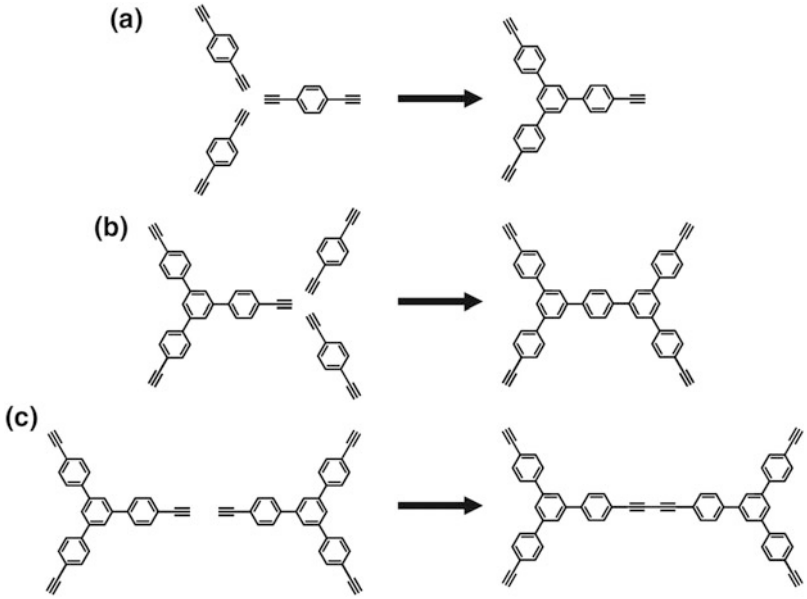

Fig. 9 Schemes of primary and secondary coupling reactions observed for DEB on Cu(111). **a** Threefold stars **b** shorter dumbbells **c** larger dumbbells

networks. Similar observations were already made for the reaction of acetylene—the smallest ethynyl molecule—on copper surfaces. Exclusive trimerization would yield benzene; however, on Cu(111) various alternative reaction products as butadiene and cyclooctatetraene were identified by temperature-programmed desorption experiments [36]. Yet, a significantly higher benzene yield on Cu(100) hints toward possibilities to enhance the regioselectivity by using different crystallographic surface orientations.

Similarly, polymerization of TEB on Ag(111) resulted in covalent, but not very well-ordered networks [37]. Even though a competition between Glaser-Hay coupling and trimerization was similarly observed, irregular, e.g., pentagonal pores are more common defects. The origin of these defects lies in the flexibility of the molecular backbone. The deformation energy associated with irregular pores is not exceedingly high [21], thereby promoting thermally activated defect formation. Moderate annealing of TEB on Ag(111) only leads to dimers, while full polymerization required higher temperatures [37]. A possible origin was proposed on the basis of elaborate DFT calculations: The substrate registry of the covalent dimer is less favorable, resulting in an enlarged molecule–surface distance. This reduces the catalytic effect of the surface, and gives rise to a higher activation barrier for coupling beyond the dimer. Such registry effects might also be important for other surface-catalyzed reactions, as the growing covalent aggregates are less flexible and cannot easily adopt to the surface as supramolecular structures.

A combined STM and DFT study of ethynyl trimerization on Au(111) proposes a reaction mechanism via a dimeric intermediate state and a significantly lower reaction temperature on the surface as compared to solution [38]. Interestingly, on Au(111) a clear preference for trimerization was observed for TEB [39], again indicating possibilities to selectively catalyze a specific coupling reaction by the choice of surface.

Imposing additional geometrical constraints on the adsorbed monomers is an interesting concept to promote regioselectivity. An experimental implementation thereof is working on vicinal surfaces that consist of small terraces of defined width and crystallographic orientation. Confining monomers on smaller terraces can prohibit certain molecular arrangements that are necessary for specific couplings. A proof of principle experiment is the polymerization of ethynyl terminated p-oligophenylenes on Ag(877) [40]. Constraining the 18.8 Å long monomers on the 36.6 Å wide terraces could suppress trimerization and exclusively yielded graphdiyne wires by Glaser-Hay type coupling. Even though this approach is elegant and very appealing, its application is most likely limited to the targeted synthesis of 1D structures.

7 Conclusions and Outlook

On-surface polymerization has already demonstrated its potential as a facile bottom-up approach for the fabrication of novel covalent nanostructures that are synthetically not accessible by any other means. Limited solubility of larger molecules and aggregates is a serious limitation for solution chemistry that does not necessarily apply to surface chemistry. The holy grail of structural perfection has so far only been achieved for polymerization under slightly reversible reaction conditions or for one-dimensional structures that are less prone to defect formation. In principle, bond reversibility is a matter of the ratio bond energy to thermal energy, i.e., kT. However, the limited thermal stability of organic molecules precludes extremely high temperatures that have helped to improve the structural quality of bottom-up fabricated graphene. The currently best covalent 2D networks are synthesized by condensation reactions. Yet, alternative coupling reactions might be desirable in terms of chemical stability or electron mobility.

Long-range order is not a strict requirement for any type of application. However, crystallinity promotes evolution of a defined band structure for electronic applications, but is also very advantageous for simulations. Similarly, membrane applications, e.g. for gas separation, become much more powerful through atomically precise pores. Long-range order is difficult to achieve for several reasons: one reason is the kinetically driven and irreversible formation of topological defects as, for instance, irregular pentagonal or heptagonal pores in hexagonal networks. Competing coupling reactions can be a further problem. Obviously, this is a severe issue for crosscoupling, but is, for instance, similarly crucial for homocouplings of chemically versatile ethynyls. Even though it is hard to imagine strategies to

completely avoid defects during kinetically controlled growth, a detailed study of defect formation is worthwhile. An atomistic understanding of defect formation is the first step toward a systematic development of strategies to avoid or at least minimize defects.

On surfaces, Ullmann coupling is the best studied and most applied polymerization reaction. It works reliably on metals, in a sense that the topology of ideal networks is predefined by the halogen substitution pattern of the precursor molecule. Since unwanted side-reactions do not occur for Ullmann coupling, topological defects remain the most severe issue. These defects are associated with bond distortion; consequently, energy is required for their formation. A promising concept would thus be the development of low-temperature polymerization schemes to suppress thermally activated defect formation.

The most appealing property of covalent nanostructures is the prospect of charge transport [41]. A requirement for meaningful experiments in this direction is working on insulating surfaces, which means either in situ synthesis or subsequent transfer. In the common Ullmann approach, the metal surface is needed to initiate the coupling by dehalogenation. However, first experiments on calcite surfaces have shown that Ullmann coupling on bulk insulator surfaces is feasible [42]. In this particular case, carboxylic acid groups were used as anchors to prevent desorption during heating until sufficiently high temperatures for the dehalogenation have been reached. Yet, other strategies are similarly conceivable. Since adatoms may play a so far unrevealed role for the dehalogenation, hybrid metal–insulator approaches, where metal atoms are deposited onto an insulator, might also be worthwhile pursuing. Alternatively, transfer procedures as template stripping have been further developed for graphene research, but might be similarly applicable to covalent organic nanostructures.

Organic chemistry is extremely diverse, thus an obvious strategy is to further explore different coupling reactions on surfaces. Boronic acid condensation and ethynyl polymerization was inspired from bulk COF synthesis. In this respect, the ionothermal synthesis of carbonitride COFs by nitrile trimerization appears particularly rewarding, as there are no known side-reactions and byproducts in this atom-economic reaction [43]. However, the harsh reaction conditions at temperatures of 400 °C in liquid $ZnCl_2$ may already indicate a low reactivity, and it remains to be explored if nitrile trimerization on surfaces is possible at all. Even though for a limited number of couplings, the potential energy landscape of a presumed reaction pathway has been simulated by DFT [33, 37, 44], on-surface chemistry remains far from being predictable. In many cases, the intuition even of most experienced organic synthetic chemists fails to predict whether and how a particular reaction proceeds on a specific surface. Many examples have proven that the geometric templating effect in combination with the chemically active role of the surface and/or the interplay with adatoms can totally alter reaction geometries and barriers or even mechanisms.

In summary, the current approach is mostly empiric. This can be cumbersome not only due to the inherent slowness of UHV experiments, but also due to the almost infinite parameter space. A reaction that does not work on one surface might

readily proceed on another surface. Nevertheless, the increasing number of joint surface scientists and organic chemists' teams will inevitably generate a wealth of interesting, insightful, and surprising results as well as novel organic nanostructures, and even maybe the perfect 2D polymer.

References

1. Zwaneveld, N.A.A., Pawlak, R., Abel, M., Catalin, D., Gigmes, D., Bertin, D., Porte, L.: Organized formation of 2d extended covalent organic frameworks at surfaces. J. Am. Chem. Soc. **130**, 6678–6679 (2008)
2. Grill, L., Dyer, M., Lafferentz, L., Persson, M., Peters, M.V., Hecht, S.: Nano-architectures by covalent assembly of molecular building blocks. Nat. Nanotechnol. **2**, 687–691 (2007)
3. Zhong, D.Y., Franke, J.H., Podiyanachari, S.K., Blomker, T., Zhang, H.M., Kehr, G., Erker, G., Fuchs, H., Chi, L.F.: Linear alkane polymerization on a gold surface. Science **334**, 213–216 (2011)
4. Cai, J.M., Ruffieux, P., Jaafar, R., Bieri, M., Braun, T., Blankenburg, S., Muoth, M., Seitsonen, A.P., Saleh, M., Feng, X.L., et al.: Atomically precise bottom-up fabrication of graphene nanoribbons. Nature **466**, 470–473 (2010)
5. Ruffieux, P., Cai, J.M., Plumb, N.C., Patthey, L., Prezzi, D., Ferretti, A., Molinari, E., Feng, X. L., Müllen, K., Pignedoli, C.A., et al.: Electronic structure of atomically precise graphene nanoribbons. ACS Nano **6**, 6930–6935 (2012)
6. Kanuru, V.K., Kyriakou, G., Beaumont, S.K., Papageorgiou, A.C., Watson, D.J., Lambert, R. M.: Sonogashira coupling on an extended gold surface in vacuo: reaction of phenylacetylene with iodobenzene on Au(111). J. Am. Chem. Soc. **132**, 8081–8086 (2010)
7. Cote, A.P., Benin, A.I., Ockwig, N.W., O'Keeffe, M., Matzger, A.J., Yaghi, O.M.: Porous, crystalline, covalent organic frameworks. Science **310**, 1166–1170 (2005)
8. El-Kaderi, H.M., Hunt, J.R., Mendoza-Cortes, J.L., Cote, A.P., Taylor, R.E., O'Keeffe, M., Yaghi, O.M.: Designed synthesis of 3d covalent organic frameworks. Science **316**, 268–272 (2007)
9. Sassi, M., Oison, V., Debierre, J.M., Humbel, S.: Modelling the two-dimensional polymerization of 1,4-benzene diboronic acid on a Ag surface. ChemPhysChem **10**, 2480–2485 (2009)
10. Ourdjini, O., Pawlak, R., Abel, M., Clair, S., Chen, L., Bergeon, N., Sassi, M., Oison, V., Debierre, J. M., Coratger, R. et al.: Substrate-mediated ordering and defect analysis of a surface covalent organic framework. Phys. Rev. B **84** (2011)
11. Guan, C.Z., Wang, D., Wan, L.J.: Construction and repair of highly ordered 2d covalent networks by chemical equilibrium regulation. Chem. Commun. **48**, 2943–2945 (2012)
12. Dienstmaier, J.F., Medina, D., Dogru, M., Knochel, P., Bein, T., Heckl, W.M., Lackinger, M.: Isoreticular two-dimensional covalent organic frameworks synthesized by on-surface condensation of diboronic acids. ACS Nano **6**, 7234–7242 (2012)
13. Dienstmaier, J.F., Gigler, A.M., Goetz, A.J., Knochel, P., Bein, T., Lyapin, A., Reichlmaier, S., Heckl, W.M., Lackinger, M.: Synthesis of well-ordered C of monolayers: surface growth of nanocrystalline precursors versus direct on-surface polycondensation. ACS Nano **5**, 9737–9745 (2011)
14. Liu, X.H., Guan, C.Z., Ding, S.Y., Wang, W., Yan, H.J., Wang, D., Wan, L.J.: On-surface synthesis of single-layered two-dimensional covalent organic frameworks via solid-vapor interface reactions. J. Am. Chem. Soc. **135**, 10470–10474 (2013)
15. Boz, S., Stöhr, M., Soydaner, U., Mayor, M.: Protecting-group-controlled surface chemistry-organization and heat-induced coupling of 4,4′-Di(Tert-Butoxycarbonylamino) biphenyl on metal surfaces. Angew. Chem. Int. Ed. **48**, 3179–3183 (2009)

16. Faury, T., Clair, S., Abel, M., Dumur, F., Gigmes, D., Porte, L.: Sequential linking to control growth of a surface covalent organic framework. J. Phys. Chem. C **116**, 4819–4823 (2012)
17. Schlögl, S., Sirtl, T., Eichhorn, J., Heckl, W.M., Lackinger, M.: Synthesis of two-dimensional phenylene-boroxine networks through in-vacuo condensation and on-surface radical addition. Chem. Commun. **47**, 12335–12357 (2011)
18. Tanoue, R., Higuchi, R., Enoki, N., Miyasato, Y., Uemura, S., Kimizuka, N., Stieg, A.Z., Gimzewski, J.K., Kunitake, M.: Thermodynamically controlled self-assembly of covalent nanoarchitectures in aqueous solution. ACS Nano **5**, 3923–3929 (2011)
19. Björk, J., Hanke, F., Stafstrom, S.: Mechanisms of halogen-based covalent self-assembly on metal surfaces. J. Am. Chem. Soc. **135**, 5768–5775 (2013)
20. McMillen, D.F., Golden, D.M.: Hydrocarbon bond-dissociation energies. Ann. Rev. Phys. Chem. **33**, 493–532 (1982)
21. Schlögl, S., Heckl, W.M., Lackinger, M.: On-surface radical addition of triply iodinated monomers on Au(111)—the influence of monomer size and thermal post-processing. Surf. Sci. **606**, 999–1004 (2012)
22. Blunt, M.O., Russell, J.C., Champness, N.R., Beton, P.H.: Templating molecular adsorption using a covalent organic framework. Chem. Commun. **46**, 7157–7159 (2010)
23. Lafferentz, L., Eberhardt, V., Dri, C., Africh, C., Comelli, G., Esch, F., Hecht, S., Grill, L.: Controlling on-surface polymerization by hierarchical and substrate-directed growth. Nat. Chem. **4**, 215–220 (2012)
24. Eichhorn, J., Nieckarz, D., Ochs, O., Samanta, D., Schmittel, M., Szabelski, P.J., Lackinger, M.: On-surface ullmann coupling: the influence of kinetic reaction parameters on the morphology and quality of covalent networks. ACS Nano **8**, 7880–7889 (2014)
25. Eichhorn, J., Strunskus, T., Rastgoo-Lahrood, A., Samanta, D., Schmittel, M., Lackinger, M.: On-surface Ullmann polymerization via intermediate organometallic networks on Ag(111). Chem. Commun. **50**, 7680–7682 (2014)
26. Russell, J.C., Blunt, M.O., Garfitt, J.M.J.S.D., Alexander, M., Champness, N.R., Beton, P.H.: Dimerization of Tri(4-Bromophenyl)Benzene by Aryl-Aryl coupling from solution on a gold surface. J. Am. Chem. Soc. **133**, 4220–4223 (2011)
27. Eder, G., Smith, E.F., Cebula, I., Heckl, W.M., Beton, P.H., Lackinger, M.: Solution preparation of two-dimensional covalently linked networks by polymerization of 1,3,5-Tri (4-Iodophenyl)Benzene on Au(111). ACS Nano **7**, 3014–3021 (2013)
28. Lipton-Duffin, J.A., Ivasenko, O., Perepichka, D.F., Rosei, F.: Synthesis of polyphenylene molecular wires by surface-confined polymerization. Small **5**, 592–597 (2009)
29. McCarty, G.S., Weiss, P.S.: Formation and manipulation of protopolymer chains. J. Am. Chem. Soc. **126**, 16772–16776 (2004)
30. Gutzler, R., Walch, H., Eder, G., Kloft, S., Heckl, W. M., Lackinger, M.: Surface mediated synthesis of 2d covalent organic frameworks: 1,3,5-Tris(4-Bromophenyl)Benzene on graphite (001), Cu(111), and Ag(110). Chem. Commun. **7**: 4456–4458 (2009)
31. Bieri, M., Blankenburg, S., Kivala, M., Pignedoli, C.A., Ruffieux, P., Mullen, K., Fasel, R.: Surface-supported 2d heterotriangulene polymers. Chem. Commun. **47**, 10239–10241 (2011)
32. Saywell, A., Gren, W., Franc, G., Gourdon, A., Bouju, X., Grill, L.: Manipulating the conformation of single organometallic chains on Au(111). J. Phys. Chem. C **118**, 1719–1728 (2014)
33. Bieri, M., Nguyen, M.T., Groning, O., Cai, J.M., Treier, M., Ait-Mansour, K., Ruffieux, P., Pignedoli, C.A., Passerone, D., Kastler, M., et al.: Two-dimensional polymer formation on surfaces: insight into the roles of precursor mobility and reactivity. J. Am. Chem. Soc. **132**, 16669–16676 (2010)
34. Jiang, J.X., Su, F., Niu, H., Wood, C.D., Campbell, N.L., Khimyak, Y.Z., Cooper, A. I.: Conjugated microporous poly(phenylene butadiynylene)s. Chem. Commun. 486–488 (2008)
35. Eichhorn, J., Heckl, W.M., Lackinger, M.: On-surface polymerization of 1,4-diethynylbenzene on Cu(111). Chem. Commun. **49**, 2900–2902 (2013)

36. Kyriakou, G., Kim, J., Tikhov, M.S., Macleod, N., Lambert, R.M.: Acetylene coupling on Cu (111): formation of butadiene, benzene, and cyclooctatetraene. J. Phys. Chem. B **109**, 10952–10956 (2005)
37. Zhang, Y.Q., Kepcija, N., Kleinschrodt, M., Diller, K., Fischer, S., Papageorgiou, A.C., Allegretti, F., Bjork, J., Klyatskaya, S., Klappenberger, F. et al.: Homo-coupling of terminal alkynes on a noble metal surface. Nat. Commun. **3**, 1286 (2012)
38. Zhou, H.T., Liu, J.Z., Du, S.X., Zhang, L.Z., Li, G., Zhang, Y., Tang, B.Z., Gao, H.J.: Direct visualization of surface-assisted two-dimensional diyne polycyclotrimerization. J. Am. Chem. Soc. **136**, 5567–5570 (2014)
39. Liu, J., Ruffieux, P., Feng, X.L., Müllen, K., Fasel, R.: Cyclotrimerization of arylalkynes on Au(111). Chem. Commun. **50**, 11200–11203 (2014)
40. Cirera, B., Zhang, Y.Q., Bjork, J., Klyatskaya, S., Chen, Z., Ruben, M., Barth, J.V., Klappenberger, F.: Synthesis of extended graphdiyne wires by vicinal surface templating. Nano Lett. **14**, 1891–1897 (2014)
41. Perepichka, D.F., Rosei, F.: Chemistry extending polymer conjugation into the second dimension. Science **323**, 216–217 (2009)
42. Kittelmann, M., Rahe, P., Nimmrich, M., Hauke, C.M., Gourdon, A., Kühnle, A.: On-surface covalent linking of organic building blocks on a bulk insulator. ACS Nano **5**, 8420–8425 (2011)
43. Kuhn, P., Antonietti, M., Thomas, A.: Porous, covalent triazine-based frameworks prepared by ionothermal synthesis. Angew. Chem. Int. Edit. **47**, 3450–3453 (2008)
44. Arado, O.D., Monig, H., Wagner, H., Franke, J.H., Langewisch, G., Held, P.A., Studer, A., Fuchs, H.: On-surface azide-alkyne cycloaddition on Au(111). ACS Nano **7**, 8509–8515 (2013)

On-Surface Dynamic Covalent Chemistry

Jie-Yu Yue, Li-Jun Wan and Dong Wang

Abstract On-surface synthesis has become a very promising bottom-up approach to obtain a functional surface with designable chemical structures. Dynamic covalent chemistry is an interesting reaction strategy to form thermodynamically controlled products utilizing the reversible covalent bond as linkage, which can be formed, broken, and reformed during the reaction and therefore provide an incidence of error-checking and self-healing. In this chapter, we focused on the surface-assisted synthesis of molecular nanostructures using dynamic covalent linkers. By proper tuning the on-surface dynamic covalent reaction processes, highly ordered covalent bond connected nanostructures can be obtained on surfaces.

1 Introduction

One of the exciting prospects with the development of nanoscience and nanotechnology is to build up functional systems using molecules, which is not only a subject for fundamental surface science study, but also closely related to many emerging technologically important applications, such as catalysis, sensor, and organic electronics. The self-assembled molecular nanostructures on surface are driven by the molecule–substrate interaction and intermolecular interaction. The most important feature of the self-assembly is the highly ordered structure, which is generally thermodynamically favored. The key to achieve thermodynamic equilibrium is that the non-covalent interactions are generally weak and reversible. By tuning the weak but appreciable non-covalent interactions, a variety of supramolecular nanostructures on surfaces have been constructed. At the same time, the weak nature of the non-covalent interaction imposes great challenge to the molecular engineering of molecular nanostructures. For example, the self-assembly

J.-Y. Yue · L.-J. Wan · D. Wang (✉)
Institute of Chemistry, Chinese Academy of Sciences,
Beijing 100190, People's Republic of China
e-mail: wangd@iccas.ac.cn

A. Gourdon (ed.), *On-Surface Synthesis*, Advances in Atom and Single Molecule Machines, DOI 10.1007/978-3-319-26600-8_11

is generally very difficult to predict. Slight modification of molecular structures, even for homologue molecules with the very same functional groups, may result in the significant change of interaction modes and therefore the resulting architectures [1]. Moreover, molecular nanostructures fabricated by non-covalent interaction generally lack the necessary stability to be used in functional systems.

Recently, great attention has been paid to construct molecular nanostructures via covalent synthetic chemistry on surface [2]. The covalent bond is robust and suitable to be used to direct the topology of the resulted nanostructures. On one hand, the on-surface synthesis chemistry has unique features from the viewpoint of fundamental surface science. At a first glance, the chemical reactions taking place on the surface seem quite similar to the corresponding bulk reaction, since utilizing the same reaction precursors and reaction process. However, the introduction of surface provides an active element to modulate the reaction. Due to the surface-confinement effect, many reaction routes, which can take place in the three-dimensional space, probably cannot act [3]. In addition, the surface–molecule interaction may modulate the configuration and diffusion of precursors and intermediates on the surface and thereafter affect the reaction process. More obviously, the surface, especially the transition metal surface, may catalyze the reactions [4–8]. On the other hand, on-surface synthesis provides new venue to obtain molecular architectures. The covalent bond not only significantly improves the stability of the resulted nanostructures, but also may facilitate the charge transportation and thus brings great application prospects of the resulted nanostructures for electronic device application. Furthermore, the surface-assisted synthesized strategy could be a facile route to achieve novel nanostructures that cannot be constructed by other methods. For example, on-surface polymerization can overcome the solubility issue and has been applied to obtain highly regular polythiophene [9]. In addition, surface can be used as template and support to synthesize highly ordered 2D polymers, which is difficult to achieve from a solution-phase synthesis route [10].

Recently, great progress has been made in the field of on-surface synthesis [11–14]. A variety of nanostructures, including one-dimensional lines, oligomers or polymers, macrocycles, and two-dimensional porous networks, have been successfully fabricated. The typical coupling reactions investigated in these studies include Glaser coupling, Ullmann coupling, Sonogashira coupling, boronic acid condensation, the reaction between boronic acid and diols, the schiff base coupling reaction, the polyester formation reaction, the polyimide formation reaction, and the polyimide formation reaction. Among them, we are particularly interested in applying dynamic covalent bonds as linkers during the construction of surface-assisted organic nanostructures. Compared to conventional covalent bond, the formation of the dynamic covalent bond is a thermodynamically controlled process. Dynamic covalent bond is reversible and can be reconstructed, and therefore, an error-checking and self-healing process can be realized during the reaction. By applying the dynamic covalent bonds, the most thermodynamically stable product can be obtained. Previously, dynamic covalent chemistry [15] has been widely explored to construct molecular nanostructures and to form responsive materials. When interfacing dynamic covalent bond with on-surface synthesis

strategy, the benign feature of reversibility has been demonstrated to be very important to facilitate the formation of highly ordered covalently linked molecular nanostructures.

In this chapter, we focus on the on-surface dynamic chemical reactions. The chapter is sectioned by coupling reaction types, such as boronic acid dehydration reaction, Schiff base coupling reaction, and others. Furthermore, each section is organized in term of the dimensionality of the targeted molecular nanostructures. Finally, a conclusion and outlook section conclude the chapter.

2 Boronic Acid Dehydration Reaction

The dynamic covalent chemistry involving boronic acid group has been well known. As shown in Scheme 1, self-condensation of three boronic acids with elimination of three water molecules can form the boroxine rings, whereas the condensation between boronic acid and catechol can lead to a boronate ester. Both reactions are highly reversible and can be applied to synthesize 2D and 3D materials. The first bulk covalent organic framework (COF) [16] material was synthesized by boronic acid dehydration reaction. The boronic acid-based coupling reactions have been applied to construct nanostructures on the surface. A series of boronic acid-based and boronate ester-based surface covalent organic frameworks (SCOFs) have been obtained as shown in Scheme 1. 1,4-benzenediboronic acid (BDBA) was utilized as building blocks to construct surface covalent organic frameworks on Ag(111) surface in ultrahigh vacuum (UHV) as shown in Fig. 1a [17]. Hexagonal network with pore size about 1.5 ± 0.1 nm was formed by BDBA on Ag(111) surface. SCOF-2, a hexagonal network with pore size about 2.9 nm as displayed in Fig. 1b, was synthesized by the co-condensation of BDBA and 2,3,6,7,10,11-hexahydroxytriphenylene (HHTP). During the synthesis process of SCOF-2, in order to avoid the self-condensation of the BDBA, a small amount of HHTP was untimely dropped on the Ag(111) surface.

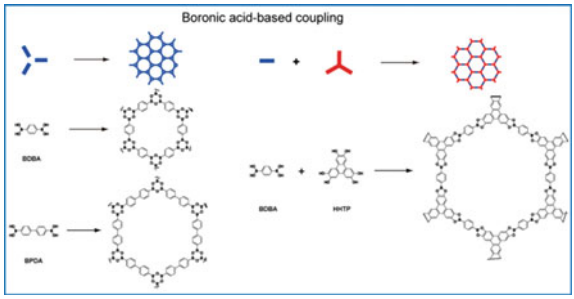

Scheme 1 Molecular structures of diboronic acid and catechol building blocks. BDBA (1,4-benzenediboronic acid). HHTP (2,3,6,7,10,11-hexahydroxytriphenylene). BPDA (biphenyl-diboronic)

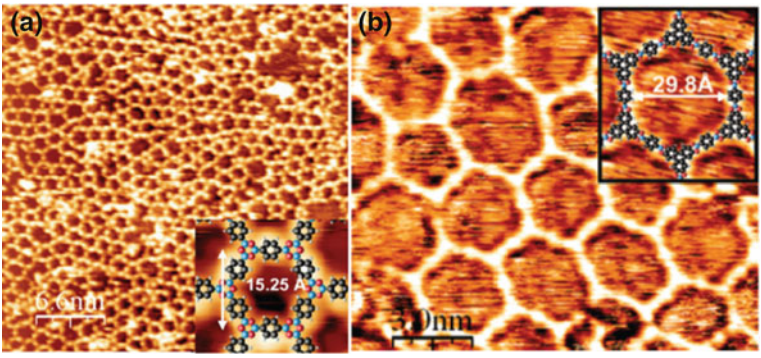

Fig. 1 **a** Self-condensation of BDBA. **b** Co-condensation of BDBA and HHTP. The corresponding structural models and the lattice parameters as indicated in the *Insets*. Copyright 2008 American Chemical Society

Other than the regular hexagonal networks, many polygon structures such as pentagon, heptagon, and octagon were formed at the same time. In the formation of covalent bond, a small number of faults resulted in the irregular polygon distribution. Deformation of the perfect hexagon structure or an incomplete ring closure in the boroxine may lead to the different polygons. Unfortunately, annealing the network at high temperature has little effect to remove the bond faults.

Obviously, the orderliness of the covalent networks from boronic acid-based condensation reactions is not comparable to that of supramolecular assembly. Since then, great efforts have been made to improve the quality of the boronic acid-based covalent networks. Dienstmaier and coworkers synthesized ordered surface covalent organic framework based on the condensation of BDBA (Scheme 1) in two different methods [18]. In method 1, the precursors were prepolymerized in a solvothermal condition to form oligomers, which were then casted on HOPG. Hexagonal frameworks with small domains up to 40 nm, which is related to the reaction temperature, were obtained. In method 2, they deposited the BDBA solvent on HOPG and directly heated the precursor-containing surface. By applying method 2, hexagonal frameworks with larger domain size were formed compared with method 1. Such a procedure was applied to reticular synthesis of a series of porous networks with tunable pore size ranging from 1.0 to 3.2 nm by choosing precursors with the same two boronic acid functionalities and different skeleton lengths [19].

In order to improve the regularity and increase the typically domain size of the SCOFs, thermodynamic equilibrium control method has been utilized in the surface-assisted synthesis. Guan and coworkers synthesized three highly ordered boronic acid-based SCOFs with large scales on the HOPG [20]. Figure 2a, b displays the SCOF from BPDA as the reaction precursor. They introduced $CuSO_4 \cdot 5H_2O$ powder into the sealed autoclaves, which can release water molecular during the heating process. The water molecular can shift the reaction direction and control the chemical equilibrium of the dehydration reaction of

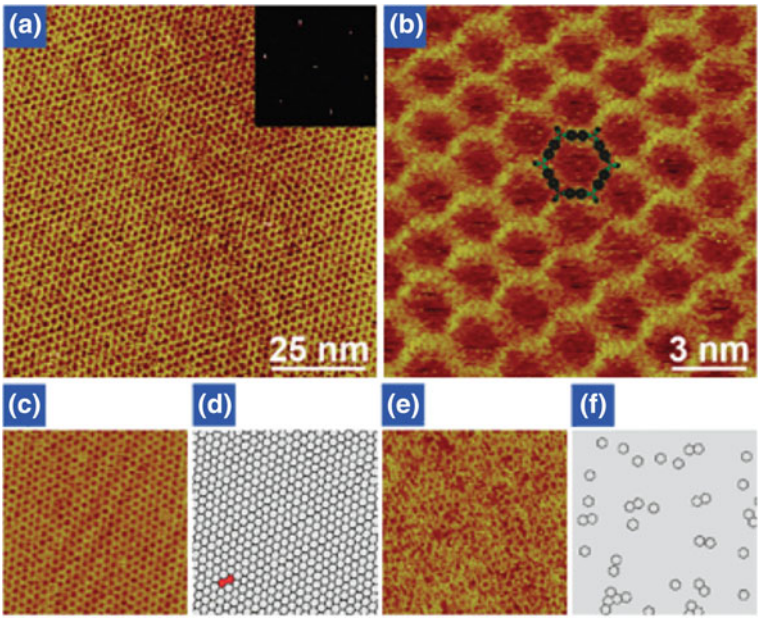

Fig. 2 **a** A STM image of SCOF on HOPG formed after dehydration of BPDA precursors at 150 °C. The *inset* depicts the corresponding FFT of the image. **b** A high-resolution STM image showing the hexagonal structure. Model of the hexagonal structures is overlaid and drawn to scale. **c** and **d** A STM image and the delineated image of SCOF obtained in the presence of H_2O. **e** and **f** A STM image and the delineated image of SCOF obtained without the presence of H_2O. Copyright Royal Society of Chemistry

boronic acid. Therefore, this strategy significantly promoted the degree of the reversible dehydration reaction, and the miss-linked defects have more chances to be remedied. As shown in Fig. 2c, d, the coverage of the ordered hexagonal SCOF can achieve 98 % and the size of ordered domain can reach more than 200 nm when using H_2O as equilibrium control agent. In contrast, without the present of water, only about 7 % hexagonal ring was found on the HOPG as shown in Fig. 2e, f, according to the statistical analysis. Similarly, by applying water as chemical equipment agent, a series of boronic acid dehydration-based 2D COFs with different pore sizes and large domain sizes were synthesized on the surface. Such an equilibrium control method can be understood by Le Chatelier's principle. The boroxine reaction is a dynamic covalent reaction with H_2O as by-product. Adding water to the closed system can change the Gibbs energy of the reaction and shift the reaction backward to favor the correction of defects and promote the self-healing abilities. Finally, the highly ordered surface nanostructures with thermodynamically more favored hexagonal structures were obtained.

A covalent organic framework based on a two-step strategy though the sequential boronic acid dehydration reaction and Ullmann reaction has been prepared by Faury et al. [21]. They utilized p-bromo-benzene boronic acid, a

bifunctional molecule, and had the potential to take place boronic acid dehydration reaction and Ullmann reaction, as building block. When annealing the molecules under UHV conditions on Au(111) surface, the boronic acid dehydration reaction firstly took place and resulted in boroxine rings-linked trimers. With increasing temperature, the Ullmann reaction was activated and a final porous network could be formed. This sequential synthesis strategy gives us new inspiration in the surface-assisted synthesis of complex structures.

3 Schiff Base Reaction

Imines, or C=N, is an important functional unit and has multiple applications in organic synthesis, such as for the preparation of metal complex and shape-persistent macrocycles [22, 23]. The generation of imine bond from aldehyde and amine groups is reversible and is a dynamic covalent bond. The Schiff base reaction unusually takes place under mild reaction conditions and has attracted great interests for on-surface synthesis. Many surface nanostructures with different topologies, such as the molecules, the oligomers, and the COFs, have been successfully constructed.

3.1 Surface Schiff Base Reactions

Weigelt et al. utilized octylamine and aromatic dialdehyde as building blocks and directly got a covalent interlinked product through surface-assisted synthesis. Experiments were carried out on Au(111) under UHV conditions. The ex situ STM and near-edge X-ray absorption fine structure spectroscopy experiments certified that the diimine can be directly obtained by on-surface synthesis [24].

Exchange reaction is an important feature of dynamic covalent chemistry. For example, the primary amine can react with imine group to result in transimination. Such process has been extensively explored in solution phase to form so-called dynamic covalent library. Ciesielski and coworkers investigated surface-mediated transamination process and compared with solution processes. The reactions were carried out between a long aliphatic-equipped dialdehyde (A) and three α,ω-diamines (B_2, B_6, B_{12}) with different lengths of aliphatic chains at the liquid–solid surface [25]. Firstly, the formation of monolayer diimines A_2B_2, A_2B_6, and A_2B_{12} was achieved by the reaction of A with B_2, B_6, and B_{12}, respectively, and observed by in situ STM. When B_6 solution was added to the preexisting A_2B_2 structure, A_2B_6 layer was obtained. Then, the addition of B_{12} solution led to the formation of A_2B_{12} monolayer. However, the reverse experiment from A_2B_{12} to A_2B_6 can only be realized by the presence of large excess of B_6 at the solid–liquid interface and over a period of time. More interestingly, the A_2B_2 cannot be formed even further adding the concentration of B_2 solution. The control experiments carried out in solution phase indicate that the transamination reaction can take place smoothly and

the mixture of the A_2B_2, A_2B_6, and A_2B_{12} can be obtained independently to the transformation sequence. The results confirmed that the molecule–surface interaction is the critical selective force that drives the on-surface reactions, which is different from the solution reaction.

3.2 *Schiff Base Reaction Induced Self-assembly*

Generally, self-assembly process is driven by weak interactions, such as van der Waals forces and hydrogen bonds. In most cases, building blocks were firstly synthesized in solution by normal organic routes and then loaded on the surface for surface self-assembly process. However, by dynamic covalent chemistry, the formation process of building blocks and the reaction process of building blocks can take place on the surface at the same time. When surface reactions are combined with self-assembly process, the surface nanostructures can be tuned and novel nanoarchitectures can be obtained.

Li and coworkers demonstrated the Schiff base reaction induced transformation of surface assembly. 1,3,5-tri(4-formylphenyl)benzene, which carries three aldehyde groups, is observed to form lamellar structures on HOPG by self-assembly [26]. When another building block 5-aminoisophthalic acid was added, the nanostructure changed from lamella to honeycomb network. The structure transition resulted from the reaction of the two building blocks. The Schiff base reaction occurring at the liquid–solid interface between aldehyde and amine led to a carboxyl group-containing triangular imine oligomers. By the hydrogen bonds of the carboxyl terminus, the triangular imine oligomers self-assembled and the hexagonal nanostructure were formed. Furthermore, the on-surface Schiff-base reaction can be utilized to construct chiral nanostructures [27].

Liu and coworkers constructed nanoporous networks by self-assembly of melamine-capped molecules through surface-assisted synthesis method [28]. When melamine (MA) reacted with twofold symmetrical terephthalaldehyde (TPA) as shown in Fig. 3a, a hexagonal porous network was obtained as shown in Fig. 3c. Two molecules MA reacted with one molecule TPA leading to the formation of candy-shaped imine oligomers. Then, the imine oligomers self-assembled through the hydrogen bonds existing at the unreacted MA units, and therefore, a porous network was formed. When MA reacted with threefold symmetrical 1,3,5-triformylbenzene (TFB) displayed in Fig. 3b, a hexagonal nanostructure with pore size about 1.3 nm was obtained as shown in Fig. 3d. Three molecules MA reacted with one molecule TFB leading to windmill-shaped imine oligomers. Then, the imine oligomers self-assembled through the hydrogen bonds existing at the unreacted MA units, and therefore, a porous network was formed. The on-surface Schiff base reaction taking place between melamine and aldehyde with different symmetries resulted in molecules terminated by MA. The hydrogen bonds formed between the unreacted amines of the MA play a significant role in the nanostructure

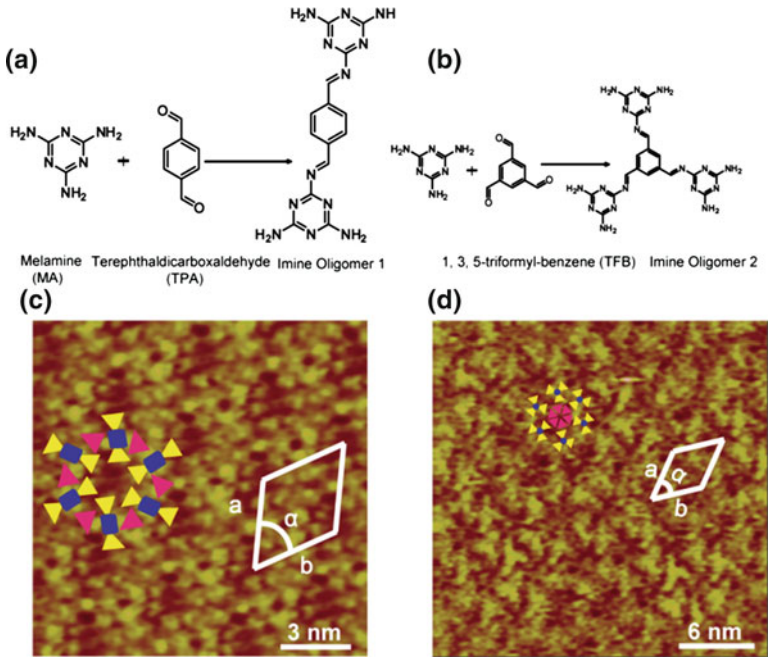

Fig. 3 **a** Chemical structures of imine oligomer 1. **b** Chemical structures of imine oligomer 2. **c** High-resolution STM image of imine oligomer 1. **d** High-resolution STM image of imine oligomer 2. Copyright Wiley-VCH

formation process. The combination of the surface coupling reaction and assembly processes provides a new perspective to the fabrication of surface nanostructures.

3.3 The Schiff Base Reaction-Based Covalent Organic Frameworks

Two-dimensional COFs, which have monolayer thick sheet and covalently bonded linkage, are expected to display unique properties resulting from the reduced dimensionality, planer structures. Many SCOFs have been fabricated on the surface by Schiff base coupling.

Tanoue and coworkers synthesized a series of 1D imine-linked polymers and 2D porous networks at the interface of Au(111) surface through thermodynamic control method by controlling the pH of the solution [29]. A pair of the building blocks 4,4′-diaminostilbene dihydrochloride (ASB) and terephthaldicarboxaldehyde (TPA) was utilized as example. Mixing the ASB and TPA in water at room temperature results in an irreversible oligomer. However, when the pH was lower than the pK_a of the amine group of the ASB, the reaction shifted to the left direction

because of the protonation of the amine. By tuning pH of the solution, the chemical equilibrium of the Schiff base reaction can be controlled, and thus, more ordered domains of polymeric structures can be obtained.

Liu and coworkers constructed highly ordered SCOFs through Schiff base coupling [30]. Molecules with threefold symmetry and twofold symmetry were chosen as precursors for on-surface Schiff base reaction, as shown in Fig. 4a. A gas–solid interface method was exploited. As shown in Fig. 4b, the building block A was first deposited on HOPG by drop-casting, and the substrate was then placed in a sealed autoclave containing another building block B. During the heating progress, building block B can be vaporized and deposited on the HOPG, and therefore, the polymerization progress between building block A and B took place. During the reaction progress, the gas-phase dosing of the building block B determines the growth, and the disordered oligomers can be significantly reduced. As shown in Fig. 4c, d, the method can be applied to obtain highly ordered SCOFs with typical domain size larger than 200 nm. In contrast, heating the HOPG

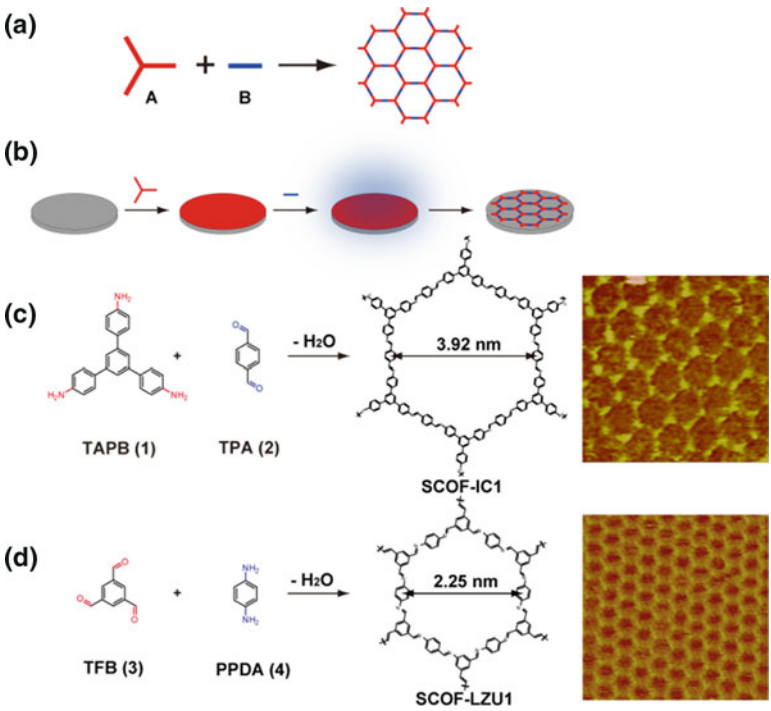

Fig. 4 Schematic diagram of SCOFs formation. **a** Condensation of two precursors A and B carrying different reactive partner groups results in the formation of SCOF. **b** Scheme diagram for solid–vapor interface reaction. **c**, **d** Condensation of trigonal precursors TAPB or TFB and linear precursors TPA or PPDA can form SCOF-IC1 or SCOF-LZU1, respectively. Copyright American Chemical Society

preloaded with the mixtures of precursors A and B in the same experimental conditions only gives SCOFs with small domains and lot of defects. The results confirm the importance of the growth process control for on-surface synthesis.

From the viewpoint of reticular design, the porous networks with the same dimension can be designed by isomeric routes via exchanging the reaction groups on precursors with different symmetry. It is interesting to carry out comparative study to understand the thermodynamics and kinetics of the isomeric routes. Liu and coworkers fabricated a range of isomeric SCOFs with larger pore size by schiff base coupling reaction and investigated their growth processes [31]. One pair of the

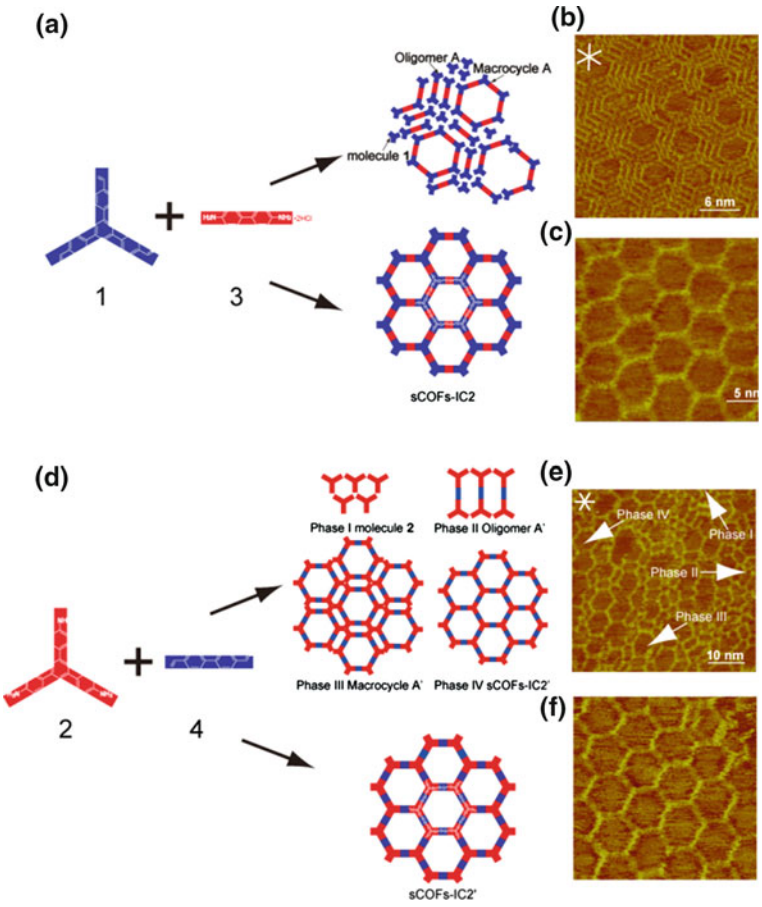

Fig. 5 **a** Molecular structures of monomers **1**, **3** and their reaction products. **b** High-resolution STM images of reaction product of **1** + **3** at lower temperature. *White lines* indicate graphite symmetry axes. **c** High-resolution STM image of $SCOF_{1+3}$ at higher temperature. **d** Molecular structures of monomers 2,4 and their reaction products. **e** High-resolution STM images of reaction product of 2 + 4 at lower temperature. *White lines* indicate graphite symmetry axes. **f** High-resolution STM image of $SCOF_{2+4}$ at higher temperature. Copyright Wiley VCH

building blocks was a threefold symmetrical aromatic aldehyde 1 and a two-old symmetrical aromatic amine **3** as shown in Fig. 5a. At a lower reaction temperature, a mixed assembly structure composed of unreacted monomer **3**, partially coupled linear oligomer, and ring structure. Interestingly, the mixed assembly shares the similar assembly motif to the close-packing assembly of pure molecule 1 on HOPG at room temperature. When reacted at a high temperature, SCOFs$_{\mathbf{1+3}}$ can be obtained as displayed in Fig. 5c. In the isomeric synthetic route, the terminal reactive groups were exchanged in two aromatic skeletons, as shown in Fig. 5d. At a low reaction temperature, mixed assembly structures of molecule **2**, the oligomer A′ and macrocycle A′, and SCOFs$_{\mathbf{2+4}}$ were got as shown in Fig. 5e. Again, the assembly motif is determined by the intermolecular interactions between the terminal amine groups. At a high temperature, large scales of SCOFs$_{\mathbf{2+4}}$ can be obtained. This experimental phenomena demonstrated that there exists a competition between the self-assembly and surface reaction. By changing the reaction temperature, the surface mobility of the building blocks and the molecular–surface interaction is changing, which leads to the evolutions of the nanostructure from blended assemblies structures to SCOFs.

A condensation reaction between aromatic amine and aldehyde was performed by Xu and coworkers on HOPG at solid–liquid interface at room temperature or by moderate heating under the conditions of low vacuum [32]. Through this mild method, SCOFs have been constructed on HOPG. Xu and coworkers used a threefold symmetric 1,3,5-tricarbaldehyde and a series of diamines with different aromatic backbone lengths as building blocks and obtained a series of SCOFs with tunable pore size ranging from 1.7 to 3.5 nm. They also fabricated the COFs on single-layer graphene on copper foil by CVD and applied DFT simulations to investigate the electronic structures and the SCOF–graphene interaction [33].

4 Other Dynamic Chemical Reactions for On-Surface Synthesis

Apart boronic acid dehydration reaction and schiff base coupling, many chemical reactions have been applied in surface-assisted synthesis, as shown in Scheme 2. Based on the reaction displayed in Scheme 2a, a trifunctional acid chloride and a bifunctional amine have been utilized as precursors to fabricated nanostructures on Ag(111) surface in UHV conditions [34]. By changing the annealing conditions, a series of corresponding oligomers and disordered two-dimensional polyamide covalent networks with different pore sizes were obtained. Jensen and coworkers applied melamine and trimesoyl chloride as building blocks and carried out on-surface synthesis experiment on Au(111) surface under UHV conditions [35]. They found that new diamide structures formed between adjacent melamine domains at room temperature. With annealing temperature increase, larger oligoamides were formed and the melamine domains transformed into a close-packed arrangement resulting from the incorporation of melamines into the original phase. Based on the

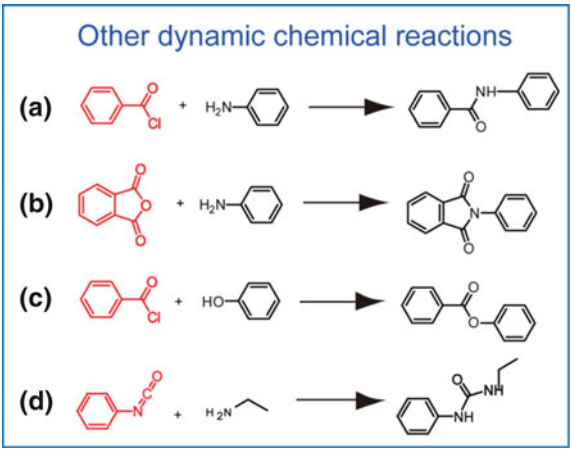

Scheme 2 Other dynamic chemical reactions utilized in the surface-assisted synthesis

reaction shown in Scheme 2b, 3,4,9,10-perylenetetracarboxylic dianhydrides and 2,4,6-tris(4-aminophenyl)-1,3,5-triazine have been used as building block of on-surface synthesis on Au(111) surface under UHV conditions [36, 37]. When annealing at a low temperature, the authors could only get H-bonded structures increasing temperatures, and amic acid intermediates began to be formed. Further temperature increase resulted in surface polyimide networks. By applying 1,3,5-tris (4-hydroxyphenyl)benzene and benzene-1,3,5-tricarbonyl trichloride as building blocks, a novel COF based on polyester condensation as shown in Scheme 2c has been fabricated on Au(111) surface [38]. Variable-temperature STM and XPS were adopted for in situ characterization, which confirmed the growth of hexagonal porous networks with uniform pore size about 2 nm. By means of low-temperature STM, the construction of polyimide films resulting from the condensation between diamines and dianhydrides in the UHV conditions has been investigated on Au(111). Based on the chemical reaction shown in Scheme 2d, the condensation reaction of 1,4-diaminobutane(1,4-DAB) with 1,3- and 1,4-phenylene diisocyanate (PDI) on Au(111) in UHV has been investigated by Greenwood and coworkers [39]. They chose an aliphatic diamine as one of their building blocks, which introduced chirality into the final structures by functionalizing the sp^3-hybridized methylene backbone. Urea oligomers formed at room temperature for each isocyanate isomer. When the temperature was increased, the length of the oligomer chains increased and finally extended ordered domains of oligomers were formed.

5 Conclusions and Outlook

Dynamic covalent bond not only has the robustness of conventional covalent bond but also can be reformed like the weak interaction in supramolecular chemistry. Through dynamic covalent chemical reaction, the growth process is more inclined to produce ordered structures due to the existence of correction and self-healing

process thanks to the natural reversibility of these formed bonds. Therefore, applying dynamic covalent chemistry in the surface-assisted synthesis is a promising bottom-up strategy to obtain regular nanostructures with covalent linker.

Compared to the solution-phase reaction, on-surface dynamic covalent chemistry has some unique features. When the reaction takes place on a surface, due to the surface confined effect, the mobility and movement of the building blocks is severely restricted. The precursors have different freedom on the surface compared to in the solution-phase reaction conditions. The involvement of adsorption, desorption, diffusion, and reaction steps in the whole process makes on-surface synthesis equally, if not more, complicated than the solution-phase reaction. Therefore, simply introducing the dynamic covalent chemistry into the on-surface synthesis is not a guarantee to achieve ordered nanostructures due to the characterization of the surface science. A lot of factors must be taken into consideration to regulate the reversibility of the dynamic covalent bond and the kinetics of the chemical reaction.

With great efforts in the past decade, a deep insight into the physical chemistry of on-surface synthesis has been gained and effective synthesis methods have been developed to make the final nanostructure more regular. Through surface-assisted synthesis based on dynamic covalent chemical bonds, we have achieved a series of macromoleculars, novel nanostructures, and two-dimensional covalent porous networks which combine stability and regularity. In particular, the chemical equilibrium control has been demonstrated in several different reaction systems and could be a universal strategy to tune the regularity. By surface-assisted synthesis, functionalized surfaced have been achieved, which can be and has the potential to be applied in making molecular devices, solar cells, molecular sieves, and gas absorbtion [40, 41]. In particular, two-dimensional organic frameworks, which have a structure similar to graphene, are the most challenging covalent structures to date from a synthesis perspective. By applying proper reaction control methods, highly ordered SCOF structures have been achieved. This gives a new perspective to design and fabricate complex nanostructures. Finally, we envision that the fundamental principle gained from the study of on-surface dynamic covalent chemistry can be beneficial to tailor more challenging non-reversible coupling reactions.

References

1. Zhang, X., Chen, T., Yan, H.-J., Wang, D., Fan, Q.-H., Wan, L.-J., Ghosh, K., Yang, H.-B., Stang, P.J.: Engineering of linear molecular nanostructures by a hydrogen-bond-mediated modular and flexible Host−Guest assembly. ACS Nano **4**(10), 5685–5692 (2010)
2. Gourdon, A.: On-surface covalent coupling in ultrahigh vacuum. Angew. Chem. Int. Ed. **47** (37), 6950–6953 (2008)
3. Lin, T., Shang, X.S., Liu, P.N., Lin, N.: Multicomponent assembly of supramolecular coordination polygons on a Au(111) surface. J. Phys. Chem. C **117**(44), 23027–23033 (2013)
4. Fan, Q., Wang, C., Han, Y., Zhu, J., Hieringer, W., Kuttner, J., Hilt, G., Gottfried, J.M.: Surface-assisted organic synthesis of hyperbenzene nanotroughs. Angew. Chem. Int. Ed. **52** (17), 4668–4672 (2013)

5. Liu, J., Ruffieux, P., Feng, X., Mullen, K., Fasel, R.: Cyclotrimerization of arylalkynes on Au (111). Chem. Commun. **50**(76), 11200–11203 (2014)
6. Lewis, E.A., Murphy, C.J., Liriano, M.L., Sykes, E.C.H.: Atomic-scale insight into the formation, mobility and reaction of Ullmann coupling intermediates. Chem. Commun. **50**(8), 1006–1008 (2014)
7. Eichhorn, J., Strunskus, T., Rastgoo-Lahrood, A., Samanta, D., Schmittel, M., Lackinger, M.: On-surface Ullmann polymerization via intermediate organometallic networks on Ag(111). Chem. Commun. **50**(57), 7680–7682 (2014)
8. Fan, Q., Wang, C., Han, Y., Zhu, J., Kuttner, J., Hilt, G., Gottfried, J.M.: Surface-assisted formation, assembly, and dynamics of planar organometallic macrocycles and zigzag shaped polymer chains with C–Cu–C bonds. ACS Nano **8**(1), 709–718 (2013)
9. Lipton-Duffin, J.A., Miwa, J.A., Kondratenko, M., Cicoira, F., Sumpter, B.G., Meunier, V., Perepichka, D.F., Rosei, F.: Step-by-step growth of epitaxially aligned polythiophene by surface-confined reaction. Proc. Natl. Acad. Sci. USA **107**(25), 11200–11204 (2010)
10. Schlutter, F., Rossel, F., Kivala, M., Enkelmann, V., Gisselbrecht, J.P., Ruffieux, P., Fasel, R., Mullen, K.: Pi-conjugated heterotriangulene macrocycles by solution and surface-supported synthesis toward honeycomb networks. J. Am. Chem. Soc. **135**(11), 4550–4557 (2013)
11. Mendez, J., Lopez, M.F., Martin-Gago, J.A.: On-surface synthesis of cyclic organic molecules. Chem. Soc. Rev. **40**(9), 4578–4590 (2011)
12. Zhang, X., Zeng, Q., Wang, C.: On-surface single molecule synthesis chemistry, a promising bottom-up approach towards functional surfaces. Nanoscale **5**(18), 8269–8287 (2013)
13. El Garah, M., MacLeod, J.M., Rosei, F.: Covalently bonded networks through surface-confined polymerization. Surf. Sci. **613**, 6–14 (2013)
14. Liu, X.-H., Guan, C.-Z., Wang, D., Wan, L.-J.: Graphene-like single-layered covalent organic frameworks, synthesis strategies and application prospects. Adv. Mater. **26**(40), 6912–6920 (2014)
15. Rowan, S.J., Cantrill, S.J., Cousins, G.R.L., Sanders, J.K.M., Stoddart, J.F.: Dynamic covalent chemistry. Angew. Chem. Int. Ed. **41**(6), 898–952 (2002)
16. Côté, A.P., Benin, A.I., Ockwig, N.W., O'Keeffe, M., Matzger, A.J., Yaghi, O.M.: Porous, crystalline, covalent organic frameworks. Science **310**(5751), 1166–1170 (2005)
17. Weigelt, S., Busse, C., Bombis, C., Knudsen, M.M., Gothelf, K.V., Strunskus, T., Wöll, C., Dahlbom, M., Hammer, B., Lægsgaard, E., Besenbacher, F., Linderoth, T.R.: Covalent interlinking of an aldehyde and an amine on a Au(111) surface in ultrahigh vacuum. Angew. Chem. **119**(48), 9387–9390 (2007)
18. Dienstmaier, J.F., Gigler, A.M., Goetz, A.J., Knochel, P., Bein, T., Lyapin, A., Reichlmaier, S., Heckl, W.M., Lackinger, M.: Synthesis of well-ordered COF monolayers: surface growth of nanocrystalline precursors versus direct on-surface polycondensation. ACS Nano **5**(12), 9737–9745 (2011)
19. Dienstmaier, J.F., Medina, D.D., Dogru, M., Knochel, P., Bein, T., Heckl, W.M., Lackinger, M.: Isoreticular two-dimensional covalent organic frameworks synthesized by on-surface condensation of diboronic acids. ACS Nano **6**(8), 7234–7242 (2012)
20. Guan, C.-Z., Wang, D., Wan, L.-J.: Construction and repair of highly ordered 2D covalent networks by chemical equilibrium regulation. Chem. Commun. **48**(24), 2943–2945 (2012)
21. Faury, T., Clair, S., Abel, M., Dumur, F., Gigmes, D., Porte, L.: Sequential linking to control growth of a surface covalent organic framework. J. Phys. Chem. C **116**(7), 4819–4823 (2012)
22. Acharyya, K., Mukherjee, S., Mukherjee, P.S.: Molecular marriage through partner preferences in covalent cage formation and cage-to-cage transformation. J. Am. Chem. Soc. **135**(2), 554–557 (2013)
23. Jin, Y., Zhu, Y., Zhang, W.: Development of organic porous materials through schiff-base chemistry. Cryst. Eng. Comm. G **15**, 1484–1499 (2013)
24. Weigelt, S., Busse, C., Bombis, C., Knudsen, M.M., Gothelf, K.V., Lægsgaard, E., Besembacher, F., Linderoth, T.R.: Surface synthesis of 2D branched polymer nanostructures. Angew. Chem. Int. Ed. **47**(23), 4406–4410 (2008)

25. Ciesielski, A., El Garah, M., Haar, S., Kovaricek, P., Lehn, J.M., Samori, P.: Dynamic covalent chemistry of bisimines at the solid/liquid interface monitored by scanning tunnelling microscopy. Nat. Chem. **6**(11), 1017–1023 (2014)
26. Li, Y., Wan, J., Deng, K., Han, X., Lei, S., Yang, Y., Zheng, Q., Zeng, Q., Wang, C.: Transformation of self-assembled structure by the addition of active reactant. J. Phys. Chem. C **115**(14), 6540–6544 (2011)
27. Hu, F.-Y., Zhang, X.-M., Wang, X.-C., Wang, S., Wang, H.-Q., Duan, W.-B., Zeng, Q.-D., Wang, C.: In Situ STM investigation of two-dimensional chiral assemblies through schiff-base condensation at a liquid/solid interface. ACS Appl. Mater. Interfaces **5**(5), 1583–1587 (2013)
28. Liu, X.-H., Wang, D., Wan, L.-J.: Surface tectonics of nanoporous networks of melamine-capped molecular building blocks formed through interface schiff-base reactions. Chem. Asian J. **8**(10), 2466–2470 (2013)
29. Tanoue, R., Higuchi, R., Enoki, N., Miyasato, Y., Uemura, S., Kimizuka, N., Stieg, A.Z., Gimzewski, J.K., Kunitake, M.: Thermodynamically controlled self-assembly of covalent nanoarchitectures in aqueous solution. ACS Nano **5**(5), 3923–3929 (2011)
30. Liu, X.-H., Guan, C.-Z., Ding, S.-Y., Wang, W., Yan, H.-J., Wang, D., Wan, L.-J.: On-surface synthesis of single-layered two-dimensional covalent organic frameworks via solid-vapor interface reactions. J. Am. Chem. Soc. **135**(28), 10470–10474 (2013)
31. Liu, X.-H., Mo, Y.-P., Yue, J.-Y., Zheng, Q.-N., Yan, H.-J., Wang, D., Wan, L.-J.: Isomeric routes to schiff-base single-layered covalent organic frameworks. Small **10**(23), 4934–4939 (2014)
32. Xu, L., Zhou, X., Yu, Y., Tian, W.Q., Ma, J., Lei, S.: Surface-confined crystalline two-dimensional covalent organic frameworks via on-surface schiff-base coupling. ACS Nano **7**(9), 8066–8073 (2013)
33. Xu, L., Zhou, X., Tian, W.Q., Gao, T., Zhang, Y.F., Lei, S., Liu, Z.F.: Surface-confined single-layer covalent organic framework on single-layer graphene grown on copper foil. Angew. Chem. Int. Ed. **53**(36), 9564–9568 (2014)
34. Schmitz, C.H., Ikonomov, J., Sokolowski, M.: Two-dimensional polyamide networks with a broad pore size distribution on the Ag(111) surface. J. Phys. Chem. C **115**(15), 7270–7278 (2011)
35. Jensen, S., Greenwood, Früchtl H.A., Baddeley, C.J.: STM investigation on the formation of oligoamides on Au(111) by surface-confined reactions of melamine with trimesoyl chloride. J. Phys. Chem. C **115**(17), 8630–8636 (2011)
36. Treier, M., Fasel, R., Champness, N.R., Argent, S., Richardson, N.V.: Molecular imaging of polyimide formation. Phys. Chem. Chem. Phys. **11**(8), 1209–1214 (2009)
37. Treier, M., Richardson, N.V., Fasel, R.: Fabrication of surface-supported low-dimensional polyimide networks. J. Am. Chem. Soc. **130**(43), 14054–14055 (2008)
38. Marele, A.C., Mas-Balleste, R., Terracciano, L., Rodriguez-Fernandez, J., Berlanga, I., Alexandre, S.S., Otero, R., Gallego, J.M., Zamora, F., Gomez-Rodriguez, J.M.: Formation of a surface covalent organic framework based on polyester condensation. Chem. Commun. **48** (54), 6779–6781 (2012)
39. Greenwood, J., Früchtl, H.A., Baddeley, C.J.: Surface-confined reaction of aliphatic diamines with aromatic diisocyanates on Au(111) leads to ordered oligomer assemblies. J. Phys. Chem. C **117**(9), 4515–4520 (2013)
40. Wan, S., Guo, J., Kim, J., Ihee, H., Jiang, D.: A belt-shaped, blue luminescent, and semiconducting covalent organic framework. Angew. Chem. Int. Ed. **48**(18), 3207 (2009)
41. Baughman, R.H., Eckhardt, H., Kertesz, M.: Structure-property predictions for new planar forms of carbon: Layered phases containing sp^2 and *sp* atoms. J. Chem. Phys. **87**(11), 6687–6699 (1987)

Synthesis of Atomically Precise Graphene-Based Nanostructures: A Simulation Point of View

L. Talirz, P. Shinde, D. Passerone and C.A. Pignedoli

Abstract We illustrate how atomistic simulations can complement experimental efforts in the bottom-up synthesis of graphene-based nanostructures on noble metal surfaces. After a brief introduction to the field, we review the state of the art of relevant computational methods. We then proceed by example through questions related to adsorption and diffusion, reactions and electronic structure, indicating both the strengths and limitations of computational approaches.

1 Introduction

In graphene-based nanotechnology, the motivation to explore *bottom-up* approaches emerges from a need for atomic precision that cannot be satisfied by traditional *top-down* fabrication methods.

Graphene, "a flat monolayer of carbon atoms tightly packed into a two-dimensional (2D) honeycomb lattice" [1], is a material with many extraordinary properties [2, 3]. From the perspective of applications in electronic switching devices, there is first of all the exceptional electron mobility that has enabled switching speeds exceeding 400 GHz [4]. Furthermore, the two-dimensional nature of graphene is beneficial to the electrostatics in transistor configurations, allowing to move source and drain contacts very close together before adverse short-channel effects set in [5]. And last, but not least, graphene is mechanically flexible, making

L. Talirz · P. Shinde · D. Passerone · C.A. Pignedoli (✉)
Nanotech@surfaces Laboratory, Empa, Swiss Federal Laboratories for Materials Science and Technology, Überlandstrasse, 129, 8600 Dübendorf, Switzerland
e-mail: carlo.pignedoli@empa.ch

L. Talirz
e-mail: Leopold.Talirz@empa.ch

C.A. Pignedoli
NCCR MARVEL, Empa, Swiss Federal Laboratories for Materials Science and Technology, Überlandstrasse, 129, 8600 Dübendorf, Switzerland

A. Gourdon (ed.), *On-Surface Synthesis*, Advances in Atom and Single Molecule Machines, DOI 10.1007/978-3-319-26600-8_12

it a promising candidate for applications in high-frequency organic electronics on flexible substrates. When it comes to room temperature digital logic applications, however, sufficient on-off ratios can be achieved only by introducing a sizeable band gap into the electronic structure of the semimetal graphene [5]. And one way of achieving this goal is by quantum confinement at the nanoscale.

There are different classes of nanostructures in this category. Prominent examples are stripes of graphene with widths in the low nm range, termed graphene nanoribbons (GNRs), but also their rolled-up counterparts, the single-wall carbon nanotubes (SWCNTs). While this chapter is dedicated to GNRs and other flat graphene nanostructures, we point out that on-surface chemistry is relevant also to the field of SWCNTs, where the surface-supported synthesis of specifically designed end-caps has recently enabled the controlled fabrication of monodisperse SWCNTs for the first time [6].

An obvious difference between GNRs and SWCNTs is that GNRs have edges, and it has been predicted early on that the atomic structure of the edges plays an important role in determining their electronic properties [58]. Therefore, the limited control over edge roughness and edge passivation in *top-down* approaches, such as lithography and etching [7], sonochemical cutting and breaking [8], or even unzipping of carbon nanotubes [9] seriously hampers the production of GNRs with reliable electronic transport characteristics. But while the need for atomically smooth edges seems to call for a *bottom-up* strategy, traditional solution-based polymerization chemistry faces a solubility problem, when macromolecules containing several hundreds to thousands of atoms are to be synthesized.

This is, where on-surface chemistry has come in to play, following pioneering works in the years 2007–2009 that described the surface-supported covalent assembly of networks and conjugated molecular wires [10–12]. Figure 1 summarizes the bottom-up approach for the synthesis of GNRs developed in collaboration between the nanotech@surfaces Laboratory at Empa, led by Roman Fasel, and the Department for Synthetic Chemistry at the Max Planck Institute for Polymer Research, led by Klaus Müllen [13]. The starting point is a molecular precursor that is designed specifically to yield a particular GNR. Figure 1 shows the 10,10′-dibromo-9,9′-bianthryl (DBBA) molecule, which yields an armchair graphene nanoribbon of width $N = 7$ (7-AGNR). The molecular precursor is then deposited onto a noble metal substrate under UHV conditions. Upon annealing at a characteristic temperature T_1, the molecules undergo dehalogenation and the radical intermediates start diffusing across the surface. When the radicals meet, they self-assemble into flexible polymer chains via aryl–aryl coupling, similar to the classical Ullmann reaction [14]. Finally, annealing at a temperature $T_2 > T_1$ activates the cyclodehydrogenation reaction, which transforms the polymers into planar GNRs.

While on-surface chemistry has proven to deliver a framework that works, this new route is not without its challenges. In particular, approaching the design of suitable precursors on the basis of trial and error risks substantial waste of resources both during precursor synthesis and subsequent on-surface coupling trials. Strong computational support can therefore be of great value, not only in order to avoid

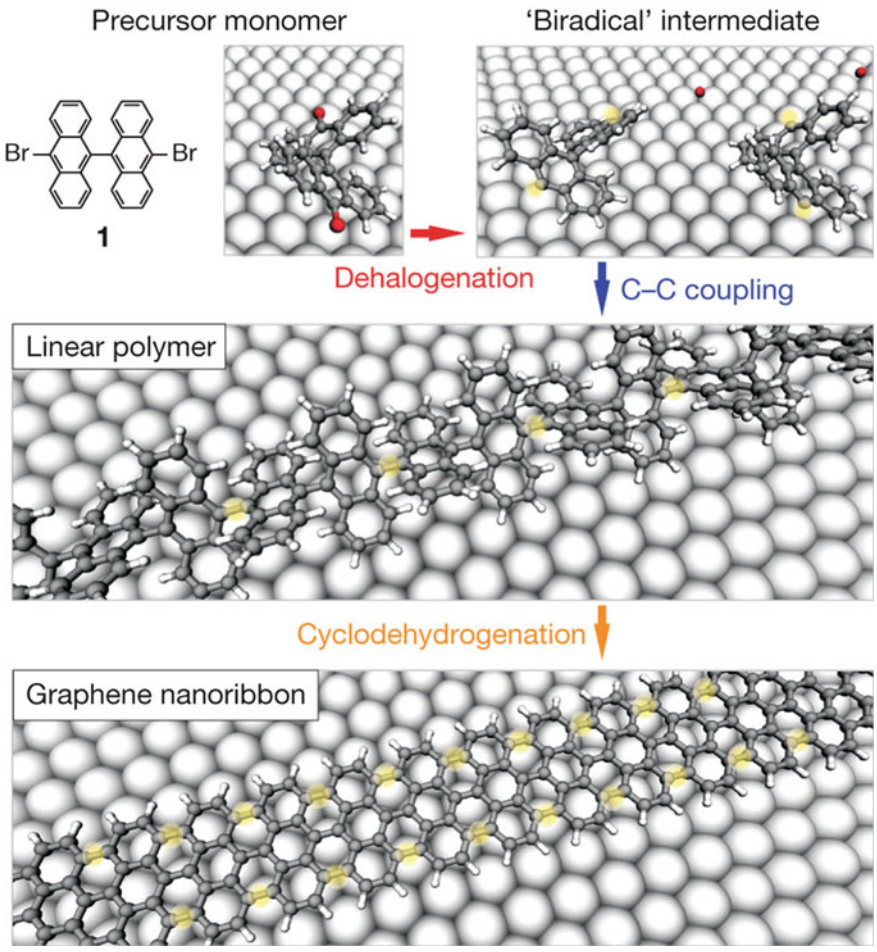

Fig. 1 Basic steps of surface-supported GNR synthesis. *Top* Dehalogenation of precursor monomers (here, 10,10′-dibromo-9,9′-bianthryl) after deposition on noble metal substrate. *Center* Formation of linear polymers by covalent coupling of diffusing dehalogenated intermediates. *Bottom* Formation of fully aromatic GNRs (here, 7-AGNR) by cyclodehydrogenation. Figure and caption reproduced with permission from Macmillan Publishers Ltd: [13], Copyright (2010)

synthesis routes that are predicted to fail or to provide products with unwanted properties, but also in aiding the interpretation of microscopy and spectroscopy data as well as in unraveling the underlying reaction mechanisms, allowing for the systematic optimization of processing parameters.

In order to be successful at this ambitious task, atomistic calculations must reach appropriate levels of precision in describing the following aspects:

(I) The closely related processes of adsorption and diffusion on the surface. This concerns questions about preferred adsorption sites, adsorption energies, the

cleaving of weaker bonds (activating precursors for the reaction with other molecules), and diffusion coefficients.

(II) The chemical reaction between molecules. This entails the prediction of reaction paths and activation energies that determine the required annealing temperatures, possibly including limiting factors such as the presence of hydrogen on the surface.

(III) The electronic properties of the reaction product. Of interest are both its intrinsic properties in order to judge its potential for applications and the influence of the nearby surface in order to enable comparison with microscopy and spectroscopy experiments. Important figures of merit include the fundamental and optical gap, the density of states (band structure) and the optical absorption spectrum.

After an overview of the relevant tools offered by state-of-the-art atomistic simulations, the remaining sections of this chapter will address each of the above aspects through recent examples from the field of graphene-based nanostructures, illustrating how experiment and theory can join forces on the path toward a nanodesign strategy that is reliable, accurate, and efficient at the same time.

2 Computational Methods

The study of molecules on surfaces represents an interface between two well-established fields of computational research. Molecules traditionally are considered the domain of quantum chemistry, meaning wave-function-based methods with an underlying variational principle, using localized basis sets. Solids and their surfaces on the other hand are the domain of computational solid-state physics, with methods such as density functional theory (DFT) [15] using plane-wave basis sets with periodic boundary conditions. Combining molecules and surfaces thus requires some level of choice and compromise.

When choosing to adopt periodic boundary conditions, a typical unit cell is shown in Fig. 2. The molecule is supported by a slab of several atomic layers of the substrate. Spurious interactions between periodic replica of the molecule are minimized by increasing the lateral dimensions of the unit cell, while spurious interactions between slabs are avoided by introducing sufficient amounts of vacuum. Starting from a precursor molecule consisting of several tens of atoms, the unit cell may contain several hundreds, sometimes thousands of atoms. Systems of this size are currently out of reach for most quantum chemistry methods, and they remain challenging even for the most efficient DFT codes commonly used for large-scale ab initio simulations, such as CPMD, CP2K, or SIESTA [16–18].

In the following, we describe different ways of modeling the interaction between molecule and surface and their consequences for the simulation of on-surface

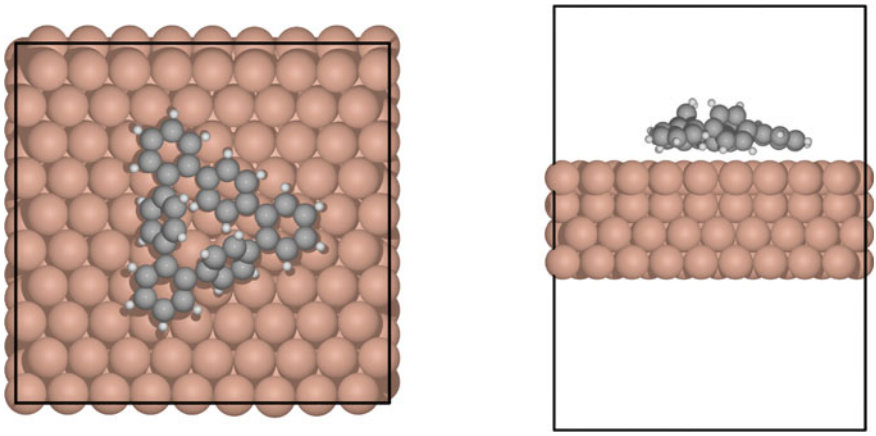

Fig. 2 *Top* and *side view* of slab geometry adapted from [19]. The cyclohexa-*o*-*p*-*o*-*p*-*o*-*p*-phenylene (CopP) molecule is supported by a Cu(111) slab of four atomic layers. While the molecule itself consists of 60 atoms, the unit cell (*black lines*) contains 420 atoms

chemistry (see also [20] for a recent review on the topic). The last part of the section is dedicated to the prediction of the valence electronic structure of graphene-based nanomaterials, both on a qualitative level and with the goal of comparing to (inverse) photoemission, tunneling, or optical absorption spectroscopy. For ab initio calculations of core-level [21, 22], infrared [23] and Raman spectra [23–25], we point the interested reader to the corresponding references.

2.1 Physisorption

If the molecule–substrate interactions are dominated by dispersion forces, a combination of quantum mechanics and molecular mechanics (QM/MM) [26, 27] can be considered. In the example illustrated by Fig. 3, the metallic substrate is treated within the empirical embedded atom method (EAM) [28]. The molecule is described by standard Kohn–Sham DFT [15, 29] and interacts with the substrate through an atomic pair potential [30] giving rise to an interaction energy

$$E = \sum_{AB} C_v^{AB} \mathrm{e}^{-\alpha_v^{AB} R_{AB}} + C_c^{AB} \mathrm{e}^{-\alpha_c^{AB} R_{AB}} - \frac{C_6^{AB}}{(R_{AB})^6}$$

where the sum goes over all atoms A of the molecule and B of the slab. The first two terms describe the Pauli repulsion due to valence and core electrons of the metal substrate, while the third term describes the attractive dispersion force. The considerable computational advantage of such a QM/MM approach provides access to the dynamics of the system, allowing for an unbiased search for possible reaction

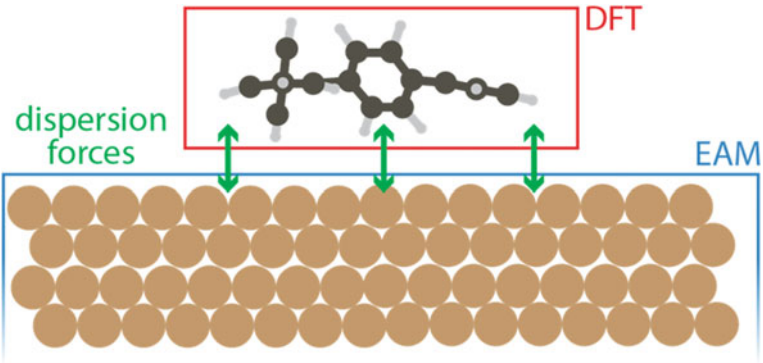

Fig. 3 Schematic representation of the QMMM approach used in [31] to study the cyclodehydrogenation of CopP on a Cu(111) substrate. While the physisorbed molecule is described within DFT, the substrate is modeled with the EAM. The two systems are coupled via an empirical potential [30] mimicking van der Waals attraction and Pauli repulsion

paths. If the process of interest involves significant energy barriers, making it a "rare event," the molecular dynamics need to be accelerated.

In the case of direct metadynamics [32, 33], the system begins moving freely, but over time is biased against revisiting configurations that have already been explored. The repulsive bias potential is placed not on the set of atomic positions x visited by the system, but on the corresponding values of a limited number of collective variables (CVs) $S_\alpha(x)$, $\alpha = 1 \ldots d$, thereby drastically reducing the dimensionality of the problem. In typical applications, $d = 2$ or $d = 3$, and the CVs describe distances, angles, or coordination numbers that are deemed important indicators of the reaction of interest. By keeping track of the bias potential deposited during the time evolution of the system, the free energy surface can be constructed in the space of the collective variables.

We note that while the concept of collective variables is very flexible [34], finding adequate CVs for complex reactions can be delicate and attempts have been made to automate this process [35]. For a recent review, we refer interested readers to [36].

2.2 *Chemisorption*

In many cases, bond formation between the molecule and the substrate is an essential ingredient of the reaction. Since no empirical potentials are available that accurately model the formation of metal–organic bonds, a complete quantum mechanical description of the system is then the only option. Kohn–Sham DFT

using (semi-)local approximations to the exchange-correlation functional has a very successful track record in applications of dense matter and covalently bound molecules. However, it was recognized early on that this type of approximation is, by construction, unable to capture the non-local nature of dispersion forces [37]. Since these forces are a crucial component of the interaction between molecules and surfaces, we discuss three common approaches to ameliorate the problem (for more details see [38]).

To some degree, it is possible to adapt semi-local exchange-correlation functionals to emulate dispersion effects at near-equilibrium atomic distances. At the expense of higher computational complexity, further improvements can be made by admixing a portion of the non-local Hartree–Fock exchange ("hybrid functionals") and including the second derivative of the density as a variable ("meta functionals") [39]. Nevertheless, a (semi-)local approximation of the correlation energy ultimately leads to an exponential decay of the interaction for large atomic separations [37]. These functionals can therefore not be expected to adequately describe systems such as large molecules or molecules on surfaces, if interactions over larger distances are important.

Another class of dispersion corrections approaches the problem in a semi-classical manner, neglecting all knowledge of the electron density and formulating the dispersion interaction in terms of an interatomic potential [38]:

$$E_{\text{disp}} = -\sum_{AB} \sum_{n=6,8,\ldots} s_n \frac{C_n^{AB}}{(R_{AB})^n} f_{\text{damp}}(R_{AB})$$

Here, AB runs over all pairs of atoms, R_{AB} is their distance and C_n^{AB} denotes the averaged (isotropic) nth-order dispersion coefficient between atoms of the corresponding kind, which can be computed ab initio. This dispersion energy is then simply added to the total DFT energy, thus ensuring the asymptotic form $1/(R_{AB})^6$ of the interaction. In order to avoid double-counting of correlation, the dispersion interaction is damped at short distances by a continuous function $f_{\text{damp}}(R_{AB})$, where details of the damping function as well as the scaling factors s_n may be used to adapt to particular (semi-)local density functionals. Extensions of the scheme include the treatment of three-body interactions [40] as well as the effects of the hybridization state on the dispersion coefficients, based on fractional occupation numbers [40] or atomic volumes [41]. This class of corrections delivers a computationally cheap way to add dispersion forces on top of various (semi-)local exchange-correlation functionals, providing, in the case of DFT-D3, dispersion coefficients for the first 94 elements of the periodic table [40]. While this has lead to a widespread adoption, some criticism remains. The first concerns the dispersion coefficients, which need to be determined on one or several reference systems, be it computationally or experimentally. These are traditionally chosen to be either the bare elements or small molecules containing the elements in question [40], which is suitable for applications in molecular systems, but provides an electronic environment that can be very different from bulk materials. For the particular

application of molecules on coinage metal surfaces, a scheme has been proposed to include screening and polarization effects at the level of atomic pairwise interactions [42]. The second and perhaps more worrying remark concerns the finding that molecular binding energies in many cases depend more sensitively on the empirical parameterization of the damping function than on the physically sound dispersion coefficients [43].

A third approach that has gained popularity in recent years is a density-based treatment of the non-local correlation energy, which takes the form

$$E_c^{nl}[n] = \int n(r)\phi[n](r,r')n(r')\,d^3r\,d^3r'$$

The kernel ϕ is derived from first principles using a plasmon pole approximation to the local dielectric function and is a function of $|r - r'|$, the electron density n and its gradient at positions r, r' [44, 45]. Treated self-consistently, the variational derivative $V_c^{nl}(r) = \delta E_c^{nl}/\delta n(r)$ modifies the exchange-correlation potential $V_{xc} = V_{xc}^{l} + V_c^{nl}$ and thus acts directly on the Kohn–Sham wave functions. One significant advantage over DFT-D methods is therefore that the effect of the electronic environment, including charge transfer, on dispersion interactions is captured in a general and physically sound manner [38]. Contrary to DFT-D methods, the non-local correlation term is not damped at short distances, meaning that particular care needs to be taken in selecting the (semi)-local exchange-correlation functional in order to avoid double-counting of correlation. Besides existing functionals, such as PW86 [45], some have thus been designed specifically for this purpose [46]. Regarding computational cost, linear scaling algorithms are available [47] that render the overhead of these so-called van der Waals density functionals negligible as compared to standard semi-local calculations.

Using DFT with dispersion corrections, the calculation of adsorption geometries and adsorption energies is feasible for systems containing several hundred [48] to more than thousand atoms. Dynamics and thus free energy profiles are typically out of reach. If the initial and final states of a process are known, the pioneering methods of Elber and coworkers [49], the nudged elastic band (NEB) [50, 51], and string [52] methods can be used to compute 0K reaction barriers and provide a description that can afterward be extended to finite-temperature free energy effects [53, 54].

As illustrated by Fig. 4, the NEB method requires not only the knowledge of the initial (green bead) and the final states (red bead), but also an initial guess for the reaction path that connects the two (white beads). After optimization of the "elastic" band, the intermediate configurations, also known as "images," follow the minimum energy profile and one image (black bead) has climbed to the saddle point [51]. In simple cases, a first guess for the images is obtained by linear interpolation between initial and final coordinates or a sequence of constrained geometry optimizations. However, the initial guess constitutes a strong bias of the overall picture of the reaction and in general different paths have to be considered (on top of the possibility of different final states).

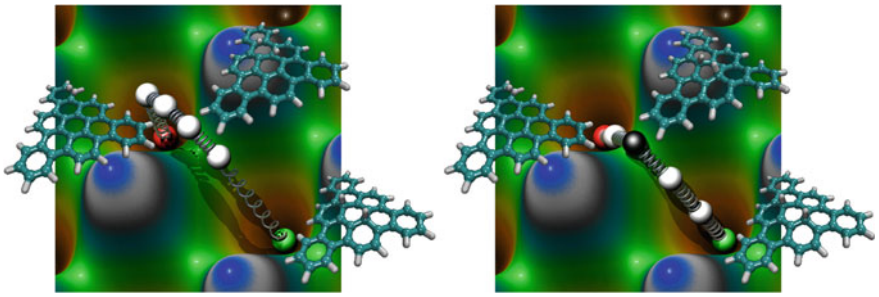

Fig. 4 Pictorial representation of a NEB calculation describing a dehydrogenation step in the synthesis of tribenzo[a,g,m]coronene. *Left panel* Initial guess of the reaction path from initial state (*green* bead) to final state (*red* bead) on the potential energy surface. *Right panel* After optimization, the intermediate configurations (*white* beads) follow the minimum energy profile. One configuration (*black* bead) has climbed to the saddle point

2.3 Electronic Structure

Since the synthesis of graphene-based nanostructures is often aimed at electronics applications, a reliable prediction of the intrinsic electronic structure of different possible targets is very useful. The main focus tends to lie on the sp^2-hybridized carbons and their π-electronic structure. Some insights can be gained already with pen and paper, using intuitive chemistry rules such as Clar's theory of the aromatic sextet [55]. These include qualitative information about the π–electron distribution, bond-length alternation and, in the case of zigzag edges, the presence of edge-localized unpaired electrons [56].

The next level of understanding is provided by tight-binding models. Considering only the π-electrons, the system is described by a Hamiltonian

$$H = -t \sum_{\langle ij \rangle} a_j^\dagger a_i + h.c.$$

where $t \approx 3$ eV is the hopping integral, $a_i^\dagger$, a_i are the electron creation and annihilation operators at carbon site i and the sum runs over nearest neighbors [57, 58]. In the case of armchair and zigzag GNRs, this model can be solved analytically [59, 60], allowing for in-depth investigations of the width- and edge-dependence of the electronic band structure. Further physics can be introduced by including site-dependent potentials [61], hopping between 3rd-nearest neighbors [62], Coulomb interactions between electrons [63] or larger basis sets [64]. These models, however, need to be parameterized and are typically fitted to band structures calculated ab initio.

Kohn–Sham DFT with (semi-)local exchange-correlation functionals provides qualitatively correct answers to many relevant questions, including band ordering, band gap hierarchy, band dispersion, shape of wave functions, and spin polarization [65–67]. This makes Kohn–Sham DFT suitable for comparing the electronic

structure of different nanostructures. Still, direct comparison with experiments is challenging, even at this level. One area, where DFT can be of great value, is the interpretation of scanning tunneling microscopy (STM) images. The shape of the Kohn–Sham orbitals is typically very accurate [68] and adequate adsorption geometries can be obtained by including the substrate together with a suitable dispersion correction. For a quantitative prediction of spectroscopic information, however, the independent-particle approximation is too simplistic. Not only does the Kohn–Sham gap significantly underestimate the band gap of bulk semiconductors [68], the discrepancy is amplified in low-dimensional materials, such as the quasi-one-dimensional GNRs or carbon nanotubes, where screening of the Coulomb interaction between electrons is strongly reduced [65].

One approach to tackle the problem is many-body perturbation theory (MBPT), in which the strongly interacting electrons are replaced by the concept of weakly interacting quasi-particles. In the form of the GW approximation [69], MBPT has provided very accurate quasi-particle band gaps of bulk materials [70] and is increasingly applied also to graphene-based nanomaterials [65, 71]. While we refer interested readers to [72] for an extensive introduction of the underlying theory, we stress one important fact: In nanostructures, where the Coulomb interaction is screened only weakly, the energy gap extracted from spectroscopy experiments strongly depends on the nature of the excitation. In the case of (inverse) photoemission spectroscopy and scanning tunneling spectroscopy (STS), the system under study is promoted from an N-electron ground state to an excited state with $N \pm 1$ electrons. The *fundamental* gap associated with these charged excitations is defined as

$$\Delta = IP - EA = E(N) - E(N+1) - (E(N-1) - E(N)),$$

where IP (EA) denote the ionization potential (electron affinity) of the system and $E(N)$ the ground-state energy of a system with N electrons. Δ coincides with the quasi-particle gap in the GW approximation. In optical absorption experiments, using techniques such as reflectance anisotropy spectroscopy, electron–hole pairs are created and the number of electrons is conserved. Within MBPT, these neutral excitations are described by the Bethe–Salpeter equation [73], often using the GW electronic structure as a starting point. The resulting *optical* gap is reduced with respect to the fundamental gap by the binding energy of the lowest-lying exciton. In graphene-based nanostructures, this energy can be substantial, even exceeding 1 eV [71, 74, 75].

Finally, additional complications arise from the presence of the nearby substrate, which significantly increases the screening of the Coulomb interaction with respect to the nanostructures in vacuum. The computational cost of GW calculations scales with $M^3 - M^4$, where M is the number of atoms in the system [76], making systems with $M > 100$ extremely challenging to handle. Full GW calculations of molecules on surfaces have thus far concentrated on small molecules and correspondingly small surface unit cells [77, 78, 81] and/or thin supporting substrates [79]. Alternatively, substrate effects may be included into GW calculations of the isolated molecule via classical image charge models [77, 80–82].

3 Adsorption and Diffusion

Once the molecular precursors are adsorbed on a metallic substrate, the factors influencing their diffusion are the surface geometry (the presence of steps, corrugations, defects, or adatoms), the surface–molecule interactions (dominated either by dispersion forces or by chemical bonding) and the molecule–molecule interactions. The study of diffusion mechanisms starts from the identification of stable adsorption sites and requires a systematic verification of all geometrically possible and chemically sound adsorption sites by means of geometry optimization. This analysis can be performed at different levels of theory, the system size typically being a limiting factor for beyond-DFT methods.

Some general insight into molecular self-assembly can be obtained from simple models, such as the "patchy-disk" model [83], accounting only for the geometry and the strength of the interaction. As illustrated in Fig. 5, Whitelam et al. concentrate on threefold-coordinated building blocks, which are represented as disks with angular domains that either allow for bond formation (green) or do not (blue). Bond strength and bond flexibility are characterized by the interaction energy $-\epsilon$ and the opening angle 2ω of the interacting stripes. Varying only these two parameters within Monte Carlo simulations, Whitelam et al. are able to reproduce the characteristics of networks ranging from graphene to DNA-based polymers with building blocks spanning three orders of magnitude in length scale.

We now turn our focus to graphene-based nanostructures formed by polymerization through Ullman-type reactions [14] on noble metal surfaces. We concentrate on high-symmetry close-packed surfaces, in particular the (111) surface, although vicinal surfaces [82, 89] as well as the (110) surface [90] have also been explored.

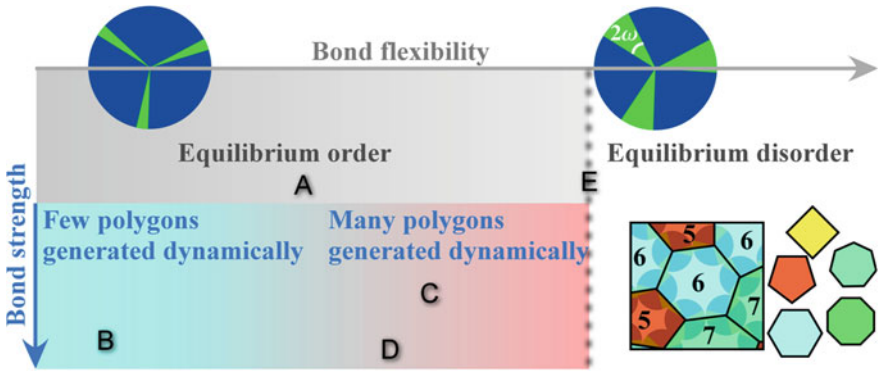

Fig. 5 "Patchy-disk" model of threefold-coordinated building blocks. In equilibrium, the periodic honeycomb network [84] (*A*) or a non-periodic polygon network [85] (*E*) can be formed. Out-of-equilibrium structures include honeycomb polycrystals [86] (*B*), polygon networks that can evolve to the honeycomb [87] (*C*), or kinetically trapped polygon network glasses [88] (*D*). Figure and caption adapted with permission from [83]. Copyright (2014) American Physical Society

A selection of successful molecular precursors is shown in Fig. 6. The molecules contain carbon–halogen (typically Br or I) bonds that are intended to be cleaved by the formation of metal–organic bonds on the surface. The broken C–halogen bonds

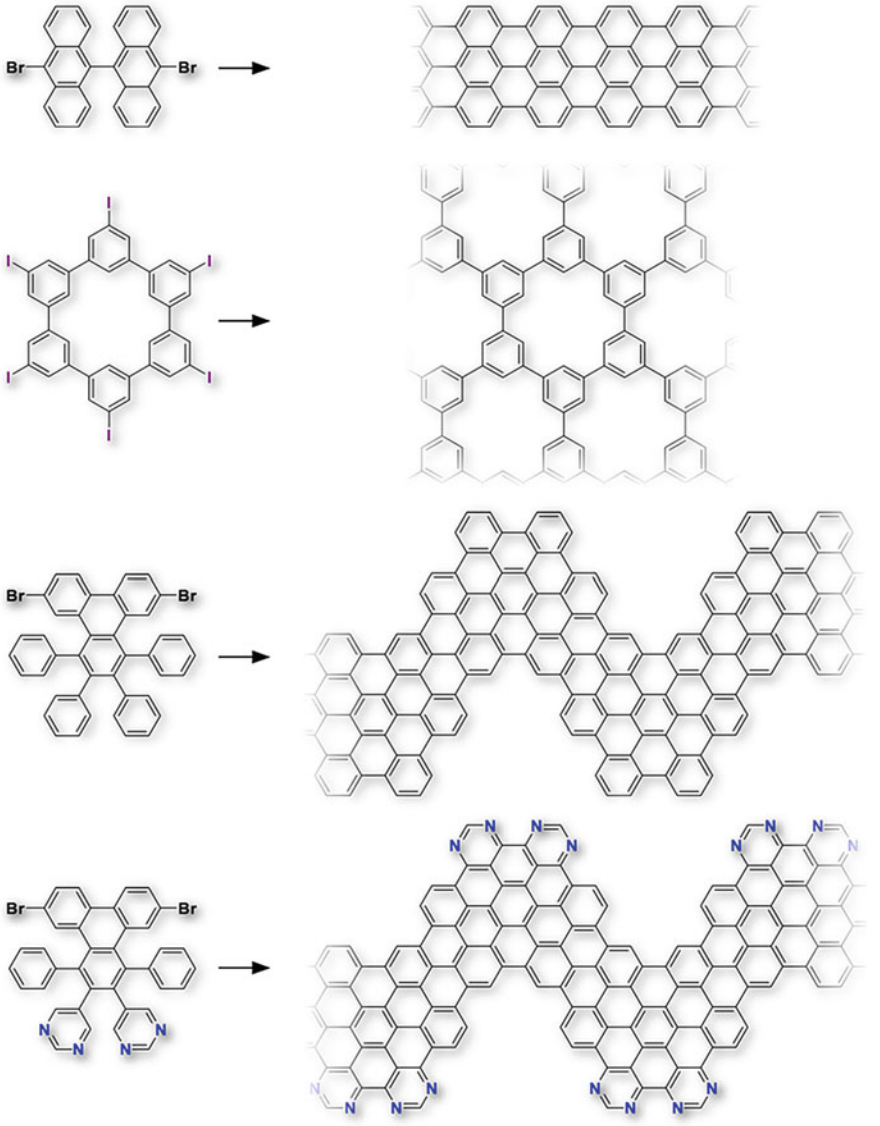

Fig. 6 Chemical drawings of molecular precursors for the metal-supported synthesis of atomically precise graphene nanostructures. Besides DBBA (*top*) used for the synthesis of 7-AGNRs [13] and hexaiodo-substituted cyclohexa-*m*-phenylene (CHP) used for the synthesis of porous graphene [92], the dibromo-tetraphenyltriphenylene molecule provides chevron-like GNRs [13], including the possibility of atomically precise doping with nitrogen atoms [93, 94]

are then the anchoring points for the self-assembly into polymers. In most of the cases (but not always [91]), dehalogenation occurs at low temperature and diffusion needs to proceed in the presence of metal–organic bonds that stabilize the radicals.

In the case of iodine, the dehalogenation process starts already below room temperature. Scission of C–I is reported at 166 K on Au(111) [95] and is completed at room temperature also on other noble metal substrates (see e.g., [92, 96]). However, iodine can still be present on the substrate at 500 K, as reported in [12] for Cu(110).

A simple case of the interplay between adsorption sites and the diffusion process is offered by the Ullmann coupling of two iodobenzene molecules on Cu(111). Starting from the evidence that iodobenzene undergoes dehalogenation already at room temperature, Nguyen and coworkers studied the adsorption sites and diffusion paths for phenyl radicals on the Cu(111) surface [97]. The formation of a single metal–organic bond leaves high rotational freedom to the adsorbed molecule. Figure 7 depicts the most energetically favorable adsorption geometry. The molecule is bound to the surface atom and may diffuse to its six first neighbors with equal probability. A direct jump between initial state (IS) and final state (FS) is associated with a high energy barrier, but a different initial guess for the NEB allows to identify a low-energy, two-step diffusion mechanism. This mechanism can be ported to the (111) surfaces of the other noble metals.

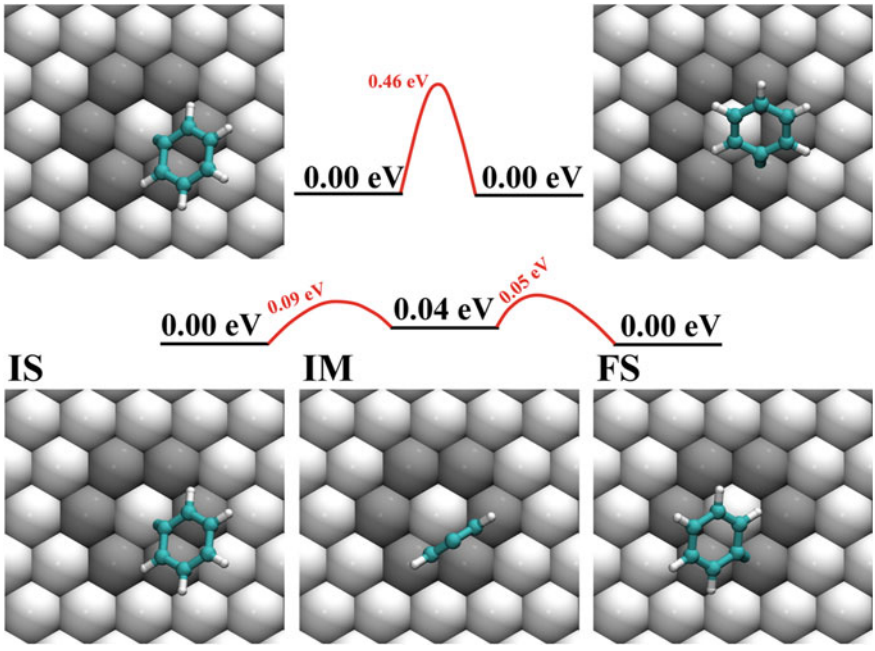

Fig. 7 Possible high-energy (*top*) and low-energy (*bottom*) diffusion pathways for a phenyl radical on the (111) surface of a noble metal. Figure and caption adapted from [97] with permission from PCCP Owner Societies

As demonstrated by this simple example, the rotational freedom of the molecule and the number of metal–organic bonds formed with the substrate can play a pivotal role in the diffusion process. Increasing complexity of the molecular precursor is reflected by a more complex diffusion mechanism. A remarkable example of the diffusion of a large molecular precursor is provided by the case of hexaiodo-substituted cyclohexa-*m*-phenylene (CHP) used to synthesize networks of porous graphene [86]. Again, the experimental evidence, supported by ab initio calculations, suggests that the C–I bonds are broken upon adsorption and iodine desorbs, when the temperature is increased to promote diffusion. The molecule is able to form six metal–organic bonds, one for each lost iodine atom. Due to the strong anchoring to the substrate, a naive initial guess for a NEB calculation of the diffusion pathway leads to very high activation barriers. A low-energy diffusion path, where the molecule rotates around one of the metal–organic bonds to diffuse to neighboring sites, can be identified with appropriate NEB guesses.

Also in this case, the "geometric" details of the diffusion mechanism apply in a similar fashion to Ag(111), Cu(111) and Au(111). Diffusion barriers vary due to the different matching of the molecular size with the substrate lattice and the different nature of the metal–organic binding. However, the transition from a dendritic growth mode of the network to a 2D growth mode, reported as shown in Fig. 8,

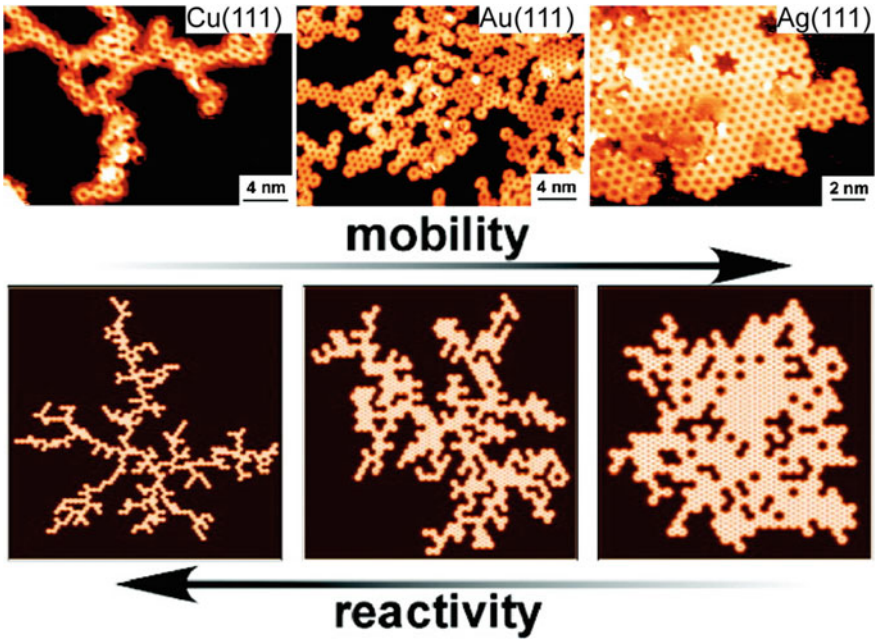

Fig. 8 The dramatic effect of the substrate on the network geometry obtained by self-assembly of CHP on noble metal substrates [Cu(111), Au(111) and Ag(111)] is explained by the interplay between mobility of the molecules at the surface and reactivity of the molecules toward C–C coupling. Figure and caption adapted with permission from [92]. Copyright (2010) American Chemical Society

cannot be attributed solely to the difference in diffusion barriers. As will be discussed in the next section, the barrier to form the "irreversible" coupling between two molecular species also plays a crucial role.

Compared to the C–I bond, scission of the C–Br occurs at higher temperature. While the C–Br bond is reported to be cleaved at room temperature on the Cu(111), Cu(110) and Ag(110) surfaces [98], it is reported to remain intact on Au(111) and Au(110) [88, 90, 98, 99]. In the case of Ag(111), the onset of C–Br bond cleavage is reported at room temperature [98, 100].

Desorption of Br typically occurs at temperatures above 200 °C [90, 98, 101]. At least in the case of brominated precursors, halogen atoms are therefore present on the surface during the diffusion of the precursor molecules. We are not aware of any study that investigates how the presence of halogen atoms on the metallic substrate influences the diffusion of the molecular precursors and their assembly. An exhaustive unbiased analysis of possible processes is challenging for computational approaches, but would be highly welcome.

4 Reactions

The synthetic approach toward nanographenes described here relies on annealing procedures to activate the two sequential steps of the reaction. If the temperature ranges for intermolecular polymerization and intramolecular cyclodehydrogenation are not well separated, the formation of large homogeneous polymers can be seriously hampered by steric hindrance between dehydrogenated monomers or by saturation of the radical species with hydrogen [66]. For this reason, the characteristic activation temperatures for a particular combination of substrate and precursor molecule are valuable information that may be predicted by atomistic simulations.

Also in this case, mechanisms identified for simple precursors can help in understanding more complex scenarios. Regarding the polymerization through Ullmann coupling, we start again from the investigation of iodobenzene [97]. As illustrated in Fig. 9, NEB calculations reveal that the coupling requires the dehalogenated molecules to reach a common surface atom. As a result of the metal–organic bonds, the shared metal atom pops out of the surface plane. When the two molecules approach each other and form the C–C bond, the surface atom retracts to its equilibrium position. This simple mechanism was later confirmed by Björk and coworkers on different noble metal substrates, including an investigation of the dehalogenation process [102].

While the mechanism is simple, the intrinsic properties of the metal substrate, such as its cohesive energy, and the interplay between molecular geometry and molecule–substrate interactions can result in quite different barriers along the

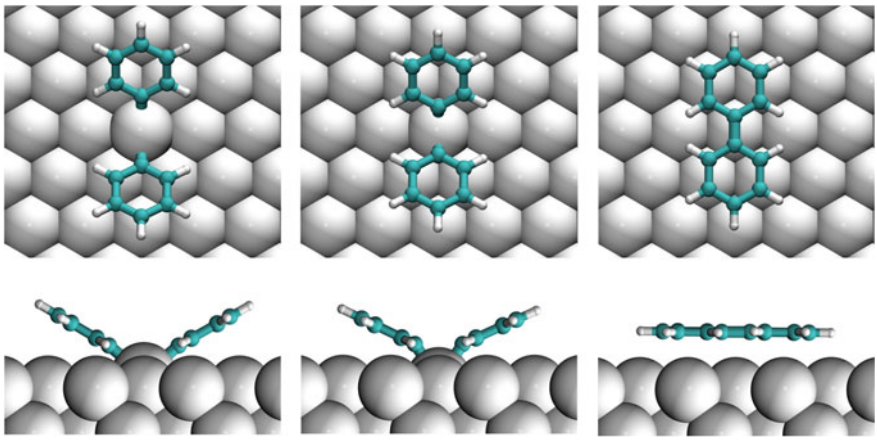

Fig. 9 Final step of the Ullmann coupling of phenyl radicals on a noble metal substrate. The two radicals share a surface atom that pops out from the surface plane (*left*). The transition state shows a partial bending of the molecules and a partial retraction of the surface atom (*center*). Upon completion, the surface atom retracts to its equilibrium surface position (*right*). Figure and caption adapted from [97] with permission from PCCP Owner Societies

reaction path. One example mentioned previously is the polymerization of cyclohexa-*m*-phenylene radicals (CHPR). As in the case of phenyl radicals, the reaction pathway in Fig. 10 [92] suggests that coupling can proceed, once two precursor molecules bind to the same surface atom. However, the large differences in diffusion barriers and activation energies between Cu(111) and Ag(111) drive a dramatic change in the network topology, as shown in Fig. 8. Diffusion of CHPR on Cu(111) is more difficult compared to the Ag(111) substrate, since the perfect lattice match in the case of copper allows the molecule to anchor strongly with six metal–organic bonds. The imperfect matching with the Ag(111) substrate makes it much easier to break C–Ag bonds. On the other hand, the different cohesive properties of the two metals result in different barriers for the coupling step.

In analogy with the picture provided by the "patchy-disk" model [83], a simple Monte Carlo simulation reproduces the phenomenology of the networks depicted in Fig. 8 [92]. In this particular case, a single parameter, representing the ratio between diffusion probability and sticking probability, is sufficient. A nice rationalization of the interplay between diffusion and coupling reaction for this kind of systems is also given in [102].

Once polymerization of the molecular precursors is achieved, the temperature has to be increased to activate the cyclodehydrogenation reaction. While surface-supported cyclodehydrogenation reactions were reported as early as 1999 [103], no theoretical investigations of the atomistic details of the reaction were available at the time. In a pioneering study, Treier and coworkers [19] investigated the fundamental role played by van der Waals dispersion forces in these processes. Dispersion forces favor flat geometries, meaning that significant distortions of the

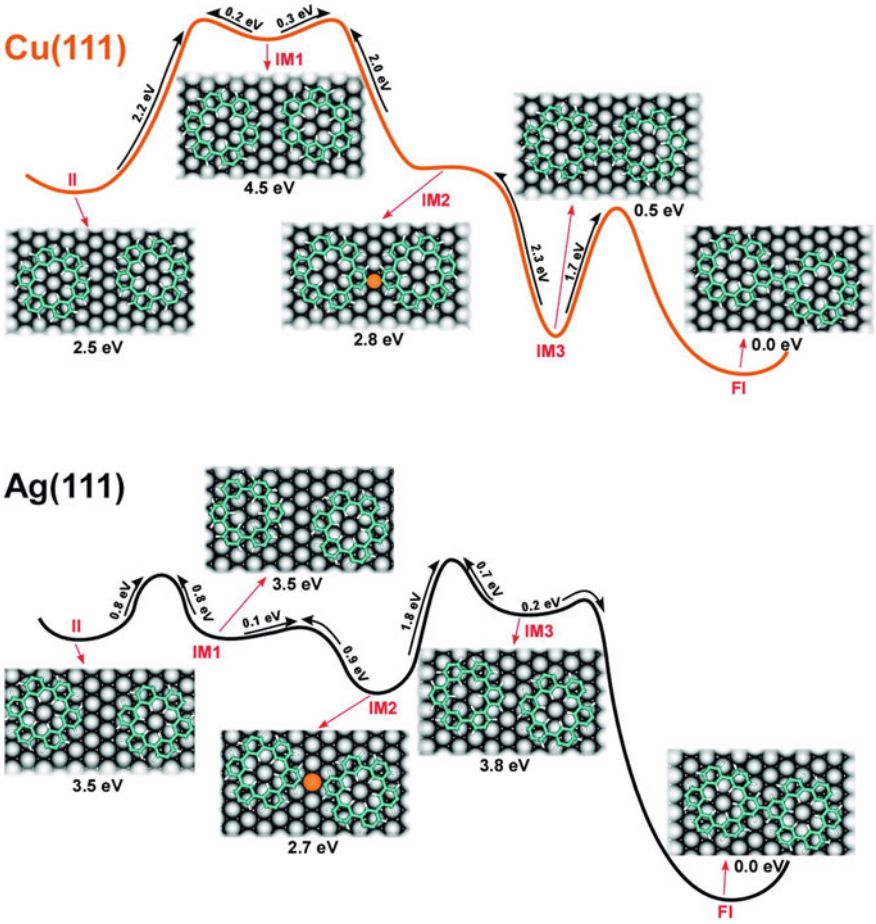

Fig. 10 Energy diagrams of the reaction pathways for CHPR−CHPR coupling on Cu(111) (*top*) and Ag(111) (*bottom*) obtained via NEB calculations. Pictorial representations of the molecule −surface configuration are given for the initial (II), intermediate (IM), and final (FI) states. The energies below each configuration are given with respect to the total energy of the final state. On both surfaces, the *orange sphere* indicates the central metal atom bonded to both CHPRs prior to intermolecular bond formation. Figure and caption reproduced with permission from [92]. Copyright (2010) American Chemical Society

molecules or polymers may be necessary in order to form metal–organic bonds. Activation energies are thus determined by a delicate interplay between short-range interactions during bond formation and long-range dispersion forces.

An example of this concept is provided by the first step in the cyclodehydrogenation of cyclohexa-*o*-*p*-*o*-*p*-*o*-*p*-phenylene (CopP). As shown in Fig. 11, the molecule contains three *para*-phenylene rings that are free to rotate (containing C

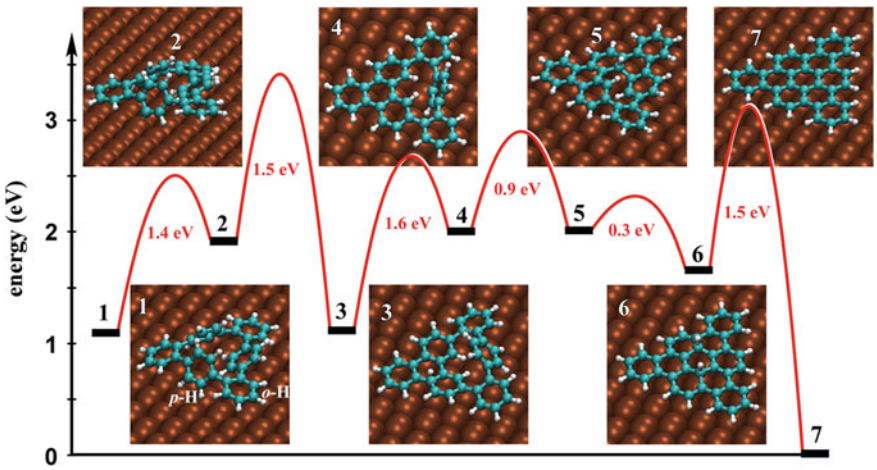

Fig. 11 Cyclodehydrogenation of CopP. As indicated in step 1, *o*-H and *p*-H denote hydrogen atoms of *ortho*- and *para*-phenylene units, respectively. Figure and caption adapted from [19] with permission

atoms labeled from 1 to 6) and three "rigid" *ortho*-phenylene rings. When the annealing temperature is properly controlled, each *para*-phenylene ring looses two hydrogens, while the hydrogens of the *para*-phenylene rings all remain attached: In the case of *o*-H cleavage, the formation of a metal–organic bond would be associated with considerable distortion of the molecule, driving up the corresponding energy barrier. In the case of *p*-H, the rotational freedom of the mobile *para*-phenylene unit enables metal–organic bond formation with little distortion. The full reaction path from CopP to tribenzo[a,g,m]coronene is essentially a sequential repetition of simple reaction steps, where dispersion forces aid in the approach of flexible subunits, hydrogen atoms are detached due to the formation of metal–organic bonds and irreversible C–C bonds are formed.

Another remarkable example of a cyclodehydrogenation reaction proceeding by the repetition of simple atomic mechanisms is given by the transformation of polyanthryl chains into 7-AGNRs. This particular reaction was studied first by Björk and coworkers [104] and later by Blankenburg and coworkers [105] in more detail. As illustrated in Fig. 12, the reaction is initiated by an approach of the terminal phenyl rings of two neighboring anthryl units. After the formation of a C–C bond, the hydrogen atom pointing downward is collected by the catalytic surface. The hydrogen atom pointing upward migrates to an edge carbon atom of the polymer, which adopts the sp^3 configuration. The mechanism is repeated until planarity of the full structure is reached. Provided that the temperature is high enough, the downward-pointing hydrogens at the edge are removed as well, leaving behind a monohydrogenated armchair edge.

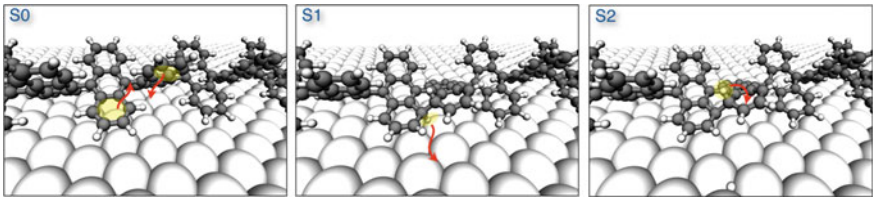

Fig. 12 First three steps in the cyclodehydrogenation reaction that transforms a polyanthryl chain into a 7-AGNR. Van der Waals interactions favor proximity of phenyl rings (*S0*) that then react forming a C–C bond (*S1*). After formation of the bond, hydrogen atoms pointing toward the surface are detached through catalytic action of the substrate and hydrogen atoms pointing upward migrate to the edge of the polymer (*S2*). These three basic steps are iterated during the whole dehydrogenation process. Figure and caption adapted with permission from [105]. Copyright (2012) American Chemical Society

The detailed understanding of this sequence revealed that the reaction, once started on one side of the polymer chain, tends to proceed on the same side. Guided by this insight, a consistent tuning of the annealing temperature allowed to obtain partially reacted structures that represented the first realization of an atomically precise heterojunction between two GNRs with different band gaps. Intraribbon quantum dots formed in between two successive heterojunctions were predicted earlier to have interesting optical properties with potential for optoelectronic applications [106].

5 Electronic Structure

The prediction of electronic properties can aid the synthesis of graphene-based nanostructures already at the design stage: only structures with desired electronic properties are worth the effort of synthesis experiments. This pruning of undesirable structures is typically based on the "gas-phase" calculations that consider the bare nanostructures without a supporting substrate. In the field of GNRs, early theoretical predictions of their edge-related electronic and magnetic properties date back to 1996 [57, 58]. Since then, they have been studied extensively, moving from the framework of tight binding [60] to ab initio methods such as DFT [61] and many-body perturbation theory [65, 74].

Apart from the well-studied armchair and zigzag GNRs, GNRs with chiral edges can also have interesting electronic and magnetic properties [107]. A more exotic example is a class of GNRs with a backbone of zigzag edges, surmounted by a triangular-notched region of variable size, as depicted in Fig. 13. The asymmetry in their atomic structure gives rise to a ferromagnetic ground state, whose total magnetization can be tuned by changing the imbalance between the "A" and "B" sublattices [108, 109]. Furthermore, substitutional doping by boron or nitrogen induces half-metallicity. The most effective doping sites can be inferred from the

spatial distribution of the frontier electronic states of the undoped GNR (see Fig. 13). Experiments for the synthesis of polymers with very large spin have been described [110], and the analogous realization of magnetic graphene-derived structures can be envisaged for the future [111].

Another important question concerns the stability of electronic and magnetic properties with respect to defects. With the motivation of synthesizing corresponding GNRs in the laboratory, we have considered GNRs with cove defects as

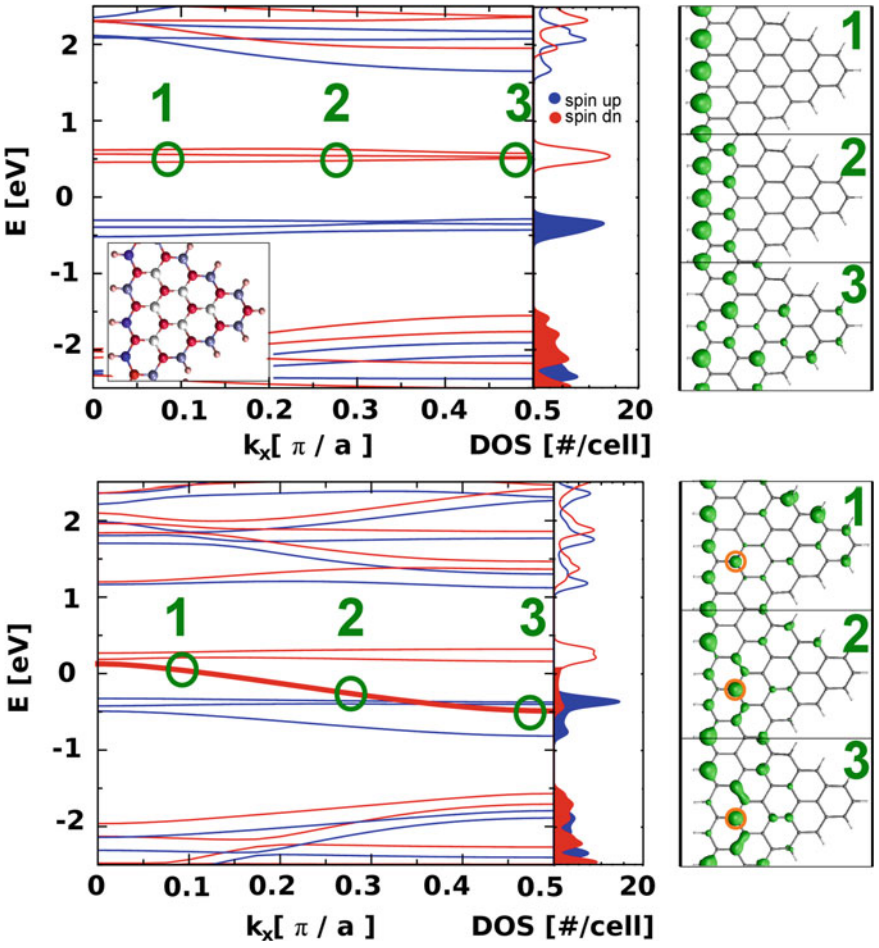

Fig. 13 Spin-resolved band structure and density of states for pristine (*top*) and nitrogen-doped (*bottom*) asymmetric zigzag GNR. The *right panels* show Kohn–Sham states of the indicated band at selected wave vectors. Upon doping with nitrogen (position marked by an *orange circle*) a spin-down band crosses the Fermi energy, signaling half-metallicity. Figure and caption adapted from [109]

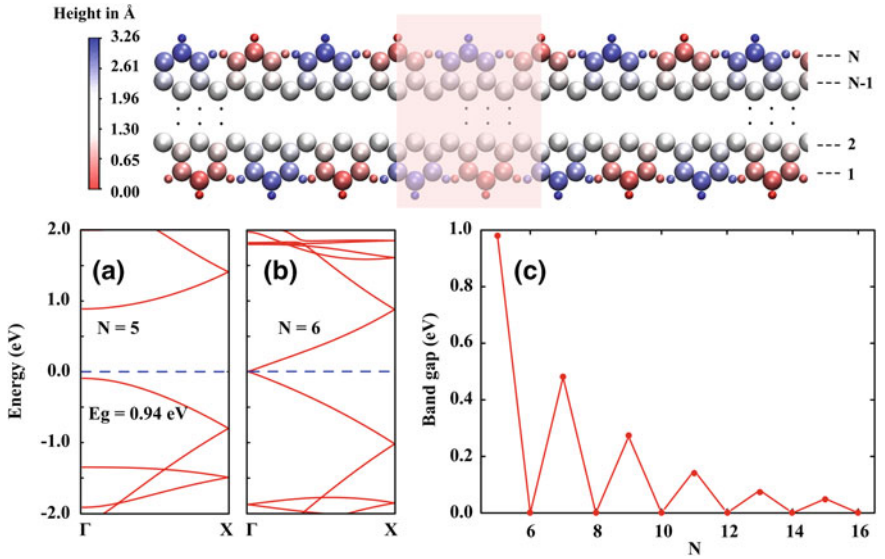

Fig. 14 Electronic structure of zigzag GNRs (ZGNRs) with cove defects. *Top panel* Geometry of freestanding GNR with unit cell indicated in *red*. Non-planarity arises from steric hindrance between nearby hydrogen atoms. *Bottom panel* **a**, **b** Band structures for odd and even cases of width *N*. **c** Band gap as a function of the width *N* indicating alternation between finite and zero gap. Unpublished data from the authors

depicted in Fig. 14. While the case of cove defects facing each other leads to a monotonous decrease in band gap with increasing width of the GNR [112], the staggered geometry shown in Fig. 14 gives rise to an interesting alternation between finite and zero band gap within DFT using the PBE exchange-correlation functional [113]. We find that spin polarization is suppressed at least up to $N = 9$, with further investigations needed into possible antiferromagnetic solutions for wider GNRs.

We note, however, that the magnetism of freestanding GNRs may easily be quenched, when the GNRs are adsorbed on a substrate. The case of zigzag GNRs adsorbed on the (111) surfaces of the coinage metals has recently been investigated using DFT with dispersion corrections in the DFT-D2 scheme [114]. For unpassivated zigzag edges, edge magnetism is shown to be suppressed on Cu, Ag, and Au due to strong hybridization of the carbon 2p with the metal d states. But even for hydrogen-passivated zigzag edges, n-doping of the GNR is reported to suppress edge magnetism on the more reactive Cu and Ag surfaces.

Unfortunately, charge transfer predicted by Kohn–Sham DFT with semi-local exchange-correlation functionals is often unreliable due to its inherent self-interaction error [115, 116]. The case of hydrogen-passivated ZGNRs on metal surfaces is particularly delicate: it tends to fall in between the regimes of physisorption and chemisorption, meaning that the semi-local exchange-correlation functional and the dispersion correction need to join seamlessly in order to obtain correct adsorption geometries. Preliminary results from the authors indicate that

varying the ribbon–substrate distance by as little as 0.2 Å can strongly affect its magnetization, making the outcome of calculations critically dependent on the van der Waals correction employed.

Besides guiding at the design stage, simulations can provide important insights also during and after the experimental synthesis, for example, by helping to interpret and rationalize spectroscopy data. While this often requires taking the substrate into account or going beyond mean-field theories, standard gas-phase DFT calculations can also provide very useful information.

One interesting example concerns the band bending in heterojunctions between pristine and nitrogen-doped chevron-type GNRs [94]. Figure 7 shows two different precursor monomers for obtaining chevron-type GNRs, in one of which four carbon atoms have been replaced by nitrogens. Heterojunctions between pristine and N-doped GNRs can simply be obtained by sequential deposition and polymerization of pristine and doped precursors. Since nitrogen is more electronegative than carbon, the band onsets in the N-doped domains are expected at lower energy than in the pristine domains and band bending has to occur at the interface. DFT predicts a band shift of 0.5 eV and an electric field of 0.2 V/nm at the interface, in agreement with STS experiments of the heterojunctions measured on the Au(111) substrate. While STS involves electronic excitation of the GNR, we note here that the electric field at the heterojunction (and thus in essence also the band bending) is a ground-state property, providing justification for the use of DFT. Based on the established agreement with experiment, DFT can now tell us how to design the details of the band bending (see Fig. 15), for example, in view of possible applications in photovoltaics and electronics.

Another frequent task is the simulation of STM images. Since the tunneling current is exponentially sensitive to the tip–sample distance, an accurate description of the adsorption geometry is mandatory. If metal–organic bond formation between substrate and adsorbate can be excluded, it can be sufficient to model the substrate with empirical potentials in a QM/MM approach (see Sect. 2.1). This is the case in the example of the polyanthryl chain on Au(111) shown in the left panel of Fig. 16.

If, however, the substrate interacts chemically with the adsorbate, both need to be treated on the quantum mechanical level. The right panel of Fig. 16 shows the termini of the 7-AGNR on Au(111), where simulations considered different possible bonding partners of the central carbon at the terminus. In case II, a metal–organic bond is formed between the substrate and the radical, leading to a downward bend of the central carbon atom by about 1Å. This geometrical effect distinguishes the electronically similar cases II and III and would be missed using an empirical model for the substrate.

Besides the adsorption geometry, one important question in STM simulations concerns the geometry of the tip. In experiments with metal tips, information on the tip shape is typically not available. The popular Tersoff–Hamann approximation [117] therefore assumes a tip wave function with perfect *s*-wave character, making both the calculation and the physical interpretation of STM images particularly easy. As illustrated by Fig. 16, this simple approximation can provide simulations in good qualitative agreement with experiment, if the sample wave functions are

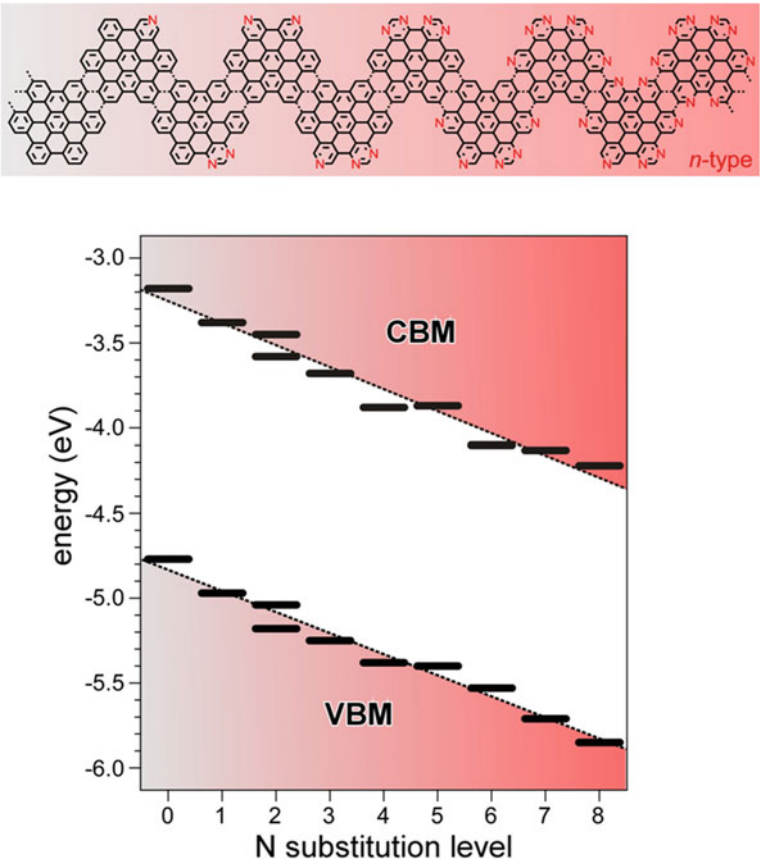

Fig. 15 Control of band bending in GNRs via monomer chemical substitution. *Top* Illustration of GNR consisting of molecules with increasing degrees of nitrogen substitution. *Bottom* Energies of valence band maxima (VBM) and conduction band minima (CBM) for GNRs with increasing degrees of nitrogen substitution. A linear fit yields a band shift of −0.13 eV per nitrogen atom. Energies are given with respect to the vacuum level. Figure and caption adapted with permission from [94]

properly extrapolated into the vacuum region [118]. Tip wave functions with higher angular momentum, as required, for example, when using a CO molecule as the tip [119], can be treated in a similar fashion using Chen's derivative rule [120]. For studies with quantitative aspirations, the tip shape can be taken into account through simple step functions [121] or even through explicit treatment of the tip atoms [122, 123].

Going beyond qualitative predictions, however, can be a challenging task. In the following, we present two recent attempts, where substrate effects have been shown to play an essential role in determining the quantitative electronic and optical properties.

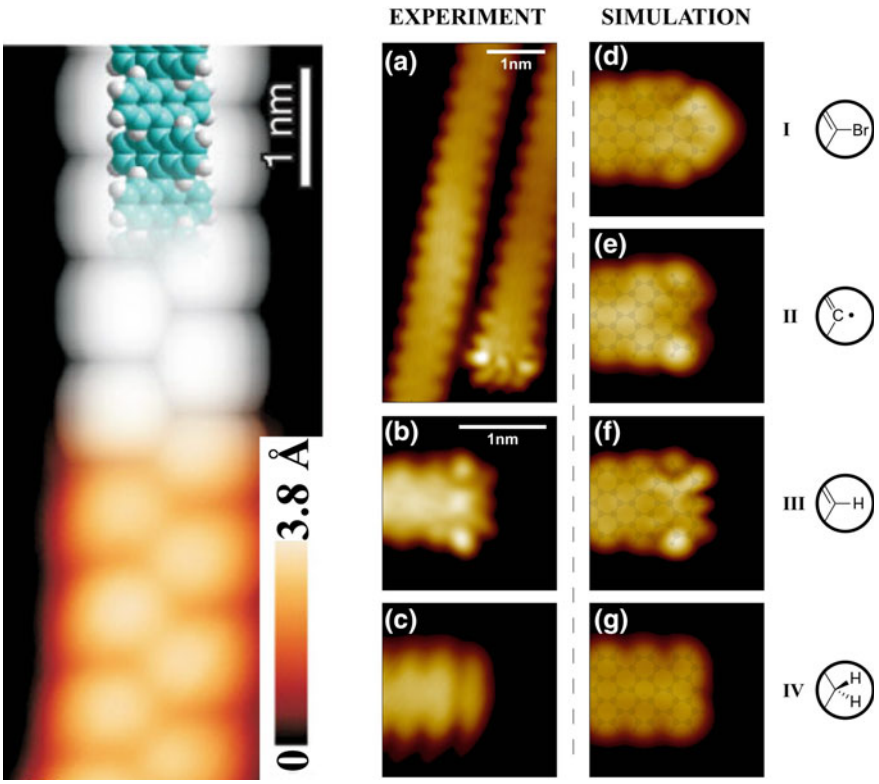

Fig. 16 Comparing STM simulations and experiments. The *left panel* shows STM images of the polyanthryl chains obtained in the synthesis of 7-AGNRs. STM simulations (*top*) were performed using an empirical model for the substrate. Figure and caption reproduced with permission from Macmillan Publishers Ltd: [13], copyright (2010). The *right panel* shows STM images of the 7-AGNR terminus (b–c experiment, d–g simulation) with different bonding partners (I–IV) for the central carbon atom. The substrate was treated within DFT using the DFT-D3 dispersion correction [40]. Figure reproduced with permission from [66]. Copyright (2010) American Chemical Society

Ruffieux and coworkers measured the band gap of 7-AGNRs supported on Au (111) [82] through scanning tunneling spectroscopy (STS). The reported value of $\Delta \approx 2.3$eV appears to contradict the theoretical prediction of $\Delta \approx 3.7$eV for the fundamental gap obtained from GW calculations [65]. The origin of the discrepancy lies in the screening of the Coulomb interaction by the nearby substrate. Unfortunately, accurate GW calculations of the 7-AGNR on the Au(111) substrate are not yet attainable with reasonable computational effort (although calculations on "simpler" substrates are being undertaken [79]). In this particular case, however, hybridization of molecular states with the substrate is weak and there is no appreciable charge transfer [82], making it possible to include the screening effect through classical image charge corrections [77, 124]. As illustrated in Fig. 17, the

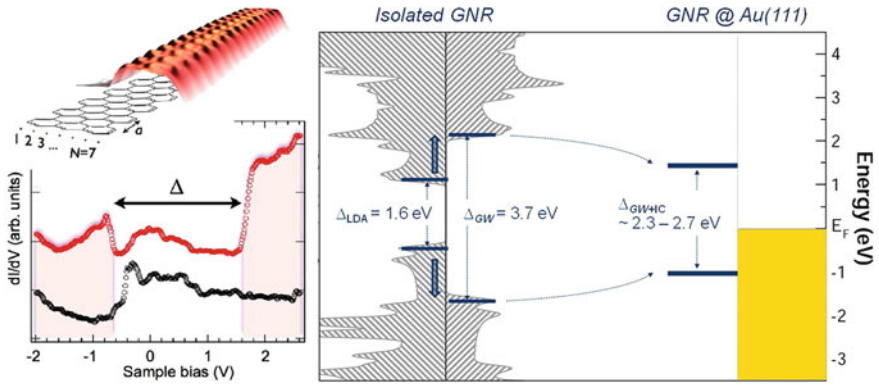

Fig. 17 Density of states (DOS) and electronic band gap Δ of the 7-AGNR. *Left* Scanning tunneling spectra recorded on the GNR (*red*, offset for clarity) and on the Au(111) substrate (*black*). *Right* LDA and GW-corrected DOS for the 7-AGNR in the gas phase and band gap reduction *via* image charge corrections on Au(111). Figure and caption adapted with permission from [82]. Copyright (2012) American Chemical Society

GW correction brings the DFT gap of the isolated 7-AGNR from 1.6 to 3.7 eV. The IC correction that mimics the presence of the metallic substrate reduces the energy gap by 1.0–1.4 eV. Overall, this results in an energy band gap of 2.3–2.7 eV for the 7-AGNR on Au(111), in agreement with the experimental value of 2.3 eV.

More recently, the optical properties of 7-AGNRs aligned on stepped Au(788) surfaces have been measured with reflectance difference spectroscopy (RDS) [125]. RDS measures the difference in complex reflectance for incident light polarized along two orthogonal directions, chosen here to point along and across the aligned GNRs (Fig. 18a). Since Au is optically isotropic [126], the RD signal is determined essentially by the optical response of the GNRs, which absorb light polarized along the GNR axis much more efficiently. The RD spectra shown in Fig. 18b are used to construct the dielectric function of the GNR, which is characterized by three discrete transitions at 2.1, 2.3, and 4.2 eV. The energies of these optical transitions are compared to calculations for freestanding 7-AGNRs in the GW/Bethe–Salpeter framework, yielding 1.9, 2.3, and 4.1 eV. It is interesting to observe that the optical gap computed for freestanding GNRs is in good agreement with experiment, while their fundamental gap is strongly affected by screening from the substrate. This suggests that the substrate-induced reduction in the fundamental gap is outbalanced by a corresponding reduction in the electron–hole binding energy. As discussed in [81] in more detail, this is expected, when the corresponding transition dipole moment vanishes. In this particular study, the clear assignment of RDS spectra also allowed to discriminate between the signatures of precursor molecules, polymers, and the planar GNRs, thus making RDS a powerful tool to monitor the synthesis during the different annealing phases in real time.

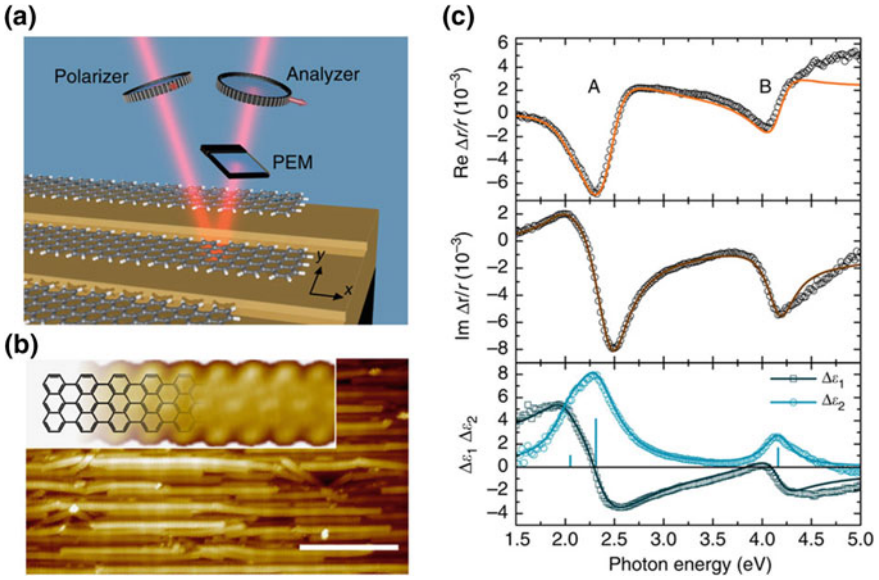

Fig. 18 Reflectance difference spectroscopy (RDS) on 7-AGNRs. **a** Schematic of the RDS experiment on 7-AGNRs aligned uniaxially on a vicinal surface. **b** STM topography image of 7-AGNRs grown on Au(788) (scale bar 20 nm) with *inset* in high resolution. **c** RD spectra (*open circles*) measured in situ after GNR synthesis. The *bottom panel* shows the differential dielectric function $\Delta\varepsilon$ obtained by applying the three-phase model [126] (*open symbols*). $\Delta\varepsilon$ is fitted to a model including three discrete harmonic oscillator transitions (*lines*). The *blue bars* indicate the energy position and oscillator strength of the determined optical transitions. Figure and caption adapted with permission from [125]

Acknowledgments The authors acknowledge the Swiss National Science Foundation (SNF) for funding and the Swiss Supercomputing Centre (CSCS) for computational resources.

References

1. Geim, A.K., Novoselov, K.S.: The rise of graphene. Nat. Mater. **6**, 183–191 (2007)
2. Novoselov, K.S., Geim, A.K., Morozov, S.V., Jiang, D., Zhang, Y., Dubonos, S.V., Grigorieva, I.V., Firsov, A.A.: Electric field effect in atomically thin carbon films. Science **306**, 666–669 (2004)
3. Castro Neto, A.H., Peres, N.M.R., Novoselov, K.S., Geim, A.K.: The electronic properties of. Rev. Mod. Phys. **81**, 109–162 (2009)
4. Schwierz, F.: Graphene transistors: status, prospects, and problems. Proc. IEEE **101**, 1567–1584 (2013)
5. Schwierz, F.: Graphene transistors. Nat. Nanotechnol. **5**, 487–496 (2010)
6. Sanchez-Valencia, J.R., Dienel, T., Gröning, O., Shorubalko, I., Mueller, A., Jansen, M., Amsharov, K., Ruffieux, P., Fasel, R.: Controlled synthesis of single-chirality carbon nanotubes. Nature **512**, 61–64 (2014)

7. Han, M., Özyilmaz, B., Zhang, Y., Kim, P.: Energy band-gap engineering of graphene nanoribbons. Phys. Rev. Lett. **98**, 206805 (2007)
8. Wu, Z.-S., Ren, W., Gao, L., Liu, B., Zhao, J., Cheng, H.-M.: Efficient synthesis of graphene nanoribbons sonochemically cut from graphene sheets. Nano Res. **3**, 16–22 (2010)
9. Kosynkin, D.V.D., Higginbotham, A.A.L., Sinitskii, A., Lomeda, J.R., Dimiev, A., Price, B. K., Tour, J.M.: Longitudinal unzipping of carbon nanotubes to form graphene nanoribbons. Nature **458**, 872–876 (2009)
10. Grill, L., Dyer, M., Lafferentz, L., Persson, M., Peters, M.V., Hecht, S.: Nano-architectures by covalent assembly of molecular building blocks. Nat. Nanotechnol. **2**, 687–691 (2007)
11. Lafferentz, L., Ample, F., Yu, H., Hecht, S., Joachim, C., Grill, L.: Conductance of a single conjugated polymer as a continuous function of its length. Science **323**, 1193–1198 (2009)
12. Lipton-Duffin, J.A., Ivasenko, O., Perepichka, D.F., Rosei, F.: Synthesis of polyphenylene molecular wires by surface-confined polymerization. Small **5**, 592–597 (2009)
13. Cai, J., Ruffieux, P., Jaafar, R., Bieri, M., Braun, T., Blankenburg, S., Muoth, M., Seitsonen, A.P., Saleh, M., Feng, X., Müllen, K., Fasel, R.: Atomically precise bottom-up fabrication of graphene nanoribbons. Nature **466**, 470–473 (2010)
14. Ullmann, F., Bielecki, J.: Ueber Synthesen in der Biphenylreihe. Berichte der Dtsch. Chem. Gesellschaft. **34**, 2174–2185 (1901)
15. Hohenberg, P., Kohn, W.: Inhomogeneous electron gas. Phys. Rev. **155**, B864 (1964)
16. CPMD v3.17 Copyright IBM Corp 1990–2013, Copyright MPI fuer Feskoerperforschung Stuttgart 1997-2001
17. Hutter, J., Iannuzzi, M., Schiffmann, F., VandeVondele, J.: CP2K: atomistic simulations of condensed matter systems. Wiley Interdiscip. Rev. Comput. Mol. Sci. **4**, 15–25 (2014)
18. Artacho, E., Anglada, E., Diéguez, O., Gale, J.D., García, A, Junquera, J., Martin, R.M., Ordejón, P., Pruneda, J.M., Sánchez-Portal, D., Soler, J.M.: The SIESTA method; developments and applicability. J. Phys. Condens. Matter. **20**, 064208 (2008)
19. Treier, M., Pignedoli, C.A., Laino, T., Rieger, R., Müllen, K., Passerone, D., Fasel, R.: Surface-assisted cyclodehydrogenation provides a synthetic route towards easily processable and chemically tailored nanographenes. Nature Chem. **3**, 61–67 (2011)
20. Björk, J., Hanke, F.: Towards design rules for covalent nanostructures on metal surfaces. Chemistry **20**, 928–934 (2014)
21. Iannuzzi, M., Hutter, J.: Inner-shell spectroscopy by the Gaussian and augmented plane wave method. Phys. Chem. Chem. Phys. **9**, 1599–1610 (2007)
22. Ljungberg, M.P., Mortensen, J.J., Pettersson, L.G.M.: An implementation of core level spectroscopies in a real space projector augmented wave density functional theory code. J. Electron Spectros. Relat. Phenomena. **184**, 427–439 (2011)
23. Baroni, S., de Gironcoli, S.: Phonons and related crystal properties from density-functional perturbation theory. Rev. Mod. Phys. **73**, 515 (2001)
24. Lazzeri, M., Mauri, F.: First-principles calculation of vibrational raman spectra in large systems: signature of small rings in crystalline SiO_2. Phys. Rev. Lett. **90**, 036401 (2003)
25. Venezuela, P., Lazzeri, M., Mauri, F.: Theory of double-resonant Raman spectra in graphene: intensity and line shape of defect-induced and two-phonon bands. Phys. Rev. B. **84**, 035433 (2011)
26. Warshel, A., Levitt, M.: Folding and stability of helical proteins: carp myogen. J. Mol. Biol. **106**, 421–437 (1976)
27. Senn, H.M., Thiel, W.: QM/MM methods for biomolecular systems. Angew. Chem. Int. Ed. Engl. **48**, 1198–1229 (2009)
28. Foiles, S., Baskes, M., Daw, M.: Embedded-atom-method functions for the fcc metals Cu, Ag, Au, Ni, Pt, and their alloys. Phys. Rev. B, Pd (1986)
29. Kohn, W., Sham, L.: Self-consistent equations including exchange and correlation effects. Phys. Rev. **140**, A1133 (1965)
30. Levi, A.C., Calvini, P.: Elastic theory of surface deformation in C60 adsorption. Surf. Sci. **601**, 1494–1500 (2007)

31. Pignedoli, C.A., Laino, T., Treier, M., Fasel, R., Passerone, D.: A simple approach for describing metal-supported cyclohexaphenylene dehydrogenation. Eur. Phys. J. B **75**, 65–70 (2010)
32. Laio, A., Parrinello, M.: Escaping free-energy minima. Proc. Natl. Acad. Sci. U.S.A. **99**, 12562–12566 (2002)
33. Laio, A., Gervasio, F.L.: Metadynamics: a method to simulate rare events and reconstruct the free energy in biophysics, chemistry and material science. Reports Prog. Phys. **71**, 126601 (2008)
34. Pietrucci, F., Andreoni, W.: Graph theory meets ab initio molecular dynamics: atomic structures and transformations at the nanoscale. Phys. Rev. Lett. **107**, 085504 (2011)
35. Tribello, G., Ceriotti, M., Parrinello, M.: Using sketch-map coordinates to analyze and bias molecular dynamics simulations. Proc. Natl. Acad. Sci. **109**, 5196–5201 (2012)
36. Rohrdanz, M.A., Zheng, W., Clementi, C.: Discovering mountain passes via torchlight: methods for the definition of reaction coordinates and pathways in complex macromolecular reactions. Annu. Rev. Phys. Chem. **64**, 295–316 (2013)
37. Rydberg, H., Dion, M., Jacobson, N., Schröder, E., Hyldgaard, P., Simak, S., Langreth, D., Lundqvist, B.I.: Van der Waals density functional for layered Structures. Phys. Rev. Lett. **91**, 126402 (2003)
38. Grimme, S.: Density functional theory with London dispersion corrections. Wiley Interdiscip. Rev. Comput. Mol. Sci. **1**, 211–228 (2011)
39. Zhao, Y., Truhlar, D.G.: Exploring the limit of accuracy of the global hybrid meta density functional for main-group thermochemistry, kinetics, and noncovalent interactions. J. Chem. Theory Comput. **4**, 1849–1868 (2008)
40. Grimme, S., Antony, J., Ehrlich, S., Krieg, H.: A consistent and accurate ab initio parametrization of density functional dispersion correction (DFT-D) for the 94 elements H-Pu. J. Chem. Phys. **132**, 154104 (2010)
41. Tkatchenko, A., Scheffler, M.: Accurate molecular Van der Waals Interactions from ground-state electron density and free-atom reference data. Phys. Rev. Lett. **102**, 073005 (2009)
42. Ruiz, V.G., Liu, W., Zojer, E., Scheffler, M., Tkatchenko, A.: Density-functional theory with screened Van der Waals interactions for the modeling of hybrid inorganic-organic systems. Phys. Rev. Lett. **108**, 146103 (2012)
43. Hanke, F.: Sensitivity analysis and uncertainty calculation for dispersion corrected density functional theory. J. Comput. Chem. **32**, 1424–1430 (2011)
44. Dion, M., Rydberg, H., Schröder, E., Langreth, D.C., Lundqvist, B.I.: Van der Waals density functional for general geometries. Phys. Rev. Lett. **92**, 246401 (2004)
45. Lee, K., Murray, É.D., Kong, L., Lundqvist, B.I., Langreth, D.C.: Higher-accuracy Van der Waals density functional. Phys. Rev. B. **82**, 081101 (2010)
46. Hamada, I.: van der Waals density functional made accurate. Phys. Rev. B. **89**, 121103 (2014)
47. Gulans, A., Puska, M., Nieminen, R.: Linear-scaling self-consistent implementation of the Van der Waals density functional. Phys. Rev. B. **79**, 201105 (2009)
48. Björk, J., Stafström, S.: Adsorption of large hydrocarbons on coinage metals: a Van der Waals density functional study. Chem. Phys. Chem. **15**, 2851–2858 (2014)
49. Elber, R., Karplus, M.: A method for determining reaction paths in large molecules: application to myoglobin. Chem. Phys. Lett. **139**, 375–380 (1987)
50. Henkelman, G., Jónsson, H.: A dimer method for finding saddle points on high dimensional potential surfaces using only first derivatives. J. Chem. Phys. **111**, 7010–7022 (1999)
51. Henkelman, G., Uberuaga, B.P., Jónsson, H.: A climbing image nudged elastic band method for finding saddle points and minimum energy paths. J. Chem. Phys. **113**, 9901–9904 (2000)
52. Ren, W., Vanden-Eijnden, E.: String method for the study of rare events. Phys. Rev. B. **66**, 052301 (2002)
53. Ren, W., Vanden-Eijnden, E.: Finite temperature string method for the study of rare events. J. Phys. Chem. B. **109**, 6688–6693 (2005)

54. Branduardi, D., Gervasio, F.L., Parrinello, M.: From A to B in free energy space. J. Chem. Phys. **126**, 054103 (2007)
55. Clar, E.: The aromatic sextet. J. Wiley (1972)
56. Wassmann, T., Seitsonen, A.: Clar's theory, n-electron distribution, and geometry of graphene nanoribbons. J. Am. Chem. Soc. **132**, 3440–3451 (2010)
57. Nakada, K., Fujita, M., Dresselhaus, G., Dresselhaus, M.: Edge state in graphene ribbons: nanometer size effect and edge shape dependence. Phys. Rev. B. **54**, 17954–17961 (1996)
58. Fujita, M., Wakabayashi, K.: Peculiar localized state at zigzag graphite edge. J. Phys. Soc. Japan. **65**, 1920–1923 (1996)
59. Wakabayashi, K., Sasaki, K., Nakanishi, T., Enoki, T.: Electronic states of graphene nanoribbons and analytical solutions. Sci. Technol. Adv. Mater. **11**, 054504 (2010)
60. Enoki, T., Ando, T.: Physics and Chemistry of Graphene: Graphene to Nanographene. Pan Stanford (2013)
61. Son, Y.-W., Cohen, M.L., Louie, S.G.: Energy gaps in graphene nanoribbons. Phys. Rev. Lett. **97**, 216803 (2006)
62. Gunlycke, D., White, C.: Tight-binding energy dispersions of armchair-edge graphene nanostrips. Phys. Rev. B. **77**, 115116 (2008)
63. Girao, E., Cruz-Silva, E., Meunier, V.: Electronic transport properties of assembled carbon nanoribbons. ACS Nano **6**, 6483–6491 (2012)
64. Boykin, T.B., Luisier, M., Klimeck, G., Jiang, X., Kharche, N., Zhou, Y., Nayak, S.K.: Accurate six-band nearest-neighbor tight-binding model for the π-bands of bulk graphene and graphene nanoribbons. J. Appl. Phys. **109**, 104304 (2011)
65. Yang, L., Park, C.-H., Son, Y.-W., Cohen, M., Louie, S.: Quasiparticle energies and band gaps in graphene nanoribbons. Phys. Rev. Lett. **99**, 186801 (2007)
66. Talirz, L., Söde, H., Cai, J., Ruffieux, P., Blankenburg, S., Jafaar, R., Berger, R., Feng, X., Müllen, K., Passerone, D., Fasel, R., Pignedoli, C.A.: Termini of bottom-up fabricated graphene nanoribbons. J. Am. Chem. Soc. **135**, 2060–2063 (2013)
67. Ijäs, M., Ervasti, M., Uppstu, A., Liljeroth, P.: Electronic states in finite graphene nanoribbons: effect of charging and defects. Phys. Rev. B. **88**, 075429 (2013)
68. Louie, S.G.: Conceptual Foundations of Materials—A Standard Model for Ground—and Excited-State Properties. Elsevier, Philadelphia (2006)
69. Hedin, L.: New method for calculating the one-particle green's function with application to the electron-gas problem. Phys. Rev. **139**, A796 (1965)
70. van Schilfgaarde, M., Kotani, T., Faleev, S.: Quasiparticle self-consistent GW theory. Phys. Rev. Lett. **96**, 226402 (2006)
71. Spataru, C.D., Ismail-Beigi, S., Benedict, L.X., Louie, S.G.: Quasiparticle energies, excitonic effects and optical absorption spectra of small-diameter single-walled carbon nanotubes. Appl. Phys. A Mater. Sci. Process. **78**, 1129–1136 (2004)
72. Onida, G., Reining, L., Rubio, A.: Electronic excitations: density-functional versus many-body Green's-function approaches. Rev. Mod. Phys. **74**, 601 (2002)
73. Salpeter, E., Bethe, H.: A relativistic equation for bound-state problems. Phys. Rev. **84**, 1232 (1951)
74. Yang, L., Cohen, M.L., Louie, S.G.: Excitonic effects in the optical spectra of graphene nanoribbons. Nano Lett. **7**, 3112–3115 (2007)
75. Prezzi, D., Varsano, D., Ruini, A., Marini, A., Molinari, E.: Optical properties of graphene nanoribbons: the role of many-body effects. Phys. Rev. B. **77**, 041404 (2008)
76. Deslippe, J., Samsonidze, G., Strubbe, D.A., Jain, M., Cohen, M.L., Louie, S.G.: BerkeleyGW: a massively parallel computer package for the calculation of the quasiparticle and optical properties of materials and nanostructures. Comput. Phys. Commun. **183**, 1269–1289 (2012)
77. Neaton, J., Hybertsen, M., Louie, S.: Renormalization of molecular electronic levels at metal-molecule interfaces. Phys. Rev. Lett. **97**, 216405 (2006)

78. Freysoldt, C., Rinke, P., Scheffler, M.: Controlling polarization at insulating surfaces: quasiparticle calculations for molecules adsorbed on insulator films. Phys. Rev. Lett. **103**, 056803 (2009)
79. Jiang, X., Kharche, N., Kohl, P., Boykin, T.B., Klimeck, G., Luisier, M., Ajayan, P.M., Nayak, S.K.: Giant quasiparticle bandgap modulation in graphene nanoribbons supported on weakly interacting surfaces. Appl. Phys. Lett. **103**, 133107 (2013)
80. Li, Y., Lu, D., Galli, G.: Calculation of quasi-particle energies of aromatic self-assembled monolayers on Au(111). J. Chem. Theory Comput. **5**, 881–886 (2009)
81. Garcia-Lastra, J.M., Thygesen, K.S.: Renormalization of optical excitations in molecules near a metal surface. Phys. Rev. Lett. **106**, 187402 (2011)
82. Ruffieux, P., Cai, J., Plumb, N.N.C., Patthey, L., Prezzi, D., Ferretti, A., Molinari, E., Feng, X., Müllen, K., Pignedoli, C.A., Fasel, R.: Electronic structure of atomically precise graphene nanoribbons. ACS Nano **6**, 6930–6935 (2012)
83. Whitelam, S., Tamblyn, I., Haxton, T.K., Wieland, M.B., Champness, N.R., Garrahan, J.P., Beton, P.H.: Common physical framework explains phase behavior and dynamics of atomic, molecular, and polymeric network formers. Phys. Rev. X. **4**, 011044 (2014)
84. He, Y., Chen, Y., Liu, H.: Self-assembly of hexagonal DNA two-dimensional (2D) arrays. J. Am. Chem. Soc. **127**, 12202–12203 (2005)
85. Lichtenstein, L., Heyde, M., Freund, H.-J.: Crystalline-vitreous interface in two dimensional silica. Phys. Rev. Lett. **109**, 106101 (2012)
86. Bieri, M., Treier, M., Cai, J., Aït-Mansour, K., Ruffieux, P., Gröning, O., Gröning, P., Kastler, M., Rieger, R., Feng, X., Müllen, K., Fasel, R.: Porous graphenes: two-dimensional polymer synthesis with atomic precision. Chem. Commun. (Camb). **45**, 6919–6921 (2009)
87. Palma, C.-A., Samorì, P., Cecchini, M.: Atomistic simulations of 2D bicomponent self-assembly: from molecular recognition to self-healing. J. Am. Chem. Soc. **132**, 17880–17885 (2010)
88. Blunt, M.O., Russell, J.C., Champness, N.R., Beton, P.H.: Templating molecular adsorption using a covalent organic framework. Chem. Commun. (Camb.) **46**, 7157–7159 (2010)
89. Linden, S., Zhong, D., Timmer, A., Aghdassi, N., Franke, J., Zhang, H., Feng, X., Müllen, K., Fuchs, H., Chi, L., Zacharias, H.: Electronic structure of spatially aligned graphene nanoribbons on Au(788). Phys. Rev. Lett. **108**, 216801 (2012)
90. Batra, A., Cvetko, D., Kladnik, G., Adak, O., Cardoso, C., Ferretti, A., Prezzi, D., Molinari, E., Morgante, A., Venkataraman, L.: Probing the mechanism for graphene nanoribbon formation on gold surfaces through X-ray spectroscopy. Chem. Sci. **5**, 4419–4423 (2014)
91. Pham, T.A., Song, F., Nguyen, M.-T., Stöhr, M.: Self-assembly of pyrene derivatives on Au (111): substituent effects on intermolecular interactions. Chem. Commun. **50**, 14089 (2014)
92. Bieri, M., Nguyen, M.-T., Gröning, O., Cai, J., Treier, M., Aït-Mansour, K., Ruffieux, P., Pignedoli, C.A., Passerone, D., Kastler, M., Müllen, K., Fasel, R., Gröning, O.: Two-dimensional polymer formation on surfaces: insight into the roles of precursor mobility and reactivity. J. Am. Chem. Soc. **132**, 16669–16676 (2010)
93. Bronner, C., Stremlau, S., Gille, M., Braße, F., Haase, A., Hecht, S., Tegeder, P.: Aligning the band gap of graphene nanoribbons by monomer doping. Angew. Chem. Int. Ed. Engl. **52**, 4422–4425 (2013)
94. Cai, J., Pignedoli, C.A., Talirz, L., Ruffieux, P., Söde, H., Liang, L., Meunier, V., Berger, R., Li, R., Feng, X., Müllen, K., Fasel, R.: Graphene nanoribbon heterojunctions. Nat. Nanotechnol. **9**, 896–900 (2014)
95. Kanuru, V.K., Kyriakou, G., Beaumont, S.K., Papageorgiou, A.C., Watson, D.J., Lambert, R.M.: Sonogashira coupling on an extended gold surface in vacuo: reaction of phenylacetylene with iodobenzene on Au(111). J. Am. Chem. Soc. **132**, 8081–8086 (2010)
96. Sykes, E.C.H., Han, P., Kandel, S.A., Kelly, K.F., McCarty, G.S., Weiss, P.S.: Substrate-mediated interactions and intermolecular forces between molecules adsorbed on surfaces. Acc. Chem. Res. **36**, 945–953 (2003)
97. Nguyen, M.-T., Pignedoli, C.A., Passerone, D.: An ab initio insight into the Cu(111)-mediated Ullmann reaction. Phys. Chem. Chem. Phys. **13**, 154–160 (2011)

98. Gutzler, R., Cardenas, L., Lipton-Duffin, J., El Garah, M., Dinca, L.E., Szakacs, C.E., Fu, C., Gallagher, M., Vondráček, M., Rybachuk, M., Perepichka, D.F., Rosei, F.: Ullmann-type coupling of brominated tetrathienoanthracene on copper and silver. Nanoscale. **6**, 2660–2668 (2014)
99. Simonov, K., Vinogradov, N.A., Vinogradov, A.S., Generalov, A.V., Zagrebina, E.M., Martenson, N., Cafolla, A.A., Carpy, T., Cunniffe, J.P., Preobrajenski, A.B.: Effect of substrate chemistry on the bottom-up fabrication of graphene nanoribbons: combined core-level spectroscopy and STM study. J. Phys. Chem. C **118**, 12532–12540 (2014)
100. Eichhorn, J., Strunskus, T., Rastgoo-Lahrood, A., Samanta, D., Schmittel, M., Lackinger, M.: On-surface Ullmann polymerization via intermediate organometallic networks on Ag (111). Chem. Comm. **50**, 7680–7682 (2014)
101. Bronner, C., Björk, J., Tegeder, P.: Tracking and removing Br during the on-surface synthesis of a graphene nanoribbon. J. Phys. Chem. C **119**, 486–493 (2015). doi:10.1021/jp5106218
102. Björk, J., Hanke, F., Stafström, S.: Mechanisms of halogen-based covalent self-assembly on metal surfaces. J. Am. Chem. Soc. **135**, 5768–5775 (2013)
103. Weiss, K., Beernink, G., Dötz, F., Birkner, A., Müllen, K., Wöll, C.H.: Template-mediated synthesis of polycyclic aromatic hydrocarbons: cyclodehydrogenation and planarization of a hexaphenylbenzene derivative at a copper surface. Angew. Chem. Int. Ed. Engl. **38**, 3748–3752 (1999)
104. Björk, J., Stafström, S., Hanke, F.: Zipping up: cooperativity drives the synthesis of graphene nanoribbons. J. Am. Chem. Soc. **133**, 14884–14887 (2011)
105. Blankenburg, S., Cai, J., Ruffieux, P., Jaafar, R., Passerone, D., Feng, X., Fasel, R., Müllen, K., Pignedoli, C.A.: Intraribbon heterojunction formation in ultranarrow graphene nanoribbons. ACS Nano **6**, 2020–2025 (2012)
106. Prezzi, D., Varsano, D., Ruini, A., Molinari, E.: Quantum dot states and optical excitations of edge-modulated graphene nanoribbons. Phys. Rev. B. **84**, 041401 (2011)
107. Yazyev, O.V., Capaz, R.B., Louie, S.G.: Theory of magnetic edge states in chiral graphene nanoribbons. Phys. Rev. B. **84**, 115406 (2011)
108. Wang, W., Yazyev, O., Meng, S., Kaxiras, E.: Topological frustration in graphene nanoflakes: magnetic order and spin logic devices. Phys. Rev. Lett. **102**, 157201 (2009)
109. Adams, D.J., Gröning, O., Pignedoli, C.A., Ruffieux, P., Fasel, R., Passerone, D.: Stable ferromagnetism and doping-induced half-metallicity in asymmetric graphene nanoribbons. Phys. Rev. B. **85**, 245405 (2012)
110. Rajca, A., Wongsriratanakul, J., Rajca, S.: Magnetic ordering in an organic polymer. Science (80-.). **294**, 1503–1505 (2001)
111. Wang, W.L., Meng, S., Kaxiras, E.: Graphene nanoflakes with large spin. Nano Lett. **8**, 241–245 (2008)
112. Wakabayashi, K., Okada, S., Tomita, R., Fujimoto, S., Natsume, Y.: Edge States and flat bands of graphene nanoribbons with edge modification. J. Phys. Soc. Japan. **79**, 034706 (2010)
113. Perdew, J., Burke, K., Ernzerhof, M.: Generalized gradient approximation made simple. Phys. Rev. Lett. **77**, 3865–3868 (1996)
114. Li, Y., Zhang, W., Morgenstern, M., Mazzarello, R.: Electronic and magnetic properties of zigzag graphene nanoribbons on the (111) surface of Cu, Ag, and Au. Phys. Rev. Lett. **110**, 216804 (2013)
115. Ke, S.-H., Baranger, H.U., Yang, W.: Role of the exchange-correlation potential in ab initio electron transport calculations. J. Chem. Phys. **126**, 201102 (2007)
116. Cohen, A.J., Mori-Sánchez, P., Yang, W.: Insights into current limitations of density functional theory. Science **321**, 792–794 (2008)
117. Tersoff, J., Hamann, D.R.: Theory of the scanning tunneling microscope. Phys. Rev. B. **31**, 805–813 (1985)
118. Tersoff, J.: Method for the calculation of scanning tunneling microscope images and spectra. Phys. Rev. B. **40**, 11990–11993 (1989)

119. Gross, L., Moll, N., Mohn, F., Curioni, A., Meyer, G., Hanke, F., Persson, M.: High-resolution molecular orbital imaging using a p-Wave STM tip. Phys. Rev. Lett. **107**, 086101 (2011)
120. Chen, C.: Tunneling matrix elements in three-dimensional space: the derivative rule and the sum rule. Phys. Rev. B. **42**, 8841 (1990)
121. Gaspari, R., Blankenburg, S., Pignedoli, C.A., Ruffieux, P., Treier, M., Fasel, R., Passerone, D.: S-orbital continuum model accounting for the tip shape in simulated scanning tunneling microscope images. Phys. Rev. B. **84**, 125417 (2011)
122. Blanco, J., González, C., Jelínek, P., Ortega, J., Flores, F., Pérez, R.: First-principles simulations of STM images: from tunneling to the contact regime. Phys. Rev. B. **70**, 085405 (2004)
123. Lewis, J.P., Jelínek, P., Ortega, J., Demkov, A.A., Trabada, D.G., Haycock, B., Wang, H., Adams, G., Tomfohr, J.K., Abad, E., Wang, H., Drabold, D.A.: Advances and applications in the FIREBALL ab initio tight-binding molecular-dynamics formalism. Phys. Status Solidi B **248**, 1989–2007 (2011)
124. Thygesen, K., Rubio, A.: Renormalization of molecular quasiparticle levels at metal-molecule interfaces: trends across binding regimes. Phys. Rev. Lett. **102**, 046802 (2009)
125. Denk, R., Hohage, M., Zeppenfeld, P., Cai, J., Pignedoli, C.A., Söde, H., Fasel, R., Feng, X., Müllen, K., Wang, S., Prezzi, D., Ferretti, A., Ruini, A., Molinari, E., Ruffieux, P.: Exciton-dominated optical response of ultra-narrow graphene nanoribbons. Nat. Commun. **5**, 4253 (2014)
126. Weightman, P., Martin, D.S., Cole, R.J., Farrell, T.: Reflection anisotropy spectroscopy. reports. Prog. Phys. **68**, 1251–1341 (2005)

Formation Mechanisms of Covalent Nanostructures from Density Functional Theory

Jonas Björk

Abstract In this chapter, it is demonstrated how electronic structure calculations, with focus on density functional theory, can be used to gain insight about on-surface reactions. I first give a brief introduction to how density functional theory can be used to study reactions. The focus is then shifted to two different types of on-surface reactions, highlighting the theoretical work that has been performed to gain detailed atomistic insight into them. First, the state of the art of the theory behind on-surface Ullmann coupling is described. In this reaction, molecular building blocks dehalogenate, which enables them to covalently couple. The most crucial reaction parameters are identified—the diffusion and coupling barriers of surface-supported radicals—and the potential for theory to optimize these is discussed. We then concentrate on the homo-coupling between terminal alkynes, a rudimentarily different process where molecules initially couple before undergoing a dehydrogenation step. The theory of the mechanism behind this coupling strategy is less developed than that of the on-surface Ullmann coupling, where fundamental questions remain to be unraveled. For example, by the subtle change of substrate from Ag to Au, the on-surface alkyne chemistry is completely altered from the homo-coupling to a cyclodehydrogenation reaction for the same molecular building block, of which origin remains unknown. The main objective of the chapter is to give an impression of what kind of information theory can obtain about reaction on surface, as well as to motivate and inspire for future theoretical studies, which will be needed to turn on-surface synthesis into a more predictive discipline.

J. Björk (✉)
Department of Physics, Chemistry and Biology, IFM, Linköping University, Linköping, Sweden
e-mail: jonas.bjork@liu.se; jonbj@ifm.liu.se

A. Gourdon (ed.), *On-Surface Synthesis*, Advances in Atom and Single Molecule Machines, DOI 10.1007/978-3-319-26600-8_13

1 Introduction

As demonstrated throughout this book, on-surface synthesis is a versatile tool for tailoring novel covalent nanostructures. At the moment, though, it is difficult to predict how a molecule will react on a surface, mainly due to that the on-surface reactions in many cases behave rudimentarily different from their wet chemistry counterparts. In order to make use of the true potential of the on-surface synthesis approach toward covalent nanostructures, we need to gain full control over each step of the relevant on-surface reaction protocols. An important course of action toward such a control is the detailed understanding of the reaction mechanisms governing the various on-surface synthesis strategies. Such information is in most often not accessible from experiments, due to short-lived transition and intermediate states of the reactions. Instead, atomic-level theoretical modeling is employed to study reaction mechanisms of on-surface synthesis. The immediate impact of such theoretical modeling is to establish a chemical intuition of on-surface reaction that is currently missing, aiding surface scientists in making more qualified choices when designing their experiments.

This chapter aims to highlight some of the work that has been performed from theory to obtain an understanding of the fundamental mechanisms underlying on-surface reactions. We will further identify questions of particular importance about on-surface synthesis, which theory will have to encounter during the forthcoming years. The chapter is divided into three main parts: First, it will be briefly discussed how density functional theory can be used to study reaction mechanisms. Secondly, the current state of the art of the theory behind on-surface Ullmann coupling will be discussed. Finally, the complexity of on-surface synthesis will be demonstrated, showing a completely different type of coupling scheme recently introduced [33], namely the homo-coupling of terminal alkynes. The chapter is concluded by a brief outlook.

2 Studying Reaction Mechanisms with Density Functional Theory

The method of choice for studying on-surface reactions is density functional theory (DFT), which is basically the highest level of theory that is numerically affordable for treating the adsorption of relatively large organic molecules on surfaces. Furthermore, it has been successful in studying reactions relevant to heterogenous catalysis, such as ammonia synthesis [27]. In DFT, the total energy of a system is calculated as a functional of the electron density $n(\mathbf{r})$ [24]

$$E[n(\mathbf{r})] = T_s[n(\mathbf{r})] + \int \mathrm{d}\mathbf{r}\, v(\mathbf{r}) n(\mathbf{r}) + \frac{1}{2}\int \mathrm{d}\mathbf{r}\mathrm{d}\mathbf{r}' \frac{n(\mathbf{r})n(\mathbf{r}')}{|\mathbf{r}-\mathbf{r}'|} + E_{xc}[n(\mathbf{r})], \qquad (1)$$

where the first term is the kinetic energy of non-interacting electrons, the second and third terms give the electron-nuclei and electron-electron Coloumb energy, respectively, and the final term is the so-called exchange-correlation (XC) energy. All these terms can be determined exactly, except for the XC energy, which has to be approximated. Popular approximations include for example the local density approximation and the generalized gradient approximation.

An important point when computing molecules on surfaces with DFT is how to treat the so-called van der Waals (vdWDF) interactions, or London dispersion forces. By construction, the conventionally used generalized gradient approximation and local density approximation fail to describe these interactions, with the result that adsorption heights are generally overestimated for weakly adsorbed systems, which may result in that the computed reactivity between a molecule and a surface is not described correctly. Two main schools of thought for treating vdW interactions have emerged: dispersion-corrected DFT [18, 31] and the van der Waals density functional [12, 32]. Without going into any details about either of the methods, considering their most recent advances, both approaches have demonstrated the ability of describing adsorption heights with an accuracy of about 0.1 Å [4, 7, 28, 31].

The relevant reactions for on-surface synthesis are often rare-event processes, occurring at rates order of magnitudes smaller than typical vibrational frequencies of molecules. Simulating the complete atomistic dynamics of these reactions at the DFT level of theory is therefore not computationally feasible, nor even possible with state-of-the-art computational resources in most cases, and we have to relate on alternative methods. The work presented in this chapter has all been performed with transition state theory, where we describe a reaction by the energy at the initial state, the final state, and the transition state, which is the lowest-energy saddle point separating the final from the initial state.

2.1 Methods for Finding Transition States

The initial and final states of a reaction are local minima at the potential energy surface, which can be found by means of standard minimization algorithms. Finding a transition state, which is a saddle point at the potential energy surface, is less straightforward and requires minimization algorithms with special constraints ensuring that a saddle point, rather than a local minimum, is found. There are several methods for finding transition states using electronic structure theory, which can be divided into two groups: chain of state methods and minimum mode following methods.

The most popular chain-of-state method is probably the nudged elastic band (NEB) method [21], including the climbing image NEB (CI-NEB) [22], which is a slightly tweaked version of NEB for more efficient convergence of transitions states. In the NEB method, one starts from an initial guess of the reaction path, leading from the initial to the final state. The path is represented by a number of

images (atomic configurations). The reaction path is optimized by minimizing the forces on the atoms of each image perpendicular to the tangent of the path (nudging). Furthermore, images are kept separate from one another by springs (elastic bands). In the CI-NEB method, the spring force is removed for the image with highest energy and is replaced with the negative of the force parallel to the tangent of the path [22]. This way, the highest energy image is forced to move up-hill along the path toward the saddle point. In other words, the highest energy image converges toward the transition state of the reaction pathway. It should be noted that a reaction path determined by the NEB methods depends on the initial guess of the path (how we interpolate between initial and final states). Depending on the type of reaction, we may need to consider several initial guesses when calculating reaction paths with NEB and CI-NEB.

With some caution, the NEB and CI-NEB methods present reliable ways of optimizing reaction paths, and in particular they provide information of how many barriers separate the initial and final states. However, they rely on an accurate tangent of the reaction path (determined by finite differences between images) and thus require a sufficient number of images to converge the reaction path. Therefore, the method becomes numerically expensive since an individual DFT calculation is needed for each image. Minimum mode following methods, which we exemplify by the Dimer method [20, 23], provide a numerically cheaper approach since we focus on the optimization toward a transition state without having the information about the complete reaction path. Using the Dimer method, there are different ways to make an initial guess for the calculation. We can either move the dimer in different directions from the initial state (even without knowledge of the final state), interpolate between initial and final states, or use the results from a NEB calculation to initialize the calculation. For complex multidimensional reactions, often encountered in on-surface synthesis, the last alternative is most appealing, since we have the full trajectory between initial and final states from NEB and thus know how many barriers separate the final from the initial state, and we use for example the Dimer method to refine the transition state(s) found from NEB.

2.2 *A Recipe for Efficient Reaction Path Determination Using the Nudged Elastic Band and Dimer Methods*

In the previous section, we deduced that the NEB and Dimer methods in combination give a reliable method for finding the transition states separating an initial and a final state of a reaction. It should nevertheless be noticed that all barriers found with DFT should be taken with caution since they to some extent will depend on the employed exchange-correlation functional. If we play with the idea that our density functionals can be trusted, which is certainly not always the case, the *recipe* for finding transition states along for a reaction goes as follows:

1. Determine initial and final states of the reaction (high numerical accuracy).
2. Interpolate between initial and final states to obtain an initial guess for the reaction path.
3. Use the NEB method to preoptimize the reaction path (low numerical accuracy). If a multibarrier reaction is found, divide the overall reaction into several sub-paths and return to point 1 for each of these paths.
4. Use the CI-NEB method [21] to further optimize the reaction path and find an initial guess of the transition state (low numerical accuracy).
5. Use the Dimer method to optimize the initial guess of the transition state obtained in Step 4 (high numerical accuracy).

The numerical accuracy for each step refers to for example the size of basis set and the *k*-point sampling used in the calculations. A relatively low numerical accuracy may be used for the NEB and CI-NEB calculations, since we are mainly interested in determining the number of barriers of the reaction, and obtaining initial guesses for transition states to be used as input in the Dimer method. Thus, we only need to describe the pathway with NEB and CI-NEB at a qualitative level. Numerically converged reaction energies and energy barriers are ensured by the high numerical accuracy in the calculations of initial and final states, as well as of the transition state using the Dimer method.

Already at point 1 in the above *recipe*, we can calculate the overall reaction energy according to

$$E_{\text{react}} = E_{\mathbf{FS}} - E_{\mathbf{IS}}, \tag{2}$$

where $E_{\mathbf{IS}}$ and $E_{\mathbf{FS}}$ are the energies of the initial and final states, respectively. Finally, after optimizing the transition state in Step 5, we can calculate the energy barrier of the reaction

$$E_{\text{barrier}} = E_{\mathbf{TS}} - E_{\mathbf{IS}}, \tag{3}$$

where $E_{\mathbf{TS}}$ is the energy of the transition state.

3 Theory of On-Surface Ullmann Coupling

The Ullmann-type coupling is probably the most frequently used reaction scheme in on-surface synthesis. Within the concept of covalent organic nanostructures, it was introduced by Grill et al. in 2007 [17], who shown that porphyrins can be coupled into 0D, 1D, and small 2D structures, depending on the number of halogens attached to each molecular precursor. Since then, it has been used numerous of times to form different types of structures [11, 14, 25], such as porous graphene [1], and atomically precise graphene nanoribbons [8]. It should, however, be noted that the principle of on-surface Ullmann coupling was proven earlier for the formation of biphenyl from iodobenzene on Cu(111) [34].

The on-surface Ullmann coupling is conceptually easy to grasp. Firstly, halogen-substituted molecules are deposited on a surface. Since the halogen–carbon bonds are more easily dissociated than other intramolecular bonds, for example carbon–hydrogen bonds, it is possible to tune the temperature such that only the halogens are abstracted from the molecules. A dehalogenated molecule diffuses on the surface until it finds another dehalogenated molecule, with which it can covalently couple. By designing molecules with different dimensions and with halogens at different sites, one could in principle tailor any type of covalent nanostructures. This is, of course, not the case as there are factors obstructing the assembly process. In particular, self-healing, which is inherent in supramolecular self-assembly, is in general missing, making the assembly into well-ordered two-dimensional covalent networks a formidable task.

Bieri and coworkers identified [2] two processes that are of extra importance for the on-surface synthesis of well-ordered two-dimensional covalent networks, namely the diffusion of dehalogenated molecules and the coupling between two dehalogenated molecules. They defined a recombination probability between two molecules as [2]

$$P_{\text{recomb}} = \frac{v_{\text{couple}}}{v_{\text{couple}} + v_{\text{diffuse}}}, \tag{4}$$

where v_{couple} is the coupling rate and v_{diffuse} is the diffusion rate. It was shown that small recombination probabilities, in other words $v_{\text{diffuse}} \gg v_{\text{couple}}$, are necessary for limiting the number of defects in two-dimensional networks. Later, we have demonstrated that the overall recombination rate may be approximated as [5]

$$v_{\text{recomb}} = \theta \frac{v_{\text{couple}}\ v_{\text{diffuse}}}{v_{\text{couple}} + v_{\text{diffuse}}}, \tag{5}$$

where θ is a parameter depending on the coverage of molecules and the fraction of molecules that has already reacted. This has the implications that the recombination rate is given by

$$v_{\text{recomb}} = \theta v_{\text{couple}} \quad \text{for} \quad v_{\text{diffuse}} \gg v_{\text{couple}}, \tag{6}$$

for coupling-limited processes, and

$$v_{\text{recomb}} = \theta v_{\text{diffuse}} \quad \text{for} \quad v_{\text{diffuse}} \ll v_{\text{couple}}, \tag{7}$$

for diffusion-limited processes.

For a *diffusion-limited process,* the rate of diffusion is much smaller than that of coupling, while for a *coupling-limited process* the rate of diffusion is much larger than that of coupling. For the formation of well-ordered

two-dimensional covalent networks, a *coupling-limited process* is a prerequisite.

Reaction rates are directly related to energy barriers E_{barrier} through the Arrhenius relation

$$v = A \exp[-E_{\text{barrier}}/k_{\text{B}}T], \tag{8}$$

where A is a pre-exponential factor, k_{B} is the Boltzmann's constant, and T the temperature. Knowledge about the barriers of the different processes in the on-surface Ullmann coupling is a necessary step toward the controlled fabrication of covalent materials with this approach. In particular, how the energy barriers depend on the type of molecule and the choice of substrate will aid us choosing the right molecule–surface combination for the assembly of a certain structure. With sufficient amount of information about these reactions, we may be able to derive *rules*, or a chemical intuition, governing the on-surface reactions [3]. Here, we use the formation of biphenyl from halogen-substituted benzene molecules as a model reaction for the on-surface Ullmann coupling. By eventually increasing the complexity of the studied processes, through alteration of the size of, and number of halogens in, the molecule, the trends of the various reaction parameters can be studied, with the intention to arrive at the aforementioned rules/chemical intuition.

3.1 The Formation of Biphenyl from Halogenated Benzenes

We consider the formation of biphenyl from halogenated benzene molecules as a model reaction of on-surface Ullmann coupling. The reaction is divided into three fundamental processes: (i) dehalogenation of the molecular building blocks; (ii) diffusion of dehalogenated molecules; and (iii) coupling of two dehalogenated molecules. The dehalogenation step is described in a separate section, while the diffusion and coupling are described as an overall recombination step because of the reasons discussed above.

3.1.1 Dehalogenation of Bromobenzene and Iodobenzene

The dehalogenation of both bromobenzene and iodobenzene is characterized by an intact physisorbed molecule in the initial state, and a chemisorbed halogen atom and phenyl radical in the final state [5]. The initial and final states are separated by a transition state where the halogenated carbon has initiated a chemical bond with the metal surface and the carbon–halogen bond has begun to break. The initial, transition, and final states are demonstrated for bromobenzene on Ag(111) in Fig. 1,

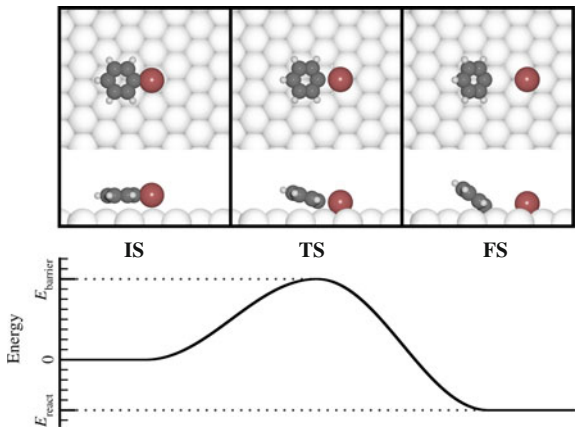

Fig. 1 **a** The dissociation of bromobenzene on Ag(111) showing *top* and *side views* of the initial state (**IS**), transition state (**TS**), and final state (**FS**), exemplifying a typical dehalogenation reaction on a (111)-surface of a noble metal. **b** Representative energy profile of a dehalogenation reaction, indicating the reaction energy (E_{react}) and the energy barrier ($E_{barrier}$) as refined by Eqs. (2) and (3), respectively

and the picture is universal for both bromobenzene and iodobenzene on all the three surfaces Cu(111), Ag(111), and Au(111). Figure 1 also depicts a typical energy profile for a dehalogenation reaction, indicating the reaction energy and energy barrier, as defined by Eqs. (2) and (3), respectively.

Using these definitions of the energy barrier and reaction energy, we can compare these for the different surfaces. Figure 2a shows the energy barrier for bromobenzene and iodobenzene on the three surfaces. Given that both reactions are

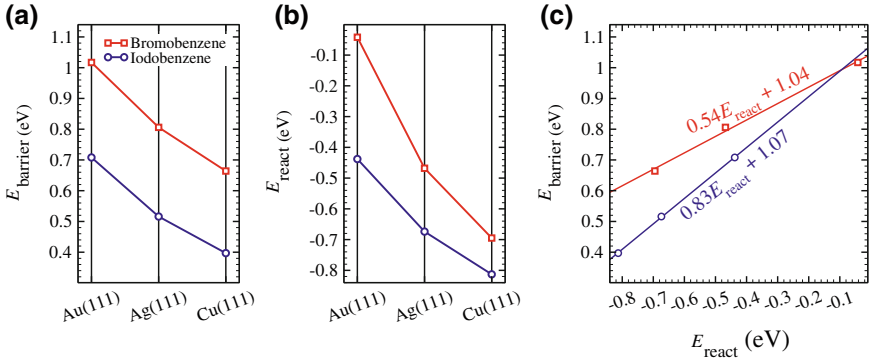

Fig. 2 **a** Energy barriers ($E_{barrier}$) and **b** reaction energies for the dehalogenation of bromobenzene and iodobenzene on the (111)-facets of the coinage metals, as indicated. **c** Relationship between the energy barrier and the reaction energy; the two molecules follow separate Brønsted–Evans–Polanyi relationships. The figure was produced with data from Ref. [5]

highly endothermic in gas phase, with reaction energies of 3.85 and 3.33 eV for bromobenzene and iodobenzene, respectively, it is evident that all the three surfaces have a prominent catalytic effect for abstracting the halogens. For bromobenzene, the barrier ranges from 1.02 eV on Au(111) to 0.66 eV on Cu(111). The exact same trend is found for iodobenzene, with the barriers shifted by roughly 0.3 eV, now ranging from 0.71 eV on Au(111) and 0.40 eV on Cu(111). Interestingly, the reaction energies follow a quite different trend, with a significant larger difference between the two molecules on Au(111) than on Cu(111), as shown in Fig. 2b.

With the small database of reaction characteristics for bromobenzene and iodobenzene, we can investigate the relationship between the reaction energy and the energy barrier. Such a relation would be valuable since reaction energies are much more easily calculated than energy barriers, in the sense of requirements on the computational resources, since we would only need to carry out Step 1 of the recipe in Sect. 2.2. In other words, we would save plenty of time if the energy barrier for a dehalogenation reaction for a given molecule could be estimated directly from the reaction energy. As it turns out, for each of the molecules there exist a Brønsted–Evans–Polanyi relationship; a linear relationship between the energy barrier and the reaction energy

$$E_{\text{barrier}} = aE_{\text{react}} + b, \tag{9}$$

which is illustrated in Fig. 2, where also the values of the parameters a and b are indicated for the two molecules. Importantly, we have to consider the molecules one-by-one to find such a relationship. Thus, there is not a single rule determining the barrier from the reaction energy for dehalogenation reactions, which is not surprising considering that the molecules have different reaction energies in the gas phase. It should be further noted that it is not clear whether the relationship for bromobenzene holds for other brominated molecules (and similar for iodobenzene). One of the objectives of future research will thus be to investigate barriers and reaction energies for other halogenated molecular building blocks, to derive a more general rule for how the barrier height relates to the reaction energy.

To better understand the splitting-off of halogens from molecular precursors, the common step in all on-surface Ullmann coupling schemes, we are encouraged to investigate different types of halogen-substituted molecules. We will build a database of reaction characteristics that can later be used to derive general rules for on-surface dehalogenation reactions.

It is important to point out that dehalogenation on atomically flat surfaces is not necessarily the most realistic model for describing this reaction. In reality, a surface has defects, such as step edges and thermally generated adatoms that diffuse over the terraces of the surface. The latter case may be of particular importance, as it has been shown that on both Cu(110) [11], Cu(111) [19], and Ag(111) [14], following

the dehalogenation but prior to the covalent bond formation, metal-organic networks can be formed with the dehalogenated molecules coordinated to thermally generated adatoms. At this point, we do not know the exact role of these adatoms; whether they participate in the dehalogenation process or form the bond with the dehalogenated molecules at a later stage. This is a question theory should be able to answer during the next few years.

3.1.2 Recombination of Surface-Supported Phenyl Radicals

Following the dehalogenation, the surface-supported radicals will diffuse on the surface until they meet another molecule with which it can covalently couple. Notice the use of the term surface-supported radical. A dehalogenated molecule is formally considered a radical in gas phase. However, due to the strong interaction with the metal surface, its unpaired spin is quenched. This is actually the reason why the dehalogenation barrier is significantly reduced on a metal surface. Thus, in case of on-surface Ullmann coupling a surface-supported radical refers to a dehalogenated molecule interacting chemically with the underlying surface. As previously discussed, both the diffusion and the coupling barriers are of uttermost importance, since they determine whether the overall recombination process is coupling limited or diffusion limited, see the discussion around Eqs. (6) and (7).

The diffusion on Au(111) is slightly different compared to Ag(111) and Cu(111). As shown in Fig. 3, it is a single-barrier process, in which the molecule is standing

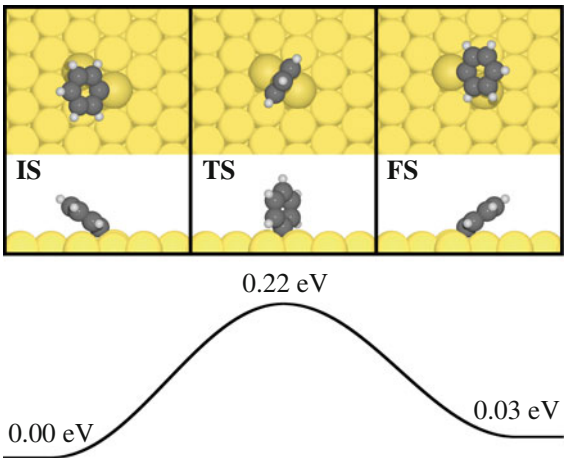

Fig. 3 Diffusion of the phenyl radical on Au(111). The initial, transition, and final states are depicted in (**a**), with the two surface atoms that the phenyl diffuses between rendered darker than other surface atoms. In (**b**) the energy profile is shown for the diffusion with energies indicated with respect to the initial state. The small difference in energy between the initial and the final states is due to difference in adsorption geometry with respect to the subsurface layers. Data from Ref. [5]

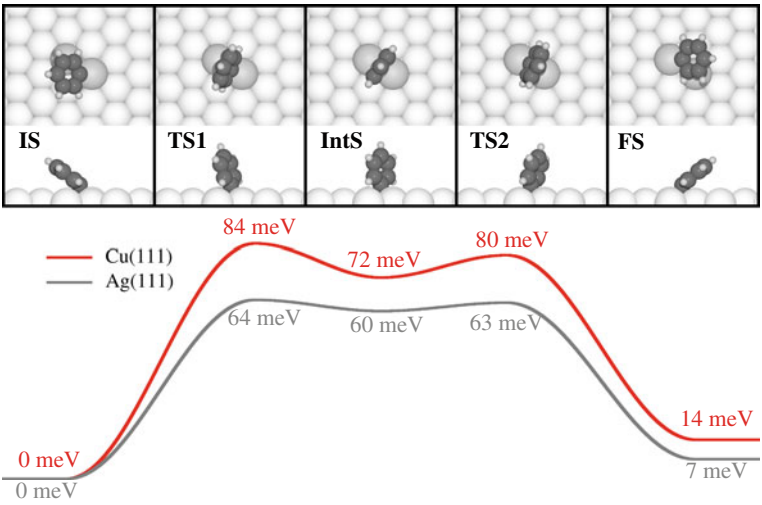

Fig. 4 Diffusion of the phenyl radical on Ag(111) and Cu(111). On both surfaces the initial and final states are separated by an intermediate state and two transition states, depicted for Ag(111) in (**a**). In (**b**) the energy profiles for the two surfaces are shown with energies indicated with respect to the initial state. Data from Ref. [5]

up-right on the surface in the transition state. On the other hand, the diffusion on Ag (111) and Cu(111), illustrated for Ag(111) in Fig. 4a, is a two-barrier process. Similarly to Au(111), the molecule goes through a state where it is standing up-right on the surface, but for Ag(111) and Cu(111) this is a shallow intermediate state in an overall two-step process. It should be noted that the phenyl radical points in opposite direction with respect to the surface in the intermediate and final states for all surfaces such that it is in a way *flipping* across the surface [5], a conclusion that was previously made for the Cu(111) surface [30].

Considering the diffusion barrier, it is significantly larger for Au(111) compared to Ag(111) and Cu(111). For Ag(111) and Cu(111), there also exist an alternative reaction path, in which the molecule has the same orientation in the initial and final states without going through the up-right intermediate state [5]. This may better resemble the behavior for a larger molecule, which will not be able to *flip* between one site and another via an up-right intermediate. In this case, the diffusion barriers on Ag(111) and Cu(111) are increased to 0.29 and 0.44 eV, respectively. This correlates well with the diffusion of the surface-stabilized cyclohexa-*m*-phenylene radical, which has a significantly larger barrier on Cu(111) than Ag(111) [2], while no barrier has been calculated on Au(111).

When two surface-stabilized phenyl radicals are close enough together they may couple to form biphenyl. Figure 5 shows the coupling path of two phenyl radicals given an initial state where the two molecules are chemically bonded to the same surface atom; in other words, they are as close to each other they could possibly be without coupling. The energy profiles in Fig. 5b are given with respect of having

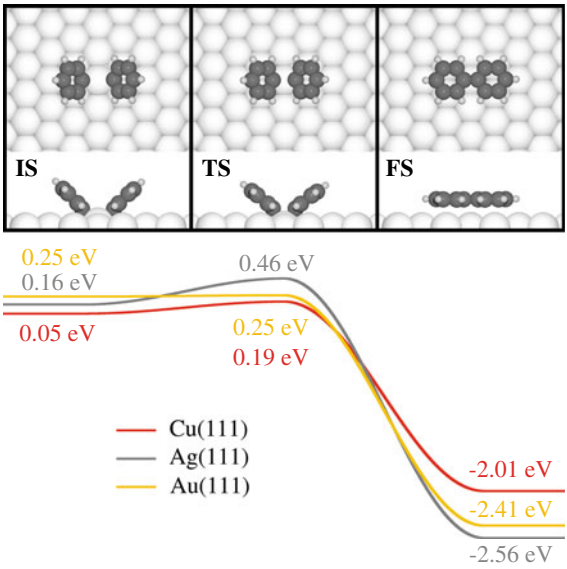

Fig. 5 Coupling of two phenyl radicals into biphenyl, illustrated on Ag(111) in (**a**). The initial state, in which the two phenyls share the same surface atom, and the final state with the molecules covalently coupled are separated by a single transition state. In (**b**) the energy profiles are compared for the reaction on Cu(111), Ag(111) and Au(111). The energies are given with respect to a state where the two molecules are well separated from each other. Notably, on Au(111) there is no barrier separating the initial from the final state. Data from Ref. [5]

the molecules well separated from each other, thus the energy of the initial state gives the net energy cost of bringing the molecules to this position. Notably, on Au (111) there is no barrier separating the initial from the final state. However, the reaction is not spontaneous since one needs to pay a net energy to bring the molecules into the position of the initial state. Also worth noting is that the coupling barrier is largest on Ag(111). The coupling reaction is exothermic with an energy gain larger than 2 eV on all surfaces, resulting from that the carbon–carbon bond is much stronger than a carbon–metal bond. This basically expresses the irreversibility of the coupling reaction.

We previously discussed diffusion-limited versus coupling-limited processes. In case of the biphenyl formation, Ag(111) is the most prominent surface from such an analysis. On this surface, the phenyl diffusion has a barrier of 0.06 eV, while the barrier of the phenyl–phenyl coupling is considerably larger (0.46 eV); in other words, a coupling-limited reaction is expected. In fact, the same conclusions were drawn for the surface-stabilized cyclohexa-*m*-phenylene radical, for which also a coupling-limited process was found on Ag(111) and was also verified from experiments [2].

Similar to the dehalogenation reaction, it will be of great interest to understand how the diffusion and coupling barriers depend on the molecular size and the number of halogen sites. Furthermore, of particular concern will be how adatoms, in

particular on Cu and Ag surfaces, affect these processes. Again, the suggested approach would be to step-wise increase the complexity of the problem and investigate the trends that may emerge. Scrutinizing the trends of diffusion and coupling may be even more crucial than those for dehalogenation considering the importance whether a process is diffusion or coupling limited.

4 Homo-Coupling of Terminal Alkynes

Another type of on-surface reaction that has become quite popular the last few years is the homo-coupling of terminal alkynes. It was first reported as late as 2012 [33] on Ag(111) with the two molecular building blocks 1,3,5-triethynyl-benzene (TEB) and 1,3,5-tris-(4-ethynylphenyl)benzene (Ext-TEB), depicted in Fig. 6a. Since then, it has been demonstrated also with other molecules on different surfaces [9, 10, 13, 16]. The basic principle of the reaction is illustrated in Fig. 6b: Two terminal alkynes couple on a surface together with the release of two hydrogen atoms. An advantage of this coupling scheme compared to the on-surface Ullmann coupling is that the only by-product is in the form of hydrogen instead of halogens.

Regarding the overall reaction process, it has been evidenced that the covalent coupling occurs together with the release of hydrogen [6, 33]. However, as will be discussed in this section, there are fundamental aspects of the reaction mechanism that are not completely clear, and which will require additional attention in the future.

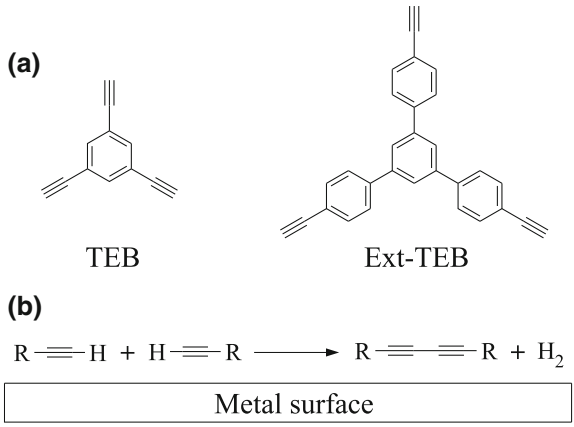

Fig. 6 **a** The molecular building blocks 1,3,5-triethynyl-benzene (TEB) and 1,3,5-tris-(4-ethynylphenyl)benzene (Ext-TEB) that was initially used to demonstrate the homo-coupling of terminal alkynes on Ag(111) [33]. **b** The basic principles of this reaction scheme: terminal alkyne groups of two molecules couple and release hydrogen

4.1 Initial Coupling of Two Molecules

Two independent studies for the reaction mechanisms of the homo-coupling have been carried out [6, 15]. Both studies made the conclusion that instead of removing the hydrogen atoms from the molecular building blocks, the reaction is initiated by the covalent coupling between two molecules. This is illustrated in Fig. 7 for the TEB molecule on Ag(111). Notably, the initial coupling barrier of 0.90 eV is just half the barrier for splitting-off a hydrogen atom directly from a single TEB molecule [6]. Similar values were found for a model component on both the Ag (111) and the Au(111) surfaces [15], and has to be considered as the commonly accepted initial step of the reaction mechanism.

Following the coupling of two TEB molecules on Ag(111), the TEB dimer can exist in two isomeric forms: a trans-isomer (**IntS1**$_{trans}$) in which one carbon is chemically bond to the surface, and a cis-isomer (**IntS1**$_{cis}$) with two carbon atoms chemically bonded to the surface. Considering that the cis-isomer is the considerably more stable of the two, it appears likely that following the initial coupling, the majority of dimers will at some point reside in this form prior to further reactions. The stability of cis-compared to the trans-isomer is due to that the dimer has two carbon atoms chemically bonded in the former while only one in the latter.

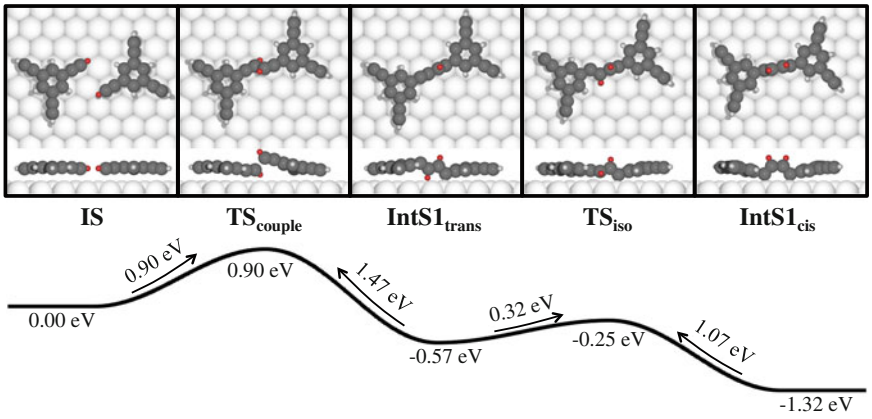

Fig. 7 The homo-coupling of terminal alkynes is initiated by the covalent bond formation between two molecules, with the hydrogen remaining on the molecules, here illustrated for TEB molecules on Ag(111). The coupled intermediate state can exist in a trans- and cis-isomer, where the latter is the more stable one. The two hydrogen atoms taking part in the coupling are shown in red for clarity. Reprinted (adapted) with permission from Ref. [6]. Copyright (2014) American Chemical Society

4.2 Removing Hydrogen from a Covalent Intermediate State

Starting from the cis-isomer of the coupled TEB dimer, one needs to climb two rather large energy barriers, of 1.27 and 1.53 eV, respectively, to split-off the two hydrogen atoms in order to reach the final state of the reaction, shown in Fig. 8. Having in mind that the reaction takes place at temperatures as low as 330 K [33] in particular the second barrier is considerably larger than expected. It is clear that the hydrogen atoms are abstracted following the covalent coupling step; however, it is not completely trivial how. It should be noted that several alternative pathways for removing the hydrogens have been investigated, but without success [6].

One possibility may be that the system has no time to thermally equilibrate following the highly exothermic coupling step. In other words, the energy gained in the coupling is invested into the dehydrogenation steps, reminiscent with the hot adsorbates that can be formed following dissociative adsorption [29]. This would also explain why none of the intermediate states have been observed experimentally. However, to challenge this hypothesis one would need to go beyond basic transition state theory. Importantly, as hydrogen is known to desorb associatively from Ag(111) well below room temperature, the split-off hydrogens will leave the surface and are therefore kinetically hindered to recombine with the molecules.

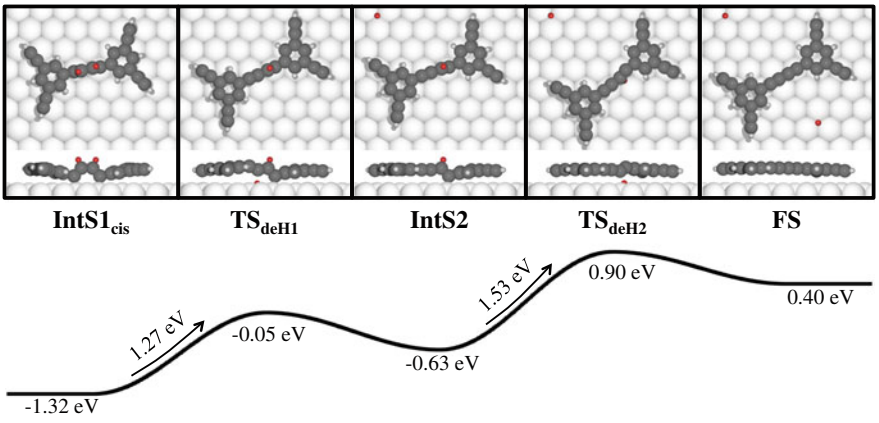

Fig. 8 Following the initial coupling of two TEB molecules, shown in Fig. 7, the dimer undergoes two dehydrogenation steps in order to finalize the overall homo-coupling. The two hydrogen atoms being dehydrogenated are shown in *red* for clarity. Reprinted (adapted) with permission from Ref. [6]. Copyright (2014) American Chemical Society

4.3 *Additional Aspects of the Surface Chemistry of Terminal Alkynes*

It is important to note that the homo-coupling discussed here is not the only possible reaction between terminal alkynes on metals. For example, by using linear molecular building blocks, a variety of products have been obtained on both Au (111) [16] and Ag(111) [10]. In the latter case, the chemoselectivity toward the homo-coupling was retained when using the Ag(887) vicinal surface [10]. The role of the vicinal surface is to *line-up* the molecules along the step edges, effectively quenching other reaction possibilities.

The importance of the underlying surface for controlling the reaction was also demonstrated by Liu and coworkers [26]. Putting the Ext-TEB molecule on Au (111), which on Ag(111) yield the homo-coupling [33], activates a cyclotrimerization reaction, resulting in the formation of a porous graphene structure [26]. Comparisons of the pathways of the cyclotrimerization and homo-coupling are anticipated to provide valuable clues for how to control the chemoselectivity of the multifaceted surface chemistry of terminal alkynes.

5 Outlook

This chapter has given a quite rough overview of how density functional theory can be used to investigate chemical reactions on surface and illustrated a couple of examples where it has been employed for processes relevant for the formation of covalent nanostructures. We have highlighted some of the limitations by considering the formation of biphenyl from halogenated benzenes as model reactions for on-surface Ullmann coupling and it is quite clear that further studies are needed for a more comprehensive theory. For example, we will need to take into account how the dimension of the molecular building blocks, number of halogens per molecule, and positions of halogens within the molecules affect the different reaction steps. This needs to be done systematically, by step-wise increasing the complexity of the studied reaction. When we have reached a critical complexity of the studied systems, patterns will hopefully emerge and we should be able to predict the reaction behavior of far more complex systems, without the requirement to explicitly calculate them.

Whereas the on-surface Ullmann coupling has quite well-defined fundamental reaction steps, where the main challenge remains how to tune the barriers of the various processes, the homo-coupling of terminal alkynes presents a challenge at a more fundamental level. First of all, we do not have the full understanding of how the hydrogen atoms are released in the overall reaction process. Secondly, and maybe more importantly, due to versatile on-surface alkyne chemistry we will need to investigate, and compare, pathways of alternative reactions. This includes not only the cyclotrimerization reaction that has been observed on Au(111) [26], but

also understanding the various reaction products that are formed, particularly for linear molecular building blocks.

This chapter has covered only two of the many possible reaction schemes that can be employed in on-surface synthesis, several of which very limited information about the reaction mechanism exist. During the next decade theoretical surface scientists have a quite daunting, but exciting, task in front of them, to develop accurate and, for experimentalists, useful theories that can be used to bring the field of on-surface synthesis forward, toward a more predictive theory.

Acknowledgements Without the close collaboration with experimental partners, much of the presented work would not have been possible. In particular, Dr. Yi-Qi Zhang, Dr. habil. Florian Klappenberger, and Prof. Johannes Barth at Technische Universität München are acknowledged for their groundbreaking experiments on the homo-coupling of terminal alkynes. Furthermore, I am grateful to Prof. Sven Stafström at Linköping University for encouraging me to follow this exciting line of research.

References

1. Bieri, M., Treier, M., Cai, J., Aït-Mansour, K., Ruffieux, P., Gröning, O., Gröning, P., Kastler, M., Rieger, R., Feng, X., Müllen, K., Fasel, R.: Porous graphenes: two-dimensional polymer synthesis with atomic precision. Chem. Commun., 6919–6921 (2009)
2. Bieri, M., Nguyen, M.-T., Gröning, O., Cai, J., Treier, M., Aït-Mansour, K., Ruffieux, P., Pignedoli, C.A., Passerone, D., Kastler, M., Müllen, K., Fasel, R.: Two-dimensional polymer formation on surfaces: insight into the roles of precursor mobility and reactivity. J. Am. Chem. Soc. **132**, 16669–16676 (2010)
3. Björk, J., Hanke, F.: Towards design rules for covalent nanostructures on metal surfaces. Chem. Eur. J. **20**, 928–934 (2014)
4. Björk, J., Stafström, S.: Adsorption of large hydrocarbons on coinage metals: a van der Waals density functional study. ChemPhysChem **15**, 2851–2858 (2014)
5. Björk, J., Hanke, F., Stafström, S.: Mechanisms of halogen-based covalent self-assembly on metal surfaces. J. Am. Chem. Soc. **135**, 5768–5775 (2013)
6. Björk, J., Zhang, Y.-Q., Klappenberger, F., Barth, J.V., Stafström, S.: Unraveling the mechanism of the covalent coupling between terminal alkynes on a noble metal. J. Phys. Chem. C **118**, 3181–3187 (2014)
7. Bürker, C., Ferri, N., Tkatchenko, A., Gerlach, A., Niederhausen, J., Hosokai, T., Duhm, S., Zegenhagen, J., Koch, N., Schreiber, F.: Exploring the bonding of large hydrocarbons on noble metals: diindoperylene on Cu(111), Ag (111), and Au (111). Phys. Rev. B **87**, 165443–165447 (2013)
8. Cai, J., Ruffieux, P., Jaafar, R., Bieri, M., Braun, T., Blankenburg, S., Muoth, M., Seitsonen, A.P., Saleh, M., Feng, X., Müllen, K., Fasel, R.: Atomically precise bottom-up fabrication of graphene nanoribbons. Nature **466**, 470–473 (2010)
9. Cirera, B., Zhang, Y.-Q., Klyatskaya, S., Ruben, M., Klappenberger, F., Barth, J.V.: 2D self-assembly and catalytic homo-coupling of the terminal alkyne 1,4-Bis (3,5-diethynyl-phenyl)butadiyne-1,3 on Ag(111). ChemCatChem **5**, 3281–3288 (2013)
10. Cirera, B., Zhang, Y.-Q., Björk, J., Klyatskaya, S., Chen, Z., Ruben, M., Barth, J.V., Klappenberger, F.: Synthesis of extended graphdiyne wires by vicinal surface templating. Nano Lett. **14**, 1891–1897 (2014)

11. Di Giovannantonio, M., El Garah, M., Lipton-Duffin, J., Meunier, V., Cardenas, L., Fagot Revurat, Y., Cossaro, A., Verdini, A., Perepichka, D.F., Rosei, F., Contini, G.: Insight into organometallic intermediate and its evolution to covalent bonding in surface-confined Ullmann polymerization. ACS Nano **7**, 8190–8198 (2013)
12. Dion, M., Rydberg, H., Schröder, E., Langreth, D.C., Lundqvist, B.I.: Van der Waals density functional for general geometries. Phys. Rev. Lett. **92**, 246401–246404 (2004)
13. Eichhorn, J., Heckl, W.M., Lackinger, M.: On-surface polymerization of 1,4-diethynylbenzene on Cu(111). Chem. Commun. **49**, 2900–2902 (2013)
14. Eichhorn, J., Strunskus, T., Rastgoo-Lahrood, A., Samanta, D., Schmittele, Lackinger, M.: On-surface Ullmann polymerization via intermediate organometallic networks on Ag(111). Chem. Commun. **50**, 7680–7682 (2014)
15. Gao, H.-Y., Franke, J., Wagner, H., Zhong, D., Held, P.-A., Studer, A., Fuchs, H.: Effect of metal surfaces in on-surface glaser coupling. J. Phys. Chem. C **117**, 18595–18602 (2013)
16. Gao, H.-Y., Wagner, H., Zhong, D., Franke, J.-H., Studer, A., Fuchs, H.: Glaser coupling at metal surfaces. Angew. Chem. Int. Ed. **52**, 4024–4028 (2013)
17. Grill, L., Dyer, M., Lafferentz, L., Persson, M., Peters, M.V., Hecht, S.: Nano-architectures by covalent assembly of molecular building blocks. Nature Nanotechnol. **2**, 687–891 (2007)
18. Grimme, S.: Semiempirical GGA-type density functional constructed with a long-range dispersion correction. J. Comp. Chem. **27**, 1787–1799 (2006)
19. Gutzler, R., Walch, H., Eder, G., Kloft, S., Hecklab, W.M., Lackinger, M.: Surface mediated synthesis of 2D covalent organic frameworks: 1,3,5-Tris(4-Bromophenyl)benzene on graphite (001), Cu(111), and Ag(110). Chem. Commun. **45**, 4456–4458 (2009)
20. Henkelman, G., Jónsson, H.: A dimer method for finding saddle points on high dimensional potential surfaces using only first derivatives. J. Chem. Phys. **111**, 7010–7022 (1999)
21. Henkelman, G., Jónsson, H.: Improved tangent estimate in the nudged elastic band method for finding minimum energy paths and saddle points. J. Chem. Phys. **113**, 9978–9985 (2000)
22. Henkelman, G., Uberuaga, B.P., Jónsson, H.: A climbing image nudged elastic band method for finding saddle points and minimum energy paths. J. Chem. Phys. **113**, 9901–9904 (2000)
23. Kästner, J., Sherwood, P.: Superlinearly converging dimer method for transition state search. J. Chem. Phys. **128**, 014106–014111 (2008)
24. Kohn, W., Sham, L.J.: Self-consistent equations including exchange and correlation effects. Phys. Rev. **140**, A1133–A1138 (1965)
25. Lafferentz, L., Eberhardt, V., Dri, C., Africh, C., Comelli, G., Esch, F., Hecht, S., Grill, L.: Controlling on-surface polymerization by hierarchical and substrate-directed growth. Nature Chem. **4**, 215–220 (2012)
26. Liu, J., Ruffieux, P., Feng, X., Müllen, K., Fasel, R.: Cyclotrimerization of arylalkynes on Au (111). Chem. Commun. **50**, 11200–11203 (2014)
27. Logadottir, A., Rod, T.H., Nørskov, J.K., Hammer, B., Dahl, S., Jacobsen, C.J.H.: The BrønstedEvansPolanyi relation and the volcano plot for ammonia synthesis over transition metal catalysts. J. Catal. **197**, 229–231 (2001)
28. Matena, M., Björk, J., Wahl, M., Lee, T.-L., Zegenhagen, J., Gade, L.H., Jung, T.A., Persson, M., Sthr, M.: On-surface synthesis of a two-dimensional porous coordination network: unraveling adsorbate interactions. Phys. Rev. B **90**, 125408–125415 (2014)
29. Meyer, J., Reuter, K.: Modeling heat dissipation at the nanoscale: an embedding approach for chemical reaction dynamics on metal surfaces. Angew. Chem. Int. Ed. **53**, 4721–4724 (2014)
30. Nguyen, M.-T., Pignedoli, C.A., Passarone, D.: An Ab initio insight into the Cu(111)-mediated Ullmann reaction. Phys. Chem. Chem. Phys. **13**, 154–160 (2011)
31. Ruiz, V., Liu, W., Zojer, E., Scheffler, M., Tkatchenko, A.: Density-functional theory with screened van der Waals interactions for the modeling of hybrid inorganic-organic systems. Phys. Rev. Lett. **108**, 146103–146107 (2012)
32. Thonhauser, T., Cooper, V.R., Li, S., Puzder, A., Hyldgaard, P., Langreth, D.C.: Van der Waals density functional: self-consistent potential and the nature of the van der Waals bond. Phys. Rev. B **76**, 125112–125122 (2007)

33. Zhang, Y.-Q., Kepčija, N., Kleinschrodt, M., Diller, K., Fischer, S., Papageorgiou, A.C., Allegretti, F., Björk, J., Klyatskaya, S., Klappenberger, F., Ruben, M., Barth, J.V.: Homo-coupling of terminal alkynes on a noble metal surface. Nat. Commun. **3**, 1286 (2012)
34. Xi, M., Bent, B.E.: Iodobenzene on Cu(111): formation and coupling of adsorbed phenyl groups. Surf. Sci. **278**, 19–32 (1992)